Advances in GEOPHYSICS

VOLUME 63

Geophysical Exploration of the Solar System

VOLUME SIXTY THREE

ADVANCES IN **GEOPHYSICS**

Geophysical Exploration of the Solar System

This page intentionally left blank

VOLUME SIXTY THREE

ADVANCES IN **GEOPHYSICS**

Geophysical Exploration of the Solar System

Volume Editors

CEDRIC SCHMELZBACH
Institute of Geophysics,
ETH Zürich,
Zürich, Switzerland

SIMON CHRISTIAN STÄHLER
Institute of Geophysics,
ETH Zürich,
Zürich, Switzerland

Serial Editor

CEDRIC SCHMELZBACH
Institute of Geophysics,
ETH Zürich,
Zürich, Switzerland

ACADEMIC PRESS
An imprint of Elsevier

Academic Press is an imprint of Elsevier
125 London Wall, London EC2Y 5AS, United Kingdom
525 B Street, Suite 1650, San Diego, CA 92101, United States
50 Hampshire Street, 5th Floor, Cambridge, MA 02139, United States
The Boulevard, Langford Lane, Kidlington, Oxford OX5 1GB, United Kingdom

Notices

Knowledge and best practice in this field are constantly changing. As new research and experience broaden our understanding, changes in research methods, professional practices, or medical treatment may become necessary.

Practitioners and researchers must always rely on their own experience and knowledge in evaluating and using any information, methods, compounds, or experiments described herein. In using such information or methods they should be mindful of their own safety and the safety of others, including parties for whom they have a professional responsibility.

To the fullest extent of the law, neither the Publisher nor the authors, contributors, or editors, assume any liability for any injury and/or damage to persons or property as a matter of products liability, negligence or otherwise, or from any use or operation of any methods, products, instructions, or ideas contained in the material herein.

ISBN: 978-0-443-18698-1
ISSN: 0065-2687

Publisher: Zoe Kruze
Acquisitions Editor: Jason Mitchell
Editorial Project Manager: Laarni Agustin
Production Project Manager: Vijayaraj Purushothaman
Cover Designer: Christian J. Bilbow
Cover Image: Géraldine Zenhäusern

Typeset by VTeX

Contents

Contributors

Amirhossein Bagheri
Institute of Geophysics, ETH Zürich, Zürich, Switzerland

Doris Breuer
DLR Institute of Planetary Research, Berlin, Germany

Julie Castillo-Rogez
Jet Propulsion Laboratory, California Institute of Technology, Pasadena, CA, United States

Michael Efroimsky
US Naval Observatory, Washington, DC, United States

Domenico Giardini
Institute of Geophysics, ETH Zürich, Zürich, Switzerland

Sander Goossens
NASA Goddard Space Flight Center, Greenbelt, MD, United States

Amir Khan
Institute of Geophysics, ETH Zürich, Zürich, Switzerland
Physik-Institut, University of Zürich, Zürich, Switzerland

Martin Knapmeyer
DLR Institute of Planetary Research, Berlin, Germany

Ana-Catalina Plesa
DLR Institute of Planetary Research, Berlin, Germany

Nicolas Rambaux
IMCCE, CNRS, Observatoire de Paris, PSL Université, Sorbonne Université, Paris, France

Alyssa Rhoden
Southwest Research Institute, Boulder, CO, United States

Attilio Rivoldini
Royal Observatory of Belgium, Brussels, Belgium

Simon C. Stähler
Institute of Geophysics, ETH Zürich, Zürich, Switzerland

Michaela Walterová
DLR Institute of Planetary Research, Berlin, Germany

Mark Wieczorek
Université Côte d'Azur, Observatoire de la Côte d'Azur, CNRS, Laboratoire Lagrange, Nice, France

This page intentionally left blank

Preface

Volume 63 of Advances in Geophysics is dedicated to the topic of *geophysical exploration of the solar system*. This volume consists of a collection of contributions that cover various aspects on studying the internal structure of the planets of our solar system with geophysical techniques.

A. Khan provides an introduction to this volume putting the following contributions into the context of planetary science. *S. Stähler* reviews chances and challenges of future seismic investigations of planetary bodies, while *M. Knapmeyer* presents a historical review of core size estimates given limited data with implications for exoplanet studies. *A. Plesa* summarizes our current knowledge about internal structures and evolution of terrestrial planets from a geodynamical perspective. Finally, *A. Bagheri* presents a review on how observations of bodily tides can be exploited to study the internal structure of planets. While these contributions focus on our solar system and the inner terrestrial planets, techniques to investigate these bodies are also relevant for studies beyond our solar system to explore exoplanets.

We thank all authors for their contributions and appreciate the work by the reviewers to ensure the high quality of this volume. Enjoy your reading of volume 63 of Advances in Geophysics.

Simon Stähler, Volume Editor
Cedric Schmelzbach, Serial Editor

This page intentionally left blank

CHAPTER ONE

Introduction to special issue

Amir Khan[a,b]
[a]Institute of Geophysics, ETH Zürich, Zürich, Switzerland
[b]Physik-Institut, University of Zürich, Zürich, Switzerland
e-mail address: amir.khan@erdw.ethz.ch

Contents

From the earliest recorded times, the planets have been the subject of wonder to man. Since their positions in the sky change continuously they were named the Wandering Ones. The Greek astronomers, most notably Ptolemy, had shown that the motions of the planets, the Sun, and the Moon could be accounted for in an elaborate Earth-centered cosmology. This early cosmology was eclipsed in the Renaissance by the ideas of Copernicus, who abolished the geocentric world view. Instead, he placed the motion of the planets around the Sun that were carefully tracked by Kepler, who availed himself of the systematic observations carried out by Brahe over a period of 20 years. Building on the laws derived by Kepler, Newton was led to the idea of universal gravitation, while Galileo, with his watchful eyes to the telescope, observed that the Jovian system formed a miniature solar system (Taylor, 2001).

Continued and more detailed observations of the planets revealed ever more intricate departures of the paths of the planets from Kepler's ellipses and steered Herschel, Adams, and Leverrier, standing on the shoulders of giants, to the discovery of Uranus and Neptune. With the sighting of the trans-Neptunian objects, including Pluto, and the presence of the asteroid belt, our system of planets has come to completion. Presently, we can state that the major dynamical features of the planets are relatively well understood. This also encompasses many minor features, such as the effects arising from general relativity theory.

Solar system research has come a long way since the beginning of the space age, especially in the last four decades, where a cornucopia of new information has been unwielded by space exploration. In spite hereof, hypothesizing on the origin of the solar system has proved difficult until

Advances in Geophysics, Volume 63
ISSN 0065-2687
https://doi.org/10.1016/bs.agph.2022.07.001

comparatively recently, because of the complexity of having to assimilate large amounts of data from differing fields (Taylor, 1999). A common assumption prior to the Apollo lunar landings was reflected in Harold Urey's view that the Moon is geologically inactive (Urey, 1952), as a result of which it would contain the evidence needed for unraveling its origin and, in turn, that of the solar system, providing the justification for the manned lunar missions. The Moon, however, turned out to be highly differentiated, and while it preserved a record of early igneous activity and geochemical fractionation in a small body, it did not preserve the record of its formation (Heiken et al., 1982). Although the lunar sample return provided prescient information on ages, chemistry, and the significance of cratering, the evidence from the observed wide range of impact crater sizes led to the notion that a hierarchy of objects existed during accretion from which the planets formed (Taylor, 1982).

Prior to the space age, meteorites constituted the only extraterrestrial material available to us on Earth. These samples were recognized to have originated from within the asteroid belt and become Earth-crossing as a result of the direct perturbation by Jupiter. The latter's early rise and the action of its gravitational attraction is believed to have prevented the formation of a planet by starving the asteroid belt of accreting material, as a result of which it is left as a relic of the solar system at the time of planetary accretion and therefore is of tremendous importance for our understanding of the early solar environment and of the chemical fractionation processes that occurred during formation of the terrestrial planets (Taylor, 1982).

The planets are formed from the solar nebula, which is a flattened, rotating disk of gas and dust surrounding the early Sun that formed from the collapse of an interstellar cloud of gas and dust. Any gas and dust that was not swept up by the Sun coalesced to form the planets. Processing of the major elements silicon, oxygen, and iron through nucleation, condensation, and coagulation into dust grains and their subsequent growth through collisions and sticking together produced bodies of size 10–100 m within 1000 years, revolving about the Sun in nearly circular orbits and in the midplane of the solar nebula (Cameron, 1995). The protoplanets finally grew into the terrestrial planets through run-away growth, producing Mars-sized objects in times as short as 10^6 years (Lissauer, 1993). Simulations have shown that in the final stages of accretion about 100 objects of lunar mass, 10 of the mass of Mercury and a few Mars-sized bodies populate the inner solar system, with the final four planets being accreted from this hierarchy of planetesimals and protoplanets in about 10^8 years (Chambers, 2001).

Of the inner solar system planets, the Earth is most likely the only body with a natural satellite. The highly inclined orbit of the Moon to the ecliptic of 5.1°, their combined anomalously high angular momentum compared to other planets and the largest mass ratio of any satellite-planet system (1/81.3), render the Moon and the Earth-Moon system unique in our solar system (Hood, 1986). The Moon, however, has a much a lower bulk density (3.34 g/cm^3) than the Earth (5.51 g/cm^3) or any of the other inner planets, implying that the Moon is composed largely of silicate minerals and deficient in metallic iron, the main constituent responsible for the high densities of the inner planets (Taylor, 2001). The two small satellites of Mars, Phobos and Deimos, most probably represent captured bodies from the nearby asteroid belt given their close resemblance to outer-belt asteroidal material (Singer, 2007), although dynamical evidence, including their almost circular orbits that are confined to the equatorial plane, would seem to suggest otherwise (Lambeck, 1979; Szeto, 1983; Bagheri et al., 2021). The satellites of the outer planets, on the other hand, are mostly ice-rock mixtures (Nimmo and Pappalardo, 2016).

Early in this century, definite ideas about the internal constitution of the Earth saw the light, while estimates of the densities of the planets were mainly available from dynamical investigations. Mercury, Venus, and Mars, including the Moon, were found to be similar to the Earth, while the outer planets, with much lower densities, clearly differed. The terrestrial planets consist of metal and their silicates and oxides, while the outer planets must consist mostly of hydrogen. This led to the division of our solar system into the inner terrestrial planets, of low mass and high density, and the outer gas giants, with high masses and low densities (Taylor, 2001).

With the proliferation of seismometers that began in the early 20th century, seismological studies have enabled Earth's internal structure to be worked out in considerable detail and today we know the density and elastic moduli as functions of pressure from its surface to the center of the core (Dziewonski and Anderson, 1981). Through comparison of empirical equations of state for the major constituents of the Earth with equations of state found experimentally in the laboratory, it has been possible to identify the chemical constituents of the Earth (Birch, 1952). This picture is continuously being refined through a combination of novel developments in experimental technique, use of first-principles calculations to simulate the physical properties of the constituents that make up the planets, theoretical and numerical advances, and developments in instrumentation that enable pushing the frontier ever deeper.

Most of our present-day knowledge of the planets is, apart from the Moon and only until very recently Mars, based on the assessment of geophysical measurements that are acquired from orbit. From gravity and magnetic measurements obtained from orbiting spacecraft, information about planetary interiors can be inferred that is otherwise not possible. Magnetic measurements, for example, can provide evidence for the past history, and the presence of subsurface oceans, while observations of the gravitational field can be used to determine the density distribution through measurements of the moments of inertia of a planet (Bills and Rubincam, 1995). Yet, of all geophysical methods, seismology is uniquely suited to determine many of the parameters that are important for understanding the deep interior structure of a planetary body.

Extraterrestrial seismology saw its advent with the Apollo lunar landings and the installation of seismometers on the lunar surface (Lognonné and Johnson, 2007; Khan et al., 2013). Seismic investigations were also conducted on Mars during the Viking missions, but, because the seismometer was placed on the lander, the seismic recordings were dominated by wind-induced shaking of the lander (Anderson et al., 1977). Efforts to detect quakes on Venus were also attempted as part of the Venera 13 and 14 landers, but the environmental conditions only allowed for observations for a very short duration (∼1 hr) during which no venusquakes were recorded (Ksanfomaliti et al., 1982). With the recent arrival of InSight (Interior Exploration using Seismic Investigations, Geodesy and Heat Transport) and the deployment of SEIS (Seismic Experiment for Interior Structure) on the Martian surface, Mars represents the second planet for which seismic data have been acquired (Banerdt et al., 2020). The seismic data acquired from InSight have afforded us a unique insight of the large-scale structure of the planet (Knapmeyer-Endrun et al., 2021; Khan et al., 2021; Stähler et al., 2021; Durán et al., 2022) and while it, to first order, appears to be a scaled-down version of the Earth, it nevertheless is sufficiently distinct in terms of seismicity, and crust, mantle, and core structure, and bulk chemical composition that our views of its origin and evolution need to be carefully considered (Khan et al., 2022).

The collection of chapters constituting this volume of Advances in Geophysics covers fundamental aspects of "Geophysical exploration of the solar system" and include four topical reviews: 1) *Seismology in the solar system* by Stähler and Knapmeyer (Stähler and Knapmeyer, 2022) that discusses the application of seismology to planetary bodies in our solar system; 2) *Planetary core radii: from Plato towards PLATO* by Knapmeyer and Walterová

(Knapmeyer and Walterová, 2022) investigates how planetary cores have been assessed over time and the constraints these impose on the large-scale structure of planets; 3) *Interior dynamics and thermal evolution of Mars – a geodynamic perspective* by Plesa et al. (Plesa et al., 2022) consider the thermal history of planets from a numerical modeling perspective; and finally 4) *Tidal insights into rocky and icy bodies: an introduction and overview* by Bagheri et al. (Bagheri et al., 2022) who use tides and tidal dissipation as a means of constraining interior structure and orbital evolution. The set of chapters should also prove of great interest in the context of the study of extrasolar system objects and the search and the conditions required for habitable zones in our universe to develop.

References

Anderson, Don L., Miller, W.F., Latham, G.V., Nakamura, Y., Toksöz, M.N., Dainty, A.M., Duennebier, F.K., Lazarewicz, A.R., Kovach, R.L., Knight, T.C.D., 1977. Seismology on Mars. Journal of Geophysical Research (1896–1977) 82 (28), 4524–4546. https://doi.org/10.1029/JS082i028p04524.

Bagheri, Amirhossein, Efroimsky, Michael, Castillo-Rogez, Julie, Goossens, Sander, Plesa, Ana-Catalina, Rambaux, Nicolas, Rhoden, Alyssa, Walterová, Michaela, Khan, Amir, Giardini, Domenico, 2022. Tidal insights into rocky and icy bodies: an introduction and overview. In: Advances in Geophysics. https://doi.org/10.1016/bs.agph.2022.07.004. This volume.

Bagheri, A., Khan, A., Efroimsky, M., Kruglyakov, M., Giardini, D., 2021. Dynamical evidence for Phobos and Deimos as remnants of a disrupted common progenitor. Nature Astronomy 5 (6), 539–543.

Banerdt, W. Bruce, Smrekar, Suzanne E., Banfield, Donald, Giardini, Domenico, Golombek, Matthew, Johnson, Catherine L., Lognonné, Philippe, Spiga, Aymeric, Spohn, Tilman, Perrin, Clément, Stähler, Simon C., Antonangeli, Daniele, Asmar, Sami, Beghein, Caroline, Bowles, Neil, Bozdag, Ebru, Chi, Peter, Christensen, Ulrich, Clinton, John, Collins, Gareth S., Daubar, Ingrid, Dehant, Véronique, Drilleau, Mélanie, Fillingim, Matthew, Folkner, William, Garcia, Raphaël F., Garvin, Jim, Grant, John, Grott, Matthias, Grygorczuk, Jerzy, Hudson, Troy, Irving, Jessica C.E., Kargl, Günter, Kawamura, Taichi, Kedar, Sharon, King, Scott, Knapmeyer-Endrun, Brigitte, Knapmeyer, Martin, Lemmon, Mark, Lorenz, Ralph, Maki, Justin N., Margerin, Ludovic, McLennan, Scott M., Michaut, Chloe, Mimoun, David, Mittelholz, Anna, Mocquet, Antoine, Morgan, Paul, Mueller, Nils T., Murdoch, Naomi, Nagihara, Seiichi, Newman, Claire, Nimmo, Francis, Panning, Mark, Thomas Pike, W., Plesa, Ana-Catalina, Rodriguez, Sébastien, Rodriguez-Manfredi, Jose Antonio, Russell, Christopher T., Schmerr, Nicholas, Siegler, Matt, Stanley, Sabine, Stutzmann, Eléanore, Teanby, Nicholas, Tromp, Jeroen, van Driel, Martin, Warner, Nicholas, Weber, Renee, Wieczorek, Mark, 2020. Initial results from the InSight mission on Mars. Nature Geoscience (ISSN 1752-0894) 13 (3), 183–189. https://doi.org/10.1038/s41561-020-0544-y.

Bills, B.G., Rubincam, D.P., 1995. Constraints on density models from radial moments: applications to Earth, Moon, and Mars. Journal of Geophysical Research 100, 26305–26315.

Birch, F., 1952. Elasticity and constitution of the Earth's interior. Journal of Geophysical Research 57 (2), 227–286.

Cameron, A.G.W., 1995. The first ten million years in the solar nebula. Meteoritics 30 (1).

Chambers, J.E., 2001. Making more terrestrial planets. Icarus 152 (2), 205–224. https://doi.org/10.1006/icar.2001.6639.

Durán, C., Khan, A., Ceylan, S., Zenhäusern, G., Stähler, S., Clinton, J.F., Giardini, D., 2022. Seismology on Mars: an analysis of direct, reflected, and converted seismic body waves with implications for interior structure. Physics of the Earth and Planetary Interiors (ISSN 0031-9201) 325, 106851. https://doi.org/10.1016/j.pepi.2022.106851.

Dziewonski, A.M., Anderson, D.L., 1981. Preliminary reference Earth model. Physics of the Earth and Planetary Interiors 25, 297–356. https://doi.org/10.1016/0031-9201(81)90046-7.

Heiken, G.H., Vanima, D.T., French, B.M., 1982. Lunar Source Book. Cambridge Univ. Press, New York, New York, USA. 736 pp.

Hood, L.L., 1986. Geophysical constraints on the lunar interior. In: Hartmann, W.K., Phillips, R.J., Taylor, G.J. (Eds.), Origin of the Moon. Lunar and Planetary Institute, Houston, Texas, USA, pp. 361–410.

Khan, Amir, Ceylan, Savas, van Driel, Martin, Giardini, Domenico, Lognonné, Philippe, Samuel, Henri, Schmerr, Nicholas C., Stähler, Simon C., Duran, Andrea C., Huang, Quancheng, Kim, Doyeon, Broquet, Adrien, Charalambous, Constantinos, Clinton, John F., Davis, Paul M., Drilleau, Mélanie, Karakostas, Foivos, Lekic, Vedran, McLennan, Scott M., Maguire, Ross R., Michaut, Chloé, Panning, Mark P., Pike, William T., Pinot, Baptiste, Plasman, Matthieu, Scholz, John-Robert, Widmer-Schnidrig, Rudolf, Spohn, Tilman, Smrekar, Suzanne E., Banerdt, William B., 2021. Upper mantle structure of Mars from insight seismic data. Science 373 (6553), 434–438. https://doi.org/10.1126/science.abf2966.

Khan, A., Pommier, A., Neumann, G.A., Mosegaard, K., 2013. The lunar Moho and the internal structure of the moon: a geophysical perspective. Tectonophysics 609, 331–352. https://doi.org/10.1016/j.tecto.2013.02.024.

Khan, A., Sossi, P.A., Liebske, C., Rivoldini, A., Giardini, D., 2022. Geophysical and cosmochemical evidence for a volatile-rich Mars. Earth and Planetary Science Letters (ISSN 0012-821X) 578, 117330. https://doi.org/10.1016/j.epsl.2021.117330.

Knapmeyer, Martin, Walterová, Michaela, 2022. Planetary core radii: from Plato towards PLATO. In: Advances in Geophysics. https://doi.org/10.1016/bs.agph.2022.07.003. This volume.

Knapmeyer-Endrun, Brigitte, Panning, Mark P., Bissig, Felix, Joshi, Rakshit, Khan, Amir, Kim, Doyeon, Lekić, Vedran, Tauzin, Benoit, Tharimena, Saikiran, Plasman, Matthieu, Compaire, Nicolas, Garcia, Raphael F., Margerin, Ludovic, Schimmel, Martin, Stutzmann, Éléonore, Schmerr, Nicholas, Bozdağ, Ebru, Plesa, Ana-Catalina, Wieczorek, Mark A., Broquet, Adrien, Antonangeli, Daniele, McLennan, Scott M., Samuel, Henri, Michaut, Chloé, Pan, Lu, Smrekar, Suzanne E., Johnson, Catherine L., Brinkman, Nienke, Mittelholz, Anna, Rivoldini, Attilio, Davis, Paul M., Lognonné, Philippe, Pinot, Baptiste, Scholz, John-Robert, Stähler, Simon, Knapmeyer, Martin, van Driel, Martin, Giardini, Domenico, Bruce Banerdt, W., 2021. Thickness and structure of the martian crust from insight seismic data. Science 373 (6553), 438–443. https://doi.org/10.1126/science.abf8966.

Ksanfomaliti, L.V., Zubkova, V.M., Morozov, N.A., Petrova, E.V., 1982. Microseisms at the VENERA-13 and VENERA-14 landing sites. Soviet Astronomy Letters 8, 241.

Lambeck, K., 1979. On the orbital evolution of the Martian satellites. Journal of Geophysical Research: Planets 84, 5651–5658. https://doi.org/10.1029/JB084iB10p05651.

Lissauer, J.J., 1993. Planet formation. Annual Review of Astronomy and Astrophysics 31 (1), 129–172.

Lognonné, P., Johnson, C., 2007. 10.03 – planetary seismology. In: Schubert, Gerald (Ed.), Treatise on Geophysics. Elsevier, Amsterdam, pp. 69–122.

Nimmo, F., Pappalardo, R.T., 2016. Ocean worlds in the outer solar system. Journal of Geophysical Research: Planets 121 (8), 1378–1399. https://doi.org/10.1002/2016JE005081.

Plesa, Ana-Catalina, Wieczorek, Mark, Knapmeyer, Martin, Rivoldini, Attilio, Walterova, Michaela, Breuer, Doris, 2022. Interior dynamics and thermal evolution of Mars – a geodynamic perspective. In: Advances in Geophysics. https://doi.org/10.1016/bs.agph.2022.07.005. This volume.

Singer, S. Fred, 2007. Origin of the Martian satellites Phobos and Deimos. In: Exp. Phobos and Deimos, vol. 1377, p. 36.

Stähler, Simon C., Khan, Amir, Bruce Banerdt, W., Lognonné, Philippe, Giardini, Domenico, Ceylan, Savas, Drilleau, Mélanie, Duran, A. Cecilia, Garcia, Raphaël F., Huang, Quancheng, Kim, Doyeon, Lekic, Vedran, Samuel, Henri, Schimmel, Martin, Schmerr, Nicholas, Sollberger, David, Stutzmann, Éléonore, Xu, Zongbo, Antonangeli, Daniele, Charalambous, Constantinos, Davis, Paul M., Irving, Jessica C.E., Kawamura, Taichi, Knapmeyer, Martin, Maguire, Ross, Marusiak, Angela G., Panning, Mark P., Perrin, Clément, Plesa, Ana-Catalina, Rivoldini, Attilio, Schmelzbach, Cédric, Zenhäusern, Géraldine, Beucler, Éric, Clinton, John, Dahmen, Nikolaj, van Driel, Martin, Gudkova, Tamara, Horleston, Anna, Thomas Pike, W., Plasman, Matthieu, Smrekar, Suzanne E., 2021. Seismic detection of the martian core. Science 373 (6553), 443–448. https://doi.org/10.1126/science.abi7730.

Stähler, Simon C., Knapmeyer, Martin, 2022. Seismology in the solar system. In: Advances in Geophysics. https://doi.org/10.1016/bs.agph.2022.07.002. This volume.

Szeto, A., 1983. Orbital evolution and origin of the Martian satellites. Icarus 55 (1), 133–168.

Taylor, S.R., 1982. Planetary Science: A Lunar Perspective. Lunar and Planetary Institute, Houston, Texas, USA. 481 pp.

Taylor, S.R., 1999. On the difficulties of making Earth-like planets. Meteoritics & Planetary Science 34 (3), 317–329. https://doi.org/10.1111/j.1945-5100.1999.tb01342.x.

Taylor, S.R., 2001. Solar System Evolution: A New Perspective. Cambridge Univ. Press, New York, New York, USA. 460 pp.

Urey, H., 1952. The Planets, Their Origin and Development. Yale Univ. Press, New Haven, Connecticut, USA. 245 pp.

This page intentionally left blank

CHAPTER TWO

Seismology in the solar system

Simon C. Stähler[a,*] **and Martin Knapmeyer**[b]
[a]Institute of Geophysics, ETH Zürich, Zürich, Switzerland
[b]DLR Institute of Planetary Research, Berlin, Germany
*Corresponding author: e-mail address: simon.staehler@erdw.ethz.ch

Contents

Advances in Geophysics, Volume 63
ISSN 0065-2687
https://doi.org/10.1016/bs.agph.2022.07.002

1. Introduction

Seismology is the classic method to investigate the deep interior of the Earth, as well as its dynamic behavior. Seismic observations confirmed the existence of Earth's core (Oldham, 1906), gave the first indication of a mineralogically distinct mantle (Mohorovičić, 1909) as well as layering of the mantle and core (Dahm, 1934; Lehmann, 1936; Bullen, 1956). For a more detailed overview, see Chapter 3 of this book (Knapmeyer and Walterova, 2022). Seismometers were therefore among the first instruments installed on the surface of the Moon by the Apollo astronauts in 1969 (Latham et al., 1971; Toksöz et al., 1972) and were part of the Viking instrument suite on Mars 1976 (Anderson et al., 1977). For a variety of reasons, among them the apparent failure of the Viking seismic experiment (Lazarewicz et al., 1981), the focus on human spaceflight in the 1980s, the absence of American landers until 1995, the crash of the Russian Mars-96

lander (Lognonné et al., 1998), and a focus on Martian geochemistry in the 2000s and 2010s, no seismic measurements were done on a planet for the 4 decades after. On 14 November 2014, the Philae lander on the comet 67/P Churyumov–Gerasimenko for the first time since Apollo measured elastic waves on a celestial object, excited by its sampling mechanism. On 5 May 2018, an Atlas V rocket finally launched the NASA InSight mission towards Mars, where it landed on 26 November 2018 and installed a seismometer (Lognonné et al., 2019) on the surface in the weeks thereafter. This mission has since repeated many of the successes of a century of seismology within a good 3 years (Banerdt et al., 2020; Giardini et al., 2020; Lognonné et al., 2020; Knapmeyer-Endrun et al., 2021; Khan et al., 2021; Stähler et al., 2021; Hobiger et al., 2021), constraining the Martian interior structure from near surface to core.

The successful execution of the InSight mission has renewed interest in seismic measurements as a natural part of landed missions to other planets (Fig. 1 shows seismograms recorded over the solar system). This article reviews possible scientific goals of seismic measurements on the major bodies of the solar system. As a graphical aide, we show a visualization of the seismic wavefield on the major planets from spectral element simulations, following the approach of Astiz et al. (1996), where red, green, and blue denote transversal, longitudinal, and vertical ground motion, see Figs. 3, 4, 9, 10, 11, 12. We follow Metzger et al. (2022) in defining a "planet" as an object of significant geological complexity. Large moons, i.e. objects of a few 100 km radius with tectonic processes shaping the surface and a complicated interior thermal budget are still planets, even if they happen to orbit another planet instead of the sun. For each object, we also summarize what little is known about its seismic sources. Further, it is discussed which missions are possible given current technical limitations as well as the programmatic landscape of the Voyage 2050 program of the European Space Agency (ESA) (Tacconi et al., 2021) and the Decadal Survey for Planetary Sciences and Astrobiology 2023–2033 by the National Academies of Sciences of the USA (Nat. Academies, 2022). The Voyage 2050 program and the Decadal survey are officially only recommendations to the individual agencies (ESA and NASA respectively), due to the participation of members from the global scientific community, both represent a true international effort and are therefore likely to shape programmatic efforts by all space agencies.

The article will hopefully serve as an introduction into the future of extraterrestrial seismology for seismologists. Beyond this, it should highlight

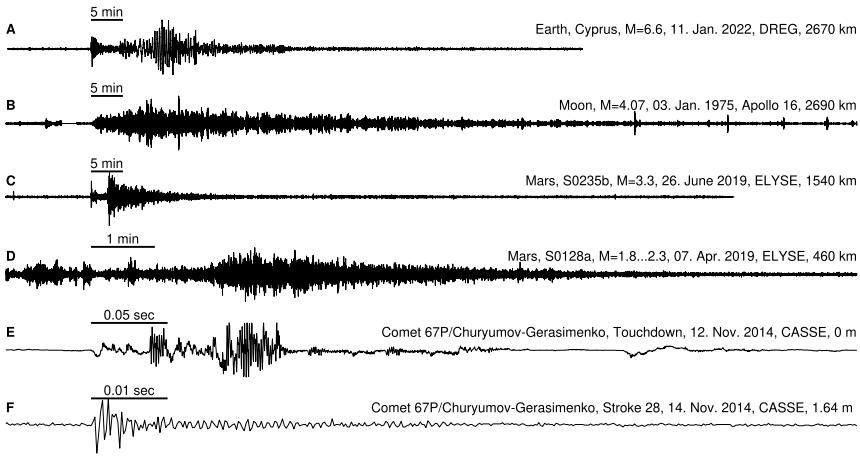

Figure 1 Seismograms recorded on four celestial bodies: Earth, the Moon, Mars, and comet 67P.

to planetary scientists in general, which gaps in our understanding seismological data can fill. It is written to be readable by an interested reader with a general geological background.

2. Mercury

2.1 Potential scientific goals

Mercury is widely understood as a planet that was stripped of much of its mantle since formation (Chau et al., 2018). The core radius is 85% of the planet's radius with a mantle of only 400 km (Spohn et al., 2001) above. While the density is well-estimated from geodetic measurements (Rivoldini et al., 2009), the distribution of weight between mantle and core is not. As shown on Mars (Stähler et al., 2021; Khan et al., 2018), probing the mass and radius of a planet's layers very precisely, can lead to strong constraints on the composition of the planet.

2.2 Seismicity

The level of background seismicity on Mercury is unknown. Compared to Mars and Earth, recent volcanism plays a minor role in shaping the surface of the planet (see Byrne, 2020, for an extended comparison). Painted with very broad strokes, seismicity on Earth and Mars is connected to volcanism: On Earth, the mid ocean ridges are expressions of extension driven at

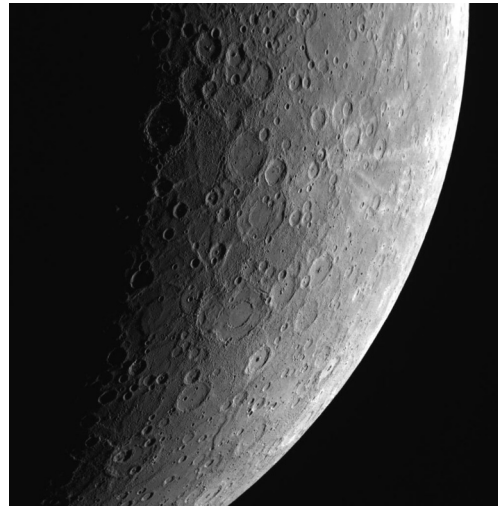

Figure 2 Mercury limb as seen by MESSENGER. The strong cratering of the surface is immediately visible and suggests that the megaregolith and its strong crustal scattering will be about as problematic for any seismometer mission, as it was on the Moon. The interior of Mercury with its large core might be much more interesting, though. Image: NASA/Johns Hopkins University Applied Physics Laboratory/Carnegie Institution of Washington. PIA 17280.

least partially by volcanism. Subduction zones on the other hand harbor the largest earthquakes known to date, at the thrust front, while the subduction process itself produces back-arc volcanism. Only transform faults are not producing co-located volcanism on their own, even though many strike-slip faults are located at the end of convergent faults. On Mars, the strongest clusters of seismicity are found connected to recent volcanism. Dike intrusion is weakening the crust in Western Elysium Planitia, leading to a large number of marsquakes observed in Cerberus Fossae (Giardini et al., 2020; Clinton et al., 2021). Given the absence of plate tectonics or recent volcanism on Mercury, it is not clear what the driver of seismicity is. Wrinkle ridges, i.e. buried thrust faults are distributed over the whole planet and are interpreted as the result of global crustal contraction due to secular cooling (Byrne et al., 2014). While the cumulative amount of deformation from this process can be estimated easily, it is not known whether the process is still ongoing or whether it has stalled. On the terrestrial moon, seismicity is triggered by tidal deformation, although it is disputed whether the tidal stresses directly cause the quakes or whether they just weaken normal stress on the fault temporarily so that rupture is possible. However, as shown by

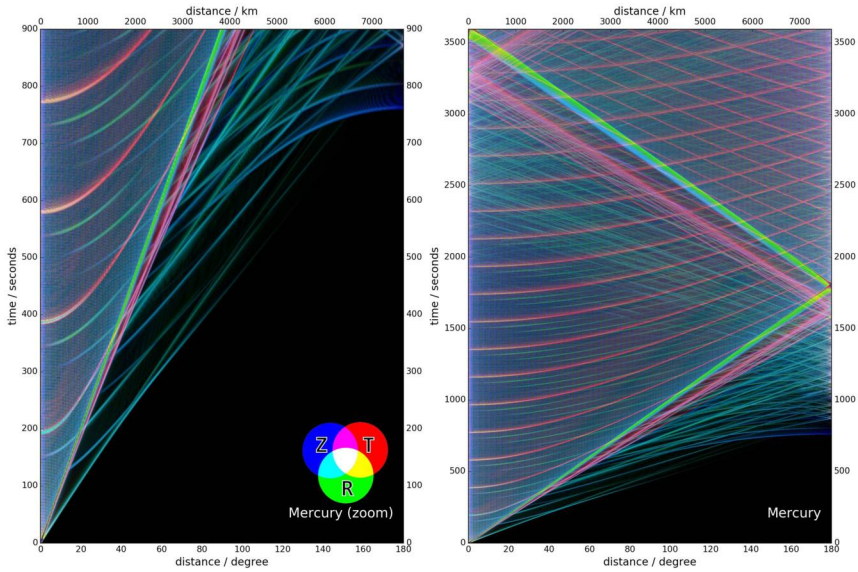

Figure 3 Global seismic wavefield stack for Mercury, using the interior model of Rivoldini et al. (2009). This stack shows surface acceleration in all 3 directions: blue for vertical, red for radial (horizontal in direction of the source) and red for transversal (horizontal, orthogonal to the source). The plot is a synthetic version of the global seismogram stack of Astiz et al. (1996) and computed using AxiSEM and Instaseis (Nissen-Meyer et al., 2014; van Driel et al., 2015). Due to the large core size, the first core-reflected shear wave (ScS) arrives already after 200 seconds and is followed by regular multiples. A seismometer on a lander could use these phases to determine the core radius. Note that these numerical simulations do not reproduce scattering, so real waveforms could be much less clear.

(Hurford et al., 2020, for a summary see Table 1), the tidal energy deposited in Mercury is significantly less than that of the moon. However, the temperature difference of more than 600 K between day and night, is likely to form transient thermally-induced seismicity along the terminator. The strong surface cratering (Fig. 2) however suggests strong seismic scattering, comparable to the Moon. The shallow core mantle-boundary implies that core reflected phases will dominate the seismogram (red hyperbola in Fig. 3).

2.3 Mission perspectives

Mercury places tight constraints on any landed mission. The place deep in the gravity well of the sun means that a lander mission will require at least one flyby on Venus or Earth to reduce its ΔV to an acceptable level. The

Ames trajectory database (Foster and Daniels, 2010) lists no trajectories with a single Venus flyby and $\Delta V < 20$ km/s until 2040. Therefore, any mission would involve rather complex and long duration trajectories. The ESA BepiColombo mission needs to do a total of eight flybys (Earth once, twice at Venus and then six times Mercury itself) between 2021 and 2025 to enter an orbit.

After landing, the spacecraft would be subject to two separate realms of operations. Due to the 3:2 spin–orbit resonance of the planet, one solar day takes 176 Earth days. Therefore, temperatures vary extremely over time across the surface, between 100 K and 700 K in equatorial planes. Due to the low inclination of the orbit, temperatures at the poles, where the sun never rises more than 2 arcminutes above horizon, are more stable below 150 K. Since the low temperatures of the night can be relatively easily accommodated by electric heaters, most proposed missions target landing after sunset and limit the mission duration to a single night. Ernst et al. (2021) present a mission concept to study the geology around an equatorial landing site over the course of a single Mercury night (88 Earth days) in 2045. The mission study includes an accelerometer for seismic studies. The mission is proposed as a New Frontiers class mission and is currently the only serious lander concept for the innermost planet. The decadal survey (Nat. Academies, 2022) questioned whether this mission can be done within a New Frontiers budget and estimated a total cost of 2.8 billion USD, i.e. a flagship mission. Because of the narrower scientific scope of the mission as proposed compared to an ice giant system mission, it was ranked behind the Uranus Orbiter and the Enceladus Orbilander.

3. Venus

3.1 Potential scientific goals

Venus is comparable in size and density to Earth, yet little is known about its surface tectonics compared to Mars or even Mercury, due to the thick cloud cover. The surface has undergone significant reworking and its oldest parts, the so-called tesserae are likely younger than 600 million years. Based on available radar images from Magellan and the Arecibo radio telescope, the surface is undergoing strong deformation until today (Smrekar et al., 2014). In the next decade, the Envision (Ghail et al., 2020) and Veritas (Smrekar et al., 2020) missions planned by ESA and NASA respectively will increase the resolution of radar images significantly and help to constrain the dominant mechanisms of surface tectonics based on geomorphology.

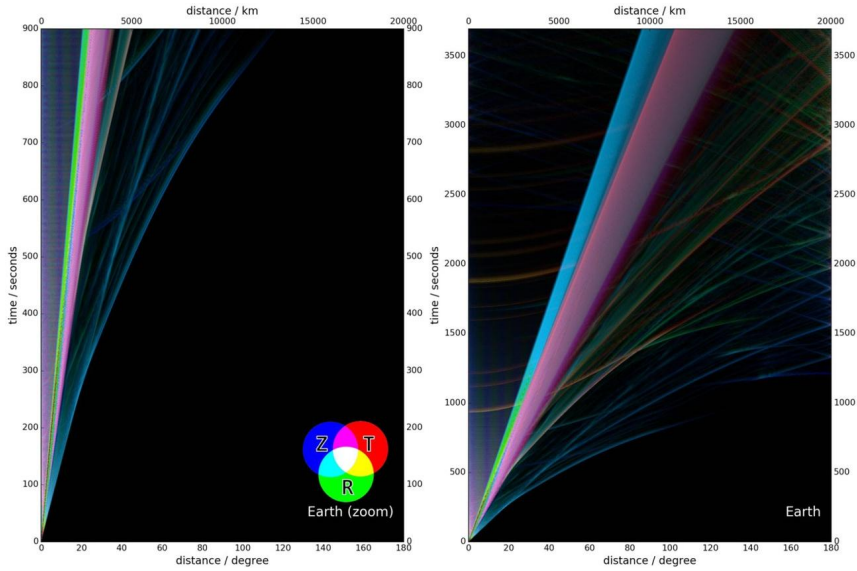

Figure 4 Global seismic wavefield stack for Earth, using the interior model of Kennett et al. (1995). Venus may show similar seismic phases, given its comparable radius and density.

Plate tectonics in the terrestrial sense of the word is unlikely to exist on Venus, since the high temperature inhibits a strong lithosphere. Locations of venusquakes could however constrain whether active faults cluster, as they do on Earth and Mars or whether deformation is widespread, as on the Moon. The global seismic wavefield of Venus is likely similar to Earth's, and identification of core-phases will be crucial in determining the minor differences in the deep interior of the two worlds. Fig. 4 shows a synthetic seismogram stack of Earth for comparison.

3.2 Seismicity

The seismicity of Venus is unknown. The relatively low crater density suggests an average surface age of 250–750 Myr, which can either be accomplished by a steady state of crater formation and removal by volcanic or tectonic processes (Phillips, 1992) or catastrophic short term subduction or overturn of the whole lithosphere at regular intervals (Strom et al., 1994). Both scenarios suggest high, though different strain rates and therefore tectonic seismicity. However, given the high surface temperature, it is actually not clear how much of this deformation is occurring in a brittle regime

and thus capable of producing venusquakes. The rate of volcanic eruption is likely higher than on Earth, with a recent study based on scaling the terrestrial rate to Venus estimating 120 discrete eruptions per (terrestrial) year (Byrne and Krishnamoorthy, 2022), which could be observed either seismically or from infrasound (see below).

3.3 Mission perspectives

Venus' orbit is relatively well accessible by spacecraft from Earth. Every 18 months, a launch window of 3 months opens with flight duration between 80 and 120 days. Landing and operating on the surface is of course an entirely different story. At this time, there are no seismic instruments at high technological readiness level that would be able to operate over extended periods under Venus conditions. The Soviet Venera landers relied on significant overdesign in terms of mass, which allowed survival of a few hours, by delaying the warming of the core electronics. The currently most promising candidate are Silicate Carbide (SiC) electronics that are able to operate at temperatures of 800 K, at least theoretically. The main application for SiC at this stage are high voltage, low loss systems, specifically power circuits, as well as simple amplification systems for sensors in high temperature environments (Zetterling, 2015). The complexity of the electronic systems that can be manufactured in SiC is far lower than for Si systems, and only basic integrated circuits have become available recently. A decisive problem is that the business case for high temperature SiC electronics is weak on Earth and development of a Venus lander would not be able to profit from commercial innovation cycles as much as it is the case for Si-based electronics. Specifically, industry development focuses on single components that cannot be moved to a cooler part of a system (such as sensors or preamplifiers), while a Venus lander would need to operate virtually all of its electronics at temperatures > 700 K. Even with SiC electronics, a lander interior would have to be cooled actively. Solar irradiation is 3–5 W/m^2, so that a mission would have to rely on a radio-thermal generator, which would operate at low efficiency, given the high outside temperature. A European concept for a long-lived lander with a seismic package based on microelectronics was presented by Wilson et al. (2016), with a life time of 100 days, banking on further progress in SiC electronics over the next decade.

An alternative approach is to operate from the upper atmosphere, where temperatures are stable and moderate around 290 K. The lifetime of such a mission would be limited primarily by the escape of Helium from the carrying balloon, to the order of 120 (Earth) days, but at much lower technical

complexity compared to a surface mission. A balloon mission equipped with infrasound sensors could detect air-coupled Rayleigh waves. Terrestrial analog concepts are currently studied on two scales: A JPL-led team studies the lower range of signal amplitudes that can be observed, using earthquakes of magnitudes 3–4 in California (Brissaud et al., 2021), as well as induced seismicity in Oklahoma. A French group centered on ISAE supaero uses free floating, long-lived meteorological balloons on equatorial trajectories to observe the global signature of large earthquakes above magnitude 7, as well as volcanic explosions (Podglajen et al., 2022). In both cases, signal detection was demonstrated, for a variety of events. The obvious drawback of the method would be that the polarization of the actual seismic wave would not be accessible directly. Garcia et al. (2021) demonstrated two possibilities to overcome this limit: A string of infrasound sensors on the balloon tether could determine the incident angle of the infrasound wave, as a proxy of the distance to the event's hypocenter. A second option is the inclusion of accelerometers into the balloon, which would record the acceleration of the balloon due to the arrival of the pressure wave. Similar techniques are used in marine seismic surveys, usually termed multisensor streamers (Robertsson et al., 2008). The advantage is that the sensor effectively measures the pressure gradient of the infrasound wave, which allows recording the signal at higher frequencies (since the spatial derivative of observing the gradient is equivalent to recording the time derivative of the signal). The final application will likely see a combination of multiple infrasound sensors and accelerometers, from which the full pressure gradient field is reconstructed and transferred to Earth.

An unknown issue is that the coupling into the air is most effective for Rayleigh waves, preferably at frequencies above 0.1 Hz. As the InSight example showed, surface waves are not regularly observed, if hypocenters are not very shallow and event magnitudes are below $M_W = 4$. A curious question would be where Venus stands in terms of seismic scattering. The dense atmosphere reduces the meteorite impact rate and thus impact gardening that produces the lunar regolith. The high surface temperature and availability of volatiles likely allows for healing of cracks and thus increases the mean free path length of seismic waves. So in terms of seismic waves, Venus might be the most "transparent" planet in the solar system, even compared to Earth.

4. Moon

4.1 Potential scientific goals

The moon hosted the first extraterrestrial seismic network between 1970 and 1979, when it was switched off due to lack of further interest in the seismic community (Lognonné and Johnson, 2007). The Apollo seismic network helped exploring the Moon in a number of ways, from the shallow subsurface (Sollberger et al., 2016) to the crust (Khan et al., 2000) and the core (Weber et al., 2011). See Khan et al. (2013); Garcia et al. (2019b) for an overview of the knowledge on the lunar interior gained from Apollo. The network further observed significant numbers of tectonic quakes and impacts (Kawamura et al., 2017). Since a network was used, a tentative identification of shallow tectonic quakes with surface faults was possible in a few cases, allowing to estimate the energy budget of the moon due to shrinking (Watters et al., 2019).

Seismometers have been part of all proposals for future network science on the moon, specifically the Lunar Geophysical Network (Weber et al., 2021). One scientific goal would be to explore the lunar crust in more detail. Since the Apollo age, it is known that significant parts of it are KREEP terrains, understood to be mantle material from an overturn in an early lunar magma ocean. These can be distinguished spectrally from orbit, but should produce a significant imprint in crustal thickness. The crustal density models of the moon are actually those of highest resolution in the whole solar system, due to data from the GRAIL mission (Wieczorek et al., 2013), but nonunique with respect to the average thickness of the crust, as well as the inner-crustal layering. Receiver function analysis to detect layering in the crust, was limited by the infamously strong scattering in lunar seismograms, but also by the low performance of the Apollo horizontal component seismometer.

A future seismic network on the moon would consist of state of the art three-component seismometers, to better detect shear waves and converted phases. Central nodes could be equipped with very high fidelity sensors (Kawamura et al., 2022), based on optical readout or superconducting gravimeters to directly observe normal modes. These would have resolution on the structure around the chemical layer above the core-mantle boundary and a potential inner core. Both features were seen in the analysis of Weber et al. (2011) and are of high importance to formation models not only of the Moon, but also of Earth, since the giant impact model derives the Moon from the Earth and a mars-sized impactor.

4.2 Seismicity

The lunar seismicity is famously divided into two families: the shallow and deep moonquakes. While the shallow moonquakes happen independently of another (their distribution in time is a Poisson process), the deep moonquakes follow a tidal cycle. The seismogram signals are so similar, that several clusters can be identified, in which moonquakes of similar focal mechanism repeat. This waveform similarity has been used to identify new moonquakes in the noise by template matching (Bulow et al., 2005). In general, all moonquakes show a very high corner frequency compared to their moment magnitude (Oberst, 1987). The peaked response curve of the Apollo seismometers makes the estimation of the absolute event magnitude challenging (Kawamura et al., 2017), but most estimates agree that the lunar seismicity is about four orders of magnitude below the terrestrial one (Knapmeyer et al., 2006). The seismicity of the Moon is relatively well known after nearly eight years of registrations by the Apollo stations. New mission concepts even rely on the recognition and re-use of source clusters that were identified in the Apollo data. The Apollo data is however of limited value when concerning the far side of the Moon, where it is unknown if it is entirely aseismic, or if the core and partial melt layer on top of the core mantle boundary absorb all seismic waves from far side sources. Specifically the polar regions and the far side might harbor more regional tectonic activity that has been impossible to observe.

4.3 Mission perspectives

The good accessibility of Moon, with launch windows almost every month means that mission complexity is significantly reduced. The NASA CLPS program tries to leverage this by buying delivery of scientific instruments to the lunar surface from commercial companies without prescribing a mission architecture. It is therefore likely that very different designs of seismic stations and network will be deployed over the next decade, starting with the Farside seismic suite (FSS), which is to land near Schrödinger crater in 2025 (Panning et al., 2021). Among the main challenges are the high amount of radiation (essentially equivalent to interplanetary space, with the chance for solar extremes), the high temperature difference between day and night and the 14-day long cold night. The two latter require significant battery capacity to ensure heating and therefore survival of a lander through the night. The Apollo 11 EASEP station is an example for instrumentation that did not survive the lunar night.

A lunar geophysical network of multiple nodes, each equipped with a seismometer (Weber et al., 2021) has been mentioned as a New Frontiers Class mission in the Decadal Survey of 2010 and 2022. The currently planned human landings during the Artemis program would allow to bring significant amounts of scientific payload with them, specifically, if the lander is a SpaceX "starship". However, at the time of writing, the specifics of the Artemis program, the exact landing concept and therefore, the scientific program are not yet defined. The European Large Logistics Lander (EL3) foresees to deliver about 100 kg of scientific payload to the lunar surface in the early 2030s, which could easily form another geophysical node.

5. Mars

5.1 Potential scientific goals

Apart from the Earth and the Moon, Mars is the only planet on which a seismometer has been operated for an extended period of time. The NASA-led InSight mission landed in Southern Elysium Planitia with the seismometer SEIS developed by a range of European partners under leadership of the French space agency CNES and the Institute de Physique du Globe (IPGP) Paris (Lognonné et al., 2019). The InSight mission (Banerdt et al., 2020) has shown that Mars is tectonically active, with a seismicity above that of the moon; similar to quiet intraplate regions on Earth. Post-InSight seismic investigations could focus on one of three aspects:

- To ensure good ground coupling, SEIS was deployed to the surface of Mars using a robot arm (Trehu-Ollennu et al., 2018). Due to the absence of active obstacle avoidance systems, the InSight landing site was selected to be flat and devoid of craters. This resulted in a location with sand as top layer and limited InSight's ability to observe long period signals (below 50 mHz). This prohibited observation of tidal deformation at the period of the Phobos orbit, which would have added a strong constraint on the rheology of the mantle (Lognonné et al., 2019; Van Hoolst et al., 2003). A future long period seismic observatory would therefore have to be installed at least on bedrock to improve coupling to the ground at long periods. This installation would require either guided landing on exposed bedrock or a rover to deploy the seismometer on suitable ground in some distance of the lander. A significant noise source was the tether, the rigid connector from SEIS to the lander, which contained 80 analog channels for scientific and housekeeping data (Zweifel et al., 2021; Hurst et al., 2021; Scholz et

al., 2020). A future mission would benefit from a much thinner tether, possibly only for power transmission, while data is transmitted wireless or on only two wires in serial digitized form. The long period background noise could be further reduced by burying the whole sensor assembly. This however would require a careful selection of a site where burial is possible to a depth of significantly compacted ground.

- While first layered models of the crust and mantle, including the radius of the core were obtained by InSight using a single station only (Drilleau et al., 2022; Durán et al., 2022; Khan et al., 2021; Knapmeyer-Endrun et al., 2021; Stähler et al., 2021), many unknowns remain: The interior of the core has not been observed yet (e.g. by SKS waves), and even though tentative observations of Pdiff were made (Horleston et al., 2022), the lowermost mantle is constrained only very sparsely by seismic data. The detection of magnitude 4 quakes in Southern Tharsis (Horleston et al., 2022) suggests that much more small seismicity could be present there, unobservable from InSight's location. At the same time, Plesa et al. (2021) showed that geodynamical models predict significant lateral variations in seismic wave speed, potentially higher than on Earth. A global network of 4–6 seismometers, combined with other geophysical sensors could observe the full global seismicity, seismic phases over a wider distance range, and potentially also the above-mentioned three-dimensional structures in the Martian interior, as deviations from the wavefield predicted for a purely layered planet (Fig. 5).
- InSight observed localized tectonic activity near the Cerberus Fossae graben (Fig. 6), in contradiction to existing models of wide-spread compressive stress from lithospheric cooling (Phillips, 1991; Knapmeyer et al., 2006). This observation has strong implications for the general mechanisms of tectonic activity on terrestrial planets. To better understand the mechanisms, it would be worth while to locate marsquakes precisely in one of the active systems, for which a multistation seismic network is necessary. Due to the low intrinsic seismic attenuation, energy above frequencies of 1 Hz is transmitted well and observable, which allows to use light-weight, short period instruments, such as the InSight SP-sensor (Stähler et al., 2022).

5.2 Mission perspectives

Landing on Mars has been executed successfully nine times by NASA and once each by the Soviet Union (Mars 3 on December 2, 1971, Perminov,

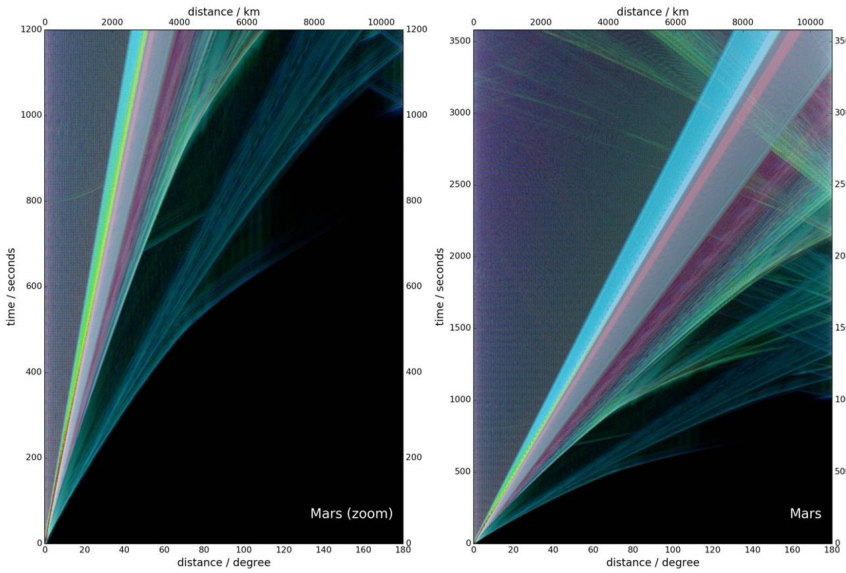

Figure 5 Global seismic wavefield stack for Mars, using the interior model InSight_KKS21_GP of Stähler et al. (2021).

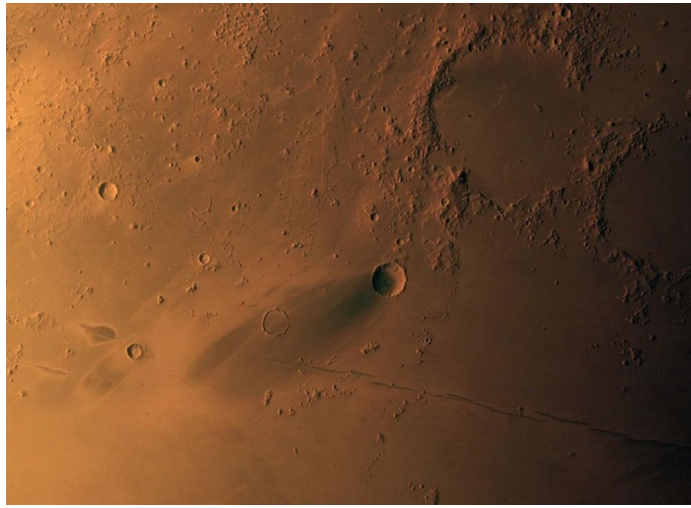

Figure 6 Image of South Western Elysium Planitia on Mars, taken on March 15, 2021, by the digital exploration camera (EXI) of the UAE Hope probe. The horizontal lines in the lower part of the image are the grabens of Cerberus Fossae, the source of most marsquakes recorded by the InSight mission so far (Giardini et al., 2020; Perrin et al., 2022; Zenhäusern et al., 2022). Image: MBRSC/UAE Space Agency/CU-LASP/EMM-EXI.

1999) and the Chinese Space Agency (Zhurong on May 14, 2021). All these landers were fundamentally operating a combination of a heat-shield and parachute for initial deceleration. The Mars Exploration Rovers Spirit and Opportunity used airbags for final approach and landing, while the large Perseverance and Curiosity rovers were lowered to the ground from a separate spacecraft, colloquially termed *sky crane*. The Discovery class missions InSight and Phoenix used hydrazine retrothrusters for final deceleration and had no active obstacle-avoidance systems. These techniques are currently considered to place a lower limit of about 200 million USD on any mission, before scientific instruments are even considered, requiring at least a Discovery class budget for future landed missions.

A potentially cheaper option is to use penetrators, i.e. spacecraft that are landing with terminal velocity and decelerate either by penetrating up to a few meters into ground or by having a deformable front part. As described in Lorenz (2011), the concept has been proposed several times over the last decades, but was never successfully executed. However, it must be noted that no penetrator mission failed during landing; Mars-96 was lost due to failed upper stage separation after launch, while DS-2 likely got lost with the mother spacecraft Mars Polar Lander. Overall, Mars is the location suited best for simple penetrator missions, since the atmosphere can fulfill initial deceleration and – more importantly for a low-cost mission – attitude control, removing the need for active propulsion. A semihard lander concept has recently been proposed by engineers from JPL under the name SHIELD (Barba et al., 2021). It would utilize a deployable drag skirt of 2 meter diameter for deceleration to obtain a low ballistic coefficient and therefore terminal velocity of < 70 m/s without the use of a parachute. At least four of such landers could be stored in a single Falcon-9 sized payload fairing and would therefore allow to build a seismic network on Mars. During landing, instruments, including the seismometer would have to survive deceleration of up to 2000 g, depending on surface character. The JAXA seismometer planned for the Lunar-A mission (Mizutani, 1995; Shiraishi et al., 2008) is specified for 5000 g and would therefore be a candidate instrument. The seismometers of the Ranger 3/4/5 missions was tested up to 3000g (Lehner et al., 1962). For a free-fall landing on the Moon, it was encapsulated in a balsa wood impact limiter sphere and submerged in freon. Other instruments, such as the InSight SP seismometer could be hardened in a similar way during flight and landing.

A ultra-high sensitivity mission would require a soft lander, likely in combination with a rover to reach a suitable installation site after landing.

While such a mission is well within the technical possibilities of NASA and likely also CNSA and ESA, it would likely require a flagship class budget for landing and operations and could therefore only be executed as part of a larger rover mission. However, NASA and ESA are currently executing the Mars Sample Return campaign, involving the Perseverance rover and likely 3 more launches until 2030. Given the size of the mission and its considerable strain on the budget of both involved agencies, it is unlikely that any additional scientific payload will be added to it, to avoid mission and budget creep. The delay of the ESA ExoMars landing due to the stop in collaboration with Roscosmos will further affect all Western Mars missions.

As a final word, it should be noted that the landscape of possibilities on Mars is likely to change, if various private space companies, foremost SpaceX, succeed in constructing reusable high performance launch vehicles, that would increase mission cadence and lessen weight limitations. However, launch cost is not at all a constraining factor typically and other factors (e.g. the availability of a high bandwidth communication network) limit mission design on Mars.

6. Phobos and Deimos

6.1 Potential scientific goals

For the two Martian moons, it is not even known whether they consist of consolidated material or form rubble piles (Le Maistre et al., 2019; Dmitrovskii et al., 2022). If they form rubble piles, seismic wave propagation in a usual sense is not possible and the strongest signal will instead be the normal modes of the moons. A more consolidated object however could be propagating seismic waves efficiently; due to the small size with high amplitudes even for small quakes. The high thermal gradient and strong tidal signal from Mars is likely to trigger a significant amount of small phobos- or deimosquakes, if the moons as a whole are consolidated enough. The rigidity of the uppermost surface layer could be estimated from the deceleration of a lander, information on mechanical properties of the soil surface will also be gained from the JAXA MMX rover, which will land and drive on the surface of Phobos.

6.2 Mission perspectives

The launch windows for Phobos and Deimos are identical to those of Mars, yet landing requires an entirely different skill set. A sample return mission to

Phobos, MMX (Martian Moon eXplorer) is planned by JAXA for launch in 2024 (Kuramoto et al., 2022), building on their extensive expertise in missions to asteroids. The mission will not carry a seismometer, but during the landed time windows, the spacecraft's IMU will listen for ground vibrations. Given that the lander stays on the surface for only a few hours and performs sampling operations during that time, the detection of a phobosquake would be a lucky event. The mission will perform a geodetic experiment, mapping the shape of Phobos using imaging and LIDAR and combining it with Doppler radio tracking of the spacecraft to obtain gravity coefficients from which the interior can be inferred (Matsumoto et al., 2021).

7. Ceres

7.1 Potential scientific goals

Ceres shows trace of a subsurface ocean, which would contain a significant amount of the water of the asteroid belt. Surface morphology indicates that this ocean is indeed partially liquid and forms yet another ocean world. A seismic mission could explore the depth of the ice/ocean interface, the thickness of the ocean, but also the homogeneity of the ice layer above. A warm ocean would result in slushy layers at the bottom of the ice that would significantly increase attenuation.

Since the planet has no moons, the tidal dissipation is insignificant. Yet, the NASA Dawn mission observed signs of recent cryovolcanism (Ruesch et al., 2016): The Ahuna Mons topographic feature is 4 km high at a width of 16 km and only lightly cratered. The age is estimated to be 210 ± 30 million years, i.e. very young in the context of a small planet. It is debated whether the dominant tectonic process on Ceres is solid state convection inside the icy crust, leading to dome formation (Bland et al., 2019) or instead global contraction, as evidenced by ubiquitous thrust faults (Ruiz et al., 2019). It is well possible that these thrust faults were indeed created in an early stage of the planet's formation and are thus fossils of the planet's ancient tectonics. The latter seems to be the case on Mars, too, where no seismicity could be attributed to thrust faults, lobate scarps or wrinkle ridges so far. Following the example of Mars, where Cerberus Fossae, one of the youngest surface features is also the most seismically active, Occator crater would be a prime target. The crater shows bright spots (faculae), interpreted as deposits of salts from eruption of brines (Nathues et al., 2020;

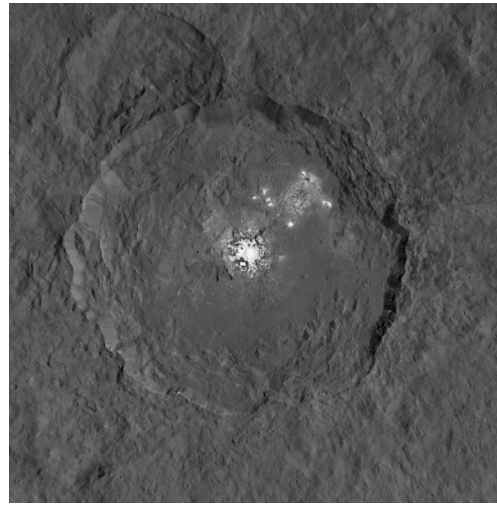

Figure 7 Occator crater on Ceres, the proposed landing site for a NF-class Ceres sample return mission (Castillo-Rogez et al., 2022). The bright spots are understood to be young carbonate salt deposits from subsurface brines. A seismometer could help to constrain the current tectonic activity and from it the deposition rate. The view is a composite of two DAWN images, avoiding overexposure of the bright spots. Image credit: NASA/JPL-Caltech/UCLA/MPS/DLR/IDA, PIA19889.

Schenk et al., 2020) (see Fig. 7). If these brines are deposited by an endogenic process, it would also lead to contemporary seismic activity, that could be picked up even by a short period seismometer.

A broadband Ceres seismometer would investigate the global distribution of tectonic activity. Since high resolution orbital images exist from the Dawn mission, at a resolution of 35 m, attribution to individual fault systems or centers of cryovolcanism would be possible. Assuming large enough Ceresquakes, the seismic data could be used to investigate layering of the planet, including the depth of the ocean.

7.2 Seismicity

The seismicity of Ceres is unknown. Given the absence of a partner object for tidal forcing and low interior heat flow, it is likely to be low. The presence of recently deposited brines (Nathues et al., 2020) suggests that seismicity driven by interior processes might be present. Due to the location of Ceres in the Asteroid belt, meteorite impacts are a likely seismic source.

7.3 Mission perspectives

Ceres can be reached relatively easily, typically with a Mars flyby, leading to a 3–4 year trajectory for orbiter missions. The Dawn mission used solar electric propulsion, leading to a 6 year trajectory, including a 400 day research trip to asteroid Vesta.

In the aftermath of the Dawn mission, lander missions have been proposed; due to the low gravity, even sample return missions are feasible. An interesting concept is proposed by Castillo-Rogez et al. (2022), in form of an electrically propulsed orbiter that is able to land and relaunch as a whole, returning samples to Earth. The mission is supposed to collect samples of carbonate salts as well as the darker reference surface materials and return it to Earth at $\leq 20\,°C$ to prevent alteration. The mission would benefit from investigating recent tectonic activity in Occator crater, to determine the samples' context. Unfortunately no seismometer is currently foreseen. A slightly modified version of this mission was proposed as a candidate for a New Frontier class mission in the Decadal Survey 2023–2033 (Nat. Academies, 2022), still without seismic measurements.

A tip to the hat goes to the student participants of the 42nd Alpbach summer school 2018, who developed Calathus, a more classical dual orbiter/lander sample return mission, in the cost range of a NASA flagship mission or an ESA L-class mission (Gassot et al., 2021).

8. Jupiter and Saturn – the giant planets

8.1 Potential scientific goals

For this topic, see the excellent overview in Gaulme et al. (2015). Seismology in the common sense, using a landed mass-and-spring sensor is of course impossible on a gas giant, instead measurements focus on long period deformation, detected by astronomical means. As all bodies, the giant planets have normal modes whose shape and frequency depends on their interior's elastic parameters. Since the bulk of the interior is in fluid state without shear modulus and yet gravity is significant given their size, the nomenclature of helioseismology is typically used. Compared to Earth, where the elastic moduli dominate as restoring force and gravity and self-rotation (the Coriolis force) can be treated as second order parameters, in the sun or the gas giants, the modes need to be treated separately by their primary restoring force (Guillot and Gautier, 2015).

- Pressure modes (p-modes) are the closest analog to normal modes on Earth. The restoring force is the pressure field, or the gradient of the

scalar potential $p = \nabla\phi$, analog to the case of the acoustic wave equation. Their sensitivity is typically constrained to the outer layers.

- Gravity modes (g-modes) have the gravity, or more precisely buoyancy as restoring force. They can therefore only form in convectively stable regions, where no density inversions exist and lateral density contrasts are low.
- Surface gravity modes (f-modes) are analogous to deep water gravity waves in the ocean, with the weight of surface vertical displacement as restoring force. Their sensitivity is therefore highly constrained to the outermost shell of the planet.
- Inertial modes (i-modes) can occur in rapidly rotating planets, such as Jupiter and Saturn, restored by the Coriolis force.

All in all, these modes create a complex overlapping picture of spectral peaks in the surface displacement and of course cross terms and coupling exist. Over time, four approaches have been considered to observe the normal modes of Jupiter remotely.

- Variations in infrared brightness, caused by temperature perturbations from p-modes. A 1 m/s velocity field corresponds to 10 mK in temperature perturbation, visible in mid-infrared, which are difficult to observe, given the limited sensitivity of photometric sensors in this optical wavelength window. Because of these difficulties, no dedicated instrument has been developed so far.
- Spectroscopy of reflected light. This method has been improved considerably on instrument side since in response to the exoplanet detection campaigns. In 2011, the seismology-dedicated SYMPA Fourier spectro-imager detected radial modes of maximum amplitude of 49^{+8}_{-10} cm, at a frequency of 1213 ± 50 μHz, with a mean large frequency spacing between radial harmonics of 155.3 ± 2.2 μHz (Gaulme et al., 2011), placing a weak constraint on the planets interior structure. Spectroscopy needs to take into account the large rotation contribution at the fringes of around 25 km/s.
- Photometry of reflected light. Here, brightness variations in reflected light are used. Compared to the other two methods, the signal-to-noise ratio is low, but sensors in visible wavelengths are widespread. However, the complex surface pattern of the Jovian clouds means that only specific modes can be observed. Another problem arose when trying to apply this method to Neptune with the extended NASA Kepler mission "K2", which observed the planet for 50 days at a 1-min cadence. No oscillations of Neptune could be detected (Rowe et al., 2017). But

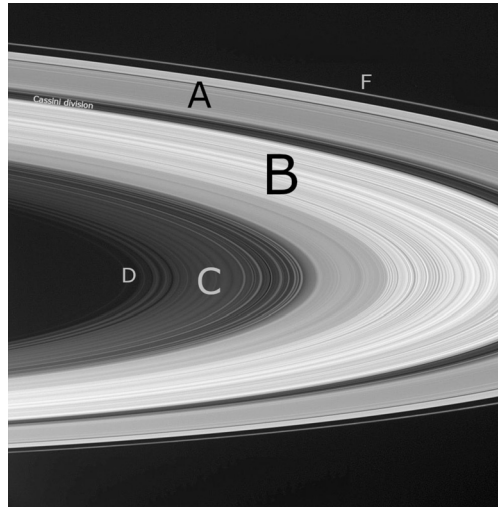

Figure 8 Cassini image of Saturn's rings taken by the ISS infrared camera. Major subdivisions are labeled by the author. Kronoseismology is done using density waves in the broad, but faint C-ring. Image credit: NASA/JPL/Space Science Institute, PIA06536.

it became apparent that oscillations of the Sun in the reflected light perturbed the signal.

- Kronoseismology: The rings of Saturn are shaped by resonance with the interior modes of the planet. Density waves exist in all rings, but specifically in the innermost C-ring (see Fig. 8), they are excited by certain normal modes of the planet (Hedman and Nicholson, 2013). This is observationally accessible via photometry of the exact ring pattern during stellar occultations during the Cassini mission (Fuller, 2014) and led to the discovery of a diffuse, but stable stratified core of the planet (Mankovich and Fuller, 2021).

8.2 Mission perspectives

Using ring seismology, the interior models of Saturn cannot be refined any further, given the high resolution on density waves in the C-ring obtained by Cassini from radio occultation experiments. Future research would therefore focus on Jupiter. Gravimetric observations by Juno (Durante and Iess, 2021) detected gravity perturbations that are compatible with the presence of p-modes, which proved the existence and excitation of these modes, although they could not be further identified.

A Doppler imaging camera for Jupiter seismology was proposed as a payload for the ESA JUICE mission (Soulat et al., 2011), but ultimately not selected. Given that Juno, a general purpose mission is currently active in the Jupiter system and two flagship class orbiter missions (JUICE and Europa Clipper) are due to launch until 2025 (although both focused on the icy moons), the need for another large Jupiter orbiter has not been foreseen by the Decadal Survey. Instead, Doppler spectroscopy from Earth will likely be the only possible method for the foreseeable future. The success of SYMPA was followed on by the JOVIAL sensor (Gonçalves et al., 2019) and dedicated instruments to measure Jupiter's zonal wind speeds, e.g. PMODE-I on the AEOS 3.6 m telescope atop Mount Haleakalā, Maui, Hawai'i (Shaw et al., 2022) are built. Observations of the normal modes with increased precision compared to SYMPA would however be fortuitous, possibly due to a large impact. To measure Jupiter's interior modes with high enough precision, multiweek continuous observation campaigns (at stable weather) would be necessary, which are likely only possible from Antarctica (Shaw et al., 2022). In the far future, it could also be done from a long-lived optical Jupiter observatory at Lagrange-point L1, as proposed by the Chinese space agency CNSA (Hsu et al., 2021).

9. Io

9.1 Potential scientific goals

While Europa, Ganymede, and Callisto are all icy moons, Io is a terrestrial planet without any surface ices (or water absorption features whatsoever Smith et al., 1979). The ice fraction on these moons actually increases with distance from Jupiter, which is one of the problems moon formation models face (Shibaike et al., 2019). In how far the interior structure and composition of Io is related to the structures of the other icy moon's rocky cores, and in how far these permit certain formation scenarios, can be understood only if the interior structures of them all are better resolved. While Io's active volcanism (discovered by Voyager I, Smith et al., 1979) is a fascinating mission goal in itself, the moon is also a perfect natural laboratory to understand tidal heating in multibody systems. To quote the KISS report on Tidal heating: "The Io–Europa–Ganymede system is a complex and delicately built tidal engine that powers Io's extreme volcanism and warms water oceans in Europa. Io's gravity generates a tidal bulge within Jupiter, whose dissipation transfers some of Jupiter's rotational energy into Io's orbit, moving it outwards and deeper into a 2:1 eccentricity resonance with

Europa. This in turn increases Io's eccentricity, resulting in enhanced tidal heating. Ultimately, Jupiter's rotational energy is converted into a combination of gravitational potential energy (orbits of the satellites) and heat via dissipation in both Jupiter and the satellites" (de Kleer et al., 2019). The tidal heating is ultimately the cause of Europa's liquid ocean, which may be a permanent feature or periodic (Hussmann and Spohn, 2004). Since tidal heating is the process creating the many ocean worlds in the Solar system (Nimmo and Pappalardo, 2016) and in other exoplanet systems, understanding it has significant consequences for habitability, as well as evolution of planetary systems. Prior to the observations of Voyager I, Peale et al. (1979) predicted that the deep interior of Io should be largely molten because of the tidal heating. Schubert et al. (1981), in explicit contradiction, proposed a thin, molten layer between the crust and a solid interior and an iron core. The thickness of the molten layer is estimated to be at least 50 km, with a melt fraction exceeding 20% (Khurana et al., 2011). Van Hoolst et al. (2020) even consider a magma ocean possible. The size of the core is somewhere between 19% and 50% of Io's radius (Anderson et al., 2001). Seismological experiments could determine layer thicknesses and core radius, and, via shear modulus and attenuation, constrain the melt fraction in the asthenosphere.

9.2 Seismicity

As with all other large moons of the giant planets, Io's seismicity is not known. However, the planet shows obvious surface tectonic activity, which implies large strain and regular brittle failure, i.e. ioquakes. A popular approach to estimate seismicity has been to use the (relatively well known) tidal dissipation and assume that a certain part of that energy is released seismically. Hurford et al. (2020) estimated the ratio between tidal dissipation and seismic energy over an orbital cycle for the Earth's moon to be $1.7 \cdot 10^{-3}$ and assumed that this ratio would be a good first order estimate for other tidally active worlds. From this assumption, they found that Io would release an annual seismic moment on the order of $5 \cdot 10^{19}$ Nm/a (see Table 1, where the values are per ten orbital cycles). Assuming that the largest possible ioquake releases 70% of the available moment (in analogy to Shallow Moonquakes), this implies that one to two magnitude 6 ioquakes would occur per month – a rate comparable to that of the Earth. The assumptions behind this scaling analysis may of course be simplistic, but it's nevertheless highly plausible that Io may be the most seismically active solid body after Earth. The existence of ridges structures oriented according to

Table 1 Estimated tidally-induced seismic moment in various planets, released over ten rotational cycles and per (terrestrial) year. The table is slightly modified from Hurford et al. (2020) and references therein. The columns are: m_{partner}, the mass of the partner body in the two-body system; T, the rotation period in (terrestrial) days, R, the radius of the planet; a, the half-axis, e, the ellipticity of the orbit, k_2/Q, the normalized tidal Love number, E_T, the estimated tidal dissipation energy; $\sum M_0$, the total seismic moment per ten orbital cycles; M_{w}, the equivalent moment magnitude. Note that this table assumes that the ratio of tidal dissipation to seismically released energy found on the moon ($1.7 \cdot 10^{-3}$) is applicable to the other worlds. Planets in italics are systems where tidal dissipation is due to rotation and not due to orbit eccentricity. For comparison, the average annual seismic moment release of the whole Earth is shown in the last column, illustrating that interior dynamics can lead to vastly higher seismicity.

	m_{partner} **[kg]**	T **[days]**	R **[km]**	a **[km]**	e **[%]**	k_2/Q	$\sum M_0$ **[Nm/10 cyc]**	M_{w}	$\sum M_0$ **[Nm/yr]**	M_{w}
Io	$1.90 \cdot 10^{27}$	1.769	1821.6	421,700	0.41	0.015	$2.3 \cdot 10^{18}$	6.2	$4.8 \cdot 10^{19}$	7.1
Europa	$1.90 \cdot 10^{27}$	3.551	1560.8	670,900	1	0.0054	$1.5 \cdot 10^{17}$	5.4	$1.5 \cdot 10^{18}$	6.1
Titan	$5.68 \cdot 10^{26}$	15.945	2575	1,200,000	2.88	0.004	$2.7 \cdot 10^{16}$	4.9	$6.2 \cdot 10^{16}$	5.1
Moon	$5.97 \cdot 10^{24}$	27.3	1737.2	384,399	5.5	0.0012	$8.0 \cdot 10^{14}$	3.9	$1.1 \cdot 10^{15}$	4.0
Enceladus	$5.68 \cdot 10^{26}$	1.37	252	237,948	0.47	0.0036	$1.0 \cdot 10^{14}$	3.3	$2.7 \cdot 10^{15}$	4.2
Earth/Lunar	–	1	–		–	–	$1.2 \cdot 10^{15}$	4	$4.4 \cdot 10^{16}$	5.0
Mars/Solar	–	1.03	–		–	–	$1.5 \cdot 10^{13}$	2.7	$5.3 \cdot 10^{14}$	3.8
Mars/Phobos	–	0.32	–		–	–	$1.6 \cdot 10^{10}$	0.7	$1.8 \cdot 10^{12}$	2.1
Mercury/Solar	–	58.65	–		–	–	$1.2 \cdot 10^{15}$	4	$7.5 \cdot 10^{14}$	3.8
Earth (tectonic)	–	–	–		–	–	–	–	$7.61 \cdot 10^{21}$	8.5

the directions of tidal stresses supports that tidally driven tectonism could be active (Bart et al., 2004).

While the existence of tectonic events is currently hypothetical, the volcanic activity of Io is obvious and documented photographically (Smith et al., 1979). One can thus expect to record seismic signals of the kind known from volcanos on Earth, i.e. distinct transient events as well as a more or less continuous tremor. Optical observation of volcanic centers on the surface could provide epicenter information and thus support the construction of travel time curves and the inversion for interior structure.

9.3 Mission perspectives

Despite the spectacular surface colors, landing on Io is actually not particularly dangerous, since the surface volcanism is locally constrained. A larger problem is Io's place very deep in Jupiter's gravity well, which would require considerable ΔV reserves and a launcher of SLS or Falcon Heavy class. The location in Jupiter's radiation belt poses a major design driver for lander electronics – contrary to orbiter missions which can minimize the radiation dose by performing only brief, repeated flybys, as in the IVO mission profile (Adams et al., 2012; McEwen et al., 2014), while a lander would need dedicated shielding of electronics.

A more realistic option for seismology may therefore be an orbital detection of seismic deformation using Interferometric Synthetic Aperture Radar (InSAR) during multiple flybys or deployment of a few retroflectors that can be queried with a laser on an orbiter. A more realistic option for seismology may therefore be an orbital detection of coseismic deformation using Interferometric Synthetic Aperture Radar (InSAR) during multiple flybys, a technique which is routinely applied to significant Earthquakes, or deployment of a few retroflectors that can be queried with a laser on an orbiter (Laser vibrometry, see de Kleer et al. (2019), and references therein). Via the latter, normal modes could be observed to constrain the deep interior of the planet, while the former would mostly serve to understand shallower lithospheric strength (Fig. 9).

10. Europa

10.1 Potential scientific goals

A liquid subsurface ocean on Europa was first predicted from the internal energy budget by radioactive decay and tides (Lewis, 1971; Cassen et al.,

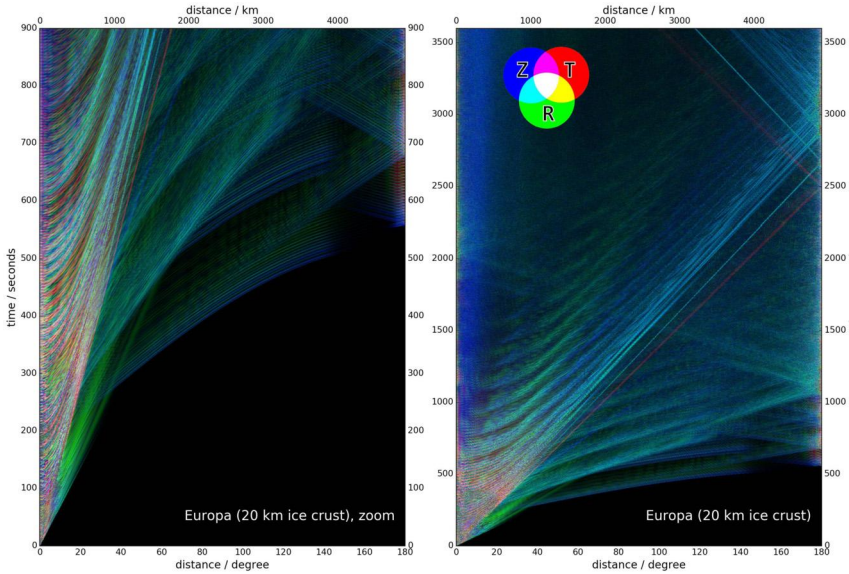

Figure 9 Global seismic wavefield stack for Europa, using an interior model of Vance et al. (2018b) with a crustal thickness of 20 km.

1979), and later supported by flyby measurements during the Galileo mission (Schubert et al., 2004). The thickness of the ice layer above the ocean is related to composition and temperature of the water; measurements of said value would therefore constrain these parameters, which have strong implications for habitability of the ocean. The ESA JUICE mission, as well as the NASA Europa Clipper will therefore both carry radars to measure the thickness during multiple flybys (Bruzzone et al., 2013; Phillips and Pappalardo, 2014). At this stage, the attenuation of electromagnetic waves by ice under Europa conditions is not well known, and the detection of a reflection of the ice bottom by either of the mission's radars is likely, but not certain (Eluszkiewicz, 2004; Aglyamov et al., 2017). A surface-deployed seismometer would be sensitive to ice thickness via 3 routes:

- A layer above a fluid half space forms a specific seismic phase, termed Crary phase after it's first descriptions on floating arctic ice (Press and Ewing, 1951; Crary, 1954). The phase is an almost monochromatic, radially horizontally polarized superposition of SV reverberations. Its central frequency is $f_{\mathrm{Cr}} = \frac{v_{\mathrm{S}}}{2d\sqrt{1-\left(\frac{v_{\mathrm{S}}}{v_{\mathrm{P}}}\right)^2}}$, where d is the ice thickness and v_{S}, v_{P} are S- and P-wave speeds, respectively. For the range of ice thicknesses predicted for Europa (5–30 km) (Vance et al., 2018a), f_{Cr} would

be between 0.11 Hz and 0.44 Hz, i.e. well-observable by a short period seismometer. This has made it a prominent candidate for ice thickness determination since 20 years (Kovach and Chyba, 2001); the phase is also well-determinable in synthetic seismograms (Stähler et al., 2018), but its robustness against heterogeneous ice of varying thickness is at this stage not known.

- Since the ocean cannot propagate shear waves, S-waves and specifically horizontally polarized SH waves will be reflected almost fully at the ice-ocean interface. Any seismic signal should therefore contain strong reverberations of shear waves, whose traveltime T_{rev} would be directly proportional to ice thickness d: $T_{\mathrm{rev}} = 2d/v_{\mathrm{S}}$. The observability of direct reverberating phases would be affected by seismic attenuation, which reduces shear wave amplitude strongest. However, the reverberating waves would also be present in the ambient seismic noise of Europa and could be retrieved by autocorrelation (Stähler et al., 2018).
- The ice thickness places an upper limit on the period of Rayleigh waves. If the ice is on the thinner side of previous estimates (below 10 km), this limit would be below 5 seconds, i.e. potentially observable by a short period sensor (Panning et al., 2006; Stähler et al., 2018).

All in all, the different potential observables provide a certain redundancy in determining the ice thickness using seismic methods, which is one of the reasons, why a seismometer has been an element of the Europa lander mission concept, that is currently awaiting NASA adoption and funding (Hand et al., 2017).

This mission described several other science goals of a seismometer, specifically to observe water or brine lenses within the ice. Seismic methods are usually good at detecting heterogeneities at depth, but as it was ruthlessly pointed out by (Grimm et al., 2021), the elastic impedance contrast between mushy ice and liquids is not particularly strong and determining even a "1D" layered seismic velocity profile below a lander is by no means a trivial process. Yet, the nonuniqueness of geophysical observations in a single station is even worse for electromagnetic, specifically potential-based methods. Also, Hobiger et al. (2021) demonstrated using InSight data that long-term observation of ambient vibrations at a single location can constrain even complicated subsurface structure, using geological context information, if available.

The habitability of Europa's ocean would be increased by transport of surface material into the ocean, since the Jovian radiation oxidizes surface material, creating a potential energy source for primitive life, if transferred

back into the ocean. Subduction in the ice has been proposed based on the geomorphology of linea on Europa's surface (Prockter and Pappalardo, 2000), but has not been observed in-situ. As InSight demonstrated on Mars, locations of seismic sources can be determined well using a single seismometer and shed light into the dominant tectonic process on a planet. Subduction zones on Earth cause well-observable continuous seismicity even in between the largest events, so a seismometer deployed close to a linea should be able to pick up its signature. This would confirm imaging data from orbit in one location and would allow inference over the whole planet (and in similar locations on Enceladus).

A separate question of high importance for habitability is the geological activity of the sea floor. The mid ocean ridges on Earth provide habitable environments independent of sunlight and subocean volcanism on Europa could play a similar role. Such activity, even in the past could be inferred from the chemistry of the dark patterns on Europa's surface, but europaquakes in the silicate crust or mantle would be a unique indication of current activity. Marusiak et al. (2022c) estimated that rocky europaquakes above magnitude 5 would be observable by a surface seismometer of the kind proposed for the Europa lander. Such magnitudes would be quite significant and are at the upper end of what is observed on Earth's mid-ocean ridges directly (not counting the adjacent transform faults, which often produce earthquakes of 7 and higher), but by no means impossible.

Finally, the sound speed in the ocean itself is affected by the ocean's chemistry. A final seismic velocity model of the planet at the end of the mission would be contingent of the ocean's salt content. Durán et al. (2022) demonstrated a fully consistent inversion of different seismic observables with other geophysical, as well as mineralogical data in a thermodynamically consistent model for Mars. Such an effort could be the final result of an observation campaign on Europa as well, delivering uncertainty limits on composition of the ocean, the thickness of the various layers and the wave speeds in the silicate interior.

10.2 Seismicity

Panning et al. (2018) estimated the seismicity rate of Europa based on the available energy from tidal dissipation to be between $10^{16} - 10^{18}$ Nm/a, which is above the value of $10^{15} - 10^{16}$ Nm/a observed for Mars (Banerdt et al., 2020), but 5 orders of magnitude below the Earth. Assuming this value is correct, a few dozen europaquakes from the icy crust should be observable over a month by a Europa seismometer as defined in (Hand et

al., 2017). Assuming that the ratio of tidal dissipation to seismic moment is about the same on all tidally active moons in the solar system (Hurford et al., 2020), Europa would be the second most active moon after Io (see Table 1).

10.3 Mission perspectives

Europa is challenging to land and operate on. Landing needs to be entirely propulsive, due to the lack of an atmosphere and Europa is deep in the gravity well of Jupiter. Since Europa is in the distance of highest radiation within Jupiter's magnetic field, a surface mission requires extensive and heavy metal shielding, which *worsens* the effect of the high-δV landing. Within realistic weight constraints, a surface mission is limited to a duration of a few weeks and a scientific payload of tens of kg. The Europa lander concept (Hand et al., 2017) managed to fit a seismometer into these constraints. The instrument would be similar in performance to the InSight SP seismometer (Lognonné et al., 2019; Pike et al., 2016), with the goal of listening to body waves of europaquakes in the ice. Observation of long period surface waves, flexural ice modes or normal modes of the whole planet would likely not be possible with an instrument of this sensitivity. The observability of seismic waves from quakes in the silicate mantle would highly depend on their magnitude, but would be made less likely by the presence of soft layers on the seafloor or the ice bottom (Marusiak et al., 2022c). In general, operation of a warm lander on ice will pose challenges to coupling of seismic sensors due to melting and tilting (Marusiak et al., 2022b).

A spacecraft in orbit at Jupiter distance can still operate on solar panels, but their size would be prohibitive for a landed mission. Power would therefore have to come from an RTG, or for a short-lived mission from high-power-density batteries.

The Europa Lander concept is the last iteration of a 3 decade long process of missions to explore the planets surface and interior. The ups and downs of this history are excellently described in Brown (2021). At this stage, it is a well-developed concept with a surface lifetime of 60-90 days. Yet, it would be the most expensive planetary robotic mission ever executed by NASA, which is why the Decadal Survey 2023–2033 did not recommend its execution as a Flagship mission until missions to Enceladus and Uranus have been realized.

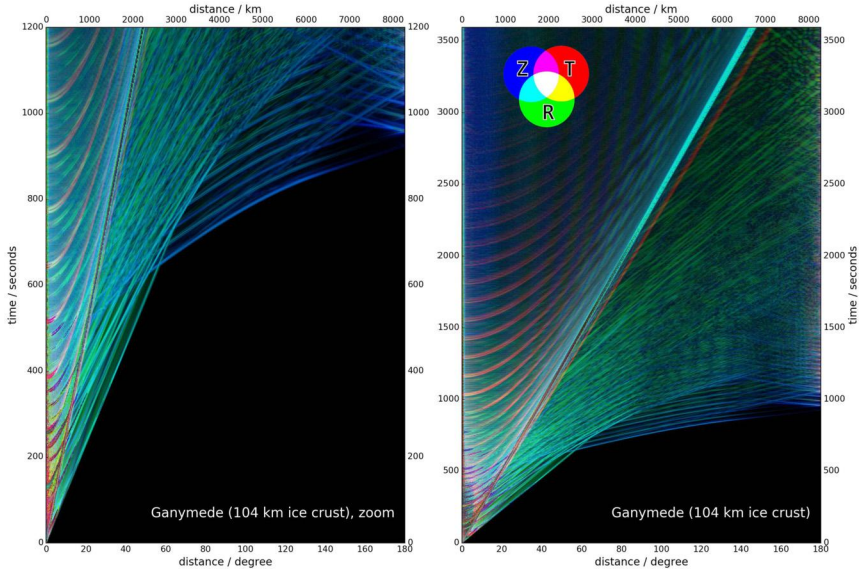

Figure 10 Global seismic wavefield stack for Ganymede, using the interior model of Vance et al. (2018b).

11. Ganymede and Callisto

11.1 Potential scientific goals

Ganymede, Callisto, and Titan form the three large ice moons of the solar system and yet, each one has at least one peculiarity that makes it difficult to sum them in one group: Ganymede is the only moon with a current-day magnetic field, Callisto has a very low moment of inertia, suggesting only partial differentiation (Nagel et al., 2004) and Titan is Titan (see next section). For all three planets, the low density implies an ocean deep enough for high-pressure ices to form, inhibiting flow of reductants from the mantle into the ocean (Vance et al., 2018b). The presence or absence of these ice layers however depends strongly on the salt content of the ocean, as well as on the poorly known equation of state of salty water at high pressures and low temperatures. Measuring the surface ice thickness could constrain the salt content of the ocean and thus the presence of a high pressure ice layer, even if no direct phases from the high pressure ice can be observed (Stähler et al., 2018). Seismology could therefore directly address questions of habitability (Vance et al., 2018a). In the case of Ganymede, quakes from beyond the core shadow could give insight into the size of a liquid core and the existence of a solid core, as implied by the magnetic field. For Cal-

listo, the question of differentiation of the rocky mantle could be answered much clearer by seismology than by moment of inertia (MoI) measurements from space. As described in Chapter 3 (Knapmeyer and Walterova, 2022), moment of inertia estimates can come with significant errors and lead to long-lived misestimation of core sizes (Fig. 10).

11.2 Seismicity

Ganymede shows strong indication of surface tectonics, although its age is difficult to estimate from existing images. Knowledge about current-day tectonics will improve significantly with data from the JUICE mission in the next decade. Callisto's heavily cratered surface indicates that current-day resurfacing and thus tectonic activity is limited. The higher distance to Jupiter, compared to Europa, means that the tidal energy budget for seismicity is low, but both planets have significant interior heat stored from formation that could drive tectonic deformation.

11.3 Mission perspectives

Tidal deformation, will be measured by the Ganymede Laser Altimeter GALA, to estimate the ice layer thickness (Enya et al., 2022) during the late stage of the JUICE mission, when the spacecraft is orbiting Ganymede. This may be seen as a long period proxy to seismology and likely the closest for some time. Landing on Ganymede or Callisto has been proposed since the Voyager age at least (Boain and Beckman, 1980) and penetrators have been proposed specifically by European institutions as payloads for Jupiter system flagship missions regularly (e.g. Vijendran et al., 2010), similar to the Huygens Titan probe on the Cassini mission. Just as regularly, these payloads were canceled to reduce mission complexity. After JUICE, another Ganymede mission with a lander to either Ganymede or Callisto is not likely to happen before the 2040s. In the meantime, one may watch the 1976 German dystopian movie "Operation Ganymed" starring Jürgen Prochnow about the difficult return of astronauts from a mission to find life on Jupiter's largest moon.

12. Titan

12.1 Potential scientific goals

Since Titan will be visited by a seismometer in 2034, the science goals of a seismic experiment have been described well already, see e.g. Barnes et

al. (2021) for an overview. A primary goal is the confirmation of a liquid ocean below the surface via observation of an interface with strong seismic impedance contrast at depth. A peak near 36 Hz in electric field signals measured during the Huygens descent were interpreted as the Schumann resonance of a 55–80 km deep conductor (Béghin et al., 2012), i.e. the ice-ocean interface. These values are plausible given thermodynamical modeling of the whole ice layer (Vance et al., 2018b), but far from undisputed. As on other ocean worlds, shear waves will be completely trapped in the ice layer and should lead to well observable reverberations. Compared to other ocean worlds, Titan is likely to harbor methane clathrates (i.e. ice-methane hybrids) near the surface (Mousis et al., 2015), which would have a significant effect on the thermal conductivity and therefore convection of the planet (Kalousová and Sotin, 2020). These clathrates will have reduced seismic velocities by up to 10% compared to pure ice (Marusiak et al., 2022a), which could be detectable by Rayleigh wave dispersion curves. An open question is the level of viscoelastic attenuation in the ice layer, given the high temperature of the ice below a few 100s of meters of depth. As described in Chapter 5 (Bagheri et al., 2022), ice has a very low quality factor $Q \approx 10$ at tidal periods, but the scaling to seismic frequencies is not well constrained.

Due to the existence of large lakes, as well as an atmosphere, Titan might be the only other place in the Solar System in which ocean-generated microseisms can be observed (Stähler et al., 2019). A seismometer deployed north of 60° latitude could likely observe the waves created on Kraken mare by a hurricane, enabling remote sensing of the atmosphere.

12.2 Seismicity

The tidal deformation of Titan's ice crust (Mitri et al., 2007) shown by Cassini gravity measurements is a plausible source of seismic activity. While Titan's orbital period is significantly higher than Europa's or Ganymede's (15.9 vs 3.6/7.2 d), its orbit's high eccentricity could allow tidal forces to drive significant tectonism (see Table 1). Whether or not the rocky core of the planet shows significant tectonic activity, is unknown. As on Europa, the science value of detecting quakes from the core would be high, since it seafloor tectonics would enrich the ocean with potential nutrients, but the detection limit is significantly higher than for an iceshell quake.

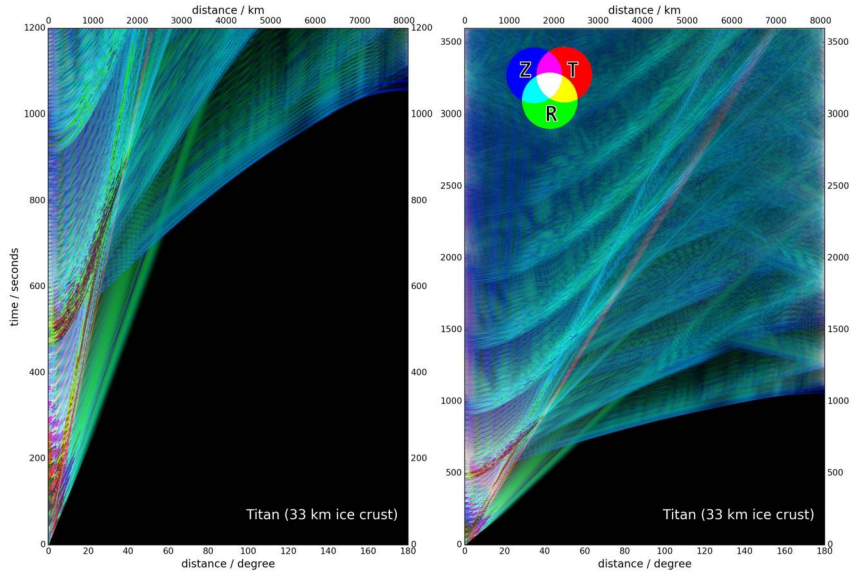

Figure 11 Global seismic wavefield stack for Titan, using an interior model from Vance et al. (2018b) with a crustal thickness of 33 km.

12.3 Mission perspectives

Titan is one of the 2 places in the solar system with a seismic experiment in preparation: The dragonfly lander will be launched in 2027 and deploy a relocatable octocopter on Titan in 2034. The mission will contain a single vertical component seismometer, delivered by JAXA and based on the instrument planned for the Lunar-A mission (Mizutani, 1995; Shiraishi et al., 2008), plus two or more horizontal geophones. The instrument will not be comparable to the InSight VBB seismometer, but should be able to detect local seismicity.

13. Enceladus

13.1 Potential scientific goals

Enceladus is the only ocean world where water from the subsurface ocean is accessible in situ without drilling through kilometers of ice. A long-lived plume of water vapor and ice has been observed near five distinct fissures (called tiger stripes) near Enceladus' south pole (see Fig. 13). The Cassini orbiter was able to probe these ejecta directly and found strong indications for a source in the subsurface ocean (Teolis et al., 2017). This means that a

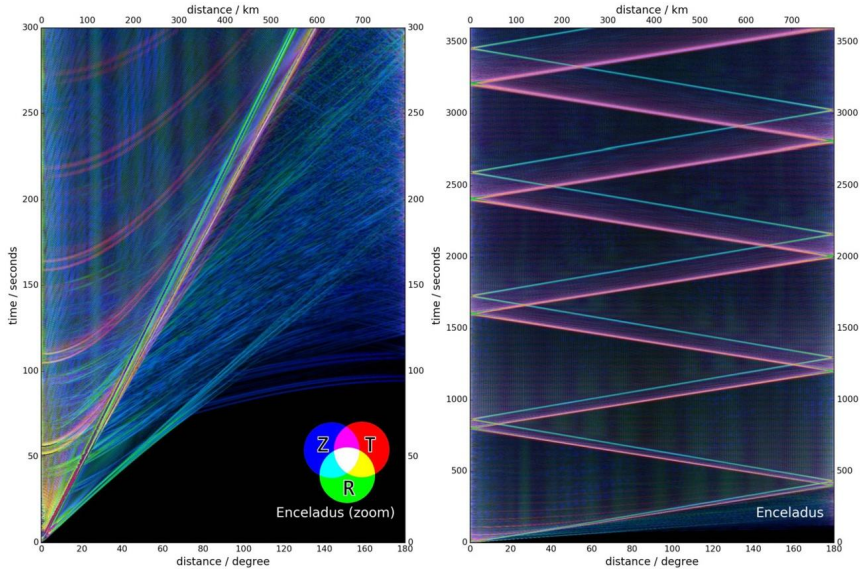

Figure 12 Global seismic wavefield stack for Enceladus, using an interior model from Vance et al. (2018b). Note that for modeling reasons, a constant ice thickness of 15 km over the whole planet is assumed, while it gravimetric observations indicate that the ice is significantly thinner near the south pole (Porco et al., 2006).

mission to Enceladus would be directly tasked with determining whether the ocean supports life today or at least has done so in the past (Choblet et al., 2021).

13.2 Seismicity

Enceladus has a tidal dissipation larger than Earth's moon, but at a radius of only 252 km. It can therefore be expected that the strain rate of the crust is very significant. The water plume sources near the tiger stripes could produce similar long-duration seismic signals as geysers on Earth. The small diameter and relatively thick ice layer facilitates seismic waves orbiting the planet multiple times (Fig. 12).

13.3 Mission perspectives

Sampling the plumes could be done from orbit, but the high impact velocities would limit the observability of large molecules (as it has been the case for Cassini's measurements), so the science return of a lander would be significantly higher. The last decadal survey recommended an Enceladus

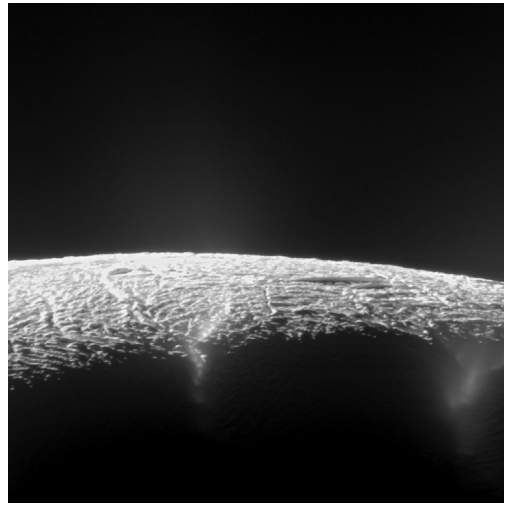

Figure 13 Cassini image of two "tiger stripe" fissures near Enceladus' south pole with water vapor emerging (visible against the dark surface below the terminator). The fissures have been identified as the source of the plumes by (Porco et al., 2014). Image by NASA/JPL/Space Science Institute, PIA 17183.

orbiter at low priority, so the design has been updated into a "Orbilander" concept, i.e. an orbiter that is capable of landing on the surface after an extended reconnaissance and remote sensing phase (MacKenzie et al., 2021). The current decadal survey (Nat. Academies, 2022) recommended this mission concept as a flagship mission after finalization of the Uranus orbiter mission, with a launch date after 2037 and landing during favorable communication geometries to Earth in the 2050s.

14. The Uranus and Neptune system

Uranus and Neptune are the two ice giants of the solar system and are thereby representing a class of planets that is very common amongst exoplanets discovered so far. Both of them have a number of planet-like moons that are potential targets for landed missions. However, all of them are known from a few images only, obtained during the flyby of Voyager 2 through the Uranus (Stone, 1987) and Neptune systems (Stone and Miner, 1989) in 1987 and 1989, respectively. Primary science goals would therefore be to research the surface geology, including geomorphology.

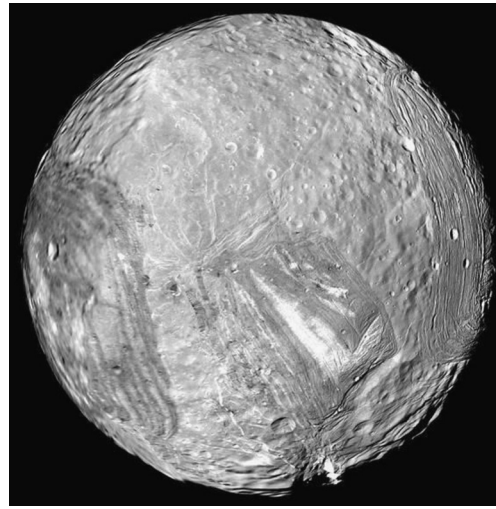

Figure 14 Voyager 2 image of the Uranus moon Miranda. The surface shows linea and TODO. Image by NASA/JPL, PIA 18185.

14.1 Potential scientific goals

Uranus has 4 large moons, Ariel, Umbriel, Titania and Oberon, between 1100 and 1550 km radius, all of which have densities between 1.4–1.7 grams per cubic cm, implying a rock to ice ratio of 2 to 3. A fifth large moon, Miranda, has a diameter of 470 km, but a density of only 1.2 g/cm^3, implying an even higher amount of water ice. The surface morphology of Miranda (Fig. 14) implies that the outer ice layer underwent subduction-like processes in the past, at a similar rate to Europa (Hammond and Barr, 2014; Stern et al., 2018), which suggests that due to tidal heating, a significant part of this ice was in liquid form at least at one point in the past (Nimmo and Pappalardo, 2016). An Uranus orbiter mission will perform dedicated flybys on the large moons and thereby constrain their interiors from gravimetric measurements, similar to what Galileo did in the Jupiter system (Sohl and Spohn, 1997). The question whether the liquid ocean still exists today is one that could be answered by a seismic experiment (see the Europa section for details), but as on Europa and Titan, measuring the seismicity of the planet alone would go a long way in constraining its energy budget.

Neptune has one major moon: Triton, which is comparable in size to the Jovian moon Europa and at an average density of 2.061 g/cm^3 widely understood to be covered by several hundred km of frozen or liquid ice

(Nimmo and Pappalardo, 2016). As on the icy moons of the gas giants, the thickness of the ice and the existence and depth of a potential ocean would be primary science targets for a seismic installation. A unique feature of Triton is its retrograde orbit, which is not found for any other moon of comparable size (the next largest moon, Phoebe with a retrograde orbit around Saturn, has only 0.08 times the mass of Triton), likely the result of capture, possibly due to collision with an original satellite. Similar to Europa, Triton has a relatively young surface age, around 100 Ma (Stern and McKinnon, 2000), as demonstrated by the small number of visible impact craters, implying geological activity over most of the age of the solar system and therefore most likely until today. As on Europa, a relatively thin ice shell opens the possibility of ice convection, potentially even subduction and thus the possibility of large thrust faults with tritonquakes of magnitudes of 5 and larger.

Of the other neptunian moons, two (Proteus and Nereid) are around 400 km in diameter, but both are irregular in shape, and possibly formed during the capture of Triton (Goldreich et al., 1989), when the natural neptunian satellites were cannibalized or deorbited by the newcomer.

14.2 Seismicity

No estimations of the level of seismicity of these moons are available up to now.

14.3 Mission perspectives

The Decadal Survey 2023–2033 (Nat. Academies, 2022) recommended a flagship mission to one of the ice giants, and preferred a Cassini-like orbiter in the Uranus system over one to Neptune, on grounds of feasibility. Specifically, launch opportunities arise in 2031 and 2032 for a 13 year cruise without the need of inner solar system gravity assists. A Neptune mission would require significant technical development, specifically relies on the SLS rocket, while planning for a Uranus orbiter could start immediately. ESA's "Voyage 2050" report (Tacconi et al., 2021) has expressed interest in contributing an atmospheric entry probe or moon lander to a NASA flagship mission to an ice giant, similar to the Cassini/Huygens contribution, where ESA delivered the Huygens Titan lander. The next years will show whether this contribution will materialize and whether it will be in form of a Uranus entry probe or a lander on Miranda or another large moon.

A mission to the Neptune system is therefore very unlikely to be even considered before the 2040s. At this time, there would likely be a push for such a mission to contain at least a short-lived lander probe to Triton.

Due to the distance to the sun, solar power is not feasible for sustained operation and as for the Europa Lander, such a mission would have to rely on high performance batteries or RTGs.

15. Interstellar objects

15.1 Potential scientific goals

The first discovery of an interstellar object is less than five years old, when 1I/2017 U1 ('Oumuamua) was observed on 2017 October 19 by the Pan-STARRS1 telescope system and confirmed to be traveling on a hyperbolic orbit, i.e. not been bound by the sun's gravity (Meech et al., 2017). The limited amount of observations that were possible in the short time window of observation confirmed a rocky, red surface without any trace of degassing, as it would be observed for a comet from the Solar System's Oort cloud (Bannister et al., 2019). Surprisingly, a second interstellar object was found only 2 years later, this time before aphelion, so that its dynamical behavior during approximation of the sun could be observed and the object 2I/Borisov could be confirmed to be an ice-rich comet (Bodewits et al., 2020; Guzik et al., 2020).

The investigation of interstellar objects is obviously interesting. Interstellar objects entering the solar system on hyperbolic trajectories are the only solid matter from outside the solar system that will be accessible to in situ characterization in the foreseeable future. A lander mission would carry simple instruments to obtain a chemical composition of the top layers. The rigidity of the object however is difficult to assess from the outside, but the distinction on whether the object is a homogeneous body, an ice-rock mixture or even a "rubble ball", a very weakly consolidated object, is of high interest to constrain the source context. The SESAME/CASSE seismic experiment on the Philae mission to comet 67P/Churyumov-Gerasimenko showed a mechanically extremely weak core below a harder surface layer (Knapmeyer et al., 2018). The latter is likely the result of previous encounters of the comet to the sun (Groussin et al., 2019). Whether similar layering exists for true interstellar objects would be quite interesting. As the contact of the TAG sampler on the OSIRIS-REx mission to Bennu showed, even asteroids can have surprisingly low rigidity in its uppermost layers (Berry et al., 2022).

15.2 Seismicity

Interstellar objects of the size encountered so far are unlikely to sustain significant tectonic activity themselves. A possible mechanism for seismic sources is thermal stress induced by the approximation of the sun or cooling while leaving the solar system. Another option would be the combination of a slow impactor mission with a landed seismometer or some kind of repeatable source on the lander, like the hammering devices used on Philae and InSight, or the mortars used on Apollo 14 and 16.

15.3 Mission perspectives

The observation of two interstellar objects in relatively short time has triggered significant interest in developing a mission for in situ exploration of objects to be detected in the near future (Hein et al., 2019; Seligman and Laughlin, 2018; Castillo-Rogez et al., 2019). Proposals exist for missions that are prepared and wait in storage for the discovery of a suitable object, either on Earth, or the sun-earth L2 point. Even though fly-by missions are significantly easier, a lander using solar-electric propulsion could be feasible (Hein et al., 2022). A landed mission would bear similarity to Philae on the ESA Rosetta mission and could do seismic or acoustic investigations to constrain subsurface properties either during landing Biele et al. (2015) or by listening to seismic waves excited during operation of a drill or similar instrument (Knapmeyer et al., 2016, 2018). The intercept point to any interstellar object would likely be outside of Jupiter's orbit and therefore solar energy is not an option for a small lander. The lifetime of a surface mission would therefore be limited by battery capacity and seismic experiments would be coordinated with sampling or impactor operations. The primary mission of Philae on comet 67P, sustained by the primary battery only, for example, was about 68 hours.

16. Lessons learned from Insight

16.1 Scattering

Terrestrial seismology builds on clearly separated arrivals of ground motion, called "phases". Only the fact that seismic waves travel mostly unperturbed through the earth and thus arrive in short pulses made it possible to disentangle the plethora of signals being reflected and converted at various layers and interfaces inside the planet. A necessary condition for such clean phases is that the length scale of heterogeneities inside the planet is larger than the

wave lengths involved (Aki and Richards, 2002). The first seismograms observed on the moon showed that this condition is not fulfilled there and that instead, the lunar crust scatters all seismic phases beyond recognition (Blanchette-Guertin et al., 2012). The classical explanation for this is a high impact rate due to the lack of an atmosphere and a lack of mechanisms to heal small cracks, due to the absence of fluids, combined with very low intrinsic attenuation, again due to extremely low water content. Preliminary analyses of Martian seismic data showed surprisingly high amount of scattering (Menina et al., 2021; Karakostas et al., 2021), at least close to the InSight landing site. Since this scattering seems limited to the uppermost kilometers, investigations of "clean" mantle phases were possible nevertheless (Durán et al., 2022; Drilleau et al., 2022).

It is likely however, that at least all airless rocky planets (Mercury) will be more similar to the Moon in terms of problematic scattering. Strongly cratered icy worlds like Ceres or Callisto might be similar, while the tidal heating in Europa, Titan and Enceladus may lead to ductile deformation of the crust and healing of heterogeneities.

This scattering will affect single station, three component seismic measurements. It is possible that gradiometric measurements, e.g. measurements of rotational motion (Bernauer et al., 2021) or distributed measurements at multiple locations (Walter et al., 2020) could allow to detect coherent wavefronts even in presence of strong scattering. However, sensitivity of such sensors is typically too low for planetary applications still (Bernauer et al., 2020), even though the field is rapidly progressing, e.g. with the PIONEERS sensor currently developed by a European collaboration (Garcia et al., 2019a).

16.2 Timing

The Sesame Casse experiment on the ESA Rosetta mission was the first seismic experiment that used vibrations from a mechanical hammer as source in 2014. An issue encountered in the analysis, was the limited coordination between instruments. A dedicated trigger line from the MUPUS hammer to the SESAME recording system was considered too complex in the preparation phase. Instead, the two instruments exchanged messages in a common part of the onboard computer memory to coordinate hammering and recording, and an on-ground assessment of the seven involved clocks and their individual drift rates was carried out during the evaluation (Knapmeyer et al., 2016). This made initial experimentation much more difficult (Knapmeyer et al., 2018). The Rosetta mission was launched in 2004,

the problem was encountered in 2014, but surprisingly, the same problem occurred again during the InSight HP3 seismic experiment, launched in 2018, when the seismometer SEIS was listening for seismic waves produced by the hammer of the HP^3 heat flow probe (Spohn et al., 2021; Sollberger et al., 2021). The lack of a joint time signal between the two instruments HP^3 and SEIS meant that a convoluted process was necessary to infer the exact time of each hammer blow from the seismic signal itself, significantly increasing the uncertainty of the observation. Since the distance between any hammering or drilling instrument and a seismic sensor is unlikely to be more than a few meters and seismic velocities > 500 m/s are expected, the precision of the joint timing source needs to be < 100 μs, which is below the typical resolution of spacecraft bus clocks.

16.3 Bandwidth

InSight was able to transmit 6 seismic channels of 20 sps each over much of the mission due to availability of orbiters with relay capacity (Odyssey, Mars Reconnaissance Orbiter and the ESA Trace Gas Orbiter). This far exceeded the premission planning, where a single 10 sps vertical channel and the 3 native channels of the seismometer were foreseen. In retrospect, one event type, the "super high frequency events", likely thermal cracking near the lander, would not have been detected with the original configuration (Dahmen et al., 2020), while another type, the very high frequency events, would have been much more difficult to spot, given that their energy is mainly on the horizontal channels above 2 Hz. It was specifically foreseen to retrieve higher bandwidth data of specific events by manual requests. Such events were either to be detected in the low bandwidth streams or in one specific "ESTA-SP" channel, that contained the integrated signal energy in a narrow frequency band above 10 Hz. This process worked successfully overall, with the caveat that the ESTA-SP channel was polluted too much by glitches and wind-related transient signals to be of much use overall.

Any future seismic mission (save for a lunar one) will likely be dramatically more constrained in terms of bandwidth, so that only a subset of data can be transmitted. At the same time, low sampling rates risk omitting interesting signals of local events. Classic, lossless seismic compression (Ahern et al., 2012) reduces the amount of data by 30–50%, which is by far not enough.

Another possibility would be advanced preprocessing of data onboard. Fig. 15 (top) shows a spectrogram of 26 hours of vertical component VBB

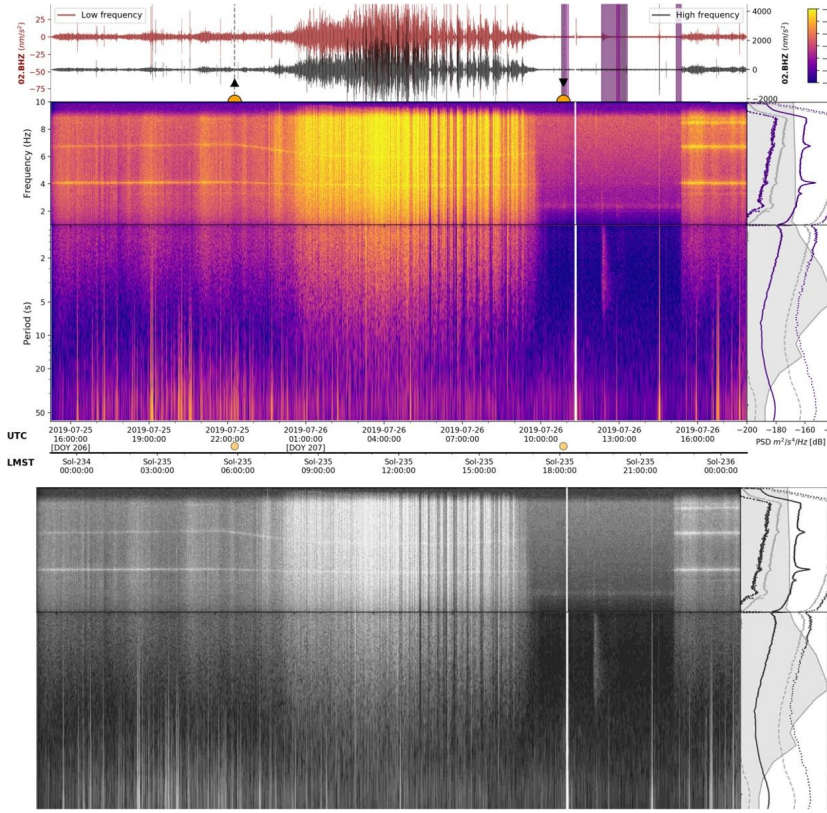

Figure 15 Top: Spectrogram of one Sol of seismic data, plot in the style of Giardini et al. (2020), fig. 1a. 3 marsquakes can be identified easily. Bottom: Same plot, subjected to level 10% lossy JPEG compression. The size of this figure is 108 kByte, i.e. 2% of the original seismic data, yet the marsquake time windows can still be identified.

data of InSight, as described by (Giardini et al., 2020). Over the course of the day, the wind noise increased dramatically over noon, masking all potential marsquakes. In the evening, S0235b, the highest SNR event of the first Martian year, can be seen. This spectrogram is equivalent to 24.7 3600 20 24 = 41.4 MBit or 5.2 MByte of seismic data. As described in (Clinton et al., 2021), operationally, all significant marsquakes can be easily detected in one such spectrogram. Fig. 15 (bottom) shows the same spectrogram as JPEG graphic, stored with high compression. The 3 marsquakes can still be detected in this graphic, yet the file size of this graphic is 108 kByte, i.e. 2% of the original seismic data. From this small file, interesting time windows could easily be identified for transfer of data at full bandwidth.

Whether spectrograms or similar, wavelet based time-frequency representations are the optimal way of producing low bandwidth daily overview files needs to be investigated and weighted against the computational power available onboard.

For certain mission concepts in the outer solar system, e.g. the Europa Lander (Hand et al., 2017), the short mission duration will require the lander to exercise its scientific campaign mostly autonomously without "Earth in the loop". This may mean that seismic events need to be identified autonomously by the lander itself. Given the phenomenology of nonseismic events, even in terrestrial planets (Ceylan et al., 2021; Dahmen et al., 2021; Stähler et al., 2020), let alone on icy ocean worlds, this process is nontrivial and will require significant theoretical work over the next years. Given the surprises we saw with both moonquakes and marsquakes, it is unlikely that a fully autonomous processing can find all kinds of events without prior knowledge of typical examples.

17. Conclusion

The InSight mission to Mars has demonstrated that even a single, two year seismometer mission is enough for a first global determination of the deep interior of a planet. It did confirm geodetic observations from orbit concerning the core radius, as well as imaging-based inferences of current day tectonics in Cerberus Fossae. Furthermore, it allowed to constrain previously inaccessible parameters, such as the crustal thickness or the rate of quakes. Finally, unexpected discoveries were made, such as the high amount of scattering in the shallow crust or the strong concentration of seismicity in Cerberus Fossae. The seismic observations, like travel times also provide a quantitative dataset to test future interior models of Mars against for the coming decades.

A similar dataset would be highly valuable for any of the other planets and moons of the solar system. Yet, given the difficulty and cost of landing, it needs to be weighted against orbital data, geodetic, radar or image based, which is easier to obtain. From a purely subjective perspective, five questions stand out that can be only addressed by seismology.

1. The tectonic mechanisms of Mars. InSight has shown that seismicity on the red planet is very focused on one young volcanic feature: Cerberus Fossae. This suggests that seismicity needs weakening of the crust by locally high heat flow, with constraints on the crustal thickness and

composition. Cerberus Fossae would therefore be a unique place in the solar system to study coseismic crustal deformation of terrestrial planets.

2. The tectonic context of samples on Ceres. A Ceres sample return mission in Occator crater would rely heavily on knowledge of the age and deposition mechanism of these briny samples. Even a low-sensitivity seismometer could pick up small quakes near the landing site to determine whether signals related to active cryovolcanism exist and suggest a young age of the deposits.
3. The ice thickness and ocean depth of Europa and Titan. The Europa Clipper radar will have a good shot at finding a reflection from the ice-ocean interface, but the success of this measurement is subject to the poorly constrained electromagnetic absorption in the icy crust. Yet, the crustal thickness and ocean depth are the strongest quantitative constraints on composition of the ocean and thus its habitability. A seismic experiment could give an independent constraint. Hopefully, the Dragonfly seismometer will perform good enough to prove this concept.
4. The formation history and tidal heating of the large moons. The four Galilean moons differ so strongly in their interior profiles (as constrained from geodetic data) that it is difficult to judge whether our formation models work on them. Given that tidally heated planets and moons in resonance might be significantly more common in other planetary systems (think of Trappist-1), constraining even only the interior of Ganymede or Io seismically would go a long way in calibrating the models we apply to exoplanets.
5. The meteoroid impact rate throughout the solar system. At the time of writing, there are no confirmed detections of meteoroid impacts by InSight, even though candidate signals exist and are reviewed. The rate of crater formation is assumed to be known when determining the age of planetary surfaces, yet the rate of new impacts cannot be constrained well, due to the strong effect of target material on observability of fresh craters. A seismic observatory on a planet can constrain this rate directly, which also has a direct implication for estimating the density of small bodies in the solar system and the resulting hazard for Earth and interplanetary spaceflight.

The experience from InSight will make it possible to build smaller, low-power seismometers, which can be added to any future landed mission at a low cost in terms of complexity and energy.

References

Adams, E., et al., 2012. Io Volcano Observer's (IVO) integrated approach to optimizing system design for radiation challenges. In: 2012 IEEE Aerospace Conference, pp. 1–13.

Aglyamov, Y., Schroeder, D.M., Vance, S.D., 2017. Bright prospects for radar detection of Europa's ocean. Icarus 281, 334–337. https://doi.org/10.1016/j.icarus.2016.08.014.

Ahern, T.K., et al., 2012. Seed Reference Manual. Tech. Rep. p. 224.

Aki, K., Richards, P.G., 2002. Quantitative Seismology, Vol. II. Ellis, J. (Ed.), 2nd edition. University Science Books. ISBN 0-935702-96-2. p. 700.

Anderson, D.L., Miller, W.F., et al., 1977. Seismology on Mars. Journal of Geophysical Research 82 (28), 4524–4546. https://doi.org/10.1029/JS082i028p04524.

Anderson, R.C., Dohm, J.M., et al., 2001. Primary centers and secondary concentrations of tectonic activity through time in the western hemisphere of Mars. Journal of Geophysical Research: Planets (ISSN 2156-2202) 106 (E9), 20563–20585. https://doi.org/10.1029/2000JE001278.

Astiz, L., Earle, P., Shearer, P.M., 1996. Global stacking of broadband seismograms. Seismological Research Letters 67 (4), 8–18. https://doi.org/10.1785/gssrl.67.4.8.

Bagheri, A., et al., 2022. Tidal insights into rocky and icy bodies: an introduction and overview. In: Geophysical Exploration of the Solar System. In: Advances in Geophysics.

Banerdt, W.B., Smrekar, S., et al., 2020. Initial results from the InSight mission on Mars. Nature Geoscience 13 (3), 183–189. https://doi.org/10.1038/s41561-020-0544-y.

Bannister, M.T., et al., 2019. The natural history of 'Oumuamua. Nature Astronomy (ISSN 2397-3366) 3 (7), 594–602. https://doi.org/10.1038/s41550-019-0816-x.

Barba, N., et al., 2021. Access to Mars surface using a low-cost rough lander. In: 2021 IEEE Aerospace Conference (50100), pp. 1–7. https://doi.org/10.1109/AERO50100.2021.9438338.

Barnes, J.W., et al., 2021. Science goals and objectives for the dragonfly Titan rotorcraft relocatable lander. Planetary Science Journal (ISSN 2632-3338) 2 (4), 130. https://doi.org/10.3847/PSJ/abfdcf.

Bart, G.D., et al., 2004. Ridges and tidal stress on Io. In: Special Issue: Io After Galileo. Icarus (ISSN 0019-1035) 169 (1), 111–126. https://doi.org/10.1016/j.icarus.2004.01.003.

Béghin, C., et al., 2012. Analytic theory of Titan's Schumann resonance: constraints on ionospheric conductivity and buried water ocean. Icarus (ISSN 0019-1035) 218 (2), 1028–1042. https://doi.org/10.1016/j.icarus.2012.02.005.

Bernauer, F., Behnen, K., Wassermann, J., et al., 2021. Rotation, strain, and translation sensors performance tests with active seismic sources. Sensors 21 (1), 264. https://doi.org/10.3390/s21010264.

Bernauer, F., Garcia, R.F., Murdoch, N., et al., 2020. Exploring planets and asteroids with 6DoF sensors: utopia and realism. Earth, Planets and Space 72 (1), 191. https://doi.org/10.1186/s40623-020-01333-9.

Berry, K., et al., 2022. Contact with Bennu! Flight performance versus prediction of OSIRIS-REx "TAG" sample collection. In: AIAA SCITECH 2022 Forum. American Institute of Aeronautics and Astronautics. https://doi.org/10.2514/6.2022-2521.

Biele, J., et al., 2015. The landing(s) of Philae and inferences about comet surface mechanical properties. Science 349 (6247), aaa9816. https://doi.org/10.1126/science.aaa9816.

Blanchette-Guertin, J.-F., Johnson, C.L., Lawrence, J.F., 2012. Investigation of scattering in lunar seismic coda. Journal of Geophysical Research 117 (E6), E06003. https://doi.org/10.1029/2011JE004042.

Bland, M.T., et al., 2019. Dome formation on Ceres by solid-state flow analogous to terrestrial salt tectonics. Nature Geoscience (ISSN 1752-0908) 12 (10), 797–801. https://doi.org/10.1038/s41561-019-0453-0.

Boain, R.J., Beckman, J.C., 1980. A Ganymede lander mission. In: Astrodynamics Conference, p. 142.

Bodewits, D., et al., 2020. The carbon monoxide-rich interstellar comet 2I/Borisov. Nature Astronomy (ISSN 2397-3366) 4 (9), 867–871. https://doi.org/10.1038/s41550-020-1095-2.

Brissaud, Q., et al., 2021. The first detection of an earthquake from a balloon using its acoustic signature. Geophysical Research Letters 48 (12), e2021GL093013. https://doi.org/10.1029/2021GL093013.

Brown, D.W., 2021. The Mission. Custom House. ISBN 978-0-06-308557-2.

Bruzzone, L., et al., 2013. RIME: Radar for Icy Moon Exploration. In: 2013 IEEE International Geoscience and Remote Sensing Symposium – IGARSS. IEEE. ISBN 978-1-4799-1114-1, pp. 3907–3910. https://doi.org/10.1109/IGARSS.2013.6723686.

Bullen, E.K., 1956. Seismology and the broad structure of the Earth's interior. Physics and Chemistry of the Earth 1, 68–93. https://doi.org/10.1016/0079-1946(56)90006-4.

Bulow, R.C., Johnson, C.L., Shearer, P.M., 2005. New events discovered in the Apollo lunar seismic data. Journal of Geophysical Research: Planets 110 (E10), 2156–2202. https://doi.org/10.1029/2005JE002414.

Byrne, P.K., 2020. A comparison of inner solar system volcanism. Nature Astronomy 4 (4), 321–327.

Byrne, P.K., Klimczak, C., et al., 2014. Mercury's global contraction much greater than earlier estimates. Nature Geoscience (ISSN 1752-0908) 7 (4), 301–307. https://doi.org/10.1038/ngeo2097.

Byrne, P.K., Krishnamoorthy, S., 2022. Estimates on the frequency of volcanic eruptions on Venus. Journal of Geophysical Research: Planets (ISSN 2169-9100) 127 (1), e2021JE007040. https://doi.org/10.1029/2021JE007040.

Cassen, P.S., Peale, J., Reynolds, R.T., 1979. Is there liquid water on Europa? Geophysical Research Letters 6, 731–734.

Castillo-Rogez, J.C., Meech, K., et al., 2019. Approach to exploring interstellar objects and long-period comets. In: Topputo, F., et al. (Eds.), 29th AAS/AIAA Space Flight Mechanics Meeting. American Astronautical Society, San Diego, CA. ISBN 978-0-87703-659-3, pp. 2115–2128. 68.

Castillo-Rogez, J.C., Brophy, J., et al., 2022. Concepts for the future exploration of dwarf planet Ceres' habitability. Planetary Science Journal (ISSN 2632-3338) 3 (2), 41. https://doi.org/10.3847/PSJ/ac34ee.

Ceylan, S., Clinton, J., Giardini, D., et al., 2021. Companion guide to the marsquake catalog from InSight, Sols 0–478: data content and non-seismic events. Physics of the Earth and Planetary Interiors 310, 106597. https://doi.org/10.1016/j.pepi.2020.106597.

Chau, A., et al., 2018. Forming Mercury by giant impacts. The Astrophysical Journal (ISSN 0004-637X) 865 (1), 35. https://doi.org/10.3847/1538-4357/aad8b0.

Choblet, G., et al., 2021. Enceladus as a potential oasis for life: science goals and investigations for future explorations. Experimental Astronomy (ISSN 1572-9508). https://doi.org/10.1007/s10686-021-09808-7.

Clinton, J.F., et al., 2021. The marsquake catalogue from InSight, Sols 0–478. Physics of the Earth and Planetary Interiors 310. https://doi.org/10.1016/j.pepi.2020.106595.

Crary, A.P., 1954. Seismic studies on Fletcher's ice island, T-3. Transactions, American Geophysical Union 35 (2), 293. https://doi.org/10.1029/TR035i002p00293.

Dahm, C.G., 1934. New values for dilatational wave-velocities through the Earth. Eos, Transactions American Geophysical Union (ISSN 2324-9250) 15 (1), 80–83. https://doi.org/10.1029/TR015i001p00080.

Dahmen, N.L., Clinton, J., et al., 2020. Super high frequency events: a new class of events recorded by the InSight seismometers on Mars. Journal of Geophysical Research: Planets. https://doi.org/10.1029/2020je006599.

Dahmen, N.L., Zenhäusern, G., et al., 2021. Resonances and lander modes observed by InSight on Mars (1–9 Hz). Bulletin of the Seismological Society of America (ISSN 0037-1106) 111 (6), 2924–2950. https://doi.org/10.1785/0120210056.

Dmitrovskii, A.A., et al., 2022. Constraints on the interior structure of Phobos from tidal deformation modeling. Icarus (ISSN 0019-1035) 372, 114714. https://doi.org/10.1016/j.icarus.2021.114714.

van Driel, M., Krischer, L., Stähler, S.C., et al., 2015. Instaseis: instant global seismograms based on a broadband waveform database. Solid Earth (ISSN 1869-9529) 6 (2), 701–717. https://doi.org/10.5194/se-6-701-2015.

Drilleau, M., Samuel, H., Garcia, R.F., et al., 2022. Marsquake locations and 1-D seismic models for Mars from InSight data. Journal of Geophysical Research: Planets. https://doi.org/10.1002/essoar.10511074.2. In press.

Durán, C., Khan, A., Ceylan, S., et al., 2022. Seismology on Mars: an analysis of direct, reflected, and converted seismic body waves with implications for interior structure. Physics of the Earth and Planetary Interiors (ISSN 0031-9201) 325, 106851. https://doi.org/10.1016/j.pepi.2022.106851.

Durante, D., Iess, L., 2021. A peek into Jupiter's normal modes from Juno gravity data. In: EGU General Assembly. Online, EGU21–15398. https://doi.org/10.5194/egusphere-egu21-15398.

Eluszkiewicz, J., 2004. Dim prospects for radar detection of Europa's ocean. Icarus (ISSN 0019-1035) 170 (1), 234–236. https://doi.org/10.1016/j.icarus.2004.02.011.

Enya, K., et al., 2022. The Ganymede Laser Altimeter (GALA) for the Jupiter icy moons explorer (JUICE): mission, science, and instrumentation of its receiver modules. Advances in Space Research (ISSN 0273-1177) 69 (5), 2283–2304. https://doi.org/10.1016/j.asr.2021.11.036.

Ernst, C.M., et al., 2021. Mercury lander: planetary mission concept study for the 2023–2032 decadal survey. arXiv:2107.06795 [astro-ph].

Foster, C., Daniels, M., 2010. Mission opportunities for human exploration of nearby planetary bodies. In: AIAA SPACE 2010 Conference & Exposition. American Institute of Aeronautics and Astronautics, Anaheim, California. ISBN 978-1-60086-966-2. https://doi.org/10.2514/6.2010-8609.

Fuller, J., 2014. Saturn ring seismology: evidence for stable stratification in the deep interior of Saturn. Icarus (ISSN 0019-1035) 242, 283–296. https://doi.org/10.1016/j.icarus.2014.08.006.

Garcia, R.F., Martire, L., et al., 2021. An active source seismo-acoustic experiment using tethered balloons to validate instrument concepts and modelling tools for atmospheric seismology. Geophysical Journal International (ISSN 0956-540X) 225 (1), 186–199. https://doi.org/10.1093/gji/ggaa589.

Garcia, R.F., Shariati, S., Guattari, F., et al., 2019a. Innovative ground motion sensors for planets and asteroids: Pioneers H2020-Space European Project. Seismological Research Letters 90, 969.

Garcia, R.F., Khan, A., Drilleau, M., et al., 2019b. Lunar seismology: an update on interior structure models. Space Science Reviews (ISSN 1572-9672) 215 (8), 50. https://doi.org/10.1007/s11214-019-0613-y.

Gassot, O., et al., 2021. Calathus: a sample-return mission to Ceres. Acta Astronautica (ISSN 0094-5765) 181, 112–129. https://doi.org/10.1016/j.actaastro.2020.12.050.

Gaulme, P., Mosser, B., et al., 2015. Seismology of giant planets. In: García, R.A., Tong, V.C.H. (Eds.), Extraterrestrial Seismology. Cambridge University Press, Cambridge. ISBN 978-1-107-04172-1, pp. 189–202. https://doi.org/10.1017/CBO9781107300668.017.

Gaulme, P., Schmider, F., et al., 2011. Detection of Jovian seismic waves: a new probe of its interior structure. Astronomy and Astrophysics 531 (16903), 104. https://doi.org/10.1051/0004-6361/201116903.

Ghail, R., et al., 2020. The Science Goals of the EnVision Venus Orbiter Mission. Tech. Rep. EPSC2020-599. Copernicus Meetings. https://doi.org/10.5194/epsc2020-599.

Giardini, D., et al., 2020. The seismicity of Mars. Nature Geoscience (ISSN 1752-0908) 13 (3), 205–212. https://doi.org/10.1038/s41561-020-0539-8.

Goldreich, P., et al., 1989. Neptune's story. Science 245 (4917), 500–504. https://doi.org/10.1126/science.245.4917.500.

Gonçalves, I., et al., 2019. First measurements of Jupiter's zonal winds with visible imaging spectroscopy. Icarus (ISSN 0019-1035) 319, 795–811. https://doi.org/10.1016/j.icarus.2018.10.019.

Grimm, R., et al., 2021. A magnetotelluric instrument for probing the interiors of Europa and other worlds. Advances in Space Research (ISSN 0273-1177) 68 (4), 2022–2037. https://doi.org/10.1016/j.asr.2021.04.011.

Groussin, O., et al., 2019. The thermal, mechanical, structural, and dielectric properties of cometary nuclei after Rosetta. Space Science Reviews (ISSN 1572-9672) 215 (4), 29. https://doi.org/10.1007/s11214-019-0594-x.

Guillot, T., Gautier, D., 2015. Giant planets. https://doi.org/10.1016/B978-0-444-53802-4.00176-7. arXiv:1405.3752 [astro-ph, physics:cond-mat], 2015.

Guzik, P., et al., 2020. Initial characterization of interstellar comet 2I/Borisov. Nature Astronomy (ISSN 2397-3366) 4 (1), 53–57. https://doi.org/10.1038/s41550-019-0931-8.

Hammond, N.P., Barr, A.C., 2014. Global resurfacing of Uranus's Moon Miranda by convection. Geology (ISSN 0091-7613) 42 (11), 931–934. https://doi.org/10.1130/G36124.1.

Hand, K.P., et al., 2017. Report of the Europa Lander Science Definition Team. Tech. Rep. Pasadena, California. p. 264.

Hedman, M.M., Nicholson, P.D., 2013. Kronoseismology: using density waves in Saturn's C ring to probe the planet's interior. The Astronomical Journal (ISSN 1538-3881) 146 (1), 12. https://doi.org/10.1088/0004-6256/146/1/12.

Hein, A.M., Eubanks, T.M., et al., 2022. Interstellar now! Missions to explore nearby interstellar objects. Advances in Space Research (ISSN 0273-1177) 69 (1), 402–414. https://doi.org/10.1016/j.asr.2021.06.052.

Hein, A.M., Perakis, N., et al., 2019. Project lyra: sending a spacecraft to 1I/'Oumuamua (former A/2017 U1), the interstellar asteroid. Acta Astronautica (ISSN 0094-5765) 161, 552–561. https://doi.org/10.1016/j.actaastro.2018.12.042.

Hobiger, M., Hallo, M., Schmelzbach, C., et al., 2021. The shallow structure of Mars at the InSight landing site from inversion of ambient vibrations. Nature Communications (ISSN 2041-1723) 12 (1), 6756. https://doi.org/10.1038/s41467-021-26957-7.

Van Hoolst, T., Dehant, V., et al., 2003. Tidally induced surface displacements, external potential variations, and gravity variations on Mars. Icarus (ISSN 0019-1035) 161 (2), 281–296. https://doi.org/10.1016/S0019-1035(02)00045-3.

Van Hoolst, Tim, Baland, Rose-Marie, et al., 2020. The librations, tides, and interior structure of Io. Journal of Geophysical Research: Planets (ISSN 2169-9100) 125 (8), e2020JE006473. https://doi.org/10.1029/2020JE006473.

Horleston, A., Clinton, J., Ceylan, S., et al., 2022. The far side of Mars – two distant marsquakes detected by InSight. The Seismic Record 2 (2). https://doi.org/10.1785/0320220007.

Hsu, Hsiang-Wen, et al., 2021. Jupiter system observatory at Sun–Jupiter Lagrangian point one. Bulletin - American Astronomical Society 53 (4). https://doi.org/10.3847/25c2cfeb.e19d6296.

Hurford, T.A., et al., 2020. Seismicity on tidally active solid-surface worlds. Icarus 338, 113466. https://doi.org/10.1016/j.icarus.2019.113466. November 2018.

Hurst, Kenneth, et al., 2021. Resonances of the InSight seismometer on Mars. Bulletin of the Seismological Society of America (ISSN 0037-1106) 111 (6), 2951–2963. https://doi.org/10.1785/0120210137.

Hussmann, Hauke, Spohn, Tilman, 2004. Thermal-orbital evolution of Io and Europa. Icarus (ISSN 0019-1035) 171 (2), 391–410. https://doi.org/10.1016/j.icarus.2004.05.020.

Kalousová, K., Sotin, C., 2020. The insulating effect of methane clathrate crust on Titan's thermal evolution. Geophysical Research Letters 47 (13), e2020GL087481. https://doi.org/10.1029/2020GL087481.

Karakostas, F., et al., 2021. Scattering attenuation of the Martian interior through coda-wave analysis. Bulletin of the Seismological Society of America (ISSN 0037-1106). https://doi.org/10.1785/0120210253.

Kawamura, T., Grott, M., et al., 2022. An autonomous lunar geophysical experiment package (ALGEP) for future space missions. Experimental Astronomy (ISSN 1572-9508). https://doi.org/10.1007/s10686-022-09857-6.

Kawamura, T., Lognonné, P., et al., 2017. Evaluation of deep moonquake source parameters: implication for fault characteristics and thermal state. Journal of Geophysical Research: Planets 122 (7), 1487–1504. https://doi.org/10.1002/2016JE005147.

Kennett, B.L.N., Engdahl, E.R., Buland, R., 1995. Constraints on seismic velocities in the Earth from traveltimes. Geophysical Journal International 122 (1), 108–124. https://doi.org/10.1111/j.1365-246X.1995.tb03540.x.

Khan, A., Ceylan, S., et al., 2021. Imaging the upper mantle structure of Mars with InSight seismic data. Science 373 (6553), 434–438.

Khan, A., Liebske, C., et al., 2018. A geophysical perspective on the bulk composition of Mars. Journal of Geophysical Research: Planets (ISSN 2169-9100) 123 (2), 1–37. https://doi.org/10.1002/2017JE005371.

Khan, A., Mosegaard, K., Rasmussen, K.L., 2000. A new seismic velocity model for the Moon from a Monte Carlo inversion of the Apollo lunar seismic data. Geophysical Research Letters 27 (11), 1591–1594. https://doi.org/10.1029/1999GL008452.

Khan, A., Pommier, A., et al., 2013. The lunar Moho and the internal structure of the Moon: a geophysical perspective. Tectonophysics 609, 331–352. https://doi.org/10.1016/j.tecto.2013.02.024.

Khurana, K.K., et al., 2011. Evidence of a global magma ocean in Io's interior. Science 332 (6034), 1186–1189. https://doi.org/10.1126/science.1201425.

de Kleer, K., et al., 2019. Tidal Heating: Lessons from Io and the Jovian System. Final Report CaltechAUTHORS:20191023-151847724. Keck Institute for Space Studies (KISS), Pasadena, CA.

Knapmeyer-Endrun, B., Panning, M.P., et al., 2021. Thickness and structure of the Martian crust from InSight seismic data. Science (ISSN 0036-8075) 373 (6553), 438–443. https://doi.org/10.1126/science.abf8966. ISSN 1095-9203.

Knapmeyer, M., Fischer, H.-H., Knollenberg, J., et al., 2018. Structure and elastic parameters of the near surface of Abydos site on comet 67P/Churyumov–Gerasimenko, as obtained by SESAME/CASSE listening to the MUPUS insertion phase. Icarus (ISSN 0019-1035) 310, 165–193. https://doi.org/10.1016/j.icarus.2017.12.002.

Knapmeyer, M., Fischer, H.H., Knollenberg, J., et al., 2016. The SESAME/CASSE instrument listening to the MUPUS PEN insertion phase on comet 67P/Churyumov–Gerasimenko. Acta Astronautica 125, 234–249. https://doi.org/10.1016/j.actaastro.2016.02.018.

Knapmeyer, M., Oberst, J., et al., 2006. Working models for spatial distribution and level of Mars' seismicity. Journal of Geophysical Research E: Planets (ISSN 0148-0227) 111 (11), 1–23. https://doi.org/10.1029/2006JE002708.

Knapmeyer, M., Walterova, M., 2022. Planetary core radii: from Plato towards PLATO. In: Geophysical Exploration of the Solar System. In: Advances in Geophysics, vol. 63.

Kovach, R.L., Chyba, C.F., 2001. Seismic detectability of a subsurface ocean on Europa. Icarus 150 (2), 279–287. https://doi.org/10.1006/icar.2000.6577.

Kuramoto, K., et al., 2022. Martian moons exploration MMX: sample return mission to Phobos elucidating formation processes of habitable planets. Earth, Planets and Space (ISSN 1880-5981) 74 (1), 12. https://doi.org/10.1186/s40623-021-01545-7.

Latham, G.V., et al., 1971. Moonquakes. Science 174 (4010), 687–692. https://doi.org/10.1126/science.174.4010.687.

Lazarewicz, A.R., et al., 1981. The Viking Seismometry Final Report. Tech. Rep. p. 60.

Le Maistre, S., Rivoldini, A., Rosenblatt, P., 2019. Signature of Phobos' interior structure in its gravity field and libration. Icarus (ISSN 0019-1035) 321, 272–290. https://doi.org/10.1016/j.icarus.2018.11.022.

Lehmann, I., 1936. Bureau Central Séismologique International, Série A, Travaux Scientifiques 14, 87–115.

Lehner, F.E., et al., 1962. A seismograph for lunar experiments. Journal of Geophysical Research 67 (12), 4779–4786.

Lewis, J.S., 1971. Satellites of the outer planets: thermal models. Science 172, 1171–1172. https://doi.org/10.1126/science.172.3988.1127.

Lognonné, P., Zharkov, V.N., Karczewski, J.F., et al., 1998. The seismic OPTIMISM experiment. Planetary and Space Science 46 (6-7). https://doi.org/10.1016/S0032-0633(98)00009-9.

Lognonné, P., Banerdt, W.B., Giardini, D., Pike, W.T., et al., 2019. SEIS: Insight's Seismic Experiment for Internal Structure of Mars. Space Science Reviews 215 (1). https://doi.org/10.1007/s11214-018-0574-6.

Lognonné, P., Banerdt, W.B., et al., 2020. Constraints on the shallow elastic and anelastic structure of Mars from InSight seismic data. Nature Geoscience 13 (3), 213–220. https://doi.org/10.1038/s41561-020-0536-y.

Lognonné, P., Johnson, C.L., 2007. Planetary Seismology, Vol. 10. ISBN 978-0-444-52748-6, p. 122. https://doi.org/10.1016/B978-044452748-6.00154-1.

Lorenz, R.D., 2011. Planetary penetrators: their origins, history and future. Advances in Space Research (ISSN 0273-1177) 48 (3), 403–431. https://doi.org/10.1016/j.asr.2011.03.033.

MacKenzie, S.M., et al., 2021. The Enceladus orbilander mission concept: balancing return and resources in the search for life. Planetary Science Journal (ISSN 2632-3338) 2 (2), 77. https://doi.org/10.3847/PSJ/abe4da.

Mankovich, C.R., Fuller, J., 2021. A diffuse core in Saturn revealed by ring seismology. Nature Astronomy (ISSN 2397-3366) 5 (11), 1103–1109. https://doi.org/10.1038/s41550-021-01448-3.

Marusiak, A.G., Panning, M.P., Vance, S.D., et al., 2022a. Methane clathrate effects on seismic propagation within Titan. In: 53rd Lunar and Planetary Science Conference. Vol. 2678. Lunar and Planetary Institute, The Woodlands (TX, USA), p. 1128.

Marusiak, A.G., Schmerr, N.C., et al., 2022b. The detection of seismicity on icy ocean worlds by single-station and small-aperture seismometer arrays. Earth and Space Science (ISSN 2333-5084) 9 (3), e2021EA002065. https://doi.org/10.1029/2021EA002065.

Marusiak, A.G., Panning, M.P., Vance, S.D., et al., 2022c. Seismic detection of euroquakes originating from Europa's silicate interior. Earth and Space Science. https://doi.org/10.1029/2021EA002041.

Matsumoto, Koji, et al., 2021. MMX geodesy investigations: science requirements and observation strategy. Earth, Planets and Space (ISSN 1880-5981) 73 (1), 226. https://doi.org/10.1186/s40623-021-01500-6.

McEwen, Alfred, et al., 2014. Io Volcano Observer (IVO): budget travel to the outer solar system. Acta Astronautica (ISSN 0094-5765) 93, 539–544. https://doi.org/10.1016/j.actaastro.2012.05.028.

Meech, Karen J., et al., 2017. A brief visit from a red and extremely elongated interstellar asteroid. Nature (ISSN 0094-5765) 552 (7685), 378–381. https://doi.org/10.1038/nature25020.

Menina, Sabrina, et al., 2021. Energy envelope and attenuation characteristics of high-frequency (HF) and very-high-frequency (VF) Martian events. Bulletin of the Seismological Society of America (ISSN 0037-1106), 0037. https://doi.org/10.1785/0120210127.

Metzger, Philip T., et al., 2022. Moons are planets: scientific usefulness versus cultural teleology in the taxonomy of planetary science. Icarus (ISSN 0019-1035) 374, 114768. https://doi.org/10.1016/j.icarus.2021.114768.

Mitri, G., et al., 2007. Hydrocarbon lakes on Titan. Icarus 186 (2), 385–394.

Mizutani, Hitoshi, 1995. Lunar interior exploration by Japanese lunar penetrator mission, LUNAR-A. Journal of Physics of the Earth 43 (5), 657–670. https://doi.org/10.4294/jpe1952.43.657.

Mohorovičić, Andrija, 1909. Das Beben Vom 8. Oktober 1909 (Translated Title). Jahrbuch des meteorologischen Observatoriums in Zagreb 4 (1), 1–67.

Mousis, Olivier, et al., 2015. Methane clathrates in the solar system. Astrobiology (ISSN 1531-1074) 15 (4), 308–326. https://doi.org/10.1089/ast.2014.1189.

Nagel, K., Breuer, D., Spohn, T., 2004. A model for the interior structure, evolution, and differentiation of Callisto. Icarus (ISSN 0019-1035) 169 (2), 402–412. https://doi.org/10.1016/j.icarus.2003.12.019.

Nathues, A., et al., 2020. Recent cryovolcanic activity at occator crater on Ceres. Nature Astronomy (ISSN 2397-3366) 4 (8), 794–801. https://doi.org/10.1038/s41550-020-1146-8.

National Academies of Sciences, Engineering, and Medicine, 2022. Origins, Worlds, and Life: A Decadal Strategy for Planetary Science and Astrobiology 2023–2032. National Academies Press, Washington, D.C. ISBN 978-0-309-47578-5. https://doi.org/10.17226/26522.

Nimmo, F., Pappalardo, Robert T., 2016. Ocean worlds in the outer solar system. Journal of Geophysical Research: Planets. https://doi.org/10.1002/2016JE005081.

Nissen-Meyer, Tarje, et al., 2014. AxiSEM: broadband 3-D seismic wavefields in axisymmetric media. Solid Earth (ISSN 1869-9529) 5 (1), 425–445. https://doi.org/10.5194/se-5-425-2014.

Oberst, J., 1987. Unusually high stress drops associated with shallow moonquakes. Journal of Geophysical Research 92 (B2), 1397–1405. https://doi.org/10.1029/JB092iB02p01397.

Oldham, Richard Dixon, 1906. The constitution of the interior of the Earth, as revealed by earthquakes. Quarterly Journal of the Geological Society 62 (1–4), 456–475. https://doi.org/10.1144/GSL.JGS.1906.062.01-04.21.

Panning, Mark P., Kedar, Sharon, et al., 2021. Farside seismic suite (FSS): first seismic data from the farside of the Moon delivered by a commercial lander. In: AGU Fall Meeting 2021. AGU.

Panning, Mark P., Lekic, V., et al., 2006. Long-period seismology on Europa: 2. predicted seismic response. Journal of Geophysical Research 111 (E12), E12008. https://doi.org/10.1029/2006JE002712.

Panning, Mark P., Stähler, Simon C., et al., 2018. Expected seismicity and the seismic noise environment of Europa. Journal of Geophysical Research: Planets 123 (1), 163–179. https://doi.org/10.1002/2017JE005332.

Peale, S.J., Cassen, P., Reynolds, R.T., 1979. Melting of Io by tidal dissipation. Science 203 (4383), 892–894. https://doi.org/10.1126/science.203.4383.892.

Perminov, V.G., 1999. The Difficult Road to Mars: A Brief History of Mars Exploration in the Soviet Union. no. 15. National Aeronautics and Space Administration Headquarters, Washington, D.C. ISBN 978-0-16-058859-4.

Perrin, C., et al., 2022. Geometry and segmentation of Cerberus Fossae, Mars: implications for marsquake properties. Journal of Geophysical Research: Planets (ISSN 2169-9100) 127 (1), e2021JE007118. https://doi.org/10.1029/2021JE007118.

Phillips, Cynthia B., Pappalardo, Robert T., 2014. Europa clipper mission concept: exploring Jupiter's ocean moon. Eos, Transactions American Geophysical Union 95 (20), 165–167. https://doi.org/10.1002/2014EO200002.

Phillips, R.J., 1991. Expected Rate of Marsquakes. Tech. Rep. pp. 35–38.

Phillips, Roger, 1992. Is there subduction on Venus? Physics World (ISSN 2058-7058) 5 (11), 25–27. https://doi.org/10.1088/2058-7058/5/11/26.

Pike, William T., et al., 2016. A silicon seismic package (SSP) for planetary geophysics. In: Lunar and Planetary Science Conference, vol. 47, p. 2081.

Plesa, A.-C., et al., 2021. Seismic velocity variations in a 3D Martian mantle: implications for the InSight measurements. Journal of Geophysical Research: Planets (ISSN 2169-9100). https://doi.org/10.1029/2020JE006755.

Podglajen, Aurélien, et al., 2022. Stratospheric Observations of Acoustic-Gravity Waves from the Hunga-Tonga Eruption. Tech. Rep. EGU22-13593. Copernicus Meetings. https://doi.org/10.5194/egusphere-egu22-13593.

Porco, C.C., Helfenstein, P., et al., 2006. Cassini observes the active South pole of Enceladus. Science 311 (5766).

Porco, Carolyn, DiNino, Daiana, Nimmo, Francis, 2014. How the geysers, tidal stresses, and thermal emission across the South polar terrain of Enceladus are related. The Astronomical Journal (ISSN 1538-3881) 148 (3), 45. https://doi.org/10.1088/0004-6256/148/3/45.

Press, Frank, Ewing, Maurice, 1951. Propagation of elastic waves in a floating ice sheet. Transactions - American Geophysical Union 32 (5), 673. https://doi.org/10.1029/TR032i005p00673.

Prockter, Louise M., Pappalardo, Robert T., 2000. Folds on Europa: implications for crustal cycling and accommodation of extension. Science 289 (5481), 941–943.

Rivoldini, A., Van Hoolst, T., Verhoeven, O., 2009. The interior structure of Mercury and its core sulfur content. Icarus (ISSN 0019-1035) 201 (1), 12–30. https://doi.org/10.1016/j.icarus.2008.12.020.

Robertsson, J.O., et al., 2008. On the use of multicomponent streamer recordings for reconstruction of pressure wavefields in the crossline direction. Geophysics (ISSN 0016-8033) 73 (5), A45–A49. https://doi.org/10.1190/1.2953338.

Rowe, J.F., Gaulme, P., Lissauer, J.J., et al., 2017. Time-series Analysis of Broadband Photometry of Neptune from K_2. The Astronomical Journal (ISSN 1538-3881) 153 (4), 149. https://doi.org/10.3847/1538-3881/aa6119.

Ruesch, O., et al., 2016. Cryovolcanism on Ceres. Science 353 (6303), aaf4286. https://doi.org/10.1126/science.aaf4286.

Ruiz, Javier, et al., 2019. Evidence of thrust faulting and widespread contraction of Ceres. Nature Astronomy (ISSN 2397-3366) 3 (10), 916–921. https://doi.org/10.1038/s41550-019-0803-2.

Schenk, P., et al., 2020. Impact heat driven volatile redistribution at occator crater on Ceres as a comparative planetary process. Nature Communications (ISSN 2041-1723) 11 (1), 3679. https://doi.org/10.1038/s41467-020-17184-7.

Scholz, John-Robert, et al., 2020. Detection, analysis, and removal of glitches from InSight's seismic data from Mars. Earth and Space Science 7 (11), 1–31. https://doi.org/10.1029/2020EA001317.

Schubert, G., Anderson, J.D., et al., 2004. Interior composition, structure and dynamics of the Galilean satellites. In: Jupiter: The Planet, Satellites and Magnetosphere, pp. 281–306.

Schubert, G., Stevenson, D.J., Ellsworth, K., 1981. Internal structures of the Galilean satellites. Icarus (ISSN 0019-1035) 47 (1), 46–59. https://doi.org/10.1016/0019-1035(81)90090-7.

Seligman, Darryl, Laughlin, Gregory, 2018. The feasibility and benefits of in situ exploration of 'Oumuamua-like objects. Astronomical Journal (ISSN 1538-3881) 155 (5), 217. https://doi.org/10.3847/1538-3881/aabd37.

Shaw, Cody L., et al., 2022. PMODE I: design and development of an observatory for characterizing giant planet atmospheres and interiors. Frontiers in Astronomy and Space Sciences (ISSN 2296-987X) 9.

Shibaike, Yuhito, et al., 2019. The Galilean satellites formed slowly from pebbles. The Astrophysical Journal (ISSN 0004-637X) 885 (1), 79. https://doi.org/10.3847/1538-4357/ab46a7.

Shiraishi, H., et al., 2008. The present status of the Japanese penetrator mission: LUNAR-A. Advances in Space Research (ISSN 0273-1177) 42 (2), 386–393. https://doi.org/10.1016/j.asr.2007.08.022.

Smith, Bradford A., et al., 1979. The Jupiter system through the eyes of Voyager 1. Science 204 (4396), 951–972. https://doi.org/10.1126/science.204.4396.951.

Smrekar, Sue, et al., 2020. VERITAS (Venus Emissivity, Radio Science, InSAR, Topography and Spectroscopy): a Proposed Discovery Mission. Tech. Rep. EPSC2020-447. Copernicus Meetings. https://doi.org/10.5194/epsc2020-447.

Smrekar, Sue, et al., 2014. Venus: Surface and Interior. Encyclopedia of the solar system (third edition). https://doi.org/10.1016/B978-0-12-415845-0.00015-3.

Sohl, F., Spohn, T., 1997. The interior structure of Mars: implications from SNC meteorites. Journal of Geophysical Research: Planets 102 (E1), 1613–1635. https://doi.org/10.1029/96JE03419.

Sollberger, D., Schmelzbach, C., Andersson, F., et al., 2021. A reconstruction algorithm for temporally aliased seismic signals recorded by the InSight Mars lander. Earth and Space Science 8 (8). https://doi.org/10.1029/2020EA001234.

Sollberger, D., Schmelzbach, C., Robertsson, J., et al., 2016. The shallow elastic structure of the lunar crust: new insights from seismic wavefield gradient analysis. Geophysical Research Letters 43 (19), 078. https://doi.org/10.1002/2016GL070883.

Soulat, L., et al., 2011. Echoes: a new instrumental concept of Doppler spectro-imager for the ESA mission project JUICE. In: Optical Complex Systems: OCS11, vol. 8172. SPIE, pp. 169–180. https://doi.org/10.1117/12.896710.

Spohn, T., Hudson, T.L., et al., 2021. The InSight HP^3 penetrator (mole) on Mars: soil properties derived from the penetration attempts and related activities. arXiv: 2112.04438 [astro-ph, physics:physics].

Spohn, T., Sohl, F., et al., 2001. The interior structure of Mercury: what we know, what we expect from BepiColombo. Planetary and Space Science 49 (14–15), 1561–1570. https://doi.org/10.1016/S0032-0633(01)00093-9.

Stähler, S.C., Khan, A., et al., 2021. Seismic detection of the Martian core. Science 373 (6553), 443–448. https://doi.org/10.1126/science.abi7730.

Stähler, S.C., Panning, M.P., Hadziioannou, C., et al., 2019. Seismic signal from waves on Titan's seas. Earth and Planetary Science Letters 520, 250–259. https://doi.org/10.1016/j.epsl.2019.05.043.

Stähler, S.C., Panning, M.P., Vance, S.D., et al., 2018. Seismic wave propagation in icy ocean worlds. Journal of Geophysical Research: Planets 123 (1), 206–232. https://doi.org/10.1002/2017JE005338.

Stähler, S.C., Panning, M., et al., 2022. A Cerberus Fossae seismic network. In: Low-Cost Science Mission Concepts for Mars Exploration. LPI Contributions. Lunar and Planetary Institute, Pasadena.

Stähler, S.C., Widmer-Schnidrig, R., et al., 2020. Geophysical observations of Phobos transits by InSight. Earth and Space Science Open Archive, 15. https://doi.org/10.1002/essoar.10503257.1.

Stern, R.J., Gerya, T., Tackley, P.J., 2018. Stagnant lid tectonics: perspectives from silicate planets, dwarf planets, large moons, and large asteroids. Geoscience Frontiers. Lid Tectonics (ISSN 1674-9871) 9 (1), 103–119. https://doi.org/10.1016/j.gsf.2017.06.004.

Stern, S.A., McKinnon, W.B., 2000. Triton's surface age and impactor population revisited in light of Kuiper belt fluxes: evidence for small Kuiper belt objects and recent geological activity. The Astronomical Journal (ISSN 1538-3881) 119 (2), 945. https://doi.org/10.1086/301207.

Stone, E.C., 1987. The Voyager 2 encounter with Uranus. Journal of Geophysical Research: Space Physics (ISSN 2156-2202) 92 (A13), 14873–14876. https://doi.org/10.1029/JA092iA13p14873.

Stone, E.C., Miner, E.D., 1989. The Voyager 2 encounter with the Neptunian system. Science 246 (4936), 1417–1421. https://doi.org/10.1126/science.246.4936.1417.

Strom, R.G., Schaber, G.G., Dawson, D.D., 1994. The global resurfacing of Venus. Journal of Geophysical Research: Planets (ISSN 2156-2202) 99 (E5), 10899–10926. https://doi.org/10.1029/94JE00388.

Tacconi, Linda, et al., 2021. ESA Voyage 2050. Report of the Senior Committee. European Space Agency.

Teolis, Ben D., et al., 2017. Enceladus plume structure and time variability: comparison of Cassini observations. Astrobiology (ISSN 1531-1074) 17 (9), 926–940. https://doi.org/10.1089/ast.2017.1647.

Toksöz, M. Nafi, et al., 1972. Lunar crust: structure and composition. Science 176 (4038), 1012–1016. https://doi.org/10.1126/science.176.4038.1012.

Trehu-Ollennu, A., Kim, W., Ali, K, et al., 2018. InSight Mars Lander robotics instrument deployment system. Space Science Reviews 214 (5), 93. https://doi.org/10.1007/s11214-018-0520-7.

Vance, Steven D., Kedar, Sharon, et al., 2018a. Vital signs: seismology of icy ocean worlds. Astrobiology 18 (1), 37–53. https://doi.org/10.1089/ast.2016.1612.

Vance, Steven D., Panning, Mark P., et al., 2018b. Geophysical investigations of habitability in ice-covered ocean worlds. Journal of Geophysical Research: Planets 123 (1), 180–205. https://doi.org/10.1002/2017JE005341.

Vijendran, Sanjay, et al., 2010. A penetrator for the Jupiter Ganymede orbiter mission. In: Proceedings of the 7th International Planetary Probe Workshop, p. 12.

Walter, F., et al., 2020. Distributed acoustic sensing of microseismic sources and wave propagation in glaciated terrain. Nature Communications 11 (1). https://doi.org/10.1038/s41467-020-15824-6.

Watters, Thomas R., et al., 2019. Shallow seismic activity and young thrust faults on the Moon. Nature Geoscience 12 (6), 411–417. https://doi.org/10.1038/s41561-019-0362-2.

Weber, Renee C., Lin, P.-Y., et al., 2011. Seismic detection of the lunar core. Science 331 (6015), 309–312. https://doi.org/10.1126/science.1199375.

Weber, Renee, Neal, Clive R., et al., 2021. The scientific rationale for deployment of a long-lived geophysical network on the Moon 53, 098. https://doi.org/10.3847/25c2cfeb.674dcfdf.

Wieczorek, Mark A., et al., 2013. The crust of the Moon as seen by GRAIL. Science 339 (6120), 671–675. https://doi.org/10.1126/science.1231530.

Wilson, Colin Frank, Zetterling, Carl-Mikael, Pike, William Thomas, 2016. Venus long-life surface package. arXiv:1611.03365 [astro-ph].

Zenhäusern, Géraldine, et al., 2022. Low-frequency marsquakes and where to find them: back azimuth determination using a polarization analysis approach. Bulletin of the Seismological Society of America (ISSN 0037-1106). https://doi.org/10.1785/0120220019.

Zetterling, Carl-Mikael, 2015. Integrated circuits in silicon carbide for high-temperature applications. MRS Bulletin (ISSN 0883-7694) 40 (5), 431–438. https://doi.org/10.1557/mrs.2015.90. ISSN 1938-1425.

Zweifel, Peter, et al., 2021. Seismic high-resolution acquisition electronics for the NASA InSight mission on Mars. Bulletin of the Seismological Society of America (ISSN 0037-1106). https://doi.org/10.1785/0120210071.

CHAPTER THREE

Planetary core radii: from Plato towards PLATO

Martin Knapmeyer* **and Michaela Walterová**
DLR Institute of Planetary Research, Berlin, Germany
*Corresponding author: e-mail address: martin.knapmeyer@dlr.de

multa venientis aevi populus ignota nobis sciet, multa saeculis tunc futuris, cum memoria nostri exoleverit, reservantur. pusilla res mundus est, nisi in illo, quod quaerat omnis mundus habeat.

(Seneca, Naturales Quaestiones, VII 30.5)

Contents

Advances in Geophysics, Volume 63
ISSN 0065-2687
https://doi.org/10.1016/bs.agph.2022.07.003

1. Introduction

After almost two thousand years, the wisdom of Seneca's words still holds: "*Much that is still unknown to us will be known to mankind in the future only, and much is preserved for times when memories of us are long gone. The world would be a small thing if it took not the entire world to fathom it*" (after the German translation by O. and E. Schönberger, English by MK). They are found in the conclusion of the seventh book of his *Naturales Quaestiones*, which also concludes the entire work.

Like Seneca took the occasion of a recent violent earthquake in Pompeji to discuss the origins of Earthquakes in the sixth book of the *Quaestiones*, we here take the occasion of the recent seismological determination of the core radius of Mars (Stähler et al., 2021) to step back and examine how our knowledge about the sizes of planetary cores evolved with time. Fortunately, we do not yet live in times when the memories of the natural philosophers of antiquity are forgotten – quite the contrary, the digitalization of old journals and books facilitates and accelerates the access to much of the relevant literature, and to literature of which we did not know beforehand that it exists, or might be relevant. This allows investigating how far back into time we have to go to find out when and where thinking about planetary cores actually started.

Plato was not at the beginning of the story. Not even close. But as it turned out during our research, the developments during the renaissance can't be understood without Aristotle. Plato was Aristotle's teacher, and the recognition of the Earth as a globe fell into their time – no globe, no core. On the other hand, PLATO (Rauer et al., 2016) will not be at the end, not even close. But it may open doors, or vistas, rather, to places where seismic experiments will be reserved to future generations, when the present study is long forgotten. The name Plato is thus found at – approximatively – two ends of a story: from a flat earth to an infinite universe, from a cosmos who is a "Living Creature" to searching the cosmos for living creatures ("Living Creature" with capitals is used to designate the universe in R.G. Bury's translation of Plato's *Timaeus*).

1.1 Why are cores interesting?

The core-mantle boundary (CMB) is the most significant discontinuity within the solid Earth, in terms of density contrast, change in composition, change in elastic properties and electric conductivity.

The core has been the source of the Earth's magnetic field for a very long time, while Mars' magnetic field died out a long time ago (Acuña et al., 1999). It is an ongoing debate in how far the longevity of the Earth's geodynamo depends on the formation and growth of its inner core (e.g. Landeau et al., 2017; Driscoll and Du, 2019, and references therein), and while a solid inner core has unexpectedly been found in the Moon (Weber et al., 2011), the existence of an inner core in Mars is generally doubted, but the question not yet finally settled.

The Earth's core contains 16.3% of the volume of the planet, and contributes 32.5% of its mass (computed for PREM, Dziewonski and Anderson, 1981). With these proportions, and with 32 weight-% of the bulk Earth, but 85.5 weight-% of the core being iron (e.g. Henderson and Henderson, 2009), almost 87 weight-% of the Earth's inventory of iron are contained in the core.

On the other hand, with only 11.4%, the contribution of the $R_c = 3480$ km core to the Earth's moment of inertia is the same as that of the outermost approx. 215 km (PREM: 5.7% of the mass in 10% of the volume). About half of the moment of inertia results from the outermost 1000 km, the upper mantle alone contributes almost three times as much as the entire core.

As is described in sections 4.1 and 4.3, one explanation for the existence, composition, and properties of planetary cores that was discussed in the past was that the core mantle boundary is the result of a phase transition. This turned out to be not the case, but the core nevertheless interacts with the phase transitions of the mantle: In the Earth, the transition to post-Perovskite occurs just above the core mantle boundary. In a similar fashion it was uncertain for a long time, if the Wadsleyite–Bridgmanite transition, occurring at 660 km depth in Earth, also occurs in Mars – or if the CMB is above the depth where the necessary pressure is reached. Simulations of mantle convection (Harder and Christensen, 1996; Harder, 1998) showed that this endothermic transition would have a thermal blanketing effect – thus the question for its existence is crucial for the planform of mantle convection in Mars, and, ultimately, might be connected to the formation of Tharsis.

Theories of the formation of the Moon have to explain the similarities, but also the differences between the compositions of Earth and Moon. "*The existence of a lunar core … provides a reservoir for missing siderophile elements which are of great value in constraining lunar origin models*" (Mueller et al., 1988, pp. 6349–6350) – a large core within the Moon would thus help to explain the

low abundance of siderophile elements, when it can be made plausible that a significant portion of them segregated into the core.

The above are only a few trivia and contexts, one can possibly name many more, and in much more detail – which would be a review of its own right. The question for a single number, the radius of the core, is thus connected to questions concerning the formation, evolution, and inner workings of the terrestrial planets.

1.2 Structure of this work

To limit the scope of this study, we will understand as a planetary core only metallic cores that were segregated from an initially rocky mantle, where "metallic" means especially iron-nickel alloys as found in meteorites, but not the relaxed astronomical definition of "being heavier than Helium" or elements that changed into a metallic state under high pressure. This excludes metallic hydrogen zones within the giant planets as well as the rocky parts of icy moons (which still may contain iron cores) from the consideration. However, as we will see, it was not always accepted that the Earth's core is an iron-nickel alloy, so some room must be given to rock-based core models nevertheless. A treatment of the interiors of icy moons, under special consideration of tidal deformation, is given by Bagheri et al. (2022, this volume).

We will first describe how we evaluate the literature, especially concerning different conventions that were used to express the moment of inertia factor, and the handling of measurement uncertainty (section 2). We then explore the farther past to find out when and how the notion of an inner structure of the Earth was developed (section 3). The main part of the study is devoted to the determination of the core radii of Earth, Moon, and Mars, and the progress especially in the 20th and 21st century (section 4). We add considerations of exoplanets and the observational constraints and conceptual approaches to describe their interiors (section 5). In some concluding remarks (section 6) we attempt to distill a few lessons that can be learned so far.

Our study is based on a large collection of numerical values which we present only graphically. All numbers, together with precise references, are collected in an accompanying document (Knapmeyer and Walterová, 2022) which is published on a file hosting service. This document precisely proves the sources of all numbers, and contains a few extra paragraphs of peripheral interest. Where we explicitly refer to these paragraphs, we give their numbers, preceded by an "S" (for "supporting information").

2. Methods: evaluation of the literature

The present work is a compilation of literature from more than two millenia, during which the scientific thinking of the world changed significantly, as did the formats of publication and the style in which publications are written. Fortunately, vast libraries of scientific literature are available in digital form via the internet nowadays, making even treatises written in the 17th century available in a near original form. Some of the cited sources are in Latin, French or German. Where we cite verbatim from these, we provide loose translations to English as well, but we think it is sometimes worthwhile to present the original formulations.

A review, by definition, requires condensation and, to a certain degree, simplification of the reviewed materials. This section describes some rules we followed during the evaluation and compilation of the references used.

Concerning the moment of inertia factor (*MoIF* for short), we focused on studies that provided new estimates. This is however not as straightforward as one might think. An important part of the discussion of the Martian MoIF deals with how to correct for the Tharsis anomaly (see section 4.3 Mars for details), and new approaches in this regard influence later publications concerning the interior structure of Mars without re-evaluating old or adding new measurements. Community consensus is also expressed in what values e.g. modeling studies use, not only in what is measured.

The moment of inertia factor depends on the reference mass and radius used: ideally, one would rescale all published values to common references. An obstacle is, however, that many studies do not make explicit which reference mass and radius was used, but assume a reader well-informed about the state of research at the time. A review like the present one could be used to provide reasonable assumptions about the state of the art at any time, but these would nevertheless only be educated guesses. Since feasible resolutions of the comparative plots shown in this study hardly show any difference between published and rescaled values, no rescaling was applied.

While the designation of an ellipsoid's moments of inertia as A, B, and C, and I for the mean moment of inertia, is consistently used throughout the literature, different normalizations were used to signify a central mass concentration. The more recent literature usually speaks of quantities like C/MR^2 and I/MR^2 as the moment of inertia factor, i.e. normalizes the planetary moment of inertia to that of a point mass rotating about an axis at a distance given by the reference radius. Some earlier works sometimes apply an additional normalization to the moment of inertia of a homogeneous

sphere, i.e. divide this by 2/5 (e.g. See, 1905a,b). Another representation is $g' = 3C/2MR^2$ (e.g. Jones, 1932; Jeffreys, 1961; Eckert, 1965; Lamar and McGann, 1966), originating in lunar libration theory, which yields $g' = 1$ for a hollow shell of infinitesimal thickness. For easier comparison, we convert all numerical values to the $1/MR^2$-normalization.

Uncertainties of the MoIF, but also for the Love number k_2, are usually not found in the older literature (e.g. See, 1905a,b; Jeffreys, 1937; Ramsey, 1948; Eckert, 1965). The more recent satellite-geodetic publications meticulously analyze the error budgets, including e.g. relativistic effects of spacecraft velocity, or accelerations due to solar light pressure, among others (e.g. Christensen and Balmino, 1979; Konopliv et al., 2013, 2016). Some unaccounted discrepancies nevertheless remain, and formal uncertainties are artificially inflated by factors of 2 (Konopliv et al., 2016, 2020), 3 (Genova et al., 2016), 5 (Folkner et al., 1997; Konopliv et al., 1998), 10 (Konopliv et al., 2001; Goossens and Matsumoto, 2008), or even 40 (Konopliv et al., 2013) to account for unknown or unmodeled error sources. Many authors however do not make explicit what statistical meaning their uncertainty boundaries have (i.e. whether they are formal standard deviations, or inflated). Comparing one author's 1σ to another's $n\sigma$ without further explanation appears misleading, although we acknowledge that unknown sources of error may exist and must be accounted for. We show both the formal and inflated uncertainties in our figures to illustrate the impact of uncertainty inflation.

Concerning the core radius itself, it is even less obvious what constitutes a new estimation: most of the literature applies similar methods to the same measured data, and mainly varies the additional assumptions necessary to arrive at an inversion problem that is not hopelessly underdetermined. We tried to gather from the literature what authors think is a plausible value or range of values. Ranges given nevertheless will be too wide in some cases, as it makes sense to set up parameter studies with boundaries slightly exceeding the plausible range, just to make sure that all possible solutions are covered.

Some authors do not provide numerical values for the core radius, but graphical representations of structural models only (e.g. Jeffreys and Bullen, 1967; Cole, 1972; Bertka and Fei, 1998a; Kavner et al., 2001). In these cases, measurements in the paper's figures were made to obtain the core radius. Sometimes, we had the impression that the values given in texts are only weakly supported by the shown histograms or other graphics. In these rare cases, values were also measured in the figures and preferred to what is

given in the text. The commented tables in the Knapmeyer and Walterová (2022) document from where each and every value originates.

This review will not discuss the evolution of our knowledge of planetary masses in great detail. Mass estimations result in the product GM of the Newtonian constant of gravity, G, and the mass M in question. The uncertainty attached to M (and consequently the mean density) is often dominated by the uncertainty of G (e.g. Birch, 1952; Bills and Ferrari, 1978; Pätzold et al., 2019, see also S4), which is notoriously difficult to measure, and still the least known of all fundamental constants (with an uncertainty in the order of 100 *ppm*, while other fundamental constants are known at sub-*ppb* level, NIST, 2019). Section S4 of Knapmeyer and Walterová (2022) gives a brief overview on the evolution of our knowledge of G, and for which celestial objects its uncertainty dominates that of the mass.

Measurements of the MoIF were conducted telescopically even in the early 20th century, but meanwhile, spacecraft missions play a crucial role. We therefore complement our depictions of the MoIF and core radius time series with timelines of these missions. We distinguish between fly-by, orbiter, and lander missions, but not between hard and soft landing, stationary landers vs. rovers etc., as this would require too many symbols and colors, and finally become illegible. For each mission, we document arrival and mission end dates, sometimes also launch dates, in UTC time. We also distinguish between "failures" and "successes", although this is not always straightforward, e.g. when a Lunar orbit could not be reached, but a fly-by was managed and valuable radio tracking data was returned. Our classification of successes might thus be different from what is found elsewhere.

3. Ye olden days: early and earliest history

When studying the evolution of our modern knowledge about planetary cores, one question arises first: How far into the past do we have to look to find the origins of this knowledge, and especially of the concept of a core within the Earth?

This also touches the question of which opinions or results should be reported: In general, it is a mistake to judge historical decisions, opinions, and events in hindsight, from the perspective of today's knowledge. It is anachronistic to say, from the hindsight perspective of our knowledge, that Gutenberg got the core radius of Earth right already in 1914: There were other authors after 1914 who presented radii more than 20 km,

at times more than 50 km different from his value, and in 1914 it was not obvious how good Gutenberg's solution was. The views concerning the Earth's interior of Athanasius Kircher (1602–1680) were somewhere between mainstream and avantgarde in his time, and deserve being mentioned, while discussions concerning the prison of damned souls partly belong to another storyline. Finding the point in time at which different lines of thought start diverging is not straightforward, and, following Wootton (2015), it might not even exist. We nevertheless found it enlightening to read the arguments concerning hell, as they shed light on the overall mindset of renaissance natural philosophers, who developed modern science while being deeply rooted in their religious traditions.

We here first look back into the more distant past, as natural philosophy in the Renaissance was directly influenced by antique Greek and Roman texts, some just rediscovered, some embedded into the official religious doctrine. We also attempt to obtain a sketchy impression of ideas from outside the European tradition. Then we fast forward to the 16th century, where we find the roots of our modern views.

3.1 The subsurface world in mythology and early natural philosophy

Theories about what is underneath our feet were developed since the earliest times. All cultures that were exposed to volcanoes and earthquakes, caves, sources of rivers, and other phenomena that connect the subsurface to human experience, have some kind of related theory or mythology.

Gods and demons related to earthquakes are indeed found in many cultures – examples are Kabrakan, the Maya "Destroyer of the Mountains" and the Aztec god of caves and earthquakes Tepeyollotli, the Polynesian Mahuike, the Norse Loki (convulsing in pain in his captivity), the Greek "Shaker of the Earth" Poseidon Ennosigaios, or Raluvimbha, the god of all natural phenomena of the Baventa in Transvaal (the list is derived from Lurker, 1989, whose spelling of names we follow). Japanese mythology knows of the giant catfish Namazu, who is immobilized with a large boulder by the Kashima and Ebisu deities. Sometimes, Ebisu is unable to hold the pressure, allowing Namazu to wiggle – and earthquakes result (e.g. Ludwin et al., 2007). Well known to probably all geologists is the Hawai'ian goddess of volcanoes and lightning, Pele, who came to Hawai'i after being banned from Tahiti (Lurker, 1989).

Taylor (1995) interprets two legends from the Tonga islands of Niuafo'ou and Tofua, in terms of volcanic eruptions: Both report that Samoan

demons stole the summit of a mountain, but were caught in the act, and henceforth dropped it into the ocean in a hectic getaway.

In the light of the obliteration of most of the Hunga Tonga / Hunga Ha'apai islands in January 2022 (scientific papers about which are just being published) one can imagine that the idea of theft might occur to people who intend to sail to an island and find nothing. Hunga Tonga is (or was) approx. 100 km south of Tofua.

Indications for a possible relation of the Israelite's god YHWH to volcanism are reviewed by Dunn (2014). Given that the biblical god YHWH is an evolution of one or more earlier tribal deities, associations with a mountain or volcano deity are possible, even though the appearance in thunderstorms (e.g. in the book Exodus) are better known and prevailing among scholars (Lurker also lists YHWH among the mountain deities). A number of verses of the Old Testament dealing with apparitions of YHWH describe phenomena well known from volcanic eruptions, like fire, black smoke, earthquakes, and others. One example is found in the Psalms: "*The earth rocked and shook; the foundations of the mountains trembled; they shook as his wrath flared up. / Smoke rose in his nostrils, a devouring fire poured from his mouth; it kindled coals into flame. / He parted the heavens and came down, a dark cloud under his feet.*" (Psalm 18.8-10, cited from the New American Bible, 2002). Having witnessed a number of thunderstorms personally, and seen video footage from eruptions of the last decades, we agree that Psalm 18 does not refer to a thunderstorm.

It has been suggested that the Greek myths of Cyclopes actually refer to volcanoes (Scarth, 1989, and references therein). Scarth indeed interpreted the blinding of Polyphemus by Odysseus as description of an eruption of Mt. Etna, and Polyphemus' cave as Etna's main crater, while the other cyclopes are metaphors for the subsidiary craters. Scarth also suggested that most details of the Polyphemus story could be interpreted as related to Etnean eruptions, from the cyclops' violence towards Odysseus' comrades to his tenderness towards his sheep, and even the sheep's black wool.

On the other hand, Hine (2002) did not see the Cyclopes live under volcanoes and argues that Greek authors had only hearsay knowledge of volcanoes, since before 79 CE the Etna was the only active volcano visible from any major city, thus mainland Greeks never saw one (despite the catastrophic effects of volcanism on earlier cultures in the Eastern Mediterranean). Another indication for the lack of experience with volcanos, in Hine's view, is the absence of specific words for "volcano" in both classical

Greek and Latin (the island named Vulcano today was known to ancient writers as Hiera; Vulcan was the god of fire and patron of blacksmiths).

In any case, we consider the description of Polyphemus' rage an interesting parallel to the Tahitian legend of stolen summits: Upon Odysseus' provocations, Polyphemus "*became all the more angry at heart, and broke off the peak of a high mountain and hurled it at us*" (Homer, Odyssey, Book 9, p. 351, English by A.T. Murray and G.E. Dimock), and a little later he "*lifted up again a far greater stone, and swung and hurled it, putting into the throw infinite strength. He threw it a little behind the dark-prowed ship*, [...] *And the sea surged beneath the stone as it fell, and the wave bore the ship onward and drove it to the shore*." (Odyssey, Book 9, p. 355).

In religion and mythology, narrative is more important than description, but Greek and Roman writers also provided more factual accounts.

Descriptions of earthquakes and volcanism often speak of fires – n.b. that without Newtonian gravity and accretional heat, and without nuclear processes, combustion is the only way to produce heat and thus the only explanation of volcanic heat available to ancient scholars. The pseudo-Aristotelian collection of phenomena, *On Marvellous Things Heard* (see Aristotle, *Minor works*, 4th cent. BCE c; since this book is part of the traditional text corpus and at least considered to originate from one of Aristoteles' successors in the peripatetic school, authorship questions are of little relevance here), paraphrases e.g. "*πυρὸς ῥεῦμα*" ("*fiery streams*", Aristotle, 4th cent. BCE c, marvelous thing no. 154), "*stream of fire*" (Aristotle, 4th cent. BCE c, no. 38), or "*outpouring fire*" (Aristotle, 4th cent. BCE c, no. 105).

Fire is also behind volcanism for Lucretius (e.g. "*ex imis vero furit ignibus impetus Aetnae*", "*from the depths come the fiery eruptions of Etna*", Lucretius, ca. 60 BCE, *De Rerum Natura*, book 2, 593, translation W.H.D. Rouse, revised by M.F. Smith), and Seneca (63 CE; e.g." *ignesque nonnumquam per aliquod ignotum antea montis aut rupis foramen emittat, aliquando notos et per saecula nobiles comprimat*.", "*and sometimes it* [the Earth] *emits fires from a previously unknown opening of a mountain or a rupture, sometimes it conceals those that were known and famous for ages*." Seneca, *Naturales Quaestiones*, book VI, chapter 4, article 1, translation MW). Pliny the Elder (77 CE) lists several mountains that are on fire: "*ardet Aetna noctibus semper*", "*flagrat in Phaselitis mons Chimaera*, [...]" ("*Etna always glows at night*", "*Mount Chimaera* [...] *is on fire*", Pliny the Elder, 77 CE, *Naturalis Historia*, book II, CX, transl. H. Rackham), "*montem Epopon, cum repente flamma ex eo emicuisset*" ("*Mount Epopos, is said to have suddenly shot up a great flame*", Pliny, 77 CE, Naturalis

Historia, book II, LXXXIX, transl. H. Rackham). His nephew, Pliny the Younger (104 CE?) theorized little, but gave a famous description of the 79 CE eruption of Mt. Vesuvius, where he said "*Interim e Vesuvio monte pluribus locis latissimae flammae altaque incendia relucebant, quorum fulgor et claritas tenebris noctis excitabatur.*" ("*Meanwhile on Mount Vesuvius broad sheets of fire and leaping flames blazed at several points, their bright glare emphasized by the darkness of night.*", Letters, book VI, XVI, transl. B. Radice).

Besides the connection of volcanic phenomena with fire, the mentioned authors agreed that the interior of the Earth contains caves or voids. The idea that earthquakes are caused by flows of water or air (e.g. "*So the cause of earth tremors is neither water nor earth but wind*", Aristotle, 4th cent. BCE b, *Meteorologica*, book II, chapter VIII, transl. H.D.P. Lee) requires open space in which these can flow. According to Aristotle, "*the severest earthquakes occur in places where the sea is full of currents or the earth is porous and hollow*" (Aristotle, 4th cent. BCE b), and the underlying motions of air are even the cause for the Earth's internal fire: "*for when the air is broken up into small particles, percussion then causes it to catch fire.*" (Aristotle, 4th cent. BCE b). Lucretius (60 BCE) thought that "*primum totius subcava montis / est natura, fere silicum suffulta cavernis*" ("*Firstly, the whole mountain is hollow beneath, being supported for the most part upon caverns in the basalt rock.*", Lucretius, *De Rerum Natura*, book 6, 682–683, translation W.H.D. Rouse, revised by M.F. Smith).

Much later, Strabo (7 BCE?b, *Geography*, book 6, 2.8) describes that a liquid pours out of Etna's crater ("ρύακας", a small river), and also that it emits flames, smoke, and "μύδρους", i.e. glowing, nearly molten material. In book 5, 4.9, Strabo repeats Pindar's suggestion of a subterranean connection from the Naples regions "*and extending as far as Sicily, is full of fire, and has caverns deep down in the earth that form a single whole, connecting not only with one another but also with the mainland; and therefore not only Aetna clearly has such a character* [...], *but also the Lipari Islands, and the districts round about Dicaearchia, Neapolis, and Baiae, and the island of Pithecussae* [called Procida today, MK]" (Strabo, 7 BCE?a, *Geography*, book 5, 4.9, transl. H.L. Jones).

Strabo's is the most extended system of interconnected cavities we found explicitly described in the antique literature, although the unknown author of the Latin poem *Aetna* (written prior to the 63 CE destructive earthquake around Pompeji) compares the Earth to a living organism, with large clefts and chasms instead of veins (*Aetna*, 95–105). In lines 445–448 the author says about the island named after Vulcan (i.e. Vulcano island north of Sicily): "*atque haec ipsa tamen iam quondam exstincta fuisset, / ni furtim aggereret Siculi vicinia montis / materiam silvamque suam, pressove canali / huc illuc ageret ventos*

et pasceret ignes" ("*And yet this very island would long ago have been extinct had not its neighbor, the Sicilian mountain, always been secretly providing it with its own fuel and material, or through some sunken channel been driving the winds this way and that to feed the flames*", *Aetna*, translation Duff and Duff, 1934).

As the source of the volcanic heat, *Aetna* identifies the volcanic rock itself: "*sed maxima causa molaris / illius incendi lapis est*" ("*But the paramount source of that volcanic fire is the lava-stone*", *Aetna*, 400-401, translation Duff and Duff).

Seneca (after the 63 CE Pompeji earthquake) also imagines enormous voids: "[...] *sunt et illic specus vasti ingentesque recessus ac spatia suspensis hinc et inde montibus laxa; sund abrupti in infinitum hiatus, qui saepe illapsas urbes receperunt et ingentem ruinam in alto condiderunt*" ("*there are also vast caverns, corridors and hallways, with mountains rising here and there. There are also abrupt abysses of infinite depth, which often devoured entire cities and bury their ruins in their depths*", Seneca, *Naturales Quaestiones*, book III, chapter 16, article 4, after the German translation by O. and E. Schönberger, English by MK). Seneca also cites Democritus with the words "*aliqua pars terrae concava est*" ("*a considerable part of the Earth is hollow*", Seneca, *Naturales Quaestiones*, book VI, chapter 20, article 1, after the German translation by O. and E. Schönberger, English by MK).

3.2 Celestial bodies in early natural philosophy

Plato's cosmos, as described in his dialogue *Timaeus* (Plato, 4th cent. BCE) is made of four elements (Tim., 32c), and is unique (32b), finite (33b-c) spherical (33b, 62d), artificial (69b-c), alive (30b), blessed (34b), aesthetic (33b), teleologic (38c-e, 39b-c), and anthropocentric (91d-e).

The Sun and the planets are created for a specific purpose: "[...] *the sun and moon and five other stars, which bear the appellation of "planets", came into existence for the determining and preserving of the numbers of Time*" (*Timaeus*, 38c/d, translation R.G. Bury). They apparently needed some training, though: "[...] *and when they had been generated as living creatures, having their bodies bound with living bonds, and had learnt their appointed duties; then they kept revolving* [...]" (*Timaeus*, 38e). And there is no suggestion of any other planets.

The plan of the creating God worked out, and humans learned time keeping, astronomy, mathematics, and philosophy from observing the sky: "*Vision, in my view, is the cause of the greatest benefit to us, inasmuch as none of the accounts now given concerning the Universe would ever have been given if men had not seen the stars or the sun or the heaven. But as it is, the vision of day and night*

and of months and circling years has created the art of number and has given us not only the notion of Time but also means of research into the nature of the Universe. From these we have procured Philosophy in all its range, than [sic] *which no greater boon ever has come or will come, by divine bestowal, unto the race of mortals. This I affirm to be the greatest good of eyesight*" (Plato, *Timaeus*, 47a/b, translation Bury). These lines, although in a different, unspecified translation, are the motto above the PLATO mission definition study report of ESA (PLATO, 2017). In how far Plato's narrating character, or the Timaeus of Locri after whom he is apparently modeled (see Bury's introduction to the dialogue), would be bewildered by our considerations on exoplanets and their habitability must remain as speculative as the notion that Giordano Bruno would have applauded the PLATO project.

Plato did not say of what material the planets and the Moon consist, but the sphere of the fixed stars "*He wrought for the most part out of fire* [...]" [*Timaeus*, 40a]. The stars rotate not only around the axis of the cosmos as a whole, but also around themselves ("*uniform motion in the same spot*", *Tim.*, 40b, as Bury translates). This idea of rotating stars, however, is not foreboding something Plato could impossibly know, but by this motion each star "*conceives always identical thoughts about the same objects*" (*Tim.*, 40b), i.e. the idea of a rotation is embedded in the animistic-teleologic concept and has nothing to do with conservation of an angular moment.

It is difficult to say if Plato thought the Earth spherical, drum-shaped, flat, or otherwise. The *Timaeus* is very unspecific here. Morrison (1959) analyzed the usage of words in Plato's *Phaedo* and several works of other authors to argue that Socrates' description in the *Phaedo*, contrary to the interpretation of many others, should not be understood as the description of a globe. Instead he suggested that Socrates had a hemispherical Earth in mind, where the entirety of the inhabited surface is the flat face of the hemisphere, while the volume contains Hades and Tartaros and is dedicated to the post mortem treatment of souls. Couprie (2005) took Socrates' comparison of the Earth with a dodecahedral leather ball more verbatim, but also thought that the entire description of the Earth in the *Phaedo* is a mixture of geography and mythology, and, given Plato's thoughts about reality and our perception of it, one even has to be careful with words like "schematic" and "real".

By all means, the idea of a spherical Earth was apparently new at Plato's time, and Aristotle considered it necessary to defend this view against earlier concepts.

Aristotle (4th cent. BCE a) was convinced that the Earth is spherical. His *On the Heavens* gives several correct arguments, and even considers possible to reach India by sailing westwards. The circumference he cites for the Earth is 85% too large (see S2.1) but of the right order of magnitude (Eratosthenes carried out his famous experiments long after Aristotle's death). He was obviously aware of the Earth's volume. Aristotle concluded that the Earth is "μὴ μέγαν πρὸς τὸ τῶν ἀστρων ἔγεθος" ("*not large in comparison with the size of the other stars*" (*On The Heavens*, book II, ch. XIV, transl. W.K.C. Guthrie). The pseudo-Aristotelian *On the Cosmos* (the authorship and dating of which is uncertain) has "*set in the depth at the center of the cosmos, densely packed and compressed, is the whole mass of the earth, unmoved and unshaken* [ἀκίνητος καὶ ἀσάλευτος]" (*On the Cosmos*, section 3, translation Furley). In general, Aristotle was more interested in the Earth's exterior than in its interior.

Aristotle knew that the Moon is spherical (*On the Heavens*, book II, ch. XI, see also S2.1). According to his five elements cosmology, the Moon and all other heavenly bodies needed to consist of Aether, and only Aether, since this is the only element that allows for eternal existence and motion (see also S2.1).

Lucretius (60 BCE) saw both Sun and Moon moving through air rather than Aether, only the part of the cosmos beyond the Sun is in Aether ("*Hunc exordia sunt solis lunaeque secuta / interutrasque globi quorum vertuntur in auris*", "*This was followed by the beginnings of sun and moon, whose globes revolve in the air between the two*", Lucretius, *De Rerum Natura*, book 5, 471–472, translation W.H.D. Rouse, revised by M.F. Smith).

At least part of the Moon is – accidentally – made of earth material according to Pliny the Elder (77 CE): The Moon and the stars are nourished by the Earth's moisture and the Moon can apparently take material of the Earth with it in the process of drinking, hence "*maculas enim non aliud esse quam terrae raptas cum humore sordes*" ("*her spots being merely dirt from the earth taken up with the moisture*", Pliny, 77 CE, Naturalis Historia, book II, VI, 46, transl. H. Rackham).

Plutarch (approx. 85 CE) went a step further and concluded from the Moon's ability to reflect light that it must consist of earth-like material, since "*... if we see that the moon is illuminated not as the air is rather than as the earth, the things upon which the same agent produce the same effects must be of similar nature*" (Plutarch, 80 CE?, *Concerning the face...*, 931c, transl. Cherniss and Helmbold).

As a tentative (as our survey of ancient literature is cursory and incomplete) conclusion we get the impression that witnessing earthquakes and volcanos were at the brink of the comprehensible for early civilizations. Language and ideas formed from everyday experiences were hardly suitable to describe, not to mention understand, these kinds of events. There was hardly even a word for lava, both Greek and Roman authors used fire metaphors for centuries. Analogies with combustion and fire are abound, but explanations were mostly limited to what is visible at the surface. The subterranean caves often mentioned in the explanation of earthquakes appear to be limited to what we would call crustal depths today, at least we found little that unequivocally describes the deep interior of the Earth. Planets were mere lights in the sky, and especially the Aristotelian philosophy, which became dominant in Christian Europe, denies any analogy between Earth on the one hand side, and the Moon and the planets on the other side.

3.3 At the dawning of the age of science

Before Galileo, it was hardly possible for European natural philosophers to think, not to mention write, about the interior of celestial bodies. At Galileo's time, the prevalent model of the world was still that of Aristotle, with its inherent heresies fixed by the work of Albertus Magnus, Thomas Aquinas and the Dominican Order of Preachers (e.g. Flasch, 2013). In Aristotle's thinking, the universe consisted of five elements, four of which were found only in the sublunar world (earth, water, air, and fire), while the supralunar world, including the Moon, entirely consisted of a fifth element, the aether (Aristotle, *On the Heavens*). The four sublunar elements were assorted around the center of the Universe in concentric shells, earthen the innermost, surrounded by water, air, and fire, in this order. The supralunar world was thought as a spherical contraption, where a number of rotating aether-shells held the planets and stars. Aristotle insisted that this universe has a finite diameter, that there is no outside, and that there is only one such universe – this one world is everything that exists (Aristotle, *On the Heavens*).

Leonardo da Vinci, in the early 16th century, applied his mechanical understanding to the Aristotelian model of – ideally – concentric spheres consisting of the elements earth and water. Since Aristotle thought the earth-element heavier than the water-element, the former should be within the latter, and both concentric with the center or the cosmos. Which is obviously not the case. Leonardo understood that rivers, by means of eroding

mountains, move mass from the dry part of the earth into the submerged part, shifting the center of gravity of the whole: the earth-sphere "[...] *will make itself lighter and in consequence will make itself more remote from the center of the gravity of the earth, that is from the center of the universe which is always concentric with the center of the gravity of the earth*." (codex Leicester, 17, translation MacCurdy, 1955, p. 325) "[...] *and the earth and the mountains will emerge out of the sphere of the water lightened by this part, and will also make itself lighter by the weight of the water which rested upon it, and will come so much the more to raise itself towards the sky. And the sphere of the water in this case does not change its position, because its water fills up the place from which the gravity of that part of the earth that fell divided itself;* [...]" (Leic. 36 r., translation MacCurdy, p. 356). What Leonardo describes here is a center-of-mass-center-of-figure offset of the earth-sphere, caused and continually increased by the erosion of mountains. He recognizes that this will ultimately bring former sea floor above the water level, giving an explanation for fossilized shells and oysters in the mountains.

Balance requires that "*it must needs be therefore that there is a great mass of water within the earth, in addition to that which is diffused through the lower parts of the atmosphere and runs through the rivers and springs*" (Leic. 36 r., translation MacCurdy, p. 355) and "*Necessity makes the machine of the earth empty of earth and full of water, after the fashion of a vessel filled with water* [...]" (Leic. 35 v., translation MacCurdy, p. 352), i.e. the earth-sphere is hollow and filled with water.

At the same time, non-Aristotelian cosmologies, denying the entire five-elements concept, circulated at least since 1417. In this year, Poggio Bracciolini re-discovered Lucretius' *De Rerum Natura* (60 BCE) – Lucretius states that there is "*illimitable space empty in every direction*" (p. 177), and that in this "[...] *unfathomable universe* [...] *it cannot by any means be thought likely that this is the only round earth*" (p. 177) and one is "[...] *bound to confess that there are other worlds in other regions and different races of men*" (p. 178).

In Galileos time, such ideas were dangerous: Giordano Bruno also considered the stars to be just distant suns, surrounded by other Earths with their respective inhabitants. Maybe his cosmological ideas were not considered as his most depraved heresies, but the sentence against him clearly condemned them as heretic and erroneous. Bruno burned on the stake in February 1600, and all his writings were prohibited and remained so until the roman church discontinued its *Index Librorum Prohibitorum* in 1965 (see the cited 1900 edition of the index of forbidden books; also Bruno, 1584; Rowland, 2008, see also S2.4).

A luckier opponent of the Aristotelian world model was William Gilbert (in Anglican England). In his book on magnetism (Gilbert, 1600), he described "*the true earth-matter we hold to be a solid body homogeneous with the globe, firmly coherent*" (p. 68), there are just "*certain hollows*" and "*veins and arteries*" (p. 64) that contain and transport water. Although "*the earth's center is the center of the earth's magnetic movements*" (i.e. the origin of the field at the surface, p. 150), Gilbert did not describe any specific structure that produces the field – from his experiments with a spherical magnet, he concluded that "*All the inner parts of the earth are in union and act in harmony, and produce direction to north and south*" (p. 184) thus the Earth as a whole behaves like "*loadstone*" (sic, p. 313). Also, Gilbert was aware that lodestone (i.e. magnetite), as dug from the earth, is closely related to iron ("... *the best loadstone is the most excellent iron ore ...*", p. 63).

Then Galileo published a little book (the *Sidereus Nuncius*, Galilei, 1610a,b, English translations from the former, Latin from the latter). On only 60 pages he announced the discovery of satellites around Jupiter, stars never been seen by human eyes before, and the pockmarked surface of the Moon. Galileo described the surface of the Moon as "*inæqualem, asperam, cauitatibus*" (p. 9 in 1610b, "uneven, rough, crowded with depressions", p. 42 in 1610b) and generally compared it to "*Telluris facies*" (p. 9, "*the face of the Earth*", p. 42). Galilei not only claimed that the Moon has mountains, he also measured the height of some to be "*eminentior* [...] *miliaribus Italicis 4*" (p. 19, "*higher than 4 Italian miles*", p. 54) and thus "*Lunares eminentias terrestribus esse subliminores*" (p. 19, "*the lunar prominences are loftier than the terrestrial ones*", p. 54). According to Aristotelian (and thus church-official) doctrine, the Moon consists of aether and is eternal and perfect – attributing landscapes and explicitly comparing it to the Earth, the material of which is subject to decay and corruption, was a bold move and raised suspicion against the new instrument. Nevertheless, Galileo's work was welcomed, even celebrated, not only among Copernicans, but also clerics like Cardinal Barberini, the later pope Urban VIII, who said he saw "*some very wonderful things concerning the Moon and Venus*" (commentary of A. van Helden to Galilei, 1610a, p. 112) through the telescope.

Other observations and publications contributed to the demise of the Aristotelian world model: Tycho Brahe demonstrated that the new star that appeared in the constellation Cassiopeia was not a meteorological phenomenon but must be situated in the sphere of the fixed stars (see Gingerich, 2005) – and thus that the supposedly eternal, unchangeable realm of the stars is not that unchangeable. Even more spectacular was the comet

of 1577 – of which Brahe demonstrated that it is moving at a distance larger than that of the Moon, contrary to Aristotle (*Meteorologica*), who considered comets as a meteorological phenomenon. Kepler (1609) knew that the perfection of circles is unsuitable to describe the observed motion of Mars. His attempt to explain the motion of planets by some force emanated by the sun (rather than by live souls as in the Aristotelian view) were considered by contemporaries as "*whimsical speculations, that do not belong to astronomy, but to physics … How is that supposed to serve astronomy?*" (from a letter of Gdansk astronomer P. Crüger, translated by MK after M. Caspar's introduction to Kepler, 1609). Astronomy, at that time, was a purely descriptive endeavor.

In parallel to the new views of the outer cosmos, the thinking about the interior of the Earth also changed. Although Aristotle explained earthquakes by winds flowing into and out of the subsurface, and although he was aware of the Earth's immense circumference, he did not describe the bulk of its interior any further.

One approach to further detail the Earth's interior is the hypothesis of the central fire. The existence and widely used therapeutical effects of hot springs called for an explanation of their heat, and a whole body of literature developed around this problem, as Vermij (1998) describes. The suggested heat sources however needed to be close to where the springs are found.

In his *Principia Philosophiae*, Descartes (1644) attempted to develop a Grand Unified Theory (as we would call it today) and claims to describe all known phenomena: "*Nullae naturae Phaenomena in hac tractatione fuisse praetermissa*" – "*No natural phenomena were omitted in this treatise*" (book IV, article 199, English by MK after the German edition of Descartes, 1644). With a theory of matter similar to that of Lucretius, i.e. small particles of different shapes and sizes and purely mechanical interactions like collisions, friction, and locking. The described phenomena include comets, the supernova of 1572, sunspots, magnetism, earthquakes, volcanoes, the nature of mercury, the reason why water does not burn, and the production of glass, among others. In 1663, the atomistic nature of his treatise granted Descartes a number of entries in the *Index Librorum Prohibitorum*, which are still found in the 1900 edition (Index, 1900, see also Wohlers' introduction to his translation of Descartes, 1644).

Sunspots play a major role in Descartes' hypothesis about the origin of the Earth: the Earth originally was a fixed star (*"antea fuerit sidus lucidum"*, "*once was a luminous star*", III, 150; "*Fingamus itaque Terram hanc, quam incolimus, fuisse olim ex sola materia primi elementi conflatam, instar Solis, quamvis ipso*

esset multo minor;", "*Let us assume that the Earth was initially made only of the first element, like the Sun, although it was much smaller.*", IV, 2), and formed independently of the Sun (IV, 2). This star produced more and more sunspots, which finally completely encrusted it, and it slid into the dominion of the Sun and became a planet (IV, 2). Some of the particles of which the Earth's sunspots consisted transformed into particles of other sizes and shapes, and formed layers around a core of stellar material ("*Harum prima & intima I continere tantum videtur materiam primi elementi*", "*The first and innermost region I obviously contains matter of the first element* [of which the stars and the Sun consist, MK] *only*", IV, 3) – from the center outward the Earth now consists of stellar matter, sunspot material ("[...] *maculis Solis, quae cum sint ejusdem naturae atque hoc corpus M* [...]", "*sunspots, which are of the same nature as the body M* [the second layer from the center, MK]", IV, 4), a layer in which metals form, the land surface with its topography, water, and air (IV, 3, 4, 44). Descartes shows a schematic and obviously unscaled cross-section through the earth, but does not estimate the dimension of the innermost region. His entire treatise is a purely qualitative narrative.

Ciancio (2018) considers Descartes as the one who finally helped the idea of a central fire to acceptance, although Descartes explains volcanic "fire" by burning sulphur and bitumen (Descartes, 1644, IV, 78) rather than by the stellar material in the Earth's center. Before, the central fire hypothesis was dismissed by many, since it was at odds with emerging views about the genesis of rock and ore, the nature of fire as such, Aristotelian philosophy, and the widespread beliefs about the Christian hell (a discussion of the evolution of the central fire hypothesis is given by Ciancio, 2018, from which our summary is derived). The two still famous cross-sections of the Earth in tome 1, book 4 of Athanasius Kircher's *Mundus Subterraneus* (Kircher, 1664) were probably inspired by Kircher's expedition into the summit crater of the Vesuvius, which convinced him that some fire must exist within the Earth, to drive and fuel volcanic eruptions. While the figures appear to simply show a network of caves and furnaces of fire which feed the volcanoes at the Earth's surface, and an independent plumbing that feeds the sources of rivers and the oceans, Kircher's text equates the shown central fire with the Christian hell, the eternal prison of damned souls. It must be noted that the association of the Christian hell with fire and heat is not universal and likely rather young. In 1320, Dante Alighieri describes hell as a cold place with Satan frozen mid-breast in ice, in accordance with the Aristotelean order of elements (Dante, ca. 1321).

Figure 1 The center of the Earth is occupied by hell, as illustrated in this early cross-section. Credit: The circles of hell and limbo (containing Abraham and Lazarus) beneath the earth; snakes appear at the surface of the earth. Engraving by J. Wierix, 1595. Wellcome Collection. Public Domain Mark.

One contradiction to Aristotle lies in the dictum that fire is lighter than air and will rise to its natural place, directly below the Moon. A marginal note on Kircher's page 171 summarizes a discussion of how – in Kircher's view – this contradiction could be resolved: "*Ignis sub Luna non est elementum*." – Fire below the Moon is not a (pure) element, and hence it does not ascend moonwards. Some authors (Cesi, Cabeo, Riccioli, see Ciancio, 2018, and references therein) accepted the presence of internal fires, but avoided mentioning a large central fire, and thus the confrontation with Aristotle. They also avoided the confrontation with the catholic church and the inquisition – a widespread belief was that the place of eternal damnation is at the location farthest from god, i.e. in the center of the universe, which coincides with the center of the Earth as illustrated in Fig. 1 (Fabbri, 2018, see also S2.2. This traditional belief is also what Harold Jeffreys referred to in his letter of 01. June 1932 to Inge Lehmann: "*I should have thought a good Jesuit would have jumped at the discovery of hell, but he reacts all wrong*." – Lehmann argued that Jesuit scientist J.B. Macelwane misunderstood her discussion of PKP amplitudes and structure within the core. Cited after Hjortenberg, 2009, p. 691).

Ciancio (2018) also cites the *Mathematicae totius*, a comprehensive educational book on mathematics, astronomy, geography, optics, music and other topics by Kircher's fellow Jesuit Pierre Gautruche (1668). In this book, Gautruche sketches an interior of the Earth where Kircher's heating and plumbing is limited to an outer region (Tabula IX, in the figure section that follows p. 208 of Gautruche's book). The majority of the Earth's interior is homogeneous, and only a small central region is reserved for a central fire, which also constitutes "*carcerem damnatorum*" (p. 219), the prison of the damned souls. For Gautruche, the homogeneous material of the deep interior imparts its magnetism on iron whenever ore or lodestone is formed ("*Nam primo, constat, virtutem Magneticam a Terra derivari in ferrum*", "*It is clear, that the magnetic power of iron derives from Earth*", transl. MW and S. Schwinger, Gautruche, 1668, p. 226), and since he knew Gilbert's work and his description of how to demagnetize a needle with fire (Gilbert, 1600, p. 190), he concluded "*Ignes subterranei vim illam Magneticam prorsus interimerent*." ("The subterranean fires would have completely suppressed the magnetic force.", transl. Ciancio, 2018; Gautruche, 1668, p. 228). Gautruche nevertheless does not rule out the central fire, but concludes that it has no physical effect. Although Gautruche gives the diameter (3436 leagues) and volume (21254065200 cubic leagues, p. 219 – too much even when using $\pi = 22/7$ from Gautruche's p. 44) of the Earth with great

precision, he does not assign a radius to the innermost zone. The *Mathematicae totius* appears to be an attempt to bring together the emerging scientific and the traditional religious views, but does not provide an unequivocal description.

Gautruche was not the only one to discuss the physical dimensions of hell. Galileo (1588) already analyzed Dante's descriptions geometrically. Burton (1651) cites two brothers of the Societas Jesu, Franciscus Ribera and Leonardus Lessius (Lessius, 1620). Ribera arrives at a diameter of "*200 italian miles* [...] *stadia mille sexcenta*", (Burton, 1651, p. 246), but his confrere Lessius disagrees, because this would be an unnecessarily vast cavern – too much space for the damned could alleviate the severity of their punishment. According to Lessius' own computations, a much smaller hell is more than sufficient: "*Quod ad magnitudinem illius cavitatis attinet, etiam si diameter eius esset solum unius leucae seu quatuor milliarium Italicorum, hoc est pedum viginti milium, satis capax esset, non solum ad omnia damnatorum corpora excipienda, sed etiam ad multitudinem decuplo maiorem* [...]" ("*Regarding the magnitude of that cavity, then if its diameter were only one league, or four Italian miles, that is twenty thousand feet* [or about 6 km, MW], *it would be spacious enough to contain not only all bodies of the damned men but also an amount ten times greater* [...]", Lessius, 1620, p. 474, translation MW). These estimations make clear that their authors think of hell as a physical place, not a supernatural or spiritual one. Also, they locate it in the center of the Earth.

In 1683, Halley suggested that the Earth is actually not a dipole, but a quadrupole magnet, since the magnetic declinations he listed are incompatible with a dipole field. Contrary to previous authors he was convinced that the reasons for the declination must be in the source of the terrestrial magnetic field, rather than in local disturbances like ore bodies. Later on, he noticed two major obstacles to his theory, firstly, that all known magnets have only two poles, and secondly, that the four poles are not fixed but moving. In 1692, Halley came up with a hypothesis he thought might appear "*Extravagant or Romantick* [sic]" to some (Halley, 1692, p. 564): Since moving large masses within the earth might change its center of gravity, resulting in "*very wonderful Effects ... as History never yet mentioned*" (p. 567), he suggested that "*a Nucleus or inner Globe included within ours, with a fluid medium in between*" (p. 568) might be rotating around the same axis of rotation, but at a slightly different rate to explain the observed westward drift of the field. Then the outer shell could have two magnetic poles, and the nucleus two additional ones. Anticipating the Aristotelian teleologic argument that his magnetic nucleus lacks a reasonable final cause and is too

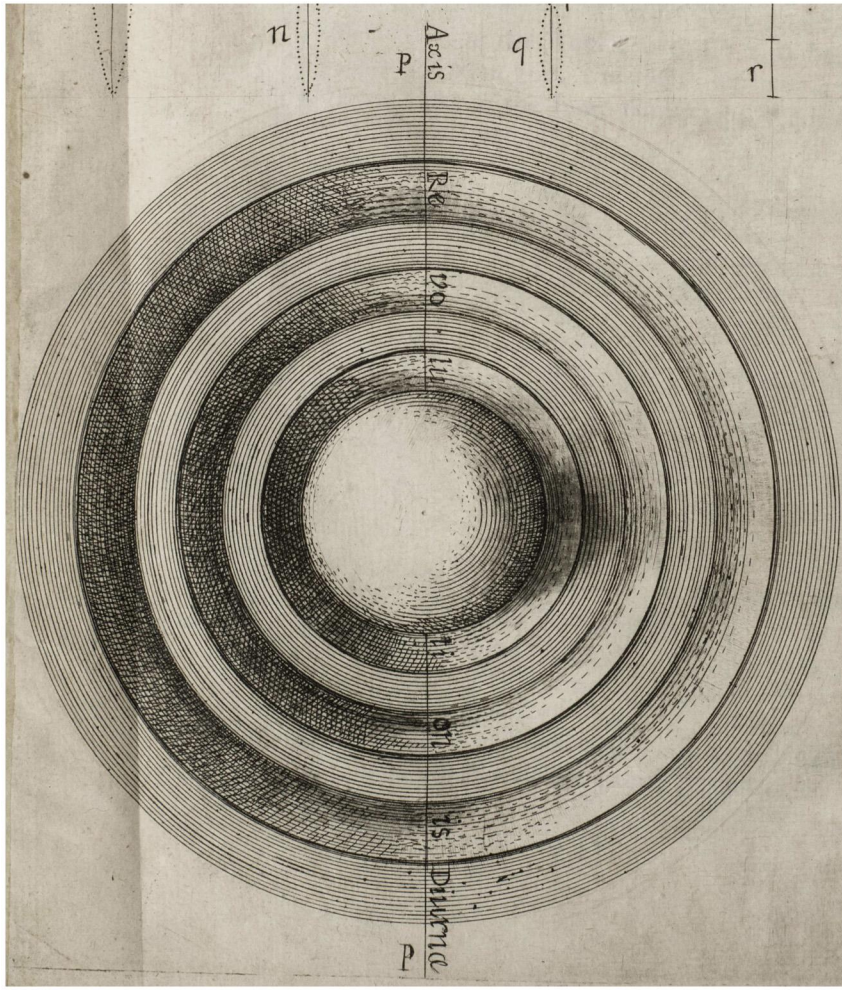

Figure 2 The Earth's internal shells as suggested by Edmund Halley in 1692, motivated by the observation of a nondipole magnetic field. The vertical line indicates the axis of daily rotation. Credit: The Royal Society, Phil. Trans. R. Soc., vol. 17, iss. 195, https://doi.org/10.1098/rstl.1686.0106, reproduced with generic permission for articles older than 70 years or in open access. Clipped graphs at the top of the figure belong to an article by Hon. Francis Roberts on trumpets. Approx. 30% of the original page were clipped from the top, and approx. 15% from the right.

useless to exist, he suggests that there might be even more internal shells, separated by a few hundreds of miles of atmosphere and possibly inhabited (Fig. 2). Today, this reminds us of Verne (1864) in the best case, but pro-

viding space for inhabitants is an excellent final cause in an anthropocentric philosophy. Halley suggested that the innermost magnetic nucleus has a diameter of "*about two thousand miles*" (p. 577), but his only argument was that the proportions of the internal shells shall reflect the proportions of Mercury, Venus, and Mars.

In 1687, just between Halley's 1683 and 1692 papers, Newton published his *Philosophiae Naturalis Principia Mathematica* (see Newton, 1726). In this massive volume, subdivided into three books, Newton introduced the concepts of mass and inertia, refined the concept of density, and replaced the "heaviness" and "lightness" of the Aristotelian elements with a quantitative force of gravitation. Newton not only described new methods and theories, but also demonstrated their power by solving a number of astronomical problems. Among these were the determination of the masses of the planets, including that of the Earth (book III, proposition 8). Newton's analysis of the shape of the Earth (book III, prop. 39) and different densities found at the surface of the Earth and in mine shafts (book III, prop. 10), allowed asking for the density structure of the earth. The formulation of proposition 8 can also be seen as the first suggestion of a radially symmetric internal structure of planets:

> *Si Globorum duorum in se mutuò gravitantium materia undique, in regionibus quae à centris aequaliter distant, homogenea sit: erit pondus Globi alterutrius in alterum reciprocè ut quadratum distantiae inter centra. (Newton, 1687)*

> *If two globes gravitate toward each other, and their matter is homogeneous on all sides in regions that are equally distant from their centers, then the weight of either globe toward the other will be inversely as the square of the distance between the centers. (Newton, 1726)*

A remark found in a preliminary manuscript version, published posthumously (Newton, 1728a,b, see also S3), gave rise to a method to extend density comparisons to whole mountains, and ultimately led to the first results on the Earth's core as described in section 4.1 (p. 89).

The 17th century saw what Wootton (2015, p. 111) called a "*silent revolution*" from the ancient natural philosophy to modern science, as it was a process extended over a century or more, rather than being centered around a few key persons as the above might suggest. Wootton points out that Galileo, when he stated "*prima fosse d'accertarsi del fatto*" ("*First, we have to make certain what the facts are*", cited after Wootton, 2009), he had to borrow the word "fact", and the concept of the undeniable scientific truth, from jurisprudence. Also, Galileo had to use "*convoluted phrases*" (Wootton, p. 58) to announce that he discovered Jupiter's moons, since a word for

discovery did not exist in Latin, and the possibility of discovering something new was not a concept in natural philosophy.

Because of these developments, and because of what is found about the Earth's interior in the literature cited, it appears meaningful to take the 17th century as the beginning of any discussion that could involve the Earth's core, and not to search for any earlier contributions.

4. Core radii of Earth, Moon, and Mars

In this section, we review the research on the terrestrial planets, first for the Earth, then follows the Moon, and finally Mars. It is impossible to completely disentangle all storylines, as many of the involved people were active in several fields, and working about several planets. Therefore, it was not possible to avoid all redundancies.

4.1 Earth

Much of what is presented here is also found in histories of geophysics, like those by Bolt (1982), Kertz (1999, in German), or Musson (2013), but for a complete view of the development, and its implications for the geophysics of other planets, it appears useful to have a closer look on the investigation of the Earth's core. From the 1950s onward, however, the body of literature on the Earth's core grows quickly, and we do not attempt to achieve complete coverage.

As a test of Newton's new physics, Bouguer's 1735 expedition to Peru aimed at testing if the Earth is indeed the oblate spheroid predicted by Newton (1726, book III, prop. 39), or if it has the prolate shape favored by Cassini (see Smallwood, 2010, and references therein). One of the experiments carried out was to determine the deflection of the plumb-line by the edifice of the Chimborazo, a relatively isolated stratovolcano (which was not recognized as a volcano at the time). Bouguer dismissed the Cotopaxi since, as a volcano, "*il y tout lieu de croire qu'elle n'a pas beaucup de solidité*" ("*there is every reason to believe that it is not very massive*", translation MK, Bouguer, 1749, p. 377) and he did not expect it to produce a sufficient effect. With a height of more than 6200 m, the Chimborazo is close to the three-miles dome Newton used to estimate the expected amount of deflection (S3). The observed deflection was however much smaller than the expected, and the experiment was generally considered as a failure (the simulation of Smallwood, 2010, shows that the small deflection found by Bouguer was correct, and that the then-unknown isostatic compensation

has a significant effect). Bouguer suggested "*Il y a beaucup d'apparence qu'on trouvera en France ou en Angleterre quelque montagne d'une grosseur suffisante ...*" ("*It appears that one might find a sufficiently large mountain in England or France ...*", translation MK, Bouguer, 1749, p. 389) to repeat the experiment under more comfortable conditions.

The idea that volcanoes are not very massive, even hollow (see also Lucretius, section 3.1), was supported by Leopold von Buch (1825, cited after Mather and Mason, 1967, p. 210) in his upheaval theory, which assumes that the first stage of the formation of a volcano is the build-up of a giant, bubble-like dome. Von Humboldt (1845) explicitly said "[...] *heben elastische Dämpfe entweder einzelne Theile* [sic] *der Erdrinde zu domförmigen, ungeöffneten Massen* [...]" ("*... elastic vapours lift either single parts of the Earth's crust into dome-shaped, closed masses ...*", translation MK, p. 254), i.e. volcanoes initially form like bubbles on boiling water. Verne (1869) adopted this concept when his Captain Nemo operates a coal mine under the circus-tent like shell of an extinct volcano.

In 1772 (printed 1775), Maskelyne proposed that suitable mountains are indeed found in Britain. Field campaigns to Mt. Schiehallion (spelled Schehallien back then) were finished by 1776, and results were published by Hutton in 1778. The observed deflection of the plumb-line was 11.6", and the mean density of the Earth determined as 4.5 $g\,cm^{-3}$, larger than that of surface rock. Hutton's interpretation was that "*great quantities of metals, or such like dense matter*" (Hutton, 1778, p. 783) must be present in the Earth's interior, and assuming a density of 10 $g\,cm^{-3}$ for a mixture of known metals, Hutton concluded that "*nearly 2/3 of the diameter of the earth, is the central or metalline part*" (Hutton, 1778, p. 784). In short, he suggested that the Earth is layered, has a discontinuous density structure, and a metal core (Playfair, 1811, collected an array of rock samples from the Schiehallion and concluded that Hutton's density is a little too low, but did not revise Hutton's core radius).

Benjamin Franklin (1793) concluded, from the presence of fossilized oyster shells in rocks above sea level, that much deformation of the surface occurred in the past, and had difficulties to imagine this to happen when the Earth is entirely solid. He suggested that the solid surface is that of a thin shell floating on a dense liquid, and, extrapolating pressure experiments with air, he supposed that air can be compressed to densities beyond that of gold, and thus constitute this dense fluid.

Cavendish (1798) found a larger mean density for the Earth (even larger than Playfair's), but did not discuss the Earth's interior any further. Gravity

experiments concerning the Earth's mean density are also related to experiments to determine the Newtonian constant of Gravity, G, (see S4), and research branched into Earth interior on the one hand, and nongeological G-measurements on the other – nowadays, Cavendish's result is usually converted into a determination of G and the relation of his work to the constitution of Earth is rarely mentioned.

The 19th century saw a complex debate about the interior structure of the Earth, reviews of which are given by Zöppritz (1881, in German), or Brush (1979). With a mean density and Newton's law of gravity, it was possible to compute the hydrostatic pressure down to the Earth's center (where $P = 7180593750$ lbs ft^2 or 343 GPa, according to Sayles, 1888), temperature could be estimated from gas theory (e.g. Richter, 1879, p. 62, who found $T = 103400$ °C for the Earth's center, and $T = 19000$ °C at 637 km depth) or from geological evidence (geologists considered volcanos as direct connection to a completely liquid interior underneath a thin crust, as many laypersons still do today). The question arose what materials could withstand the conditions of the Earth's interior. Since the surface is obviously solid, one question was to which depth the solid material, termed "crust" to distinguish it from any nonsolid below, may extend. It must be kept in mind when reading about crustal thicknesses of hundreds of kilometers, that the vocabulary of the 19th century was different from today's – language was not yet differentiated into crust and mantle.

Humphry Davy (1808) offered an alternate approach to explain volcanic heat: He found that metals like Potassium and Sodium (which he discovered and named) "*cannot exist at the surface of the globe; but it is very possible that they may form a part of the interior*" (p. 369), and then "*their accidental exposure to the action of air and water, must produce the effect of subterranean fire, and a product of earth and stony matter analogous to lavas*" (footnote on p. 369). To further investigate this, he traveled to Vesuvius, Italy, several times from 1814 to 1820 and conducted a number of experiments on freshly erupted lava (Davy, 1828) and "*... from known facts, there appears to me no other adequate source* [for volcanic fires, MK] *than the oxidation of the metals ...*" (Davy, 1828, p. 250), but admits that hot springs and temperatures in mines "*render it probable that the interior of the globe possesses a very high temperature: and the hypothesis of the nucleus of the globe being composed of fluid matter, offers a still more simple solution of the phænomena* [sic] *of volcanic fires*" (p. 250) than his theory. Maybe he would have liked that Potassium indeed plays an important role in planetary heat production, although by radioactive decay rather than oxidation.

When Hopkins (1842) interpreted the Earth's precession and found a solid shell thickness of at least 800 km, he only distinguished between a solid outer shell and a liquid core below, although he recognized the existence of a solid inner nucleus as another possibility. The absence of any fluid layer at all, was however excluded by the precession. Hopkins did not discuss the nature of the liquid material, but focused on the implications of his result for volcanos: the global subterranean lava ocean is reduced to small lava lakes embedded in a thick shell.

Hennessy (1851) further elaborated the approach of Hopkins (1842), adding the volume change during solidification to the theory, and arrived at a shell thickness of at least 18 and at most 600 miles. He explicitly excluded the existence of a solid inner nucleus (on the grounds that solidification can't start at center and surface at the same time, although Hopkins argued for the opposite) and considered the effects of temperature and pressure on density as more important than composition – apparently to refute Hutton's conclusion concerning a metal core.

Haughton (1851, cited after Pratt, 1859) computed an equilibrium thickness, due to the depth- and temperature-dependent melting point, and increased the maximum thickness to 768 miles (1235 km) – which Pratt (1859) did not accept, claiming that Haughton made a mathematical error and uses unphysical arguments. Haughton (1859) felt personally attacked, but assumed that the controversy suffered from the separation of Calcutta (where Pratt resided) from Dublin (Haughton).

Pratt (1859) also cites Haughton with the words "*the subject would appear to be excluded from the domain of positive science, and to possess an interest for the mathematician only*" (p. 327) – which Oldham (1906) confirmed: "*... geologists have turned in despair from the subject, and become inclined to confine their attention to the outermost crust of the earth* [sic], *leaving its centre as a playground for mathematicians*" (p. 456, Oldham however referred to the state of the core, while Haughton meant its size).

The idea of a gaseous interior was re-invented by Ritter (1879, referring neither to Descartes, 1644, nor to Franklin, 1793), based on the discovery of the critical temperature at which the phase boundary between liquid and gas no longer exists, concluding "*... dass die Erdkugel aus einem gasförmigen Kerne und einer denselben umschliessenden festen Rinde besteht*" ("*... that the Earth consists of a gaseous core, enclosed by a solid crust.*" Ritter, 1879, p. 16), in which any chemical compound dissociates, and only the elements are present.

Sayles (1888, p. 19), on the contrary, insisted that *"Even hydrogen would be as hard as diamond* [...]" under the conditions of the Earth's center, but gives no further argument for this view.

Supporting the idea of a gaseous core, Milne (1903) argued that crustal material would melt below a depth of about 65 km ("*40 miles*", Milne, 1903, p. 539), due to high temperature and pressure melting. Below about 320 km ("*200 miles*", Milne, 1903, p. 539), the material would become gaseous, but still have a very dense atomic packing. He suggested that the iron-nickel alloy found in meteorites might be a condensate form of this substance that he calls "*Gēite*" (Milne, 1903, p. 539, the word is composed from "geo" and the usual suffix "-ite", the intended pronunciation is apparently "geïte" or "ge-ite"). This material is supposed to have a density of approximately 6 g cm^{-3} and a P-wave velocity above 9.5 km s^{-1} as indicated by velocity observations also reported by Milne.

Building on the magnetism arguments of Halley's, Thomson (Lord Kelvin) found that, "... *if there were a spheroidal iron core 2000 miles diameter, cool and magnetic to within 100 miles of its surface, sunk to the centre of a spheroidal space of lighter fluid 3000 miles diameter, enclosed within a solid crust 2500 miles thick, the moment of inertia would be only about one-half per cent.* [sic] *less than it would be if the whole were rigid* [i.e. solid]." (Thomson, 1863, p. 581), thus he combined the magnetic field constraint with geodesy. As origin of this iron sphere, he suggested a big iron meteorite that hit the early Earth. In addition, he hinted that the actual rigidity of the Earth's interior might be determined from "*the velocity of natural or artificial earthquake waves*" (Thomson, 1863, p. 581) – Thomson recognized the potential of seismic methods and of the joint interpretation of different geophysical observables.

Wiechert (1896, 1897) maintained that molecules are strong enough to withstand the conditions at depth, and to limit the density to which materials can be compressed. To him, iron was the most likely constituent of the core, because of its abundance in the Sun, in meteorites, and the depth-dependent iron content of magmas (Wiechert, 1896). He used measurements of the Earth's ellipticity to constrain the size of the iron core.

Thomas J.J. See considered "*Professor Wiechert's hypothesis that the Earth has an iron core* [as] *ingenious rather than probable*" (See, 1905a, column 125) – to him, "... *our Earth is still effectively a gaseous sphere, except that the increase of density under tremendous pressure has rendered it highly rigid like a ball of steel*" (See, 1905a, column 130). See himself computed internal pressures to a

high precision, but offered little in terms of material properties to support this view.

The debate so far generally suffered from the inaccessibility of its subject. The properties of matter under extreme conditions, i.e. the equations of state, even solidification at surface pressure (e.g. Zöppritz, 1881), were known much worse than today. Mistrust between protagonists, who were concerned that their opponents misjudge or ignore evidence from other disciplines (see Brush, 1979) sometimes increased the temperature of arguments (e.g. Pratt, 1859, vs. Haughton, 1859). And, most importantly, the geodetic observations available (surface and mean density, ellipticity, precession) left the problem of the internal structure underdetermined. New types of observations were necessary, but already underway.

Mallet (1849), in the Admiralty's "Manual of Scientific Enquiry", described for the members of the Navy not only what observations should be made during earthquakes, but also how to build makeshift seismoscopes from materials available on ships, and what kind of rocks to collect for the later determination of their elastic moduli. The progresses that could be made with self-recording seismometers, rather than seismoscopes, were known at least since the early 1840s (Forbes, 1844, see also Musson, 2013, and Wood, 1988, and references therein). The first teleseismic recording was that of an earthquake in Tokio, using horizontal pendulums in Potsdam and Wilhelmshaven (von Rebeur-Paschwitz, 1889).

At that time, it was not well understood what is actually visible in a seismogram, and what kind of wave motion could be expected. Rebeur-Paschwitz described distinct phases of motion in his recordings, but did not distinguish wave types. In 1900, Oldham described analogous three phases of motion in recordings of 11 events at several observatories, and presented travel time curves for all three phases. He identified the first two phases with "*condensational*" (i.e., longitudinal, p. 165) and "*distortional*" (i.e. transverse, p. 165) waves, and the third with surface waves, possibly of the type suggested by Rayleigh (1885). Oldham concluded from the curvature of the travel time curves, that ray paths are curved and propagation velocities increase with depth, as predicted e.g. by Schmidt (1888). Using Snell's law, he connected the surface velocity at the source to the velocity at the ray's turning point and obtained velocities of 10, 12.5, and 15 km/s at depths of 1000, 2000, and 3000 km, respectively, and also estimates of the bulk modulus at these depths, similar to what Thomson (1863) suggested. Oldham also predicted that the presence of a core of solid iron ("*which may reasonably be supposed to exist*", Oldham, 1900, p. 168) would result in a sudden veloc-

ity increase, and complications of the ray path. On density considerations, Oldham (1900) predicted that the radius of this metallic core is about 0.55 times the Earth's radius, and that "*paths which emerge at a distance of 90° of arc from the origin*" (p. 168) will just touch it, and observations from more than 90° "*will be interesting to see*" (p. 168).

Three years later, evaluating 14 different earthquakes, Oldham (1906) found that S-waves arriving at more than 120° of distance are much delayed with respect to an extrapolation of arrivals from shorter distances. He concluded that "*the central four-tenths of the* [Earth's] *radius are occupied by matter possessing radically different physical properties, inasmuch as the rate of propagation of the first phase* [a P wave, MK] *is but slightly reduced, while the second-phase waves* [i.e., S waves, MK] *are either not transmitted at all, or, more probably, transmitted at about half the rate which prevails in the outer shell*" (Oldham, 1906, p. 472). So, Oldham identified a low velocity material, but he neither claimed that it is liquid, nor that it is metallic or gaseous, but only that there is a significant physical difference (Muir and Tsai, 2020, showed that Oldham's P wave data, although perhaps mixing P, Pdiff, PP, and PKiKP, is sufficient to infer the existence of a core in a Bayesian framework and assuming that only P and PKP are involved. This demonstration does however not answer the question asked in the title of Muir and Tsai's paper, whether Oldham actually did discover the core, as Oldham mainly relied on S arrivals. It only supports that his data set was sufficient to infer a core from P arrivals).

In the first contribution of the series of papers *Über Erdbebenwellen* (*On Earthquake Waves*), Wiechert and Zoeppritz (1907) first reconsidered arguments concerning the Earth's interior based on flattening of the ellipsoid and implications in terms of the density laws of Laplace and Roche. These however require a volume reduction of the rock by an implausible 80%. Wiechert and Zoeppritz preferred a compositional change to a significant density change under pressure. Based on Wiechert's older idea of an iron core, a reasonable range for rock density and the observed flattening of the Earth, they suggested that the core has a radius of 75% to 80% of the Earth's radius, with a density of the iron slightly above 8 g cm^{-3}.

Wiechert and Zoeppritz (1907) suspected that Oldham's observations of delayed arrivals were based on a confusion of SS with S phases (in our modern nomenclature, which did not exist in 1907; the claim is easily supported today by comparing Oldham's data to model travel time curves, as e.g. in Muir and Tsai, 2020), and Wiechert stated "*Ich muß mich auch der Ansicht von Dr. Zoeppritz anschließen, daß den Oldam'schen* [sic] *Folgerungen nicht beigepflichtet werden kann* [...]" ("*I must concur with Dr. Zoeppritz' view that*

Oldham's conclusions cannot be endorsed", transl. MK, Wiechert and Zoeppritz, 1907, p. 519). In a footnote added in proof (p. 508), Wiechert and Zoeppritz (1907) announced that, by comparing seismograms from Samoa with European stations, it was possible to trace rays down to 3370 km depth, into the core, showing that the velocity within the core is lower than that immediately above it. Further results for the thickness of the rocky "crust" are summarized in Wiechert's introduction to the posthumous paper of Zoeppritz and Geiger (1909), based on ray path constructions for P and S waves.

This paper also details the announced ray tracings and turning point depths below 3000 km depth (Zoeppritz and Geiger, 1909, Fig. 2 on p. 420). Using the turning point depths, Zoeppritz and Geiger also computed P- and S-wave velocities as function of depth (their Fig. 4, on p. 424), showing a linear increase down to 1500 km or 1600 km depth, and constant velocity below.

It turned out, however, that the data set used so far was insufficient, and that earthquakes at larger distances revealed that velocities below 3000 km depth are not constant. In addition, travel times for large distances turned out to be too uncertain. Zoeppritz proposed to augment the travel time observations with evaluations of amplitudes, which was applied by Zoeppritz et al. (1912, published posthumously). An amplitude theory for geometric spreading of spherical P-wave fronts in an ideally elastic medium was applied to amplitude measurements from 71 earthquakes. This resulted in replacing the velocity-discontinuity at a depth of 1500 km, and the constant velocity below that depth, by three discontinuities (at 1194 ± 50 km, 1677 ± 100 km, and 2436 ± 150 km, where the given uncertainties are only rough estimates) and nonconstant velocities. Zoeppritz et al. (1912) do however not interpret any of these discontinuities as the core-mantle boundary.

Geiger and Gutenberg (1912) extended the analysis to the amplitudes of S waves and multiples like PP, PPP, or SPS (and introduced the reader to this previously unused shorthand nomenclature in an extra paragraph). Combining their results with those of Zoeppritz et al. (1912) they arrived at discontinuity depths of 1193 ± 50 km, 1712 ± 100 km, and 2454 ± 100 km (Geiger and Gutenberg, 1912, p. 668). They also obtained S-wave velocities for turning point depths and found that Poisson's ratio at the depths of the discontinuities takes values of 0.273, 0.270, and 0.282, respectively (p. 669). The authors do however not claim that any of their discontinuities ("*Unstetigkeitsflächen*") mark the limit of the core, and from a Poisson's ratio

below 0.3 one can obviously not conclude the presence of liquid material (and they didn't).

Gutenberg (1914) further continued these analyses by the introduction of more rigid selection criteria. The target he aimed at could be hit only with registrations of earthquakes with well-known epicenters (to within 2° of distance); his catalog comprises 78 events from 1904 to 1911 from distances beyond $\Delta = 80°$. Some of these were already used in the previous papers of the Göttingen group, but reanalyzed, with an assumed travel time accuracy of ±3 s. Seismograms used were recorded in Göttingen in most cases. Again, amplitudes were used to support the interpretation of uncertain travel times. As a first conclusion, the small amplitudes of P beyond $\Delta = 103°$ suggest that the P wave turning points enter a low velocity zone for these distances, only to reappear again somewhere between $\Delta = 136°$ and $\Delta = 144°$. This low velocity layer made impossible the application of the Wiechert-Herglotz method, as used before, and required Gutenberg to compare candidate models with his observations in order to find the best velocity structure. To better constrain the distance at which P reappears, Gutenberg (1914) uses 14 additional stations, most of them for only one event.

Gutenberg (1914) compared 28 different velocity models with his data. For depths below 2480 km, he assumed $v_P/v_S = 1.8$, or a Poisson's ratio of roughly $\nu = 0.28$, as it was apparently not possible to compute the S-wave velocities for such depths. From page 153 onwards, Gutenberg suddenly starts to speak of mantle ("*Mantel*") and core ("*Kern*", the latter reaching up to a radius of 3480 km), without having argued why any of his observations is related to the core. When writing his manuscript, he probably knew the results already. His final result is: "*Die Erde besteht demnach aus einem Kern* ($r = 3500$ km) *und aus einem Mantel, dessen Konstitution sich an 3 Stellen ungleichmäßig, jedoch nicht sprungweise, ändert.*" ("*The Earth therefore consists of a core and a mantle, the constitution of which* [*i.e.*, *the mantle*] *changes unevenly, but not discontinuous, at 3 depths.*", transl. MK, Gutenberg, 1914, p. 176, signed Göttingen, 18 July 1912). By the assumed Poisson's ratio, Gutenberg implied that the core is solid, and he did not exclude the possibility of S waves transmitted through the core. His figure 9 actually shows an S-wave leg through the core, for a phase the modern nomenclature not even has a name for (akin to SKS, where the core-leg is an S-wave rather than a P-wave, Storchak et al., 2003).

Usually, Gutenberg's (1914) paper is cited as the one which determined the Earth's core radius, but as Fig. 3 shows, this is a little bit too simple:

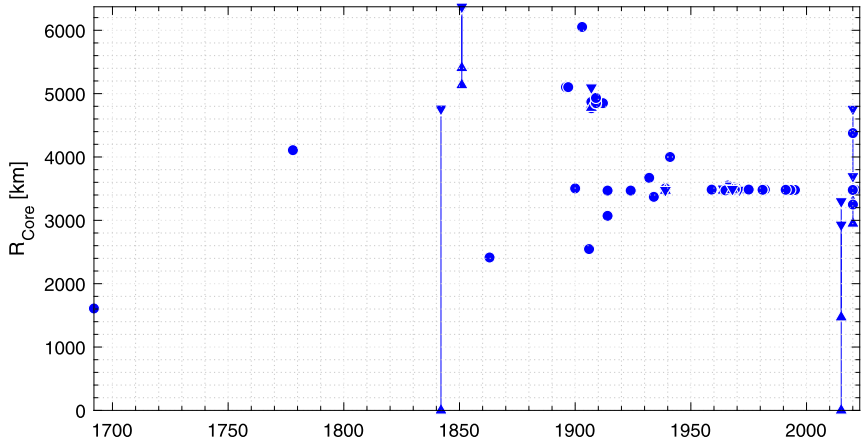

Figure 3 Evolution of Earth core radius with time. A circle indicates a single value, a line ended with triangles indicates the interval from the upward pointing triangle to the downward pointing triangle. All symbols are drawn at the year the respective publication appeared. Numerical values in Knapmeyer and Walterová (2022).

Several works in the following decades found rather different radii. But the work of Gutenberg indeed marks a considerable decrease of the disagreement between authors.

In the same year, Rudolph and Szirtes (1914) undertook it to construct a global travel time curve based on 74 events from the years 1906 to 1913, recorded at 1570 stations worldwide. They saw continuous P and S travel time curves without any gap between 108° and 150° and trace both up to 149° (Rudolf and Szirtes give distances in km, tracing arrivals up to 16600 km). They report that "*Von der ersten reflektierten P-Welle zweigt sich bei* $\Delta = 12500$ km *ein stark ausgeprägter und durch sehr viele Beobachtungen gestützter Wellenzug ab*" ("*PP branches into a pronounced wavetrain at* $\Delta = 112°$, *which is supported by very many observations*", Rudolph and Szirtes, 1914, p. 738), which they interpret as a wave "*welche an dem Erdkern gebrochen, oder was vielleicht wahrscheinlicher ist, reflektiert ist*" ("*which was refracted, or perhaps more likely, reflected, and the Earth's core*", Rudolph and Szirtes, 1914, p. 738). From the shapes of their travel time curves they conclude, that the velocity discontinuity at the core-mantle boundary is less pronounced than assumed before, and too weak to produce any conversions.

Angenheister (1921) basically confirmed the findings of Rudolph and Szirtes (1914) from his analysis of 26 Events that occurred in the Tonga region between 1907 and 1916, and showed a figure of the P, PP, and P'

travel time curves (P' denoting the additional phase that branches from PP). The core is however not his main concern, and by locating the CMB "*in rund 3000 km Tiefe*" ("*at about 3000 km depth*", Angenheister, 1921, p. 124), he kept himself out of that discussion.

Macelwane (1922) however cited the works of Rudolph and Szirtes (1914) and Angenheister (1921) as "*have since shown that the latter belong to a branch of the first reflected waves*" (Macelwane, 1922, p. 480), i.e. claimed that Angenheister's P' phase (simply called P by Gutenberg, 1914, but interpreted as P wave entering the core, i.e. PKP, and interpreted as PcP by Rudolph and Szirtes, 1914) is neither PKP nor PcP, but PP, and also maintains that the state of the core – liquid or solid – is undecided, although "*seismologists and geophysicists suppose the core of the earth to be a rigid solid*" (Macelwane, 1922, p. 480). Comparison with travel times for the ak135 model (Kennett et al., 1995) shows, that Angenheister actually traced PKP and PKIKP.

Two years later, Macelwane (1924) reported the observation of an S wave that passed through the core, supporting his view that the core is solid, i.e. has a nonzero rigidity, and consists of heavy metals like iron.

Another two years later, Jeffreys (1926) combined the results of Oldham (1906) and Gutenberg (1914) with Love numbers and density estimations based on the Adams–Williamson equation, in order to infer that "*There seems to be no reason to deny that the earth's metallic core is truly fluid*" (Jeffreys, 1926, p. 383).

During the late 1920s, Inge Lehmann already suspected the existence of a velocity discontinuity within the core. In a letter to Harold Jeffreys, dated 31 May 1932, she wrote "*There is hardly anything to disprove the existence of such a surface in present observational data*" (facsimile of the letter in Hjortenberg, 2009, p. 688). In a paper with what is about the shortest possible title, Lehmann used a two-layer model with constant velocities to illustrate the reflection and refraction of P waves in the core, and the resulting travel time curves. Considering amplitudes and arrival times of core phases she found that what she called the P'_3 branch of the travel time curve is actually a reflection from within the core (i.e. PKiKP in modern nomenclature, Storchak et al., 2003), and concludes: "*We take it that, as before, the earth* [sic] *consists of a core and a mantle, but that inside the core there is an inner core in which the velocity is larger than in the outer one.*" (Lehmann, 1936, p. 97).

By combining observations of PcP and ScS with those of phases transmitted through the core (PKP, SKS, but also multiples), Jeffreys (1939a,b) could determine the P-wave velocities within the outer and inner core,

but left the S-wave velocities undetermined. Jeffreys (1939c) then provides extensive travel time tables, and P- and S-wave velocities for phases observed at distances up to 107°, and derives the core radius with a formal uncertainty of less than 5 km.

Since a propagation velocity of 0 means that no signal is observed, the S velocity in a liquid core can't be measured directly but must be inferred from other constraints. The continued nonobservation of seismic phases with S-wave legs in the outer core, even in modern compilations (e.g. Astiz et al., 1996) is not a proof, since S-wave legs through the inner core also keep escaping from observation, although consensus is that they should exist.

Concerning the state of the core, Gutenberg (1929) warns that the properties "solid" and "liquid" should not be confused with the aggregate state with which they are connected in everyday experience, but that a body is "*fest, wenn er eine meßbare Righeit* (*Formstabilität*) *besitzt, als flüssig, wenn ihm diese fehlt, er dabei sein Volumen durch Druckminderung nur wenig vergrößert*" ("*solid, when it has a measurable rigidity* (*form stability*), *liquid, when it lacks this but increases its volume only little under pressure reduction*", p. 455, translation MK).

In his *Seismological Tables*, Jeffreys adds that the observed amplitude of SKS "*seems to indicate that the core must be fluid even to the shortest periods*" (Jeffreys, 1939c, p. 408), i.e. the material behaves like a fluid under stresses acting at the time scale of seismic waves as well as on the 12-hour scale of the tides.

It appears like, by 1939, the description of the Earth's core was basically as is found in any modern textbook, but this is not the case. In the 1950s, the question of the core radius was re-iterated (or maybe continued after WWII), and the discussion of the composition and interior constitution of the Earth was also not finished.

In 1941, Kuhn and Rittmann revived the gaseous interior concept once more (without referring to Descartes, 1644; Franklin, 1793, or Ritter, 1879, and ignoring or unaware of Lehmann, 1936): "*Insbesondere zeigt sich, daß die Hypothese, wonach die Erde einen im wesentlichen aus Eisen bestehenden Kern besitzen sollte, voraussichtlich aufgegeben werden muß*" ("It especially turns out that the hypothesis, that the Earth has a core predominantly consisting of iron, likely needs to be abandoned", transl. MK, Kuhn and Rittmann, 1941, p. 216). Instead, they proposed that "*... die innersten Teile der Erde aus praktisch unveränderteter, stark wasserstoffhaltiger Solarmaterie bestehen*" ("*... the innermost parts of the Earth consist of basically unmodified solar matter with a high*

hydrogen content", transl. MK, Kuhn and Rittmann, 1941, p. 216). They did not generally doubt the abundances of elements in meteorites and the Sun, but the possibility of a differentiation within a reasonable time. In their view, the Earth's core has a much larger radius than previously thought (4000 km) and consists of "*Solarmaterie*" ("*solar matter*", P. 231), i.e. gas with the composition of the Sun. The discontinuity at 2900 km depth, and the S wave opacity of deeper regions, is not due a change in composition, but due to a reduction of the Maxwell relaxation time under pressure and temperature.

Kuhn and Rittmann (1941) provided a coherent framework of thought, and their arguments were taken seriously, although they were in stark contrast to Goldschmidt's argument that a separation into silicate and iron shells is "*... unumgänglich, falls die Erde ursprünglich schmelzflüssig gewesen ist*" ("*... unavoidable, if the Earth was initially molten and liquid*", Goldschmidt, 1922, p. 919), which is based on processes used in steel production as well as on the structure of meteorites, especially Pallasites.

Kronig et al. (1946) however found that Kuhn and Rittmann provide too little motivation for the proposed change of the Maxwell relaxation time and suggested that this might be found by a phase transition of Hydrogen: Specifically, they suggested that Hydrogen undergoes a transition from the molecular H_2 to an alkali-like atomic grid. From energy considerations they found that such a state would indeed have a lower energy, and that the transition would occur at a pressure compatible with that at a depth of 2900 km within the Earth. The required density could be obtained by 10 mass-percent of Hydrogen with heavier elements. (It should not go unnoticed that Kronig et al., 1946, grossly underestimated the necessary pressure, and that metallic hydrogen has not yet been demonstrated in the lab, see Gregoryanz et al., 2020, and references therein.)

Ramsey (1948) further supported this case by showing that the known densities and moments of inertia of terrestrial planets can be reproduced with the metallic-hydrogen model. He extended the energy argument towards a stability criterion and found "*If the mass is* 0.793 M_E *the radius of the core is approximately* 1000 *km, and this is the smallest core possible in a stable configuration*" (Ramsey, 1948, p. 413). Interestingly, although he denies that the Earth's core consists of iron, he sets up his model calculations with "*No allowance ... for the tendency of heavier elements to condense towards the centre of the Earth*" (p. 411), i.e. he denies that an iron core could form in spite of the separation effect.

Ramsay took a contribution of J.D. Bernal to a discussion held by the Royal Astronomical Society in April 1936 (Bernal, 1936) as example for a discontinuous density change without alteration of composition: "*Dr. Bernal had been asked whether a new state of the old material, probably olivine, was likely at high pressure*" (Bernal, 1936, p. 268) and might be responsible for what was then called the "20°-Discontinuity" and located by Jeffreys at 480 km depth in the same meeting (the travel time triplications of the olivine phase transitions at 410 km and the 660 km depth overlap around 20° distance, which probably posed an additional challenge in seismogram interpretation). Referring Goldschmidt's experiments on Magnesium germanate, Bernal answered that "*By analogy it therefore seemed probably that at high pressure olivine would adopt a cubic form*" (Bernal, 1936, p. 268). Ramsey (1948), and also Jeffreys (1937, 1939c), refer to this statement by Bernal like to a study conducted by him, although it was an oral assessment of results obtained by Goldschmidt.

In his discussion of the hypotheses of Kuhn & Rittmann and Ramsay, Birch (1952) hardly left any doubt that he considers them inappropriate. He found that it "*is evidently more reasonable to reserve hydrogen for the giant planets ... than to attempt the construction of small planets having mean densities between 4 and 5.5 of so light a component*" (Birch, 1952, p. 275). Neither the density of the Earth, nor those of the other terrestrial planets (for which Birch had the newer data compared to Kuhn and Rittmann, or Ramsay), nor the equations of state provide a reasonable argument for large amounts of hydrogen in the core. He also dismissed Kuhn and Rittmann's claim that iron can't segregate into the core as being based on inadequate assumptions on viscosity. Both outer and inner core may be alloys, but according to Birch, iron is very likely the dominant constituent. According to a recent review, Hydrogen contributes less than about 0.25 weight-percent to the composition of the core (Hirose et al., 2021).

While not referring to phase transitions, Bullen (1949) also preferred the idea that the core-mantle boundary does not constitute a change in composition but only reflects an effect of pressure. He argued that astronomical observations of both Earth and Mars are better explained if only the inner core consists of iron. He later detailed this (Bullen, 1957a) such that the mantle is a mixture of metallic iron, and several oxides down to a depth where all these, except the metallic iron, melt and thus allow the iron to sink downwards and form the inner core, again supported by astrometric data of Mars. Keith Edward Bullen in 1966, stated that his "... *attitude has been to express formal results in the form 'If P, then Q', rather than 'Because*

P, therefore Q' and to discuss the limitations, as well as the strengths, of particular models." (Bullen, 1966b, p. 237). He wanted his studies to be understood such that his models explain the data better than other models, while being open to yet different models that provide even better explanations.

The composition of the core is an important part of the discussion of the bulk composition of the terrestrial planets in general. Hypotheses about the origin and evolution of all planets could be tested by comparison of Earth with the few data available for the other planets. This will be detailed further in the following sections, especially that on Mars (section 4.3, p. 126).

After World War II, a new type of data became available: Nuclear explosions provided a controlled source strong enough to sound not only the crust, but also the lower mantle and core (Gutenberg and Richter, 1946; Gutenberg, 1946). Underwater explosions conduced at the Bikini atoll coupled better seismically into the solid Earth than airborne explosions such as "Trinity" (Carder and Bailey, 1958). The test named "Bikini Baker" (24 July 1946, 09:34:59.7 GMT, yield about 20 ktTNT; according to Shurcliff, 1947) was the first recorded at up to 79° distance, and PcP phases were identified at $\Delta = 35°$ and $\Delta = 63°$ (Carder and Bailey, 1958). In preparation of the International Geophysical Year 1957, seismic stations were deliberately deployed to record seismic waves from nuclear explosions (Carder and Bailey, 1958) and several seismologists of the time, such as Keith Bullen got ever so slightly carried away in demanding dedicated "clean" nuclear explosion campaigns for seismology (Bullen, 1957b; Griggs and Press, 1961). Carder (1964) further evaluated the observed core reflections to estimate the core radius.

Core radius determinations using PcP did not satisfy Sacks (1966), who returned to determining the boundary of the core shadow from the amplitude ratio between P and P_{diff}. As an additional advantage of this approach, he considered that the decay of P_{diff}, according to analog model studies of Rykunov (1957, citation in Sacks, 1966), depends on the rigidity within the core. Sacks obtained an upper limit rigidity of 10^8 dyne/cm^2 (i.e. 10 MPa) for the interior of the (outer) core. Knopoff and Gilbert (1961) however showed that the potential for the diffracted P wave is the same for rigid and liquid spheres for high frequencies, and Guttenberg (1960; actually, this is by the well-known Gutenberg with a single "t", but the name is misspelled on the paper) already argued that Rykunov's wavelengths are too large. Continuing the previous study, Sacks (1967) slightly revised his radius estimate and suggested that the discrepancies between his result, those of other authors, and the Jeffreys–Bullen standard solution might also be

due to mantle structures not yet recognized. He did not elaborate on core rigidity.

A previous estimate by Press, comparing the amplitudes of ScS with those of ScSScS, concluded that the rigidity of the outer core is at most 10 *GPa*, and, considering its incompressibility, indicated "*a state unlike that of a normal solid*" (Press, 1956, p. 124). Anderson and Kovach (1964) could further reduce this upper limit estimation by a factor of 5. In the introduction to the 1967 compilation of the *Seismological Tables*, Jeffreys said "*S below* [the core-mantle boundary] *does not appear to exist. For this and other reasons this central core is generally believed to be liquid*." (Jeffreys and Bullen, 1967, p. 3).

Another new type of data became available on 22 May 1960, with the great Chile earthquake ($M_W \approx 9.5$, Purcaru and Berckhemer, 1982): free oscillations. Ironically, Benioff et al. (1959) essentially reported the nonobservation of free oscillations in weeks to months of gravimeter and strain meter data from different locations shortly before this event. Benioff et al. (1961) then presented free oscillations spectra from two earthquakes (Chile, and Kamchatka, Nov. 1952).

Several authors (see Dorman et al., 1965, and references therein) found that the observed free oscillation periods can be explained only if the core is larger than assumed before. Press (1968) constructed five million models in a Monte Carlo search and found necessary an even larger (by 6 km) radius increase than Dorman did. This was also supported by Haddon and Bullen (1969).

Buchbinder (1971) mentioned the frequency dependence of Q in the liquid core, but since he considered only a narrow frequency range around 1 Hz, an evaluation is not possible. He only noted a Q contrast between outer and inner core which might be the result of the transition from liquid to solid.

The phase-transition theory for the Earth's core was essentially abandoned by Bullen in 1973, when he suggested that the outer core consists predominantly of Fe_2O, which is unstable under surface conditions, but becomes stable under core conditions, as was found theoretically just briefly before. The location of the core mantle boundary still retains a pressure-dependency, but also marks a chemical boundary. The inner core, according to this model, would consist of pure iron. Bullen saw the necessity for a new model arising from improved values for the Earth's moment of inertia factor, among other reasons. He did not consider the phase-transition

hypothesis as falsified, "*But the case against it is sufficiently strong to make it desirable to seek alternatives*" (Bullen, 1973, p. 68).

In the early 1970s, the necessity of a new physically self-consistent Earth model became clear, i.e., of a model that can be used as a self-consistent reference for astronomical, seismological, and geodetic studies. An IUGG working group for the development of such a model was set up in 1971. With wide applicability in mind, mass, radius and moment of inertia were introduced as constraints in addition to seismological data, which consisted of body waves, surface waves, and free oscillations. With their PEM series of models, Dziewonski et al. (1975) demonstrated that the construction of a physically meaningful Earth model from the given constraints and with the envisioned parameterization is feasible. The ultimate result of these efforts is PREM (Preliminary Reference Earth Model, Dziewonski and Anderson, 1981). In the late 1980s, IASPEI initiated the replacement of the Jeffreys–Bullen travel time tables with a more accurate and versatile set of tables, based on a larger data set and employing modern computational methods. The resulting IASP91 model (Kennett and Engdahl, 1991) is intended as a tool for seismogram analysis only and thus focuses on precise travel time fits and computational pragmatism.

A central shortcoming of IASP91 is its core structure, since PKP travel times do not have turning points in the outermost 1000 km of the core, and no shear wave observations in the inner core (PKJKP) were available. Several studies investigated alternative core structures to find an improvement.

Morelli and Dziewonski (1993) considered IASP91 to be biased by the dominance of paths from pacific hypocenters to European stations, resulting in predicted travel times that are systematically too fast (P) or too slow (S). Their model SP6 has a modified PREM lower mantle and core structure, but Morelli and Dziewonski found "*no need to change*" (p. 188) the core radius of PREM.

Kennett et al. (1995) also recognized that IASP91 travel times deviate from observations by one to a few seconds. They relocated events from the ISC catalog and constructed an improved model with reduced velocity gradients in the deeper core, and a core radius adopted from SP6, but subsequently reduced by 0.5 km.

Kaneshima and Helffrich (2013) evaluated multiple reflections within the core, namely SmKS phases, where m is the number of reflections at the CMB underside. These phases are sensitive for those regions within the core where PKP has no turning points. The core radius of PREM was

retained, only the velocity structure was modified, and the fit with respect to SmKS phases was evaluated.

Kennett (2020) was cautious against using PREM as body wave travel time fit, since its construction is dominated by free oscillations data at frequencies much lower than those of body waves. In addition to the accuracy of predicted travel times, he aimed at the derivatives of elastic moduli in terms of which equations of state are formulated. He used starting models produced by combining several previous models, and optimized these. The resulting preferred model has a core radius 0.5 km smaller than that of PREM, and an improved velocity structure – size matters less than internal structure here. The data used is a mixture of mantle, but especially core phases in order to better constrain the outermost outer core.

A new twist on the question of the state of the core came from first-principle computations of Belonoshko et al. (2019), who predicted that the inner core consists of iron in a bodycentric cubic rather than hexagonal close-packed crystal phase – and that this bcc iron, under inner core conditions, has a viscosity below 150 Pas, comparable to liquid iron, while the hcp configuration is unstable under the assumed conditions and thus not expected to exist in the inner core. The bodycentric cubic phase is also supposed to better fit the anelastic attenuation and density of the inner core. This result, at least, confirms that rheology and state of matter are unintuitive and should not be used synonymously, as Gutenberg (1929, see above) warned.

Dorn et al. (2015) and Baumeister et al. (2020) deliberately hurled themselves back into the preseismological era by reducing the used constraints to those that might be available for Exoplanets: mass, radius, assumptions on the composition, and Love numbers, but evaluated with algorithms not available in the early 20th century. Dorn et al. assumed that the composition of the host star is a good proxy for the bulk composition of the planet, and ran a Markov Chain Monte Carlo inversion. Baumeister et al. (2020) trained a neural network to circumvent CPU-expensive model evaluations, and investigated the relative importance of composition and Love number k_2 as constraints. Both estimated the Earth's core radius (of PREM) as validation test. The approach of Dorn et al. yielded an underestimation, where the PREM radius is outside the 95% confidence interval, although not entirely excluded. The radius interval to which 95% of the Baumeister et al. (2020) parameter space are mapped contains the PREM radius, even if k_2 is not used, but is biased high. When using k_2, the distribution is biased slightly low, but much narrower than without. Baumeister et al.

saw their approach as a tool for a quick first interpretation, to guide more time-consuming detailed modeling with modified compositions. A critical factor for both Dorn et al. and Baumeister et al. is the assumed composition. Dorn et al. named the assumption of a pure Fe core as cause for the underestimation of its radius, and intended to include lighter elements in future models. It remained open, however, how the core alloy can be inferred from the host star composition. In a follow up study with a generalized implementation, Dorn et al. (2017a,b) took the previous paper as demonstration of relative importance of compositional results, but stick to the pure Fe core. The improved method was not validated against Earth, but against Neptune.

A new view on the seismic wavefield is the evaluation of seismogram cross-correlations between stations, giving access to structures not directly illuminated by rays from a source to one of the stations. Ma and Tkalčić (2021) used only 10 carefully selected events, but all stations from which data is available, to construct a correlogram with global coverage, and derive a global 1D velocity model. The core radius is however inherited from PREM.

The investigation of the Earth's core started more than 300 years ago, a period which covers several independent developments. These include the development of the modern concept of science – in contrast to natural philosophy – during the 17th and 18th century, as foundation of the development of physical and chemical theories allowing for the description of the Earth's interior, and for the development of suitable measurement methods. The continuous improvement of technology, including seismographs and telescopes, but also computational aids, accelerated the gain of knowledge during the past decades.

One has to keep in mind that not even the mathematical notation we use today was available in the 17th century (see also Cajori, 1928). For example, the symbol "÷" was first used for division in 1659, before that it was used for subtraction by many; Leibnitz introduced ":" for division in 1684. Kepler wrote $\overset{VI}{8}$ instead of $8x^6$. Descartes introduced the now common superscript notation for positive integer exponents in 1637, but today's use of negative and noninteger exponents is found first in a 1676 letter by Newton. Geiger and Gutenberg (1912) refer to graphical integration methods (p. 656), slide rules (*"Rechenschieber"*, p. 664) and the "*fünfstelligen Tafeln für Maschinenrechnen von Dr. F.G. Gauß*" ("*five-digits tables for* [mechanical] *machine computations by Dr. F.G. Gauß*", p. 664; this Dr. F.G. Gauß

is not to be confused with the better-known namesake C.F. Gauß) for their numerical computations.

Seismogram recording on (smoked) paper or film limited the possibilities of data exchange; filtering and deconvolution of instrument responses was impossible. The development of the seismological phase name notation is apparent in the publications from the first half of the 20th century cited above, and reflects the growing understanding of wave propagation within the Earth, and of the structure of the Earth.

Francis Birch stated that the core-mantle boundary "*is the best determined ... discontinuity of the interior*" (Birch, 1952, p. 231). The community's interest in determining the size of the core, rather than its physical properties, apparently decreased since the 1960s, and the investigation of fine structure shifted into focus, i.e. that of the small-scale velocity structure around the core mantle boundary, and possible topography of the core, the very nature of the D" zone, and to the fitting of depth derivatives of parameters. These topics, however, are outside the scope of the present study, and will not be followed.

4.2 Moon

While the diameter of the Moon and its distance from the Earth were known already in antiquity (Hipparcus of Nicaea found a smallest distance of 71 and a largest of 83 earth radii in the 2nd century BCE, see van Helden, 1985), the determination of mass, density, and moment of inertia had to wait until Newton developed the respective concepts.

Once the theory of gravity was established, physical interpretations of astronomical observations could evolve as quickly as mechanics in general. In the 5th volume of his *Mécanique Céleste*, Laplace already gave the relative moments of inertia $(C-A)/C = 0.00059701$ and $\gamma = (B-A)/C = 0.000563916$ for the Moon (Laplace, 1825, p. 287). Wichmann (1848) obtained $(C-A)/C = 0.000599$ and $\gamma = 0.000564$. Both Laplace's and Wichmann's results are based on observations of the physical libration. Houzeau (1882) reported two more such results, obtained by Nicollet in 1823 and Stambucchie and Kreil in 1837.

The first solution that assigns an explicit value to C is apparently that given by See (1905a), which he derived by assuming that the Moon follows Laplace's density law for a chemically homogeneous body. Hence his value can't be used to infer the interior structure of the Moon, since it is a prediction, not a measurement.

The estimated polar MoIF of de Sitter (1915, cited after Jeffreys, 1936) exceeds that of the homogeneous sphere, although the uncertainty is such that a mass concentration towards the lunar center still appears possible. This MoIF is based on actual observations of the lunar orbit and the motion of its perigee and nodes, including relativistic effects. De Sitter corrected it to a slightly lower value in 1927, the mean value still pointing to a density decrease with depth, but with increased uncertainty.

Jones (1932) evaluated stellar occultations observed between 1672 and 1908 to improve the orbital elements of the Moon. Here, the Moon's (and also the Earth's) radius, mass and moments of inertia enter into the secular motion of perigee and orbital nodes. The polar moment of inertia was determined from libration theory as $C/MR^2 = 0.58$. This result is "*very improbable*" (p. 51), as Jones remarked. It contains a systematic error due to the deviation δk of the reciprocal flattening of the Earth from 297, which enters as a bias term $0.14\delta k$. Jones (1932) thought that "*Such a discordance is not alarming*" (p. 51) and considered a reciprocal flattening of 296 "*quite possible*" and 295 "*reasonable*" (p. 51), but considered the evidence for 297 too strong (as in the International Ellipsoid 1930, e.g. Kahle, 1984). The corresponding value of the Geodetic Reference System 1980 is, however, 298.257 (e.g. Kahle, 1984), resulting in an even larger value of $C/MR^2 = 0.697$. Since a hollow sphere with an infinitesimally thin shell has $C/MR^2 = 2/3$, this and other high values suggested that the density within the Moon decreases considerable with depth, leading to a gravitationally unstable configuration of its interior.

Jeffreys (1934) relied on the mean densities of planets only when he inferred that the Moon has no core at all, since the average density of the Moon is too close to that of Olivine to allow for any heavy metal core. Jeffreys (1937) expanded this thought with regard to the phase transitions of Olivine, which he estimated to occur at 474 km depth in the Earth but not occurring at all in the Moon. He thus maintained the conclusion that the mean density of the Moon does not allow for an iron core.

A more plausible value for the Moon's polar moment of inertia, i.e. smaller than 0.4, is that cited by Wildt (1947). The reference given by Wildt ("*H. Jeffreys, M.N., Geophys. Suppl., 4, 62, 1940*") could not be found; the closest match for the cited moment of inertia factor is that of Jeffreys (1936).

Ramsey (1948) used the Moon, among other bodies, to test his theory, that the Earth's core is a metallic high-pressure modification of mantle minerals (Kozlovskaya, 1967, cites this as the Lodochnikov–Ramsey hy-

pothesis, apparently – bot not explicitly – referring to Lodochnikov, 1939, which we could unfortunately not obtain. Brush, 1982, discusses the various compositional hypotheses in more detail). To this end he assumed that all terrestrial planets share the same composition. For the Moon he modeled a mean moment of inertia close to that for homogeneous density. Following his arguments lined out in section 4.1 the Moon can't have a core as it would be unstable under lunar pressure conditions. The high moment of inertia factor appears to be a sufficient argument to Ramsey to see his theory corroborated. He did not attempt to predict the Moon's flattening, via the Radau–Darwin equation, since he considered the observed flattening to be too large to be compatible with the hydrostatic equilibrium that is prerequisite to the equation.

After a re-evaluation of the lunar libration and shape, Jeffreys (1961) still obtains a mean MoIF above 0.4, but again with an uncertainty that easily allows for a central mass concentration.

Eckert (1965) obtains an even larger value from a new evaluation of the motions of the orbital nodes of the Moon, and considers the deviation from a constant-density sphere as too large to reject the result as a simple error. As possible cause he proposes deviations from an elliptical shape, and considers further investigation necessary.

The sensitivity of density models for the polar moment of inertia factor used in the inversion was investigated by Solomon and Toksöz (1968) in a relatively rarely cited paper (a survey on Google Scholar on 17 Feb. 2022 resulted in only 13 citations, compared e.g. to 94 for Kuhn and Rittmann, 1941 in German language, and 130 for Ramsey, 1948; Scopus knows of only 3 citations for Solomon and Toksöz). Using a polynomial density model that allowed for analytical inversion they showed the nonuniqueness of the inversion and the insensitivity of observables for the central portion of the Moon.

The "*hollow moon* [sic] *paradox*" (Kaula, 1969, p. 1584) did not just vanish from one paper to the next, but was resolved by improved understanding of motions in the Earth–Moon-System. On a seminar held at JPL in 1967, van Flandern (1968) suggested that all previous observations of lunar libration were flawed by a combination of effects: firstly, new charts of the lunar limb showed a systematic offset in the limb determination due to the higher mountains on the southern hemisphere of the Moon. In addition, it became clear during the preparation of these charts that "*the geometric center shifts back and forth with respect to the center of mass*" (van Flandern, 1968, p. 13) while it was assumed before to remain at a constant offset to the

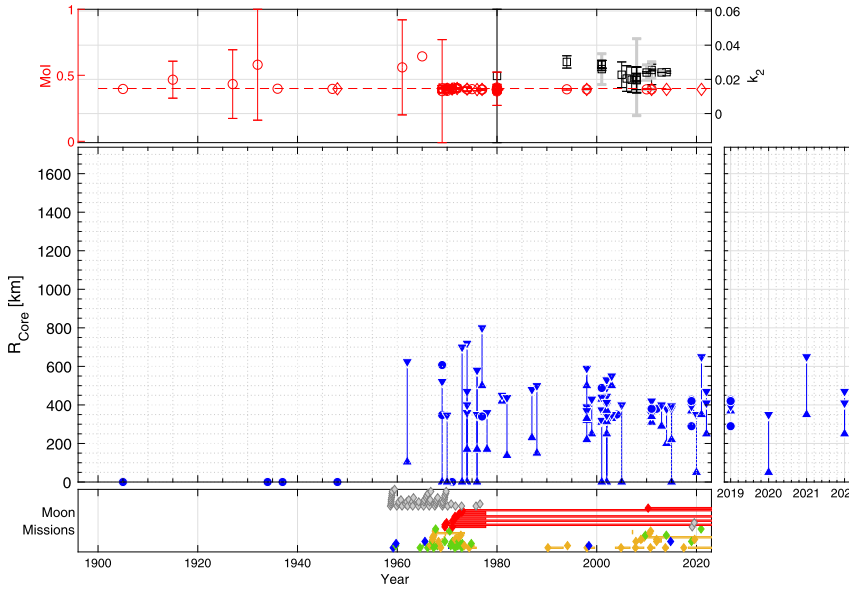

Figure 4 Evolution of parameter estimations for the Moon. Top: Moment of inertia factor (circles for polar, diamonds for mean MoIF), and k2 (squares), middle: Core radius, symbols as in Fig. 3, bottom: Spacecraft missions (gray: failed, blue: fly-by, green: lander, orange: orbiter, red: Apollo ALSEP. Diamonds indicate arrival times, bars indicate life time.), right: core radius estimations since 2019. Mission data is mostly from Siddiqi (2018), for details and all other numerical values see Knapmeyer and Walterová (2022).

south of the center of mass, i.e. the locations of the two were not determined correctly before. And, finally, the availability of atomic clocks led to the insight that Earth's rotation is not as uniform as implied in earlier evaluations, an effect which Kaula (1969) considered the most important one, and the correction of which resulted in a MoIF close to 0.4.

Using radio tracking on missions Mariner II and IV, and Ranger III to IX, the uncertainties of the Earth's and Moon's masses were reduced by a factor 6.8 and 48, respectively (the Mariners contributed to the determination of the lunar mass via a monthly trajectory perturbation; Sjogren et al., 1966). The trajectory of Luna 10, as evaluated by Akim (1966) is the oldest spacecraft-based estimation of the polar moment of inertia factor given by Ferrari et al. (1980), who present re-evaluations of 14 results from the earlier literature.

Beginning in the mid-sixties, new MoIF estimates resulting from spacecraft tracking were produced in rapid succession, corresponding to the high launch rates up to the late 1970s. We found only six publications of moment

of inertia factors larger than 0.4 after 1966 (not counting those re-evaluated by Ferrari et al., 1980), and none of these was published after 1972: Having spacecraft near the Moon was the game changer (clearly visible in Fig. 4).

The Lunar Orbiter missions allowed determining low order spherical harmonic coefficients of the lunar gravity field up to degree and order 4, plus C_{50}, C_{60}, C_{70}, C_{80}, from two years of data and five orbiters (Lorell, 1970). At the time, this was a major computational effort, since "*The amount of data is so great as to cause a handling problem even for modern high-speed computers*" (p. 191). In combination with moment of inertia ratios obtained from libration observations, it was then possible to estimate the polar moment of inertia factor. This gravity solution could be extended to degree 15 by Liu and Laing (1971), who also obtained a revised moment of inertia factor. Sjogren (1971) provided a cross-check of these results with previously unused tracking data from Lunar Orbiter IV.

Cook (1970) complained that many authors do not make explicit to which radius they normalize their moment of inertia factors, thus introducing unnecessary difficulty into the discussion of the fluctuations between published values of J_s and C_{22}. He made clear that the same radius should be used as in the determination of J_2, and that a phrase like "mean radius" is not enlightening and does not correspond to mathematical requirements in the definition of the respective series expansions. He adds, however, that the uncertainty introduced by using different radius values "*is less than other sources of error*" (p. 193).

From the overall abundance of iron in the universe at large, and estimations that all bodies with radii in excess of 100 km would experience an early molten phase, Firsoff (1969) concluded that "*The Moon must have a nife* [sic] *core*" (i.e. Ni-Fe, Firsoff, 1969, p. 193) and proposed a three-layer structure of crust, mantle, and core, where the core covers 35% of the lunar radius (or 608 km) and contains 10% of the lunar mass. With a 174 km crust, a plausible mass partitioning appears possible that fits the overall mass and hydrostatic equilibrium figure.

Using a thermodynamical approach that allowed for a pressure and temperature dependent density, Nakamura and Latham (1969) investigated the possibility of a chemically homogeneous Moon. Even when including a thin low-density layer to match the expected basaltic density at the surface, the modeled moment of inertia factors were too large, and Nakamura and Latham concluded that, if the actual MoIF is smaller than 0.401 ± 0.001, the Moon can't be chemically homogeneous. Assuming iron as constituent

of a candidate core, they found that this core most likely covers 20% (or 347 km) of the radius, but at most 30% (or 521 km).

Cook (1970) however suggests that, although the presence of Mascons and the "*likely*" (p. 193) offset between the center of figure and the center of mass are evidence against a homogeneous density, the available data are insufficient to determine if a real concentration of mass towards the center exists. He also remarks that C for a triaxial ellipsoid of homogeneous density will exceed 0.4 when referenced to the radius of a sphere of equal volume, implying that the interpretation of the MoIF is less straightforward than often assumed.

The lunar gravity field was not the only window to the lunar interior that was opened by spacecraft missions. Runcorn et al. (1970) investigated the magnetic properties of samples returned by Apollo 11, including remanent magnetization. From the magnetization of these samples, but also field and gradient measurements in situ, they concluded that mare lava must be magnetized, and that an internal dipole field is a likely explanation – and a small iron core would be its source. Runcorn (1962) already interpreted the nonspherical shape of the Moon as the result of internal convection that deforms the rigid outer shell. From the parameters of the shape, and using a then recent result on the relation between the planform of convection and the thickness of the convecting layer, he deduced a possible range for the radius of a lunar core, as well as the driving temperature difference. The possible core radius range inferred from magnetization partially overlaps with that of Runcorn (1962), although it also allows smaller cores.

In a theoretical study using a two-layered Moon-model consisting of a light crust of 50 to 100 km thickness and a mantle, but without core, Cole (1971) demonstrated that the mass and Moment of Inertia factor of the Moon could be satisfied without the assumption of an iron (or otherwise heavy) core. He did not deny the possibility of a lunar core, but showed that the MoIF alone does not require one.

The Apollo 15 Laser altimeter data supported that the lunar center of mass is offset towards the earth from its center of figure, by about 2 km (Michael and Blackshear, 1972). To account for this, Michael and Blackshear tested models with dense crustal slabs on the near side of the Moon, in addition to a spherically symmetric structure. It turned out that this yields a reduction of the polar moment of inertia factor and thus indeed contributes to the solution of the "hollow moon paradox". Concerning the difficulties in the mathematical description of the lunar gravity field they comment "... *that the Moon is a wonderfully complicated gravitational object with many localized*

gravitational anomalies near its surface and perhaps in its interior, and these anomalies are difficult to represent in a finite mathematical formulation. There is very little that can be done about [this], *except perhaps to enjoy the challenge*" (p. 389).

At about the same time, the geodetic interpretation of Kaula et al. (1974) obtained a maximum possible radius of an iron core of 400 km, under a mantle of olivines and pyroxenes to account for the necessity of a material from which surface basalts could be derived.

Signals from one deep moonquake cluster (A33) suspected to be on the far side, and a "*large*" (Nakamura et al., 1973, p. 49) meteoroid impact that occurred in the evening of 17th July 1972 near Mare Moscoviense provided seismic signals on the Apollo seismic stations that were sensitive for the deep interior. S waves from the impact were missing at the Apollo 14 and 16 stations, as were P from A33 at Apollo 16, and S from A33 at Apollo 14. This lack of signals gave rise to the concept of a partial melt layer in the central region of the Moon, with a melt fraction of a few percent. The radius of this region was estimated to be between 700 and 800 km, but "*The possibility of a very dense, molten, metallic core similar to that of the earth is ruled out by considerations of both moments of inertia and seismic wave velocities. The radius of about 700 km is too large for such a core*" (Nakamura et al., 1973, p. 51) – a statement which probably does not intend to exclude an iron core at all, but only to state that it cannot have such a large radius. In any case, the dictum was later modified by Toksöz et al. (1974), who find a 700 km FeS core compatible with the constraints.

With one additional distant impact on the 19 Sep. 1973, Nakamura et al. (1974, 1976) further differentiated between partial melt layer and iron core and concluded from the P wave delays "*suggests that the moon has a central, low-velocity core*" (Nakamura et al., 1974, p. 137) with a radius between 170 km and 360 km and perhaps consisting of iron sulfide, although they didn't consider the available data a sufficient constraint for conclusions on composition.

The interpretation of the July 1972 impact was doubted by Goins et al. (1981), who argued that the signal is weak, the signal-to-noise ratio low, and the uncertainty of arrival times so high that the alleged P-wave delay is not significant – and thus the evidence for a core is inconclusive. Goins et al. considered a region of increased shear wave attenuation possible, but conclude that "*The existence of a lunar core remains an open question. All lunar data … allow but do not require a core*" (p. 5027).

Absent any additional seismic sources on the far side, and without successful detection of free oscillations (the authors "*recently searched*" (p. A121),

and also refer to an otherwise apparently unpublished master thesis), Nakamura et al. (1982) agree that "*... the question of the existence of a metallic core remains unresolved*" (p. A121), at least from the seismological point of view.

Cook (1975) also concluded that neither the moment of inertia – due to the large uncertainty of the MoIF – nor the seismic data, nor the magnetization of rocks provides sufficient evidence to make definitive statements about the deep interior of the Moon. He emphasized that the MoIF is very close to that of a homogeneous sphere and, even if smaller than 0.4, "*the uncertainty is at present too great to make any useful statement about the maximum density of a core with a radius of 2–300 km*" (p. 290). Based on an estimation of the central pressure of the Moon, and the bulk modulus of Earth's mantle rock under that pressure, he did not expect a density increase by more than 5%.

Bills and Ferrari (1976; 1977) however showed that an additional density contrast within the Moon, besides that at the base of the crust, must exist to obtain the observed deformation and moment of inertia tensor. They demonstrated how a step-wise combination of assuming a Fe-FeS eutectic core, the mean density of the entire Moon, and the polar MoIF pose incremental constraints on the density profile. The density in the core region is determined by the assumed composition only, but regions above 800 km depth are well constrained. Introducing the full moment of inertia tensor and "*some a priori knowledge on each of the* [eleven] *parameters*" yields an overdetermined problem, but still the outer regions are better constrained than the core region. The multi-layered models of Bills and Ferrari (1977) all share the same, predefined core.

Levin (1979) was more certain that a core must exist, and that the combination of seismological results and the moment of inertia factor rules out a pure FeS core – the core could be pure iron, or contain a small amount of FeS.

Lunar magnetism provided another clue via the induced field resulting from the Moon's passage through the Earth's Magnetic tail once per month. Data from Explorer 35, Apollo 12, and the Apollo 15 and 16 subsatellites, evaluated with two different methods, either require or allow a small iron core (Goldstein et al., 1976a,b). The evaluation of Wiskerchen and Sonett (1977) supports the existence of a metal core, but point to a larger radius than that of Goldstein et al. (1976a).

In addition to tracking orbiting spacecraft (Lunar Orbiter, Apollo subsatellites, e.g. Ferrari, 1977; Explorer 35, Explorer 49, e.g. Blackshear and Gapcynski, 1977), and laser ranging of cube corner reflections on the lu-

nar surface (e.g. Dickey et al., 1994), the landings of the Apollo missions offered another opportunity: tracking the transmitters of the surface experiments (ALSEP), in relation to background Quasars (Slade et al., 1977). The ALSEP stations were however shut down in September 1977 (Bates et al., 1979) and it appears that this approach did not contribute to the geodesy of the Moon. It did contribute to the geodesy of Mars, as we shall see in section 4.3.

The shutdown of the ALSEPs also ended the passive seismic experiment on the Moon, only the Laser Ranging Retro-Reflectors remained usable. At that time, the only seismic constraints on the core radius were still the recordings of the 1972 impact mentioned above (Latham et al., 1978). The Apollo LRRR as well as the reflector on the Lunokhod 2 rover were continuously in use by ranging stations on Earth (Müller et al., 2019). The reflector on the Lunokhod 1 rover was considered lost for decades due to a km-range uncertainty in the rover's location, but was identified on images taken by the Lunar Reconnaissance Orbiter in 2010, and after a first successful measurement in April 2010, its location could be determined to within centimeters, and the reflector added to the network of lunar laser ranging stations (Murphy et al., 2011).

Ferrari et al. (1980) not only presented a new solution for the polar moment of inertia factor, but also a table that places it into relation to values since 1969, to justify the new approach of combining tracking (of Lunar Orbiter 4 only) and laser ranging data. This table is essentially a conversion of the table of C_{20} and C_{22} values of Ananda (1977), using new values of libration parameters. The Ferrari et al. (1980) solution is within 0.5σ the mean of their comparison table, but slightly below its mean. The uncertainty of the new result is controlled mainly by the Doppler data, pointing to a way of future improvements. The harmonic coefficients were determined only to degree and order 5 here, an improvement to the degree and order 16 solution of Ferrari (1977) was not intended. The lunar laser ranging data also provided the first solution for the lunar elastic Love number k_2 that we found, although with a rather large uncertainty.

When considered in parallel, as Russell et al. (1981) suggested, magnetic sounding, gravity, and seismology are all "*consistent with some sort of small lunar core*" (p. 835), but do not agree on its size, are sensitive to different properties, and thus allow for different compositions. As Russell et al. pointed out, the radius constraint from magnetic sounding with the Apollo 15 and 16 subsatellites gives a lower limit of the core radius. This constraint furthermore depends on the iron content of the crust, and requires only

that the core is conductive, but is not quantitative. Russell et al. suggested that even molten basalt could explain the observations. Their conclusion is to suggest dedicated missions to obtain better data in all geophysical disciplines.

With the Apollo dataset completed, and without new missions, compositional studies could be based on a static set of observations and improvement of the underlying techniques. Hood and Jones (1987) used the seismic velocity model of Nakamura (1983) as well as the mean and crustal density, and also the Moment of inertia factor, and constructed models for different compositions and thermal evolution histories. They found that, depending on core composition and other model details, core radii from about 280 km to about 480 km are compatible with their constraints, and slightly less if magnetic sounding constraints are added.

While Hood and Jones conducted forward modeling, Mueller et al. (1988) attempted an inverse method to interpret the Nakamura (1983) velocity model in order to obtain compatible compositions and core radii. This approach allowed better assessment of the trade-offs between unknowns, e.g. between crustal thickness and core radius. They found "*no petrological information that can be utilized to constrain core size*" (p. 6346). The focus of this study, however, was on the composition, and the related question of the origin of the Moon.

The k_2 estimation of Dickey et al. (1994) has a reduced uncertainty, about small enough to constrain the core radius to a 100 km interval. The estimation however builds on a roughly estimated core radius, rather than providing one.

Using gravity field coefficients and librational observations, one obtains four equations to determine the three principal moments of inertia of the Moon, i.e. the problem is overdetermined. Authors often use only three of the possible constraints, depending on their respective uncertainties or other considerations. Bills (1995) analyzed the four different approaches that arise from omitting one constraint, and also a way to test for the self-consistency of gravitational and librational measurements. He demonstrated that the mean moment of inertia factor, which is the most important constraint on the density distribution, depends most on the choice of constraints used for its computation. Bills suggested that the origin of the discrepancies between the different solutions lies in the assumption that the Moon is rotating as a rigid body – while a viscous, fluid core would likely remove them.

The magnetometer onboard of Lunar Prospector provided a measurement of the induced magnetic dipole moment that results from passages through the Earth's magnetotail. An electrically conductive core would reject the outer field, and the resulting perturbation could be translated into an estimation of the core radius (Hood et al., 1999). The authors favor a metallic core, but point out that the electric conductivity of a molten silicatic core could be large enough to produce the same effect. They however considered it difficult to keep a silicatic core molten up to today, and also argued that other constraints are in favor for a liquid metallic core. The core radius range of Hood et al. was confirmed by a corresponding analysis of Kaguya magnetometer data (Shimizu et al., 2013), which yielded an interval that is slightly narrower, but is completely contained within the Hood et al. interval.

In the early 21st century, interest in the re-interpretation of Apollo seismic records renewed and a series of new publications was produced by several authors across the globe. This arose mainly from the availability of much more powerful computers than in the 1970s, and also new analysis techniques (Nakamura, 2015).

Khan et al. (2000) re-evaluated the arrival times of Nakamura (1983) using a fully nonlinear Markov-Chain Monte Carlo technique rather than a linearized inversion and produced an ensemble of compatible velocity models for the lunar interior down to 1000 km depth. Although this study did thus not contribute to the question of the core size, it shows advantages of modern computational methods: the fully nonlinear treatment of the problem, and the uncertainty estimation implied by the distribution of velocities in the solution ensemble. A direct comparison of older and younger velocity models (Knapmeyer and Weber, 2015) shows that the Khan et al. (2000) ensemble generally suggests higher velocities than other studies below 500 km depth but also a general compatibility. Also, Khan et al. (2000) are an early example for an inversion method that became increasingly popular in the 21st century.

From their own mantle composition calculations, which are based on the Nakamura (1983) velocity model, Kuskov and Kronrod (2001) found "*insuperable objections to the seismic velocities proposed by Khan et al. (2000) in the lunar lower mantle*" (p. 208), although Khan et al. (2000) invert the same data that Nakamura (1983) used, and can thus be considered as improvement of the older model. Kuskov et al. (2002) renew this rejection and add that the "[...] *velocity estimates of Goins et al. (1981) and Nakamura (1983) are in general agreement with the allowed field of theoretical velocities*. [...] *Petrologi-*

cally and geophysically admissible ranges of velocities and densities may be utilized as a significant constraint for analysis of the internal structure of the Moon using the Apollo seismic data." (p. 188). The formulation is somewhat awkward as it suggests that petrological modeling, which needs assumptions on composition and temperature, is epistemologically superior to the inversion of seismic arrival times into seismic velocities. The velocities depend on shear and bulk moduli, and also density, which reflect composition only indirectly via the equations of state of the material. Evaluation of these requires knowledge of pressure and temperature, where the latter bears a considerable uncertainty even on the Earth. At the same time, structural parameters can be derived from the seismological data directly, without any recurrence to composition.

The same inversion approach was used by Khan and Mosegaard (2001), and extended to a greater depth: after careful selection of suitable data, spectral analysis of five meteoroid impact yielded a spectrum of free oscillations, thus allowing to invert for shear wave velocity and density down to the center of the Moon, using total mass and moment of inertia as additional constraints. The resulting model ensemble shows near-constant densities throughout the upper mantle, and a gradual density increase below about 1200 km depth. For a liquid core, one expects zero shear wave velocity as in the Earth's outer core, but S-wave velocities in the central region are 4.7 ± 1.5 km/s according to this inversion. Also, "*Densities seem to be more in the realm of an FeS or silicate core, although an Fe core cannot rigorously be excluded*" (p. 1794): the density at the center is only 4.7 ± 0.4 g/cm^3. The question of the state of the core was investigated by Khan et al. (2004) and Khan and Mosegaard (2005) in dedicated studies with a liquid-vs.-solid hypothesis testing design, both concluding that, with the used data, a liquid core is more likely than a solid one.

The inversion of Khan and Mosegaard (2001) considers only the seismic data (plus mass and MoIF), but not the already available constraints from magnetic sounding, with which any Moon model must be compatible as well. Wieczorek and Zuber (2002) pick up the low central density of Khan and Mosegaard as a central argument in their suggestion that the core of the Moon is a titanium rich silicate mixture as result of Ilmenite segregation from the lunar magma ocean. The electrical conductivity of the proposed composition could be high enough to produce the observed magnetization without requiring much larger cores than with a Fe/FeS composition. Contrary to Hood et al. (1999), Wieczorek and Zuber argue that an iron

core would be frozen today, while a silicate core could be maintained in liquid state today.

Laser ranging determinations of k_2 led to a series of slightly different values and allowed estimating the flattening of the lunar core, thus supporting the case for its liquid state (Williams et al., 2005, 2006, 2007, 2008; Williams and Boggs, 2008). A systematic offset between k_2 solutions from Laser ranging on the one hand, and spacecraft tracking on the other hand, was resolved by Goossens and Matsumoto (2008) in a joint evaluation of data from several spacecrafts (the Lunar Orbiters I to V, Apollo 15 and 16 subsatellites, Clementine, Lunar Prospector, and SMART-1). A limitation that could not be overcome is the necessity to inflate the formal uncertainty to account for sources of uncertainty that could not be modeled. An important step in the determination of the lunar gravity field was achieved with the twin satellites of the Japanese SELENE mission, which for the first time allowed measurements over the far side, which is invisible to Earth-based tracking stations (Matsumoto et al., 2010; Goossens et al., 2011). The discrepancy between Laser ranging and spacecraft tracking solutions for k_2 however reappeared.

The GRAIL mission, also with a twin-satellite system, resulted in a much higher spatial resolution of the gravity field, and a substantial reduction of the uncertainty on k_2 (Konopliv et al., 2013; Williams et al., 2014). The mission used Ka-Band rather than S-Band communication between satellites, i.e., frequencies roughly ten times higher than in the ground-based tracking, which "*provides a stunning 4 orders-of-magnitude improvement in measurement of the spacecraft along-track velocity*" (Konopliv et al., 2013, p. 1416).

Structural information, the dynamical behavior of the Moon in its orbit, and compositional information from rock samples and meteorites can be used to construct compositional models for the crust, mantle and core of the Moon. Even with seismic velocity models that do not reach down to the lunar center, such modeling can predict the core radius based on the available amounts of iron and thermodynamic stability criteria. The study of Mueller et al. (1988) is mentioned above, and similar studies followed at the end of the 1990s.

Kuskov and Kronrod (1998) used the same velocity model (Nakamura, 1983) and building blocks (but added Sulfur as possible core constituent). Two different ranges for the core radius resulted, depending on the presence or absence of Sulfur in the core. In a subsequent study (Kuskov and Kronrod, 2001), with a slightly more complex set of building blocks, these

radius ranges were modified and narrowed down. In both studies, Kuskov and Kronrod concluded with regard to the origin of the Moon that "*The chemical composition of the Moon is different from that of the Earth's upper mantle and bears no genetic relationship to the terrestrial material as well as to any of the known chondrites*." (Kuskov and Kronrod, 2001, p. 221, almost the same formulation is found on p. 302 of Kuskov and Kronrod, 1998).

After a re-evaluation of the raw data, involving re-reading of arrival times, relocation of the seismic sources, and construction of a new seismic velocity model, Lognonné et al. (2003) arrived at an essentially opposite conclusion, namely that "*This composition can be explained by the collision between the primitive Earth and an impactor with a composition close to enstatite chondrites*." (p. 42).

With a massive processing of seismogram stacks of 38 Deep Moonquake clusters (chosen after determining S-wave arrival times for all known 106 clusters), involving polarization filtering and array-beamforming with respect to the expected arrival times of a variety of reflected phases (combinations of P-to-S and S-to-P conversion at different interfaces) for a broad range of core and inner core radii, Weber et al. (2011) identified shear wave energy reflected from the top of the alleged partial melt zone, the core-mantle boundary, and the boundary between the solid inner and liquid outer core of the Moon. The conversion of the respective arrival times into absolute radii depends on the shear wave velocities in mantle and crust and is thus somewhat model dependent. However, since the travel time of waves is an integral over all velocities along their path, the result is not very dependent on details of the velocity model. The reflection from the inner-core-outer-core boundary (ICB) could be identified as a liquid-solid interface by the lack of SH-polarized waves – in a liquid, the incoming wave would be a P-wave (K-leg of SKiKS), and reflection can thus occur only in SV polarization, as the SH-polarization does not couple with P. While the radii of interfaces inherit some epistemic uncertainty from the mantle structure, their presence is probably the most robust result of Weber et al. (2011).

While Weber et al. (2011) reported the results of seismic waveform processing (and their figure 2, from which interface depths are measured, is derived directly from the seismograms), Garcia et al. (2011) followed an inverse modeling approach in which an ensemble of velocity and density models is constructed, using arrival times (involving source relocation), mass and moment of inertia as constraints. The energy of SH-polarized ScS phases was then computed based on the obtained mantle models, and

compared to the Apollo seismograms to identify the best fitting core radius. A range of likely core radii resulted, the middle of which was adopted for the sought (very preliminary) reference model. An erratum (Garcia et al., 2012), with a correction for an erroneous pressure computation, contains the final VPREMOON model but does not change the core radius. The VPREMOON core radius is about 50 km larger than that of Weber et al. (2011), and the radius ranges given in the two papers overlap only slightly: A certain allowance for the depth-velocity tradeoff must be considered when comparing the two results, as Weber et al. (2011) used a prescribed mantle structure. Despite the differences between approaches, the two studies obtained very similar results that differ by much less than the range of values in previous publications.

Garcia et al. (2011) did not investigate the existence of an inner core and do not search for seismic phases related to an inner-core-outer-core boundary. In consequence, the resulting VPREMOON model does not contain an inner core. The authors nevertheless acknowledge the likely existence of an inner core for thermodynamical reasons and point out that the density VPREMOON assigns to the core is of limited value without further constraints on the inner core, and that GRAIL and KAGUYA might provide important clues. That VPREMOON does not contain an inner core does thus not imply that Garcia et al. denied its existence.

Neither Weber et al. (2011) nor Garcia et al. (2011) provide core phase travel times in numerical form. The beamforming-approach of Weber et al. (2011) does not require the determination of individual arrival times, which is actually a strength, since phase picking is a somewhat uncertain, subjective endeavor. The resulting absence of respective tables however makes the subsequent use of core phase constraints in other studies difficult.

While Weber et al. and Garcia et al. were searching for ScS phases and building their core models, the GRAIL mission worked on improving the mass, moment of inertia, and Love number constraints, that are necessary to constrain the density of the core. Since the entire core contains less than 1.5%, and the inner core less than 1% of the lunar mass (Williams et al., 2014), resolving their respective contributions involved improvements on the Earth's gravitational coefficients and the lunar ephemeris as well. Williams et al. (2014) conducted a detailed analysis of the GRAIL results to analyze the constraints arising from the new data. A tradeoff between the radii of the outer and inner core and their densities remained, but the existence of a solid inner core was shown explicitly to be compatible with the geodetic information. In addition, Matsumoto et al. (2015) confirm

that the combined GRAIL and LLR data require a low viscosity zone at the base of the lunar mantle.

Dorn et al. (2015, see also our discussion of their results for the Earth on p. 27), benchmark their approach, which is intended for the analysis of exoplanets, using the lunar core radius of Kuskov and Kronrod (2001). The latter obtained 310 km to 320 km for a pure iron core, and Dorn et al. (2015) conclude that their result "*matches the independent estimate* [i.e. Kuskov and Kronrod] *reasonably well with* $0 \leq R_c \leq 380$ km (*95% credible interval*)" (p. A38). They do not comment on the core radii obtained by Weber et al. (2011) and Garcia et al. (2011).

Kuskov and Belashchenko (2016) undertake molecular dynamics simulations to estimate properties (density and sound velocity, among others) of FeS alloys under lunar core conditions and find, in comparison with Garcia et al. (2011) and Weber et al. (2011), a "[...] *good agreement of P-wave velocities in the liquid outer core, while the calculated core density does not match* [...]" (p. 49), and from this discrepancy between their own modeling and the data processing and inversion of Garcia et al. and Weber et al., Kuskov et al. conclude that "[...] *the most probable outer core radius should be less than 330 km* [...] *found by Weber et al.* [...]" (p. 49). Moreover, "*It can be concluded from these results that future seismic measurements are needed to provide further observational constraints on the composition and physical properties of the core.*" (p. 49), a conclusion at which Kuskov and Kronrod (1998) and Kuskov et al. (2002) also arrived, in similar words.

From 2017 onwards, an international team at the International Space Science Institute Bern/Beijing started compiling a new reference data set for the seismological analysis of the Moon from the wealth of literature that accumulated in the previous almost 50 years, and also to improve the accessibility of the data (Nunn et al., 2020). Based on this data, and using three different parameterizations and inversion methods, Garcia et al. (2019) produced three new velocity and density models for the lunar interior. These show that, with the most recent methods, the crust and mantle up to a depth of approx. 600 km are relatively well resolved, while the distributions of Apollo stations and seismic sources leave "*Deep mantle and core structure* [...] *poorly constrained*" (p. 37). New seismic data would be required to further improve our knowledge of the deepest regions.

Viswanathan et al. (2019) again combined GRAIL and Lunar Laser Ranging Data (meanwhile 48 years of observation) to estimate the mean radius and flattening of the core-mantle boundary, assuming a hydrostatic liquid core within a nonhydrostatic lithosphere of a frozen-in shape. A criti-

cal parameter for their resulting radius range is the assumed crustal thickness and density, which was provided by GRAIL (Wieczorek et al., 2013). Although the flattening of the CMB naturally plays an important role in the interpretation, it remains unclear to what extent the asymmetric distribution of crustal thicknesses between near and far side, with hemispheric average thicknesses outside of the adopted thickness interval is relevant for the result. The interior model was deliberately set up without an inner core, justified by a brief remark in the supplementary information ("*recent GRAIL analyses (Konopliv et al., 2013, Lemoine et al., 2013) showed no signature thereof*", p. 3). This is however not supported by the given references. According to Konopliv et al. (2013), detection of the periodic variation of gravity field coefficients C_{21} and S_{21} would require including the acceleration of the spacecraft due to its heat radiation, which is not included in the force budget of their gravity model GL0660B. Lemoine et al. (2013) state explicitly "*In this paper we have not estimated the periodic harmonics of* $\overline{C}_{21}$ *and* $\overline{S}_{21}$ *that represent the expected signature of core motion* [...]. *The estimation of these periodic terms will be the subject of future work*." Williams et al. (2014) finally estimate the inner core's radius from GRAIL data. The effect of omitting the inner core on the uncertainty of the core radius estimate by Viswanathan et al. (2019) remains unclear.

Kronrod et al. (2018) attempted a joint inversion of seismic travel times, geodetic and tidal, geothermal, geochemical and petrological constraints, the latter from an assumed set of constituents. The results of this study were somewhat inconclusive, and in order to obtain any solution at all, it was necessary to relax the constraints from seismic travel times (by inflating their uncertainties by a factor 3 compared to the reference they were taken from) and to introduce additional constraints, like fixing the crustal parameters. The authors were dissatisfied themselves with this outcome.

In a new attempt, Kronrod et al. (2020) used a similar set of constraints, and fixed another subset of model parameters (e.g. thickness, density and seismic velocities of the crust, inner core density) with a slightly extended set of observables (bulk contents of Al_2O_3 and FeO were treatedas observables). Again, inflating the uncertainties of seismic travel times was considered necessary. Under the assumed conditions and constraints, the authors concluded that a completely solid core is ruled out. The most likely core radius is 300 km, but with an uncertainty range from 50 km to 350 km.

A previously unused nonlinear optimization method, Particle Swarm Optimization, was employed by Zhong et al. (2021) to invert the mass,

radius, and moment of inertia as derived from a degree and order 1500 GRAIL gravity field solution for core structure. The most likely core radius reported by the authors is relatively large, compared to other studies from the 21st century, and the admissible range of core radii (according to their Fig. 2) reaches the upper boundary of the explored range (650 km). For the inner core, a most likely radius could be estimated, but admissible values are found within the entire explored range (100 to 350 km).

Kronrod et al. (2022) attempted to reconcile seismological, geodetic, and geochemical data in order to estimate not only the size but also the composition of the core. The core radius, in their formulation, is derived from thermodynamically feasible compositional models. They assumed that the core is subdivided into a liquid outer and a solid inner core, as found by Weber et al. (2011). No seismological data beyond this result was included, the seismic constraints used were only the P and S travel times (no crustal conversions) underlying the mantle model of Weber et al. (2011), but not the beamforming results on which Weber et al. (2011) based their interpretations, or other numerical constraints concerning core phases. It was thus not possible for Kronrod et al. (2022) to fully employ the seismological constraints on core size. The posterior probability functions shown by Kronrod et al. (2022) have nonzero values for core radii between 250 and 470 km. The authors however name 300 to 350 km as the possible interval.

Based on the experience from Earth one would have expected that passive seismology would solve the problem of the lunar core size. Geophysical investigations, i.e. mainly seismology and measurements of magnetic and electric properties of the core indeed draw a relatively clear picture. Nevertheless, core radii discussed in studies published since 2011 differ little from those published between 1980 and 2000. Compared to the 1960s, only the largest radii were abandoned, and it is commonly accepted that the Moon has a core, and also that it is subdivided into an outer and inner core. That the range of discussed core radii is nevertheless relatively large may in part result from the difficulty to reconcile the seismological results on core size, partial melt directly above the CMB, and deep moonquake source depth with compositional models. In part, the radius discussion is however impeded by the format of numerical representation of the seismological evidence, and the challenges that apparently arise from fully integrating them into modeling procedures. It remains to be seen whether a future lunar seismic network (as part of a lunar geophysical network) with more global station distribution can lead to a travel time dataset that is used more widely

by the community (see also the discussion of future seismic experiments in Chapter 2, Stähler and Knapmeyer, 2022).

4.3 Mars

Mars is one of the five planets known since antiquity; there are few objects in the sky that shine brighter. It played a major role in the development of modern astronomy and for overcoming the geocentric cosmos, as the motion of Mars is the central topic of the near 500 pages of Kepler's *Astronomia Nova* (1609), where he found the first and second of the Keplerian laws of planetary motion – without telescope.

At this time, first estimations of Mars' true radius were already made; the oldest one we found is due to Albategnius, who saw Mars at a visible diameter of 94 arc seconds, which translates into a radius of nearly 34100 km (880 CE, cited after Houzeau, 1882). The first radius estimation that captures the correct order of magnitude was apparently that of Le Monnier, who reported an optical diameter corresponding to an equatorial radius of 3590 km (1746, cited after Houzeau, 1882). Radius measurements conducted throughout the 19th century are scattered between 3200 km and 4100 km, with a mean of 3490 ± 160 km (see Fig. 5, S6.3.1), and biased toward high radii.

In 1784, Herschel reported a series of observations of bright spots in the polar regions of Mars, and how they change with time. After meticulous analysis, he concluded "*that the bright polar spots are owing to the vivid reflection of light from frozen regions; and that the reduction of those spots is to be ascribed to their being exposed to the sun*" (Herschel, 1784, p. 260). Herschel continued reporting observations of the diameter of Mars, and found, after corrections for perspective that "*The true proportion, therefore, of the equatorial to the polar diameter will be as 1355 to 1272*" (p. 268). Finally, supporting earlier observations made by Cassini with his own observations of star occultations, Herschel concludes "*that this planet is not without a considerable atmosphere*" and that some individual observations require "*the variable disposition of clouds and vapours floating in the atmosphere of that planet*" (p. 273), such that "*its inhabitants probably enjoy a situation in many respects similar to ours*" (p. 273).

Six different types of observational errors, all of which lead to an increased diameter, were discussed by Campbell (1895). Caring for all of them, and using a yellow glass filter, he obtained a radius only about 58 km too large, and only few of the newer values in our collection deviate from the true radius by more than that. The precision that could be achieved by

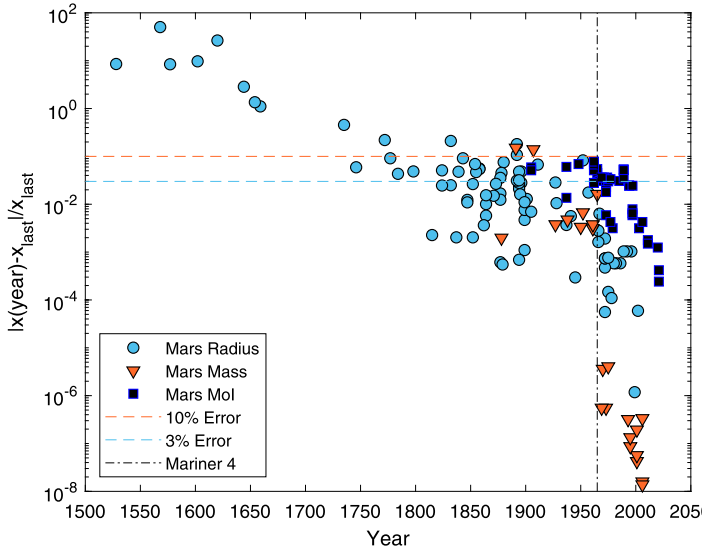

Figure 5 Relative uncertainties of Mars' radius, mass, and moment of inertia factor over time, computed with respect to the most recent values. Horizontal lines indicate the accuracy goals of the PLATO mission (10% in mass, 3% in radius, Rauer et al., 2016), the vertical line indicates the arrival of the Mariner IV mission at Mars. Numerical values in Knapmeyer and Walterová (2022).

careful observation gave rise to another source of error, which Campbell eliminated coincidentally by blocking red and blue wavelengths in order to reduce chromatic aberration: With a series of photographs taken systematically with different color filters from infrared to violet, Wright (1924) demonstrated that the radius of Mars appears larger in violet than in infrared: "*we have in round numbers 120 miles* [approx. 190 km, MK] *as the radial excess of the violet over the infra-red images*" (Wright, 1924, p. 251). His interpretation is that the infrared photos show the planetary surface, while the disc visible on the violet photos is only the atmosphere, which scatters short-wavelength light. With an orange-yellow filter, Campbell's result is thus closer to the true radius than it could be in white light.

The significance of Wright's observation for our study lies in the fact that a +5% bias in radius results in a near -10% bias in I/MR^2 and a near -15% bias in mean density when mass and moment of inertia are held fixed.

A spacecraft came to the rescue, in the form of the Mariner IV flyby in 1965: When the spacecraft went into occultation behind Mars, the local radii at the entrance and exit points could be determined (Fjeldbo et al., 1966) and translated into a mean radius (Bullen, 1966). The accuracy

of Radius, Mass, and MoI improved considerably with the presence of spacecraft near Mars (Fig. 5). We'll return to the space age later.

Long before that, See (1905a,b) provided a first estimate of the Martian moment of inertia factor, by inverting Laplace's density law to the observed mass and radius. The resulting density distribution is coreless, as Laplace's law is a continuous function for the entire planet, but allowed an estimation of the flattening of Mars, and its moment of inertia.

An example for how comparative planetology can help solving problems concerning the Earth is the work of Jeffreys (1937). He aimed to obtain constraints on the depth of a seismic discontinuity within the Earth from a comparison of Earth, Moon, and Mars. The discontinuity in question was determined to be at either 350 km or around 474 km depth within the Earth (depending on who was asked), and the question was if it might indicate a phase transition of Olivine. The Moon, being small, provided an estimation of the densities above the discontinuity. For Mars, Jeffreys pointed out that the uncertainty in its radius makes the main contribution to the uncertainty of its density. Using the relation between depth and density found for Earth, Jeffreys found that the hypothesis of a phase transition at the given depth in Earth, when transferred to the size and mass of Mars, requires the presence of a heavy core. If the discontinuity announces the presence of a new material, the Martian data can be reproduced without core. However, "*The evidence from Mars is indecisive; it shows at any rate that the central core must be much smaller than in the Earth, and possibly absent* [...]" (Jeffreys, 1937, p. 67). Jeffreys compared his density models to the real Mars via the flattening of the Martian ellipsoid, which could be derived from observation of Phobos' orbit, and which Jeffreys connected to the moment of inertia factor of his density models via the Radau–Darwin equation.

The theory of phase transitions led Ramsey (1948) to the same conclusion he already got for the Moon: Mars is too small to support the phase transition he considered to be behind the Earth's seismic discontinuity at 2900 km depth. Therefore, like the Moon and all small bodies, Mars cannot have a core at all.

This view is supported by Bullen (1949), who also constructs an Earth model where the outer core is a pressure effect and only the inner core is chemically distinct from the material between crust and inner core. In this view, the Earth's outer core is a high-pressure phase of mantle material, while Mars can again not support the required pressure, but has a (metal) inner core. A revised radius for Mars led Bullen (1957a) to revisit his eval-

uations, but he still concludes that neither the Earth's nor Mars' core need to be thought as containing much elemental iron.

To deal with the problem of the uncertain planetary radius, MacDonald (1962) constructed models on a number of different planetary radii. Like Jeffreys (1937); MacDonald used a constraint obtained from the Phobos orbit observations: these yielded a J_2 corresponding to a rather high polar moment of inertia, close to a homogeneous body, and hence required a small core only.

Lyttleton (1965) also supported the hypothesis that the outer core of the Earth is a high pressure phase of mantle material, and consequently, by comparison of pressures and likely temperatures in Mars and Earth, excluded the possibility of a liquid core in Mars. He argued that all of Mars is rocky material, and can be described by a "*two-zone model with the inner core having physical properties similar to those of the mantle of the Earth*" (Lyttleton, 1965, p. 24). Based on this, and with material parameters informed by seismological data for the Earth's mantle, Lyttleton constructed a series of Mars models with different fractions of mass contained below the phase transition. Interestingly, the material behavior under high pressure results in a lower limit of the moment of inertia factor, which, according to Lyttleton's theory for Mars, must exceed 0.38. As Lyttleton noticed himself, his model ensemble can't be used to infer the actual core radius, since the planetary mass and radius (still before Mariner 4) are too uncertain. In addition, he suggested that observations from spacecraft could settle the question of mountains – he considered the formation of mountains an important clue to internal temperature and processes, but neither limb nor shadow observations produced unambiguous evidence for mountains on Mars so far.

Kovach and Anderson (1965) introduced a third hypothesis into the controversy between chemically identical or different terrestrial planets: The bulk composition of the planets might be identical, but the compositions of the different cores might differ by their content of light alloys, and they show that Earth and Mars models based on this hypothesis can satisfy the astronomical observations, namely mean density and polar moment of inertia. They find that, if the radius of Trumpler (1927, 3310 ± 12 km), is combined with the Phobos-based moment of inertia factor, "*Mars must be a* [sic] *undifferentiated and nearly homogeneous body, but it is not necessary to violate compositional identity with the earth*" (Kovach and Anderson, 1965, p. 2879). Even a "*somewhat larger mean radius* [...] *of 3325 km*" (p. 2879) still allows for a near identical composition. Nevertheless, "*If a core is formed by downward drainage of heavy elements, we can say that Mars is in an earlier stage of*

evolution than the earth" (p. 2879), and an interpretation of the Earth's core-mantle boundary as pressure-induced phase transition is not inevitable. As we know now, both mentioned planetary radii are too small, while the adopted $C/MR^2 = 0.3836$ is too large, and far-fetched conclusions are thus to be taken with a grain of salt.

Ironically, the differentiated Mars model of Kovach and Anderson (1965) has a core radius very close to that of Stähler et al. (2021), but they dismissed the differentiation option because the associated polar moment of inertia (0.35) is much smaller than the value they considered realistic.

Bullen (1966b) dismissed the entire approach of Kovach and Anderson (1965) as an "*ad hoc device*" (Bullen, 1966b, p. 236) and maintained the phase transition hypothesis.

After a re-assessment of the available mass, radius and flattening data, and with modified equations of state, Kozlovskaya (1967) constructs a number of Mars models which require the existence of a small iron core. Although she supports that all terrestrial planets formed from the same pristine material, she allows for different compositions of Earth, Venus, and Mars, since the thermal conditions at the places where these formed might have differed, i.e. a differentiation of the pristine material with respect to the distance of the Sun took place.

The first to use data from the Mariner IV fly by is apparently Binder (1969; Bullen, 1966a, only suggested that the new radius may have significant implications). The Mariner IV observations reduced the uncertainties on radius, mass, and moment of inertia significantly; the latter was now clearly below that of a homogeneous sphere (Fig. 6). In consequence, Binder found an iron core necessary to reconcile his compositional model with these observations. Binder apparently thinks this core as solidified, but also assumes that it might have maintained a dynamo in the past.

An alternative hypothesis for the composition of Mars is that of Ringwood (see Ringwood and Clark, 1971, and references therein), who suggested that the different mean densities of Venus, Earth, and Mars are due to different oxidation states. Ringwood and Clark (1971) reject the hypothesis that the Martian iron did not differentiate into a core on the grounds of the oxidation state of the Martian atmosphere, and also the (by then only likely) oxidation of surface rocks. Their preferred model has a large core, mostly consisting of solid Magnetite in a high-pressure *hpp* lattice, and possible a thin (100 km) liquid outer core. A large liquid core is excluded by the authors, also because of the absence of a magnetic field.

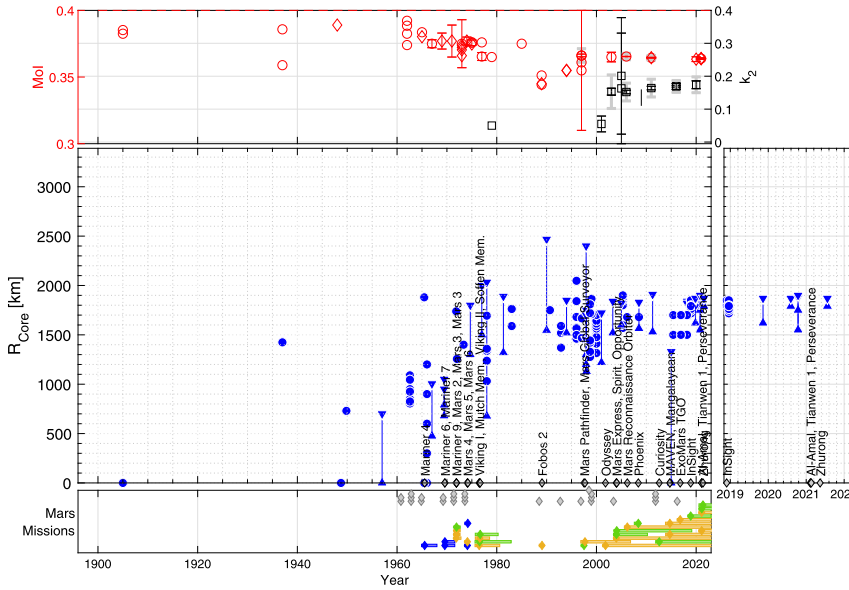

Figure 6 Evolution of parameter estimations for Mars. See Fig. 4 for a description of plot elements. Mission names are indicated in the middle panel. Mission data is mostly from Siddiqi (2018), for details and all other numerical values see Knapmeyer and Walterová (2022).

Shortly afterwards, Bullen (1973) suggested that planetary cores are chemically distinct and consisting of iron, but, depending on the internal pressure, outer cores of Fe_2O would form in the larger planets. Mars is too small for Fe_2O to be stable, and thus its core would consist of Fe only, and, by analogy with the Earth's inner core, be entirely solid. With this model, it was possible to reconcile geodetic data from the planets with the overarching concept of a shared bulk composition.

Johnston et al. (1974) build their core models of an Fe-FeS mixture and do not discuss the possibility of magnetite or Fe_2O.

Mariner 4 reduced not only the accepted value of the moment of inertia factor (Lorell and Shapiro, 1973 give $C = 0.375 \pm 0.006$, scratching the theoretical *lower* bound of Lyttleton, 1965, from *below*), but also the expectations concerning Mars as neighboring planet: While the late 19th century thought Mars as a largely earthlike world, but aged and dying, research in the 20th century step by step replaced biology and imagination with geology, as described in the first chapter of Hartmann and Raper (1974). The fly-by of Mariner 4 resulted in 21 complete pictures and revealed a

Moon-like surface (all reproduced in Leighton et al., 1967). Mariner 4 was followed by Mariners 6 and 7, which returned another 200 images. Collins (1971) summarizes that "*The Mariner 6 and 7 flights have finally revealed a unique Martian character, distinctly different from that of either the Earth or the Moon*" (p. 147). After these three fly-by missions, Mariner 9 entered an orbit around Mars (Mariner 8 failed) and, with more than 7000 images returned (Hartmann and Raper, 1974), allowed for a detailed topographic map of the entire surface of Mars. With the first preorbital science picture of Mariner 9 it became clear that Nix Olympica, originally the name of an albedo feature, was a giant mountain, recognizable as such since it protruded above the dust storm active during approach. The next two images showed that there are three other mountains of comparable height to the east (Hartmann and Raper, 1974), and initially named South Spot, Middle Spot, and North Spot (McCauley et al., 1972). Mariner 9 also discovered Valles Marineris, rampart craters, dunes, and many other features. Knowledge about the Martian surface was revolutionized, and it even became necessary to define a new nomenclature (exit Nix Olympica, enter Olympus Mons, enter the dichotomy), which was adopted by IAU in 1973 (following a recommendation of Commission 16 at the XV. IAU general assembly, Trans. IAU, 1973, see also de de Vaucouleurs et al., 1975). The planet which was suspected to have no mountains at all (see Lyttleton, 1965) has in fact the largest mountains of the solar system.

Mariner 9 confirmed the smaller moment of inertia value obtained from Mariner 4, even indicated a still smaller value, and also allowed mapping of the global gravity field and improving the mass measurement (Lorell and Shapiro, 1973). The degree 9 gravity solution of Jordan and Lorell (1975) identifies Tharsis not only as topographic, but also as a gravimetric maximum, which even distorts the low-degree gravity coefficients.

Binder and Davis (1973) recognized that the Mariner 9 observations of the Martian shape imply that a straightforward interpretation of J_2 in terms of hydrostatic equilibrium is probably too simple, and corrections for isostatic and nonisostatic contributions from the crust are necessary to compare a spherically symmetric model with real Mars. Since they lacked information on the structure of the crust, they could only evaluate a series of test models.

Doppler tracking of the Mariner 9 spacecraft allowed for the reconstruction of the gravity field of Mars. Reasenberg et al. (1975) produced a sixth degree and order spherical harmonics solution, while Sjogren et al. (1975) first fitted a set of discrete point masses and then derived a ninth de-

gree and order solution from their combined gravity field. Both solutions match closely and find a significant anomaly associated with Tharsis, with a gravity high between Pavonis Mons and Ascraeus Mons. Sjogren et al. (1975) show that a single mass anomaly connected to Tharsis is responsible for most of the variability of the gravity field.

Therefore, Reasenberg (1977) concluded, the J_2 coefficient of the gravity field expansion contains a contribution from a nonisostatic mass distribution under Tharsis, which must be considered when converting J_2 into a moment of inertia. From a geometric model of Tharsis, based on assumptions of its geological origin and structure, Reasenberg computed a considerable reduction of the polar moment of inertia from $C/MR^2 = 0.377$ down to $C/MR^2 = 0.3654$, which is the lowest value resulting from measurement so far (with the exception of the lower end of Lorell and Shapiro's uncertainty interval).

A different approach towards a nonhydrostatic correction was presented by Cook (1977), in terms of an analysis of the deviation in spherical harmonic coefficients, attempting to determine the deviation in J_2 from coefficients which should be zero in the hydrostatic case, but are nonzero in reality. Cook concluded that the necessary correction on the moment of inertia factor is much smaller than those by Binder and Davis (1973) and Reasenberg (1977), and that it does not invalidate models constructed with an uncorrected value.

Kaula (1979) found the discrepancy between Binder and Davis (1973), Cook (1977), and Reasenberg (1977) rather dissatisfying, even more so as the previous works do not explain where the discrepancy might originate. He presented an approach to Reasenberg's Tharsis-removal concept in simpler expressions. His conclusion is that Reasenberg's "*deterministic solution is better than Cook's* [...] *statistical extrapolation plus his opposite interpretation of the significance of the large* J_{22}" (Kaula, 1979, p. 195, emphasis in the original).

The arguments of Reasenberg (1977) and Kaula (1979) were in turn considered insufficient by Bills (1989), who proposed that their common result should be considered as the upper bound of the plausible range. In his view, Mars must be considered as a triaxial ellipsoid, on the grounds that a random distribution of inhomogeneities on a comparatively massive homogeneous sphere most likely results in a triaxial ellipsoid, and that Venus actually showed this configuration (according to Bills, 1989, and references therein). Bills also points out that the only means to solve the problem is by measuring the precession rate of Mars, which would provide a direct scaling factor between J_2 and the polar moment of inertia. With an approach

based on the modeling of Tharsis' gravity anomaly in terms of a spherical harmonics expansion, Zuber and Smith (1997) obtained a corrected polar moment of inertia factor of $0.361 < C/MR^2 < 0.366$, supporting the approach of Reasenberg.

The last publication of a core radius smaller than 1000 km (with the notable exception of Dorn et al., 2015) after Binder (1969), is, to our knowledge, that of Okal and Anderson (1978, see Fig. 6). In preparation for the Viking missions, they aimed at identifying the kind of seismic observations most useful to discriminate between the different theories. Okal and Anderson did thus not predict that the core might be small, but provide new criteria for the recognition of a small core. Their preferred model (well known in the literature as AR model) is not small, but has a core radius of 1694 km.

One can thus say that the most significant single event in the determination of the Martian core radius was the Mariner 9 mission: With Mariner 9, small cores disappeared from the discussion of Mars.

A remarkable outlier in terms of the investigated core radii is the study of Schubert and Spohn (1990), who have the largest of all cores in our collection in their model suite (with $R_c = 2468.06$ km). This value resulted from, on the one hand, assuming a Fe-FeS composition of the core to limit the possible densities, and, on the other hand, the uncertainty of the mean moment of inertia factor resulting from the ongoing discussion of how the observed J_2 coefficient has to be converted into the polar moment of inertia. The lower limit of their core radii is attained for a pure iron core ($R_c = 1546.44$ km). This underlines the importance of both compositional assumptions, and appropriate uncertainty propagation for core radius studies.

The Viking twin missions were launched only four years after Mariner 9, and resulted in additional milestones of Martian research. In the 1960s, Wänke already argued for Mars as the SNC parent body (see Dreibus and Wänke, 1985, and references therein), by the end of the 1970s, several authors argued for a Martian origin of the SNC meteorites. The soil sample analyses of Viking showed "close compositional similarities" between Martian soil and Shergotty meteorites (Wood and Ashwal, 1981, and references therein), while trace gases trapped are similar to the trace gas content of the Martian atmosphere, again based on Viking measurements (McSween, 1984, and references therein). Dreibus and Wänke (1985) considered the trapped gases as the most striking evidence for a Martian origin, and argue that the SNC thus support that a CI chondritic composition explains

neither the composition of the Earth nor that of Mars, and also not that of Venus. The SNC meteorites thus became important witnesses of the composition of Mars, and even allowed conclusions about the evolution of Mars.

The Viking missions also allowed determining the precession rate, and provided a handle on the polar moment of inertia without the assumption of hydrostatic equilibrium (Yoder and Standish, 1997). Since the period of precession is much longer than the typical mission life time (the rate of 7.83 arc sec estimated by Yoder corresponds to about 165000 years), its uncertainty is considerable and the resulting uncertainty of the moment of inertia factor relatively large. The obtained value of $C/MR^2 = 0.355 \pm 0.015$ encompasses the corrected moments of inertia of Reasenberg (1977), Kaula (1979) and Bills (1989) as well.

An improvement of the uncertainty on precession became possible with the Mars Pathfinder lander (Folkner et al., 1997). Although short-lived itself, the long time between Viking and Pathfinder (about 20 years) resulted in a significant advance in the orientation of Mars' rotational axis. Further improvement resulted from the recovery of previously unused tracking data of the Viking I lander. The new precession rate led to an increase of the resulting C and a decrease of its uncertainty, $C/MR^2 = 0.3662 \pm 0.0017$ now clearly excluded the low value of Bills (1989). It also showed that the old, uncorrected value of 0.377 was indeed to high, and corroborated Reasenberg's (1977) interpretation of the Tharsis bulge, as Folkner et al. (1997) pointed out: "*Our estimate favors the Reasenberg interpretation*" (Folkner et al., p. 1750). In terms of the core radius, the new precession rate implies that "[...] *the core radius can range from 1200 to 2400 km without an additional constraint such as core composition*" (Folkner et al., 1997, p. 1750).

Bertka and Fei (1998a) nevertheless considered the uncertainty of the precession rate as too high and the knowledge of the crustal thickness too poor to provide a sufficiently precise estimation of the moment of inertia, but expected a significant improvement from the Mars Pathfinder mission. Based on the compositional constraints due to SNC meteorites, they constructed a series of density profiles and attempted to estimate a feasible range of moment of inertia factors, given plausible geochemical and geological assumptions. With a late-breaking new moment of inertia factor, they conclude that the iron content of the Martian mantle is larger than that of the Earth, and that the mantle may contain a perovskite layer just above the CMB. With all of their mantle and core compositions (all from the Fe-FeS system), they obtain core radii smaller than 1750 km. In a follow-

up, Bertka and Fei (1998b) adapt their models to the Pathfinder results and allow for additional light elements in the core, obtaining a feasible radius range from 1276 to 1809 km, the latter with a Fe_3O_4 composition and 27 weight-% of Oxygen in the core. Their main conclusion is that a CI chondritic composition is insufficient to explain the formation of all terrestrial planets.

Sanloup et al. (1999) suggested a new compositional model based on a mixture of three different classes of chondrites, rather than CI only, constrained by the oxygen isotopic composition of SNC meteorites, and yielding relatively large cores up to 1865 km radius. Sanloup et al. considered the MoIF range defined by the Reasenberg (1977) / Kaula (1979) estimations and the much lower value of Bills (1989) as the acceptable range, "*which has been recently confirmed by the Pathfinder mission*" (Sanloup et al., p. 51, referring to Folkner et al., 1997, see also above).

With Hydrogen instead of Oxygen in the core, and a chondritic Fe/Si ratio, Zharkov and Gudkova (2000) constructed a series of models covering core radius range of approx. 400 km in width. From the successful construction of models that fit the Pathfinder MoIF value and a composition close to that of Dreibus and Wänke, they conclude that the DW compositional model is not as unequivocally invalidated as some assumed. The largest core of Zharkov and Gudkova (2000) has a radius of 1702 km.

In a study of annual variations of snow depth on Mars with Mars Global Surveyor MOLA data, Smith et al. (2001) presented a new value and uncertainty for the k_2 Love number, in passing and without any discussion. According to their footnote, it was apparently obtained as a by-product of the inversion routine. The obtained value, $k_2 = 0.055 \pm 0.008$ could be considered as corroboration of the 0.05 assumed earlier, e.g. by Lemoine et al. (2001), or Christensen and Balmino (1979).

A new solution, $k_2 = 0.153 \pm 0.017$ (with uncertainty inflation of five), was presented by Yoder et al. (2003), derived from three years of radio tracking of Mars Global Surveyor. This solution was accompanied by a new determination of the precession rate and polar moment of inertia factor, and represents a major step in the understanding of the Martian core, as it is indicative of a fluid state, while the lower value mentioned by Smith et al. (2001) would imply that the core is solid.

With this result from Mars Global Surveyor, a new milestone was also achieved in the determination of Mars' core radius: After Yoder et al. (2003), cores smaller than 1500 km in radius disappeared from the literature (again, with the exception of Dorn et al., 2015).

Later missions consolidate this result, and even supported slightly higher values. Using of the laser altimeter of Mars Global Surveyor, MOLA, to determine the distance to Phobos instead of the Martian surface amounted to an improved tracking of Phobos. The long-lived missions Mars Global Surveyor, Mars Reconnaissance Orbiter, and Mars Odyssey provided tracking data for continuous improvements of gravity field solutions, and also love numbers, precession rates, and Moment of inertia factors.

Partly in preparation of the first purely geophysically focused mission to Mars, InSight (Banerdt et al., 2013), a number of new models was created (Khan et al., 2018; Plesa et al., 2018a,b), and a set of reference models, intended to represent the best knowledge, was compiled (Smrekar et al., 2019). Khan et al. (2018) introduced new descriptions of the viscoelastic behavior of olivine, and complex models of composition and phase transitions within Mars, to reduce the core radius range of a Bayesian ensemble of radially symmetric models. Plesa et al. (2018a) built 3D thermal evolution models, with different chemical compositions and enrichments of radioactive elements in the crust. Their modes were based on earlier studies (Plesa et al., 2015, 2016), but constraints were updated and larger cores allowed, which proved necessary since none of the models with core radius smaller than 1800 km fitted the constraints. The determination of the core radius was however not the goal of the studies of Plesa et al.

Smrekar et al. (2019) compiled a review of the knowledge on Mars' interior structure prior to the InSight mission, and show a set of reference models that reflect this knowledge, with core radii from 1718 km to 1850 km.

The core formation scenarios of Brennan et al. (2020) were published after InSight started operations on Mars, but before its first results on core radius were published, i.e. without seismological constraints. The same is true for Konopliv et al. (2020), who, like Brennan et al., were more conservative in their core radius estimations than Smrekar et al. (2019).

The first core radius estimation based on InSight seismological data was actually published by authors not in the InSight mission team. Deng and Levander (2020) used the autocorrelation of ambient vibrations ("noise") to identify discontinuities beneath the InSight lander. This method produces a time series showing maxima at times that corresponds to the travel time of reflected phases; the times of the maxima are converted into depths using a set of velocity models that were computed prior to the InSight mission, partly by members of the mission team. This yielded a core radius between 1790 and 1870 km.

Interestingly, this radius interval is identical to the 1830 ± 40 km of Stähler et al. (2021). This study is based on the more classical approach of identifying core reflected S waves, i.e. the ScS phase. Six marsquakes with sufficient SNR were identified, waveforms rotated and filtered to enhance arrivals in SH polarization, and stacked according to the predicted ScS arrival times of an ensemble 5000 velocity models compatible with other body wave arrivals. A new arrival time inversion, including k_2 and moment of inertia as additional constraints then resulted in the final core radius estimation.

When working with InSight seismogram data, it is important to know about a number of peculiarities that arise from technical and environmental conditions. These are described in a dedicated paper (Kim et al., 2021). The most severe peculiarities are probably the so-called glitches (steps in acceleration) and spikes (steps in displacement), which represent a self-noise of the sensor assembly. Methods for their detection and mitigation were described by Scholz et al. (2020). An unfortunate property of glitches and spikes is that they tend to occur in pairs, with separations of 280 and 368 s (Kim et al., 2021). Although Deng and Levander (2020) used their own processing methods to suppress artefacts, Kim et al. show that the autocorrelation nevertheless is clearly affected by them. The glitch and spike separations are near identical to the arrival times reported by Deng and Levander (280 s for the Olivine-Wadsleyite transition and 375 s for PcP). Kim et al. do not go as far to declare the results of Deng and Levander incorrect, but state that "*two strong phases in the LF ACFs interpreted as P-wave reflections* [...] *are substantially affected by the presence of glitches*" (Kim et al., 2021, p. 2998). The remarkable similarity of the core radii of Deng and Levander (2020) and Stähler et al. (2021) is then an unfortunate combination of using specific a priori velocity models and a certain periodicity in the occurrence of glitches. Deng and Levander themselves, who are both co-authors of Kim et al. (2021), are apparently not entirely convinced of this interpretation; at least not as much as to publish any comment or correction to their 2020 paper. We thus report their result, and include it into our figures, as it is a result considered correct by its authors.

Stähler et al. (2021) not only present a core radius, but also first interpretations of the planetological significance of their result. First, the observation of ScS supports the earlier finding that the core is at least partially liquid: An S-wave reflection from an interface between to solid materials would be much weaker than from a solid-liquid interface. Second, an inversion that used constraints other than the seismological also

solved for core density and suggested that light elements in addition to the traditionally assumed Sulfur are likely present in the core: "*C, O, Si, N, and H, are all potentially viable candidates*" (Stähler et al., 2021, p. 446), while a pure Fe-S core would require a sulfur concentration above 30 wt%, unknown from meteorites. A near-eutectic fracton of light elements would also make the nucleation of an inner core unlikely and thus provide a clue to the demise of the Martian geodynamo. Finally, a large core produces a larger seismic core shadow, and can thus result in a downward bias of estimations of the seismic moment rate of Mars, especially since much of the Tharsis plateau is within the core shadow for InSight. The mean density of the core found by Stähler et al. is so difficult to reconcile with cosmochemical constraints, that Khan et al. (2022) proposed a new global composition of the planet, significantly increased in volatiles. Plesa et al. (2022, this volume), describe consequences of the results of the InSight mission for our understanding of the geodynamic and thermal evolution of Mars.

The Rotation and Interior Structure Experiment (RISE) of Insight (Folkner et al., 2018) intends to augment previous measurements of the martian precession rate with a measurement of the nutation rate, and thus provide an independent determination of the core radius, and the moment of inertia of the core. At the time of writing, an updated precession rate and moment of inertia factor for the planet as a whole is published (including tracking data from Viking 1, Pathfinder, Opportunity, and InSight; Kahan et al., 2021), but the results concerning the core directly are not finalized.

As we have shown, the Mariner IV and IX missions to Mars resulted in the most pronounced changes, InSight may prove as another example. Although Mars was under close scrutiny at least since Kepler, and although surface structures, seasons, and climate could be observed telescopically from Earth for a long time, the two Mariner missions provided information without which all interpretation of Mars' interior structure would be doomed. Interestingly, the most important information, in terms of interior structure, were geometric in nature: finally a precise radius (Mariner IV), and, from Mariner IX: Mountains.

These alone do of course not determine an interior. But the determination of precession (to overcome the hypothesis of a hydrostatic figure), of the Love number (to reduce the nonuniqueness of density modeling) and, finally, of seismic reflections from the core mantle boundary, all rely on the continued presence of spacecraft in orbit and on the surface. Moreover, from the InSight seismic experiment, core phase travel times are published within the event catalog, for use in future inversions.

5. Exoplanets

Considering exoplanets in a dedicated section might appear premature, since most of them are observed only indirectly, by disturbances they cause in the observation of their host stars. Their interior structure is nevertheless subject of debate, and of interest not only for the identification of truly earthlike planets, but also for the general understanding of planetary formation.

5.1 Observational constraints

Most of the currently known exoplanets have been discovered by indirect detection techniques, such as transit photometry, radial velocity measurements (RV) or transit-timing variations (TTV).

Transit photometry stands for measuring the stellar flux and its variations caused by periodic passing of a planet in front of the host star. As might be expected, such stellar occultations can only occur if the planet is "transiting", and their probability depends on the extent and orientation of the planetary orbit relative to the observer. The quantity derived from transit light curves is the ratio between the planetary and the stellar radius.

The second method, spectroscopic RV measurements, rely on the varying Doppler shift of the host star's spectral lines, as it moves forward and backwards with respect to the observer due to the gravitational pull by the orbiting planetary companion. Such a motion can be detected even if the exoplanet is not transiting (as was the case of, e.g., Proxima Centauri b; Anglada-Escudé et al., 2016) and enables the estimation of the minimum planetary mass, relative to the stellar mass. The amplitude of the RV variations depends on the orientation of the planetary orbit. In the best-case scenario, with an orbit viewed edge-on, the actual planetary mass equals the "minimum mass" estimated by this method. In the worst-case scenario with a face-on orbit, the star's motion has no radial component and the method cannot be applied.

If there are multiple planets orbiting the host star, their mutual gravitational interaction can, in principle, affect the timing and duration of stellar occultations (in the transit light curves) as well as the timing of maximum RV variations. The TTV method is then based on fitting the transit light curves with gravitationally perturbed orbit (or orbits) and inferring the masses (and also orbital parameters) of the perturbers. This technique enables the indirect detection and characterization of planets that are not necessarily transiting and provides relatively precise estimates of planetary

masses, again with respect to the stellar mass (e.g., Agol and Fabrycky, 2018).

As we have seen in the previous paragraph, the measurements of exoplanetary parameters by indirect techniques are always relative. The precision of exoplanetary characterization can only be as high as the precision of the host star characterization. With the revised stellar parameters from the Gaia mission (Gaia Collaboration et al., 2016), the uncertainty of exoplanetary radius measurements obtained by Kepler is around 5% (Fulton and Petigura, 2018). For the PLATO mission, the radii of Earth-sized exoplanets around brighter stars (with relative magnitudes below 10) are expected to be estimated with a ~3% uncertainty (Rauer et al., 2016). The typical uncertainty of current mass estimations of small exoplanets is around 20%, but the PLATO mission aims at reducing this value down to 10% (to scale: for an Earth-sized planet, a 10% mass uncertainty corresponds to the mass of a Mars-sized planet).

Considering the continuously increasing time baseline of both photometric and spectrometric observations, combined with the expected precision of new, ongoing or planned missions (CHEOPS, JWST, PLATO), several authors discussed the possibility of measuring not only the mean radius of exoplanets but also their shape. As a consequence of rapid rotation or possible tidal interaction with the host star, the planet assumes the shape of an oblate or prolate ellipsoid, which might then affect the measured transit light curve (e.g., Seager and Hui, 2002; Carter and Winn, 2010; Correia, 2014; Zhu et al., 2014; Hellard, 2019; Hellard et al., 2020). With the orbital period known, and with an assumed interior structure of the exoplanet, the rotational flattening can constrain the planet's spin state. On the other hand, given an assumption on the spin rate (e.g., the synchronous rotation), the flattening provides an insight into the interior structure. Fitting the transit light curves by an ellipsoidal planet may also refine the resulting exoplanet radii and densities (Correia, 2014).

Hellard et al. (2020) predicted that the rotational and tidal deformation of hot Jupiters (close-in gas giants) would be observable by the CHEOPS, JWST, and PLATO missions. Akinsanmi et al. (2020) later proposed assessing the exoplanetary oblateness by a combination of photometric and spectroscopic measurements and illustrated that a Saturn-like rotational flattening might be detectable by existing high-precision spectrographs (such as ESPRESSO; Pepe et al., 2014). Needless to say that most of the present-day studies focus on detecting the deformation of gas giants as the tidal and rotational response of Earth-sized rocky planets is generally smaller. The

first estimation of an exoplanet's shape from a transit light curve has been achieved only recently. Using light curves acquired by the CHEOPS, HST, and *Spitzer* missions, Barros et al. (2022) reconstructed the tidal deformation of an extreme, exotic world: the hot Jupiter WASP-103b. Although the empirical limits on an exoplanetary Love number were also posed in an earlier work (Hellard et al., 2020; for WASP-121b), it was first in the case of WASP-103b that the deformed shape was detected at a 3σ confidence level.

In addition to measuring the shape, i.e., the rotational flattening or tidal prolateness of exoplanets, one can also consider the dynamical effects of tidal interaction reflected in the tidally-induced orbital evolution. The orbital evolution includes long-term changes in the orbital period as well as relatively short-term phenomena, such as the apsidal motion. Apsidal motion then translates to transit timing variations or changes in the transit duration (Ragozzine and Wolf, 2009). A drawback of this method, when compared to the planet shape estimation, is the dependence on a large number of unknowns: the tidal deformation and flattening of both the star and the planet, the orbital eccentricity, the contribution of relativistic precession, and the perturbations from other planetary or stellar companions. Nevertheless, the method has already yielded a few early k_2 estimations (all for hot Jupiters). For nonresonant multiplanetary systems, tidal effects combined with third-body perturbation can drive the planets' orbits to a tidal fixed point, at which they keep a constant eccentricity and aligned or anti-aligned apses (Batygin et al., 2009). The tidal Love number k_2 is then linked to the fitted orbital eccentricity. Batygin et al. (2009) apply this conclusion to the hot Jupiter HAT-P-13b and discuss its core mass. For systems with a single planet, Csizmadia et al. (2019) further proposed detecting apsidal motion in the variations of RV measurements and estimated k_2 of a massive gas giant WASP-18Ab.

Although the observational prospects are still more optimistic for close-in gas giants, Bolmont et al. (2020) also discussed the effect of tidally-induced apsidal motion on the TTV signal of the famous multiplanetary system TRAPPIST-1 (Gillon et al., 2017). The system consists of a tightly packed resonant chain of seven exoplanets with masses compatible with a rocky composition. According to the authors, the tidally-induced apsidal motion of the innermost planets with Earth-like tidal parameters should be comparable with relativistic effects, which still lie under the observational threshold. However, for more extreme tidal parameters, hypothesized for ocean worlds, the accumulated difference in observed and theoretical transit

times over several years already yields a detectable effect (Bolmont et al., 2020).

Last but not least, auxiliary information about the bulk composition of exoplanets might be acquired from measuring the elemental abundances in the spectra of the planet-hosting stars. As the other methods, this is not straightforward and only indirect, since it requires an accurate model of the stellar atmosphere and spectrum formation processes (Asplund et al., 2009). Regarding the Fe/Si, Mg/Si, and C/O abundance ratios, which are of particular importance for the exoplanet core sizes and mantle mineralogies, Sun-like values are typically being reported for nearby Sun-like stars (e.g., Gilli et al., 2006; Suárez-Andrés et al., 2018; Bedell et al., 2018). This observation inspires exoplanetary interior models assuming Earth-like composition.

In total, we can think of the following existing or potential observational constraints: the mass, the radius, the fluid Love number k_f, the dynamically-inferred Love number at the orbital frequency $k_2(\omega)$, and the relative elemental abundances in the host star's spectrum. The fluid Love number derived from rotational flattening might or might not be the same as the frequency-dependent Love number k_2, which participates in the orbital evolution. Specifically, for rocky bodies, k_2 is a function of rheology and its value depends on the ratio of the tidal loading period to a characteristic relaxation time. This period is, in most cases, cases equal to half the rotational or the orbital period. If both the rotational flattening and the dynamical effect of tides are measured, the core size and density of an exoplanet can be constrained by the same type of models that are currently used for Mercury, Venus, and other solar system bodies with lacking seismological measurements. An illustration of this approach will be provided at the end of this section.

5.2 Interior structure of exoplanets

5.2.1 Mass-radius relationships

The characterization of exoplanet interiors draws inspiration from our knowledge about the solar system bodies. The structural models are thus constructed with the assumption that the exoplanets are made of the same basic components as the planets in our immediate neighborhood: iron, silicates, water, and light elements like hydrogen and helium. In the case of solid exoplanets, a differentiated interior is typically considered, with more or less complex mantle mineralogy and with various light element concentrations in the core. The results of structural models are mass-radius

relationships. Their comparison with the observed mass and radius then yields an estimate of the planet's interior structure and core size.

One of the oldest mass-radius relationships for cold, chemically-homogeneous spheres was derived by Zapolsky and Salpeter (1969), who found the scaling law

$$M = \alpha R^3 \rho_{\mathrm{cen}}, \tag{1}$$

with M, R being the planetary mass and radius, respectively, ρ_{cen} the central density, and α symbolizing a mass- and composition-dependent dimensionless parameter. Further, more realistic models, focusing specifically on rocky bodies, were presented in the dawn of the era of exoplanetary exploration. Valencia et al. (2006) studied the interior structure and scaling laws for exo-Earths, super-Earths (large rocky exoplanets with Earth-like core mass fraction), and super-Mercuries (planets with a high core mass fraction). Regarding the core composition, the authors considered a wide range of assumptions: Fe with 8 wt% Si, pure Fe or FeO, and Fe with an alloy fitting PREM (Dziewonski and Anderson, 1981). For both the total planetary radius and the core radius, a scaling law of the form $R \propto M^{\beta}$ was proposed: for a super-Mercury with a fixed core composition and a variable core mass fraction (CMF), the dimensionless exponent β of the planetary radius or the core radius does not change much. The effect of a variable CMF on the radii is smaller than the effect of surface temperature, which affects the planet's thermal state. For a super-Earth with a fixed CMF, the effect of the assumed core composition on the resulting core radius is larger than the effect of the observed planetary radius. The discussion is further extended to the effect of water and the model is applied to a particular exoplanet in Valencia et al. (2007a,b).

A different form of the mass-radius relationship was found by Seager et al. (2007), who followed in the steps of Zapolsky and Salpeter (1969) and derived scaling laws for homogeneous spheres consisting of planet-building materials as well as for differentiated exoplanets with a simplified interior composition. For both classes of models, the authors found the relationship

$$\log_{10} \frac{R}{r_1} = c_1 + \frac{1}{3} \log_{10} \frac{M}{m_1} - c_2 \left(\frac{M}{m_1} \right)^{c_3}, \tag{2}$$

where c_1, c_2, c_3, r_1, and m_1 are composition-dependent tabulated values. Seager et al. (2007) do not discuss the effect of light elements in the core, and their results primarily reflect the bulk composition of the extrasolar worlds.

A logarithmic form of the mass-radius relationship was also found by Fortney et al. (2007), who studied a wide range of exoplanetary mass-ranges as well as the effect of stellar irradiation. A similar, two- or three-layered model with fixed composition of the individual layers (pure Fe, $MgSiO_3$, and H_2O) is presented by Zeng and Sasselov (2013). In a two-layered model with fixed core and mantle compositions, the core size (as well as the internal pressure) can be determined from the mass and radius measurements uniquely. In three-layered models, the solution is nonunique and is represented by a curve on a ternary diagram. An interesting point of the study by Zeng and Sasselov (2013) is the consideration of both differentiated and nondifferentiated planets. In the differentiated case, the variation in the CMF results in covering the mass-radius diagram by curves spanning the entire range between the two extremal homogeneous cases (e.g., pure Fe sphere and pure $MgSiO_3$ sphere). For the nondifferentiated exoplanets, the radius corresponding to a given mass might be smaller or greater, depending on the level of oxidization of iron.

Zeng et al. (2016) derived a semi-empirical mass-radius relationship with equations of state extrapolated from PREM. In the model, they explicitly address the core size. Assuming an Earth-like interior structure, they fit the results to

$$\left(\frac{R}{R_\oplus}\right) = (1.07 - 0.21 \times \mathrm{CMF})\left(\frac{M}{M_\oplus}\right)^{1/3.7}, \tag{3}$$

where $\oplus$ indicates the terrestrial value. The expression holds for CMF < 0.4 and $1M_\oplus \leq M \leq 8M_\oplus$. From Eq. (4), the CMF of Earth-like exoplanets can be obtained. The authors also note that in order to distinguish a 20% CMF apart from a 30% one, the planet radius needs to be measured with a 2% precision, or the mass needs to be measured with a 6% precision. Neither of these precisions is accessible with existing or upcoming exoplanetary missions. Li Zeng and his colleagues also apply the mass-radius relationships to exoplanets with existing mass and radius measurements, obtaining either the bulk compositions (Zeng and Sasselov, 2013), or even the CMFs (Zeng et al., 2016). In a later work (Zeng and Jacobsen, 2017), the authors present a simplified two-layered interior structure based on the assumption of the local gravitational acceleration increasing linearly in the core and staying constant in the mantle and keeping the equations of state derived from PREM (accepting an up to 20% error in the central density and an up to 16% error in the mantle density, with respect to PREM densities). They also suggest the following procedure for estimating the core radius:

1) calculate the surface gravity from observed M and R, 2) determine CMF from Eq. (3), and 3) calculate core radius fraction (CRF) from a scaling law $\mathrm{CRF} = \sqrt{\mathrm{CMF}}$. In the scope of the simplified model, the moment of inertia factor can be estimated as (Zeng and Jacobsen, 2017)

$$\mathrm{MoIF} = \frac{1}{3}\left(1 + \frac{1}{5}\mathrm{CMF}^2\right). \tag{4}$$

The models described above either treat the planetary composition as a free parameter, or they fix it to the terrestrial values. However, several authors have taken an alternative approach, relying on the following observation from the solar system: the abundances of most chemical elements in CI-type chondritic meteorites show a close agreement with the abundances in the solar photosphere (e.g., Asplund et al., 2009). This type of meteorites is also believed to represent the most pristine material from which the solar system bodies formed and serves as one source of information about the bulk Earth composition (McDonough and Sun, 1995; and references therein). On the other hand, constraining the planetary composition by the spectrum of the host star does not take into account possible heterogeneities in the accretion disc (e.g., Taylor, 1993, see also the evolution of theories about the composition of Mars in section 4.3), differential condensation of the planet-forming elements in high-temperature regions close to the host star (Thiabaud et al., 2015), or further catastrophic events, which might have led to the depletion of planetary mantles (Marcus et al., 2010). Similarly, the partitioning of Fe and the light elements Si, S, and O between core and mantle is poorly constrained.

The elemental abundances in the host star's spectrum were first considered in the model of Sotin et al. (2007). Starting with a set of five independent parameters (Mg/Si, Fe/Si, Mg-Fe partitioning, H_2O abundance, and the total planetary mass), the authors constructed interior structure models and predicted the planetary radii. The core size in their model depends uniquely on the planetary mass and the elemental abundances; its composition is fixed to 87% Fe and 13% FeS. Building on the work of Sotin et al. (2007), Grasset et al. (2009) investigated the detectability of water on a wide mass-range of solid exoplanets or ice giants. Besides the main objective of the work, the authors also discussed the effect of core and mantle composition on the resulting core size and planetary radius. For a fixed mass, the addition of FeS to the pure iron core (by up to 40 mol%) leads to an increase in the core radius (by up to 20%), but the planetary radius only increases by 1%; an observation similar to that of Valencia et al. (2006). The results

are also affected by the Mg/(Mg+Fe) ratio in silicates, which implies a 30% difference in the core size when varied over the range [0.65, 1], with the planetary radius variation below 2%. Conversely, for a fixed radius, Unterborn et al. (2016) found that the core size, the light element concentration in the core, and the consideration of low-pressure elements in the upper mantle have a major impact on the resulting mass.

Motivated by the nonuniqueness of interior models, (Dorn et al., 2015, 2017a,b) performed Bayesian probability analyses aimed to determine the sensitivity of interior structures to the observational uncertainties. They conclude that it is possible to constrain the exoplanetary core size and mantle composition from mass-radius observations informed by the host star's elemental abundances. While all observational uncertainties are equally important (especially for super-Earths and other massive planets), the accuracy of Fe/Si and Mg/Si abundances has the major effect on the inferred core size. The authors openly admit that the inferred core sizes are underestimated since a purely iron core is considered (Dorn et al., 2015, see also sections 4.1 Earth and 4.3 Mars). However, as illustrated in Dorn et al. (2017b), the elemental abundances are only known with a high uncertainty and the core size cannot be well constrained by present-day measurements.

5.2.2 Tidal parameters

The mass-radius relationships set constraints on the bulk composition of exoplanets and, with a set of assumptions on the interior structure, they provide a basic characterization of the extrasolar worlds. Although the models often predict the core size, this prediction depends on the considered concentration of light elements in the core as well as on the thermal state of the mantle. As in the case of solar system bodies, an additional constraint on the radial structure can be posed by the measurements of the tidal or rotational deformation. In particular, the fluid Love number k_f depends on the density distribution, and despite its own inherent nonuniqueness (Kramm et al., 2011), provides additional constraints.

Padovan et al. (2018) presented a method for calculating the fluid Love number of exoplanets and illustrated the effect of different central mass condensations. In a parametric study with a two-layered planet of fixed mass and radius, the authors show how k_f and MoIF depend on the relative core size and density. The smaller the core, the smaller both mentioned quantities. The ability of k_f to solve the mass-radius tradeoff is also shown in an application to three realistic interior models of a rocky exoplanet with a constant mean density. Tobie et al. (2019) used the structural model of

Sotin et al. (2007) to calculate the tidal response of silicate and ice-rich exoplanets. As in the original work, the authors considered a fixed core composition (87% Fe and 13% FeS) and derived scaling laws for the tidal Love number k_2 and the quality factor Q. Consistent with other studies, it is found that for a given mass (of an ice-less planet), the magnitude of k_2 is controlled by the core size and thus by the bulk Fe fraction. A more detailed treatment of the tidal response and its applications for interior structure studies is given by Bagheri et al. (2022, this volume).

The model of Sotin et al. (2007) was also adopted by Baumeister et al. (2020), who explored the applicability of a machine learning technique (mixture density networks) on the inference of radial structure. In particular, the authors considered the mass, radius, and the fluid Love number as an input and the distribution of relative thicknesses of individual layers as an output. Among other results, Baumeister et al. (2020) illustrated the extreme nonuniqueness of mass-radius measurements on the case of the Earth as well as the great reduction in the number of possible solutions when k_f is considered. Despite several simplifications (e.g., the prescribed core composition), the machine-learned approach enables a fast first characterization of a large number of exoplanets, which can then be studied by dedicated, more realistic models.

5.3 Simplified model "exoplanet"

In this section, we briefly discuss the sensitivity of moment of inertia factor and k_2 measurements to the size and density of an exoplanetary core. On the way to this goal, we will assume that the model planet consists of two or three homogeneous layers and its response to periodic tidal loading by the host star is purely elastic. We note, however, that the tidal Love number k_2, which can be potentially derived from the tidally-induced portion of apsidal motion, generally depends on the ratio of the orbital period to the characteristic relaxation time of the planet-forming material (e.g., Efroimsky and Lainey, 2007; Ferraz-Mello, 2013; Correia et al., 2014). For the illustration purposes, the transient as well as steady state creeping of the planetary material is neglected.

Considering a two-layered spherical planet consisting of a homogeneous core (index "C") and a mantle ("M"), the moment of inertia factor can be expressed analytically as

$$\mathrm{MoIF} = \frac{2}{5R_\mathrm{L}^2}\frac{R_\mathrm{C}^5\left(\rho_\mathrm{C}-\rho_\mathrm{M}\right)+R_\mathrm{M}^5\rho_\mathrm{M}}{R_\mathrm{C}^3\left(\rho_\mathrm{C}-\rho_\mathrm{M}\right)+R_\mathrm{M}^3\rho_\mathrm{M}}. \tag{5}$$

Similarly, for a three-layered model with a lithosphere ("L") the MoIF is

$$\mathrm{MoIF} = \frac{2}{5R_\mathrm{L}^2}\frac{R_\mathrm{C}^5\left(\rho_\mathrm{C}-\rho_\mathrm{M}\right)+R_\mathrm{M}^5\left(\rho_\mathrm{M}-\rho_\mathrm{L}\right)+R_\mathrm{L}^5\rho_\mathrm{L}}{R_\mathrm{C}^3\left(\rho_\mathrm{C}-\rho_\mathrm{M}\right)+R_\mathrm{M}^3\left(\rho_\mathrm{M}-\rho_\mathrm{L}\right)+R_\mathrm{L}^3\rho_\mathrm{L}}. \tag{6}$$

In both equations above, ρ_i are the respective densities of the individual layers and R_i are the outer radii. If we introduce the relative radii $\xi_i = R_i/R_\mathrm{upp}$ and relative densities $\lambda_i = \rho_i/\rho_\mathrm{upp}$, where "upp" indicates the uppermost layer, we can likewise write

$$\mathrm{MoIF} = \frac{2}{5}\frac{\xi_\mathrm{C}^5\left(\lambda_\mathrm{C}-1\right)+1}{\xi_\mathrm{C}^3\left(\lambda_\mathrm{C}-1\right)+1}, \tag{7}$$

or

$$\mathrm{MoIF} = \frac{2}{5}\frac{\xi_\mathrm{C}^5\left(\lambda_\mathrm{C}-\lambda_\mathrm{M}\right)+\xi_\mathrm{M}^5\left(\lambda_\mathrm{M}-1\right)+1}{\xi_\mathrm{C}^3\left(\lambda_\mathrm{C}-\lambda_\mathrm{M}\right)+\xi_\mathrm{M}^3\left(\lambda_\mathrm{M}-1\right)+1}. \tag{8}$$

The moment of inertia factor, in this simplified case, is thus fully characterized by the density contrasts at CMB and at the base of the lithosphere and by the relative thicknesses of the layers. For a known rotational flattening $f = (R_\mathrm{eq} - R_\mathrm{pol})/R_\mathrm{eq}$ and the planet's rotational period P_rot, the MoIF can be estimated from the Radau–Darwin equation (e.g., Murray and Dermott, 2000), under the explicit assumption of the hydrostatic equilibrium. However, we should also note that Eqs. (5)–(8) only hold for an idealized spherical planet. In reality, the MoIF will depend on additional geometric factors due to the deformed figure (e.g., Zharkov and Sobisevich, 2005).

An alternative measure of the density contrasts and radial stratification of the planet interior is the fluid (or secular) Love number k_f, which parameterizes the reaction of a planet in hydrostatic equilibrium to the tidal or rotational potential. An analytical expression for the fluid Love number has been derived by Folonier et al. (2015). In particular, the authors give k_f of a two-layered model, which reads as

$$k_\mathrm{f} = \frac{5\left(\lambda_\mathrm{C}+\left(1-\lambda_\mathrm{C}\right)\xi_\mathrm{C}^3\right)\left(2+3\lambda_\mathrm{C}+3\left(1-\lambda_\mathrm{C}\right)\xi_\mathrm{C}^5\right)}{\left(2+3\lambda_\mathrm{C}\right)\left(2\lambda_\mathrm{C}+5\left(1-\lambda_\mathrm{C}\right)\xi_\mathrm{C}^3\right)-9\lambda_\mathrm{C}\left(1-\lambda_\mathrm{C}\right)\xi_\mathrm{C}^5} - 1 \tag{9}$$

Additionally, it can be related to the rotational flattening by

$$k_\mathrm{f} = \frac{5}{2}\frac{f}{\epsilon_\mathrm{J}+\epsilon_\mathrm{M}} - 1, \tag{10}$$

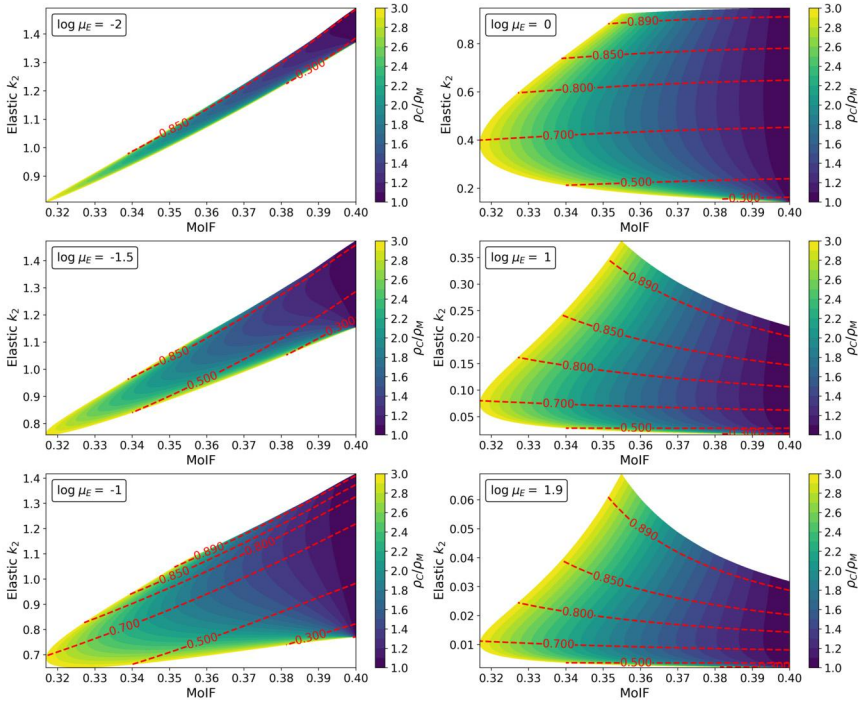

Figure 7 The core radius fraction (red isolines) and the relative core density (color-coded according to colorbar) of a two-layered model exoplanet as a function of the moment of inertia factor (x-axis), the elastic tidal Love number (y-axis), and the dimensionless mantle rigidity (individual plots). As explained in the text, larger mantle rigidities correspond to smaller bodies.

where ϵ_J and ϵ_M are the equivalent Jeans and MacLaurin homogeneous spheroids, respectively. Folonier et al. (2015) also provide a method for the analytical calculation of fluid Love numbers for planets consisting of more than two layers. The resulting formulae are, however, too complex for this simplified overview. The link between the fluid Love numbers and the mean MoIF can also be approximated by the Radau–Darwin equation (e.g., Murray and Dermott, 2000; Zharkov and Sobisevich, 2005).

The elastic Love number k_2, corresponds to the deformation of a planet with tidal loading periods below the relaxation time of planet-forming materials. It can only be expressed analytically for a homogeneous, incompressible sphere; for two-layered or even three-layered models, the resulting expression would already be extremely complex. Therefore, we calculate k_2

numerically from the normal mode theory (e.g., Sabadini and Vermeersen, 2004; Tobie et al., 2005).

With the moment of inertia factor given by (7) and with the elastic Love number k_2, we can assess the relative radius and relative density of an exoplanetary core. For the sake of this model, we assume that the planet consists of a fluid core and an elastic mantle with the dimensionless effective rigidity μ_E given by

$$\mu_E = \frac{\mu}{\rho g R}. \tag{11}$$

The dimensionless effective rigidity defines the ratio between the contributions of elasticity and self-gravity to the tidal response and depends on the tidal effective mantle rigidity μ, the average mantle density ρ, the surface gravity g, and the planet radius R. For giant planets and massive super-Earths, we may expect a self-gravity-dominated regime with $\mu_E \ll 1$. Moons and asteroids are basically in the elasticity-dominated regime with $\mu_E \gg 1$ and, for Earth-sized planets, we have $\mu_E \sim 1$. Fig. 7 illustrates the effect of the core radius fraction (CRF) and the ratio between the core and mantle densities on the observed MoIF and elastic k_2. For large and massive planets, the value of the elastic k_2 is dominated by the planet's density structure and contains the same information as MoIF (or k_f). As we consider smaller or stiffer planets (plots with higher μ_E), the ensemble of different core sizes and densities slowly unfolds. For Earth-sized worlds, k_2 is mainly sensitive to the core size, while MoIF is an indication of the core-mantle density contrast.

6. Concluding remarks

The evolution of our knowledge of planetary core radii, but also of the quantities on which the evaluation of the core radius relies, shows certain repeating patterns.

All measured quantities will always carry aleatoric and epistemic uncertainties. At the same time, most geophysical inverse problems are underdetermined, as is the inversion of a moment of inertia factor into a core radius, and their result is e.g. a tradeoff curve between two parameters. Measurement uncertainty adds an extra dimension to the nonuniqueness of inversion results, in that it extends the tradeoff curve into a band of nonzero width.

As seen best for the parameters concerning Mars, formal estimations of uncertainty sometimes result in an underestimation of the actual uncer-

tainty – which becomes obvious when successive measurements of the same quantity are mutually incompatible, although their error bars are small. Many of the older publications do not provide any uncertainty estimates at all. We did not investigate the history of planetary mass estimations, but the history of the estimation of Newton's gravitational constant *G*, shows the same: When relying on the formal error only, independent measurements yielded mutually incompatible results, even after meticulous analysis of all possible sources of error (e.g. Michaelis et al., 1995). The remaining discrepancies may be attributed to "epistemic uncertainty" (the statistical standard term), "unknown unknowns" (often attributed to Donald Rumsfeld, former US Secretary of Defense), "dark uncertainty" (Merkatas et al., 2019), and heuristic approaches (uncertainty inflation factors, see section 2) might be the only practical way to carry on with a result.

All known uncertainties should be propagated end-to-end, from measurement to inversion result, which is of course easier said than done. But although an underestimated result uncertainty might look good in an abstract, in the long run it does not support scientific progress.

A popular method of uncertainty treatment are Bayesian methods, often implemented in the form for Monte Carlo Markov Chain methods. In how far these methods can treat epistemic uncertainty, and which inversion method is most appropriate for a given problem, is outside the scope of this work. We can only suggest to make cognizant choices.

In several cases we were unable to track down the origin of numerical values, or numerical values were not given at all, when the authors apparently assumed that their value would be clear to all readers, based on explicit conventions or common use at the time of their writing, and within their scientific community. Also, some authors refer to results published only in contributions to conferences, or internal reports of their institutions. Meanwhile, many decades or even centuries later, it is not always possible to reconstruct – especially for the outsider – what alluded conventions were (how long were Greek stades again? What is the conventional reference radius for Moon gravity studies, and why?). More than five decades after the first landing on the Moon, it has become clear that the life time of data collected in space missions can be very long. Besides the well organized archives run by space agencies, each author should think of readers trying to use their results after their own retirement, and take care for traceability.

As is most obvious in the case of Mars, the uncertainty of quantities like planetary radius, mass, moment of inertia factor, and, ultimately, the core radius, may evolve discontinuously, dependent on single experiments.

Times of gradual improvement, or no improvement at all, are interrupted by sudden changes. These discontinuities in knowledge tend to occur when dedicated in-situ experiments are conducted by spacecraft. The evolution of measurements of the lunar moment of inertia factors shows this very clearly – with the spacecraft missions of the 1960s it became clear very quickly that all previous determinations were significantly too high – "significant" not only in statistical terms, but in terms of their physical and planetological implications. The recognition of systematic overestimations and resulting misinterpretations repeated when Mariner IX revealed the Tharsis bulge on Mars.

Without the Apollo seismic network, the Laser Retro Reflectors, and the rock samples, or without long-term observation of the martian precession, or a precise surface topography, it would have been impossible to reach the current state of knowledge about the interior of Moon and Mars. Encounters of spacecraft with other celestial bodies, be it 1P/Halley, 67P/Churyumov–Gerasimenko, Pluto, Io, Enceladus, Titan, and many others, have also revealed insights that revolutionized our understanding.

Seismological experiments so far require the presence of an instrument (or several) on the surface of the planet. This is not easy to achieve (Stähler and Knapmeyer, 2022), but has the great advantage that wavefields can, at least in principle, be inverted for structural parameters unambiguously, a property that potential fields do not provide. The wavelengths of seismic body waves also allow for a high spatial resolution, which is important as the discussions about phase transitions, and the effect of phase transitions on mantle convection and geodynamo operation show. Needless to mention that these are connected to the problem of habitability.

The geodetic and astrometric methods of interpreting orbital parameters, and how they change in time, have the great advantage that they can be conducted over long distances – telescopes on Earth can not only track the moons of Mars, but also determine the masses of exoplanets. The same instrument can serve to investigate many different bodies, not even restricted to planets.

The main goals of PLATO are "*to detect and characterize extrasolar planets, including terrestrial planets in the habitable zone* (*HZ*) *of their host stars. Characterization here means to derive accurate planetary radii, masses, and ages*" (Rauer et al., 2016). The "*state of our current ignorance*" (to cite a section heading from the otherwise unrelated work of Borwein et al., 1989) is such that the core radius problem for exoplanets requires assumptions that appear bold in the light of the exploration of our neighboring planets. Extrapolating from

the number of hypotheses about Moon and Mars that were dropped in the past, and given the sensitivity of some geodynamic properties for internal pressure and core size, our assumptions on exoplanets prove inappropriate. With the information we can currently hope to obtain about these objects, the inverse problem will remain underdetermined. But this might change if our understanding of planetary formation and evolution improves, driven not only by the objects in the solar system, but also by a growing ensemble of extrasolar systems at various stages of their evolution.

Scientific knowledge evolves along a meandering path. Assumptions and approximations are often unavoidable and may lead us astray for a while. One lesson to learn from the past is, that even in the early 20th century, long before spacecraft became available at all, the comparison of Earth with other planets was actively sought to test assumptions about inaccessible regions within the Earth. The inaccessibility of the interior of exoplanets surpasses the inaccessibility of the Earth's interior by far. This makes even more important to devise tests for all employed hypotheses and assumptions, and to keep in mind that models for exoplanets must not contradict the observations made in our solar system.

Acknowledgments

M. Walterova gratefully acknowledges the financial support and endorsement from the DLR Management Board Young Research Group Leader Program and the Executive Board Member for Space Research and Technology. Enlightening discussions with Brigitte Knapmeyer-Endrun (Seismological Station Bensberg, Cologne University), DLR colleagues Ana-Catalina Plesa, Frank Sohl, Philipp Baumeister, Sabrina Schwinger, Thomas Ruedas Gomez, and Nicola Tosi, former DLR colleague Athanasia Nikolaou, but no less with Tamara Gudkova (RAS Schmidt Institute), Simon Stähler (ETH Zürich), Ralph Lorenz (Johns Hopkins University), David Sollberger (ETH Zürich), Natacha Fabbri (Museo Galileo, Firenze), Rudolf Widmer-Schnidrig (Black Forest Observatory), Tilman Spohn (ISSI Bern) are gratefully acknowledged. Remaining mistakes are ours. Our librarian Silvia Pawel was always quick to procure even the unlikeliest publications.

References

Acuña, M.H., Connerney, J.E.P., Ness, N.F., Lin, R.P., Mitchell, D., Carlson, C.W., McFadden, J., Anderson, K.A., Rème, H., Mazelle, C., Vignes, D., Wasilewski, P., Cloutier, P., 1999. Global distribution of crustal magnetization discovered by the Mars Global Surveyor MAG/ER experiment. Science 284, 790–793. https://doi.org/10.1126/science.284.5415.790.

Agol, E., Fabrycky, D.C., 2018. Transit-timing and duration variations for the discovery and characterization of exoplanets. In: Handbook of Exoplanets. https://doi.org/10.1007/978-3-319-55333-7_7.

Akim, E.L., 1966. Determination of the moon's gravitational field from the motion of Luna 10. Doklady Akademii Nauk SSSR 170, 799–802 (in Russian).

Akinsanmi, B., Barros, S.C.C., Santos, N.C., Oshagh, M., Serrano, L.M., 2020. Constraining the oblateness of transiting planets with photometry and spectroscopy. Monthly Notices of the Royal Astronomical Society 497 (3), 3484–3492. https://doi.org/10.1093/mnras/staa2164.

Ananda, M., 1977. Lunar gravity: a point mass model. Journal of Geophysical Research 82, 3049–3065.

Anderson, D.L., Kovach, R.L., 1964. Attenuation in the mantle and rigidity of the core from multiply reflected core phases. Proceedings of the National Academy of Sciences 51 (2), 168–172. https://doi.org/10.1073/pnas.51.2.168.

Angenheister, G., 1921. Beobachtungen an pazifischen Beben. Ein Beitrag zum Studium der obersten Erdkruste. Nachrichten von der Gesellschaft der Wissenschaften zu Göttingen, Mathematisch-Physikalische Klasse, 113–146. Available online: http://resolver.sub.uni-goettingen.de/purl?GDZPPN002505924. (Accessed 24 November 2021).

Anglada-Escudé, G., Amado, P.J., Barnes, J., Berdiñas, Z.M., Butler, R.P., Coleman, G.A.L., de la Cueva, I., Dreizler, S., Endl, M., Giesers, B., Jeffers, S.V., Jenkins, J.S., Jones, H.R.A., Kiraga, M., Kürster, M., López-González, M.J., Marvin, C.J., Morales, N., Morin, J., Nelson, R.P., Ortiz, J.L., Ofir, A., Paardekooper, S.-J., Reiners, A., Rodríguez, E., Rodríguez-López, C., Sarmiento, L.F., Strachan, J.P., Tsapras, Y., Tuomi, M., Zechmeister, M., 2016. A terrestrial planet candidate in a temperate orbit around Proxima Centauri. Nature 536 (7617), 437–440. https://doi.org/10.1038/nature19106.

Aristotle, 4th cent. BCE a. On the Heavens. Transl. W.K.C. Guthrie. Loeb Classical Library, vol. 338. Harvard University Press, Cambridge, Mass., USA, London, GB. 379 pages.

Aristotle, 4th cent. BCE b. Meteorologica, Transl. H.D.P. Lee. Loeb Classical Library, vol. 397. Harvard University Press, Cambridge, Mass., USA, London, GB. 433 pages.

Aristotle, 4th cent. BCE c. Minor Works. Transl. W.S. Hett, F.M. Cornford. Loeb Classical Library, vol. 307. Harvard University Press, Cambridge, Mass., USA, London, GB. 516 pages.

Asplund, M., Grevesse, N., Sauval, A.J., Scott, P., 2009. The chemical composition of the Sun. Annual Review of Astronomy and Astrophysics 47 (1), 481–522. https://doi.org/10.1146/annurev.astro.46.060407.145222.

Astiz, L., Earle, P., Shearer, P., 1996. Global stacking of broadband seismograms. Seismological Research Letters 67 (4), 8–18.

Bagheri, A., Efroimsky, M., Castillo-Rogez, J., Goossens, S., Plesa, A.-C., Rambaux, N., Rhoden, A., Walterová, M., Khan, A., Giardini, D., 2022. Tidal insights into rocky and icy bodies: an introduction and overview. In: Geophysical Exploration of the Solar System. In: Schmelzbach, C., Stähler, C. (Eds.), Advances in Geophysics, vol. 63. This volume.

Banerdt, W.B., Smrekar, S., Hurst, K., Lognonné, P., Spohn, T., Asmar, S., Banfield, D., Boschi, L., Christensen, U., Dehant, V., Folkner, W., Giardini, D., Goetz, W., Golombek, M., Grott, M., Hudson, T., Johnson, C., Kargl, G., Kobayashi, N., Maki, J., Mimoun, D., Mocquet, A., Morgan, P., Panning, M., Pike, W.T., Tromp, J., van Zoest, T., Weber, R., Wieczorek, M., the InSight Team, 2013. InSight: a discovery mission to explore the interior of Mars. In: 44th Lunar and Planetary Science Conference, #1915. The Woodlands, Texas, USA, 18–22 March 2013.

Barros, S.C.C., Akinsanmi, B., Boué, G., Smith, A.M.S., Laskar, J., Ulmer-Moll, S., Lillo-Box, J., Queloz, D., Cameron, A.C., Sousa, S.G., Ehrenreich, D., Hooton, M.J., Bruno, G., Demory, B.-O., Correia, A.C.M., Demangeon, O.D.S., Wilson, T.G., Bonfanti, A., Hoyer, S., Alibert, Y., Alonso, R., Escudé, G.A., Barbato, D., Bárczy, T., Barrado, D., Baumjohann, W., Beck, M., Beck, T., Benz, W., Bergomi, M., Billot, N., Bonfils,

X., Bouchy, F., Brandeker, A., Broeg, C., Cabrera, J., Cessa, V., Charnoz, S., Damme, C.C.V., Davies, M.B., Deleuil, M., Deline, A., Delrez, L., Erikson, A., Fortier, A., Fossati, L., Fridlund, M., Gandolfi, D., Muñoz, A.G., Gillon, M., Güdel, M., Isaak, K.G., Heng, K., Kiss, L., des Etangs, A.L., Lendl, M., Lovis, C., Magrin, D., Nascimbeni, V., Maxted, P.F.L., Olofsson, G., Ottensamer, R., Pagano, I., Pallé, E., Parviainen, H., Peter, G., Piotto, G., Pollacco, D., Ragazzoni, R., Rando, N., Rauer, H., Ribas, I., Santos, N.C., Scandariato, G., Ségransan, D., Simon, A.E., Steller, M., Szabó, Gy.M., Thomas, N., Udry, S., Ulmer, B., Van Grootel, V., Walton, N. Detection of the tidal deformation of WASP-103b at 3 σ with CHEOPS. Astronomy & Astrophysics 657, A52. https://doi.org/10.1051/0004-6361/202142196.

Bates, J.R., Lauderdale, W.W., Kernaghan, H., 1979. ALSEP Termination Report, NASA Reference Publication 1036. NASA Scientific and Technical Information Office. https://nssdc.gsfc.nasa.gov/misc/documents/b32116.pdf. (Accessed 13 July 2021).

Batygin, K., Bodenheimer, P., Laughlin, G., 2009. Determination of the interior structure of transiting planets in multiple-planet systems. The Astrophysical Journal 704 (1), L49–L53. https://doi.org/10.1088/0004-637X/704/1/L49.

Baumeister, P., Padovan, S., Tosi, N., Montavon, G., Nettelmann, N., MacKenzie, J., Godolt, M., 2020. Machine-learning inference on the interior structure of low-mass exoplanets. The Astrophysical Journal 889 (42). https://doi.org/10.3847/1538-4357/ab5d32. 10 pages.

Bedell, M., Bean, J.L., Meléndez, J., Spina, L., Ramírez, I., Asplund, M., Alves-Brito, A., dos Santos, L., Dreizler, S., Yong, D., Monroe, T., Casagrande, L., 2018. The chemical homogeneity of sun-like stars in the solar neighborhood. The Astrophysical Journal 865 (1). https://doi.org/10.3847/1538-4357/aad908.

Belonoshko, A.B., Fu, J., Bryk, T., Simak, S.I., Mattesini, M., 2019. Low viscosity of the Earth's inner core. Nature Communications 10 (2483). https://doi.org/10.1038/s41467-019-10346-2.

Benioff, H., Harrison, J.C., LaCoste, L., Munk, W.H., Slichter, L.B., 1959. Searching for the Earth's free oscillations. Journal of Geophysical Research 64 (9), 1334–1337.

Benioff, H., Press, F., Smith, S., 1961. Excitation of free oscillations of the Earth by earthquakes. Journal of Geophysical Research 66 (2), 605–619.

Bernal, J.D., 1936. 1936 April 24 geophysical discussion. The Observatory 59, 265. Available online: https://articles.adsabs.harvard.edu/pdf/1936Obs....59..265. (Accessed 29 November 2021).

Bertka, C.M., Fei, Y., 1998a. Density profile of an SNC model Martian interior and the moment-of-inertia factor of Mars. Earth and Planetary Science Letters 157, 79–88.

Bertka, C.M., Fei, Y., 1998b. Implications of Mars Pathfinder data for the accretion history of the terrestrial planets. Science 281, 1838–1840. https://doi.org/10.1126/science.281.5384.1838.

Bills, B.G., 1989. The moments of inertia of Mars. Geophysical Research Letters 16 (5), 385–388.

Bills, B.G., 1995. Discrepant estimates of moments of inertia of the Moon. Journal of Geophysical Research 100 (E12), 26297–26303.

Bills, B.G., Ferrari, A.J., 1976. Lunar density structure: evidence for a core. In: Lunar and Planetary Science Conference 7, p. 64.

Bills, B.G., Ferrari, A.J., 1977. A lunar density model consistent with topographic, gravitational, librational, and seismic data. Journal of Geophysical Research 82 (8), 1306–1314.

Bills, B.G., Ferrari, A.J., 1978. Mars topography harmonics and geophysical implications. Journal of Geophysical Research 83 (B7), 3497–3508.

Binder, A.B., 1969. Internal structure of Mars. Journal of Geophysical Research 74 (12), 3110–3118.

Binder, A.B., Davis, D.R., 1973. Internal structure of Mars. Physics of the Earth and Planetary Interiors 7, 477–485.

Birch, F., 1952. Elasticity and constitution of the Earth's interior. Journal of Geophysical Research 57 (2), 227–286.
Blackshear, W.T., Gapcynski, J.P., 1977. An improved value of the lunar moment of inertia. Journal of Geophysical Research 82, 1699–1701.
Bolmont, E., Demory, B.-O., Blanco-Cuaresma, S., Agol, E., Grimm, S.L., Auclair-Desrotour, P., Selsis, F., Leleu, A., 2020. Impact of tides on the transit-timing fits to the TRAPPIST-1 system. Astronomy & Astrophysics 635, A117. https://doi.org/10.1051/0004-6361/202037546.
Bolt, B.A., 1982. Inside the Earth. Freeman & Company, San Francisco. 191 pp.
Borwein, J.M., Borwein, P.B., Bailey, D.H., 1989. Ramanujan, Modular equations, and approximations to Pi or how to compute one billion digits of Pi. American Mathematical Monthly 96 (3), 201–219.
Bouguer, P., 1749. La Figure de la Terre. Charles-Antoine Jombert, Paris, France. Approx. 410 pages. Online: https://books.google.de/books?hl=de&lr=&id=LiHvRISNxFsC&oi=fnd&pg=PR1&dq=Bouguer+&ots=S3Fwwan-r4&sig=1MgwiAJoOZ_N84Z-vymkS8_deOA#v=onepage&q=Bouguer&f=false. (Accessed 8 June 2021).
Brennan, M.C., Fischer, R.A., Irving, J.C.E., 2020. Core formation and geophysical properties of Mars. Earth and Planetary Science Letters 530, 115923. https://doi.org/10.1016/j.epsl.2019.115923.
Bruno, G., 1584. Über das Unendliche, das Universum und die Welten (De l'infinito universo et Mondi). German transl. C. Schultz. Reclam, Stuttgart, Germany. 243 pages.
Brush, S.G., 1979. Nineteenth-century debates about the inside of the Earth: solid, liquid or gas? Annals of Science 36 (3), 225–254. https://doi.org/10.1080/00033797900200231.
Brush, S.G., 1982. Chemical history of the Earth's core. EOS 63 (47), 1185–1188. https://doi.org/10.1029/EO063i047p01185.
Buchbinder, G.G.R., 1971. A velocity structure of the Earth's core. Bulletin of the Seismological Society of America 61 (2), 429–456.
Bullen, K.E., 1949. On the constitution of Mars. Monthly Notices of the Royal Astronomical Society 109 (6), 688–692.
Bullen, K.E., 1957a. On the constitution of Mars (second paper). Geophysical Supplements to Monthly Notices of the Royal Astronomical Society 7 (5), 271–278. https://doi.org/10.1111/j.1365-246X.1957.tb06693.x.
Bullen, K.E., 1957b. Seismology in our atomic age. In: Eleventh General Assembly of the International Union of Geodesy and Geophysics, pp. 29–34.
Bullen, K.E., 1966a. Implications of the revised Mars radius. Nature 211, 396.
Bullen, K.E., 1966b. On the constitution of Mars III. Monthly Notices of the Royal Astronomical Society 133, 229–238. https://doi.org/10.1093/mnras/133.2.229.
Bullen, K.E., 1973. Cores of the terrestrial planets. Nature 243, 68–70.
Burton, R., 1651. The anatomie of melancholy. Printed by R.W. for Henry Cripps of Oxford, scanned from Bayerische Staatsbibliothek. Available online: https://books.google.de/books?id=kwlBAAAAcAAJ&hl=de&pg=PP3#v=onepage&q&f=false. (Accessed 4 April 2022).
Cajori, F., 1928. A History of Mathematical Notations. Open Court Publishing, LaSalle & Chicago, Ill., USA. 2 volumes, 450 & 367 pages.
Campbell, W.W., 1895. A determination of the polar diameter of Mars. The Astronomical Journal 15 (18), 145–149.
Carder, D.S., Bailey, L.F., 1958. Seismic wave travel times from nuclear explosions. Bulletin of the Seismological Society of America 48, 377–398.
Carder, D.S., 1964. Travel times from central Pacific nuclear explosions and inferred mantle structure. Bulletin of the Seismological Society of America 54 (6, part B), 2271–2294.
Carter, J.A., Winn, J.N., 2010. The detectability of transit depth variations due to exoplanetary oblateness and spin precession. The Astrophysical Journal 716 (1), 850–856. https://doi.org/10.1088/0004-637X/716/1/850.

Cavendish, H., 1798. XXI: experiments to determine the density of the Earth. Philosophical Transactions of the Royal Society 88, 469–526. https://doi.org/10.1098/rstl.1798.0022.
Christensen, E.J., Balmino, G., 1979. Development and analysis of a twelfth degree an order gravity model for Mars. Journal of Geophysical Research 84 (B14), 7943–7953.
Ciancio, L., 2018. "Immoderatus fervor ad intra coërcendus". Reactions to Athanasius Kircher's Central Fire in Jesuit science and imagination. Nuncius 33, 464–504. https://doi.org/10.1163/18253911-03303004.
Cole, G.H.A., 1971. On inferring elastic properties of the deep lunar interior. Planetary and Space Science 19, 929–947.
Cole, G.H.A., 1972. The internal structure of planetary bodies. Contemporary Physics 13 (6), 585–600. https://doi.org/10.1080/00107517208228018.
Collins, S.A., 1971. The Mariner 6 and 7 pictures of Mars, NASA SP-263. NASA Scientific and Technical Information Office, Washington, D.C., USA. 173 pages.
Cook, A.H., 1970. The moments of inertia and the density distribution of the Moon. Monthly Notices of the Royal Astronomical Society 150, 187–194.
Cook, A.H., 1975. The internal structures of the planets. Geophysical Journal of the Royal Astronomical Society 42, 285–293.
Cook, A.H., 1977. The moment of inertia of Mars and the existence of a core. Geophysical Journal of the Royal Astronomical Society 51, 349–356. https://doi.org/10.1111/j.1365-246X.1977.tb06922.x.
Correia, A.C.M., 2014. Transit light curve and inner structure of close-in planets. Astronomy & Astrophysics 570. https://doi.org/10.1051/0004-6361/201424733.
Correia, A.C.M., Boué, G., Laskar, J., Rodríguez, A., 2014. Deformation and tidal evolution of close-in planets and satellites using a Maxwell viscoelastic rheology. Astronomy & Astrophysics 571. https://doi.org/10.1051/0004-6361/201424211.
Couprie, D.L., 2005. Some remarks on the Earth in Plato's Phaedo. Hyperboreous 11 (2), 192–204.
Csizmadia, Sz., Hellard, H., Smith, A.M.S., 2019. An estimate of the k2 Love number of WASP-18Ab from its radial velocity measurements. Astronomy & Astrophysics 623, A45. https://doi.org/10.1051/0004-6361/201834376.
Dante, Alighieri, ca. 1321. The Divine Comedy. English by H.F. Cary. Borders Classics. 659 pages.
Davy, H., 1808. XXIII. Electro-chemical researches, on the decomposition of the earths; with observations on the metals obtained from the alkaline earths, and on the amalgam procured from ammonia. Philosophical Transactions of the Royal Society 98, 333–370.
Davy, H., 1828. X. On the phænomena of volcanoes. Philosophical Transactions of the Royal Society 118, 241–250.
Deng, S., Levander, A., 2020. Autocorrelation reflectivity of Mars. Geophysical Research Letters 47. https://doi.org/10.1029/2020GL089630.
Descartes, R., 1644. Die Prinzipien der Philosophie. German transl. and introduction C. Wohlers. Meiner, Hamburg, Germany. 711 pages.
de Sitter, W., 1927. On the most probable values of some astronomical constants, first paper, constants connected with the earth. Bulletin of the Astronomical Institutes of the Netherlands IV (129), 57–61.
Dickey, J.O., Bender, P.L., Faller, J.E., Newhall, X.X., Ricklefs, R.L., Ries, J.G., Shelus, P.J., Veillet, C., Whipple, A.L., Wiant, J.R., Williams, J.G., Yoder, C.F., 1994. Lunar laser ranging: a continuing legacy of the Apollo program. Science 265, 482–490. https://doi.org/10.1126/science.265.5171.48.
Dorman, J., Ewing, J., Alsop, L.E., 1965. Oscillations of the Earth: new core-mantle boundary model based on low-order free vibrations. Proceedings of the National Academy of Sciences 54, 364–368.

Dorn, C., Khan, A., Heng, K., Connolly, J.A.D., Alibert, Y., Benz, W., Tackley, P., 2015. Can we constrain the interior structure of rocky expolanets from mass and radius measurements? Astronomy & Astrophysics 577 (A83). https://doi.org/10.1051/0004-6361/201424915.

Dorn, C., Venturini, J., Khan, A., Heng, K., Alibert, Y., Helled, R., Rivoldini, A., Benz, W., 2017a. A generalized Bayesian inference method for constraining the interiors of super earths and sub-neptunes. Astronomy & Astrophysics 597 (A37). https://doi.org/10.1051/0004-6361/201628708.

Dorn, C., Hinkel, N.R., Venturini, J., 2017b. Bayesian analysis of interiors of HD 219134b, Kepler-10b, Kepler-93b, CoRoT-7b, 55 Cnc e, and HD 97658b using stellar abundance proxies. Astronomy & Astrophysics 597. https://doi.org/10.1051/0004-6361/201628749.

Dreibus, G., Wänke, H., 1985. Mars, a volatile-rich planet. Meteoritics 20 (2, pt. 1), 367–381.

Driscoll, P.E., Du, Z., 2019. Geodynamo conductivity limits. Geophysical Research Letters 46, 7982–7989. https://doi.org/10.1029/2019GL082915.

Duff, J.W., Duff, A.M. (Eds.), 1934. Minor Latin Poets I. Loeb Classical Library, vol. 284. Harvard University, Cambridge, Mass., USA, London, GB. Transl. J.W. Duff, A.M. Duff. 419 pages.

Dunn, J.E., 2014. A god of volcanoes: did Yahwism take root in volcanic ashes? Journal for the Study of the Old Testament 38 (4), 387–424. https://doi.org/10.1177/0309089214536484.

Dziewonski, A.M., Hales, A.L., Lapwood, E.R., 1975. Parametrically simple Earth models consistent with geophysical data. Physics of the Earth and Planetary Interiors 10, 12–48.

Dziewonski, A.M., Anderson, D.L., 1981. Preliminary reference Earth model. Physics of the Earth and Planetary Interiors 25, 297–356.

Eckert, W.J., 1965. On the motions of the perigee and node and the distribution of mass in the Moon. The Astronomical Journal 70 (10), 787–792.

Efroimsky, M., Lainey, V., 2007. Physics of bodily tides in terrestrial planets and the appropriate scales of dynamical evolution. Journal of Geophysical Research: Planets 112 (E12). https://doi.org/10.1029/2007JE002908.

Fabbri, N., 2018. Threats to the christian cosmos. The reckless assault on the heavens and the debate over hell. In: Fabbri, N., Favino, F. (Eds.), Copernicus Banned. The Entangled Matter of the Anti-Copernican Decree of 1616, Biblioteca di Galileana VIII. Leo S. Olschki Editore, Firenze, Italy, pp. 29–56.

Ferrari, A.J., 1977. Lunar gravity: a harmonic analysis. Journal of Geophysical Research 82, 3065–3084.

Ferrari, A.J., Sinclair, W.S., Sjogren, W.L., Williams, J.G., Yoder, C.F., 1980. Geophysical parameters of the Earth–Moon system. Journal of Geophysical Research 85 (B7), 3939–3951.

Ferraz-Mello, S., 2013. Tidal synchronization of close-in satellites and exoplanets. A rheophysical approach. Celestial Mechanics & Dynamical Astronomy 116 (2), 109–140. https://doi.org/10.1007/s10569-013-9482-y.

Firsoff, V.A., 1969. On the internal structure of the Moon. Journal of the British Astronomical Association 79 (3), 191–199.

Fjeldbo, G., Fieldbo, W.C., Eshleman, V.R., 1966. Atmosphere of Mars: Mariner IV models compared. Science 153 (3743), 1518–1523. https://doi.org/10.1126/science.153.3743.1518.

Flasch, K., 2013. Das philosophische Denken im Mittelalter, 3rd edition. Reclam, Stuttgart, Germany. 874 pages.

Folkner, W.M., Dehant, V., Le Maistre, S., Yseboodt, M., Rivoldini, A., Van Hoolst, T., Asmar, S.W., Golombek, M.P., 2018. The rotation and interior structure experiment

on the InSight mission to Mars. Space Science Reviews 214, 100. https://doi.org/10.1007/s11214-018-0530-5.

Folkner, W.M., Yoder, C.F., Yuan, D.N., Standish, E.M., Preston, R.A., 1997. Interior structure and seasonal mass redistribution of Mars from radio tracking of Mars Pathfinder. Science 278 (5344), 1749–1752. https://doi.org/10.1126/science.278.5344.1749.

Folonier, H.A., Ferraz-Mello, S., Kholshevnikov, K.V., 2015. The flattenings of the layers of rotating planets and satellites deformed by a tidal potential. Celestial Mechanics & Dynamical Astronomy 122 (2), 183–198. https://doi.org/10.1007/s10569-015-9615-6.

Forbes, J., 1844. XIII. On the theory and construction of a seismometer, or instrument for measuring earthquake shocks, and other concussions. Transactions of the Royal Society of Edinburgh 15 (1), 219–228. https://doi.org/10.1017/S0080456800029914.

Fortney, J.J., Marley, M.S., Barnes, J.W., 2007. Planetary radii across five orders of magnitude in mass and stellar insolation: application to transits. The Astrophysical Journal 659, 1661–1672. https://doi.org/10.1086/512120.

Franklin, B., 1793. Conjectures concerning the formation of the Earth, &c. in a letter from Dr B. Franklin, to the Abbé Soulavie. Transactions of the American Philosophical Society 3, 1–5. Available online. https://www.jstor.org/stable/1004845. (Accessed 18 November 2021).

Fulton, B.J., Petigura, E.A., 2018. The California-Kepler survey. VII. Precise planet radii leveraging Gaia DR2 reveal the stellar mass dependence of the planet radius gap. The Astronomical Journal 156 (6). https://doi.org/10.3847/1538-3881/aae828.

Gaia Collaboration, Prusti, T., de Bruijne, J.H.J., Brown, A.G.A., Vallenari, A., Babusiaux, C., Bailer-Jones, C.A.L., Bastian, U., Biermann, M., Evans, D.W., Eyer, L., Jansen, F., Jordi, C., Klioner, S.A., Lammers, U., Lindegren, L., Luri, X., Mignard, F., Milligan, D.J., Panem, C., Poinsignon, V., Pourbaix, D., Randich, S., Sarri, G., Sartoretti, P., Siddiqui, H.I., Soubiran, C., Valette, V., van Leeuwen, F., Walton, N.A., Aerts, C., Arenou, F., Cropper, M., Drimmel, R., Høg, E., Katz, D., Lattanzi, M.G., O'Mullane, W., Grebel, E.K., Holland, A.D., Huc, C., Passot, X., Bramante, L., Cacciari, C., Castañeda, J., Chaoul, L., Cheek, N., De Angeli, F., Fabricius, C., Guerra, R., Hernández, J., Jean-Antoine-Piccolo, A., Masana, E., Messineo, R., Mowlavi, N., Nienartowicz, K., Ordóñez-Blanco, D., Panuzzo, P., Portell, J., Richards, P.J., Riello, M., Seabroke, G.M., Tanga, P., Thévenin, F., Torra, J., Els, S.G., Gracia-Abril, G., Comoretto, G., Garcia-Reinaldos, M., Lock, T., Mercier, E., Altmann, M., Andrae, R., Astraatmadja, T.L., Bellas-Velidis, I., Benson, K., Berthier, J., Blomme, R., Busso, G., Carry, B., Cellino, A., Clementini, G., Cowell, S., Creevey, O., Cuypers, J., Davidson, M., De Ridder, J., de Torres, A., Delchambre, L., Dell'Oro, A., Ducourant, C., Frémat, Y., García-Torres, M., Gosset, E., Halbwachs, J.-L., Hambly, N.C., Harrison, D.L., Hauser, M., Hestroffer, D., Hodgkin, S.T., Huckle, H.E., Hutton, A., Jasniewicz, G., Jordan, S., Kontizas, M., Korn, A.J., Lanzafame, A.C., Manteiga, M., Moitinho, A., Muinonen, K., Osinde, J., Pancino, E., Pauwels, T., Petit, J.-M., Recio-Blanco, A., Robin, A.C., Sarro, L.M., Siopis, C., Smith, M., Smith, K.W., Sozzetti, A., Thuillot, W., van Reeven, W., Viala, Y., Abbas, U., Abreu Aramburu, A., Accart, S., Aguado, J.J., Allan, P.M., Allasia, W., Altavilla, G., Álvarez, M.A., Alves, J., Anderson, R.I., Andrei, A.H., Anglada Varela, E., Antiche, E., Antoja, T., Antón, S., Arcay, B., Atzei, A., Ayache, L., Bach, N., Baker, S.G., Balaguer-Núñez, L., Barache, C., Barata, C., Barbier, A., Barblan, F., Baroni, M., Barrado y Navascués, D., Barros, M., Barstow, M.A., Becciani, U., Bellazzini, M., Bellei, G., Bello García, A., Belokurov, V., Bendjoya, P., Berihuete, A., Bianchi, L., Bienaymé, O., Billebaud, F., Blagorodnova, N., Blanco-Cuaresma, S., Boch, T., Bombrun, A., Borrachero, R., Bouquillon, S., Bourda, G., Bouy, H., Bragaglia, A., Breddels, M.A., Brouillet, N., Brüsemeister, T., Bucciarelli, B., Budnik, F., Burgess, P.,

Burgon, R., Burlacu, A., Busonero, D., Buzzi, R., Caffau, E., Cambras, J., Campbell, H., Cancelliere, R., Cantat-Gaudin, T., Carlucci, T., Carrasco, J.M., Castellani, M., Charlot, P., Charnas, J., Charvet, P., Chassat, F., Chiavassa, A., Clotet, M., Cocozza, G., Collins, R.S., Collins, P., Costigan, G., Crifo, F., Cross, N.J.G., Crosta, M., Crowley, C., Dafonte, C., Damerdji, Y., Dapergolas, A., David, P., David, M., De Cat, P., de Felice, F., de Laverny, P., De Luise, F., De March, R., de Martino, D., de Souza, R., Debosscher, J., del Pozo, E., Delbo, M., Delgado, A., Delgado, H.E., di Marco, F., Di Matteo, P., Diakite, S., Distefano, E., Dolding, C., Dos Anjos, S., Drazinos, P., Durán, J., Dzigan, Y., Ecale, E., Edvardsson, B., Enke, H., Erdmann, M., Escolar, D., Espina, M., Evans, N.W., Eynard Bontemps, G., Fabre, C., Fabrizio, M., Faigler, S., Falcão, A.J., Farràs Casas, M., Faye, F., Federici, L., Fedorets, G., Fernández-Hernández, J., Fernique, P., Fienga, A., Figueras, F., Filippi, F., Findeisen, K., Fonti, A., Fouesneau, M., Fraile, E., Fraser, M., Fuchs, J., Furnell, R., Gai, M., Galleti, S., Galluccio, L., Garabato, D., García-Sedano, F., Garé, P., Garofalo, A., Garralda, N., Gavras, P., Gerssen, J., Geyer, R., Gilmore, G., Girona, S., Giuffrida, G., Gomes, M., González-Marcos, A., González-Núñez, J., González-Vidal, J.J., Granvik, M., Guerrier, A., Guillout, P., Guiraud, J., Gúrpide, A., Gutiérrez-Sánchez, R., Guy, L.P., Haigron, R., Hatzidimitriou, D., Haywood, M., Heiter, U., Helmi, A., Hobbs, D., Hofmann, W., Holl, B., Holland, G., Hunt, J.A.S., Hypki, A., Icardi, V., Irwin, M., Jevardat de Fombelle, G., Jofré, P., Jonker, P.G., Jorissen, A., Julbe, F., Karampelas, A., Kochoska, A., Kohley, R., Kolenberg, K., Kontizas, E., Koposov, S.E., Kordopatis, G., Koubsky, P., Kowalczyk, A., Krone-Martins, A., Kudryashova, M., Kull, I., Bachchan, R.K., Lacoste-Seris, F., Lanza, A.F., Lavigne, J.-B., Le Poncin-Lafitte, C., Lebreton, Y., Lebzelter, T., Leccia, S., Leclerc, N., Lecoeur-Taibi, I., Lemaitre, V., Lenhardt, H., Leroux, F., Liao, S., Licata, E., Lindstrøm, H.E.P., Lister, T.A., Livanou, E., Lobel, A., Löffler, W., López, M., Lopez-Lozano, A., Lorenz, D., Loureiro, T., MacDonald, I., Magalhães Fernandes, T., Managau, S., Mann, R.G., Mantelet, G., Marchal, O., Marchant, J.M., Marconi, M., Marie, J., Marinoni, S., Marrese, P.M., Marschalkó, G., Marshall, D.J., Martín-Fleitas, J.M., Martino, M., Mary, N., Matijevič, G., Mazeh, T., McMillan, P.J., Messina, S., Mestre, A., Michalik, D., Millar, N.R., Miranda, B.M.H., Molina, D., Molinaro, R., Molinaro, M., Molnár, L., Moniez, M., Montegriffo, P., Monteiro, D., Mor, R., Mora, A., Morbidelli, R., Morel, T., Morgenthaler, S., Morley, T., Morris, D., Mulone, A.F., Muraveva, T., Musella, I., Narbonne, J., Nelemans, G., Nicastro, L., Noval, L., Ordénovic, C., Ordieres-Meré, J., Osborne, P., Pagani, C., Pagano, I., Pailler, F., Palacin, H., Palaversa, L., Parsons, P., Paulsen, T., Pecoraro, M., Pedrosa, R., Pentikäinen, H., Pereira, J., Pichon, B., Piersimoni, A.M., Pineau, F.-X., Plachy, E., Plum, G., Poujoulet, E., Prša, A., Pulone, L., Ragaini, S., Rago, S., Rambaux, N., Ramos-Lerate, M., Ranalli, P., Rauw, G., Read, A., Regibo, S., Renk, F., Reylé, C., Ribeiro, R.A., Rimoldini, L., Ripepi, V., Riva, A., Rixon, G., Roelens, M., Romero-Gómez, M., Rowell, N., Royer, F., Rudolph, A., Ruiz-Dern, L., Sadowski, G., Sagristà Sellés, T., Sahlmann, J., Salgado, J., Salguero, E., Sarasso, M., Savietto, H., Schnorhk, A., Schultheis, M., Sciacca, E., Segol, M., Segovia, J.C., Segransan, D., Serpell, E., Shih, I-C., Smareglia, R., Smart, R.L., Smith, C., Solano, E., Solitro, F., Sordo, R., Soria Nieto, S., Souchay, J., Spagna, A., Spoto, F., Stampa, U., Steele, I.A., Steidelmüller, H., Stephenson, C.A., Stoev, H., Suess, F.F., Süveges, M., Surdej, J., Szabados, L., Szegedi-Elek, E., Tapiador, D., Taris, F., Tauran, G., Taylor, M.B., Teixeira, R., Terrett, D., Tingley, B., Trager, S.C., Turon, C., Ulla, A., Utrilla, E., Valentini, G., van Elteren, A., Van Hemelryck, E., van Leeuwen, M., Varadi, M., Vecchiato, A., Veljanoski, J., Via, T., Vicente, D., Vogt, S., Voss, H., Votruba, V., Voutsinas, S., Walmsley, G., Weiler, M., Weingrill, K., Werner, D., Wevers, T., Whitehead, G., Wyrzykowski, Ł., Yoldas, A., Žerjal, M., Zucker, S., Zurbach, C., Zwitter, T., Alecu, A., Allen, M., Allende Prieto, C., Amorim, A., Anglada-Escudé, G., Arsenijevic, V., Azaz, S., Balm, P., Beck, M.,

Bernstein, H.-H., Bigot, L., Bijaoui, A., Blasco, C., Bonfigli, M., Bono, G., Boudreault, S., Bressan, A., Brown, S., Brunet, P.-M., Bunclark, P., Buonanno, R., Butkevich, A.G., Carret, C., Carrion, C., Chemin, L., Chéreau, F., Corcione, L., Darmigny, E., de Boer, K.S., de Teodoro, P., de Zeeuw, P.T., Delle Luche, C., Domingues, C.D., Dubath, P., Fodor, F., Frézouls, B., Fries, A., Fustes, D., Fyfe, D., Gallardo, E., Gallegos, J., Gardiol, D., Gebran, M., Gomboc, A., Gómez, A., Grux, E., Gueguen, A., Heyrovsky, A., Hoar, J., Iannicola, G., Isasi Parache, Y., Janotto, A.-M., Joliet, E., Jonckheere, A., Keil, R., Kim, D.-W., Klagyivik, P., Klar, J., Knude, J., Kochukhov, O., Kolka, I., Kos, J., Kutka, A., Lainey, V., LeBouquin, D., Liu, C., Loreggia, D., Makarov, V.V., Marseille, M.G., Martayan, C., Martinez-Rubi, O., Massart, B., Meynadier, F., Mignot, S., Munari, U., Nguyen, A.-T., Nordlander, T., Ocvirk, P., O'Flaherty, K.S., Olias Sanz, A., Ortiz, P., Osorio, J., Oszkiewicz, D., Ouzounis, A., Palmer, M., Park, P., Pasquato, E., Peltzer, C., Peralta, J., Péturaud, F., Pieniluoma, T., Pigozzi, E., Poels, J., Prat, G., Prod'homme, T., Raison, F., Rebordao, J.M., Risquez, D., Rocca-Volmerange, B., Rosen, S., Ruiz-Fuertes, M.I., Russo, F., Sembay, S., Serraller Vizcaino, I., Short, A., Siebert, A., Silva, H., Sinachopoulos, D., Slezak, E., Soffel, M., Sosnowska, D., Straižys, V., ter Linden, M., Terrell, D., Theil, S., Tiede, C., Troisi, L., Tsalmantza, P., Tur, D., Vaccari, M., Vachier, F., Valles, P., Van Hamme, W., Veltz, L., Virtanen, J., Wallut, J.-M., Wichmann, R., Wilkinson, M.I., Ziaeepour, H., Zschocke, S., 2016. The Gaia mission. Astronomy & Astrophysics 595. https://doi.org/10.1051/0004-6361/201629272.

Galilei, G., 1588. Due lezioni all' Accademia Fiorentina circa la figura, sito e grandezza dell'Inferno di Dante. Lezione prima. (German: Erste Lektion vor der Florentinischen Akademie über die Gestalt, Lage und Größe von Dantes "Hölle", transl. M. Köster, C. Wagner) In: Mudry, A. (Ed.), Galileo Galilei, Schriften, Briefe, Dokumente, Vol. 1. Rütten & Loening, Berlin. 439 pages.

Galilei, G., 1610a. Sidereus Nuncius, or The Sidereal Messenger. Engl. transl. and commentary A. van Helden. 2nd ed. University of Chicago Press, Chicago, USA, London, GB. 131 pages.

Galilei, G., 1610b. Sidereus Nuncius. Le Messager Celeste. French transl. and commentary by I. Pantin. Societé d'edition Les Belles Lettres, Paris. 115 pages.

Garcia, R.F., Gagnepain-Beyneix, J., Chevrot, S., Lognonné, P., 2012. Erratum to "Very Preliminary Reference Moon Model", by R.F. Garcia, J. Gagnepai-Beyneix, S. Chevrot, P. Lognonné [Phys. Earth Planet. Inter. 188 (2011) 96–113]. Physics of the Earth and Planetary Interiors 202–203, 89–91.

Garcia, R.F., Gagnepain-Beyneix, J., Chevrot, S., Lognonné, P., 2011. Very preliminary reference Moon model. Physics of the Earth and Planetary Interiors 188, 96–113.

Garcia, R.F., Khan, A., Drilleau, M., Margerin, L., Kawamura, T., Sun, D., Wieczorek, M.A., Rivoldini, A., Nunn, C., Weber, R.C., Marusiak, A.G., Lognonné, P., Nakamura, Y., Zhu, P., 2019. Lunar seismology: an update on interior structure models. Space Science Reviews 215 (50). https://doi.org/10.1007/s11214-019-0613-y.

Gautruche, P., 1668. Mathematicae Totius. Cantabrigiae, Excudebat Joan. Field, Celeberrimae Academiae Typographus, Impensis Edwardi Story, Library of the University of Michigan. Available online: https://books.google.de/books?id=7KY2AAAAMAAJ. (Accessed 14 December 2021).

Geiger, L., Gutenberg, B., 1912. Ueber Erdbebenwellen. VI. Konstitution des Erdinnern, erschlossen aus der Intensität longitudinaler und transversaler Erdbebenwellen, und einige Beobachtungen an den Vorläufern. Nachrichten von der Gesellschaft der Wissenschaften zu Göttingen, Mathematisch-Physikalische Klasse 6, 623–675.

Genova, A., Goossens, S., Lemoine, F.G., Mazarico, E., Neumann, G.A., Smith, D.A., Zuber, M.T., 2016. Seasonal and static gravity field of Mars from MGS, Mars Odyssey and MRO radio science. Icarus 272, 228–245. https://doi.org/10.1016/j.icarus.2016.02.050.

Gilbert, W., 1600. De Magnete, magneticisque corporius, et de magno magnete tellure. (De Magnete, translation P. Fleury Mottelay). Dover Publications. 1958. 368 pages.
Gilli, G., Israelian, G., Ecuvillon, A., Santos, N.C., Mayor, M., 2006. Abundances of refractory elements in the atmospheres of stars with extrasolar planets. Astronomy & Astrophysics 449 (2), 723–736. https://doi.org/10.1051/0004-6361:20053850.
Gillon, M., Triaud, A.H.M.J., Demory, B.-O., Jehin, E., Agol, E., Deck, K.M., Lederer, S.M., de Wit, J., Burdanov, A., Ingalls, J.G., Bolmont, E., Leconte, J., Raymond, S.N., Selsis, F., Turbet, M., Barkaoui, K., Burgasser, A., Burleigh, M.R., Carey, S.J., Chaushev, A., Copperwheat, C.M., Delrez, L., Fernandes, C.S., Holdsworth, D.L., Kotze, E.J., van Grootel, V., Almleaky, Y., Benkhaldoun, Z., Magain, P., Queloz, D., 2017. Seven temperate terrestrial planets around the nearby ultracool dwarf star TRAPPIST-1. Nature 542 (7642), 456–460. https://doi.org/10.1038/nature21360.
Gingerich, O., 2005. Tycho Brahe and the Nova of 1572. In: Turatto, M., Benetti, S., Zampieri, L., Shea, W. (Eds.), 1604-2004: Supernovae as Cosmological Lighthouses. Proceedings of the Conference Held 15–19 June, 2004 in Padua, Italy. In: ASP Conference Series, vol. 342. Astronomical Society of the Pacific, San Francisco, p. 3.
Goins, N.R., Dainty, A.M., Toksöz, M.N., 1981. Lunar seismology: the internal structure of the Moon. Journal of Geophysical Research 86 (B6), 5061–5074.
Goldschmidt, V.M., 1922. Über die Massenverteilung im Erdinneren, verglichen mit der Struktur gewisser Meteoriten. Naturwissenschaften 10, 918. https://doi.org/10.1007/BF01566019.
Goldstein, B.E., Phillips, R.J., Russell, C.T., 1976a. Magnetic evidence concerning a lunar core. In: Proceedings of the Lunar Science Conference 7th, pp. 3321–3341.
Goldstein, B.E., Phillips, R.J., Russell, C.T., 1976b. Magnetic permeability measurements and a lunar core. Geophysical Research Letters 3 (6), 289–292.
Goossens, S., Matsumoto, K., 2008. Lunar degree 2 potential Love number determination from satellite tracking data. Geophysical Research Letters 35, L02204. https://doi.org/10.1029/2007GL031960.
Goossens, S., Matsumoto, K., Liu, Q., Kikuchi, F., Sato, K., Hanada, H., Ishihara, Y., Noda, H., Kawano, N., Namiki, N., Lemoine, F.G., Rowlands, D.D., Harada, Y., Chen, M., 2011. Lunar gravity field determination using SELENE same-beam differential VLBI tracking data. Journal of Geodesy 85, 205–228. https://doi.org/10.1007/s00190-010-0430-2.
Grasset, O., Schneider, J., Sotin, C., 2009. A study of the accuracy of mass-radius relationships for silicate-rich and ice-rich planets up to 100 Earth masses. The Astrophysical Journal 693 (1), 722–733. https://doi.org/10.1088/0004-637X/693/1/722.
Gregoryanz, E., Ji, C., Dalladay-Simpson, P., Li, B., Howie, R.T., Mao, H.-K., 2020. Everything you always wanted to know about metallic hydrogen but were afraid to ask. Matter and Radiation at Extremes 5, 038101. https://doi.org/10.1063/5.0002104.
Griggs, D.T., Press, F., 1961. Probing the Earth with nuclear explosions. Journal of Geophysical Research 66 (1), 237–258. https://doi.org/10.1029/JZ066i001p00237.
Gutenberg, B., 1914. Ueber Erdbebenwellen. VII A. Beobachtungen an Registrierungen von Fernbeben in Göttingen und Folgerung über die Konstitution des Erdkörpers (mit Tafel). Nachrichten von der Gesellschaft der Wissenschaften zu Göttingen, Mathematisch-Physikalische Klasse, 125–176. https://gdz.sub.uni-goettingen.de/download/pdf/PPN252457811_1914/LOG_0024.pdf, 1914. Download 15.06.2021.
Gutenberg, B., 1946. Interpretation of records obtained from the New Mexico atomic bomb test, July 16, 1945. Bulletin of the Seismological Society of America 36 (4), 327–330. https://doi.org/10.1785/BSSA0360040327.
Gutenberg, B. (Ed.), 1929. Lehrbuch der Geophysik. Bornträger, Berlin, Germany. 1017 pages.
Gutenberg, B., Richter, C.F., 1946. Seismic waves from atomic bomb tests. Transactions of the American Geophysical Union 27 (4), 776.

Guttenberg, B., 1960. The shadow of the Earth's core. Journal of Geophysical Research 65 (3), 1013–1020.

Haddon, R.A.W., Bullen, K.E., 1969. An Earth model incorporating free Earth oscillation data. Physics of the Earth and Planetary Interiors 2, 35–49.

Halley, E., 1683. A theory of the variation of the Magnetical Compass, by Mr. Ed. Halley Fellow of the R. S. Philosophical Transactions of the Royal Society 13 (148), 208–221. https://doi.org/10.1098/rstl.1683.0031.

Halley, E., 1692. An account of the cause of the change of the variation of the magnetical needle, with an hypothesis of the structure of the internal parts of the earth: as it was proposed to the Royal Society in one of their late meetings. Philosophical Transactions of the Royal Society 17, 563–578. https://doi.org/10.1098/rstl.1686.0107. Accompanying figure in https://doi.org/10.1098/rstl.1686.0106.

Harder, H., 1998. Phase transitions and the three-dimensional planform of thermal convection in the Martian mantle. Journal of Geophysical Research 103 (E7), 16775–16797.

Harder, H., Christensen, U., 1996. A one-plume model of martian mantle convection. Nature 380, 507–509.

Hartmann, W.K., Raper, O., 1974. The New Mars. The Discoveries of Mariner 9. NASA SP-337. NASA Scientific and Technical Information Office, Washington, D.C., USA. 193 pages.

Haughton, S., 1859. LXIII. On the thickness of the Earth's crust. The London, Edinburgh, and Dublin Philosophical Magazine and Journal of Science 18 (122), 420–426. https://doi.org/10.1080/14786445908642790.

van Helden, A., 1985. Measuring the Universe. University of Chicago Press, Chicago, Ill., USA. 203 pages.

Hellard, H., 2019. Retrieval of the fluid Love number k_2 in exoplanetary transit curves. The Astrophysical Journal 878 (2). https://doi.org/10.3847/1538-4357/ab2048.

Hellard, H., Csizmadia, S., Padovan, S., Sohl, F., Rauer, H., 2020. HST/STIS capability for Love number measurement of WASP-121b. The Astrophysical Journal 889 (1). https://doi.org/10.3847/1538-4357/ab616e.

Henderson, P., Henderson, G.M., 2009. The Cambridge Handbook of Earth Science Data. Cambridge University Press, Cambridge, UK. 277 pages.

Hennessy, Henry, 1851. XXII. Researches in terrestrial physics – Part II. Philosophical Transactions of the Royal Society 141, 511–547. https://doi.org/10.1098/rstl.1851.0025.

Herschel, W., 1784. On the remarkable appearances at the polar regions of the planet Mars, and its spheroidical figure; with a few hints relating to its real diameter and atmosphere. Philosophical Transactions of the Royal Society 74, 233–273. https://doi.org/10.1098/rstl.1784.0020.

Hine, H.M., 2002. Seismology and vulcanology in antiquity? In: Tuplin, C.J., Rihill, T.E. (Eds.), Science and Mathematics in Ancient Greek Culture. Oxford University Press, Oxford, UK, pp. 56–75.

Hirose, K., Wood, B., Vočadlo, L., 2021. Light elements in the Earth's core. Nature Reviews Earth & Environment 2, 645–659. https://doi.org/10.1038/s43017-021-00203-6.

Hjortenberg, E., 2009. Inge Lehmann's work materials and seismological epistolary archive. Annals of Geophysics 52 (6), 679–698.

Homer, ca. 735 BCE. Odyssey, books 1–12. Transl. A.T. Murray, revised by G.E. Dimock. Loeb Classical Library, vol. 104. Harvard University Press. Cambridge, Mass., USA, London, GB. 481 pages.

Hood, L.L., Jones, J.H., 1987. Geophysical constraints on lunar bulk composition and structure: a reassessment. In: Proceedings of the 17th Lunar and Planetary Science Conference. Journal of Geophysical Research 92 (B4), E396–E410.

Hood, L.L., Mitchell, D.L., Lin, R.P., Acuña, M.H., Binder, A.B., 1999. Initial measurements of the lunar induced magnetic dipole moment using lunar prospector magnetometer data. Geophysical Research Letters 26 (15), 2327–2330.

Hopkins, W., 1842. On the thickness and constitution of the Earth's crust, III. Researches in physical geology – Third series. Philosophical Transactions of the Royal Society 132, 43–55. https://doi.org/10.1098/rstl.1842.0004.

Houzeau, J.-C., 1882. Vade-mecum de l'astronomie, vol. 1, parts 1-014. F. Hayez, Bruxelles, Belgium. 1144 pages. Online: https://books.google.de/books?id=ju3PAAAAMAAJ&hl=de. (Accessed 24 August 2021).

Humboldt, A.v., 1845. Kosmos. Entwurf einer physischen Weltbeschreibung, vol. 1. J.G. Cotta'scher Verlag, Stuttgart. 494 pages. Available online: Deutsches Textarchiv https://www.deutschestextarchiv.de/humboldt_kosmos01_1845/254. (Accessed 29 March 2022).

Hutton, C., 1778. XXXIII. An account of the calculations made from the survey and measures taken at Schehallien, in order to ascertain the mean density of the Earth. Philosophical Transactions of the Royal Society of London 68. https://doi.org/10.1098/rstl.1778.0034.

Index Librorum Prohibitorum, 1900. SSMI D.N. Leonis XIII, Iussu et auctoritate recognitus et editus, praemittuntur Constitutiones Apostolicae de examine et prohibitione librorum. Typis Vaticanis, Rome. 316 pages. Available online: https://archive.org/details/indexlibrorumpr00roma/page/72/mode/2up. (Accessed 28 September 2021).

Jeffreys, H., 1926. The rigidity of the Earth's central core. Geophysical Supplements to Monthly Notices of the Royal Astronomical Society 1 (7), 371–383. https://doi.org/10.1111/j.1365-246X.1926.tb05385.x.

Jeffreys, H., 1934. The constitution of the inner planets. Monthly Notices of the Royal Astronomical Society 94 (9), 823. https://doi.org/10.1093/mnras/94.9.823.

Jeffreys, H., 1936. On the figures of the Earth and Moon. Monthly Notices of the Royal Astronomical Society 97 (1), 3–14. https://doi.org/10.1093/mnras/97.1.3.

Jeffreys, H., 1937. On the figures of the Earth and Moon. Monthly Notices of the Royal Astronomical Society, Geophysical Supplement 4 (1), 1–13.

Jeffreys, H., 1939a. The times of the core waves. Geophysical Supplements to Monthly Notices of the Royal Astronomical Society 4 (7), 548–561. https://doi.org/10.1111/j.1365-246X.1939.tb02915.x.

Jeffreys, H., 1939b. The times of P, S and SKS, and the velocities of P and S. Geophysical Supplements to Monthly Notices of the Royal Astronomical Society 4 (7), 498–533. https://doi.org/10.1111/j.1365-246X.1939.tb02912.x.

Jeffreys, H., 1939c. Seismological tables (council report on the progress of astronomy). Monthly Notices of the Royal Astronomical Society 99, 397. https://doi.org/10.1093/mnras/99.4.397.

Jeffreys, H., 1961. On the figure of the Moon. Monthly Notices of the Royal Astronomical Society 122 (5), 421–432. https://doi.org/10.1093/mnras/122.5.421.

Jeffreys, H., Bullen, K.E., 1967. Seismological Tables. British Association for the Advancement of Science, Gray Milne Trust, Office of the British Association, London. 50 pages.

Johnston, D.H., McGetchin, T.R., Toksöz, M.N., 1974. The thermal state and internal structure of Mars. Journal of Geophysical Research 79 (26), 3959–3971.

Jones, H.S., 1932. Discussion of observations of occultations of stars by the moon, 1672–1908, being a revision of Newcomb's "Researches on the motion of the Moon, part II". Annals of the Cape Observatory XIII, part 3. 72 pages.

Jordan, J.F., Lorell, J., 1975. Mariner 9: an instrument of dynamical science. Icarus 25, 146–165.

Kahan, D.S., Folkner, W.M., Buccino, D.R., Dehant, V., Le Maistre, S., Rivoldini, A., Van Hoolst, T., Yseboodt, M., Marty, J.C., 2021. Mars precession rate determined from

radiometric tracking of the InSight lander. Planetary and Space Science 199, 105208. https://doi.org/10.1016/j.pss.2021.105208.

Kahle, H.-G., 1984. Gravity field and figure of the Earth. In: Fuchs, K., Soffel, H. (Eds.), Landolt–Börnstein Numerical Data and Functional Relationships in Science and Technology, New Series, Group V: Geophysics and Space Research, vol. 2a. Springer, Berlin, Heidelberg, New York, Tokyo, pp. 311–356.

Kaneshima, S., Helffrich, G., 2013. Vp structure of the outermost core derived rom analysing large-scale array data of SmKS waves. Geophysical Journal International 193, 1537–1555. https://doi.org/10.1093/gji/ggt042.

Kaula, W.M., Schubert, G., Lingenfelter, R.E., Sjogren, W.L., Wollenhaupt, W.R., 1974. Apollo laser altimetry and inferences as to lunar structure. In: Proceedings of the Fifth Lunar Conference. Geochimica et Cosmochimica Acta Supplement 5, 3, 3049–3058.

Kaula, W.M., 1969. The gravitational field of the Moon. Science 166 (3913), 1581–1588. https://doi.org/10.1126/science.166.3913.1581.

Kaula, W.M., 1979. The moment of inertia of Mars. Geophysical Research Letters 6 (3), 194–196.

Kavner, A., Duffy, T.S., Shen, G., 2001. Phase stability and density of FeS at high pressures and temperatures: implications for the interior structure of Mars. Earth and Planetary Science Letters 185, 25–33.

Kennett, B.L.N., 2020. Radial Earth models revisited. Geophysical Journal International 222, 2189–2204. https://doi.org/10.1093/gji/ggaa298.

Kennett, B.L.N., Engdahl, E.R., 1991. Traveltimes for global earthquake location and phase identification. Geophysical Journal International 105, 429–465.

Kennett, B.L.N., Engdahl, E.R., Buland, R., 1995. Constraints on seismic velocities in the Earth from traveltimes. Geophysical Journal International 122 (1), 108–124.

Kepler, J., 1609. Astronomia Nova, dt.: Neue Astronomie, translated from Latin by M. Caspar, R. Oldenbourg, München, Germany, reprint of the 1929 edition, 481 pages.

Kertz, W., 1999. Geschichte der Geophysik. Georg Olms, Hildesheim, Zürich, New York. 376 pages.

Khan, A., Liebske, C., Rozel, A., Rivoldini, A., Nimmo, F., Connolly, J.A.D., Plesa, A.-C., Giardini, D., 2018. A geophysical perceptive on the bulk composition of Mars. Journal of Geophysical Research: Planets 123, 575–611. https://doi.org/10.1002/2017JE005371.

Khan, A., Mosegaard, K., 2001. New information on the deep lunar interior from an inversion of lunar free oscillation periods. Geophysical Research Letters 28 (9), 1791–1794.

Khan, A., Mosegaard, K., 2005. Further constraints on the deep lunar interior. Geophysical Research Letters 32, L22203. https://doi.org/10.1029/2005GL023985. 4 pages.

Khan, A., Mosegaard, K., Rasmussen, K.L., 2000. A new seismic velocity model for the Moon from a Monte Carlo inversion of the Apollo lunar seismic data. Geophysical Research Letters 27 (11), 1591–1594.

Khan, A., Mosegaard, K., Williams, J.G., Lognonné, P., 2004. Does the Moon possess a molten core? Probing the deep lunar interior using results from LLR and Lunar Prospector. Journal of Geophysical Research 109, E09007. https://doi.org/10.1029/2004JE002294.

Khan, A., Sossi, P.A., Liebske, C., Rivoldini, A., Giardini, D., 2022. Geophysical and cosmochemical evidence for a volatile-rich Mars. Earth and Planetary Science Letters 578, 117330. https://doi.org/10.1016/j.epsl.2021.117330.

Kim, D., Davis, P., Lekić, V., Maguire, R., Compaire, N., Schimmel, M., Stutzmann, E., Irving, J.C.E., Lognonné, P., Scholz, J.-R., Clinton, J., Zenhäusern, G., Dahmen, N., Deng, S., Levander, A., Panning, M.P., Garcia, R.F., Giardini, D., Hurst, K., Knapmeyer-Endrun, B., Nimmo, F., Pike, W.T., Pou, L., Schmer, N., Stähler, S., Tauzin, B., Widmer-Schnidrig, R., Banerdt, W.B., 2021. Potential pitfalls

in the analysis and structural interpretation of seismic data from the Mars InSight mission. Bulletin of the Seismological Society of America 111, 2892–3002. https://doi.org/10.1785/0120210123.

Kircher, A., 1664. Athanasii Kircheri. Mundus subterraneus: in XII libros digestus. Amstelodami: apud Ioannem Ianssonium & Elizeum Weyerstraten, 1664. ETH-Bibliothek Zürich, Rar 1365 GF. https://doi.org/10.3931/e-rara-14326. (Accessed 25 October 2021).

Knapmeyer, M., Walterová, M., 2022. Tables of planetary core radii and underlying parameters. version 1.0.275, 122 pages. https://doi.org/10.5281/zenodo.6601798.

Knapmeyer, M., Weber, R.C., 2015. Seismicity and interior structure of the Moon. In: Tong, V.C.H., Garcia, R.A. (Eds.), Extraterrestrial Seismology. Cambridge University Press, pp. 91–106.

Knopoff, L., Gilbert, F., 1961. Diffraction of elastic waves by the core of the Earth. Bulletin of the Seismological Society of America 51 (1), 35–49.

Konopliv, A.S., Asmar, S.W., Carranza, E., Sjogren, W.L., Yuan, D.N., 2001. Recent gravity models as a result of the Lunar Prospector mission. Icarus 150, 1–18. https://doi.org/10.1006/icar.2000.6573.

Konopliv, A.S., Binder, A.B., Hood, L.L., Kucinskas, A.B., Sjogren, W.L., Williams, J.G., 1998. Improved gravity field of the Moon from Lunar Prospector. Science 281, 1476–1480. https://doi.org/10.1126/science.281.5382.1476.

Konopliv, A.S., Park, R.S., Folkner, W.M., 2016. An improved JPL Mars gravity field and orientation from Mars orbiter and lander tracking data. Icarus 274, 253–260. https://doi.org/10.1016/j.icarus.2016.02.052.

Konopliv, A.S., Park, R.S., Rivoldini, A., Baland, R.-M., LeMaister, S., Van Hoolst, T., Yseboodt, M., Dehant, V., 2020. Detection of the Chandler Wobble of Mars from orbiting Spacecraft. Geophysical Research Letters 47. https://doi.org/10.1029/2020GL090568.

Konopliv, A.S., Park, R.S., Yuan, D.-N., Asmar, S.W., Watkins, M.W., Williams, M.M., Williams, J.G., Fahnestock, E., Kruizinga, G., Paik, M., Strekalov, D., Harvey, N., Smith, D.E., Zuber, M.T., 2013. The JPL lunar gravity field to spherical harmonic degree 660 from the GRAIL Primary Mission. Journal of Geophysical Research: Planets 118, 1415–1434. https://doi.org/10.1002/jgre.20097.

Kovach, R.L., Anderson, D.L., 1965. The interiors of the terrestrial planets. Journal of Geophysical Research 70 (12), 2873–2882. https://doi.org/10.1029/JZ070i012p02873.

Kozlovskaya, S.V., 1967. Models for the internal struture of the Earth, Venus, and Mars. Soviet Astronomy 10 (5), 865–878. Translated from Astronomicheskii Zhurnal 43 (5), 1081–1097 (1967).

Kramm, U., Nettelmann, N., Redmer, R., Stevenson, D.J., 2011. On the degeneracy of the tidal Love number k2 in multi-layer planetary models: application to Saturn and GJ436b. Astronomy & Astrophysics 528, A18. https://doi.org/10.1051/0004-6361/201015803.

Kronig, R., De Boer, J., Korringa, J., 1946. On the internal constitution of the Earth. Physica XII (5), 245–256.

Kronrod, E., Kuskov, O., Matsumoto, K., Kronrod, V., 2020. Estimation of the probable size of the lunar core based on geophysical and geochemical data. Fundamental and applied problems of mechanics. Journal of Physics: Conference Series 1705. https://doi.org/10.1088/1742-6596/1705/1/012024.

Kronrod, E., Matsumoto, K., Kuskov, O., Kronrod, V., Yamada, R., Kamata, S., 2018. Joint inversion of geophysical (seismic and selenodetic) and geochemical data for internal structure and composition of the Moon. IOP Conference Series: Materials Science and Engineering 468, 012015. https://doi.org/10.1088/1757-899X/468/1/012015.

Kronrod, E., Matsumoto, K., Kuskov, O.L., Kronrod, V., Yamada, R., Kamata, S., 2022. Towards geochemical alternatives to geophysical models of the internal structure of the

lunar mantle and core. Advances in Space Research 69, 2798–2824. https://doi.org/10.1016/j.asr.2022.01.012.
Kuhn, W., Rittmann, A., 1941. Über den Zustand des Erdinnern und seine Entstehung aus einem homogenen Urzustand. Geologische Rundschau 32, 215–256. https://doi.org/10.1007/BF01799758.
2016
Kuskov, O.L., Belashchenko, D.K., 2016. Thermodynamic properties of Fe-S alloys from molecular dynamics modeling: implications for the lunar fluid core. Physics of the Earth and Planetary Interiors 258, 43–50. https://doi.org/10.1016/j.pepi.2016.07.006.
Kuskov, O.L., Kronrod, V.A., 1998. Constitution of the Moon 5. Constraints on composition, density, temperature, and radius of a core. Physics of the Earth and Planetary Interiors 107, 285–306.
Kuskov, O.L., Kronrod, V.A., 2001. Core sizes and internal structure of Earth's and Jupiter's satellites. Icarus 151, 204–221. https://doi.org/10.1006/icar.2001.6611.
Kuskov, O.L., Kronrod, V.A., Hood, L.L., 2002. Geochemical constraints on the seismic properties of the lunar mantle. Physics of the Earth and Planetary Interiors 134, 175–189.
Lamar, D.L., McGann, J., 1966. Shape and internal structure of the Moon. Icarus 5 (1–6), 10–23. https://doi.org/10.1016/0019-1035(66)90004-2.
Landeau, M., Aubert, J., Olson, P., 2017. The signature of inner-core nucleation on the geodynamo. Earth and Planetary Science Letters 465. https://doi.org/10.1016/j.epsl.2017.02.004.
Laplace, P.S., 1825. Traité de Mécanique Céleste, Tome Cinquième, Bachelier (succeseur de Mme. Ve. Courcier). Libraire, Paris. Available online: https://opacplus.bsb-muenchen.de/title/BV012175706. (Accessed 19 January 2021).
Latham, G.V., Dorman, H.J., Horvath, P., Ibrahim, A.K., Koyama, J., Nakamura, Y., 1978. Passive seismic experiment: a summary of current status. In: Proceedings of the Lunar and Planetary Science Conference 9th, pp. 3609–3613.
Lehmann, I., 1936. P', Publications du bureau central séismologique international. Série A, Travaux Scientifiques, Fascicule No. 14, 87–115.
Leighton, R.B., Murray, B.C., Sharp, R.P., Allen, J.D., Sloan, R.K., 1967. Mariner Mars 1964 Project Report: Television Experiment, Part I: Investigator's Report. Mariner IV Pictures of Mars. NASA TR 32-884. Propulsion Laboratory, Pasadena, CA, USA. 211 pages.
Lessius, L., 1620. De perfectionibus moribusque divinis, libri XIV, Antverp, Balthasatem Moretum & Viduam Ioannis Moreti & Io. Mersium. 592 pages. Available online: https://mdz-nbn-resolving.de/details:bsb10350967. (Accessed 4 April 2022).
Levin, B.J., 1979. On the core of the Moon. In: Proceedings of the Lunar and Planetary Science Conference 10th, pp. 2321–2323.
Liu, A.S., Laing, P.A., 1971. Lunar gravity analysis from long-term effects. Science 173, 1017–1020.
Lodochnikov, V.N., 1939. Nekotorye obshie voprosy, svyazannye s magmoi, dayushei bazal'tovye porody. Zap. Vserossh. Mineral. Obsh. 68, 207–223, 428–442.
Lognonné, P., Gagnepain-Beyneix, J., Chenet, H., 2003. A new seismic model of the Moon: implications for structure, thermal evolution and formation of the Moon. Earth and Planetary Science Letters 211, 27–44. https://doi.org/10.1016/S0012-821X(03)00172-9.
Lorell, J., 1970. Lunar Orbiter gravity analysis. Moon 1, 190–231.
Lorell, J., Shapiro, I.I., 1973. Mariner 9 celestial mechanics experiment: a status report. Journal of Geophysical Research 78 (20), 4327–4329.
Lucretius, 60 BCE. On the nature of things (De Rerum Natura). Transl. W.H.D. Rouse, revised by M.F. Smith. Loeb Classical Library, vol. 181, Harvard University Press, Cambridge, Mass., USA, London, GB, 602 pages.

Ludwin, R.S., Smits, G.J., Carver, D., James, K., Jonientz-Trisler, C., McMillan, A.D., Losey, R., Dennis, R., Rasmussen, J., De Los Angeles, A., Buerge, D., Thrush, C.P., Clague, J., Bowechop, J., Wray, J., 2007. Folklore and earthquakes: native American oral traditions from Cascadia compared with written traditions from Japan. Geological Society, London, Special Publications 273, 67–94. https://doi.org/10.1144/GSL.SP.2007.273.01.07.

Lurker, M., 1989. Lexikon der Götter und Dämonen, 2nd extended edition. Kröner, Stuttgart, Germany. 604 pages.

Lyttleton, R.A., 1965. On the internal structure of the planet Mars. Monthly Notices of the Royal Astronomical Society 129 (1), 21–39. https://doi.org/10.1093/mnras/129.1.21.

Ma, X., Tkalčić, H., 2021. CCREM: new reference Earth model from the global coda-correlation wavefield. Journal of Geophysical Research Solid Earth 126, e2021JB022515. https://doi.org/10.1029/2021JB022515.

MacCurdy, E., 1955. The Notebooks of Leonardo da Vinci. George Braziller, New York. 1247 pages.

MacDonald, G.F., 1962. On the internal constitution of the inner planets. Journal of Geophysical Research 67 (7), 2945–2974.

Macelwane, J.B., 1922. Some seismological evidence that is not evident. Science 56 (1452), 478–480.

Macelwane, J.B., 1924. The interior of the Earth (1). Bulletin of the Seismological Society of America 14 (2), 81–90.

Mallet, R., 1849. On observation of earthquake phenomena. In: Herschel, J.F.W. (Ed.), A Manual of Scientific Enquiry. The Lords Commissioners of the Admiralty, John Murray, London. 488 pages. Available online: https://www.biodiversitylibrary.org/item/107631#page/1/mode/1up. https://ia800501.us.archive.org/29/items/NHM19639/NHM19639.pdf. Download 18 Nov. 2021.

Marcus, R.A., Sasselov, D., Hernquist, L., Stewart, S.T., 2010. Minimum radii of super-earths: constraints from giant impacts. The Astrophysical Journal Letters. https://doi.org/10.1088/2041-8205/712/1/l73.

Maskelyne, N., 1775. XLVIII. A proposal for measuring the attraction of some hill in this kingdom by astronomical observations. Philosophical Transactions of the Royal Society 65, 495–499. https://doi.org/10.1098/rstl.1775.0049.

Mather, K.F., Mason, S.L., 1967. A Source Book in Geology 1400–1900. Harvard University Press, Cambridge, Mass., USA.

Matsumoto, K., Goossens, S., Ishihara, Y., Liu, Q., Kikuchi, F., Iwata, T., Namiki, N., Noda, H., Hanada, H., Kawano, N., Lemoine, F.G., Rowlands, D.D., 2010. An improved lunar gravity field model from SELENE and historical tracking data: revealing the farside gravity features. Journal of Geophysical Research 115, E06007. https://doi.org/10.1029/2009JE003499.

Matsumoto, K., Yamada, R., Kikuchi, F., Kamata, S., Ishihara, Y., Iwata, T., Hanada, H., Sasaki, S., 2015. Internal structure of the Moon inferred from Apollo seismic data and selenodetic data from GRAIL and LLR. Geophysical Research Letters 42, 7351–7358. https://doi.org/10.1002/2015GL065335.

McCauley, J.F., Carr, M.H., Cutts, J.A., Hartmann, W.K., Maursky, H., Milton, D.J., Sharp, R.P., Wihelms, D.E., 1972. Preliminary Mariner 9 report on the geology of Mars. Icarus 17, 289–327.

McDonough, W.F., Sun, S.-s., 1995. The composition of the Earth. Chemical Geology 120 (3–4), 223–253. https://doi.org/10.1016/0009-2541(94)00140-4.

McSween, H.Y. Jr., 1984. SNC meteorites: are they Martian rocks? Geology 12, 3–6.

Merkatas, C., Toman, B., Possolo, A., Schlamminger, S., 2019. Shades of dark uncertainty and consensus value for the Newtonian constant of gravitation. Metrologia 56. https://doi.org/10.1088/1681-7575/ab3365.

Michael, W.H. Jr., Blackshear, W.T., 1972. Recent results on the mass, gravitational field and moments of inertia of the moon. Moon 3, 388–402.
Michaelis, W., Haars, H., Augustin, R., 1995. A new precise determination of Newton's gravitational constant. Metrologia 32, 267–276.
Milne, J., 1903. Seismometry and Gēite. Nature 67 (1745), 538–539.
Morelli, A., Dziewonski, A.M., 1993. Body wave traveltimes and a spherically symmetric P- and S-wave velocity model. Geophysical Journal International 112 (2), 178–194.
Morrison, J.S., 1959. The shape of the Earth in Plato's Phaedo. Phronesis 4 (2), 101–119.
Mueller, S., Taylor, G.J., Phillips, R.J., 1988. Lunar composition: a geophysical and petrological synthesis. Journal of Geophysical Research 93 (B6), 6338–6352.
Muir, J.B., Tsai, V.C., 2020. Did Oldham discover the core after all? Handling imprecise data with Hierarchical Bayesian model selection methods. Seismological Research Letters 91, 1377–1383. https://doi.org/10.1785/0220190266.
Murray, C., Dermott, S., 2000. Solar System Dynamics. Cambridge University Press, Cambridge. https://doi.org/10.1017/CBO9781139174817.
Murphy, T.W. Jr., Adelberger, E.G., Battat, J.B.R., Hoyle, C.D., Johnson, N.H., McMillan, R.J., Michelsen, E.L., Stubbs, C.W., Swanson, H.E., 2011. Laser ranging to the lost Lunokhod 1 reflector. Icarus 211, 1103–1108. https://doi.org/10.1016/j.icarus.2010.11.010.
Musson, R.M.W., 2013. A history of British seismology. Bulletin of Earthquake Engineering 11, 715–861. https://doi.org/10.1007/s10518-013-9444-5.
Müller, J., Murphy, T.W., Schreiber, U., Shelus, P.J., Torre, J.-M., Williams, J.G., Boggs, D.H., Bouquillon, S., Bourgoin, A., Hofmann, F., 2019. Lunar Laser Ranging: a tool for general relativity, lunar geophysics and Earth science. Journal of Geodesy 93, 2195–2210. https://doi.org/10.1007/s00190-019-01296-0.
NIST, 2019. 2018 CODATA Recommended Values of the Fundamental Constants of Physics and Chemistry. National Institute of Standards and Technology, Gaithersburg, MD, USA. NIST SP 959. Available online: https://tsapps.nist.gov/publication/get_pdf.cfm?pub_id=928211. (Accessed 3 May 2021).
Nakamura, Y., 1983. Seismic velocity structure of the lunar mantle. Journal of Geophysical Research 88 (B1), 677–686.
Nakamura, Y., 2015. Planetary seismology: early observational results. In: Tong, V.C.H., Garcia, R.A. (Eds.), Extraterrestrial Seismology. Cambridge University Press, pp. 91–106.
Nakamura, Y., Lammlein, D., Latham, G., Ewing, M., Dorman, J., Press, F., Toksöz, N., 1973. New seismic data on the state of the deep lunar interior. Science 181, 49–51.
Nakamura, Y., Latham, G., Lammlein, D., Ewing, M., Duennebier, F., Dorman, J., 1974. Deep lunar interior inferred from recent seismic data. Geophysical Research Letters 1 (3), 137–140.
Nakamura, Y., Latham, G.V., 1969. Internal Constitution of the Moon: is the lunar interior chemically homogeneous? Journal of Geophysical Research 74 (15), 3771–3780.
Nakamura, Y., Latham, G.V., Dorman, H.J., 1982. Apollo lunar seismic experiment – final summary. In: Proceedings of the Lunar and Planetary Science Conference 13th. Journal of Geophysical Research 87, Supplement, A117–A123.
Nakamura, Y., Latham, G.V., Dorman, H.J., Duennebier, F.K., 1976. Seismic structure of the Moon: a summary of current status. In: Proceedings of the Lunar Science Conference 7th, pp. 3113–3121.
New American Bible, 2002. United States Conference of Catholic Bishops, Washington, DC, USA. Available online: https://www.vatican.va/archive/ENG0839/_INDEX.HTM. (Accessed 27 September 2021).
Newton, I., 1687. Philosophiae naturalis principia mathematica. London. Approx. 510 pages. Available online: https://books.google.de/books?id=ASS2vmaQRnUC&

newbks=1&newbks_redir=0&dq=newton%20Philosophiae%20Naturalis&hl=de&pg=PP11#v=onepage&q=newton%20Philosophiae%20Naturalis&f=falselast. (Accessed 17 November 2021).

Newton, I., 1726. Philosophiae Naturalis Principia Mathematica (The Principia. Mathematical Principles of Natural Philosophy, transl. I.B. Cohen, A. Whitman, 1999). University of California Press, Berkeley, CA, USA, Los Angeles, CA, USA, London, UK. 966 pages.

Newton, I., 1728a. A Treatise of the System of the World. (anonymous translation) F. Fayram, London, UK. 155 pages. Online: https://books.google.de/books?id=rEYUAAAAQAAJ&newbks=1&newbks_redir=0&hl=de&pg=PR1#v=onepage&q&f=false. (Accessed 15 November 2021).

Newton, I., 1728b. De Mundi Systemate. Tonson, Osborn & Longman, London, UK. 108 pages. Available online: https://books.google.de/. (Accessed 11 November 2021).

Nunn, C., Garcia, R.F., Nakamura, Y., Marusiak, A.G., Kawamura, T., Sun, D., Margerin, L., Weber, R., Drilleau, M., Wieczorek, M.A., Khan, A., Rivoldini, A., Lognonné, P., Zhu, P., 2020. Lunar seismology: a data and instrumentation review. Space Science Reviews 216, 89. https://doi.org/10.1007/s11214-020-00709-3. 39 pages.

Okal, E.A., Anderson, D.L., 1978. Theoretical models for Mars and their seismic properties. Icarus 33, 514–528.

Oldham, R.D., 1900. III. On the propagation of earthquake motion to great distances. Philosophical Transactions of the Royal Society of London Series A, Containing Papers of a Mathematical or Physical Character 194, 135–174. https://doi.org/10.1098/rsta.1900.0015.

Oldham, R.D., 1906. The constitution of the interior of the Earth, as revealed by earthquakes. Quarterly Journal of the Geological Society 62, 456–475.

Padovan, S., Spohn, T., Baumeister, P., Tosi, N., Breuer, D., Csizmadia, Sz., Hellard, H., Sohl, F., 2018. Matrix-propagator approach to compute fluid Love numbers and applicability to extrasolar planets. Astronomy & Astrophysics 620 (A178). https://doi.org/10.1051/0004-6361/201834181.

PLATO. Revealing habitable worlds around solar-like stars, 2017. Definition Study Report, ESA-SCI(2017)-1. Available online: https://sci.esa.int/documents/33240/36096/1567260308850-PLATO_Definition_Study_Report_1_2.pdf. https://sci.esa.int/s/8rPyPew. (Accessed 22 March 2022).

Pepe, F., Molaro, P., Cristiani, S., Rebolo, R., Santos, N.C., Dekker, H., Mégevand, D., Zerbi, F.M., Cabral, A., Di Marcantonio, P., Abreu, M., Affolter, M., Aliverti, M., Allende Prieto, C., Amate, M., Avila, G., Baldini, V., Bristow, P., Broeg, C., Cirami, R., Coelho, J., Conconi, P., Coretti, I., Cupani, G., D'Odorico, V., De Caprio, V., Delabre, B., Dorn, R., Figueira, P., Fragoso, A., Galeotta, S., Genolet, L., Gomes, R., González Hernández, J.I., Hughes, I., Iwert, O., Kerber, F., Landoni, M., Lizon, J.-L., Lovis, C., Maire, C., Mannetta, M., Martins, C., Monteiro, M., Oliveira, A., Poretti, E., Rasilla, J.L., Riva, M., Santana Tschudi, S., Santos, P., Sosnowska, D., Sousa, S., Spanó, P., Tenegi, F., Toso, G., Vanzella, E., Viel, M., Zapatero Osorio, M.R., 2014. ESPRESSO: the next European exoplanet hunter. Astronomische Nachrichten 335 (1), 8. https://doi.org/10.1002/asna.201312004.

Plato, 4th cent. BCE. Timaeus-Critias-Cleitophon-Menexenus-Epistles. Transl. R.G. Bury, Loeb Classical Library, vol. 234. Harvard University Press, Cambridge, Mass., USA, London, GB. 634 pages.

Playfair, J., 1811. XVIII. Account of a lithological survey of Schehallien, made in order to determine the specific gravity of the rocks which compose that mountain. Philosophical Transactions of the Royal Society, 347–377. https://doi.org/10.1098/rstl.1811.0020.

Plesa, A.-C., Grott, M., Tosi, N., Breuer, D., Spohn, T., Wieczorek, M.A., 2016. How large are present-day heat flux variations across the surface of Mars? Journal of Geophysical Research: Planets 121, 2386–2403. https://doi.org/10.1002/2016JE005126.

Plesa, A.-C., Knapmeyer, M., Golombek, M.P., Breuer, D., Grott, M., Kawamura, T., Lognonné, P., Tosi, N., Weber, R.C., 2018a. Present-day Mars' seismicity predicted from 3-D thermal evolution models of interior dynamics. Geophysical Research Letters 45. https://doi.org/10.1002/2017GL076124.

Plesa, A.-C., Padovan, S., Tosi, N., Breuer, D., Grott, M., Wieczorek, M.A., Spohn, T., Smrekar, S., Banerdt, W.B., 2018b. The thermal state and interior structure of Mars. Geophysical Research Letters 45 (12), 12198–12209. https://doi.org/10.1029/2018GL080728.

Plesa, A.-C., Tosi, N., Grott, M., Breuer, D., 2015. Thermal evolution and Urey ratio of Mars. Journal of Geophysical Research: Planets 120, 955–1010. https://doi.org/10.1002/2014JE004748.

Plesa, A.-C., Wieczorek, M., Knapmeyer, M., Rivoldini, A., Walterová, M., Breuer, D., 2022. Interior dynamics and thermal evolution of Mars – a geodynamic perspective. In: Geophysical Exploration of the Solar System. In: Schmelzbach, C., Stähler, C. (Eds.), Advances in Geophysics, vol. 63. This volume.

Pliny the Elder, 77 CE. Natural History, Books 1–2. Transl. H. Rackham. Loeb Classical Library, vol. 330. Harvard University Press, Cambridge, Mass., USA, London, GB. 378 pages.

Pliny the Younger, 104 CE?. Letters, books 1–7. Transl. B. Radice. Loeb Classical Library, vol. 55. Harvard University Press, Cambridge, Mass., USA, London, GB. 565 pages.

Plutarch, 80 CE?. Concerning the face which appears in the orb of the Moon (De facie quae in orbe lunae apparet). In: Moralia, vol. XII. Transl. H. Cherniss, W.C. Helmbold. Loeb Classical Library, vol. 409. Harvard University, Cambridge, Mass., USA, London, GB. 590 pages.

Pratt, J.H., 1859. On the thickness of the crust of the Earth. The London, Edinburgh, and Dublin Philosophical Magazine and Journal of Science 17 (115), 327–332.

Press, F., 1956. Rigidity of the Earth's core. Science 124, 124. https://doi.org/10.1126/science.124.3233.1204.a.

Press, F., 1968. Earth models obtained by Monte Carlo inversion. Journal of Geophysical Research 73 (16), 5223–5234.

Purcaru, G., Berckhemer, H., 1982. Quantitative relations of seismic source parameters and a classification of earthquakes. Tectonophysics 84, 57–128.

Pätzold, M., Andert, T.P., Hahn, M., Barriot, J.-P., Asmar, S.W., Häusler, B., Bird, M.K., Tellmann, S., Oschlisniok, J., Peter, K., 2019. The Nucleus of comet 67P/Churyumov–Gerasimenko – Part I: The global view – nucleus mass, mass-loss, porosity, and implications. Monthly Notices of the Royal Astronomical Society 483, 2337–2346. https://doi.org/10.1093/mnras/sty3171.

Ragozzine, D., Wolf, A.S., 2009. Probing the interiors of very hot Jupiters using transit light curves. The Astrophysical Journal 698 (2), 1778–1794. https://doi.org/10.1088/0004-637X/698/2/1778.

Ramsey, W.H., 1948. On the constitution of the terrestrial planets. Monthly Notices of the Royal Astronomical Society 108 (5), 406–413. https://doi.org/10.1093/mnras/108.5.406.

Rauer, H., Aerts, C., Cabrera, J., PLATO Team, 2016. The PLATO Mission. Astronomische Nachrichten 337 (8–9), 961. https://doi.org/10.1002/asna.201612408.

Rayleigh, L., 1885. On waves along the plane surface of an elastic solid. Proceedings of the London Mathematical Society s1–17, 4–11. https://doi.org/10.1112/plms/s1-17.1.4.

Reasenberg, R.D., 1977. The moment of inertia and isostasy of Mars. Journal of Geophysical Research 82 (2), 369–375. https://doi.org/10.1029/JB082i002p00369.

Reasenberg, R.D., Shapiro, I.I., White, R.D., 1975. The gravity field of Mars. Geophysical Research Letters 2 (3), 89–92.

von Rebeur-Paschwitz, E., 1889. The earthquake of Tokio, April 18, 1889. Nature 40 (25), 294–295. https://doi.org/10.1038/040294e0.

Ringwood, A.E., Clark, S.P., 1971. Internal constitution of Mars. Nature 234, 89–92.
Ritter, A., 1879. Anwendungen der mechanischen Wärmetheorie auf kosmologische Probleme. Carl. Rümpler, Hannover, Germany. 74 pages. Available online: https://books.google.de/books?id=59PLQXTI8lgC&ots=Zgmq49dUey&dq=Ritter%20Untersuchungen%20Annalen%20der%20Physik%20Bd.%203&lr&pg=PA1#v=onepage&q&f=false. (Accessed 17 November 2021).
Rowland, I.D., 2008. Giordano Bruno: Philosopher/Heretic. University of Chicago Press, Chicago, Ill., USA. 335 pages.
Rudolph, E., Szirtes, S., 1914. Über eine neue Laufzeitkurve. Physikalische Zeitschrift, 15. Jahrg. Staats- und Universitätsbibliothek Hamburg, pp. 737–739. Available online: https://resolver.sub.uni-hamburg.de/kitodo/PPN670034223. (Accessed 24 November 2021). (CC BY-SA 4.0 [https://creativecommons.org/licences/by-sa/4.0/deed.de]).
Runcorn, S.K., 1962. Convection in the Moon. Nature 195 (4847), 1150–1151.
Runcorn, S.K., Collinson, D.W., O'Reilly, W., Battey, M.H., Stephenson, A., Jones, J.M., Manson, A.J., Readmyn, P.W., 1970. Magnetic properties of Apollo 11 lunar samples. In: Proceedings of the Apollo 11 Lunar Science Conference, Vol. 3. Geochimica Et Cosmochimica Acta Suppl. 1, vol. 2, 2369–2387.
Russell, C.T., Coleman, P.J. Jr., Goldstein, B.E., 1981. Measurements of the lunar induced magnetic moment in the geomagnetic tail: evidence for a lunar core? In: Proceedings of the Lunar and Planetary Science Conference 12B, pp. 831–836.
Sabadini, R., Vermeersen, B., 2004. Global Dynamics of the Earth. Modern Approaches in Geophysics. Springer, Netherlands. https://doi.org/10.1007/978-94-017-1709-0.
Sacks, I.S., 1967. Diffracted P-wave studies of the Earth's core, 2. Lower mantle velocity, core size, lower mantle structure. Journal of Geophysical Research 72 (10), 2589–2594.
Sacks, S., 1966. Diffracted wave studies of the Earth's core, 1. Amplitudes, core size, and rigidity. Journal of Geophysical Research 71 (4), 1173–1181.
Sanloup, C., Jambon, A., Gillet, P., 1999. A simple chondritic model of Mars. Physics of the Earth and Planetary Interiors 112, 43–54.
Sayles, I., 1888. An inquiry into the state of Earth's interior. The American Naturalist 22 (253), 17–21. Available online: https://www.journals.uchicago.edu/doi/pdf/10.1086/274629. (Accessed 24 June 2021).
Scarth, A., 1989. Volcanic origins of the polyphemus story in the "Odyssey": a non-classicist's interpretation. The Classical World 83 (2), 89–95. https://doi.org/10.2307/4350550.
Schmidt, A., 1888. Wellenbewegung und Erdbeben. Jahreshefte des Vereins für vaterländische Naturkunde in Württemberg 44, 248–270. https://www.biodiversitylibrary.org/item/35766#page/256/mode/1up. https://ia800904.us.archive.org/21/items/jahresheftedesve44vere/jahresheftedesve44vere.pdf. Download 19 Nov. 2021.
Scholz, J.-R., Widmer-Schnidrig, R., Davis, P., Lognonné, P., Pinot, B., Garcia, R.F., Hurst, K., Pou, L., Nimmo, F., Barakaoui, S., de Raucourt, S., Knapmeyer-Endrun, B., Knapmeyer, M., Orhand-Mainsant, G., Compaire, N., Cuvier, A., Beucler, É., Bonnin, M., Joshi, R., Sainton, G., Stutzmann, E., Schimmel, M., Horleston, A., Böse, M., Ceylan, S., Clinton, J., Driel, Martin van, Kawamura, T., Khan, A., Stähler, S.C., Giardini, D., Charalambous, C., Stott, A.E., Pike, W.T., Christensen, U.R., Banerdt, W.B., 2020. Detection, analysis, and removal of glitches from InSight's seismic data from Mars. Earth and Space Science 7, e2020EA001317. https://doi.org/10.1029/2020EA001317.
Schubert, G., Spohn, T., 1990. Thermal history of Mars and the Sulfur content of its core. Journal of Geophysical Research 95 (B9), 14095–14104.
Seager, S., Hui, L., 2002. Constraining the rotation rate of transiting extrasolar planets by oblateness measurements. The Astrophysical Journal 574 (2), 1004–1010. https://doi.org/10.1086/340994.

Seager, S., Kuchner, M., Hier-Majumder, C.A., Militzer, B., 2007. Mass-radius relationships for solid exoplanets. The Astrophysical Journal 669 (2), 1279–1297. https://doi.org/10.1086/521346.

See, T.J.J., 1905a. Researches on the internal densities, pressures, and moments of inertia of the principal bodies of the planetary system. Astronomische Nachrichten 167 (o), 114–142.

See, T.J.J., 1905b. Researches on the physical constitution of the heavenly bodies. Astronomische Nachrichten 169 (21), 321–364. https://doi.org/10.1002/asna.19051692102.

Seneca, 63 CE. Naturales quaestiones / Naturwissenschaftliche Untersuchungen. Transl. O. & E. Schönberger, Reclam, Stuttgart, Germany, 542 pages.

Shimizu, H., Matsushima, M., Takahashi, F., Shibuya, H., Tsnuakawa, H., 2013. Constraint on the lunar core size from electromagnetic sounding based on magnetic field observations by an orbiting satellite. Icarus 222, 32–43. https://doi.org/10.1016/j.icarus.2012.10.029.

Shurcliff, W.A. (Ed.), 1947. Bombs at Bikini. Wm. H. Wise & Co., New York, USA. 212 pages. Available online: https://ia600201.us.archive.org/8/items/bombsatbikinioff00unit/bombsatbikinioff00unit.pdf. (Accessed 29 November 2021).

Siddiqi, A.A., 2018. Beyond Earth. A Chronicle of Deep Space Exploration 1958–2016. In: NASA History Division, Office of Communications. Washington, DC, USA. NASA History Division, Office of Communications, Washington, DC, USA. NASA SP-2018-4041, PDF version. 393 pages. https://www.nasa.gov/sites/default/files/atoms/files/beyond-earth-tagged.pdf. (Accessed 27 April 2021).

Sjogren, W.L., Lorell, J., Wong, L., Downs, W., 1975. Mars gravity field based on a short-arc technique. Journal of Geophysical Research 80 (20), 2899–2908.

Sjogren, W.L., Trask, D.W., Vegos, C.J., Wollenhaupt, W.R., 1966. Physical constants as determined from radio tracking of the Ranger lunar probes Jet Propulsion Laboratory. Technical Report 32-1057. III+22 pages. Available online: https://ntrs.nasa.gov/api/citations/19670012115/downloads/19670012115.pdf. (Accessed 8 February 2022).

Sjogren, 1971. Lunar gravity estimate: independent confirmation. Journal of Geophysical Research 76, 7021–7026.

Slade, M.A., Preston, R.A., Harris, A.W., Skjerve, L.J., Spitzmesser, D.J., 1977. ALSEP-Quasar differential VLBI. The Moon 17, 133–147.

Smallwood, J.R., 2010. Bouguer redeemed: the successful 1737-1740 gravity experiments on Pichincha and Chimborazo. Earth Sciences History 29 (1), 1–25. Available online: https://www.jstor.org/stable/24137124. (Accessed 16 November 2021).

Smith, D.E., Zuber, M.T., Neumann, G.A., 2001. Seasonal variations of snow depth on Mars. Science 294 (5549), 2141–2146. https://doi.org/10.1126/science.1066556.

Smrekar, S.E., Lognonné, P., Spohn, T., Banerdt, W.B., Breuer, D., Christensen, U., Dehant, V., Drilleau, M., Folknoer, W., Fuji, N., Garcia, R.F., Giardini, D., Golombek, M., Grott, M., Gudkova, T., Johnson, C., Khan, A., Langlais, B., Mittelholz, A., Mocquet, A., Myhill, R., Panning, M., Perrin, C., Pike, T., Plesa, A.-C., Rivoldini, A., Samuel, H., Stähler, S.C., van Driel, M., van Hoolst, T., Verhoeven, O., Weber, R., Wieczorek, M., 2019. Pre-mission InSights in the interior of Mars. Space Science Reviews 215 (3). https://doi.org/10.1007/s11214-018-0563-9.

Solomon, S.C., Toksöz, M.N., 1968. On the density distribution in the Moon. Physics of the Earth and Planetary Interiors 1, 475–484.

Sotin, C., Grasset, O., Mocquet, A., 2007. Mass radius curve for extrasolar Earth-like planets and ocean planets. Icarus 191 (1), 337–351. https://doi.org/10.1016/j.icarus.2007.04.006.

Storchak, D.A., Schweitzer, J., Bormann, P., 2003. The IASPEI standard seismic phase list. Seismological Research Letters 74 (6), 761–772.

Strabo, 7 BCE?a. Geography, Books 3–5. Transl. H.L. Jones. Loeb Classical Library, vol. 50. Harvard University Press, Cambridge, Mass., USA, London, GB. 488 pages.

Strabo, 7 BCE?b. Geography, Books 6–7. Transl. H.L. Jones. Loeb Classical Library, vol. 182. Harvard University Press, Cambridge, Mass., USA, London, GB. 401 pages.

Stähler, S.C., Khan, A., Banerdt, W.B., Lognonné, P., Giardini, D., Ceylan, S., Drileau, M., Duran, A.C., Garcia, R.F., Huang, Q., Kim, D., Lekić, V., Samuel, H., Schimmel, M., Schmerr, N., Sollberger, D., Stutzmann, E., Xu, Z., Antonangeli, D., Charalambous, C., Davis, P.M., Irving, J.C.E., Kawamura, T., Knapmeyer, M., Maguire, R., Marusiak, A.G., Panning, M.P., Perrin, C., Plesa, A.-C., Rivoldini, A., Schmelzbach, C., Zenhäusern, G., Beucler, E., Clinton, J., Dahmen, N., van Driel, M., Gudkova, T., Horleston, A., Pike, W.T., Plasman, M., Smrekar, S.E., 2021. Seismic detection of the martian core. Science 373 (6553), 443–448. https://doi.org/10.1126/science.abi7730.

Stähler, S.C., Knapmeyer, M., 2022. Seismology of the Solar System. In: Geophysical Exploration of the Solar System. In: Schmelzbach, C., Stähler, C. (Eds.), Advances in Geophysics, vol. 63. This volume.

Suárez-Andrés, L., Israelian, G., González Hernández, J.I., Adibekyan, V.Zh., Delgado Mena, E., Santos, N.C., Sousa, S.G., 2018. C/O vs. Mg/Si ratios in solar type stars: the HARPS sample. Astronomy & Astrophysics 614. https://doi.org/10.1051/0004-6361/201730743.

Taylor, P.W., 1995. Myths, legends and volcanic activity: an example from northern Tonga. The Journal of the Polynesian Society 104 (3), 323–346.

Taylor, S., 1993. Early accretional history of the Earth and the Moon-forming event. Lithos 30 (3–4), 207–221. https://doi.org/10.1016/0024-4937(93)90036-C.

Thiabaud, A., Marboeuf, U., Alibert, Y., Leya, I., Mezger, K., 2015. Elemental ratios in stars vs planets. Astronomy & Astrophysics 580. https://doi.org/10.1051/0004-6361/201525963.

Thomson, W., 1863. XXVII. On the rigidity of the Earth. Philosophical Transactions of the Royal Society 153. https://doi.org/10.1098/rstl.1863.0027.

Tobie, G., Grasset, O., Dumoulin, C., Mocquet, A., 2019. Tidal response of rocky and ice-rich exoplanets. Astronomy & Astrophysics 630. https://doi.org/10.1051/0004-6361/201935297.

Tobie, G., Mocquet, A., Sotin, C., 2005. Tidal dissipation within large icy satellites: applications to Europa and Titan. Icarus 177 (2), 534–549. https://doi.org/10.1016/j.icarus.2005.04.006.

Toksöz, M.N., Dainty, A.M., Solomon, S.C., Anderson, K.R., 1974. Structure of the Moon. Reviews of Geophysics and Space Physics 12 (4), 539–567.

Trumpler, R.J., 1927. Observations of Mars at the opposition of 1924. Lick Observatory Bulletin 387, 19–45.

Unterborn, C.T., Dismukes, E.E., Panero, W.R., 2016. Scaling the Earth: a sensitivity analysis of terrestrial exoplanetary interior models. The Astrophysical Journal 819, 32. https://doi.org/10.3847/0004-637x/819/1/32.

Valencia, D., O'Connell, R.J., Sasselov, D., 2006. Internal structure of massive terrestrial planets. Icarus 181 (2), 545–554. https://doi.org/10.1016/j.icarus.2005.11.021.

Valencia, D., Sasselov, D.D., O'Connell, R.J., 2007a. Radius and structure models of the first super-Earth planet. The Astrophysical Journal 656 (1), 545–551. https://doi.org/10.1086/509800.

Valencia, D., Sasselov, D.D., O'Connell, R.J., 2007b. Detailed models of super-earths: how well can we infer bulk properties? The Astrophysical Journal 665 (2), 1413–1420. https://doi.org/10.1086/519554.

Vermij, R., 1998. Subterranean fire. Changing theories of the Earth during the Renaissance. Early Science and Medicine 3 (4), 323–347.

Verne, J., 1864. Voyage au centre de la terre. J. Hetzel. 342 pages, Bibliothèque nationale de France, département Littérature et art, Y2-72900. https://gallica.bnf.fr/ark:/12148/bpt6k1340157. (Accessed 10 November 2021).

Verne, J., 1869. 20000 Meilen unter den Meeren. (Vingt mille lieues sous les mers, German translation V. Dehs). Deutscher Taschenbuchverlag, München, Germany. 759 pages.

Viswanathan, V., Rambaux, N., Fienga, A., Laskar, J., Gastineau, M., 2019. Observational constraint on the radius and oblateness of the lunar core-mantle boundary. Geophysical Research Letters 46, 7295–7303. https://doi.org/10.1029/2019GL082677.

Weber, R.C., Lin, P.-Y., Garnero, E.J., Williams, Q., Lognonné, P., 2011. Seismic detection of the Lunar Core. Science 331, 309–312. https://doi.org/10.1126/science.1199375.

Wichmann, M., 1848. Erster Versuch zur Bestimmung der physischen Libration des Mondes aus Beobachtungen mit dem Heliometer, angestellt und berechnet von Dr. Moritz Wichmann. Astronomische Nachrichten 26 (621), 322–336.

Wiechert, E., 1896. Ueber die Beschaffenheit des Erdinnern, Bericht über die in den Sitzungen der Physikalisch-ökonomischen Gesellschaft zu Königsberg i. Pr. im Jahre 1896 gehaltenen Vorträge. Schriften der Physikalisch-ökonimischen Gesellschaft zu Königsberg 37.

Wiechert, E., 1897. Ueber die Massenvertheilung im Inneren der Erde. Nachrichten von der Gesellschaft der Wissenschaften zu Göttingen, Mathematisch-Physikalische Klasse 3, 221–243.

Wiechert, E., Zoeppritz, K., 1907. Über Erdbebenwellen. Nachrichten von der Gesellschaft der Wissenschaften zu Göttingen, Mathematisch-Physikalische Klasse 1907, 415–549. https://gdz.sub.uni-goettingen.de/download/pdf/PPN252457811_1907/PPN252457811_1907.pdf, 1907. Download 15.06.2021.

Wieczorek, M.A., Neumann, G.A., Nimmo, F., Kiefer, W.S., Taylor, G.J., Melosh, H.J., Phillips, R.J., Solomon, S.C., Andrews-Hanna, J.C., Asmar, S.W., Konopliv, A.S., Lemoine, F.G., Smith, D.E., Watkins, M.W., Williams, J.G., Zuber, M.T., 2013. The crust of the Moon as seen by GRAIL. Science 339, 671–675. https://doi.org/10.1126/science.1231530.

Wieczorek, M., Zuber, M.T., 2002. The "Core" of the Moon: iron or titanium rich? In: Lunar and Planetary Science Confernce XXXIII. Abstract No. 1384, 11–15 March 2002, League City, TX, USA.

Wildt, R., 1947. Reports on the progress of astronomy. The constitution of the planets. Monthly Notices of the Royal Astronomical Society 107 (1), 84–107.

Williams, J.G., Boggs, D.H., 2008. Lunar core and mantle. What does LLR see? In: Proceedings of the 16th International Workshop on Laser Ranging. 12–17 Oct. 2008, Poznan, Poland, Vol. 1317.

Williams, J.G., Boggs, D.H., Ratcliff, J.T., 2005. Lunar fluid core and solid-body tides. In: Lunar and Planetary Science Conference XXXVI. Abstract 1503.

Williams, J.G., Boggs, D.H., Ratcliff, J.T., 2006. Lunar interior results and possibilities. In: Lunar and Planetary Science Conference XXXVII. Abstract 1229.

Williams, J.G., Boggs, D.H., Ratcliff, J.T., 2007. Lunar mantle and fluid core results and inner core possibilities. In: Lunar and Planetary Science Conference XXXVIII. Abstract 2004.

Williams, J.G., Boggs, D.H., Ratcliff, J.T., 2008. Lunar mantle and fluid core results and inner core possibilities. In: Lunar and Planetary Science Conference XXXIX. Abstract 1484.

Williams, J.G., Konopliv, A.S., Boggs, D.H., Park, R.S., Yuan, D.-N., Lemoine, F.G., Goossens, S., Mazarico, E., Nimmo, F., Weber, R.C., Asmar, S.W., Melosh, H.J., Neumann, G.A., Phillips, R.J., Smith, D.E., Solomon, S.C., Watkins, M.M., Wieczorek, M.A., Andrews-Hanna, J.C., Head, J.W., Kiefer, W.S., Matsuyama, I., McGovern, P.J., Taylor, G.J., Zuber, M.T., 2014. Lunar interior properties from the GRAIL

mission. Journal of Geophysical Research 119, 1546–1578. https://doi.org/10.1002/2013JE004559.
Wiskerchen, M.J., Sonett, C.P., 1977. A lunar metal core? In: Proceedings of the Lunar Science Conference 8th, pp. 515–535.
Wood, R.M., 1988. Robert Mallet and John Milne – earthquakes incorporated in Victorian Britain. Earthquake Engineering and Structural Dynamics 17, 107–142.
Wood, C.A., Ashwal, L.D., 1981. SNC meteorites: igneous rocks from Mars? In: Proceedings of the Lunar and Planetary Science Conference, 12B, pp. 1359–1375.
Wootton, D., 2009. New light on the composition and publication of the Sidereus Nuncius. Galileana VI, 123–140.
Wootton, D., 2015. The Invention of Science. A New History of the Scientific Revolution. Allen Lane, Penguin Random House, UK. 769 pages.
Wright, W.H., 1924. Photographs of Mars made with light of different colors. Publications of the Astronomical Society of the Pacific XXXVI (213), 239–254.
Yoder, C.F., Konopliv, A.S., Yuan, D.N., Standish, E.M., Folkner, W.M., 2003. Fluid core size of Mars from detection of the solar tide. Science 300 (5617), 299–303. https://doi.org/10.1126/science.1079645.
Yoder, C.F., Standish, E.M., 1997. Martian precession and rotation from Viking lander range data. Journal of Geophysical Research 102 (E2), 4065–4080.
Zapolsky, H.S., Salpeter, E.E., 1969. The mass-radius relation for cold spheres of low mass. The Astrophysical Journal 158, 809. https://doi.org/10.1086/150240.
Zeng, L., Jacobsen, S.B., 2017. A simple analytical model for rocky planet interiors. The Astrophysical Journal 837 (2). https://doi.org/10.3847/1538-4357/aa6218.
Zeng, L., Sasselov, D., 2013. A detailed model grid for solid planets from 0.1 through 100 Earth masses. Publications of the Astronomical Society of the Pacific 125 (925), 227. https://doi.org/10.1086/669163.
Zeng, L., Sasselov, D.D., Jacobsen, S.B., 2016. Mass-radius relation for rocky planets based on PREM. The Astrophysical Journal 819 (2). https://doi.org/10.3847/0004-637X/819/2/127.
Zharkov, V.N., Gudkova, T.V., 2000. Interior structure models, Fe/Si ratio and parameters of figure for Mars. Physics of the Earth and Planetary Interiors 117, 407–420.
Zharkov, V.N., Sobisevich, A.L., 2005. Moments of inertia and the chandlerian period for two- and three-layer models of the Galilean satellite Io. Astronomy Letters 31 (3), 205–212. https://doi.org/10.1134/1.1883352.
Zhong, Z., Zhang, T., Duan, L., Li, Y., Zhu, H., 2021. Estimation of the size and composition of the lunar core based on the gravity field model GL1500E and LLR physical libration parameters [J]. Geomatics and Information Science of Wuhan University 46 (2), 238–243. https://doi.org/10.13203/j.whugis20190124 (in Chinese).
Zhu, W., Huang, C.X., Zhou, G., Lin, D.N.C., 2014. Constraining the oblateness of Kepler planets. The Astrophysical Journal 796 (1). https://doi.org/10.1088/0004-637X/796/1/67.
Zoeppritz, K., Geiger, Gutenberg, B., 1912. Über Erdbebenwellen V. Konstitution des Erdinnern, erschlossen aus dem Bodenverrückungsverhältnis der einmal reflektierten zu den direkten longitudinalen Erdbebenwellen, und einige andere Beobachtungen ueber Erdbebenwellen. Nachrichten von der Gesellschaft der Wissenschaften zu Göttingen, Mathematisch-Physikalische Klasse 1912, 121–206. Online: https://gdz.sub.uni-goettingen.de/download/pdf/PPN252457811_1912/LOG_0022.pdf. Download 15.06.2021.
Zoeppritz, K., Geiger, L., 1909. Ueber Erdbebenwellen. III. Berechnung von Weg und Geschwindigkeit der Vorläufer. Die Poissonsche Konstante im Erdinnern. Nachrichten von der Gesellschaft der Wissenschaften zu Göttingen, Mathematisch-Physikalische Klasse 1909, 400–428. https://gdz.sub.uni-goettingen.de/download/pdf/PPN252457811_1909/PPN252457811_1909.pdf. Download 15.06.2021.

Zuber, M., Smith, D.E., 1997. Mars without Tharsis. Journal of Geophysical Research 102 (E12), 28673–28685.

Zöppritz, K., 1881. Ueber die Mittel und Wege zu besserer Kenntniss vom inneren Zustand der Erde zu gelangen. Verhandlungen des Ersten Deutschen Geographentages zu Berlin am 7. und 8. Juni 1881, vol. 16. Dietrich Reimer, Berlin, pp. 15–28. Available online: https://www.google.de/books/edition/Verhandlungen_des_Deutschen_Geographenta/bR77PLMV2AIC?hl=de&gbpv=0. (Accessed 16 November 2021).

de Vaucouleurs, G., Blunck, J., Davies, M., Dollfus, A., Koval, I.K., Kuiper, G.P., Masursky, H., Miyamoto, S., Moroz, V.I., Sagan, C., Smith, B., 1975. The new Martian nomenclature of the International Astronomical Union. Icarus 26, 85–98.

van Flandern, T.C., 1968. A preliminary report on a lunar latitude fluctuation. In: Mulholland, J.D. (Ed.), Proceedings of the JPL Seminar on Uncertainties in the Lunar Ephemeris. Pasadena, CA, USA, 20 July 1967. Jet Propulsion Laboratory Technical Report TR 32-1247, Pasadena, CA, USA. VII+34 pages. Available online: https://ntrs.nasa.gov/citations/19680014724. (Accessed 9 February 2022).

CHAPTER FOUR

Interior dynamics and thermal evolution of Mars – a geodynamic perspective

Ana-Catalina Plesa[a,*], **Mark Wieczorek**[b], **Martin Knapmeyer**[a], **Attilio Rivoldini**[c], **Michaela Walterová**[a], **and Doris Breuer**[a]

[a]DLR Institute of Planetary Research, Berlin, Germany
[b]Université Côte d'Azur, Observatoire de la Côte d'Azur, CNRS, Laboratoire Lagrange, Nice, France
[c]Royal Observatory of Belgium, Brussels, Belgium
*Corresponding author: e-mail address: Ana.Plesa@dlr.de

Contents

1. Introduction

A variety of numerical modeling studies have been used to investigate the thermal evolution and interior dynamics of Mars (see Breuer and Moore, 2015; Smrekar et al., 2019, for a review). These studies use either fully dynamical 2D/3D simulations that self-consistently model the evolution of mantle flow and through their nature can address local output quantities in regions of interest or 1D parametrized models that track the evolution of global quantities, such as the global mantle temperature or the average surface heat flow. Fully dynamical 2D and 3D models have been used to predict the surface heat flow and seismicity distribution on present-day Mars (Plesa et al., 2016, 2018a), the effects of impacts during the early thermochemical history (Ruedas and Breuer, 2017; Roberts and Arkani-Hamed, 2017), partial melting and crust-mantle differentiation (Ruedas et

Advances in Geophysics, Volume 63
ISSN 0065-2687
https://doi.org/10.1016/bs.agph.2022.07.005

al., 2013; Plesa and Breuer, 2014), and the formation of the martian crustal thickness dichotomy (Keller and Tackley, 2009; Golabek et al., 2011). On the other hand, 1D parametrized thermal evolution models have been applied to investigate the crustal formation and crust-mantle differentiation (Hauck and Phillips, 2002; Breuer and Spohn, 2006; Morschhauser et al., 2011), as well as mantle degassing (Fraeman and Korenaga, 2010; Grott et al., 2011), the magnetic field evolution (Breuer and Spohn, 2003; Williams and Nimmo, 2004), the thermal state of the lithosphere (Grott and Breuer, 2008; Thiriet et al., 2018), and the coupled thermal-orbital evolution of Mars and its moon Phobos (Samuel et al., 2019).

With the arrival of the InSight mission in 2018 (Banerdt et al., 2020), a new chapter of planetary geophysics has begun. Equipped with a seismometer (SEIS, Lognonné et al., 2020), a heat flow probe (HP^3, Spohn et al., 2018) and X-band telecommunication capabilities that allow to precisely measure the rotation of Mars (RISE, Folkner et al., 2018), InSight investigates the interior of Mars from its core to the surface.

InSight's measurements represent the most direct set of constraints for the interior of Mars. The crustal thickness (Knapmeyer-Endrun et al., 2021), the thickness and thermal state of the lithosphere (Khan et al., 2021), and the size of the core (Stähler et al., 2021) provide important information for modeling of thermal evolution and investigating physical processes active in the interior of Mars. In turn, numerical models of the thermal evolution combined with InSight measurements can be used to constrain poorly known parameters, such as the rheology of the mantle, distribution of heat producing elements (HPEs) between the mantle and crust, and the evolution of the surface and core-mantle boundary (CMB) heat flows. Previous 1D models that used inversion techniques for the interior structure, composition, and thermal state of the mantle or made assumptions of the present-day thermal structure have made predictions about the seismic structure of the martian mantle (e.g., Khan et al., 2018; Zheng et al., 2015; Gudkova and Zharkov, 2004; Sohl and Spohn, 1997; Mocquet et al., 1996). More recent thermal evolution models have directly addressed the seismic observations of InSight. These models investigated the effects of crustal thickness and its enrichment in HPEs on the thermal evolution and present-day partial melt distribution in the interior of Mars (Knapmeyer-Endrun et al., 2021), studied the consequences of a molten layer at the base of the mantle on the thermal history and core size measurements (Samuel et al., 2021), and estimated seismic velocities variations due to the interior temperature distribution (Plesa et al., 2021).

In this study we focus on 3D thermal evolution models and discuss results presented in previous studies and new simulations in the framework of the recent InSight data about the martian crust, mantle, and core. In Section 2 we review the mathematical equations used by geodynamic models to calculate the thermal evolution of Mars. Section 3 presents the effects of the crustal thickness variations on model predictions for heat flow and elastic lithospheric thickness variations, as well as on the distribution of partial melt zones in the mantle. The dynamics inside the martian mantle, seismic velocities variations due to mantle thermal anomalies, and constraints from tidal deformation are discussed in Section 4. In Section 5 we list the core size estimates from geodetic data and seismic observations and discuss their consequence on the mantle dynamics and convection pattern. The seismogenic layer thickness and the present-day seismicity are discussed in Section 6. In the last section (Section 7) we present a summary of geodynamic models and their findings and suggest future investigations.

We discuss in detail selected models that are compatible with the crustal thickness and core radius estimates that were derived from InSight's seismic measurements. Throughout this study we illustrate how model results can be related to available geological and geophysical observations. For our models we use both global constraints such as the thermal lithosphere thickness (Khan et al., 2021) and estimates of the tidal deformation of Mars (Genova et al., 2016; Konopliv et al., 2016, 2020), as well as local data sets, such as the present-day elastic lithosphere thicknesses at the north and south poles (Phillips et al., 2008; Wieczorek, 2008; Broquet et al., 2020, 2021) and the location of partial melt that could explain recent volcanic activity in Tharsis and Elysium volcanic centers. We highlight how our knowledge of the thermal history and present-day state of the interior has improved with the recent InSight results and discuss what future models need to address in order to further constrain the thermal evolution of Mars. Current geodynamic modeling will also help to identify scientifically interesting landing sites for a future seismic network that may become available after 2030 (Stähler and Knapmeyer, 2022).

2. Geodynamic modeling and thermal evolution of Mars

Geodynamic models that are used to investigate the interior dynamics of rocky planets in general, and of Mars in particular, numerically solve for a set of conservation equations. While a 3D spherical geometry is the choice

for investigating the convection pattern in the interior and relating the results to local observations, 2D models have the advantage of being computationally faster making it possible to test a larger parameter space with a higher spatial resolution compared to their 3D counterparts. The equations and parameters used in these models are typically nondimensional. They are scaled with the mantle thickness D as length scale, a reference thermal diffusivity κ as time scale, and the initial temperature difference ΔT across the mantle as temperature scale, although some codes use dimensional quantities (Kronbichler et al., 2012; Heister et al., 2017). The advantage of the nondimensionalization is that characteristic dimensionless numbers such as the Rayleigh number, which is defined as the ratio between parameters driving convection and those opposing it, can be used to describe the convection system without needing to know the exact detailed parameters of a simulation.

The system of equations that is solved includes the conservation of mass, linear momentum and thermal energy (e.g., Schubert et al., 2001). Their nondimensional formulation for a system assuming a Newtonian rheology, an infinite Prandtl number as appropriate for high viscosity media with negligible inertia, a variable thermal expansivity and conductivity, using the Extended Boussinesq Approximation (EBA), and including solid-solid phase transitions read (e.g., Christensen and Yuen, 1985):

$$\nabla \cdot \vec{u} = 0, \quad (1)$$

$$\nabla \cdot \left[\eta(\nabla \vec{u} + (\nabla \vec{u})^T)\right] - \nabla p + (Ra\alpha T - \textstyle\sum_{l=1}^{3} Rb_l \Gamma_l)\vec{e}_r = 0, \quad (2)$$

$$\frac{DT}{Dt} - \nabla \cdot (k \nabla T) - Di\alpha(T + T_0)u_r - \frac{Di}{Ra}\Phi - \textstyle\sum_{l=1}^{3} Di \frac{Rb_l}{Ra} \frac{D\Gamma_l}{Dt} \gamma_l (T + T_0) - H = 0, \quad (3)$$

where $\vec{u}$ is the velocity vector, u_r is its radial component, η is the viscosity, p is the dynamic pressure, α is the thermal expansivity, T is the temperature, $\vec{e}_r$ is the unit vector in radial direction, t is the time, k is the thermal conductivity, Di is the dissipation number, and $\Phi \equiv \underline{\tau} : \underline{\dot{\varepsilon}}/2$ is the viscous dissipation, where $\underline{\tau}$ and $\underline{\dot{\varepsilon}}$ are the deviatoric stress and strain-rate tensors, respectively.

The Rayleigh number that describes the vigor of convection, the internal heating rate H that controls the mantle heating due to radioactive elements (HPEs), and the dissipation number Di that accounts for the increase of temperature due to adiabatic compression effects are defined as

follows:

$$Ra = \frac{\rho g \alpha \Delta T D^3}{\eta \kappa}, \qquad H = \frac{\rho Q_{HPE} D^2}{k \Delta T}, \qquad Di = \frac{\alpha g D}{c_p}, \tag{4}$$

where g is the gravitational acceleration, c_p is the mantle heat capacity, and Q_{HPE} is the heat production rate in W kg^{-1}.

Previous geodynamic models accounted for two exothermic phase transitions, and, in case of a small core radius, for an additional endothermic phase change. While exothermic phase transitions tend to accelerate mantle flow, the endothermic one slows it down and promotes layered convection. In particular, the endothermic phase transition from wadsleyite/ringwoodite to bridgmanite has been suggested to affect the style of convection. This phase transition significantly changes the CMB heat flow and leads to a low degree convection pattern that was proposed by previous studies to explain the formation of the Tharsis volcanic province (Harder and Christensen, 1996; Breuer et al., 1998; Spohn et al., 1998; Van Thienen et al., 2006). However, this phase transition is not relevant for models with a core radius of 1700 km or larger, and in these scenarios the convection in the mantle is characterized by more than one plume (Spohn et al., 1998; Michel and Forni, 2011).

One of the most important parameters in geodynamic models is the mantle viscosity, which is temperature and pressure dependent and follows an Arrhenius law. Its nondimensional formulation (e.g., Roberts and Zhong, 2006) reads:

$$\eta(T, z) = \exp\left(\frac{E + zV}{T + T_0} - \frac{E + z_{ref} V}{T_{ref} + T_0}\right), \tag{5}$$

where z is the depth, E and V are the activation energy and activation volume, respectively, T_0 is the nondimensional surface temperature, and z_{ref} and T_{ref} are the reference depth and temperature where the reference viscosity is attained. The temperature dependence of the viscosity is controlled by the activation energy while the pressure dependence by the activation volume (e.g., Karato and Wu, 1993; Hirth and Kohlstedt, 2003).

At the temperature and pressure conditions of planetary mantles the viscosity varies over orders of magnitude and is the parameter primarily controlling the vigor of convection, the formation of a stagnant lid – an immobile layer at the top of the convecting mantle caused by the strong increase of viscosity with decreasing temperature –, and the convection

pattern in the mantle. The latter is sensitive to the increase of the viscosity with depth, and may result in a low degree convection pattern for a strong depth-dependent viscosity or a sudden viscosity increase (i.e., a viscosity jump) in the mid-mantle (Roberts and Zhong, 2006; Keller and Tackley, 2009). Such a convection pattern has been previously proposed to explain the crustal thickness dichotomy and focused volcanic activity in Tharsis, which is the largest volcano-tectonic region on Mars (e.g., Harder and Christensen, 1996; Breuer et al., 1998; Zhong and Zuber, 2001; Roberts and Zhong, 2006; Keller and Tackley, 2009).

Geodynamic thermal evolution models account for the decay of radioactive elements with time and employ a cooling boundary condition at the CMB. Using a 1-D energy balance the evolution of the CMB temperature is calculated under the assumption of a constant core density and heat capacity (Stevenson et al., 1983; Steinbach and Yuen, 1994):

$$c_c \rho_c V_c \frac{dT_{CMB}}{dt} = -q_c A_c, \tag{6}$$

where c_c, ρ_c, and V_c are the core heat capacity, core density, and core volume, respectively. T_{CMB} and q_c are the temperature and the heat flow at the CMB, respectively, while A_c is the CMB area.

Geodynamic models have been employed in previous studies to investigate the effects of crustal thickness variations, as derived from gravity and topography data, on the surface heat flow variations and the thermal state of the lithosphere (Plesa et al., 2016, 2018b). The crust in these studies does not change with time, but varies spatially according to the chosen crustal thickness model (Wieczorek and Zuber, 2004; Wieczorek et al., 2022). Results show that the crustal thickness variations and the crustal enrichment in HPEs control the surface heat flow distribution at present day, the thickness of the lithosphere and the lithospheric temperature variations. In addition to global output quantities such as the average lithosphere thickness, average surface and CMB heat flows and average mantle temperature, these models can provide local values that can be compared to regional estimates. This is essential to evaluate constraints provided by local measurements and helps to put regional scale data in a global context.

3. Crustal thickness estimates, partial melting, and the thermal state of the lithosphere

The thickness of the crust provides important constraints for later planetary differentiation after core formation and for the overall thermal evolution of the mantle. The crust that is built after the initial differentiation of the planet and the crystallization of a potential magma ocean records the magmatic activity through time, as it is formed by partial melting of the mantle. During mantle melting, incompatible elements such as heat producing elements ($U^{235,238}$, K^{40}, and Th^{242}) and volatiles (e.g., H_2O and CO_2) are preferentially enriched in the melt. The melt, due to its lower density compared to the surrounding mantle rises to the surface, where it crystallizes and produces the crust. While volatiles, such as H_2O and CO_2 are released in the atmosphere, the heat producing elements (HPEs) remain stored in the crust that becomes more enriched than the primitive mantle.

On Mars, the bulk of the crust has been built during the early history (Greeley and Schneid, 1991; Nimmo and Tanaka, 2005) with an intense volcanic activity during Noachian. Over time, volcanic activity declined and became more focused in Tharsis and Elysium, the largest volcanic provinces on Mars. Young lava flows in both Tharsis (Neukum et al., 2004; Hauber et al., 2011) and Elysium (Vaucher et al., 2009) indicate that Mars has remained volcanicaly active over most of its history and that partial melt production in the planet's interior may be ongoing. The crustal heat production rate that was derived from the surface abundances of thorium and potassium recorded by the gamma-ray spectrometer (GRS) on board Mars Odyssey (Taylor et al., 2006a) indicates a higher crustal enrichment factor compared to typical values for mid-ocean ridge basalts on Earth (Kaula et al., 1981). The GRS data shows also a rather homogeneous distribution with crustal thorium abundances between 0.2 and 1 ppm (Taylor et al., 2006b), indicating much smaller variations than those observed on the Moon (Lawrence et al., 2000). Based on this rather homogeneous distribution of thorium and potassium at the surface of Mars and assuming that the surface abundance of HPEs is representative for the entire crust, it was suggested that crustal thickness variations have a stronger effect on the crustal heat flow variations (Hahn et al., 2011).

Perhaps the most prominent geological feature on Mars is the crustal dichotomy. The cause for the difference in elevation and crustal thickness between the southern highlands and the northern lowlands is poorly known. Crustal thickness models that can explain the gravity and topography data are nonunique. While an anchor point given by a crustal thickness

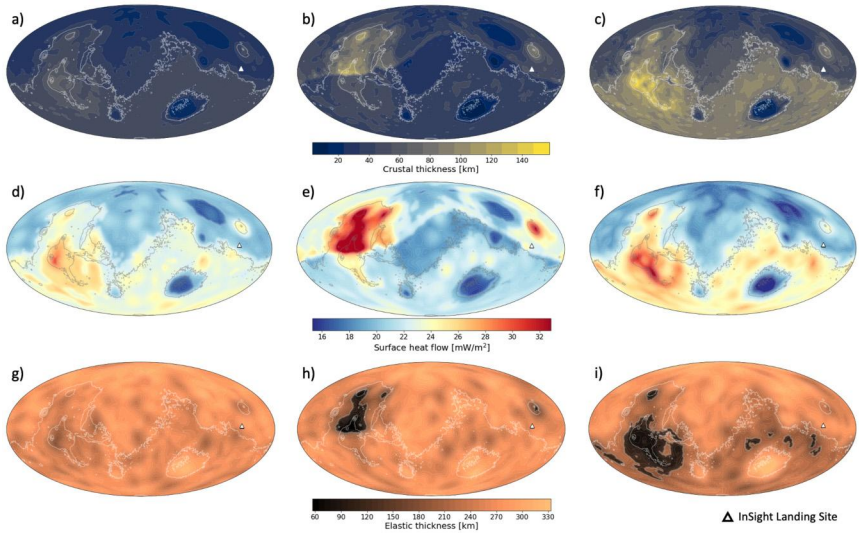

Figure 1 Distribution of the crustal thickness (a, b, and c), associated heat flow variations (d, e, and f) and elastic lithosphere thickness (g, h, and i) at present day. Panels a, d, and g show the thin crustal thickness end-member with an average crustal thickness of 40.6 km and a crustal density of 2550 kg m^{-3}. Panels b, e, and h present a crustal thickness model with and average thickness of 43.1 km and a density difference between northern lowlands (3000 kg m^{-3}) and southern highlands (2600 kg m^{-3}). In panels c, f, and i an end-member model with an average crustal thickness of 71.4 km and a crustal density of 3000 kg m^{-3}. The white and gray contour lines show the 0 km level of surface topography obtained from the Mars Orbiter Laser Altimeter (MOLA) on board Mars Global Surveyor (MGS).

value at a known location can help to constrain these models, one major assumption that remains is the density of the crust and how it varies laterally (Wieczorek et al., 2022). When considering different crustal densities for the northern lowlands and southern highlands, the difference in crustal thickness across the dichotomy boundary can be small (Fig. 1a), entirely absent (Fig. 1b), or clearly visible (Fig. 1c).

Seismic data from the InSight mission have been used to determine the crustal thickness at the InSight landing site (Knapmeyer-Endrun et al., 2021). In the initial receiver function analyses, which are sensitive to the local crustal structure beneath the Insight lander (Knapmeyer-Endrun et al., 2021), two possible crustal models were permissible: a two layer crust based on two strong seismic discontinuities below the surface at depths of about 8 and 20 km, or a three layer crust that included a third weaker discontinuity recorded in the data at about 39 km depth. These seismic

constraints can be used in combination with gravity and topography data to construct global crustal thickness models of the planet (Wieczorek and Zuber, 2004; Wieczorek et al., 2022). For the two layer model, such modeling predicts an average crustal thickness somewhere between 24 and 38 km (Knapmeyer-Endrun et al., 2021), whereas for the three layer model the average thickness is predicted to be between 30 and 72 km (Wieczorek et al., 2022). We note that the range of crustal thicknesses in Wieczorek et al. (2022) for the three layer model is slightly larger than the range of 39 to 72 km presented in Knapmeyer-Endrun et al. (2021). This is because the initial study considered that the density of the crust was laterally homogeneous, whereas the latter study considered cases where the density of the crust could differ across the dichotomy boundary.

While none of the two crustal thickness models (two layer or three layer) can be currently excluded based on the receiver function analysis, thermal evolution models typically produce a thicker crust than the average crustal thickness predicted by the two layer model (Knapmeyer-Endrun et al., 2021). Moreover, a recent study by Kim et al. (2021) that analyzed free-surface multiples of the P-wave and combined these with receiver function analysis also favors the three layer crust scenario. Therefore here we will discuss only models using the three layer crust scenario.

In Fig. 1 we show three crustal thickness models that match the gravity and topography data, and that are anchored at the InSight landing site by the three layer crustal thickness derived from the seismic observations. The crustal thickness models represent end-members in terms of crustal densities and crustal thicknesses. The thinnest crust uses a crustal thickness at the InSight landing site of 31 km and the lowest considered crustal density of 2550 $\mathrm{kg\,m^{-3}}$ (Fig. 1a) leading to an average crustal thickness of 40.6 km. An end-member model with a crustal thickness of 49 km at the InSight landing site and the highest crustal density value of 3000 $\mathrm{kg\,m^{-3}}$ (Fig. 1c) leads to an average crustal thickness of 71.4 km. In addition to the two end-member models, Fig. 1b shows another model that uses a crustal thickness at InSight landing site of 47 km and different densities for the northern lowlands (3000 $\mathrm{kg\,m^{-3}}$) and southern highlands (2600 $\mathrm{kg\,m^{-3}}$). This model has an average crustal thickness of 43.1 km. In this case, the dichotomy in crustal density largely erases the crustal thickness dichotomy that is prominent in the other two models in Fig. 1a and c.

Previously, crustal thickness models have been combined with geodynamic models to investigate the effects of crustal thickness variations on the surface heat flow variations and thermal state of the lithosphere (Plesa et

al., 2016, 2018b). These models show that crustal thickness variations are the main contributions to the heat flow variations and mantle plumes have only a minor effect (Plesa et al., 2016). Here we discuss 3D thermal evolution calculations similar to Plesa et al. (2016, 2018b) that include updated crustal thickness models, which have been constrained by InSight seismic data. A list of the parameters used in the geodynamic simulations is shown in Table 1, while details of the crustal thickness modeling are discussed in Wieczorek et al. (2022) and crustal parameters are shown in Table 2.

In the absence of direct heat flow measurements, the elastic lithosphere thickness at various times and locations can be used as a proxy for the surface heat flow, as it can be linked to the thermal state of the lithosphere. The elastic thickness characterizes the stiffness of the lithosphere in response to loading and can be related to the mechanical thickness, given a rheological model. The mechanical thickness is directly linked to the thermal state of the lithosphere, since it can be identified with an isotherm (McNutt, 1984) and thus, it can be directly compared to lithospheric temperatures from thermal evolution models (Fig. 1). This comparison can be performed at

Table 1 Parameters used in the geodynamic models in Fig. 1.

Symbol	Description	Value
D	Mantle thickness	1550 km
T_{ref}	Reference temperature	1600 K
p_{ref}	Reference pressure	3×10^9 Pa
E	Activation energy	3×10^5 J mol^{-1}
V	Activation volume	10×10^{-6} m^3 mol^{-1}
T_{init}	Initial mantle temperature	1800 K
ΔT	Initial temperature drop across the mantle	2000 K
α	Reference thermal expansivity	2.5×10^{-5} K^{-1}
η	Reference viscosity	10^{21} Pa s
c_p	Mantle heat capacity	1142 J kg^{-1} K^{-1}
ρ	Mantle density	3500 kg m^{-3}
c_c	Core heat capacity	850 J kg^{-1} K^{-1}
ρ_c	Core density	6000 kg m^{-3}
g	Surface gravity acceleration	3.72 m s^{-2}
k	Mantle thermal conductivity	4 W m^{-1} K^{-1}
k_{cr}	Crust thermal conductivity	3 W m^{-1} K^{-1}
κ	Mantle thermal diffusivity	1×10^{-6} m^2 s^{-1}
Q	Total initial radiogenic heating (mantle and crust)	23.33×10^{-12} W kg^{-1}

Table 2 Parameters of the crustal thickness models shown in Fig. 1. A detailed description of the crustal thickness models is presented in Wieczorek et al. (2022). ρ_N and ρ_S are the densities of the northern lowlands and southern highlands, respectively, avg. d_c is the average crustal thickness, min. d_c and max. d_c are the minimum and the maximum crustal thickness values, and $d_c^{InSight}$ is the crustal thickness at InSight location.

Model	ρ_N [kg m^{-3}]	ρ_S [kg m^{-3}]	avg. d_c [km]	min. d_c [km]	max. d_c [km]	$d_c^{InSight}$ [km]
Thin crust	2550	2550	40.6	11.7	72.4	31
Density dichotomy crust	3000	2600	43.1	2.9	130.4	47
Thick crust	3000	3000	71.4	5.0	157.2	49

various times during the evolution and at different locations, depending on the time and location, for which elastic thickness estimates are available.

The base of the mechanical lithosphere can be calculated following the approach of Grott and Breuer (2008) and Plesa et al. (2016, 2018a) and assuming a bounding stress of σ_B of the order of 10^7 Pa (Grott and Breuer, 2010; Burov and Diament, 1995), which gives the temperature associated with ductile failure:

$$T_e = \frac{E}{R}\left[\log\left(\frac{\sigma_B^n A}{\dot{\varepsilon}}\right)\right]^{-1}, \tag{7}$$

where E, A, and n are rheological parameters, R is the gas constant, and $\dot{\varepsilon}$ is the strain rate. A list of the rheological parameters used to calculate the mechanical thickness is shown in Table 3.

The mechanical thickness represents an upper bound for the elastic lithosphere thickness. However, it should be noted that the mechanical and elastic thickness are similar for small curvatures and bending moments

Table 3 Rheological parameters used for the calculation of the mechanical lithosphere thickness (Grott and Breuer, 2008, and references therein).

Symbol	Description	Value
E_{ol}	Activation energy, dry olivine dislocation creep	5.4×10^5 J mol^{-1}
E_{dia}	Activation energy, wet diabase dislocation creep	2.76×10^5 J mol^{-1}
A_{ol}	Prefactor, olivine dislocation creep	2.4×10^{-16} Pa^{-n} s^{-1}
A_{dia}	Prefactor, diabase dislocation creep	3.1×10^{-20} Pa^{-n} s^{-1}
n_{ol}	Stress exponent, dry olivine dislocation creep	3.5
n_{dia}	Stress exponent, wet diabase dislocation creep	3.05
σ_B	Bounding stress	10^7 Pa
$\dot{\varepsilon}$	Strain rate	10^{-14} s^{-1}

as it is the case for the large geological features that are considered here (McGovern et al., 2004; Belleguic et al., 2005). Thus in the following, we will use the term "elastic thickness".

The elastic thickness of the mantle and crust can be determined using Eq. (7) for their individual rheological parameters (Table 3). For the calculations presented here, we use parameters for a dry olivine mantle and a wet diabase crust similar to Grott and Breuer (2008). These rheological parameters have been found to match best the elastic thickness estimates available for the early history (Noachian epoch) and present-day Mars (Grott and Breuer, 2010; Breuer et al., 2016; Plesa et al., 2018b). If a layer of incompetent crust separates the elastic cores of the mantle D_m and crust D_c, then the elastic thickness of the crust and mantle system is significantly reduced and the effective elastic thickness can be calculated as follows (Grott and Breuer, 2008, 2010):

$$D_e = (D_m^3 + D_c^3)^{\frac{1}{3}}. \tag{8}$$

Otherwise, if the elastic thickness of the crust equals the crustal thickness, then the effective elastic thickness is the sum of the two contributions.

On Mars, gravity and topography analysis, lithospheric flexure studies, and estimates of the brittle to ductile transition indicate elastic lithosphere thicknesses smaller than about 25 km during the Noachian epoch (Grott et al., 2013, and references therein). These small values suggest a warm lithosphere and/or a low mantle viscosity during the early martian history (Grott et al., 2013; Thiriet et al., 2018; Plesa et al., 2018b). On the other hand, present-day elastic thickness estimates that are available for the north and south poles of Mars indicate a much thicker and colder lithosphere at these two locations. This has been concluded based on the lack of downward deflection with uncertainties of 100–200 m, beneath the north polar cap as seen by the MARSIS and SHARAD radars (Phillips et al., 2008), while for the south polar cap a maximum lithospheric flexure of 770 m has been found (Broquet et al., 2021). Previous elastic lithosphere thickness estimates with values larger than 300 km for the north pole (Phillips et al., 2008) and larger than 150 km for the south pole (Wieczorek, 2008) have been reevaluated in two recent studies (Broquet et al., 2020, 2021). The latest estimates indicate an elastic thickness between 330 km and 450 km for the north pole of Mars (Broquet et al., 2020) and a value larger than 150 km with a best fit of 360 km for the south pole (Broquet et al., 2021).

The present-day elastic thickness estimates at the north and south poles of Mars represent some of the strongest constraints for the thermal evolu-

tion models (Plesa et al., 2018b). Successful models require that the elastic lithosphere thickness values at these two locations are compatible with the present-day estimates. The elastic thickness is anti-correlated to the crustal thickness and surface heat flow (Fig. 1). Regions of thick crust typically associated with the southern hemisphere and in particular with volcanic centers show an elevated heat flow and a thin elastic thickness compared to the northern hemisphere and in particular within impact basins. This is due to the fact that a thicker crust has a higher amount of HPEs and a stronger blanketing effect than a thinner crust. The crustal blanketing effect is produced by the lower crustal conductivity compared to that of the mantle. This leads to higher subsurface temperatures in regions covered by a thick crust compared to areas with a thin crust.

The magnitude of surface heat flow and elastic thickness variations depends on the magnitude of crustal thickness variations. In the following, we discuss the effects of crustal thickness variations for the present-day surface heat flow and elastic thickness pattern taking as examples three geodynamic simulations that use the three different crustal thickness models presented in Fig. 1. The geodynamic models use the bulk heat production rate of Taylor (2013) and assume that the mantle contains about 43% of the bulk heat production rate, a value that lies in the range suggested by Knapmeyer-Endrun et al. (2021) to produce localized melting regions in the interior at present-day. A crustal thickness dichotomy leads to a dichotomy in surface heat flow and elastic thickness. The smallest surface heat flow and elastic thickness variations are obtained for the thinnest crust scenario (Fig. 1d, g), where crustal thickness variations are more than a factor two smaller compared to the thickest crust scenario. The crustal thickness variations for the case where the crustal density differs across the dichotomy boundary are about 25 km smaller than for the thickest crust scenario. However surface heat flow and elastic thickness variations are more pronounced in this case due to the difference in the crustal density and therefore the amount of crustal HPEs between the southern and northern hemispheres. Due to the lower crustal density of the southern compared to the northern hemisphere, the volumetric heat production in the northern crust is higher than in the southern crust leading to a warmer crust on the northern compared to the southern hemisphere. This is reflected also by the higher surface heat flow in the northern part of the Tharsis region compared to the southern part.

The elastic thickness is thickest in areas of thin crust where the interior cools more efficiently. These areas are typically impact basins, with the Hellas impact basin usually recording the highest elastic thickness values.

Table 4 Results obtained of the crustal thickness models shown in Fig. 1. All values represent present-day values. F_s [min, max] is the average surface heat flux with minimum and maximum values. T_e [min, max] is the average elastic thickness with minimum and maximum values calculated assuming a strain rate $\dot{\varepsilon} = 10^{-14}$ s^{-1}. $F_s^{InSight}$ is the surface heat flux at InSight location. T_e^{NP} is the elastic lithosphere thickness averaged below the north pole ice cap (i.e., within 10° from the north pole), while T_e^{SP} is the elastic lithosphere thickness averaged below the south pole ice cap (i.e., within 5° from the south pole). T_{CMB} is the core-mantle boundary temperature and F_{CMB} is the core-mantle boundary heat flux.

Output	Thin crust	Density dichotomy crust	Thick crust
F_s (min, max) [mW m^{-2}]	22.1 (16.3, 30.0)	22.2 (16.0, 38.9)	22.3 (14.4, 33.1)
T_e (min, max) [km]	267 (185, 326)	261 (61, 328)	234 (70, 348)
$F_s^{InSight}$ [mW m^{-2}]	20.1	22.6	19.1
T_e^{NP} [km]	284	288	304
T_e^{SP} [km]	264	280	236
T_{CMB} [K]	2094.2	2092.7	2086.1
F_{CMB} [mW m^{-2}]	2.3	2.4	2.4

The thinnest elastic thickness is obtained in areas covered by a thick crust, where the presence of an incompetent crustal layer (i.e., a weak crustal layer formed by high crustal temperatures) may decouple the elastic cores of the mantle and the crust, thus further reducing the elastic thickness. This has been suggested to exist at present day in the Tharsis area around Arsia Mons, where the crust is thickest (Grott and Breuer, 2010). Indeed such an incompetent crustal layer is present in the crustal density dichotomy model and the thickest crust scenario. While in the former this is located in Tharsis and in a small area in Elysium, for the latter the incompetent crustal layer is present in the Tharsis area and in smaller locations in the southern hemisphere due to the overall thicker crust in this scenario. As discussed in previous studies, the strongest constraint is given by the elastic thickness at the north pole. While at the south pole, all models present an elastic thickness greater than 150 km being compatible with the latest estimate (Broquet et al., 2021), only the thickest crust scenario presents an elastic thickness larger than 300 km (i.e., 304 km) at the north pole (Table 4), a value that is still lower than the recent estimate of Broquet et al. (2020). A higher elastic thickness may be obtained if the mantle is more depleted in HPEs than assumed in these models. However, a lower heat production in the mantle might lead to scenarios in which partial melt production stops earlier than suggested by the geological record in Tharsis and Elysium (Neukum et al.,

2004; Vaucher et al., 2009; Hauber et al., 2011). Another solution to explain the discrepancy between the elastic thickness estimates and the values obtained from geodynamic models would require that the load produced by the polar cap is not yet at elastic equilibrium as discussed by Broquet et al. (2020). This would lead to lower elastic thickness estimates, since in this case the observed deflection would be the sum of a downward deflection caused by the viscous relaxation and an upward deflection caused by some form of postglacial rebound. Whether the north pole is at elastic equilibrium strongly depends on the viscosity of the lithosphere and mantle that is linked to the parameters of the geodynamic model and would require the computation of an individual elastic thickness estimate for each thermal evolution model. Nevertheless, future work needs to address this aspect, since this may significantly affect the number of admissible models that can explain the elastic lithosphere thickness at the north pole of Mars.

In addition to the surface heat flow and elastic lithosphere, the thickness of the crust and its variations can affect the amount and distribution of partial melt that may still be produced in the interior of Mars today. Due to the pronounced crustal blanketing effect and higher amount of crustal HPEs, regions covered by a thick crust can be kept warm and their temperatures can exceed the melting temperature and produce melt up to recent times. Whether melt can still be produced in the martian mantle at present day primarily depends on the amount of mantle HPEs.

The study by Knapmeyer-Endrun et al. (2021) showed that only a limited range of crustal enrichment, i.e., containing between 55–70% of the total bulk of HPEs would lead to localized partial melt production at present day in the interior of Mars. A strong crustal enrichment containing more than 70% of the bulk amount of HPEs would lead to a mantle that is too cold to produce melt at present day. On the other hand a mantle containing more than 45% of the bulk amount of bulk amount of HPEs would be too warm and lead to wide-spread melting at present day. For a crust with an average thickness at the upper end of values obtained from InSight's seismic data this indicates a crustal enrichment in thorium and potassium similar to the surface abundance as measured by the gamma-ray instrument on board Mars Odyssey (Hahn et al., 2011; Taylor et al., 2006a). A thinner crust, on the other hand, requires an enriched component in the subsurface in order to avoid wide-spread melting in the interior of Mars at present day (Knapmeyer-Endrun et al., 2021).

In Fig. 2 we show the present-day melt fraction and the depth of the melt zone for the three models presented in Fig. 1. The melting temper-

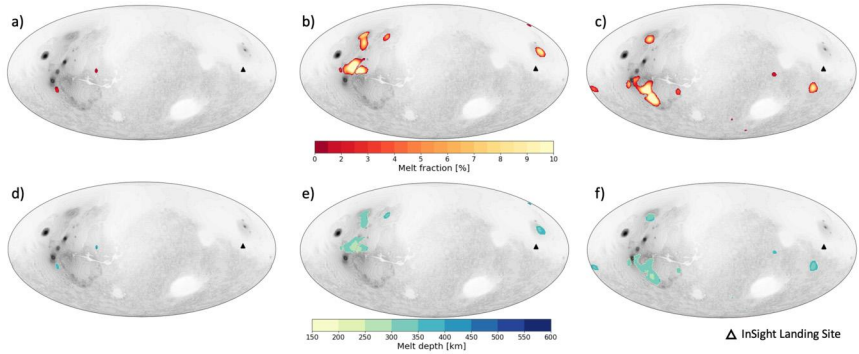

Figure 2 Distribution of partial melt zones at present day in the mantle for the models presented in Fig. 1. Panel a, b, and c show the melt fraction and panels d, e, and f show the corresponding melt depth. The thin crust end-member is shown in panels a and d, the density dichotomy crust in panels b and e, and the thick crust end-member in panels c and f.

ature is taken from Ruedas and Breuer (2017), who updated the solidus parametrization of Ruedas et al. (2013) to include more recent melting experiments from Collinet et al. (2015) and Matsukage et al. (2013). Furthermore, Ruedas and Breuer (2017) include a correction to account for the effects of Na, K, and Ca as suggested by Kiefer et al. (2015) that leads to about 35 K lower solidus for the primitive martian mantle compared to the terrestrial mantle. Additionally, the solidus used in each model in Fig. 2 considers the effect of mantle depletion due to crust formation. The solidus is increased linearly with the degree of depletion that each model experienced according to the crustal volume.

The least melt is produced at depths larger than 350 km in the thin crust model (Fig. 2a and d) that also has the smallest crustal thickness variations. The crustal blanketing effect is more pronounced for the other two models using a crustal density dichotomy and a higher density crust, respectively, due to a locally thicker crust in these models. This results in a larger amount of partial melt (higher melt fractions and more melt regions) and shallower melt zones compared to the thin crust model.

In general, geodynamic models have difficulties to produce partial melt zones at present-day beneath the Elysium volcanic province, even though mantle plumes are present there. Melting takes place mostly in Tharsis and underneath the southern hemisphere, as these areas are typically covered by a thicker crust. Since the Elysium province lies in the northern lowlands, it is difficult to focus mantle plumes underneath it that are hot enough to

produce melt at present day. Interestingly, the crustal density dichotomy model shows melting zones focused in Tharsis and Elysium. The melting zone in Elysium is likely due to a thicker crust in this region compared to the southern hemisphere and due to the reduced differences in crustal thickness between the northern and southern hemispheres caused by using a lower crustal density in the south compared to the north. We note, however, that the density difference between the southern and the northern crust is quite extreme in this model (i.e., 400 kg m^{-3}), and whether a crustal thickness model with smaller density variations between north and south can produce a partial melting zone at present day beneath Elysium needs to be tested by future studies.

4. Mantle dynamics, seismic velocities variations, and tidal dissipation

The thermal state of the mantle, the thermal lithosphere thickness, as well as the location of hot mantle plumes and cold downwellings can affect the variation of seismic velocities. Typically, the thickness of the thermal lithosphere is the sum of the stagnant lid thickness and of the thermal boundary layer where convective instabilities initiate. Below the thermal lithosphere, the mantle temperature usually follows an adiabatic profile. However, deviations from an adiabatic temperature profile may occur if convection is sluggish due to a high pressure-dependence of the viscosity or due to strong cooling of the interior, in which case the average temperature profile lies between an adiabatic and a conductive profile (Fig. 3). Parametrized thermal evolution models typically use either an adiabatic mantle temperature profile or a conductive one, if convection stops (i.e., the Rayleigh number drops below a critical value). The 2D/3D geodynamic models, on the other hand, self-consistently calculate the thermal profile, and in these models, depending on the rheological parameters, the thermal profile in the mantle may lie between an adiabatic and a conductive profile.

The thermal state of the interior is to first order affected by the mantle viscosity. However, rheological parameters such as the activation energy and activation volume that are determined by laboratory deformation experiments have large uncertainties. While the activation energy of olivine aggregates was measured to lie at about 375 ± 75 kJ mol^{-1} for diffusion and 520 ± 40 kJ mol^{-1} for dislocation creep (Hirth and Kohlstedt, 2003), the activation volume is one of the most poorly constrained parameters with

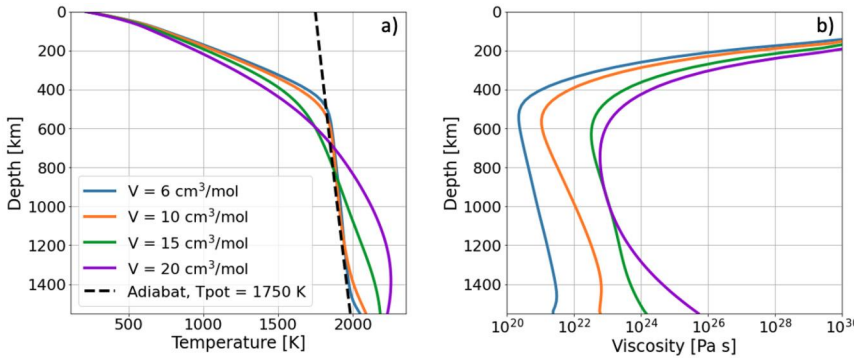

Figure 3 Effect of the pressure dependence of the viscosity, which is given by the activation volume, on the temperature (a) and viscosity (b) profiles at present day. The values for the activation volume are taken from Hirth and Kohlstedt (2003).

values between 0 and 20 $cm^3\,mol^{-1}$ (Hirth and Kohlstedt, 2003). These values will substantially affect the mantle temperature profile (Fig. 3) and also the mantle convection pattern. An activation volume of 6 $cm^3\,mol^{-1}$ leads to a larger number of plumes and downwellings compared to an activation volume of 10 $cm^3\,mol^{-1}$, as illustrated in the temperature maps at mid-mantle depth (Fig. 4a and b). However, further increasing the activation volume would lead to scenarios, in which convection in the lower part of the mantle is weak or even absent. This reduces the thickness of the convective layer and increases the wavelength of the convection pattern (Fig. 4c and d).

The viscosity could also be affected by the presence of water in the mantle. Water concentrations in excess of 100 ppm can reduce the viscosity by about two orders of magnitude (Karato and Wu, 1993) and can significantly affect mantle cooling. On Mars, recent petrological analyses of martian meteorites suggest a bulk water content of 137 ppm, with crustal abundances of 1410 ppm and mantle water contents between 14 and 72 ppm (McCubbin et al., 2016). A wet mantle rheology during most of the thermal history would not be able to reproduce strong mantle plumes in recent times (Plesa et al., 2018b) as required by the petrological evidence for local mantle temperatures (Filiberto and Dasgupta, 2015; Kiefer and Li, 2016). In addition, a dry rheology was favored by models that coupled the thermal and orbital evolution of Mars and its moon Phobos, in order to reproduce the orbital evolution of Mars' closest satellite (Samuel et al., 2019). Thus, according to thermal evolution models, water in the martian mantle was most likely lost during the earliest planetary evolution and most of

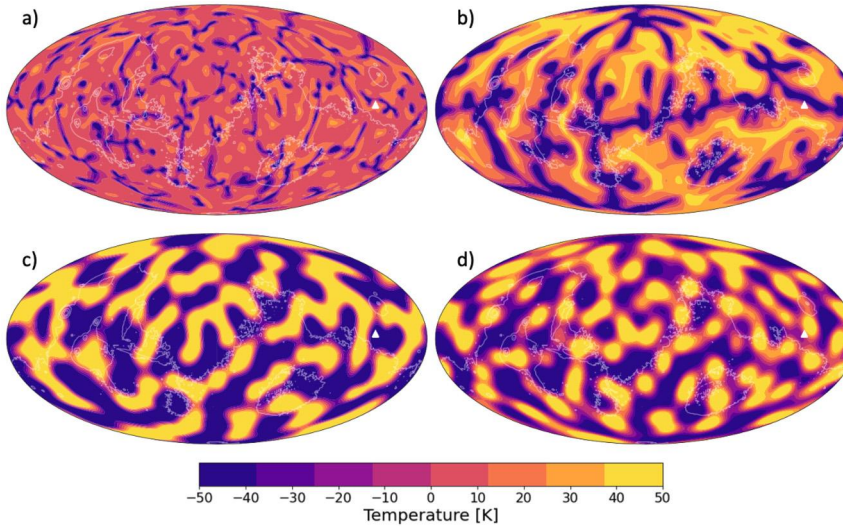

Figure 4 Temperature variations at mid-mantle depth (775 km depth) corresponding to the temperature profiles shown in Fig. 3. The models use an activation volume of 6 $cm^3\ mol^{-1}$ (panel a), 10 $cm^3\ mol^{-1}$ (panel b), 15 $cm^3\ mol^{-1}$ (panel c), and 20 $cm^3\ mol^{-1}$ (panel d). The color scale has been clipped to show the locations of mantle plumes (bright colors) and downwellings (dark colors). For orientation the 0 km level of the surface topography is indicated by white contour lines.

the thermal history was characterized by a dry mantle rheology. We note, however, that geochemical reservoirs may complicate this interpretation, as they could trap water in isolated regions inside the mantle and lithosphere (Breuer et al., 2016).

The present-day thermal state of the interior is the result of billion years of thermal evolution. Mantle plumes and cold downwellings may be present in the interior of Mars at present day and would lead to temperature variations in the interior and to variations in the thermal lithosphere thickness. These effects can only be investigated by using 2D and 3D geodynamic models. Previous models showed that the thermal lithosphere can be substantially thinner at the location of mantle plumes (Kiefer and Li, 2009), as their higher temperature decreases locally the viscosity and allows the silicate material to flow (i.e., to convect) at shallower depths. Conversely, the thermal lithosphere is thicker above cold mantle downwellings. Additionally, the variations of the thermal lithosphere thickness are affected by the crustal thickness variations, as the latter has a higher amount of HPEs and a lower conductivity compared to the mantle. This

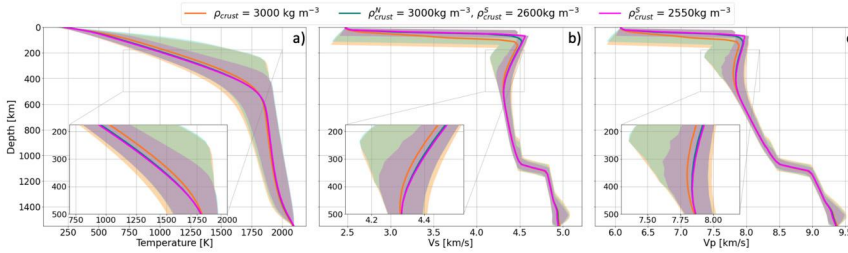

Figure 5 Profiles of the temperatures (panel a) as well as the shear wave velocities (panel b) and compressional wave velocities (panel c) for the models presented in Fig. 1. The TAY13 (Taylor, 2013) was assumed for the seismic velocities calculation. Full lines indicate the average profiles throughout the mantle, while the shaded regions show the corresponding variations.

leads to a higher lithospheric temperature and thinner lithospheric thickness beneath areas covered by a thick crust (e.g., beneath volcanic provinces) compared to regions of thin crust (e.g., impact basins). For models that include crustal thickness variations, the largest variations in temperature are observed in the lithosphere. We also note that the largest temperature variations are obtained for models with a thick crust that exhibits larger crustal thickness variations. In Fig. 5a we show average temperature profiles and corresponding temperature variations at present day for the three thermal evolution models presented in Fig. 1. The model with a crustal density dichotomy between the northern and southern hemisphere and the model with a crustal density of 3000 kg m^{-3} have crustal thickness variations of 127.2 km and 152.3 km, respectively, that lead to larger lithospheric temperature variations than the crustal thickness model with a crustal density of 2550 kg m^{-3}, which has a difference of only 60.8 km between the minimum and maximum crustal thickness values.

On Mars, the average thermal lithosphere thickness has been estimated based on the evaluation of seismic events recorded by InSight. Using direct and surface-reflected body wave phases, a thermal lithosphere thickness of 400–600 km is required to explain the differential travel times obtained for seismic events at epicentral distance between 25° and 75° from InSight location and with moment magnitudes between 3 and 4 (Khan et al., 2021). InSight's estimate of the average thermal lithosphere thickness of Mars is thicker than the thermal lithosphere on the Earth and suggests that Mars has significantly cooled during its thermal history. This thick lithosphere and its thermal gradient inferred from InSight data control the formation of low-velocity zones in the interior of Mars that have been proposed in previous

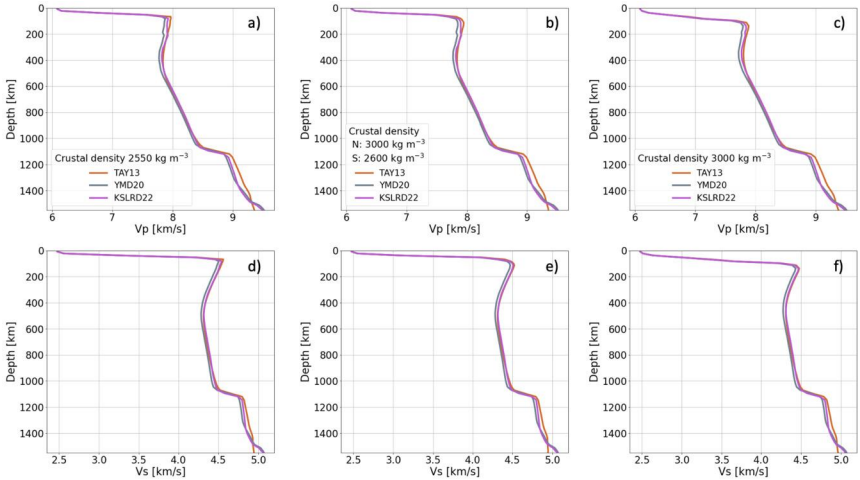

Figure 6 Effects of mantle composition on the compressional wave velocities (panels a, b, and c) and shear wave velocities (panels d, e, and f) for three different mantle compositions: TAY13 (Taylor, 2013), YMD20 (Yoshizaki and McDonough, 2020), and KSLRD22 (Khan et al., 2022). Panels a and d show the thin crust end-member case, panels b and e present the results for the density dichotomy crust, and panels c and f show the thick crust end-member case.

studies (Mocquet and Menvielle, 2000; Zheng et al., 2015). Additionally, a recent study by Plesa et al. (2021) showed that 3D thermal evolution models with a crust containing less than 20% of the bulk amount of HPEs would lead to a hot interior and a thin lithosphere. These models are incompatible with InSight observations, as they would lead to S-wave shadow zones for high-quality events in the Cerberus Fossae region, for which clear P- and S-waves arrivals were recorded.

Temperature variations affect the seismic velocities with the strongest velocities variation being present in the lithosphere and at the depth of the olivine to wadsleiyte phase-transition (Fig. 5b and c). We note that the effects of composition are minor compared to the effect of temperature variations in the lithosphere. In Fig. 6, we show the differences between the average seismic velocities profiles for the three models presented in Fig. 5. We tested three of the most recent compositions that have been proposed for Mars: the TAY13 composition (Taylor, 2013), the YMD20 composition (Yoshizaki and McDonough, 2020), and the KSLRD22 composition (Khan et al., 2022). While the seismic velocities have been computed using these compositions, the bulk amount of HPEs that was used in all thermal evolution models was taken from TAY13. Other HPEs models with a higher

abundance of radiogenic elements such as the model by Yoshizaki and McDonough (2020) would require a higher crustal enrichment in HPEs and a similar amount of mantle HPEs as the models shown here in order to avoid wide-spread melting in the mantle at present day. Thus, even for other HPEs models the mantle temperature would be similar to the profiles shown in Fig. 5.

For all three compositional models tested here, the seismic velocities are nearly identical in the upper mantle and show slight differences in the lower mantle, with minimally lower seismic velocities values for the YMD20 and KSLRD22 compositions mainly due to the lower FeO content of these models (14.7 ± 1.0 wt% for YMD20 and 13.7 ± 0.4 wt% for KSLRD22 compared to 18.1 ± 2.2 wt% for TAY13).

The temperature and hence the seismic velocities in the lithosphere follow the crustal thickness variations. The crustal thickness pattern controls their variations down to a depth of 400 km or even deeper in particular for models with a thick crust (Fig. 7). In Fig. 7, the thin crust model (average crustal thickness of 40.6 km, left column) shows a pattern of the S-wave velocity variations that closely follows the crustal thickness pattern at 150 km depth. Lower-than-average seismic velocities are observed below the southern hemisphere and are caused by the warmer temperatures due to a thicker crust compared to the northern hemisphere. Conversely, the areas covered by a thin crust, i.e., the northern hemisphere and large impact basins such as Hellas, show seismic velocities higher than the average value, due to the more efficient cooling and hence colder temperatures than those beneath the southern hemisphere. This seismic velocities pattern is no longer visible at 400 km depth. For the thick crust model (average crustal thickness of 71.4 km, right column), however, a dichotomy in the S-wave velocity variations is still visible at 400 km depth. Since all models in Fig. 7 use the same bulk heat production and the same amount of HPEs in the mantle, the difference is caused by the stronger crustal thickness variations and the more pronounced blanketing effect due to the low crustal conductivity in the thick crust scenario compared to the thin crust case. In the crustal density dichotomy case (middle column), the crustal thickness pattern is more complex than in the previous two models, but the Tharsis region is clearly distinguishable on the map of S-wave velocity variations at 400 km depth. Seismic velocities variations are small and about 1% in the convecting mantle. Larger variations are observed again closer to the CMB, where negative seismic velocity gradients may be locally present due to the stability of larger proportions of garnet and ferropericlase at the expense of

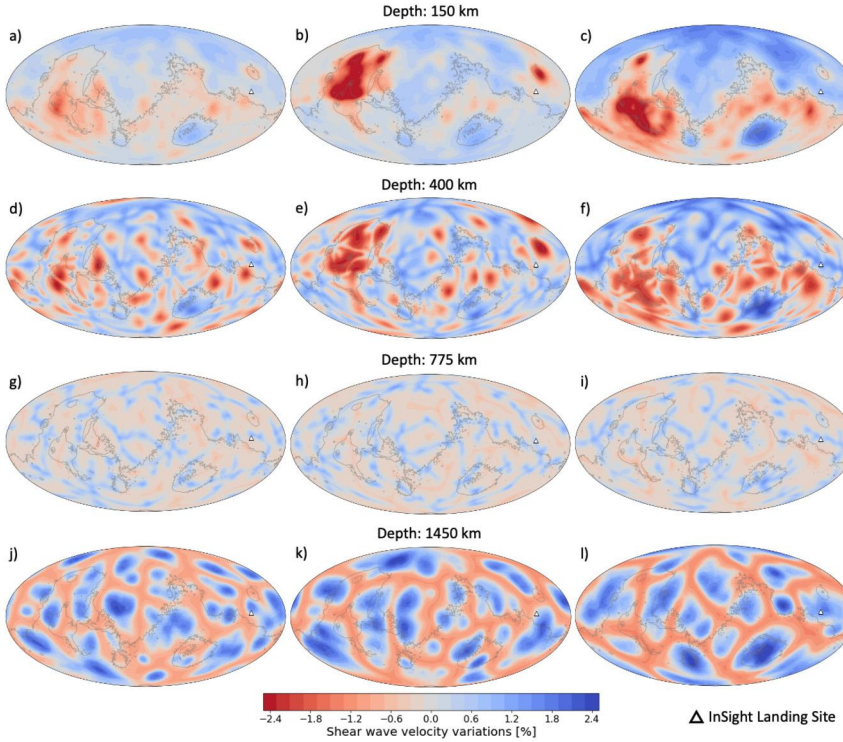

Figure 7 Seismic velocities variations at different depths throughout the mantle calculated for TAY13 composition. Left column (panels a, d, g and j) shows the thin crust end-member case. Middle column (panels b, e, h, and k) presents the density dichotomy crust model, and the right column (panels c, f, i, and l) shows the thick crust end-member case. For orientation, the gray contour lines show the 0 km level of surface topography.

ringwoodite (Plesa et al., 2021). We note however that this depends on the chosen mineralogical model and mostly appears for the Taylor-composition (Taylor, 2013), but is absent for the Yoshizaki- and Khan-compositions (Yoshizaki and McDonough, 2020; Khan et al., 2022).

Depending on the location of seismic events, the propagation of their seismic waves will encounter not only a different crustal thickness on the path to the seismic station, but also a different lithospheric thickness and lithospheric temperature. In Fig. 8 we show the differences between seismic velocities profiles at present-day at three different locations on Mars (Tharsis, Utopia, and InSight) for the three thermal evolution models presented in Fig. 1 and compare them with their corresponding average profiles. The differences in the uppermost 400 km can be substantial. The largest dif-

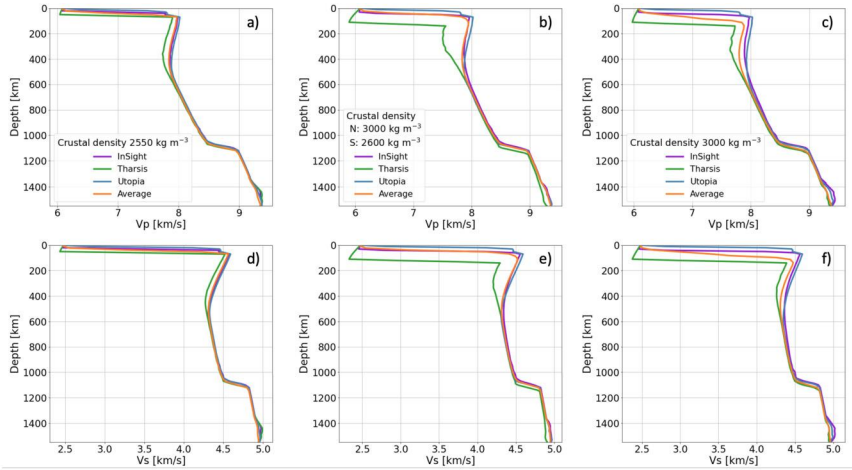

Figure 8 Seismic velocities profiles at selected locations compared to the average profiles. InSight profile is drawn at 136° longitude and 4° latitude. Tharsis profile is taken at −115° longitude and 0° latitude, while the Utopia profile was selected at 115° longitude and 45° latitude. Panels a and d show the seismic velocities profiles for the thin crust end-member, panel b and e for the density dichotomy crust case, and panels c and f for the thick end-member case.

ferences are observed between Tharsis volcanic province (profile taken at −115° longitude and 0° latitude) and Utopia impact basin (115° longitude and 45° latitude), and are most extreme for models with a thick crust in the Tharsis area (the thick crust model and the model with a different density between the northern and southern hemispheres). Interestingly, the model with a different density between the northern and southern hemispheres shows the largest variations. This is caused by the higher volumetric heat production in the northern hemisphere compared to the southern hemisphere in this model. On the other hand, the average profile and the profile at the InSight landing site are nearly identical. The largest difference between InSight and average profiles is observed for the thickest crust scenario, where crustal thickness variations between these two locations are more pronounced than in the other two crustal thickness models.

The uppermost layers are dominated by the seismic velocities of the crust. While for the individual profiles at the three locations a sharp transition occurs at the crust mantle interface, this transition is more gradual for the average profile. This is due to the fact that for the average profiles both mantle and crustal areas are present at the same depth. In the uppermost layers the crustal areas dominate but with deeper depth they become

smaller being replaced by mantle areas. Right below the crust, the seismic velocities reflect the large variations of the lithospheric temperatures, while deeper in the convecting mantle these variations become much smaller and therefore the difference in seismic velocities is minor. The olivine to wadsleyite phase transition is clearly visible for all models. The depth of the phase transition depends on the temperature, and for the Tharsis profile, which has a higher local temperature, the average phase transition depth is at about 1110 ± 10 km, depending on the thermal evolution model. For the InSight profile the average phase transition depth is shallower and about 1070–1080 km, due to a lower temperature at this location. All models show the same average depth for the olivine to wadsleyite phase transition at ~1095 km for the average profile, since the latter is nearly identical for all models (cf. Fig. 5).

In addition to the seismic velocities, the thermal state of the mantle together with the size and state of the core (solid or liquid, see Section 5) also affects the tidal deformation of a planet. The latter has been determined for Mars from radio tracking measurements from Mars Odyssey, Mars Reconnaissance Orbiter, and Mars Global Surveyor (Konopliv et al., 2016; Genova et al., 2016; Konopliv et al., 2020). The lag of the tidal deformation caused by Mars' closest moon, Phobos, is given by the phase lag ε that describes the dissipation inside Mars and is linked to the thermal state of the interior through the viscosity (Nimmo and Faul, 2013). The dissipation can be also expressed in form of the tidal quality factor Q that is defined as $1/\sin(\varepsilon)$. Low values of Q would indicate a dissipative mantle caused by a low viscosity and hence high mantle temperature, whereas a cold interior and consequently a high viscosity would lead to high Q values.

On Mars, current available estimates for the tidal quality factor Q calculated at the main tidal period of Phobos (5.55 hours) range between 72 and 105 (Ray et al., 2001; Lainey, 2016) and indicate a more dissipative interior than that of the Earth, for which a tidal quality factor of 280 was calculated at the lunar semidiurnal terrestrial tide (Ray et al., 2001). Here we recalculate the tidal quality factor using the approach from Zharkov and Gudkova (2005) that was also used by Khan et al. (2018):

$$\frac{Q}{k_2} = 559 \tag{9}$$

Using the latest k_2 estimate of 0.174 ± 0.008 (Konopliv et al., 2020), we find a tidal quality factor of 97.3 ± 4.5. However, the error bars would increase when accounting for the frequency-dependency of k_2, higher tidal

terms, and the fact that dissipation occurs in both Mars and Phobos. Thus, following the approach of Khan et al. (2018) we increase the error bars and use a tidal quality factor Q of 97 ± 12, a range that includes the previous estimates of Khan et al. (2018) as well as the new values obtained from the most recent k_2 estimate.

Previous studies have used prescribed thermal profiles (Nimmo and Faul, 2013) or temperature profiles from mantle convection models (Plesa et al., 2018b) to calculate the dissipation in the interior of Mars and compare the results with observations. The study by Nimmo and Faul (2013) uses an extended Burgers model for dry olivine and finds that, for a grain size of 1 cm, a present-day potential temperature of 1625 ± 75 K is required to explain the dissipation in the interior of Mars. Plesa et al. (2018b) used the present-day thermal state from mantle convection models and computed the tidal quality factor Q. Using Q estimates in the range of 99.5 ± 4.9 (Konopliv et al., 2016; Lainey, 2016), this study concluded that models with an inefficient cooling of the interior caused by either a high amount of HPEs in the mantle or a large increase of the viscosity with depth (i.e., due to a high activation volume) would be too dissipative to satisfy the constraints. Conversely, models that contain nearly all HPEs in the crust and have a cold present-day mantle lead to a much lower dissipation than the suggested values for Mars. Thermal evolution compatible with the Q estimates of Lainey (2016) indicates that between 37.6% and 68.3% of the bulk amount of HPEs are concentrated in the crust (Plesa et al., 2018b).

Here, we calculate the tidal deformation of the three thermal evolution models presented in Fig. 1. These models contain 57% of the total bulk amount of HPEs in their crust, and thus lie within the range of models that were found compatible with Q estimates by Plesa et al. (2018b). To compute the tidal deformation, we use a semianalytical model based on the normal mode theory for radially stratified viscoelastic bodies (Sabadini and Vermeersen, 2004). The results are shown in Fig. 9 and Table 5, and are discussed in detail below.

The model uses 100 layers for the mantle and 1 layer for the core, which is assumes to be homogeneous. It uses as inputs the density, viscosity and rigidity. While the viscosity profile comes from the geodynamic simulations, the density and rigidity profiles depend on the mineralogical model and are calculated by the thermodynamic code Perple_X (Connolly, 2009) using the thermodynamic formulation and database of Stixrude and Lithgow-Bertelloni (2011). All three profiles (i.e., viscosity, density, and

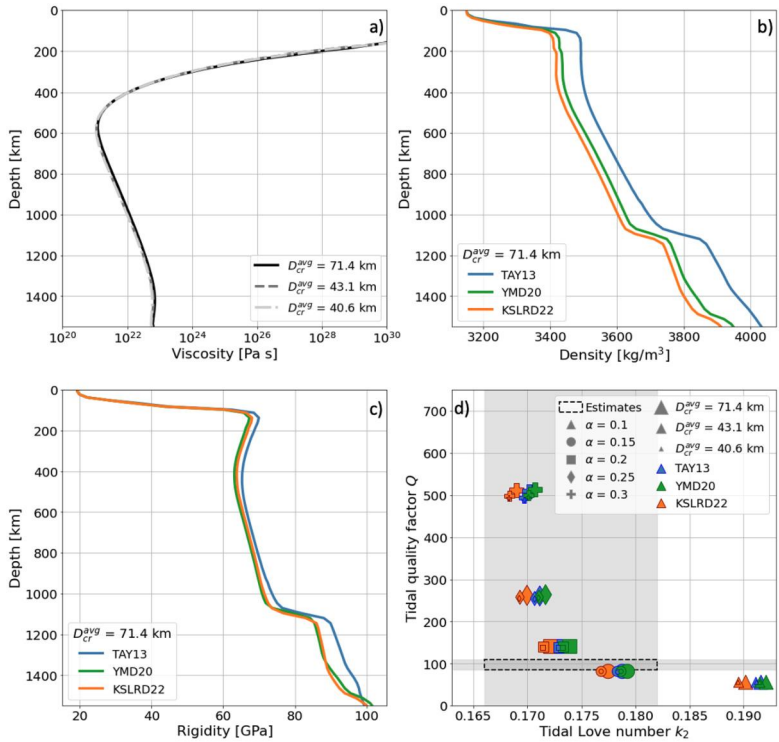

Figure 9 Panel a: Viscosity profiles throughout the mantle for the models shown in Fig. 1. Panel b and c: mantle density and rigidity profiles, respectively, for the thick crust end-member using three different mantle compositions TAY13, YMD20, and KSLRD22. Panel d: calculated tidal quality factor Q and tidal Love number k_2 for the three mantle models (panel a) and three compositions (panel b and c).

rigidity) are temperature and pressure-dependent and are calculated from the temperature profiles obtained by the geodynamic models.

For the tidal deformation calculations, we used the Andrade rheological model and assumed that the planet is incompressible. Nevertheless, we note that the assumption of compressibility might render corrections to k_2 that are of the order of the observational uncertainty. While other rheological models exist and have been applied to calculate the tidal deformation of Mars and other rocky planets, the advantage of the Andrade model is the small number of parameters it requires for the calculations (Castillo-Rogez et al., 2011; Efroimsky, 2012). A detailed review of the theory of viscoelasticity and tidal response, as well as their application to constrain the interior

Table 5 Tidal deformation results for the three models presented in Fig. 1 using an incompressible Andrade model, three different mantle mineralogies, and various values of the tidal parameter α used in the Andrade model. According to Castillo-Rogez et al. (2011) the tidal parameter ζ was set to 1 for all calculations.

Tidal parameter	Thin crust		Density dichotomy crust		Thick crust	
	TAY13 composition (Taylor, 2013)					
	Q	k_2	Q	k_2	Q	k_2
$\alpha = 0.1$	56.50	0.191	56.60	0.191	56.81	0.192
$\alpha = 0.15$	81.40	0.178	81.71	0.178	82.47	0.179
$\alpha = 0.2$	137.94	0.173	138.75	0.173	140.92	0.173
$\alpha = 0.25$	253.90	0.171	255.91	0.171	261.50	0.171
$\alpha = 0.3$	489.38	0.170	494.19	0.170	508.01	0.170
$\alpha = 0.4$	1955.25	0.169	1981.69	0.169	2060.93	0.170
	YOS20 composition (Yoshizaki and McDonough, 2020)					
	Q	k_2	Q	k_2	Q	k_2
$\alpha = 0.1$	56.76	0.191	56.86	0.191	57.09	0.192
$\alpha = 0.15$	81.90	0.179	82.21	0.179	83.00	0.179
$\alpha = 0.2$	138.98	0.173	139.81	0.173	142.03	0.174
$\alpha = 0.25$	256.20	0.171	258.24	0.171	263.93	0.172
$\alpha = 0.3$	494.50	0.170	499.37	0.170	513.42	0.171
$\alpha = 0.4$	1980.81	0.169	2007.58	0.170	2088.06	0.170
	KHA22 composition (Khan et al., 2022)					
	Q	k_2	Q	k_2	Q	k_2
$\alpha = 0.1$	56.69	0.189	56.79	0.189	57.01	0.190
$\alpha = 0.15$	81.77	0.177	82.08	0.177	82.87	0.177
$\alpha = 0.2$	138.72	0.171	139.53	0.171	141.74	0.172
$\alpha = 0.25$	255.58	0.169	257.60	0.169	263.27	0.170
$\alpha = 0.3$	493.03	0.168	497.87	0.168	511.85	0.169
$\alpha = 0.4$	1972.59	0.168	1999.18	0.168	2079.16	0.168

structure of Mercury, Venus, Mars, the Moon, and icy satellites is given in Chapter 5 (Bagheri et al., 2022).

A recent study by Bagheri et al. (2019) has compared various rheological models for Mars and found that all models can fit the observations when using a single frequency (i.e., at the main period of Phobos), but information of the dissipation at additional frequencies could help to distinguish between the current rheological models. The same study concluded that the Maxwell rheology would require very low viscosities to fit the available data and rheologies such as Andrade, extended-Burgers, or Sundberg-Cooper are more appropriate to use when studying tidal dissipation.

The Andrade model that is used here is able to describe all components of deformation (elastic deformation, viscous creep, and the transient Andrade creep) and requires in total four parameters: the viscosity, the rigidity and two empirically determined parameters α and ζ. The parameter ζ describes the ratio between the timescales of the anelastic Andrade creep and the Maxwell body and has been found to be close to one (Castillo-Rogez et al., 2011). On the other hand α describes the duration of the transient response, and values for olivine-rich mantle rocks lie between 0.1 and 0.5, and mostly between 0.2 and 0.4 (Castillo-Rogez et al., 2011).

The average thermal state of the geodynamic models, which was used to calculate the tidal deformation in Fig. 9, is very similar (cf. Fig. 5a). Although the temperature and seismic velocities variations in the lithosphere can be significantly different between the three geodynamic models (cf. Fig. 7), the average viscosity, density, and rigidity profiles are very similar (Fig. 9a, b, and c), with TAY13 composition showing slightly larger densities and higher rigidities than YOS20 and KHA21 composition, due to the higher FeO content. Thus, the tidal dissipation values mainly depend on the chosen value for α, for which a value between 0.2 and 0.15 seems to fit best the observed dissipation in the interior of Mars (Fig. 9d).

5. Core radius estimates and their implications for the interior dynamics

The core of a terrestrial planet is a witness of the earliest planetary differentiation, when metal and silicates separate to form the layers inside the planet. The size of the core is essential to determine the thickness of the silicate layer (mantle and crust), when knowing the planet's radius. The thickness of the silicate layer in turn affects the mantle flow and the convection pattern (i.e., number of mantle plumes and their distribution). The latter can be linked to surface geological features such as volcanic and tectonic provinces. For a detailed review that describes the methods and the progress in determining of the core size of the Earth, Mars, and Moon, as well as future opportunities for terrestrial exoplanets we refer the reader to Chapter 3 (Knapmeyer and Walterová, 2022).

Many geodynamic studies have investigated the formation of the martian crustal thickness dichotomy, proposing a degree-one or ridge like convection pattern. This pattern is largely favored for models using a small core that allows for the presence of an endothermic phase transition at the base of the mantle (Harder and Christensen, 1996; Breuer et al., 1998),

similar to the 660-phase transition on the Earth. Models employing a specific mantle viscosity structure with a viscosity increase in the mid-mantle (Zhong and Zuber, 2001; Roberts and Zhong, 2006; Keller and Tackley, 2009) and models that included the combined effects of a giant impact and the subsequent dynamics in the mantle (Golabek et al., 2011) were also able to produce a degree-one mantle pattern, but in these cases too the core radius was about half of the planetary radius or smaller.

InSight's measurements have revealed that the martian core has a radius of 1830 ± 40 km and is more than half the planet's radius (Stähler et al., 2021). This is consistent with estimates of the tidal Love number k_2 (Konopliv et al., 2016; Genova et al., 2016) that were previously combined with thermal evolution models and suggested a core radius strictly larger than 1800 km (Plesa et al., 2018b). The k_2 value of Konopliv et al. (2016) of 0.169 ± 0.006 has been recently updated by Konopliv et al. (2020) to 0.174 ± 0.009. The most recent estimate was corrected for atmospheric tides, and the uncertainties account for the fact that the correction for atmospheric tides depends on the atmospheric conditions at the time of observations (Konopliv et al., 2020). As shown in Fig. 9 models using a core radius of 1850 km, a value that was previously used by Plesa et al. (2018b) and is consistent with the seismic detection of the martian core (Stähler et al., 2021), are also able to fit the latest k_2 estimate of (Konopliv et al., 2020).

The large size of the core excludes the possibility of having a bridgmanite-dominated lower mantle on Mars (Stähler et al., 2021), as it is the case for the Earth. An endothermic phase transition at the base of the martian mantle will no longer occur, as the pressure is too low for this to take place. Even for models with smaller core radii (1700 – 1360 km) an endothermic phase transition at the base of the present-day martian mantle was only marginally possible requiring CMB temperatures in excess of 2100 K (Spohn et al., 1998). In addition, the large radius of the core leads to a small scale convection pattern with many small plumes distributed throughout the mantle as illustrated in Fig. 10.

All three models in Fig. 10 have been built similarly to the models presented in (Plesa et al., 2016). They use the same crustal thickness with a crustal density of 2800 $\mathrm{kg\,m^{-3}}$ and a crustal enrichment that matches the average value derived from GRS measurements. The crustal thickness is derived from gravity and topography data and matches the crust-mantle discontinuity at InSight landing site, as observed in the seismic measurements (Knapmeyer-Endrun et al., 2021; Wieczorek et al., 2022). The radius of

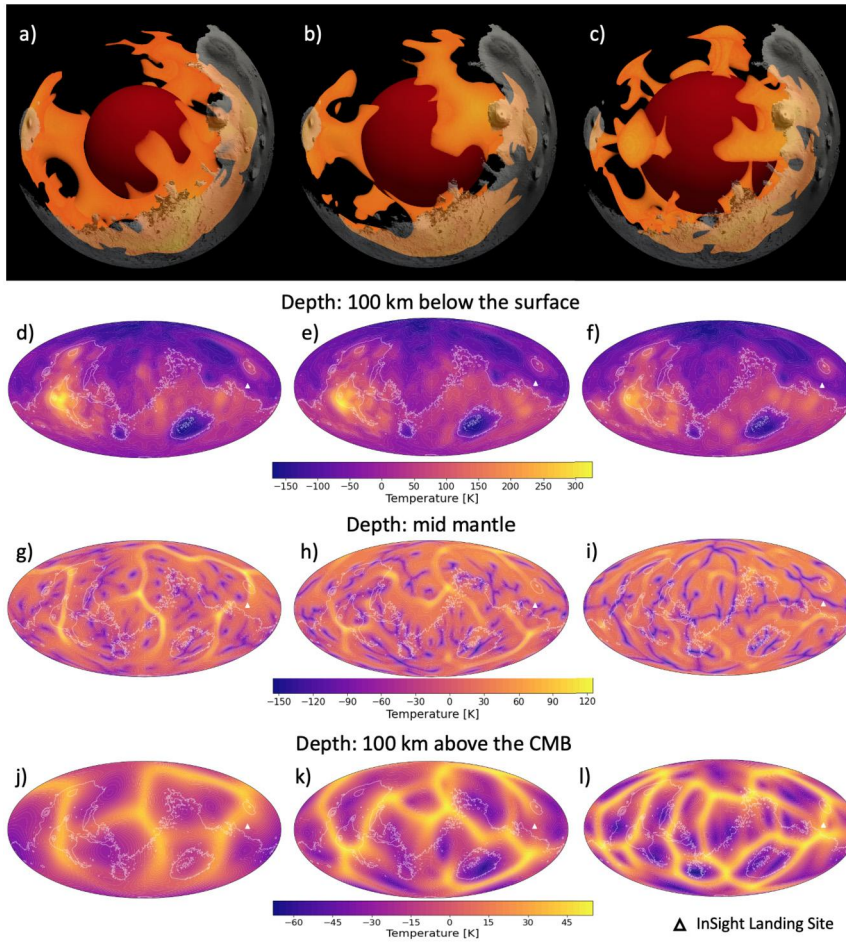

Figure 10 Mantle convection pattern (panels a, b, and c) and temperature variations throughout the mantle. All models use a crustal thickness with and average value of 61.3 km and a crustal density of 2800 kg m^{-3}. Left column (panels a, d, g, and j) shows a model with a core radius of 1500 km. Middle column (panels b, e, h, and k) shows a model with a 1700 km core radius, while right column (panels c, f, i, and l) presents a model with a core radius of 1850 km. Only the model shown in the right column is compatible with core radius estimates by InSight.

the core has been varied between the three models with values of 1500 km, 1700 km, and 1850 km. While the former two values are incompatible with the recent InSight data, the last value of 1850 km lies well within the current core radius estimates (Stähler et al., 2021).

The models show a shallow subsurface that is mostly dominated by the crustal thickness variations with a temperature pattern similar to the crustal thickness pattern (Fig. 10d–f). The effects of mantle plumes are more pronounced for 1500 km core radius compared to the 1850 km core radius. It can be observed that the case with the largest core shows a short wave-length convection pattern compared to the small core model. This is illustrated both in the temperature maps at mid-mantle depth (Fig. 10g–i) and at 100 km above the CMB (Fig. 10j–l) that show the presence of a larger number of plumes and downwellings for the model with a core radius of 1850 km compared to the case with a core radius of only 1500 km.

A large core that leads to a small scale mantle convection pattern is at odds with the formation of the martian crustal thickness dichotomy through an endogenous process. However, exogenic processes such as the sequence of one or several large impacts may represent a key mechanism (Wilhelms and Squyres, 1984; Frey and Schultz, 1988). Such scenario is compelling, as it has been proposed to explain the elliptical nature of the dichotomy (Andrews-Hanna et al., 2008; Nimmo et al., 2008; Marinova et al., 2008). The effect on the subsequent dynamics in the mantle may lead to mantle plumes in Tharsis and Elysium that with time may be stabilized by the insulating effect of a thicker crust at those locations (Schumacher and Breuer, 2006). This scenario, however, would not exclude weaker thermal anomalies at other locations, that may have led to shorter episodes of volcanic activity (e.g., Syrtis Major, the Circum Hellas province) or may have never resulted in the buildup of volcanic provinces at the surface.

Another important aspect of a large martian core is that it requires a high amount of light elements to be able to match the planet's mass. Sulfur cannot be the only light element in the core, as its amount would then exceed the abundance found in EH-chondrites, the most sulfur rich building blocks. Thus, other elements such as oxygen, carbon, and hydrogen are required to match both the core density and to be compatible with geochemical arguments (Stähler et al., 2021; Khan et al., 2022, and references therein). The composition of the martian core has major consequences for its evolution and the generation of an early magnetic field. A large amount of light elements in the core could lead to a scenario in which the core crystallizes from the top down (iron snow) by forming iron particles at the top of the core due to a steeper melting temperature than the core adiabatic profile (Stewart et al., 2007; Rivoldini et al., 2011; Breuer

et al., 2015; Helffrich, 2017; Davies and Pommier, 2018; Hemingway and Driscoll, 2021).

A recent study by Hemingway and Driscoll (2021) investigated the crystallization of the martian core and found that Mars may possess a partially solid core today. However, the large amount of light elements places the core composition close to the eutectic and likely prevented the crystallization of an inner core (Stähler et al., 2021), due to the significant decrease of the core melting temperature (Mori et al., 2017). In addition, Hemingway and Driscoll (2021) used a simple thermal evolution model without explicit treatment of the stagnant lid evolution. This most likely underestimates the mantle and core temperatures. Typical stagnant lid thermal evolution models (e.g., Breuer and Spohn, 2003; Morschhauser et al., 2011; Plesa et al., 2018b; Samuel et al., 2019, 2021) suggest that even at present day the CMB temperature is too high to allow for core crystallization, in particular for a high mantle viscosity that was found compatible with additional geophysical and seismic constraints (Plesa et al., 2018b; Samuel et al., 2019; Knapmeyer-Endrun et al., 2021). However, core crystallization would undoubtedly take place in the future, when the core temperature has sufficiently decreased to allow for core crystallization. The exact time and style of crystallization will strongly depend on the core composition and thermal state (Stewart et al., 2007).

The early martian dynamo was most likely driven by thermal buoyancy inside the core until at least 3.7 Gyr ago (Mittelholz et al., 2020), placing important constraints on the heat flow at the CMB. Thermal evolution scenarios that maintain a CMB heat flow above the critical core heat flow, above which thermal convection in the core sets in, for at least 800 Myr need to be investigated in future studies. An important step for answering this question has been undertaken by Greenwood et al. (2021), who used 1D parametrized thermal evolution models and showed that a prolonged thermally driven dynamo can be sustained. Successful models require core thermal conductivities in the range of $16 - 35$ $\mathrm{W\,m^{-1}\,K^{-1}}$ and mantle reference viscosities of 10^{21} Pa s or smaller and activation volumes smaller than 6 $\mathrm{cm^3\,mol^{-1}}$ (Greenwood et al., 2021). However, geodynamic models in a 3D geometry require higher viscosities and/or activation volumes to explain localized melting at recent times (Knapmeyer-Endrun et al., 2021) and a large present-day elastic lithosphere thickness at the north pole of Mars (Plesa et al., 2018b). Thus future models need to investigate if both constraints for the early magnetic field and recent thermal state can be matched.

6. Seismogenic layer thickness and the present-day seismicity

Seismic observations provide the most direct view into the interior of a planetary body and reveal the level of activity that the planet experiences. While seismic observations have greatly improved our understanding of the interiors of the Earth, Moon, and Mars, currently, the seismic activity for other planetary bodies such as Mercury, Venus, or icy satellites can only be indirectly estimated with large uncertainties. A comprehensive review of the current state of knowledge of planetary seismology and directions for future seismic investigations of planetary bodies is given in Chapter 2 (Stähler and Knapmeyer, 2022).

In the absence of plate tectonics and because Mars is smaller than the Earth, its seismicity was suggested to be lower than that of the Earth and mainly driven by planetary cooling. However, the level of seismic activity was expected to be larger than the seismicity of the Moon recorded by the Apollo seismic measurements (Ewing et al., 1971; Toksöz et al., 1974). Previous seismic measurements on Mars were performed by Viking in the 1970s (Anderson et al., 1976). While the seismometer on Viking 1 failed to uncage and could not record any data, Viking 2 collected data between 1976 and 1978. However, these measurements are strongly contaminated by noise caused by lander vibrations due to wind, given the location of the seismometer on the lander deck. During 146 sols of operation only one event recorded by Viking 2 seismometer could be interpreted as a marsquake (Anderson et al., 1977), but a seismic origin is difficult to establish in the absence of wind data during the event.

In the absence of unambiguous seismic recordings from Mars, previous studies have estimated the level of seismic activity based on the analysis of surface faults (Golombek et al., 1992; Golombek, 1994, 2002) and from numerical models of planetary cooling (Phillips, 1991; Knapmeyer et al., 2006; Plesa et al., 2018a). Maps of tectonic centers were compiled based on orbital imaging of the surface. Using the Mars Orbiting Laser Altimeter shaded topographic relief maps, Knapmeyer et al. (2006) compiled a global fault catalog and used it to predict the martian seismicity and the distribution of epicenters by associating the event size with fault length. Another study by Plesa et al. (2018a) used 3D geodynamic thermal evolution models combined with spatial variations of crustal thickness to evaluate the seismogenic layer thickness and the present-day martian seismicity. While all previous models predicted that Mars is seismically active today with a seis-

micity between that of the Moon and that of the Earth, the uncertainties of the annual seismic moment covered several orders of magnitude.

Since more than three years, InSight's seismometer (SEIS) has been recording seismic events on Mars. In the absence of microseismic events that are observed on the Earth, SEIS is able to record extremely small amplitude events on Mars (Lognonné et al., 2020). Although sensitive to the martian wind that leads to a noisy environment during the martian mid-day (Giardini et al., 2020), SEIS was able to record over 2000 teleseismic events (InSight Marsquake Service, 2022) mostly during the late afternoon and evening, when the noise level is low. For some of these events the location could be determined and several of them have been localized in the Cerbeus Fossae region (Zenhäusern et al., 2022) – a young fault system with a minimum age of 10 Myr situated between 20° and 40° east of the InSight landing site (Taylor et al., 2013). A recent study by (Horleston et al., 2022) reported on distant seismic events, one of which could be located in Valles Marineris (146°±7°). For many events, however, a localization is difficult in particular due to large uncertainties in the backazimuth that are caused by high scattering and noise levels in the seismic data. Therefore, for many of the recorded seismic events only a distance can be provided, while the direction that is required to determine the location of the source remains unclear (Giardini et al., 2020). Recent advances in the study of these events, by using a comprehensive polarization analysis, have been applied to improve the estimates of the distribution of seismicity on Mars (Zenhäusern et al., 2022).

On Mars planetary cooling was thought to be the main source of present day seismicity. However, high frequency events detected by InSight may be driven by solar illumination, the CO_2 cycle or annual solar tides (Knapmeyer et al., 2021). Moreover, the high level of seismicity observed in Cerberus Fossae (Zenhäusern et al., 2022) could be indicative of processes such as magma ascent thorough the crust and lithosphere that may be ongoing on Mars. Indeed, some of the low frequency marsquakes have been suggested to be related to volcanic tremor in Elysium Planitia region (Kedar et al., 2021). Thus, seismicity may not only be linked to the cooling of the interior, but also to ongoing magmatic processes, and knowledge about the level of seismic activity and location of seismic events can help to constrain the evolution and present-day state of the martian mantle. Global thermal evolution models which use crustal thickness variations derived from gravity and topography data and anchored by the seismic observations at InSight landing site, show a close correlation between the crustal thickness varia-

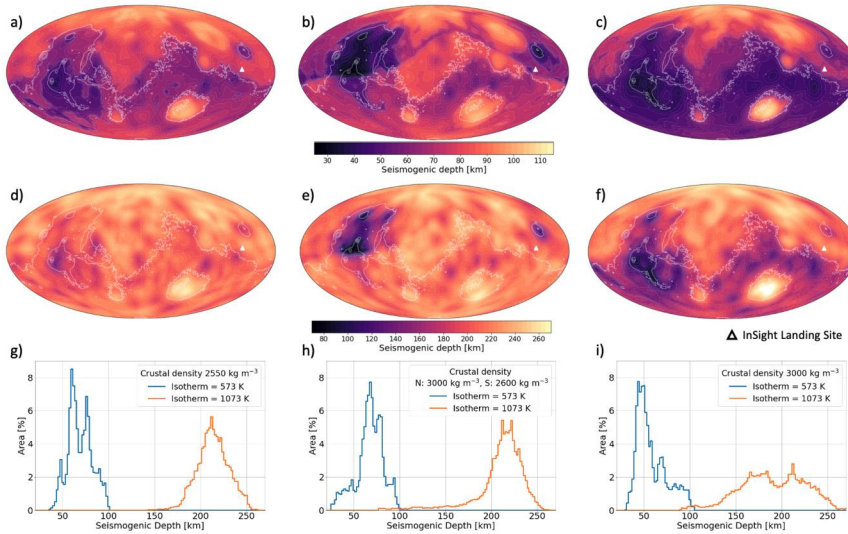

Figure 11 Maps of the seismogenic layer at present day computed using the 573 K isotherm (panels a, b, and c) and the 1073 K isotherm (panels d, e, and f). Panels g, h, and i show histograms for the seismogenic layer thickness. Panels a, d, and g show the results obtained for the thin crust end-member case, Panels b, e, and h show the seismogenic layer thickness for the density dichotomy crust, and panels c, f, and i show the values that were obtained for the thick crust end-member. For orientation, the white contour lines show the 0 km level of surface topography.

tions and the seismogenic layer thickness (Fig. 11). The latter is typically estimated by using an isotherm that describes the depth up to which seismic events could originate. In previous studies isotherms between 573 K and 1073 K have been tested (Phillips, 1991; Knapmeyer et al., 2006; Plesa et al., 2018a). The 573 K isotherm marks the temperature at which quartz, the most ductile component of a granitic crust starts to show a plastic behavior (Scholz, 1998). Thus, this temperature is often associated with the bottom of the seismogenic layer on Earth. The 1073 K isotherm is more representative for a basaltic composition, as it marks the maximum depth of oceanic intraplate quakes (Bergman, 1986; Wiens and Stein, 1983). Since the majority of the martian crust is thought to have a basaltic composition, this value has been suggested to be more representative for determining the depth of the seismogenic layer on Mars.

In Fig. 11 the depth of the seismogenic layer is shown for the three thermal evolution models discussed in Section 3 that employ the crustal thickness variations illustrated in Fig. 1. The seismogenic layer was cal-

Table 6 Seismogenic layer thickness obtained the three models presented in Fig. 1 using a 573 K and a 1073 K isotherm. Min, median, and max show the minimum, median and maximum values attained in each model.

Isotherm		Thin crust [km]	Density dichotomy crust [km]	Thick crust [km]
573 K	min	38.77	28.71	33.74
	median	76.40	75.83	58.52
	max	104.16	104.16	109.19
1073 K	min	143.42	79.48	90.07
	median	219.15	221.50	193.87
	max	265.29	266.55	281.77

culated by using the 573 K (Fig. 11a, b, and c) and 1073 K isotherms (Fig. 11d, e, and f), and the results are shown in Table 6. Similar to the models presented in Plesa et al. (2018a), due to their effects on the lithospheric temperatures, the variations of the crustal thickness control the seismogenic layer thickness variations. For the 573 K isotherm a clear dichotomy can be observed for the seismogenic layer thickness of the thin and thick crust end-members (Fig. 1a and b). For the density dichotomy crust, where variations in crustal density reduce the variations in crustal thickness, the seismogenic layer thickness is more homogeneous, but shows small values in Tharsis and Elysium provinces that are characterized by a thicker crust compared to the rest of the planet. For the 1073 K isotherm the crustal thickness dichotomy pattern is no longer visible for the thin crust model, as in this case this temperature is attained at a depth that is no longer sensitive to the temperature variations caused by the crustal thickness pattern. Due to the thicker crust and higher amount of crustal HPEs in the thick crust model, a dichotomy in the seismogenic layer is still visible for the 1073 K isotherm. The crustal density dichotomy model shows a thin seismogenic layer in Tharsis and Elysium areas and otherwise a rather homogeneous distribution.

For the 573 K isotherm the seismogenic depth is much shallower compared to the 1073 K isotherm. The seismogenic layer thickness of the models presented in Fig. 11 show values between 29 and 109 km when the seismogenic layer is defined using the 573 K isotherm, while for the 1073 K isotherm the seismogenic layer thickness extends to depths of 282 km. Compared to the 573 K isotherm, the range of seismogenic layer thicknesses obtained with the 1073 K isotherm is nearly twice as large. As already shown by Plesa et al. (2018a) the range of seismogenic layer thickness increases for large crustal thickness variations. The values presented in Fig. 11

are smaller than the high density crust models (HC models) of Plesa et al. (2018a), but similar to the values obtained for the crustal thickness of Neumann et al. (2004) (NC models) and those for a density dichotomy crust (DC models). This is due to the fact that the HC models of Plesa et al. (2018a) have a thick crust (87.1 km on average) with a high amount of crustal HPEs and a cold mantle and lithosphere that lead to a thick seismogenic layer. Later, these models were excluded, as they were found to produce a much thinner elastic thickness than the south pole estimate due to the presence of a decoupling layer between the elastic cores of the mantle and crust (Plesa et al., 2018b). Furthermore, the average thickness of the HC models exceeds 72 km and is thus incompatible with the recent seismic data of the InSight mission (Knapmeyer-Endrun et al., 2021).

The seismogenic layer thickness is directly linked to the depth of seismic events, since deep seismic events could be indicative of a cold and thick lithosphere. For the three models shown in Fig. 11 some regions such as the Tharsis region, Elysium Planitia, and Arabia Terra region show a different seismogenic thickness depending on the exact model and the isotherm used. We note, however, that deep events are necessary to be able to distinguish between seismogenic depth distributions predicted from thermal evolution models (Plesa et al., 2018a). Shallow seismic events can occur in both thin and thick seismogenic layers. In general, deep seismic events would indicate that the 1073 K isotherm is more appropriate to define the seismogenic layer thickness. Specifically, deep seismic events in e.g., Arabia Terra could be indicative of a seismogenic thickness distribution such as the one observed for the density dichotomy crust (Fig. 11), while deep seismic events in Daedalia Planum around Arsia Mons and in the adjacent Terra Sirenum region could exclude the thick crust model. Deep seismic events in the northern part of the Tharsis province around Alba Mons would favor the thin crust model, while seismic events as deep as 280 km could only be obtained in Hellas basin in the thick crust model. However, source depths of marsquakes recorded by InSight lie at about 20–50 km below the surface (Brinkman et al., 2021; Stähler et al., 2021), but depth uncertainties remain large (Brinkman et al., 2021). Thus, currently none of the seismogenic layer distributions suggested by Plesa et al. (2018a) and shown in Fig. 11 can be excluded based on the depth of seismic events.

The seismogenic layer volume can be calculated from the seismogenic layer thickness and can be used to estimate an annual seismic moment knowing the strain rate from thermal evolution models.

$$M_{cum} = \eta \dot{\varepsilon} V \mu \Delta t, \tag{10}$$

where η is the seismic efficiency with values between 0 and 1 that describe how much of the strain is released in form of seismic events compared to aseismic deformation. The strain rate $\dot{\varepsilon}$ is estimated from thermal evolution models. V is the seismogenic layer volume, μ is the shear modulus and Δt is the time interval used to compute the seismic moment.

Previous studies by Knapmeyer et al. (2006) and Phillips (1991) have used parametrized thermal evolution models and investigated the rate of planetary cooling to estimate an annual seismic moment. In a more recent study, Plesa et al. (2018a) used global 3D models and estimated the annual seismic moment distribution based on the local contributions of strain rates associated with mantle cooling and convection. The contribution associated with convective stresses was found to be high in regions covered by a thick crust that leads to higher subsurface mantle temperatures and lower viscosities allowing for material to flow. The contribution associated with cooling stresses on the other hand was found to be high in area covered by a thin crust such as the northern hemisphere or large impact basins. In the absence of a thick insulating crust, these areas cool more efficiently and can produce higher cooling stresses compared to regions covered by a thick crust. While the seismic moment contributions from convective and cooling stresses are anti-correlated, given the fact that Mars is a stagnant lid planet and thus convective stresses are negligible in the shallow subsurface, the contribution from convective stresses is typically smaller compared to that of cooling stresses. Moreover, the contribution of convective stresses is entirely absent for the 573 K isotherm, as this isotherm would lead to a thin seismogenic layer.

The distribution of the annual seismic moment is shown in Fig. 12. For the 573 K isotherm the distribution of the annual seismic moment reflects the cooling pattern of the lithosphere that is controlled by the crustal thickness variations. Areas covered by a thick crust show a lower annual seismic moment budget, due to their slower cooling compared to areas covered by a thin crust. For the 1073 K isotherm, on the other hand, the annual seismic moment distribution is rather homogeneous. The contribution associated with convective stresses illustrates that a higher seismic moment can be attained in the southern hemisphere and the Tharsis and Elysium volcanic provinces, given their thicker crust that leads to warmer temperatures in those regions. The cooling stresses are more homogeneously distributed with slightly lower values in Tharsis and the southern hemisphere in particular for the density dichotomy and thick crust models (Fig. 12h and i, respectively). Nevertheless, when combining the contribu-

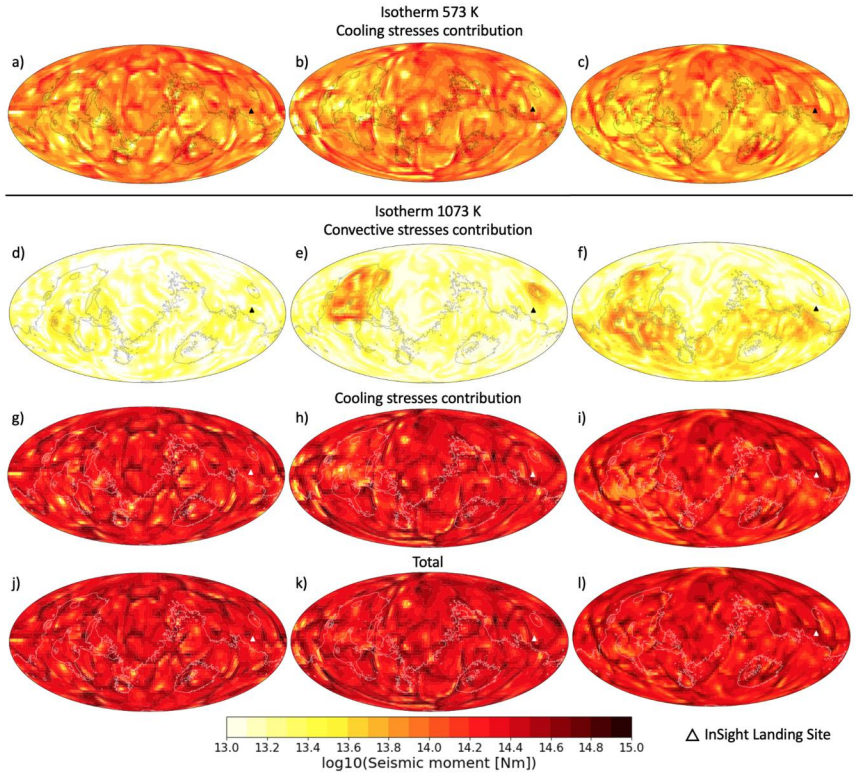

Figure 12 Spatial distribution of the annual seismic moment budget computed using the 573 K isotherm to define the seismogenic layer thickness (panels a, b, and c). Panels d, e, and f show the convective stresses contribution, panels g, h, and i the contribution associated with cooling stresses, and panels j, k, and l the total annual seismic moment budget computed using the 1073 K isotherm. Left column (panels a, d, g, and j) shows the results obtained for the thin crust end-member case, middle column (panels b, e, h, and k) shows the case with a density dichotomy crust, and right column (panels c, f, i, and l) shows the thick crust end-member case. The white and gray contour lines show the 0 km level of surface topography.

tions from cooling and convective stresses, the total contribution leads to a more homogeneous pattern, as it was also discussed by Plesa et al. (2018a).

The total available annual seismic moment budget can be used to compute a size-frequency distribution that often follows a Gutenberg-Richter law. The size-frequency distribution indicates the number of events that would be expected to occur over the course of a year with a seismic moment larger or equal to the largest assumed marsquake (seismic moment M_0). The moment release obtained from global 3D thermal evolution

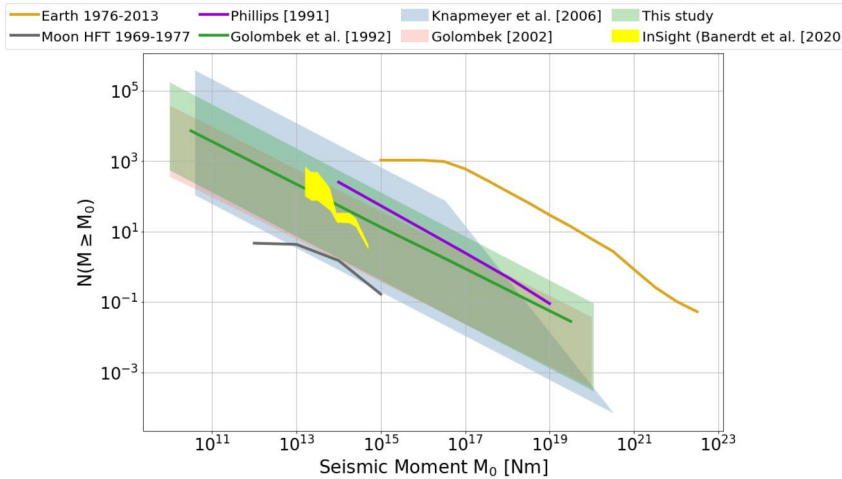

Figure 13 Comparison of the moment-frequency diagram for the Earth, Moon, and Mars. For Mars, the comparison includes the models presented in Fig. 1 (this study), previous seismicity estimates from Knapmeyer et al. (2006), Golombek (2002), Golombek et al. (1992), and Phillips (1991), as well as the values derived from the InSight data (Banerdt et al., 2020). Similar to Plesa et al. (2018a), the maximum seismic moment for a marsquake was assumed to be 10^{20} Nm and the slope was set to 0.625 (Knapmeyer et al., 2006), as suggested from the analysis of quakes occurring above the olivine-bridgmanite transition on Earth (Kagan, 2002).

models that include the recent constraints from the InSight data on core size and crustal thickness is shown in Fig. 13. Models indicate an annual cumulative seismic moment between 5.19×10^{16} and 1.52×10^{19} Nm, similar to previous values from thermal evolution calculations (Knapmeyer et al., 2006; Plesa et al., 2018a). Fig. 13 also includes previous estimates from lithospheric cooling computed using parametrized thermal evolution models (Knapmeyer et al., 2006; Phillips, 1991), as well as from total slip on surface faults (Golombek et al., 1992; Golombek, 2002). The seismic moment release of the Earth was obtained from Harvard Centroid Moment Tensor catalog between 1976 and 2013, while that of the Moon was derived from shallow moonquakes (Oberst, 1987). The seismicity of Mars was derived based on InSight observations of marsquakes and extrapolated to the entire planet to account for uncertainties in detecting small and distant events (Banerdt et al., 2020).

The size-frequency diagram in Fig. 13 is sensitive to the largest seismic moment assumed. Values of the maximum possible seismic moment for Mars were estimated based on data from oceanic and continental intraplate

quakes on Earth and lie around 10^{20} Nm yr^{-1} (Phillips, 1991; Golombek et al., 1992; Golombek, 1994). Adopting this value and using the total cumulative moment release (Eq. (10)) the moment-frequency relation can be calculated. Additional uncertainties are related to the seismic efficiency η that lies between 0.025 and 1 for events on Earth (Ward, 1998b,a), with values larger than 0.7 being representative for regions located at the border between North American and Pacific plates and small values indicating small strain regions, typical for central USA and northwest Europe (Ward, 1998b). In addition, the cumulative moment release is proportional to the shear modulus, that for PREM varies between 26.6 GPa at the surface to 68.2 GPa at the base of the crust (Dziewonski and Anderson, 1981).

It is important to note that the models of Plesa et al. (2018a) and those presented in Fig. 12 do not include the contribution of stresses produced by lithospheric flexure due to loading. Tensile-compressive stresses as well as shear stresses distribution in the martian lithosphere correlate with surface structures and can affect the seismic moment distribution in particular in areas such as Tharsis, Hellas Planitia, Argyre Planitia, Acidalia Planitia, Arcadia Planitia, and Valles Marineris (Gudkova et al., 2017; Batov et al., 2018). In addition, although the seismicity distribution Fig. 12 includes the contribution from convective stresses that reflect the presence of strong mantle plumes in the interior, it does not consider the contribution from magmatic processes that may be ongoing on Mars. This contribution may be specifically important in areas close to the large volcanic centers in Tharsis and Elysium, and may explain the observed seismicity in Cerberus Fossae. Thus future models that evaluate the present-day distribution of seismicity need to include these additional contributions.

Tectonic faults at the surface are important indicators of the internal stress distribution in the lithosphere (Banerdt et al., 1992; Carr, 1974; Golombek and Phillips, 2010; Wise et al., 1979). However, the distribution of present-day seismicity cannot be robustly estimated from the distribution of these features, as this would require knowledge of which faults are active today. The distribution of seismically active zones on present-day Mars could range from a nearly homogeneous one, if all faults are considered to be seismically active, to limited areas on the northern hemisphere and in Tharsis and Elysium, if only faults cutting Amazonian terrains are active today (Knapmeyer et al., 2006; Plesa et al., 2018a). Thus, the localization of seismic events is essential to constrain the distribution of seismicity. Maps of the location of seismic events that were recorded by InSight could be used in future studies to discriminate between scenarios of seismicity dis-

tribution proposed by the analysis of various stress contributions and fault locations on the martian surface.

7. Conclusions and future work

The large amount of data and the diversity of data sets that are now available for Mars provide a unique opportunity to investigate the planet's thermal evolution and constrain poorly known parameters such as the mantle viscosity, thermal variations in the interior, or the distribution of heat producing elements between the mantle and the crust. In particular, recent results of the InSight mission provide the most direct constraints for the martian interior. Crustal thickness values, the size of the core and information about the thickness of the thermal lithosphere can be combined with interior evolution models to constrain the thermal history and present-day state of the martian mantle and core.

Global geodynamic models show that the crustal thickness variations control the surface heat flow and elastic lithosphere thickness pattern. The present-day elastic lithosphere thickness at the north pole of Mars is one of the strongest constraints for thermal evolution models and indicates that the mantle contains less than 45% of the total heat production and/or that the polar cap has not yet reached elastic equilibrium.

Lithospheric temperatures show strong variations that correlate with the crustal thickness pattern. These variations lead to a seismic velocities pattern that can extend to depths of 400 km and deeper, depending on the exact crustal thickness model and crustal enrichment in HPEs. The seismic velocities variations due to temperature are larger than due to different compositional models for the mantle.

Thermal evolution models with a large core and a dry mantle viscosity can match the observed tidal deformation values. The size of the core indicates that the convection pattern in the mantle is characterized by several mantle plumes and downwellings, with stronger plumes preferentially focused in Tharsis due to a thick insulating crust at this location. Thus, the formation of the martian crustal dichotomy cannot be explained by an endogenous process that would require a low degree convection pattern, but is likely the result of the combined effects of large-scale impacts during the early martian history and subsequent interior dynamics.

The seismicity obtained from thermal evolution models that employ the latest crustal thickness and core radius estimates is compatible with the seismicity derived from InSight's observations. The seismogenic layer thickness

is sensitive to the crustal thickness variations and can be used to exclude thermal evolution models, if the depth of the events is known and exceeds the model predicted depth.

Several open questions, however, remain and require more modeling work and future observations. One of the largest unknowns that still remains is the surface heat flow of Mars. While estimates of the elastic lithosphere thickness at the north and south poles can be used to constrain the heat loss and the thermal state of the lithosphere at those locations, future models need to investigate scenarios, in which recent magmatic activity in Tharsis and Elysium is compatible with a large elastic thickness at the north pole of Mars.

Since the martian core is most likely liquid at present day, geodynamic thermal evolution models need to investigate whether a thermally driven dynamo can be reconciled with the duration of the martian magnetic field. While in a recent study by Greenwood et al. (2021) 1D thermal evolution models were found compatible with an internally generated magnetic field between 4.1 and 3.6 Gyr ago, it remains to be tested whether these scenarios are compatible with additional constraints on mantle cooling imposed by the large elastic lithosphere thickness at the north pole (Broquet et al., 2020) and by recent volcanic activity in Tharsis and Elysium (Neukum et al., 2004; Vaucher et al., 2009; Hauber et al., 2011).

Future models need to consider constraints from the Chandler Wobble, the movement of the pole away from the planet's average rotation axis, that have been determined from radio tracking observations of Mars Odyssey, Mars Reconnaissance Orbiter, and Mars Global Surveyor (Konopliv et al., 2020). Since the Chandler Wobble period is sensitive to the rheology of the martian mantle, this would provide, in addition to the tidal quality factor Q, a valuable constraint for the mantle viscosity and thermal state of the interior.

Seismic velocities obtained from global geodynamic models need to be combined with seismic waves propagation to test the effect of variations in the mantle and lithosphere on estimated travel times. While in the convective mantle the variations in seismic velocities are typically small, temperature variations in the lithosphere may significantly affect the travel times of seismic waves, in particular for travel paths located on the northern and southern hemispheres.

So far, the distribution of seismicity included only the contributions from cooling and convective stresses. Future models need to include stresses associated with topographic loads and evaluate the contribution from mag-

matic processes. Their predictions for the distribution of seismicity could be constrained with the observed locations of marsquakes.

Acknowledgments

A.-C. Plesa and M. Walterova gratefully acknowledge the financial support and endorsement from the DLR Management Board Young Research Group Leader Program and the Executive Board Member for Space Research and Technology. Numerical simulations presented in this work were performed on the HoreKa supercomputer funded by the Ministry of Science, Research and the Arts Baden-Württemberg and by the Federal Ministry of Education and Research. M. Wieczorek acknowledges the French Space Agency (CNES) and the French National Research Agency (ANR-19-CE31-0008-08) for funding the InSight science analysis. This is InSight Publication No. 307.

References

Anderson, D.L., Duennebier, F.K., Latham, G.V., Toksöz, M.F., Kovach, R.L., Knight, T.C.D., Lazarewicz, A.R., Miller, W.F., Nakamura, Y., Sutton, G., 1976. The viking seismic experiment. Science 194 (4271), 1318–1321.

Anderson, D.L., Miller, W.F., Latham, G.V., Nakamura, Y., Toksöz, M.N., Dainty, A.M., Duennebier, F.K., Lazarewicz, A.R., Kovach, R.L., Knight, T.C.D., 1977. Seismology on Mars. Journal of Geophysical Research 82 (28), 4524–4546.

Andrews-Hanna, J.C., Zuber, M.T., Banerdt, W.B., 2008. The Borealis basin and the origin of the Martian crustal dichotomy. Nature 453, 1212–1215.

Bagheri, A., Efroimsky, M., Castillo-Rogez, J., Goossens, S., Plesa, A.-C., Rambaux, N., Walterová, M., Khan, A., Giardini, D., 2022. Tidal insights into rocky and icy bodies: an introduction and overview. In: Schmelzbach, C. (Ed.), Advances in Geophysics, vol. 63.

Bagheri, A., Khan, A., Al-Attar, D., Crawford, O., Giardini, D., 2019. Tidal response of Mars constrained from laboratory-based viscoelastic dissipation models and geophysical data. Journal of Geophysical Research: Planets 124 (11), 2703–2727.

Banerdt, W.B., Golombek, M.P., Tanaka, K.L., 1992. Stress and tectonics on Mars. In: George, M. (Ed.), Mars, pp. 249–297.

Banerdt, W.B., Smrekar, S.E., Banfield, D., Giardini, D., Golombek, M., Johnson, C.L., Lognonné, P., Spiga, A., Spohn, T., Perrin, C., et al., 2020. Initial results from the InSight mission on Mars. Nature Geoscience, 1–7.

Batov, A., Gudkova, T., Zharkov, V., 2018. Model estimates of non-hydrostatic stresses in the Martian crust and mantle: 2- three-level model. Solar System Research 52 (3), 234–240.

Belleguic, V., Lognonné, P., Wieczorek, M.J., 2005. Strength of faults on Mars from MOLA topography. Journal of Geophysical Research 1110, E11005.

Bergman, E.A., 1986. Intraplate earthquakes and the state of stress in oceanic lithosphere. Tectonophysics 132 (1), 1–35.

Breuer, D., Moore, W.B., 2015. Dynamics and thermal history of the terrestrial planets, the Moon, and Io. Treatise on Geophysics (Second Edition) 10, 299–348.

Breuer, D., Plesa, A.-C., Tosi, N., Grott, M., 2016. Water in the Martian interior – the geodynamical perspective. Meteoritics & Planetary Science 51 (11), 1959–1992.

Breuer, D., Rueckriemen, T., Spohn, T., 2015. Iron snow, crystal floats, and inner-core growth: modes of core solidification and implications for dynamos in terrestrial planets and moons. Progress in Earth and Planetary Science 2 (1), 1–26.

Breuer, D., Spohn, T., 2003. Early plate tectonics versus single plate tectonics on Mars: evidence from the magnetic field history and crust evolution. Journal of Geophysical Research E 108.

Breuer, D., Spohn, T., 2006. Viscosity of the martian mantle and its initial temperature: constraints from crustal formation history and the evolution of the magnetic field. Planetary and Space Science 54, 153–169.

Breuer, D., Yuen, D.A., Spohn, T., Zhang, S., 1998. Three dimensional models of Martian mantle convection with phase transitions. Geophysical Research Letters 25 (3), 229–232.

Brinkman, N., Stähler, S.C., Giardini, D., Schmelzbach, C., Khan, A., Jacob, A., Fuji, N., Perrin, C., Lognonné, P., Beucler, E., et al., 2021. First focal mechanisms of marsquakes. Journal of Geophysical Research: Planets, e2020JE006546.

Broquet, A., Wieczorek, M.A., Fa, W., 2020. Flexure of the lithosphere beneath the North Polar Cap of Mars: implications for ice composition and heat flow. Geophysical Research Letters 47 (5), e2019GL086746.

Broquet, A., Wieczorek, M., Fa, W., 2021. The composition of the south polar cap of Mars derived from orbital data. Journal of Geophysical Research: Planets 126 (8), e2020JE006730.

Burov, E.-B., Diament, M., 1995. The effective elastic thickness (Te) of continental lithosphere: what does it really mean? Journal of Geophysical Research 100, 3905–3927.

Carr, M.H., 1974. Tectonism and volcanism of the Tharsis region of Mars. Journal of Geophysical Research 79 (26), 3943–3949.

Castillo-Rogez, J.C., Efroimsky, M., Lainey, V., 2011. The tidal history of Iapetus: spin dynamics in the light of a refined dissipation model. Journal of Geophysical Research: Planets 116 (E9).

Christensen, U.R., Yuen, D.A., 1985. Layered convection induced by phase transitions. Journal of Geophysical Research 90, 10291–10300.

Collinet, M., Médard, E., Charlier, B., Vander Auwera, J., Grove, T.L., 2015. Melting of the primitive Martian mantle at 0.5–2.2 GPa and the origin of basalts and alkaline rocks on Mars. Earth and Planetary Science Letters 427, 83–94.

Connolly, J., 2009. The geodynamic equation of state: what and how. Geochemistry, Geophysics, Geosystems 10 (10).

Davies, C.J., Pommier, A., 2018. Iron snow in the Martian core? Earth and Planetary Science Letters 481, 189–200.

Dziewonski, A.M., Anderson, D.L., 1981. Preliminary reference Earth model. Physics of the Earth and Planetary Interiors 25 (4), 297–356.

Efroimsky, M., 2012. Tidal dissipation compared to seismic dissipation: in small bodies, Earths, and super-Earths. The Astrophysical Journal 746 (2), 150.

Ewing, M., Latham, G., Press, F., Sutton, G., Dorman, J., Nakamura, Y., Meissner, R., Duennebier, F., Kovach, R., 1971. Seismology of the Moon and implications on internal structure, origin and evolution. Highlights of Astronomy 2, 155–172.

Filiberto, J., Dasgupta, R., 2015. Constraints on the depth and thermal vigor of melting in the Martian mantle. Journal of Geophysical Research: Planets 120 (1), 109–122.

Folkner, W.M., Dehant, V., Le Maistre, S., Yseboodt, M., Rivoldini, A., Van Hoolst, T., Asmar, S.W., Golombek, M.P., 2018. The rotation and interior structure experiment on the InSight mission to Mars. Space Science Reviews 214 (5), 100.

Fraeman, A.A., Korenaga, J., 2010. The influence of mantle melting on the evolution of Mars. Icarus 210 (1), 43–57.

Frey, H., Schultz, R.A., 1988. Large impact basins and the mega-impact origin for the crustal dichotomy on Mars. Geophysical Research Letters 15, 229–232.

Genova, A., Goossens, S., Lemoine, F.G., Mazarico, E., Neumann, G.A., Smith, D.E., Zuber, M.T., 2016. Seasonal and static gravity field of Mars from MGS, Mars Odyssey and MRO radio science. Icarus 272 (Supplement C), 228–245.

Giardini, D., Lognonné, P., Banerdt, W.B., Pike, W.T., Christensen, U., Ceylan, S., Clinton, J.F., van Driel, M., Stähler, S.C., Böse, M., et al., 2020. The seismicity of Mars. Nature Geoscience 13 (3), 205–212.

Golabek, G., Keller, T., Gerya, T.V., Zhu, G., Tackley, P.J., Connolly, J.A.D., 2011. Origin of the martian dichotomy and Tharsis from a giant impact causing massive magmatism. Icarus 215, 346–357.

Golombek, M.P., 1994. Constraints on the Largest Marsquake. LPSC XXV, Houston, Texas. Abstract #1221.

Golombek, M.P., 2002. A revision of Mars seismicity from surface faulting. LPS XXXIII, Houston, Texas. Abstract #1244.

Golombek, M.P., Banerdt, W.B., Tanaka, K.L., Tralli, D.M., 1992. A prediction of Mars seismicity from surface faulting. Science 258 (5084), 979–981.

Golombek, M.P., Phillips, R.J., 2010. Mars tectonics. In: Watters, T.R., Schultz, R.A. (Eds.), Planetary Tectonics. Cambridge University Press, pp. 183–232.

Greeley, R., Schneid, B.D., 1991. Magma generation on Mars: amounts, rates, and comparisons with Earth, Moon, and Venus. Science 254 (5034), 996–998.

Greenwood, S., Davies, C.J., Pommier, A., 2021. Influence of thermal stratification on the structure and evolution of the Martian core. Geophysical Research Letters 48 (22), e2021GL095198.

Grott, M., Baratoux, D., Hauber, E., Sautter, V., Mustard, J., Gasnault, O., Ruff, S.W., Karato, S.-I., Debaille, V., Knapmeyer, M., Sohl, F., Hoolst, T.V., Breuer, D., Morschhauser, A., Toplis, M.J., 2013. Long-term evolution of the Martian crust-mantle system. Space Science Reviews 172 (1), 49–111.

Grott, M., Breuer, D., 2008. The evolution of the Martian elastic lithosphere and implications for crustal and mantle rheology. Icarus 193, 503–515.

Grott, M., Breuer, D., 2010. On the spatial variability of the Martian elastic lithosphere thickness: evidence for mantle plumes? Journal of Geophysical Research 115 (E3).

Grott, M., Morschhauser, A., Breuer, D., Hauber, E., 2011. Volcanic outgassing of CO_2 and H_2O on Mars. Earth and Planetary Science Letters 308, 391–400.

Gudkova, T., Batov, A., Zharkov, V., 2017. Model estimates of non-hydrostatic stresses in the Martian crust and mantle: 1—two-level model. Solar System Research 51 (6), 457–478.

Gudkova, T., Zharkov, V., 2004. Mars: interior structure and excitation of free oscillations. Physics of the Earth and Planetary Interiors 142 (1–2), 1–22.

Hahn, B.C., McLennan, S.M., Klein, E.C., 2011. Martian surface heat production and crustal heat flow from Mars Odyssey Gamma-Ray spectrometry. Geophysical Research Letters 38 (14).

Harder, H., Christensen, U., 1996. A one-plume model of martian mantle convection. Nature 380, 507–509.

Hauber, E., Brož, P., Jagert, F., Jodłowski, P., Platz, T., 2011. Very recent and wide-spread basaltic volcanism on Mars. Geophysical Research Letters 38 (L10201).

Hauck, S.A., Phillips, R.P., 2002. Thermal and crustal evolution of Mars. Journal of Geophysical Research 107 (E7), 5052.

Heister, T., Dannberg, J., Gassmöller, R., Bangerth, W., 2017. High accuracy mantle convection simulation through modern numerical methods – II: Realistic models and problems. Geophysical Journal International 210 (2), 833–851.

Helffrich, G., 2017. Mars core structure—concise review and anticipated insights from InSight. Progress in Earth and Planetary Science 4 (1), 1–14.

Hemingway, D.J., Driscoll, P.E., 2021. History and future of the Martian dynamo and implications of a hypothetical solid inner core. Journal of Geophysical Research: Planets 126 (4), e2020JE006663.

Hirth, G., Kohlstedt, D., 2003. Rheology of the Upper Mantle and the Mantle Wedge: A View from the Experimentalists. American Geophysical Union, pp. 83–105.

Horleston, A.C., Clinton, J.F., Ceylan, S., Giardini, D., Charalambous, C., Irving, J.C.E., Lognonné, P., Stähler, S.C., Zenhäusern, G., Dahmen, N.L., Duran, C., Kawamura, T., Khan, A., Kim, D., Plasman, M., Euchner, F., Beghein, C., Beucler, E., Huang, Q., Knapmeyer, M., Knapmeyer-Endrun, B., Lekić, V., Li, J., Perrin, C., Schimmel, M., Schmerr, N.C., Stott, A.E., Stutzmann, E., Teanby, N.A., Xu, Z., Panning, M., Banerdt, W.B., 2022. The far side of Mars: two distant marsquakes detected by InSight. The Seismic Record 2 (2), 88–99.

InSight Marsquake Service, 2022. Mars Seismic Catalogue, InSight Mission; V9 2022-01-01. ETHZ, IPGP, JPL, ICL, Univ. Bristol.

Kagan, Y.Y., 2002. Seismic moment distribution revisited: II. Moment conservation principle. Geophysical Journal International 149, 731–754.

Karato, S.I., Wu, P., 1993. Rheology of the upper mantle: a synthesis. Science 260, 771–778.

Kaula, W.M., Head, J.W., Merrill, R.B., Pepin, R.O., Solomon, S.C., Walker, D., Wood, C.A., 1981. Basaltic Volcanism on the Terrestrial Planets.

Kedar, S., Panning, M.P., Smrekar, S.E., Stähler, S.C., King, S.D., Golombek, M.P., Manga, M., Julian, B.R., Shiro, B., Perrin, C., Power, J., Michaut, C., Ceylan, S., Giardini, D., Lognonné, P., Bandert, W.B., 2021. Analyzing low frequency seismic events at Cerberus Fossae as long period volcanic quakes. Journal of Geophysical Research.

Keller, T., Tackley, P.J., 2009. Towards self-consistent modeling of the martian dichotomy: the influence of one-ridge convection on crustal thickness distribution. Icarus 202, 429–443.

Khan, A., Ceylan, S., van Driel, M., Giardini, D., Lognonné, P., Samuel, H., Schmerr, N.C., Stähler, S.C., Duran, A.C., Huang, Q., et al., 2021. Upper mantle structure of Mars from InSight seismic data. Science 373 (6553), 434–438.

Khan, A., Liebske, C., Rozel, A., Rivoldini, A., Nimmo, F., Connolly, J.A.D., Plesa, A., Giardini, D., 2018. A geophysical perspective on the bulk composition of Mars. Journal of Geophysical Research 123 (2), 575–611.

Khan, A., Sossi, P., Liebske, C., Rivoldini, A., Giardini, D., 2022. Geophysical and cosmochemical evidence for a volatile-rich Mars. Earth and Planetary Science Letters 578, 117330.

Kiefer, W.S., Filiberto, J., Sandu, C., Li, Q., 2015. The effects of mantle composition on the peridotite solidus: implications for the magmatic history of Mars. Geochimica et Cosmochimica Acta 162, 247–258.

Kiefer, W.S., Li, Q., 2009. Mantle convection controls the observed lateral variations in lithospheric thickness on present-day Mars. Geophysical Research Letters 36, L18203.

Kiefer, W.S., Li, Q., 2016. Water undersaturated mantle plume volcanism on present-day Mars. Meteoritics & Planetary Science 51 (11), 1993–2010.

Kim, D., Lekić, V., Irving, J., Schmerr, N., Knapmeyer-Endrun, B., Joshi, R., Panning, M., Tauzin, B., Karakostas, F., Maguire, R., et al., 2021. Improving constraints on planetary interiors with PPS receiver functions. Journal of Geophysical Research: Planets 126 (11), e2021JE006983.

Knapmeyer, M., Oberst, J., Hauber, E., Wählisch, M., Deuchler, C., Wagner, R., 2006. Working models for spatial distribution and level of Mars' seismicity. Journal of Geophysical Research 111 (E11).

Knapmeyer, M., Stähler, S.C., Daubar, I., Forget, F., Spiga, A., Pierron, T., van Driel, M., Banfield, D., Hauber, E., Grott, M., et al., 2021. Seasonal seismic activity on Mars. Earth and Planetary Science Letters 576, 117171.

Knapmeyer, M., Walterová, M., 2022. Planetary core radii: from Plato towards PLATO. In: Schmelzbach, C. (Ed.), Advances in Geophysics, vol. 63.

Knapmeyer-Endrun, B., Panning, M.P., Bissig, F., Joshi, R., Khan, A., Kim, D., Lekić, V., Tauzin, B., Tharimena, S., Plasman, M., et al., 2021. Thickness and structure of the martian crust from InSight seismic data. Science 373 (6553), 438–443.

Konopliv, A.S., Park, R.S., Folkner, W.M., 2016. An improved JPL Mars gravity field and orientation from Mars orbiter and lander tracking data. Icarus 274 (Supplement C), 253–260.

Konopliv, A.S., Park, R.S., Rivoldini, A., Baland, R.-M., Le Maistre, S., Van Hoolst, T., Yseboodt, M., Dehant, V., 2020. Detection of the Chandler wobble of Mars from orbiting spacecraft. Geophysical Research Letters 47 (21), e2020GL090568.

Kronbichler, M., Heister, T., Bangerth, W., 2012. High accuracy mantle convection simulation through modern numerical methods. Geophysical Journal International 191 (1), 12–29.

Lainey, V., 2016. Quantification of tidal parameters from Solar System data. Celestial Mechanics & Dynamical Astronomy 126, 145–156.

Lawrence, D.J., Feldman, W.C., Barraclough, B.L., Binder, A.B., Elphic, R.C., Maurice, S., Miller, M.C., Prettyman, T.H., 2000. Thorium abundances on the lunar surface. Journal of Geophysical Research 105 (E8), 20307–20331.

Lognonné, P., Banerdt, W., Pike, W., Giardini, D., Christensen, U., Garcia, R., Kawamura, T., Kedar, S., Knapmeyer-Endrun, B., Margerin, L., et al., 2020. Constraints on the shallow elastic and anelastic structure of Mars from InSight seismic data. Nature Geoscience 13 (3), 213–220.

Marinova, M.M., Aharonson, O., Asphaug, E., 2008. Mega-impact formation of the Mars hemispheric dichotomy. Nature 453, 1216–1219.

Matsukage, K.N., Nagayo, Y., Whitaker, M.L., Takahashi, E., Kawasaki, T., 2013. Melting of the Martian mantle from 1.0 to 4.5 GPa. Journal of Mineralogical and Petrological Sciences, 120820.

McCubbin, F.M., Boyce, J.W., Srinivasan, P., Santos, A.R., Elardo, S.M., Filiberto, J., Steele, A., Shearer, C.K., 2016. Heterogeneous distribution of H_2O in the Martian interior: implications for the abundance of H_2O in depleted and enriched mantle sources. Meteoritics & Planetary Science 51 (11), 2036–2060.

McGovern, P.J., Solomon, S.C., Smith, D.E., Zuber, M.T., Simons, M., Wieczorek, M.A., Phillips, R.J., Neumann, G.A., Aharonson, O., Head, J.W., 2004. Correction to "Localized gravity/topography admittance and correlation spectra on Mars: implications for regional and global evolution". Journal of Geophysical Research 109 (E7).

McNutt, M.K., 1984. Lithospheric flexure and thermal anomalies. Journal of Geophysical Research Solid Earth 89 (B13), 11180–11194.

Michel, N., Forni, O., 2011. Mars mantle convection: influence of phase transitions with core cooling. Planetary and Space Science 59, 741–748.

Mittelholz, A., Johnson, C., Feinberg, J., Langlais, B., Phillips, R., 2020. Timing of the martian dynamo: new constraints for a core field 4.5 and 3.7 Ga ago. Science Advances 6 (18), eaba0513.

Mocquet, A., Menvielle, M., 2000. Complementarity of seismological and electromagnetic sounding methods for constraining the structure of the Martian mantle. Planetary and Space Science 48 (12–14), 1249–1260.

Mocquet, A., Vacher, P., Grasset, O., Sotin, C., 1996. Theoretical seismic models of Mars: the importance of the iron content of the mantle. Planetary and Space Science 44 (11), 1251–1268.

Mori, Y., Ozawa, H., Hirose, K., Sinmyo, R., Tateno, S., Morard, G., Ohishi, Y., 2017. Melting experiments on Fe–Fe3S system to 254 GPa. Earth and Planetary Science Letters 464, 135–141.

Morschhauser, A., Grott, M., Breuer, D., 2011. Crustal recycling, mantle dehydration, and the thermal evolution of Mars. Icarus 212, 541–558.

Neukum, G., Jaumann, R., Hoffmann, H., Hauber, E., Head, J., Basilevsky, A., Ivanov, B.A., Werner, S.C., van Gasselt, S., Murray, J.B., McCord, T., Team, T.H.C.-I., 2004. Recent and episodic volcanic and glacial activity on Mars revealed by the High Resolution Stereo Camera. Nature 432, 971–979.

Neumann, G.A., Zuber, M.T., Wieczorek, M.A., McGovern, P.J., Lemoine, F.G., Smith, D.E., 2004. Crustal structure of Mars from gravity and topography. Journal of Geophysical Research 109, E08002.

Nimmo, F., Faul, U.H., 2013. Dissipation at tidal and seismic frequencies in a melt-free, anhydrous Mars. Journal of Geophysical Research 118 (12), 2558–2569.

Nimmo, F., Hart, S.D., Korycansky, D.G., Agnor, C.B., 2008. Implications of an impact origin for the martian hemispheric dichotomy. Nature 453, 1220–1223.

Nimmo, F., Tanaka, K., 2005. Early crustal evolution of Mars. Annual Review of Earth and Planetary Sciences 33 (1), 133–161.

Oberst, J., 1987. Unusually high stress drops associated with shallow moonquakes. Journal of Geophysical Research 92, 1397–1405.

Phillips, R.J., 1991. Expected rates of Marsquakes, in Scientific Rationale and Requirements for a Global Seismic Network on Mars. LPI Tech. Rep., 91-02 LPI/TR-91-02:35–38. Lunar and Planet. Inst., Houston, Texas.

Phillips, R.J., Zuber, M.T., Smrekar, S.E., Mellon, M.T., Head, J.W., Tanaka, K.L., Putzig, N.E., Milkovich, S.M., Campbell, B.A., Plaut, J.J., Safaeinili, A., Seu, R., Biccari, D., Carter, L.M., Picardi, G., Orosei, R., Mohit, P.S., Heggy, E., Zurek, R.W., Egan, A.F., Giacomoni, E., Russo, F., Cutigni, M., Pettinelli, E., Holt, J.W., Leuschen, C.J., Marinangeli, L., 2008. Mars north polar deposits: stratigraphy, age, and geodynamical response. Science 320 (5880), 1182–1185.

Plesa, A.-C., Bozdağ, E., Rivoldini, A., Knapmeyer, M., McLennan, S.M., Padovan, S., Tosi, N., Breuer, D., Peter, D., Staehler, S., et al., 2021. Seismic velocity variations in a 3D Martian mantle: implications for the InSight measurements. Journal of Geophysical Research: Planets, e2020JE006755.

Plesa, A.-C., Breuer, D., 2014. Partial melting in one-plate planets: implications for thermochemical and atmospheric evolution. Planetary and Space Science 98, 50–65. Planetary evolution and life.

Plesa, A.-C., Grott, M., Tosi, N., Breuer, D., Spohn, T., Wieczorek, M.A., 2016. How large are present-day heat flux variations across the surface of Mars? Journal of Geophysical Research 121 (12), 2386–2403.

Plesa, A.-C., Knapmeyer, M., Golombek, M., Breuer, D., Grott, M., Kawamura, T., Lognonné, P., Tosi, N., Weber, R., 2018a. Present-day Mars' seismicity predicted from 3-D thermal evolution models of interior dynamics. Geophysical Research Letters 45 (6), 2580–2589.

Plesa, A.-C., Padovan, S., Tosi, N., Breuer, D., Grott, M., Wieczorek, M., Spohn, T., Smrekar, S., Banerdt, W., 2018b. The thermal state and interior structure of Mars. Geophysical Research Letters 45 (22), 12–198.

Ray, R.D., Eanes, R.J., Lemoine, F.G., 2001. Constraints on energy dissipation in the Earth's body tide from satellite tracking and altimetry. Geophysical Journal International 144 (2), 471–480.

Rivoldini, A., Hoolst, T.V., Verhoeven, O., Mocquet, A., Dehant, V., 2011. Geodesy constraints on the interior structure and composition of Mars. Icarus 213 (2), 451–472.

Roberts, J., Arkani-Hamed, J., 2017. Effects of basin-forming impacts on the thermal evolution and magnetic field of Mars. Earth and Planetary Science Letters 478 (Supplement C), 192–202.

Roberts, J.H., Zhong, S., 2006. Degree-1 convection in the Martian mantle and the origin of the hemispheric dichotomy. Journal of Geophysical Research: Planets 111.

Ruedas, T., Breuer, D., 2017. On the relative importance of thermal and chemical buoyancy in regular and impact-induced melting in a Mars-like planet. Journal of Geophysical Research: Planets 122 (7), 1554–1579, 2016JE005221.

Ruedas, T., Tackley, P.J., Solomon, S.C., 2013. Thermal and compositional evolution of the martian mantle: effects of phase transitions and melting. Physics of the Earth and Planetary Interiors 216, 32–58.

Sabadini, R., Vermeersen, B., 2004. Normal mode theory in viscoelasticity. In: Global Dynamics of the Earth. Springer, pp. 1–44.
Samuel, H., Ballmer, M.D., Padovan, S., Tosi, N., Rivoldini, A., Plesa, A.-c., 2021. The thermo-chemical evolution of Mars with a strongly stratified mantle. Journal of Geophysical Research: Planets 126 (4), e2020JE006613.
Samuel, H., Lognonné, P., Panning, M., Lainey, V., 2019. The rheology and thermal history of Mars revealed by the orbital evolution of Phobos. Nature 569 (7757), 523–527.
Scholz, C.H., 1998. Earthquakes and friction laws. Nature 391, 37–42.
Schubert, G., Turcotte, D.L., Olson, P., 2001. Mantle Convection in the Earth and Planets. Cambridge University Press, Cambridge.
Schumacher, S., Breuer, D., 2006. Influence of a variable thermal conductivity on the thermochemical evolution of Mars. Journal of Geophysical Research 111 (E02006).
Smrekar, S.E., Lognonné, P., Spohn, T., Banerdt, W.B., Breuer, D., Christensen, U., Dehant, V., Drilleau, M., Folkner, W., Fuji, N., et al., 2019. Pre-mission InSights on the interior of Mars. Space Science Reviews 215 (1), 3.
Sohl, F., Spohn, T., 1997. The interior structure of Mars: implications from SNC meteorites. Journal of Geophysical Research 102 (E1), 1613–1635.
Spohn, T., Grott, M., Smrekar, S., Knollenberg, J., Hudson, T., Krause, C., Müller, N., Jänchen, J., Börner, A., Wippermann, T., et al., 2018. The heat flow and physical properties package (HP^3) for the InSight mission. Space Science Reviews 214 (5), 96.
Spohn, T., Sohl, F., Breuer, D., 1998. Mars. The Astronomy and Astrophysics Review 8, 181–235.
Stähler, S., Knapmeyer, M., 2022. Seismology in the solar system. In: Schmelzbach, C. (Ed.), Advances in Geophysics, vol. 63.
Stähler, S.C., Khan, A., Banerdt, W.B., Lognonné, P., Giardini, D., Ceylan, S., Drilleau, M., Duran, A.C., Garcia, R.F., Huang, Q., et al., 2021. Seismic detection of the martian core. Science 373 (6553), 443–448.
Steinbach, V., Yuen, D., 1994. Effects of depth-dependent properties on the thermal anomalies produced in flush instabilities from phase transitions. Physics of the Earth and Planetary Interiors 86, 165–183.
Stevenson, D.J., Spohn, T., Schubert, G., 1983. Magnetism and thermal evolution of the terrestrial planets. Icarus 54, 466–489.
Stewart, A.J., Schmidt, M.W., Van Westrenen, W., Liebske, C., 2007. Mars: a new core-crystallization regime. Science 316 (5829), 1323–1325.
Stixrude, L., Lithgow-Bertelloni, C., 2011. Thermodynamics of mantle minerals – II. Phase equilibria. Geophysical Journal International 184 (3), 1180–1213.
Taylor, G.J., 2013. The bulk composition of Mars. Geochemistry 73 (4), 401–420.
Taylor, G.J., Boynton, W., Brückner, J., Wänke, H., Dreibus, G., Kerry, K., Keller, J., Reedy, R., Evans, L., Starr, R., Squyres, S., Karunatillake, S., Gasnault, O., Maurice, S., d'Uston, C., Englert, P., Dohm, J., Baker, V., Hamara, D., Janes, D., Sprague, A., Kim, K., Drake, D., 2006a. Bulk composition and early differentiation of Mars. Journal of Geophysical Research 111 (E3).
Taylor, G.J., Stopar, J., Boynton, W.V., Karunatillake, S., Keller, J.M., Brückner, J., Wänke, H., Dreibus, G., Kerry, K.E., Reedy, R.C., et al., 2006b. Variations in K/Th on Mars. Journal of Geophysical Research: Planets 111 (E3).
Taylor, J., Teanby, N.A., Wookey, J., 2013. Estimates of seismic activity in the Cerberus Fossae region of Mars. Journal of Geophysical Research: Planets 118 (12), 2570–2581.
Thiriet, M., Michaut, C., Breuer, D., Plesa, A.-C., 2018. Hemispheric dichotomy in lithosphere thickness on Mars caused by differences in crustal structure and composition. Journal of Geophysical Research 123.
Toksöz, M.N., Dainty, A.M., Solomon, S.C., Anderson, K.R., 1974. Structure of the Moon. Reviews of Geophysics 12 (4), 539–567.

Van Thienen, P., Rivoldini, A., Van Hoolst, T., Lognonné, P., 2006. A top-down origin for martian mantle plumes. Icarus 185 (1), 197–210.
Vaucher, J., Baratoux, D., Mangold, N., Pinet, P., Kurita, K., Grégoire, M., 2009. The volcanic history of central Elysium Planitia: implications for martian magmatism. Icarus 204 (2), 418–442.
Ward, S.N., 1998a. On the consistency of earthquake moment rates, geological fault data, and space geodetic strain: Europe. Geophysical Journal International 135, 1011–1018.
Ward, S.N., 1998b. On the consistency of earthquake moment rates, geological fault data, and space geodetic strain: the United States. Geophysical Journal International 134, 172–186.
Wieczorek, M., et al., 2022. InSight constraints on the global character of the Martian crust. Journal of Geophysical Research.
Wieczorek, M.A., 2008. Constraints on the composition of the Martian south polar cap from gravity and topography. Icarus 196 (2), 506–517.
Wieczorek, M.A., Zuber, M.T., 2004. Thickness of the martian crust: improved constraints from geoid-to-topography ratios. Journal of Geophysical Research 109 (E1), E01009. https://doi.org/10.1029/2003JE002153.
Wiens, D.A., Stein, S., 1983. Age dependence of oceanic intraplate seismicity and implications for lithospheric evolution. Journal of Geophysical Research Solid Earth 88 (B8), 6455–6468.
Wilhelms, D.E., Squyres, S.W., 1984. The martian hemispheric dichotomy could be due to a giant impact. Nature 309, 138–140.
Williams, J.-P., Nimmo, F., 2004. Thermal evolution of the Martian core: implications for an early dynamo. Geology 32 (2), 97–100.
Wise, D.U., Golombek, M.P., McGill, G.E., 1979. Tectonic evolution of Mars. Journal of Geophysical Research 84, 7934–7939.
Yoshizaki, T., McDonough, W.F., 2020. The composition of Mars. Geochimica et Cosmochimica Acta 273, 137–162.
Zenhäusern, G., Stähler, S.C., Clinton, J.F., Giardini, D., Ceylan, S., Garcia, R.F., 2022. Low-frequency marsquakes and where to find them: back azimuth determination using a polarization analysis approach. Bulletin of the Seismological Society of America.
Zharkov, V., Gudkova, T., 2005. Construction of Martian interior model. Solar System Research 39 (5), 343–373.
Zheng, Y., Nimmo, F., Lay, T., 2015. Seismological implications of a lithospheric low seismic velocity zone in Mars. Physics of the Earth and Planetary Interiors 240, 132–141.
Zhong, S., Zuber, M.T., 2001. Degree-1 mantle convection and the crustal dichotomy on Mars. Earth and Planetary Science Letters 189, 75–84.

CHAPTER FIVE

Tidal insights into rocky and icy bodies: an introduction and overview

Amirhossein Bagheri[a,*], Michael Efroimsky[b], Julie Castillo-Rogez[c], Sander Goossens[d], Ana-Catalina Plesa[e], Nicolas Rambaux[f], Alyssa Rhoden[g], Michaela Walterová[e], Amir Khan[h,a], and Domenico Giardini[a]

[a]Institute of Geophysics, ETH Zürich, Zürich, Switzerland
[b]US Naval Observatory, Washington, DC, United States
[c]Jet Propulsion Laboratory, California Institute of Technology, Pasadena, CA, United States
[d]NASA Goddard Space Flight Center, Greenbelt, MD, United States
[e]DLR Institute of Planetary Research, Berlin, Germany
[f]IMCCE, CNRS, Observatoire de Paris, PSL Université, Sorbonne Université, Paris, France
[g]Southwest Research Institute, Boulder, CO, United States
[h]Physik-Institut, University of Zürich, Zürich, Switzerland
*Corresponding author. e-mail addresses: amirhossein.bagheri@erdw.ethz.ch, amirhbagheri@yahoo.com

Contents

Advances in Geophysics, Volume 63
ISSN 0065-2687
https://doi.org/10.1016/bs.agph.2022.07.004

1. Introduction

The Solar system harbors a diverse population of planetary bodies. These include objects formed of rock, ice, gas, as well as objects of a mixed composition. Over the past two decades, our understanding of these bodies' interior structure has been considerably improved owing to the valuable data provided by several successful space missions. A combined perception of celestial bodies' interiors and the mechanisms that govern their evolution can represent an efficient means to infer information about their past history and origin which help us to understand how the Solar system has formed and evolved. Given the scarcity of seismic data for the planetary bodies except the Earth, the Moon, and Mars, our studies have to rely on remote sensing and geodetic measurements. An efficient means to infer knowledge on the planets' and moons' interior structure is their tidal response to the gravitational attraction from other objects.

A planet's side facing its satellite is attracted by the satellite stronger than the opposite side. Since the planet's rotation is, generally, not synchronized with the period of the orbiting satellite, the satellite exerts a periodically changing force field and a resulting deformation field in the hosting planet. These changes in the gravitational potential generated by the satellite are known as *tides* (Fig. 1). Aside from the well-known ocean tides on the Earth, both the Earth and other planets demonstrate atmospheric tides and, most importantly, *bodily tides*, a phenomenon on which this chapter concentrates. This phenomenon is always reciprocal; so the satellite, in its turn, is experiencing periodic perturbation of the planet-generated potential, and is developing periodic deformation. The Sun can also play the same role and generate tides in the planets and itself experiences tides generated by them.

Tidal deformation of a celestial body results in both vertical and horizontal displacement of its surface and in the ensuing perturbation of its gravitational field. These variations are described by three parameters: h, l,

and k. The two former parameters (h, l) represent the deformations caused by the tidal force on the planet in the vertical and horizontal directions, respectively, whereas k represents the induced perturbation in the gravitational field. h and k are known as Love numbers and l is known is the Shida number.

The interior of a planetary body is not perfectly elastic and is affected by internal friction, as a result of which the tidal bulge does not exactly align with the position of the tide-raising body, but exhibits a phase lag. The *quality factor* Q is defined as the inverse of the sine of the absolute value of the phase angle between the tidal bulge and the direction towards the tide-raising body. It relates to the energy dissipated by friction per loading cycle, in such a way that a lower Q implies higher dissipation. Both the tidal deformation magnitude and the phase lag are sensitive to the large-scale interior properties of the body, such that a larger deformation (higher Love numbers) would imply that the interior of the object is less rigid (contains fluid parts, highly porous material, etc.), while a larger phase lag would imply that the interior is composed of a material that is more viscous. Thus, the tidal response, represented in the form of the tidal Love numbers and tidal quality factor, is used to probe the structural properties of the planetary body. Owing to their long-wavelength nature, tides sample the large-scale interior properties of the body and can be used to probe its deep interior.

Studying the planetary tidal response dates back to Love (1911), in the early 20th century, when the response of a compressible and homogeneous Earth model was first computed. With the increasing precision of modern geodesy, the tidal response of the Earth can be measured by satellite altimetry and the Global Positioning Systems (e.g., Yuan et al., 2013); the semidiurnal tidal Love numbers and the tidal quality factor of the Earth are $k_2 = 0.3531$, $h_2 = 0.6072$, $l_2 = 0.0843$, and $Q \sim 10$, respectively (Seitz et al., 2012; Krásná et al., 2013) (For earlier measurement and analysis, see Dehant (1987); Mitrovica et al. (1994); Smith et al. (1973); Ryan et al. (1986); Haas and Schuh (1996); Petrov (2000)). Tidal dissipation in the Earth takes place predominantly in the oceans, especially in shallow seas. The dissipation in the oceans excluded, the solid-Earth tidal quality factor is found to be $Q \sim 280 \pm 70$ (Egbert and Ray, 2003). Based on such measurements, tidal tomography studies have been efficiently used to constrain the large-scale features of the Earth's deep interior, such as the nature of two large low-shear-velocity provinces (LLSVP) (Métivier and Conrad, 2008; Latychev et al., 2009; Lau et al., 2017).

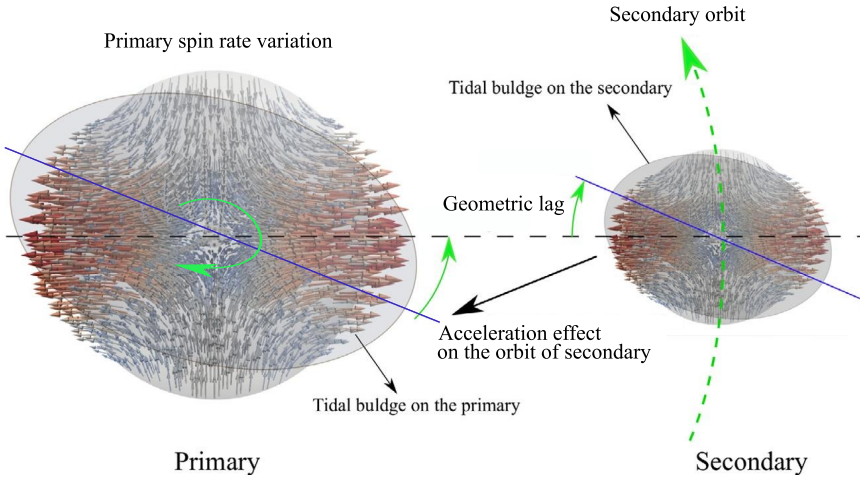

Figure 1 Tidal force field and the geometric lag induced in a planet and its satellite resulting from the gravitational attraction of the two bodies towards each another. Tension in the body is shown with red and compression with blue arrows where the size of the arrows indicates the force magnitude. The force field is shown on the unperturbed bodies. The maximum tidal force in the perturbed body is induced in the side of the body that faces the perturber. The tidal evolution changes the orbit period of the satellite and spin rate of the rotation of two bodies, driving their orbital properties towards synchronism.

The purpose of this chapter is to provide an introduction to the existing knowledge on the interior of the planetary bodies, based on studying their tidal activity. In this chapter, we cover the fundamental aspects and formulation of tidal modeling and discuss the role played by tides in understanding the planetary bodies. First, we review the general aspects of viscoelasticity followed by several viscoelastic models used to mimic dissipation in materials, next we provide the fundamental information for modeling the tidal response of a planetary body followed by a brief introduction to tidal evolution and thermal coupling. Next, we discuss the constraints obtained by using the tidal response measurements in understanding the interior properties and evolution of several rocky and icy planetary bodies in the Solar system, i.e., Mercury, Venus, the Moon, Mars, and the largest moons of gas giants. We also discuss what can be learned from measuring the tidal response by the anticipated missions to the planetary bodies on which we currently have either no measurement or measurements without enough precision. While this chapter mostly discusses the interior structure based on measurements of tidal response presented by tidal Love number and tidal

quality factor, we also provide a short summary of the surface geological features resulting from tidal activity, and of these features' interpretation for the interior properties and evolution of the planetary bodies.

2. Viscoelasticity

Tidal dissipation in a planetary body is a complex process which depends on large scale interior structure of the body and the frequency of excitations. In this section, we review the fundamentals of viscoelastic relaxation and the models used to mimic these processes. Note that tidal dissipation differs from seismic dissipation, because it is defined not only by the internal structure of the body and the dissipative properties of its layers but also by the interplay of these properties with the body's self-gravitation. Leaving the description of this interplay for Section 4, in the current section, we address the rheological properties of the materials, from which the planetary bodies are formed.

2.1 General aspects

Dissipation in a material is, essentially, a relaxation process whose effectiveness is sensitive to the material composition, temperature, confining pressure, grain size and, importantly, to the frequency of forcing. The combined influence of these parameters on the energy damping rate is highly nontrivial, and is defined by complex microscale processes such as grain-boundary interactions, dislocation migration and the presence of voids and melt (e.g., Jackson et al., 2002; Jackson and Faul, 2010; McCarthy et al., 2011; Sundberg and Cooper, 2010; Takei et al., 2014). Hence, an appropriate modeling of the viscoelastic behavior of a celestial body is crucial for the correct interpretation of its tidal measurements.

Mars, as an example, appears to be an instructive case of necessity for such modeling. Compared to the solid-Earth quality factor at semidiurnal tides ($Q = 280 \pm 70$, Ray et al. (2001)), the Martian quality factor at the period of Phobos's tides (T = 5.55 hr) is surprisingly low, i.e., $Q \approx 78 - 100$, (e.g., Jacobson and Lainey, 2014). Applying the simplistic Maxwell rheology to Mars results in an unreasonably low average viscosity ($\sim 10^{14}$ Pa s) (Bills et al., 2005), in contrast to that estimated for the Earth's mantle ($\sim 10^{22-23}$ Pa s) (Anderson and O'Connell, 1967; Karato and Wu, 1993). This result is surprising, given that Mars is expected to have cooled faster on account of its smaller size, and therefore has a higher viscosity value than the solid Earth (see, e.g., Plesa et al. (2018); Khan et al. (2018)). The issue

is resolved by employing a more realistic viscoelastic model attributing the high tidal dissipation to strong anelastic relaxation in Mars (Castillo-Rogez and Banerdt, 2012; Nimmo and Faul, 2013; Khan et al., 2018; Bagheri et al., 2019).

Another example showing the necessity for accurate rheological modeling is Venus. Application of a simplistic elastic model to the mantle would yield to an enticing but naive interpretation for the measured tidal Love number value (Dumoulin et al., 2017; Konopliv and Yoder, 1996). This interpretation would suggest a fully liquid core (Konopliv and Yoder, 1996). However, a fully solid iron core has been shown to be a plausible option, as well, when viscoelasticity is taken into account (Dumoulin et al., 2017; Yoder, 1995). Further insights about tides on Venus and Mars are provided in Sections 5.2 and 5.4, respectively. These examples reveal that accurate modeling of viscoelastic dissipation in planetary bodies is essential to understanding their interior structure.

Based on various friction mechanisms taken into account, several viscoelastic models have been proposed and constrained by means of laboratory experiments (e.g., Gribb and Cooper, 1998; Faul et al., 2004; Jackson, 2005; Jackson and Faul, 2010; Takei et al., 2014). Most of the experimental studies have focused on rocky materials such as olivine and orthopyroxene (see, e.g., Qu et al. (2021) and Jackson and Faul (2010)), whereas few studies have considered the dissipation in ice (McCarthy and Cooper, 2016). These models have been utilized to study the planetary data (Lau and Faul, 2019; Nimmo et al., 2012; Nimmo and Faul, 2013; Khan et al., 2018). Because of its ease of implementation, the Maxwell rheology has long been employed to model the viscoelastic behavior of the planets and moons, and has been especially popular in the studies of very long timescales such as glacial isostatic adjustment (Al-Attar and Tromp, 2013; Crawford et al., 2018; Ivins et al., 2021; Lau et al., 2021). This model, however, fails to accommodate the transient anelastic behavior between the fully elastic and viscous regimes (Rambaux et al., 2010; Renaud and Henning, 2018; Castillo-Rogez and Banerdt, 2012), which makes it inapplicable at seismic and oftentimes at tidal frequencies.

Due to the shortcomings of the Maxwell model, in later studies it was suggested to rely on a combined Maxwell-Andrade model, often referred to as simply the Andrade model (e.g., Andrade, 1910; Rambaux et al., 2010; Castillo-Rogez et al., 2011; Efroimsky, 2012). More sophisticated options, such as the Burgers model and the Sundberg–Cooper model incorporate anelasticity as a result of elastically-accommodated and dislocation- and

diffusion-assisted grain boundary sliding processes (Burgers, 1935; Sundberg and Cooper, 2010; Jackson, 2005, 2000; Jackson and Faul, 2010). These models can be further adjusted to take into account the effect of grain size, frequency, temperature, and pressure on the dissipation – a fundamental set of parameters that are needed to describe planetary interiors (e.g., Jackson and Faul, 2010).

Geophysical analysis enables us to test viscoelastic models against the attenuation data gleaned over a broad frequency range: from seismic wave periods ($\leq$1 s) over normal modes ($\sim$1 hr), bodily tides (hrs-days), and Chandler Wobble (months), to very long-period tides ($\sim$20 years). This frequency gamut is spanning five orders. Equipped with this knowledge, we can then model the quality factors of planets and use the available measurements to predict the dissipation behavior over a large range of periods. Fig. 2 shows the measured quality factor of the solid Earth as a function of period, ranging from seconds to years. Here, the extended Burgers viscoelastic model (described in Section 2.4) has been considered and constrained by geophysical observations (Lau and Faul, 2019). In this figure, dissipation in the measured surface waves, normal modes, semidiurnal M2 tides, Chandler Wobble, and the 18.6 yr long-period tides are taken into account. As shown in the figure, studying the dissipation in the Earth, particularly its frequency dependence, has resulted in diverse interpretation, revealing the complexity of this process and the need for further considerations.

Studying tides is not limited to rocky planets. In the recent years, substantial attention has been devoted to the tidal dynamics of icy systems such as Trans-Neptunian Objects, including the Pluto–Charon binary and Kuiper belt objects (e.g., Bierson et al., 2020; Bagheri et al., 2022; Rhoden et al., 2020; Saxena et al., 2018; Arakawa et al., 2021; Renaud et al., 2021), as well as the Galilean moons, Iapetus and Enceladus (e.g., Kamata and Nimmo, 2017; Shoji et al., 2014; Spencer, 2013; Tyler, 2009, 2014; Beuthe, 2019; Tyler, 2011). All these bodies are either presently tidally active or experienced significant tidal activity in their history. Understanding the tidal response of these bodies is essential to constrain their origin and, more importantly, to assess in some cases the potential habitability of their interior. Modeling their past evolution requires information on dissipation in ice. Due to the much lower viscosity of ice in comparison to rocks (McCarthy and Cooper, 2016), dissipation in ice can easily dominate that in the rock in the bodies containing parts composed of both ice and rock. This applies also to binaries in the outer Solar system where the temperature is

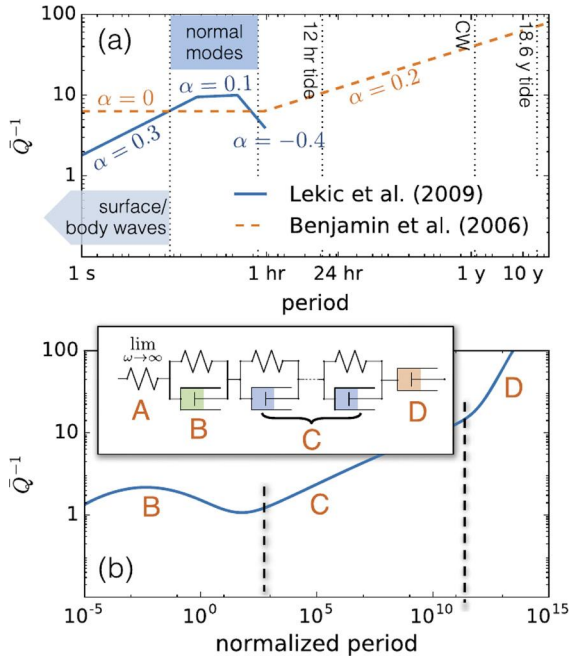

Figure 2 (a) The frequency dependence of normalized attenuation, $\bar{Q}^{-1}$ for the solid Earth, displaying the contrasting absorption bands reported by Benjamin et al. (2006) and Lekić et al. (2009) (orange–dashed and blue–solid lines, respectively). The former study used geodetic observations of the semidiurnal and long-period tides and of the Chandler Wobble (CW), whose periods are indicated by the vertical black dotted lines. The latter study used surface wave and normal mode data whose frequency bands are marked by blue boxes. (b) Main panel: schematic frequency dependence of attenuation of the Extended Burgers model (Faul and Jackson, 2015). Inset: the mechanical components of the Extended Burgers model in spring-dashpot representation. Figure and caption modified from Lau and Faul (2019). For further details on the figure, please refer to the (Lau and Faul, 2019).

too low for the rocky fraction to dissipate energy, and most of the tidal dissipation is taking place in the ice layers. The viscoelastic behavior of ice can be studied using the same models as those used for rocks (Renaud et al., 2021; Sundberg and Cooper, 2010; Bagheri et al., 2022).

The mentioned viscoelastic models have been used to study dissipation in the planetary bodies (discussed in Section 5), although the measured data for the planetary bodies other than the Earth is considerably more limited. In the next sections, we review the theoretical aspects of material viscoelastic properties followed by a summary of several laboratory-based rheological models. Note that here, we are mostly focusing on the solid

body tides, not on the dissipation in fluid parts such as the molten core or the surface and subsurface oceans. The effect of liquid parts on tidal dissipation is a complex process believed to be responsible for phenomena such as libration of Mercury (e.g., Rambaux et al., 2007; Margot et al., 2007; Peale, 2005) or precession of the Moon (e.g., Yoder, 1981; Cébron et al., 2019; Williams et al., 2001). Moreover, it has been argued that in some circumstances dissipation in the ocean can dominate that in the solid parts (Tyler, 2008; Tyler et al., 2015; Tyler, 2009). However, detailed discussion on the possibility of significant tidal dissipation in the ocean is outside the scope of this study.

2.2 Constitutive equation

Rheological properties of a material are expressed by a constitutive equation linking the present-time deviatoric strain tensor $u_{\gamma\nu}(t)$ with the values assumed by the deviatoric stress $\sigma_{\gamma\nu}(t')$ over the time $t' \leq t$. When the rheological response is linear, i.e., when the resulting strain is linear in stress (which is usually the case for strains not exceeding 10^{-6} (Karato, 2008)), the equation is a convolution, in the time domain:

$$2\,u_{\gamma\nu}(t) = \int_{-\infty}^{t} \dot{J}\,(t-t')\;\sigma_{\gamma\nu}(t')\,dt' \quad , \tag{1}$$

and is a product, in the frequency domain:

$$2\,\bar{u}_{\gamma\nu}(\chi) = \bar{J}(\chi)\,\bar{\sigma}_{\gamma\nu}(\chi) \quad . \tag{2}$$

In Eq. (1), t is time and the kernel $\dot{J}\,(t-t')$ is a time derivative of the *compliance function* $J(t-t')$, also called *creep function*, which carries all information about the (linear) rheological behavior of the material. Naturally, deformation of a viscoelastic solid depends on the time evolution of the applied load (Chawla and Meyers, 1999). In Eq. (2), χ stands for the frequency, $\bar{u}_{\gamma\nu}(\chi)$ and $\bar{\sigma}_{\gamma\nu}(\chi)$ denote the Fourier images of the strain and stress tensors, while the *complex compliance function*, or simply *complex compliance* $\bar{J}(\chi)$ is a Fourier image of $J(t-t')$. For details, see, e.g., Efroimsky (2012).

While elasticity is a result of bond-stretching along crystallographic planes in an ordered solid, viscosity and dissipation inside a polycrystalline material occur by motion of point, linear, and planar defects, facilitated by diffusion. Each of these mechanisms contributes to viscoelastic behavior (e.g., Karato, 2008). As can be observed from Eq. (1), the response

of the material to forcing comprises (a) an instantaneous elastic response, (b) a semirecoverable transient flow regime where the strain rate changes with time, and (c) a steady-state creep. Accordingly, the creep function for a viscoelastic solid consists of three terms:

$$\underbrace{J(t)}_{\text{Creep function}} = \underbrace{J}_{\text{Elastic}} + \underbrace{f(t)}_{\text{Transient strain-rate}} + \underbrace{t/\eta}_{\text{Viscous}}, \tag{3}$$

η being the shear viscosity. The Fourier image of $J(t)$ is the complex compliance $\bar{J}(\chi) = \Re[\bar{J}(\chi)] + i\Im[\bar{J}(\chi)]$, where χ is the frequency. The associated shear quality factor is given by

$$Q_s(\chi)^{-1} = \frac{|\Im[\bar{J}(\chi)]|}{\sqrt{\Re^2[\bar{J}(\chi)] + \Im^2[\bar{J}(\chi)]}}. \tag{4a}$$

For solids far from the melting point, the instantaneous (elastic) part of deformation is usually sufficiently large: $|\Re[\bar{J}(\chi)]| \gg |\Im[\bar{J}(\chi)]|$, in which case we have

$$Q_s(\chi)^{-1} \approx \frac{|\Im[\bar{J}(\chi)]|}{\Re[\bar{J}(\chi)]}. \tag{4b}$$

This quality factor is responsible for attenuation of seismic waves, and may vary in both vertical and lateral directions within a planet.[1] An intrinsic material property, $Q_s(\chi)$ is different from the degree-n tidal quality factors $Q_n(\chi)$ characterizing the planet as a whole as will be presented in Section 5.4. As explained in Efroimsky (2012, 2015) and Lau et al. (2017), the distinction comes from the fact that the tidal factors are defined by interplay of self-gravitation with the overall rheological behavior (generally, heterogeneous). In simple words, self-gravitation pulls the tidal bulge down, thus acting as an effective addition to rigidity. While at sufficiently high frequencies this effect is negligible, it becomes noticeable at the lowest frequencies available to analysis.

Below, we consider the Maxwell, Burgers, extended Burgers, Andrade, Sundberg–Cooper, and extended Sundberg–Cooper rheologies, as well as

[1] Note that seismic attenuation takes place as a result of three effects: intrinsic anelasticity, geometric spreading, and scattering attenuation. The viscoelastic models discussed here only represent the attenuation due to intrinsic anelasticity and not the other two effects, all of which have to be taken into account in the study of dissipation of seismic waves (see, e.g., Cormier, 1989; Lognonné et al., 2020; Bagheri et al., 2015; Lissa et al., 2019; Winkler et al., 1979; Margerin et al., 2000).

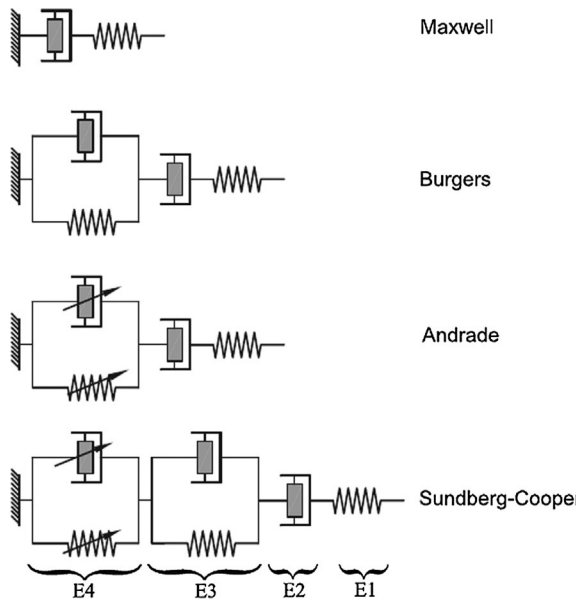

Figure 3 Schematic representation of viscoelastic models in terms of springs and dashpots. A spring element (E1) represents a purely elastic response, while a dashpot element (E2) is representative of purely viscous damping. A series connection of elements 1 and 2 is representative of the response of a Maxwell model (irrecoverable), while a connection of elements 1 and 2 in parallel (element 3) results in an anelastic (recoverable) response with a discrete (single) spectrum of relaxation times. Arrows on spring and dashpot in element 4, conversely, indicate an element that incorporates a continuous distribution of anelastic relaxation times and results in a broadened response spectrum (Bagheri et al., 2019).

a simplified power-law scheme. These models were derived from laboratory studies of various regimes of viscoelastic and anelastic relaxation. The applicability realm of each model depends on parameters such as the grain size, temperature, and pressure. Each model can be represented as an arrangement of springs and dashpots connected in series, or in parallel, or in a combination of both connection methods as shown in Fig. 3 (Findley and Onaran, 1965; Moczo and Kristek, 2005; Nowick and Berry, 1972; Cooper, 2002; Jackson et al., 2007; McCarthy and Castillo-Rogez, 2013). Instantaneous elastic response is mimicked by a spring, while a fully viscous behavior is modeled with a dashpot. A series connection (a Maxwell module) implies a nonrecoverable displacement, while a parallel connection (a Voigt module) ensures a fully recoverable deformation. Schematic diagrams of four viscoelastic models are shown in Fig. 3.

2.3 Maxwell

Maxwell is the simplest model of the viscoelastic behavior and can be interpreted as a series connection of a spring and dashpot. In the time domain, the creep function for this model is:

$$J(t) = J + \frac{t}{\eta} \ , \tag{5}$$

η being the viscosity, and J being the shear elastic compliance related to the shear elastic modulus μ by

$$J = \frac{1}{\mu} \ . \tag{6}$$

The real and imaginary parts of the complex compliance are

$$\Re[\bar{J}(\chi)] = J \ , \tag{7}$$

$$\Im[\bar{J}(\chi)] = -\frac{1}{\chi \, \eta} = -J \frac{1}{\chi \, \tau_M} \ , \tag{8}$$

where χ is the frequency, and the Maxwell time is introduced as

$$\tau_M = \eta J = \frac{\eta}{\mu} \ . \tag{9}$$

It is the timescale of relaxation of strain after the stress is abruptly turned off.

Lacking a transient term, the Maxwell model implies an elastic regime at high frequencies and a viscous-fluid regime in the low-frequency limit. It provides a reasonable approximation for reaction to very-long-period loading such as glacial isostatic adjustments (Peltier, 1974). On the other hand, the model is less adequate at tidal and especially seismic frequencies where transient processes are present.

2.4 Burgers and extended Burgers

The shortcoming of Maxwell's model in representing a transient response at the frequencies residing between the elastic and viscous bands can be rectified by introducing a time-dependent anelastic transition between these two regimes. This gives birth to the *Burgers rheology*:

$$J(t) = J_U \left[1 + \Delta \left[1 - \exp\left(-\frac{t}{\tau} \right) \right] + \frac{t}{\tau_M} \right] \ , \tag{10}$$

where J_U is the elastic compliance, Δ is the so-called *anelastic relaxation strength*, and τ is a characteristic time of the development of anelastic response. While the Maxwell model does not discriminate between the unrelaxed and relaxed values of J, the Burgers model does. From the above expression for $J(t)$, we observe that while J_U is the unrelaxed value, $J_U(1+\Delta) = J_R$ is its relaxed counterpart. This conclusion can be deduced also from the expression for the compliance in the complex domain:

$$\bar{J}(\chi) = \Re\left[\bar{J}(\chi)\right] + i\,\Im\left[\bar{J}(\chi)\right] \ , \tag{11}$$

$$\Re[\bar{J}(\chi)] = J_U\left(1 + \frac{\Delta}{1+\chi^2\tau^2}\right) \quad , \qquad \Im[\bar{J}(\chi)] = J_U\,\Delta\,\frac{\chi\,\tau}{1+\chi^2\tau^2} \quad . \tag{12}$$

By inserting these expressions for $\Re[\bar{J}(\chi)]$ and $\Im[\bar{J}(\chi)]$ into definition (4a) for Q_s^{-1}, it is easy to demonstrate that for this model the inverse quality factor possesses a peak, which makes the model applicable to realistic situations where such a peak appears in experiments.

More generally, the anelastic relaxation time τ can be replaced with a distribution $D(\tau)$ of relaxation times over an interval specified by an upper (τ_H) and lower (τ_L) bounds (Jackson and Faul, 2010). From a micromechanical point of view, this distribution is associated with diffusionally accommodated grain-boundary sliding. This is how the so-called *extended Burgers model* emerges:

$$J(t) = J_U\left[1 + \Delta\int_{\tau_L}^{\tau_H} D(\tau)\left[1 - \exp\left(-\frac{t}{\tau}\right)\right]d\tau + \frac{t}{\tau_M}\right] \ , \tag{13}$$

where $J_U\Delta$, as in the Burgers model, is the increase in compliance associated with complete anelastic relaxation.

The corresponding components of the complex compliance are:

$$\Re[\bar{J}(\chi)] = J_U\left(1 + \Delta\int_{\tau_L}^{\tau_H}\frac{D(\tau)}{1+\chi^2\tau^2}\,d\tau\right) \ , \tag{14}$$

$$\Im[\bar{J}(\chi)] = -J_U\left(\chi\ \Delta\int_{\tau_L}^{\tau_H}\frac{\tau D(\tau)}{1+\chi^2\tau^2}\,d\tau\ +\ \frac{1}{\chi\,\tau_M}\right) . \tag{15}$$

A commonly used distribution of anelastic relaxation times associated with the background dissipation is the absorption band model proposed by Minster and Anderson (1981). Within that model, $D(\tau)$ is implemented by the

function $D(\tau, \alpha)$ bearing a dependence on a fractional parameter α:

$$D_B(\tau, \alpha) = \begin{cases} 0 & \text{for } \tau \notin [\tau_L, \tau_H] , \\ \dfrac{\alpha \tau^{\alpha-1}}{\tau_H{}^{\alpha} - \tau_L{}^{\alpha}} & \text{for } \tau_L < \tau < \tau_H , \end{cases} \tag{16}$$

where $0 < \alpha < 1$, while τ_L and τ_H denote the cut-offs of the absorption band where dissipation is frequency-dependent and scales, approximately,[2] as $Q_s \propto \chi^{\alpha}$. The lower bound of the absorption band ensures a finite shear modulus at high frequencies and restricts attenuation at those periods.

Jackson and Faul (2010) found that their experimental data were better fit by including a dissipation peak in the distribution of anelastic relaxation times, which is superimposed upon the monotonic background along with the associated dispersion. This background peak is attributed mostly to sliding with elastic accommodation of grain-boundary incompatibilities (see Takei et al., 2014, for a different view). In this case, $D(\tau)$ writes as

$$D_P(\tau) = \frac{1}{\sigma \tau \sqrt{2\pi}} \exp\left(\frac{-\ln(\tau/\tau_P)}{2\sigma^2} \right) \tag{17}$$

peaked around some τ_P, a new timescale to be a part of the model.

2.5 Andrade

While the extended Burgers model incorporates a distribution of relaxation times within a restricted timescale to account for the transient anelastic relaxation, the Andrade model implies a distribution of relaxation times over the entire time domain:

$$J(t) = J_U + \beta\, t^{\alpha} + \frac{t}{\eta} , \tag{18}$$

[2] Using approximation (4b), estimating the real part of the compliance as its elastic term, and also neglecting the viscous term in the imaginary part, we observe that

$$Q_s^{-1}(\chi) \propto \chi\, \Delta \int_{\tau_L}^{\tau_H} \frac{\tau\, D(\tau)\, d\tau}{1+\chi^2\tau^2} = \frac{\alpha\, \Delta}{\tau_H^{\alpha} - \tau_L^{\alpha}} \int_{\chi\tau_L}^{\chi\tau_H} \frac{\chi^{-1}(\chi\tau)\, d(\chi\tau)}{1+\chi^2\tau^2}\, \chi^{1-\alpha} (\chi\tau)^{\alpha-1} = \frac{\alpha\, \Delta}{\tau_H^{\alpha} - \tau_L^{\alpha}}\, \chi^{-\alpha}\, A(\chi) ,$$

where

$$A(\chi) \equiv \int_{\chi\tau_L}^{\chi\tau_H} \frac{z\, dz}{1+z^2} = \frac{1}{2} \ln(1+z^2)\Big|_{\chi\tau_L}^{\chi\tau_H} = \frac{1}{2} \ln \frac{1+(\chi\tau_H)^2}{1+(\chi\tau_L)^2} .$$

Since the function $A(\chi)$ is slower that the power function $\chi^{-\alpha}$, we may say that within this crude approximation the quality factor scales as about χ^{α}.

where α defines the frequency-dependence of the compliance.[3] Having fractional dimensions, the parameter β is somewhat unphysical. For this reason, it was suggested by Efroimsky (2012, 2015) to cast the compliance as

$$J(t) = J_U \left[1 + \left(\frac{t}{\tau_A} \right)^{\alpha} + \frac{t}{\tau_M} \right] , \tag{19}$$

with the parameter τ_A defined through

$$\beta = \tau_A^{-\alpha} J_U \tag{20}$$

and named *the Andrade time*. A justification for this reformulation will be provided shortly.

With Γ denoting the Gamma function, the complex compliance corresponding to (19) writes as:

$$\bar{J}(\chi) = J_U \left[1 + (i\chi\tau_A)^{-\alpha} \Gamma(1+\alpha) - i(\chi\tau_M)^{-1} \right] , \tag{21}$$

its real and imaginary parts being

$$\Re[\bar{J}(\chi)] = J_U \left[1 + \Gamma(1+\alpha) \, (\chi\tau_A)^{-\alpha} \cos\left(\frac{\alpha\pi}{2} \right) \right] , \tag{22}$$

$$\Im[\bar{J}(\chi)] = -J_U \left[\Gamma(1+\alpha) \, (\chi\tau_A)^{-\alpha} \sin\left(\frac{\alpha\pi}{2} \right) + (\chi\tau_M)^{-1} \right] . \tag{23}$$

The absorption band in this model extends from 0 to ∞. In other words, anelastic relaxation effectively contributes across the entire frequency range from short-period seismic waves to geological timescales. This generates two problems.

First, in the situations where the anelastic behavior is dominated by defect unjamming, it has a low-frequency cut-off, as explained by Karato and Spetzler (1990, eqn 17).[4] The presence of this feature can be built into the Andrade model "by hand," by assuming that the Andrade time quickly grows to infinity (or, equivalently, that the parameter β quickly reduces to zero) as the frequency goes below some threshold value. So, for frequencies

[3] Following a long-established convention, we are denoting the Andrade dimensionless parameter with α. For the same reason, we denoted with α a parameter emerging in distribution (16). It should however be kept in mind that these two α's are different parameters and assume different values.

[4] According to Figure 3 in Karato and Spetzler (1990), for the Earth mantle the threshold is located at about 1/yr. However, due to the sensitivity of this threshold to the temperature and pressure, for the mantle as a whole this threshold is smeared into a transition zone covering a decade or two.

below this threshold, the response of the material is overwhelmingly viscoelastic, while above the threshold the response becomes predominantly anelastic. At this point, we can appreciate the convenience of employing τ_A instead of β: it turns out (Castillo-Rogez et al., 2011, Fig 4) that for olivines τ_A and τ_M are similar over an appreciable band of frequencies:

$$\tau_A \approx \tau_M \ . \tag{24}$$

Second, within the Andrade model it is impossible, by distinction from the Burgers and extended Burgers models, to write down the relaxed value of J. This problem finds its resolution within the Sundberg–Cooper and extended Sundberg–Cooper models discussed below.

2.6 Sundberg–Cooper

Similarly to the Maxwell model, in the Andrade model it is conventional to identify the elastic compliance J with its unrelaxed value J_U. Consequently, just as the Maxwell model is extended to Burgers, so the Andrade model can be extended to that of Sundberg and Cooper (2010), to account for the combined effects of diffusional background and elastically-accommodated grain-boundary sliding:

$$J(t) = J_U + J_U \Delta \left(1 - e^{-t/\tau}\right) + \beta\, t^{\alpha} + \frac{t}{\eta} \ . \tag{25a}$$

In terms of the Maxwell and Andrade times, this creep function can be written down as

$$J(t) = J_U \left[1 + \Delta \left(1 - e^{-t/\tau}\right) + \left(\frac{t}{\tau_A}\right)^{\alpha} + \frac{t}{\tau_M} \right] . \tag{25b}$$

In the frequency domain, this compliance writes as

$$\Re[\bar{J}(\chi)] = J_U \left[1 + \Gamma(1+\alpha)\ (\chi\, \tau_A)^{-\alpha} \cos\left(\frac{\alpha\pi}{2}\right) + \frac{\Delta}{1+\chi^2\tau^2} \right] , \tag{26}$$

$$\Im[\bar{J}(\chi)] = -J_U \left[\Gamma(1+\alpha)\,(\chi\, \tau_A)^{-\alpha} \sin\left(\frac{\alpha\pi}{2}\right) + \chi\, \frac{\tau\, \Delta}{1+\chi^2\tau^2} + (\chi\, \tau_M)^{-1} \right] , \tag{27}$$

the corresponding $Q_s^{-1}(\chi)$ possessing a peak.

A further extension of the Sundberg–Cooper model can be performed in analogy with the extended Burgers model. The term containing the parameter τ can be replaced with an integral specifying a distribution of anelastic relaxation times τ, as in Eq. (13).

The real and imaginary parts of the complex compliance for the extended Sundberg–Cooper model are:

$$\Re[\bar{J}(\chi)] = J_U \left[1 + \Gamma(1+\alpha)\ (\chi\,\tau_A)^{-\alpha} \cos\left(\frac{\alpha\pi}{2}\right) + \Delta \int_{\tau_L}^{\tau_H} \frac{D(\tau)}{1+\chi^2\tau^2}\, d\tau \right], \tag{28}$$

$$\Im[\bar{J}(\chi)] = -J_U \left[\Gamma(1+\alpha)\,(\chi\,\tau_A)^{-\alpha} \sin\left(\frac{\alpha\pi}{2}\right) + \chi\,\Delta \int_{\tau_L}^{\tau_H} \frac{\tau\, D(\tau)}{1+\chi^2\tau^2}\, d\tau + (\chi\,\tau_M)^{-1} \right], \tag{29}$$

where $D(\tau)$ is given either by expression (17) or by (16). In the latter case, it is important to mind the difference between the Andrade exponential α and the parameter entering distribution (16). While in Eq. (16) we denoted the parameter with the same letter α and wrote the function as $D_B(\tau, \alpha)$, in Eqs. (28)–(29) this function should appear as $D_B(\tau, \alpha_1)$, with α_1 generally different from the Andrade α.

2.7 Power-law approximation

Finally, we consider a power-law approximation sometimes used for fitting measurements (e.g., Jackson et al., 2002). As we shall now demonstrate, this description follows from the Andrade model (22)–(23) under the simplifying assumptions that the anelastic dissipation is weak and that the viscoelastic dissipation is even weaker[5]:

$$\text{Assumption 1}: \quad (\chi\,\tau_A)^{-\alpha} \ll 1\,, \tag{30a}$$

$$\text{Assumption 2}: \quad (\chi\,\tau_M)^{-1} \ll (\chi\,\tau_A)^{-\alpha}\,. \tag{30b}$$

[5] We indeed see from Eq. (22) that assumption (30a) implies the weakness of anelastic dissipation. It can also be observed from Eq. (23) that assumption (30b) implies the weakness of viscoelasticity as compared to anelasticity.

Approximations (4b) and (30b) enable us to write the inverse shear quality factor as

$$Q_s^{-1} \equiv \frac{|\Im[\bar{J}(\chi)]|}{|\bar{J}(\chi)|} \approx \frac{J_U}{|\bar{J}(\chi)|} \Gamma(1+\alpha)\,(\chi\,\tau_A)^{-\alpha} \sin\left(\frac{\alpha\,\pi}{2}\right) \tag{31}$$

or, equivalently,

$$Q_s^{-1} \cot\left(\frac{\alpha\,\pi}{2}\right) \approx \frac{J_U}{|\bar{J}(\chi)|} \Gamma(1+\alpha)\,(\chi\,\tau_A)^{-\alpha} \cos\left(\frac{\alpha\,\pi}{2}\right) . \tag{32}$$

With aid of inequalities (30), $|\bar{J}(\chi)|$ can be written down as

$$|\bar{J}(\chi)| \approx J_U \left[1 + \Gamma(1+\alpha)\,(\chi\,\tau_A)^{-\alpha} \cos\left(\frac{\alpha\,\pi}{2}\right)\right] . \tag{33}$$

Combining Eqs. (32) and (33), we arrive at

$$\frac{J_U}{|\bar{J}(\chi)|} \approx 1 - Q_s^{-1} \cot\left(\frac{\alpha\,\pi}{2}\right) . \tag{34}$$

Also, the approximate expression (31) can be concisely reparameterized through the forcing period $2\pi/\chi$:

$$Q_s^{-1} \approx A \left(\frac{2\pi}{\chi}\right)^{\alpha} , \qquad A = \Gamma(1+\alpha) \sin\left(\frac{\alpha\pi}{2}\right) (2\pi\,\tau)^{-\alpha} . \tag{35}$$

Together, Eqs. (34)–(35) constitute a simplified version of the Andrade model, a version that is valid when both assumptions (30) are fulfilled, which is often the case at seismic frequencies.

Fig. 4 compares the frequency-dependent shear modulus and the quality factors rendered by different rheological models (Bagheri et al., 2019). This figure readily reveals that Maxwell model and power-law become impractical when it is necessary to describe a wide range of periods. The other three models, i.e., the extended Burgers, Andrade, and Sundberg–Cooper ones, sometimes render similar dependencies, though in Section 5 we shall see that the choice of the right rheology may become very important in modeling of tides.

2.8 Rescaling for different values of the temperature, pressure, and grain size

To make a rheological model practical, it is necessary to endow the timescales and other parameters of the model with a dependency on the

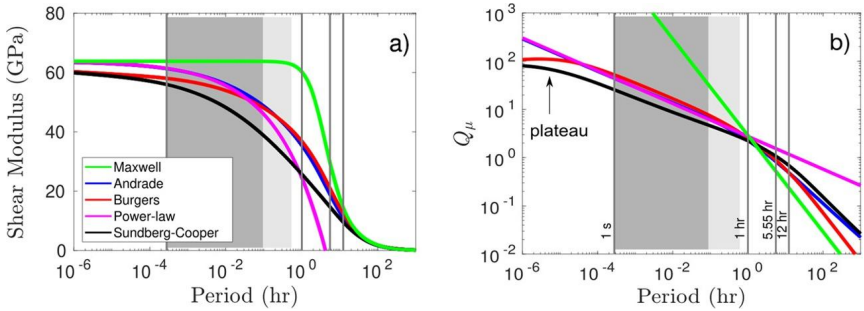

Figure 4 Computed variations of relaxed shear modulus (G_R) and shear attenuation (Q_S) with period for the five rheological models considered in this study. G_R (a) and Q_S (b) as a function of period at constant temperature and grain size; the vertical lines show periods of interest: seismic body waves (1 s), normal modes (1 hr), main tidal excitation of Phobos on Mars (5.55 hr), and main tidal excitation of the Sun (12.32 hr). Figure is modified from Bagheri et al. (2019).

grain size d, temperature T, and pressure P. For the Maxwell time, Morris and Jackson (2009), Jackson and Faul (2010), and McCarthy et al. (2011) suggested the following rescaling prescription:

$$\tau_M(T,P,d) = \tau_{M0}\left(\frac{d_g}{d_0}\right)^{m_{gv}} \exp\left[\left(\frac{E^*}{R}\right)\left(\frac{1}{T}-\frac{1}{T_0}\right)\right] \exp\left[\left(\frac{V^*}{R}\right)\left(\frac{P}{T}-\frac{P_0}{T_0}\right)\right], \tag{36}$$

where R is the gas constant, E^* is the activation energy, V^* is the activation volume, m_{gv} is the grain size exponent for viscous relaxation, P is the pressure, T is the temperature, and τ_{M0} is a normalized value of the Maxwell time at a particular set of reference conditions (d_0, P_0, and T_0). In this expression, both exponential functions come from the rescaling of viscosity η, under the assumption that the rigidity μ stays unchanged under the variations of both T and P. This assumption is acceptable for temperatures not exceeding about 3/4 of the melting temperature, which in its turn, is a function of pressure.

While the above formula is sufficient to rescale the Maxwell model, a more complicated expression is needed in the case of the Burgers model that has an additional timescale τ. An even more involved expression is required for the extended Burgers model that has three additional timescales τ_L, τ_H, τ_P. Jackson and Faul (2010) suggested to extend (36) to all these

timescales:

$$\tau_i(T, P, d) = \tau_{i0}\left(\frac{d_g}{d_0}\right)^{m_g} \exp\left[\left(\frac{E^*}{R}\right)\left(\frac{1}{T} - \frac{1}{T_0}\right)\right] \exp\left[\left(\frac{V^*}{R}\right)\left(\frac{P}{T} - \frac{P_0}{T_0}\right)\right], \tag{37}$$

where all parameters are as in Eq. (36), while $i = M, L, H, P$. The grain size exponential m_g can be different for the anelastic (m_{ga} for $i = L, H, P$) and viscous (m_{gv} for $i = M$) relaxation regimes.

In the case of the Andrade model, Jackson and Faul (2010) adjust for the variations of d, T, and P by replacing the actual period with the following pseudo-period:

$$X = \chi^{-1}\left(\frac{d_g}{d_0}\right)^{-m_g} \exp\left[\left(\frac{-E^*}{R}\right)\left(\frac{1}{T} - \frac{1}{T_0}\right)\right] \exp\left[\left(\frac{-V^*}{R}\right)\left(\frac{P}{T} - \frac{P_0}{T_0}\right)\right]. \tag{38}$$

This is equivalent to a simultaneous rescaling of both the Maxwell and Andrade times by formula (36). To apply it to the Andrade time, one may hypothesize that τ_A and τ_M either are equal or are staying proportional within the considered realm of temperatures, pressures and grain sizes. For τ_A, the power m_g should assume its anelastic value m_{ga}, like in the case of the Burgers model. While this rescaling is natural for the Maxwell time, its applicability to the Andrade time still requires justification.

Similarly to the complete Andrade model, its simplified version (34)–(35) becomes subject to prescription (38). In Eq. (35), a replacement of the actual forcing period $2\pi/\chi$ with the pseudo-period X given by Eq. (38) yields:

$$Q_s^{-1} \approx A X^{\alpha} \ . \tag{39}$$

Just as in the case of the full Andrade model, the applicability of this rule to the power law needs further study.

The parameters involved in the considered viscoelastic models often need more accurate constraining. Extensive experimental work has been carried out in this direction (Jackson, 2000, 2005; Jackson and Faul, 2010; Jackson et al., 2007, 2002; Sundberg and Cooper, 2010; Qu et al., 2021; McCarthy et al., 2011). In addition, understanding of the effects of porosity or the presence of partial melt needs further research. Constraints on the effect of the involved parameters will help to obtain more detailed insights into the interiors of the planetary bodies and to develop interpretation of the existing and upcoming measurements. In the literature on tides, each

of the afore-mentioned viscoelastic models has been used. In Sections 3 and 4, we address other aspects required for modeling the tidal response of planetary bodies. Those aspects are used in combination with the viscoelastic models to constrain interior properties of the planets and moons, as discussed in Section 5.

3. Tidal and thermal evolution in planetary systems

3.1 Tidal evolution

Viscoelastic tidal dissipation in gravitationally interacting planetary bodies results in an angular momentum exchange between the spin and orbit of the bodies. This process results in an evolution of the spin and orbital rates towards low spin-orbit resonances, e.g., 1:1 for most moons or 3:2 for Mercury, and in the damping of eccentricity and inclination of the orbit. The conservation of the angular momentum of the two-body system implies an evolution of the separation, eccentricity, and inclination, while the dissipation of the rotational kinetic energy leads to heat deposition in the orbital partners. When the perturbed body rotates faster than the perturber is orbiting above its surface, the tidal bulge leads the perturber and exerts such a torque on the perturber that the semimajor axis of the orbit expands. On the other hand, if the tidally perturbed body rotates slower than the perturber's orbital rate, the bulge lags behind and exerts on the perturber a torque contracting the semimajor axis, provided the orbital eccentricity is not very large. The boundary between these cases is commonly defined by a distance between the two bodies, known as *synchronous radius*, at which the perturber's mean motion equals the hosting body's spin rate. It however was demonstrated by Bagheri et al. (2021) that this division is valid only for low eccentricities, while at higher eccentricities a satellite originally located above the synchronous radius can cross it and migrate downwards to the hosting planet.

Studying of the orbital evolution of celestial bodies helps to constrain the history of the planetary systems and their origin. For example, numerous studies have targeted the dynamical evolution of the Earth–Moon system, exploiting the Moon's present-day separation rate of 38.08 ± 0.19 mm/yr observed from the Lunar Laser Ranging (LLR), employing various tidal evolution models (Webb, 1982; Touma and Wisdom, 1998; Williams et al., 2014; Rufu and Canup, 2020; Wisdom and Tian, 2015; Ćuk et al., 2016b; Canup and Asphaug, 2001; Zahnle et al., 2015; Farhat et al., 2022). Another important example is the discovery of the

unexpectedly rapid migration of the Saturnian moon Titan (∼11 cm/yr) (Lainey et al., 2020) that has been used to explain the large obliquity of Saturn. This measurement invalidates the traditional belief (Hamilton and Ward, 2004) that the presently observed obliquity of the rotation axis of Saturn is a result of the crossing of a resonance between the spin-axis precession and the nodal orbital precession mode of Neptune that happened during the late planetary migration more than 4 Gyrs ago. Instead, Saillenfest et al. (2021) proposed that the resonance was encountered more recently, about 1 Gyr ago, and forced Saturn's obliquity to increase from a small value to its current state. Another example is the measurement of Phobos' migration rate towards its host at a rate of ∼1.8 cm/yr. This observation has been used to constrain the Martian moons' origin and interior properties (Yoder, 1982; Bagheri et al., 2021; Singer, 1968; Samuel et al., 2019) as discussed in Section 5.4. Based on this observation, it has been also shown that Phobos will collide with Mars's surface in ∼30–50 Myrs (e.g., Bills et al., 2005).

The rate at which tidal evolution takes place depends on the orbital parameters such as the distance between the two bodies, spin and orbital periods, eccentricity of the orbit, and on the physical properties of these bodies' interiors, that affect viscoelastic dissipation. Modeling tidal evolution comprises the following major steps:

(1) Decomposition of the tidal potential into Fourier harmonic modes.

(2) Assigning to each Fourier mode a specific phase lag and magnitude.

The first step can be carried out by means of a development by Kaula (1964) who explicitly wrote down Fourier expansions for both the perturbing potential and the additional tidal potential of the perturbed body. To perform the second step, simplified tidal models such as constant phase lag model (CPL) (MacDonald, 1964; Goldreich, 1966; Murray and Dermott, 1999) and constant time lag model (CTL) (Singer, 1968; Mignard, 1979, 1980, 1981; Hut, 1981; Heller et al., 2011) were introduced for analytical treatment and applied to rocky moons and planets, as well as gas giants.

Despite their popularity, both the CTL and CPL models have been shown to suffer problems of both physical and mathematical nature (Efroimsky and Makarov, 2013, 2014). The CTL model implies that all the tidal strain modes experience the same temporal delay relative to the corresponding stress modes (Efroimsky and Makarov, 2013; Makarov and Efroimsky, 2013). The CPL model, on the other hand, is not supported by physical principles because it assumes a constant tidal response independent of the excitation frequency – which is incompatible with geophysical

and laboratory data as shown in various studies (Jackson and Faul, 2010; Jackson, 2005; Khan et al., 2018; Bagheri et al., 2019; Lau and Faul, 2019; Nimmo et al., 2012; Nimmo and Faul, 2013).

The shortcomings of the CTL and CPL models are resolved by assigning individual phase lag and amplitude decrease to each Fourier mode. This assignment is defined by the rheology of the body and is also influenced by its self-gravitation. A combination of the properly performed steps (1) and (2) provides a means for calculating spin-orbit evolution of planets and moons (Boué and Efroimsky, 2019), including modeling their capture into spin-orbit resonances (Noyelles et al., 2014). Further extensions of this approach were developed to extend the formalism to highly eccentric orbits (Bagheri et al., 2021; Renaud et al., 2021; Bagheri et al., 2022) and to include the effect of physical libration in longitude (Frouard and Efroimsky, 2017; Efroimsky, 2018a).

3.2 Tidal-thermal evolution coupling

Tidal dissipation is not only responsible for the observed orbits and spin states of celestial bodies, but also can affect these bodies' thermal evolution. Thermal evolution is responsible for the planetary bodies' differentiation, melting, and volcanism. The principal heat sources in a binary system are (see, e.g., Hussmann et al. (2006)): (a) the heating associated with accretion during planet formation, (b) the gravitational energy released during planetary differentiation, (c) radiogenic heating in the silicate component due to the decay of long-lived radioactive isotopes (U, Th, and K), and (d) tidal heating due to viscoelastic dissipation. Of these sources, only (c) and (d) are of relevance for the long-term evolution of the planet while the two first sources are mostly linked to the early stages of planetary accretion.

Thermal evolution implies heat being transported to the surface of the body either by conduction or convection, and as a consequence, the interior temperature varies with time. This results in substantial changes in the interior structure and physical properties of the body, such as viscosity and rigidity, which in turn, can considerably change the tidal response of the body and affect its orbital evolution and spin. In the solar system, we can find several examples where tidal and thermal evolution affect one another. For example, in Europa, tidal heating can be intense enough to maintain the presence of a liquid surface or subsurface ocean, though there is no consensus on whether the tidal dissipation is taking place predominantly in the ocean or the ice shell (e.g., Tyler et al., 2015; Choblet et al., 2017; Hussmann and Spohn, 2004; Tobie et al., 2003; Rhoden and Walker, 2022;

Sotin et al., 2009). Moreover, tidal heating can result in volcanism, like in Io, considerably exceeding the heating by long-term radiogenic isotopes (e.g., Peale et al., 1979; Van Hoolst et al., 2020; Kervazo et al., 2022; Foley et al., 2020; de Kleer et al., 2019a,b). When considerable portion of ice or liquid water is present inside the body, tidal heating can entail cryovolcanism. This is believed to be the case in several icy moons such as Enceladus, Titan, Europa, and Triton (e.g., Spencer et al., 2009; Sohl et al., 2014; Vilella et al., 2020; Hansen et al., 2021; Hay et al., 2020). In all of the mentioned examples, the tidal and thermal evolution have comodulating effects on each other. This, necessitating their joint consideration in evaluating the evolution and present-day state of planetary systems. Since in this chapter we mostly focus on tides with referring to thermal evolution only in cases where tidal dissipation plays an important role, we do not provide more details on thermal evolution modeling.

4. Tidal potential, Love numbers, and tidal response

4.1 Static tides

Consider a spherical body of radius R. An external perturber of mass M^*, located at a point $\boldsymbol{r}^* = (r^*, \lambda^*, \phi^*)$, in the body frame, generates the following disturbing potential at a point $\boldsymbol{R} = (R, \phi, \lambda)$ on the surface of the body:

$$W(\boldsymbol{R}, \boldsymbol{r}^*) = \sum_{n=2}^{\infty} W_n(\boldsymbol{R}, \boldsymbol{r}^*) = -\frac{GM^*}{r^*} \sum_{n=2}^{\infty} \left(\frac{R}{r^*}\right)^n P_n(\cos\gamma) \quad , \quad (40)$$

where $R < r^*$, the letter G denotes the Newton gravity constant, ϕ is the latitude reckoned from the spherical body's equator, λ is the longitude reckoned from a fixed meridian, $P_n(\cos\gamma)$ are the Legendre polynomials, while γ is the angular separation between the vectors $\boldsymbol{r}^*$ and $\boldsymbol{R}$ pointing from the center of the perturbed body.

In a static picture, the additional tidal potential arising from the deformation of the perturbed body is a sum of terms U_n each of which is equal to W_n multiplied by a mitigating factor $k_n (R/r)^{n+1}$, where k_n is an n-degree Love number. With the perturber residing in $\boldsymbol{r}^*$, the additional potential at a point $\boldsymbol{r} = (r, \phi, \lambda)$ is

$$U(\boldsymbol{r}, \boldsymbol{r}^*) = \sum_{n=2}^{\infty} U_n(\boldsymbol{r}, \boldsymbol{r}^*) = \sum_{n=2}^{\infty} k_n \left(\frac{R}{r}\right)^{n+1} W_n(\boldsymbol{R}, \boldsymbol{r}^*) \quad . \quad (41)$$

Note that in this equation, it is implied that while the surface point has the coordinates $\boldsymbol{R} = (R, \phi, \lambda)$, the coordinates of the exterior points are $\boldsymbol{r} = (r, \phi, \lambda)$, with $r \geq R$. In simple words, the point $\boldsymbol{r}$ is located right above $\boldsymbol{R}$. Along with the potential Love numbers k_n, the vertical displacement Love numbers h_n and the horizontal displacement Shida numbers l_n (Shida, 1912) are in use. They appear in the expressions for degree-n vertical displacement H_n and horizontal displacement L_n of a surface point:

$$H_n = \frac{h_n}{g} W_n(\boldsymbol{R}, \boldsymbol{r}^*) \ , \tag{42}$$

$$L_n = \frac{l_n}{g} \nabla W_n(\boldsymbol{R}, \boldsymbol{r}^*) \ , \tag{43}$$

where g is the surface gravity. While static tides imply permanent deformation of the planet or moon, on nonsynchronous orbits time-varying tides are raised in the bodies.

4.2 Actual situation: time-dependent tides

For time-dependent tides, the above formalism acquires an important additional detail: the reaction lag, as compared to the action. Within a simplistic approach, we might simply take each W_n at an earlier moment of time. In reality, this simplification is too crude, because lagging depends on frequency; so each W_n must be first decomposed into a Fourier series over tidal modes, and then each term of the series should be endowed with its own lag. The magnitude of the tidal reaction is also frequency dependent, as a result of which each term of the Fourier series should now be multiplied by a dynamical Love number of its own. Symbolically, this may be cast in a form similar to the static-case expression:

$$U(\boldsymbol{r}, \boldsymbol{r}^*) = \sum_{n=2}^{\infty} U_n(\boldsymbol{r}, \boldsymbol{r}^*) = \sum_{n=2}^{\infty} \left(\frac{R}{r}\right)^{n+1} \hat{k}_n W_n(\boldsymbol{R}, \boldsymbol{r}^*) \ . \tag{44}$$

The hat in $\hat{k}_n$ serves to remind us that this is not a multiplier but a linear operator that mitigates and delays differently each Fourier mode of W_n.

A degree-n component of potential (44) can be found by means of a convolution-type *Love operator* (Efroimsky, 2012):

$$U_n(\boldsymbol{r}, \boldsymbol{r}^*, t) = \left(\frac{R}{r}\right)^{n+1} \int_{-\infty}^{t} \dot{k}_n(t - t') \ W_n(\boldsymbol{R}, \boldsymbol{r}^*, t') \, dt' \ . \tag{45}$$

This is not surprising, because the linearity of tides implies that, at a time t, the magnitude of reaction depends linearly on the perturbation magnitudes at all the preceding moments of time, $t' \le t$. The inputs from the actions at earlier times emerge owing to the inertia (delayed reaction) of the material. A perturbation applied at a moment t' enters the integral for $U_n(\boldsymbol{r}, t)$ with a weight $\dot{k}_n(t-t')$ whose value depends on the time elapsed. Here, overdot denotes time derivative, so the weights are time derivatives of some other functions $k_n(t-t')$. Following Churkin (1998), who gave to this machinery its current form, we term the weights as *Love functions*.

In the frequency domain, the convolution operator becomes a product:

$$\bar{U}_n(\boldsymbol{r}, \omega) = \left(\frac{R}{r}\right)^{n+1} \bar{k}_n(\omega)\ \bar{W}_n(\boldsymbol{R}, \boldsymbol{r}^*, \omega)\ , \tag{46}$$

where $\omega = \omega_{nmpq}$ is a tidal mode; $\bar{U}_n(\omega)$ and $\bar{W}_n(\omega)$ are the Fourier images of the potentials $U_n(\boldsymbol{r}, t)$ and $W_n(\boldsymbol{R}, \boldsymbol{r}^*, t)$; while the complex Love numbers

$$\bar{k}_n(\omega) = |\bar{k}_n(\omega)|\, e^{-i\epsilon_n(\omega)} = k_n(\omega)\, e^{-i\epsilon_n(\omega)}\ , \tag{47}$$

are the Fourier components of the Love functions $\dot{k}_n(t-t')$.

A pioneer work devoted to development of the functions $\bar{U}_n(\omega)$ and $\bar{W}_n(\omega)$ into Fourier series was presented by Darwin (1879) who derived several leading terms of this expansion. A full expansion was later provided in a monumental work by Kaula (1961, 1964). A reader-friendly explanation of this machinery can be found in Efroimsky and Makarov (2013). The tidal Fourier modes $\omega = \omega_{nmpq}$ over which these functions are decomposed are parameterized with four integers $nmpq$ and can be approximated as

$$\omega_{nmpq} \approx (n - 2p + q)\,\dot{\mathcal{M}} - m\dot{\theta}\ , \tag{48}$$

where $\mathcal{M}$ and $\dot{\mathcal{M}}$ are the mean anomaly and mean motion of the perturber, while θ and $\dot{\theta}$ are the rotation angle and rotation rate of the tidally perturbed body.[6] The actual forcing frequencies in the body are (Efroimsky and Makarov, 2013)

$$\chi_{nmpq} = |\,\omega_{nmpq}\,|\ . \tag{49}$$

[6] An accurate expression for ω_{nmpq} includes also terms proportional to the apsidal and nodal precession rates of the perturber. Usually, these terms are small.

Below, whenever this promises no confusion, we drop the subscript and simplify the notation as

$$\omega \equiv \omega_{nmpq} \quad , \quad \chi \equiv \chi_{nmpq} \ . \tag{50}$$

The Darwin–Kaula theory of tides has to be reworked considerably for bodies experiencing physical libration (Frouard and Efroimsky, 2017). Negligible for planets and large satellites, the impact of physical libration on tidal evolution becomes strong for middle-sized satellites, and very strong for some of the small moons. For example, in Phobos, it more than doubles the tidal dissipation rate, while in Epimetheus it increases the dissipation rate by more than 25 times (Efroimsky, 2018a; Bagheri et al., 2021).

Similarly to the potential tidal Love numbers k_n, the time-dependent displacement Love numbers h_n and l_n can be derived. Except for the Earth and the Moon, no robust measurements of the displacement Love numbers for other bodies have been made. Such measurements would require delivery of precise geophysical instruments on the surface of a planetary body. Thus, most of the studies focused on tides have to rely on the measured potential Love number as discussed in Section 5.

4.3 Complex Love numbers

Expressing the degree-n Love number as

$$\bar{k}_n(\omega) \ = \ \Re\Big[\bar{k}_n(\omega)\Big] \ + \ i\,\Im\Big[\bar{k}_n(\omega)\Big] \ = \ |\bar{k}_n(\omega)|\ e^{\,-i\epsilon_n(\omega)}, \tag{51}$$

we introduce the dynamical Love number

$$k_n(\omega) \ = \ |\bar{k}_n(\omega)| \ . \tag{52}$$

We also define the phase as $-\epsilon_n$, with a "minus" sign, thus endowing ϵ_n with the meaning of phase lag. It can also be shown (Efroimsky and Makarov, 2013) that $\mathrm{Sign}\,\epsilon_l(\omega) = \mathrm{Sign}(\omega)$. The so-called *quality function*

$$K_n(\omega) \equiv \ -\,\Im\Big[\,\bar{k}_n(\omega)\,\Big] \ = \ k_n(\omega)\ \sin\epsilon_n(\omega) \tag{53a}$$

can be written down also as

$$K_n(\omega) \equiv \ -\,\Im\Big[\,\bar{k}_n(\omega)\,\Big] = \frac{k_n(\omega)}{Q_n(\omega)}\ \mathrm{Sign}(\,\omega) \quad , \tag{53b}$$

where $Q_n(\omega)$ is the tidal quality factor defined through

$$Q_n^{-1}(\omega) = |\sin\epsilon_n(\omega)| \ . \tag{54}$$

The quality function $K_n(\omega)$ appears in the expressions for tidal forces, tidal torques, tidal heating (Efroimsky and Makarov, 2014), and tidal evolution of orbits (Boué and Efroimsky, 2019).

While $\sin\epsilon_n(\omega)$ is an odd function, $Q_n(\omega)$ is even – and so is $k_n(\omega)$. Hence, no matter what the sign of ω and ϵ_n, we can always regard both $Q_n(\omega)$ and $k_n(\omega)$ as functions of the frequency $\chi \equiv |\omega|$:

$$Q_n(\omega) = Q_n(\chi) \ , \quad k_n(\omega) = k_n(\chi) \ . \tag{55}$$

The mode-dependency $\bar{k}_n(\omega)$ and, consequently, the dependencies $k_n(\omega)$, $\epsilon_n(\omega)$, $Q_n(\omega)$ can be derived from the expression for the complex compliance $\bar{J}(\chi)$ or the complex rigidity $\bar{\mu}(\chi) = 1/\bar{J}(\chi)$, functions containing the information about the rheology of a body.

Overall, tidal dissipation is a very complex process wherein self-gravitation[7] and rheology are intertwined. Its quantification necessitates elaborate viscoelastic modeling, to appropriately interpret observation of tides, and to make these observations an effective tool to constrain the deep interior.

4.4 Quality function of a homogeneous celestial body

By a theorem known as the *correspondence principle* or the *elastic–viscoelastic analogy* (Darwin, 1879; Biot, 1954), the complex Love number of a spherical uniform viscoelastic body, $\bar{k}_n(\chi)$, is related to the complex compliance $\bar{J}(\chi)$ by the same algebraic expression through which the static Love number k_n of that body is related to the relaxed compliance J_R:

$$\bar{k}_n(\chi) = \frac{3}{2(n-1)} \frac{1}{1 + \mathcal{B}_n/\bar{J}(\chi)} \ , \tag{56}$$

where

$$\mathcal{B}_n \equiv \frac{(2n^2 + 4n + 3)}{ng\rho R} = \frac{3(2n^2 + 4n + 3)}{4n\pi G\rho^2 R^2} \ . \tag{57}$$

[7] As we mentioned above, self-gravitation is pulling the tidal bulge down, effectively acting as additional rigidity. Negligible over the frequencies much higher than the inverse Maxwell time, gravity becomes an important factor at lower frequencies.

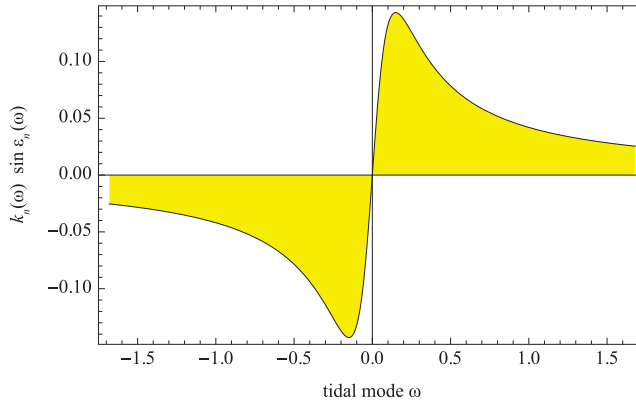

Figure 5 A typical shape of the quality function $k_n(\omega)\,\sin\epsilon_n(\omega)$, where ω is a shortened notation for the tidal Fourier mode ω_{nmpq}. (From Noyelles et al., 2014.)

In this expression, G denotes Newton's gravitational constant, while g, ρ, and R are the surface gravity, density, and radius of the body. From Eq. (56), we find how the quality function $K_n(\omega_{nmpq})$ entering an *nmpq* term of the expansions for the tidal torque and tidal dissipation rate is expressed through the rheological law $\bar{J}(\chi)$:

$$K_n(\chi) \equiv k_n(\chi)\,\sin\epsilon_n(\chi) = -\frac{3}{2(n-1)}\,\frac{\mathcal{B}_n\,\Im\left[\bar{J}(\chi)\right]}{\left(\Re\left[\bar{J}(\chi)\right]+\mathcal{B}_n\right)^2+\left(\Im\left[\bar{J}(\chi)\right]\right)^2}\,. \tag{58}$$

For the Maxwell or Andrade model, the dependence of $K_n \equiv k_n \sin\epsilon_n$ on a tidal mode has the shape of a kink, depicted in Fig. 5. It can be demonstrated (Efroimsky, 2015, eqn 45) that the frequency-dependence of the inverse quality factor $Q_n(\chi)^{-1} \equiv |\sin\epsilon_n(\chi)|$ has a similar shape, with a similarly positioned peak.

For a Maxwell body, the extrema of the kink $K_n(\omega)$ are located at

$$\omega_{peak}{}_n = \pm\,\frac{\tau_M^{-1}}{1+\mathcal{B}_n\,\mu} \approx \pm\,\frac{1}{\mathcal{B}_n\,\eta}\,, \tag{59}$$

which can be checked by insertion of formulae (7)–(8) into Eq. (58).[8]

[8] The approximation in Eq. (59) is hinging on the inequality $\mathcal{B}_n\,\mu \gg 1$. Barely valid for a Maxwell Earth ($\mathcal{B}_2\,\mu \approx 2.2$), it fulfills well for Maxwell bodies of Mars's size and smaller.

Between the peaks, the quality function $K_n(\omega) = k_n(\omega)\,\sin\epsilon_n(\omega)$ is about linear in frequency[9]:

$$|\omega| < |\omega_{peak_n}| \quad \Longrightarrow \quad K_n(\omega) \approx \frac{3}{2\,(n-1)}\,\frac{\omega}{|\omega_{peak_n}|}\,. \tag{60}$$

Outside the inter-peak interval, the function $K_n(\omega)$ falls off as the inverse frequency:

$$|\omega| > |\omega_{peak_n}| \quad \Longrightarrow \quad K_n(\omega) \approx \frac{3}{2\,(n-1)}\,\frac{|\omega_{peak_n}|}{\omega}\,. \tag{61}$$

Naturally, the insertion of $\omega = \omega_{peak_n}$ in any of these expressions renders the same value for the peak amplitude:

$$K_n^{(\mathrm{peak})} \approx \pm\,\frac{3}{2\,(n-1)}\,. \tag{62}$$

While the peaks' amplitude is insensitive to a choice of the viscosity value η, the spread between the extrema depends on η. Expression (59) indicates that for a higher viscosity the peaks are residing close to zero, i.e., to the point of resonance $\omega \equiv \omega_{nmpq} = 0$. If the viscosity evolves and assumes lower values (which happens when a body is getting warmer), the peak frequency grows, eventually superseding the orbital frequency. In realistic situations, this requires very low viscosities and happens for bodies at high temperatures or, possibly, for bodies close to rubble. Outside the inter-peak interval, the quality function $K_n(\omega)$ behaves as $\sin\epsilon_n(\omega) = Q_n^{-1}(\omega)\,\mathrm{Sign}(\omega)$, and its values change slowly with frequency.

Owing to the near-linear mode-dependence of K_n in the inter-peak interval, the tidal torque value transcends spin-orbit resonances continuously (Makarov and Efroimsky, 2013; Noyelles et al., 2014).[10] From expression (45) in Efroimsky (2015), it can be derived that for a Maxwell body with $\mathcal{B}_n\,\mu \gg 1$, the locations of extrema of the kink function

[9] This is the reason why the Constant Time Lag (CTL) tidal is applicable solely for $|\omega| < |\omega_{peak_n}|$, and renders incorrect results for higher frequencies.

[10] The linearity of $k_n \sin\epsilon_n$ in ω is equivalent to the frequency-independence of the time lag: $\Delta t_n(\omega_{nmpq}) = \Delta t$, see Efroimsky and Makarov (2013). This is why the tidal response of a terrestrial body can be described with the constant-Δt model *only when all considered tidal frequencies are lower than* $|\omega_{peak}|$ – or, equivalently, when all mean motions and spin rates are lower than $|\omega_{peak}|$. This usually requires a very low viscosity. We now see why the application of the CTL (constant time lag) tidal model to solid or semimolten silicate planets is seldom possible (while for liquified planets this entire formalism is not intended anyway).

$\sin\epsilon_n(\omega) = Q_n^{-1}(\omega)\,\mathrm{Sign}(\omega)$ virtually coincide with the locations of the extrema (59) for K_n. Each of these two functions has only one peak for a positive tidal mode, when the regular Maxwell or Andrade models are used. This changes if we insert into formula (58), and into its counterpart for $\sin\epsilon_n(\omega) = Q_n^{-1}(\omega)\,\mathrm{Sign}(\omega)$, a complex compliance corresponding to a more elaborate rheology, such as the Sundberg–Cooper one. In that situation, an additional peak will appear.

4.5 Layered bodies

Analytical solutions for the tidal response of a homogeneous planetary body using other viscoelastic models can be derived (Renaud and Henning, 2018). However, in most geophysical applications, more sophisticated modeling is required for precise interpretations. This is due to the fact that the material properties of the planetary bodies vary with depth. This results in variation of the tidal response of the planetary body compared to a homogeneous planet. The variation of temperature, pressure, and grain size within the planetary bodies can be taken into account using the viscoelastic models discussed in Section 2. Such an approach has been followed by, e.g., Bagheri et al. (2022, 2019); Khan et al. (2018); Nimmo et al. (2012); Nimmo and Faul (2013); Padovan et al. (2014); Steinbrügge et al. (2021); Plesa et al. (2018). To model a layered planetary body with depth-dependent properties, numerical methods have been used in such studies (Tobie et al., 2008; Roberts and Nimmo, 2008; Běhounková et al., 2015), while another widely used class of methods is based on the propagator matrix technique, derived in the scope of the normal mode theory (e.g., Alterman et al., 1959; Takeuchi et al., 1962; Wu and Peltier, 1982; Vermeersen et al., 1996; Sabadini and Vermeersen, 2004). Similar approach is used to calculate the tidal response by, e.g., Plesa et al. (2018); Moore and Schubert (2000); Padovan et al. (2014) to obtain the interior structure models further discussed in Section 5. Martens et al. (2016) developed a Python toolbox to compute the tidal and load Love numbers in an elastic regime and exploited it (Martens et al., 2019) to study the Earth's tides. Bagheri et al. (2019) used a numerical code based on the spectral-element-method to compute the tidal response using several viscoelastic models. Dmitrovskii et al. (2021) used the same technique in 3D to model tides in an irregularly shaped body (Phobos); but only modeled the elastic response instead of a general viscoelastic behavior.

The overall tidal response of layered bodies depends on the interplay between the individual layers. For example, an ocean or a global molten layer

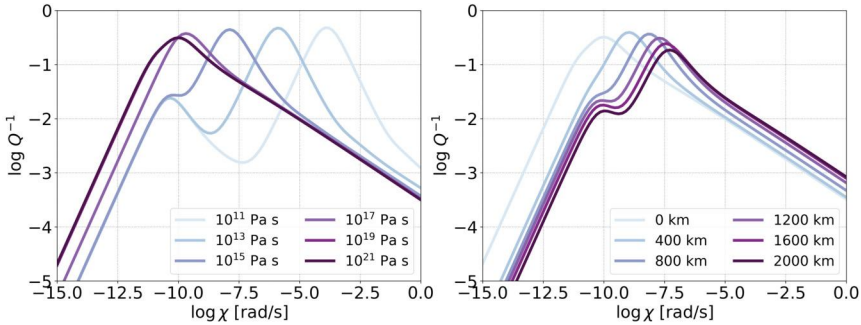

Figure 6 The inverse tidal quality factor of a model Earth-sized planet with a liquid core, a mantle of viscosity 10^{21} Pa s and rigidity $\mu = 200$ GPa, and a weak surface layer (e.g., a global icy crust). The left panel illustrates the effect of the upper layer's viscosity, keeping its thickness fixed to 200 km and its rigidity to the mantle value. On the right panel, the layer's viscosity is held constant at 10^{17} Pa s and the individual lines correspond to different thicknesses.

below the crust or lithosphere might effectively decouple the interior of the planet from the surface and diminish the tidal deformation of the lower layers. As an instructive example, a comparison between the tidal response of a planetary body incorporating layers of different physical properties is shown in Fig. 6. This figure depicts the tidal quality factor of a three-layered Earth-sized planet consisting of a liquid core, a solid mantle governed by the Andrade rheology, and a weak surface layer with the same properties as the mantle, but a lower viscosity. The presence of two dissipative layers leads to the emergence of two peaks in the Q^{-1} spectrum. In this sense, the response of a layered body might be mimicked by an advanced rheological model, for example the Sundberg–Cooper rheology (Gevorgyan, 2021) or by its extensions. Moreover the peak corresponding to the planetary mantle is shifted to higher frequencies and it becomes weaker with decreased upper-layer viscosity (or increased upper-layer thickness).

Appropriately modeling the tidal response on the layered bodies can also help in understanding the tidal dissipation pattern (e.g., Beuthe, 2013), and interpret them to infer knowledge about the interior properties. As shown by Segatz et al. (1988) in the case of Jovian moon Io, the presence of a semimolten layer (an astenosphere) between the solid mantle and lithosphere can considerably affect the pattern of surface tidal heat flow. The same is true for the tidal dissipation within icy moons with a subsurface ocean (Tobie et al., 2005b) and for hypothetical exoplanets with icy crust overlying a silicate mantle (Henning and Hurford, 2014).

5. Tides as a probe of the deep interior

Having introduced the theoretical aspects of modeling tides in previous sections, here we address particular planetary bodies, focusing on how information about their interiors was obtained by studying their tidal response. We summarize the constraints on the interior properties of Mercury, Venus, the Moon, Mars and its moons, and the largest moons of giant planets. We also mention the expected future improvements in measuring these bodies' tidal response.

5.1 Mercury

Studies of Mercury's interior have long focused on its magnetic and gravitational field, and only recently the first measurements of its tidal response were obtained. The Mariner 10 flybys in 1974 and 1975 (Dunne, 1974) provided us with the first clues of Mercury's interior, by detecting its magnetic field (Ness et al., 1974), and with the first measurements of its gravitational field (Anderson et al., 1987). A much more detailed view of Mercury and its environment was provided by NASA's MErcury Surface, Space ENvironment, GEochemistry, and Ranging (MESSENGER) spacecraft, the first to orbit Mercury (Solomon et al., 2007). Pre-MESSENGER studies of Mercury often focused on a combination of rotation and tides, together with its spin-orbit resonance, providing predictions that could later be tested against MESSENGER data (Peale et al., 2002; Van Hoolst and Jacobs, 2003; Van Hoolst et al., 2007; Rambaux et al., 2007; Rivoldini et al., 2009; Dumberry, 2011; Matsuyama and Nimmo, 2009).

One of MESSENGER's many goals was to map Mercury's gravity field, which could then be used to determine the state of Mercury's core. Peale (1976) and Peale et al. (2002) showed that, because Mercury is in a Cassini state (where its spin axis, its orbit normal, and the normal to the invariable plane are coplanar), its polar moment of inertia and the moment of inertia of the solid outer shell (mantle and crust) can be determined from 3 quantities: Mercury's obliquity, the amplitude of its longitudinal librations, and its second degree gravitational harmonic coefficients. The first two were determined from Earth-based radar data (Margot et al., 2007), and MESSENGER finally provided the first precise measurement of Mercury's second degree harmonics (Smith et al., 2012). During the MESSENGER mission, estimates of its gravity field were updated as more data were collected. Mercury's gravitational tidal response as expressed in its degree two Love number k_2 was also determined. (See Fig. 7.)

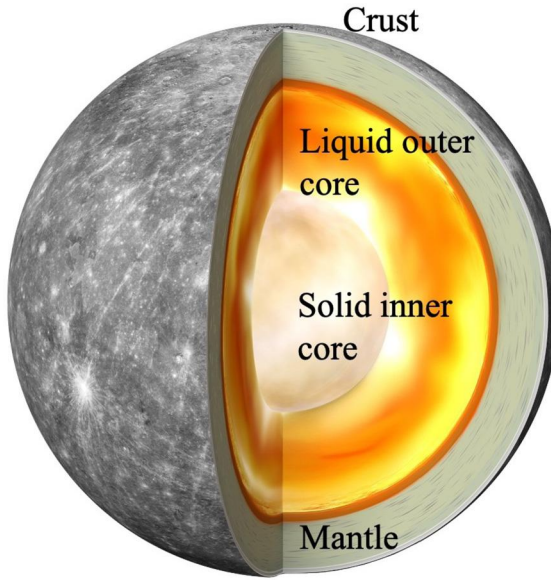

Figure 7 The view of Mercury's interior based on recent measurements of its rotational state. Adapted from Genova et al. (2019).

The first estimate of $k_2 = 0.451 \pm 0.014$ was reported by Mazarico et al. (2014b) using three years of MESSENGER radio tracking data. The Love number was coestimated along with gravity field parameters and rotational parameters, but they found that the radio data was not sensitive to parameters describing the forced librations. The value of k_2 was consistent with pre-MESSENGER analyses of Mercury's tidal response, which indicated a range of 0.4–0.6 (Van Hoolst and Jacobs, 2003; Rivoldini et al., 2009). Using the newly determined gravitational parameters, Rivoldini and Van Hoolst (2013) and Hauck et al. (2013) investigated Mercury's interior structure as constrained by its moments of inertia, but without considering the tides.

Initial results using MESSENGER data proposed the existence of an FeS layer on top of the core, to account for the higher mantle density that was a result of a larger-than-expected value for the moment of inertia of the outer shell (Smith et al., 2012). Results using MESSENGER's X-Ray Spectrometer measurements of the ratio of Ti and Si also argue against the FeS layer (Cartier et al., 2020). Mercury's core itself is mostly considered to be metallic, with light elements of S and/or Si (Rivoldini et al., 2009;

Hauck et al., 2013; Chabot et al., 2014; Knibbe and van Westrenen, 2015, 2018).

Padovan et al. (2014) were the first to comprehensively consider Mercury's tidal response in the light of MESSENGER's results. They considered several end-member models such as a hot or cold mantle, and found that the results presented in Mazarico et al. (2014b) fell in their range, and would be mostly consistent with their cold mantle, without a layer of FeS on the top of the core. The latter was initially considered by Smith et al. (2012) to account for the relatively large moment of inertia of the outer shell. Updates to the estimate of Mercury's obliquity by Margot et al. (2012) reduced this value, and an FeS layer was no longer necessary (Hauck et al., 2013; Rivoldini and Van Hoolst, 2013; Knibbe and van Westrenen, 2015). The k_2 value was also later confirmed by an independent analysis by Verma and Margot (2016), with a value of $k_2 = 0.464 \pm 0.023$. Steinbrügge et al. (2018a) further investigated Mercury's tidal response, and computed models consistent with MESSENGER measurements of mean density, mean moment of inertia, moment of inertia of mantle and crust, and k_2. They showed that the ratio of h_2 (the radial displacement Love number) and k_2 can provide better constraints on the size of a possible solid inner core than the geodetic measurements such as moments of inertia can.

The MESSENGER mission had several extensions, where the altitude and location of its periapsis changed, with lower and lower altitudes obtained in the northern hemisphere, down to 25 km above surface. This increased the sensitivity of the tracking data with respect to smaller scale gravity features, and to Mercury's tidal response. Using the entire set of tracking data, Genova et al. (2019) presented a gravity model that included estimation of Mercury's rotational parameters and tidal Love number. Their estimate of Mercury's obliquity unambiguously satisfies the Cassini state. Their obliquity value results in a lower normalized polar moment of inertia of 0.333 ± 0.005, whereas earlier results yielded normalized polar moment of inertia values around 0.346 (Margot et al., 2012; Hauck et al., 2013; Mazarico et al., 2014b). Using this updated value and smaller error, they modeled Mercury's interior with a Markov Chain Monte Carlo (MCMC) (Mosegaard and Tarantola, 1995) approach and found evidence for the existence of a solid inner core, with the most likely core size being between 0.3 and 0.7 times the size of the liquid core. Their updated Love number, $k_2 = 0.569 \pm 0.025$, was also higher than the previous estimate.

An analysis by Bertone et al. (2021) also finds Mercury's rotational parameters unambiguously satisfying the Cassini state, yet with a differ-

ent obliquity that results in a normalized polar moment of inertia value of 0.343 ± 0.006. Their analysis is based on laser altimetry data from the Mercury Laser Altimeter (MLA, Cavanaugh et al. (2007)), using crossovers (where two laser tracks intersect, the difference in measured altitude can be used to infer rotation and tidal parameters, for example). This discrepancy could point to differences in the rotation state of the entire planet as measured by gravity and the rotation state of the outer shell as measured by laser altimetry. Bertone et al. (2021) did not estimate k_2 but they did provide the first estimate of the radial displacement Love number, $h_2 = 1.55 \pm 0.65$. Due to the sparsity of crossovers, this parameter is difficult to measure. Finally, an analysis by Konopliv et al. (2020a), using the entire MESSENGER tracking data set, determined Mercury's Love number in close agreement with that of Genova et al. (2019), with a value of $k_2 = 0.53 \pm 0.03$.

The differences in moment of inertia values and newly determined Love numbers have implications for our knowledge of Mercury's interior structure, especially for the size of the liquid core. Steinbrügge et al. (2021) performed an analysis of the lower normalized polar moment of inertia value of 0.333 and the higher Love number of 0.569, and found several challenges in determining interior structure models that fit these parameters: they find a relatively large inner core (>1000 km), a relatively high temperature at the core-mantle boundary (CMB; above 2000 K), low viscosities at this boundary (below 10^{13} Pa s), and a low mantle density (markedly below 3200 kg m^{-3}). They also indicate that the low viscosities required to match k_2 imply a significantly weaker mantle. They indicate that such challenges do not exist for the higher normalized polar moment of inertia value of ~ 0.346. It should be noted that they focused their analysis on models that matched the central values of parameters such as the moments of inertia and k_2. If they take into account the quoted errors, they indicate some of the challenges are alleviated.

A recent analysis by Goossens et al. (2022) also investigated the different values for moments of inertia and k_2, using an MCMC method to map out models of Mercury's interior that satisfy the measurements and their quoted errors (see Fig. 8). They find that models that match the lower normalized polar moment of inertia value of 0.333 (Genova et al., 2019) also match or predict the Love number value of $k_2 = 0.569$. Models that match the higher normalized polar moment of inertia of ~ 0.346 indicate even higher Love numbers, larger than 0.6, with a wide spread. Their study thus indicates that the higher normalized polar moment of inertia values are not consistent with the current measurements of the Love number. In

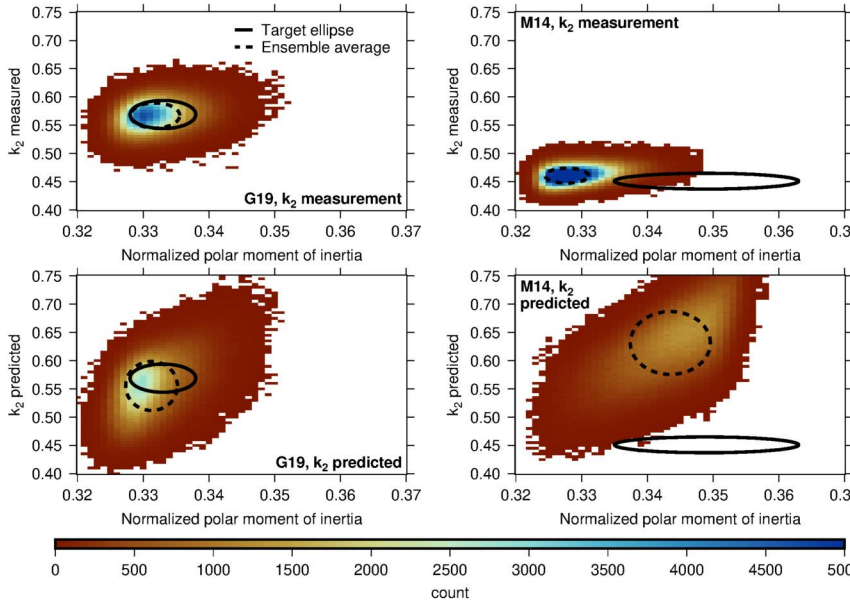

Figure 8 Results of the MCMC analysis by Goossens et al. (2022), which determined models of Mercury's interior structure using different measurements for the normalized polar moment of inertia and tidal Love number k_2. The label "G19" refers to Genova et al. (2019) and "M14" to Mazarico et al. (2014b). The results are shown as heatmaps of the mapped quantities for all accepted models in the MCMC analysis. For the top panels, k_2 was used as a measurement in the MCMC analysis, whereas it was predicted for the results in the bottom panels. These results indicate that the set of measurements of G19 s the most consistent. Higher values of the normalized polar moment of inertia, as provided by M14, cannot simultaneously fit the measured k_2, and would indeed predict an even higher value.

addition, they also find lower CMB temperatures than Steinbrügge et al. (2021) indicated, in the range of 1600–2200 K but with a peak at 1800 K. While their study does indicate low viscosity values at the CMB, models with a constant mantle temperature, mimicking a convecting mantle rather than a conducting one, predict lower temperatures and higher viscosities. Models that satisfy the lower normalized polar moment of inertia and the updated moment of inertia for the outer shell do indicate mantle densities that are lower than previously assumed (3089 ± 135 kg m^{-3}). A study by Lark et al. (2022) indicates that the presences of sulfides in the mantle can explain this lower density. Goossens et al. (2022) also provide a prediction for the radial displacement Love number $h_2 = 1.02 \pm 0.04$ for models that satisfy the measurements from Genova et al. (2019).

The next spacecraft that will orbit Mercury is the European Space Agency's BepiColombo mission (Benkhoff et al., 2010). This spacecraft will provide precise gravity measurements (Genova et al., 2021) as well as laser altimetry (Thomas et al., 2021), both with a more global coverage than was possible with MESSENGER, due to the latter's elliptical orbit around Mercury. BepiColombo data will provide updated measurements of the moments of inertia and the Love numbers k_2 and h_2 (Steinbrügge et al., 2018b; Thor et al., 2020; Genova et al., 2021), as well as for its rotational state and gravity, which will help resolve the current challenges in understanding Mercury's interior structure.

5.2 Venus

The tidal response of Venus to semidiurnal Solar tides was measured more than a quarter century ago using Magellan and Pioneer tracking data. Konopliv and Yoder (1996) estimated the 2-σ interval for the potential Love number as $k_2 = 0.295 \pm 0.066$ and concluded, following the predictions of Yoder (1995), that Venus has a fully liquid core. However, this conclusion was based on a purely elastic model of the tidal response. A new reassessment of the problem with a compressible Andrade model (Dumoulin et al., 2017) indicated that the question of size and state of the Venusian core cannot be resolved with the data available. The wide range of admissible Love numbers, combined with the absence of Q measurements and with the large uncertainties on the planet's moment of inertia (Margot et al., 2021) constrains neither the core state, nor the mantle mineralogy and temperature profile. Dumoulin et al. (2017) illustrated that only a future measurement of k_2 below 0.26 and a large phase lag[11] ($\epsilon_2 > 4°$) would indicate a fully solid core. At higher Love numbers, the core can be interpreted as at least partially liquid and a precise measurement of the phase lag would further help to discern between different mantle viscosities and thermal states (see Fig. 9).

In addition to solid-body tides, the deformation of Venus is also affected by tides raised by its thick atmosphere, which consists of two components: one due to the gravitational loading by the Sun and the other resulting from thermal forcing (Auclair-Desrotour et al., 2017; Correia et al., 2003;

[11] Dumoulin et al. (2017) define their "tidal phase lag" as $\frac{1}{2}\arcsin Q^{-1}$. For the semidiurnal tide (and, more generally, for the *nmpq* tidal components with $m = 2$), this quantity coincides with the *geometric lag*, a quantity not to be confused with the *phase lag*. See Efroimsky and Makarov (2013, eqn 26) for details.

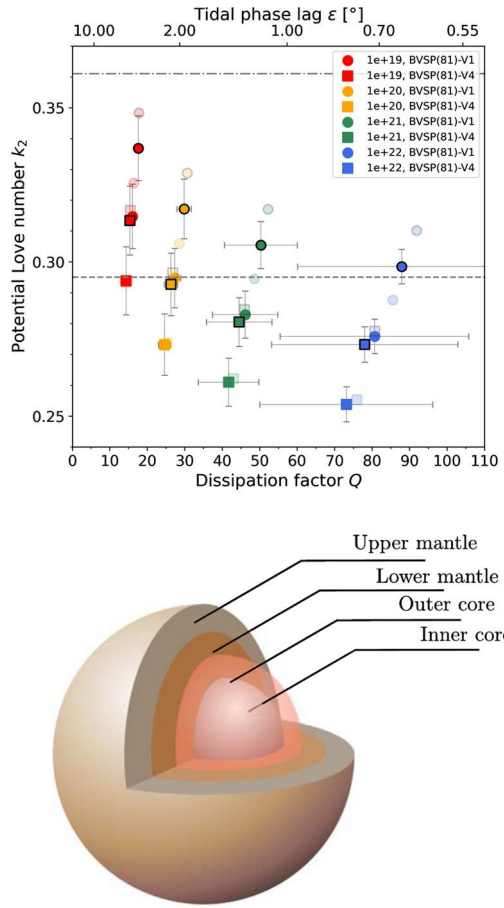

Figure 9 Top: Overview of Venusian tidal parameters for two mantle mineralogies and two mantle temperature profiles, assuming an incompressible Andrade model, reproduced after Dumoulin et al. (2017). Circles symbolize an iron-poor (0.24 wt% FeO) mantle model and squares an iron-rich (18.7 wt% FeO) model according to Basaltic Volcanism Study Project (1981). Different colors stand for different mantle viscosities; the markers with black edges correspond to a hot interior (Armann and Tackley, 2012) and the markers without contour correspond to a cold interior (Steinberger et al., 2010). The dashed and dot-dashed lines indicate the mean value and the upper bound of the 2-σ interval for the tidal Love number obtained by Konopliv and Yoder (1996) using Magellan and Pioneer data: $k_2 = 0.295 \pm 0.066$. Finally, the error bars illustrate the span of results calculated for different values of the Andrade parameter $\alpha \in (0.2, 0.3)$ (see Section 2.5), and the transparent markers, taken from Dumoulin et al. (2017), indicate the effect of compressibility. Bottom: Schematic interior structure of Venus from Shah et al. (2022).

Ingersoll and Dobrovolskis, 1978; Gold and Soter, 1969). The interplay between the gravitational and thermal tides leads to the instability of synchronous rotation and it has probably driven the planet to its present-day retrograde spin configuration. Close to its nonsynchronous, yet stationary rotation state, Venus might also be influenced by the weak gravitational pull of the Earth, as hypothesized by Dobrovolskis and Ingersoll (1980) and Gold and Soter (1969). Besides the contribution to the planet's rotational dynamics, the atmosphere acts as a global surface load and diminishes the tidal deformation of the Venusian surface by approximately 0.3% (see Remus et al., 2012; Dermott, 1979).

The tidal phase lag and thus the tidal quality factor Q can also be used to constrain the thermal state of the interior, given the temperature dependence of the mantle viscosity. In addition to the present-day values, knowing the past thermal state and Q of Venus can further help us to understand its tidally-induced rotational evolution (Bolmont et al., 2020). Since Venus and the Earth are often referred to as twin planets, due to their similar size and mass, the tidal quality factor Q may be similar between the two bodies. However, while on the Earth plate tectonics represent an efficient way to cool the interior, on Venus large scale subduction may be absent today. In fact, a recent study by Rolf et al. (2018) concluded that if Venus may have experienced one or multiple episodes of plate tectonics in the past, the last of those episodes likely ended 300–450 Myr ago, otherwise thermal evolution models cannot match the observed surface gravity spectrum. If Venus has been in a stagnant lid regime, with an immobile surface over the past 500 Myr, its interior would likely have a much higher temperature than that of the present-day Earth. This may indicate a much more dissipative interior, i.e., lower tidal quality factor Q, than that of the solid Earth, for which Q is around 280 (Ray et al., 2001). Even if Venus currently experiences some sort of surface mobilization on a much smaller scale than tectonic plates provide on the Earth, with small patches of the surface being recycled in the interior (i.e., the so-called plutonic squishy lid regime Lourenço et al. (2020)), this might still lead to a hotter interior than on present-day Earth. This type of surface mobilization is thought to have operated on the Earth in the past during the Archean, when the interior temperature was higher than it is today (Rozel et al., 2017; Lourenço et al., 2020).

That the interior of Venus may be characterized by high mantle temperatures, which in turn may indicate a higher dissipation, is also supported by the small elastic lithosphere thicknesses that are indicators for a thin and hot

lithosphere (Smrekar et al., 2018). Small elastic thicknesses are estimated at coronae (O'Rourke and Smrekar, 2018), steep side domes (Borrelli et al., 2021), and crustal plateaus (Maia and Wieczorek, 2022), and likely 20 km or less may be representative for a significant part of the planet (Anderson and Smrekar, 2006). Moreover, the temperatures inside the Venusian mantle may allow for volcanic activity at present-day. This has been suggested by several observations. For example, the presence of recently active hot-spots in the interior of Venus has been inferred based on their thermal signature (Shalygin et al., 2015) and emissivity data of Venus Express, which allow to distinguish fresh from weathered basaltic material (Helbert et al., 2008; Smrekar et al., 2010; D'Incecco et al., 2017). In addition, gravity, topography and surface deformation structures at the locations where recent volcanic activity has been suggested are consistent with the presence of mantle plumes in the interior (Kiefer and Hager, 1991; Smrekar and Phillips, 1991). Moreover, many Venusian coronae display topographic features (an outer trench and rise) that are interpreted as ongoing plume activity (Gulcher et al., 2020). Furthermore, SO_2 variations in the atmosphere of Venus recorded by Pioneer Venus Orbiter (Esposito, 1984; Esposito et al., 1988) and later by Venus Express (Marcq et al., 2013) provide additional hints at recent volcanic activity. All this evidence, although indirect, may indicate that the present-day interior of Venus is characterized by high mantle temperatures and hence low mantle viscosities that would lead to a lower dissipation factor than that of the Earth. Whether the above conclusions hold or not, it needs to be tested by future data.

Owing to the lack of recent and accurate tidal measurements, Venus still remains the most enigmatic of the terrestrial worlds. Recently revived interest in its interior and atmospheric conditions, nurtured by the putative detection of biosignatures (Greaves et al., 2021; cf. Villanueva et al., 2021), foreshadowed the selection of two geophysical mission concepts for a launch in late 2020s or early 2030s. The VERITAS mission (Venus Emissivity, Radio Science, InSAR, Topography, and Spectroscopy; Smrekar et al., 2020) of NASA's Discovery Program will address the present geological and volcanic activity, the link between interior and atmospheric evolution, and the global accurate mapping of Venusian gravity field. In order to reduce the uncertainties of the gravity field (and tidal response) measurements, introduced by the planet's rotation, the mission will combine standard Earth-based Doppler tracking with the systematic observation of surface features by the onboard instrument VISAR (Venus Interferometric Synthetic Aperture Radar). With this approach, the expected 3-σ accu-

racy of the Love number k_2 is 4.6×10^{-4} and of the tidal phase lag 0.05° (Cascioli et al., 2021).

The medium-sized ESA's Cosmic Vision Programme mission *EnVision* (Ghail et al., 2016) will focus on the geological structures of Venus that are of interest for understanding its past thermal evolution. As in the case of VERITAS, the primary objectives of the mission also include the determination of a uniform high-resolution gravity field, with a spatial resolution better than ~ 170 km. The expected 1-σ error of both the real and the imaginary parts of the Love number k_2 is 10^{-3}, implying a 0.1° uncertainty for the tidal phase lag (Rosenblatt et al., 2021). Despite the similarity of the two geophysical missions, VERITAS and *EnVision* are expected to be synergistic. First, the launch of *EnVision* is planned for a later date than the launch of VERITAS, and the two orbiters will only operate simultaneously for a part of the respective mission durations. Second, while VERITAS aims at providing a global geophysical survey, *EnVision* is designed for more targeted, repeated observations of the regions of interest identified by the former (Ghail, 2021). With the new data, a refined estimate of the Venusian core size will be possible and the first measurements of phase lag will enable constraining the average mantle viscosity within an order of magnitude (Dumoulin et al., 2017; Rosenblatt et al., 2021).

5.3 The Moon

The Moon is one of the best studied bodies in the Solar system because of its proximity to the Earth. It is only 60 Earth radii away and its surface undergoes a monthly tidal deformation of $\pm$ 0.1 m generated by the Earth's gravitational field. This tidal potential impacts also the Moon's gravity field and its orientation periodically. In addition, the Moon does not have an ocean as on the Earth and the tidal variations are only incorporated in solid tides. These variations are detected by space missions orbiting the Moon and by Lunar-Laser Ranging measurements performed from the stations on the Earth. These accurate regular measurements over the past 50 years since the Apollo program have made the Moon the best place to test tidal theory and dissipation mechanisms. The interpretation of these variations provides information about the lunar interior, but many questions remain about its internal structure and dissipation mechanisms.

The determination of the Love number k_2 at the monthly period of the Moon (its orbital period) has most recently been obtained by the Gravity Recovery and Interior Laboratory (GRAIL) space mission radio science

experiment, which consists of precise measurements of two satellites in orbit around the Moon (Zuber et al., 2013). This experiment is similar to the GRACE mission around the Earth and GRAIL has determined the lunar gravity field up to degree 900 (Konopliv et al., 2014) and provided the monthly Love k_2 number of the Moon at 0.02416 ± 0.00022 (Konopliv et al., 2013, 2014; Lemoine et al., 2013; Williams et al., 2014). The Love number h_2 is determined on the Moon using the Lunar Reconnaissance Orbiter mission which carries a laser altimeter, Lunar Orbiter Laser Altimeter LOLA which measures displacements of the Moon's surface to an accuracy of 10 cm (Smith et al., 2017). The Moon's Love number h_2 is determined to be 0.0371 ± 0.0033 (Mazarico et al., 2014a) and 0.0387 ± 0.0025 (Thor et al., 2021). Finally, the dissipation of the Moon is extracted from LLR ranging measurements by analyzing the lunar orientation and libration (Park et al., 2021; Pavlov et al., 2016; Viswanathan et al., 2018, and references therein). The Lunar-Laser Ranging (LLR) consists of precise measurements of the round-trip travel time of a photon emitted from a laser on an Earth-ground station and lunar retroreflectors deployed by US astronauts and the Russian Lunakhod robotic missions (Murphy, 2013; Chabé et al., 2020). These measurements allow to determine the Earth–Moon distance at centimeter level and the lunar rotation to the milliarcsecond level (Viswanathan et al., 2018; Park et al., 2021). Lunar orientation and libration analysis allows for extraction of the lunar dissipation. Currently, the monthly lunar tidal bulge delay time is estimated to be 0.1 days which corresponds to a monthly dissipation factor $Q = 38$ (Williams et al., 2001; Williams and Boggs, 2015).

Beyond the monthly Love number k_2 and dissipation factor Q, precise analyses of the LLR data have determined their frequency dependence. In fact, the Moon's orbit is strongly perturbed by the presence of the Sun and its orbital motion results from a three-body motion. The Moon's orbit is described by the Delaunay arguments ℓ, ℓ', F, D which represent the mean anomaly of the Moon, the mean anomaly of the Earth–Moon barycenter, the latitude anomaly of the Moon and the elongation of the Moon of periods 27.55 days, 365.25 days, 27.21 days, 29.53 days, to which must be added the precession of the lunar orbit of 18.6 years (for a description of the lunar orbit see Chapront-Touzé and Chapront (1988, 1991)). Thus, librations and tidal shifts are mixed and tidal frequencies appear as mixed combinations of these frequencies with a period spectrum ranging from 2 weeks to 18.6 years and frequencies at 1 month, 7 months and 1 year (Williams et al., 2001; Rambaux and Williams, 2011; Williams and Boggs,

2015). The extraction of dissipation factors from LLR fits and the orientation of the Moon is challenging, but the terms at 27.2 days and 365 days stand out, while two others at 1095 and 2190 days provide upper bounds on lunar dissipation, whereas the term at 206 days is more uncertain (Williams et al., 2001; Williams and Boggs, 2015). The k_2/Q curve as a function of period has a kinked shape as shown in Section 2, and the rheological models can then be compared with the observations to identify plausible internal structure patterns (Williams and Boggs, 2015).

Several rheological models, such as Maxwell, Andrade, absorption band (see Fig. 10), were employed to explain the relatively low monthly dissipation factor $Q = 38$ and the bell-shaped behavior of the k_2/Q law (see, e.g., Williams and Boggs, 2015). Three physical mechanisms to explain this dissipation have been suggested: (i) the properties of the lunar material, (ii) the presence of water at depth, and (iii) the presence of a partially molten zone.

(i) By analogy with the Earth, Nimmo et al. (2012) examined the influence of polycrystalline olivine melt-free to explain the observed dissipation. They were able to reproduce the dissipation at seismic and monthly tidal frequencies but not the slope behavior associated at longer tidal periods. Matsuyama et al. (2016) developed a Bayesian approach to test the presence or not of a transient layer above the core from the observed mass, solid moment of inertia, and elastic Love numbers k_2 and h_2 to constrain the density and rigidity profile of the Moon. Their model favors an internal structure without a transition zone. However, it should be noted that this observation is based on a purely elastic approach. Matsumoto et al. (2015) adopted a similar approach to Matsuyama et al. (2016) to study the interior of the Moon using an MCMC method. Their results are slightly different than Matsuyama et al. (2016) in that, for example, Matsuyama et al. (2016) obtain a unimodal probability distribution for the liquid outer core radius, while Matsumoto et al. (2015) obtained a bimodal distribution. Matsuyama et al. (2016) attribute this difference to the ways of computing the Love numbers, i.e., Matsuyama et al. (2016) apply a simple anelastic correction to the observed Love numbers, while Matsumoto et al. (2015) use a viscoelastic model to compute the Love numbers at the tidal forcing period, or, alternatively, to the use of additional tidal quality and seismic constraints by Matsumoto et al. (2015).

(ii) Karato (2013) proposed that water concentration would be the mechanism behind dissipation, also by analogy with the Earth's asthenosphere. Although this model reproduces the low value of the dissipation factor it does not describe the frequency dependence.

(iii) Finally, the molten layer model proposed by Nakamura as early as 1973 from seismic data seems to be the most robust. A Bayesian approach developed by Khan et al. (2014) used Love number, mass distribution, composition and electromagnetic data to explore the parameter space and conclude that the melt layer is present. An attempt to fit the LLR data to the power scaling law $Q \sim \chi^p$ resulted in a small *negative* value of the exponential: $p = -0.19$ (Williams et al., 2001). A subsequent reprocessing of the data in Williams and Boggs (2009) rendered the value $p = -0.07$. Efroimsky (2012) proposed that since the frequency-dependence of k_2/Q has a kink form, as in Fig. 5, the negative slope found by the LLR measurements may be located slightly to the left of the pick of the kink. For a Maxwell Moon, this necessitates the mean viscosity as low as $\sim 3 \times 10^{15}$ Pa s, implying the presence of a considerable amount of partial melt. Explaining the origin of the sign of p has been a problem for rheological models (see e.g. Nimmo et al., 2012). However, according to the seismic data, the Moon can have a low viscosity zone just above the core. Recent viscoelastic models have therefore introduced this low viscosity layer which will generate an additional dissipation peak with respect to the astenosphere dissipative background and at the same time shift its position to explain the LLR data (e.g., Harada et al., 2014, 2016; Rambaux et al., 2014; Williams and Boggs, 2015; Tan and Harada, 2021; Briaud et al., 2022). Fig. 10 coming from Williams and Boggs (2015) shows the effect of various rheological models to explain the k_2/Q coming from LLR analysis at four frequencies.

With all the mentioned complexities, we are at the beginning of the study of lunar dissipation, and our knowledge is still fragmentary. Several directions of improvement are now possible. Firstly, from an observational point of view, the installation of new, more compact and optimized single lunar Cube Corner Retroreflectors (Turyshev et al., 2013; Dell'Agnello et al., 2015), better distributed spatially on the Moon during the next Artemis missions, will make it possible to improve the return of the photon number and the precision of the measurements (Dell'Agnello et al., 2011; Dehant et al., 2012). The accuracy of these measurements is about 1–2 centimeter (Viswanathan et al., 2018; Park et al., 2021) while theoretically the accuracy is expected to be around one millimeter (Samain et al., 1998). This means that data analysis and dynamic models need to be improved to reach the theoretical accuracy. Finally, a better knowledge of long-period lunar tides will be possible by combining other measurements, such as altimetry, active retroreflectors, differential lunar laser ranging or from the zenith telescope (Petrova and Hanada, 2013; Zhang et al., 2020; Dehant et al., 2012; Thor et

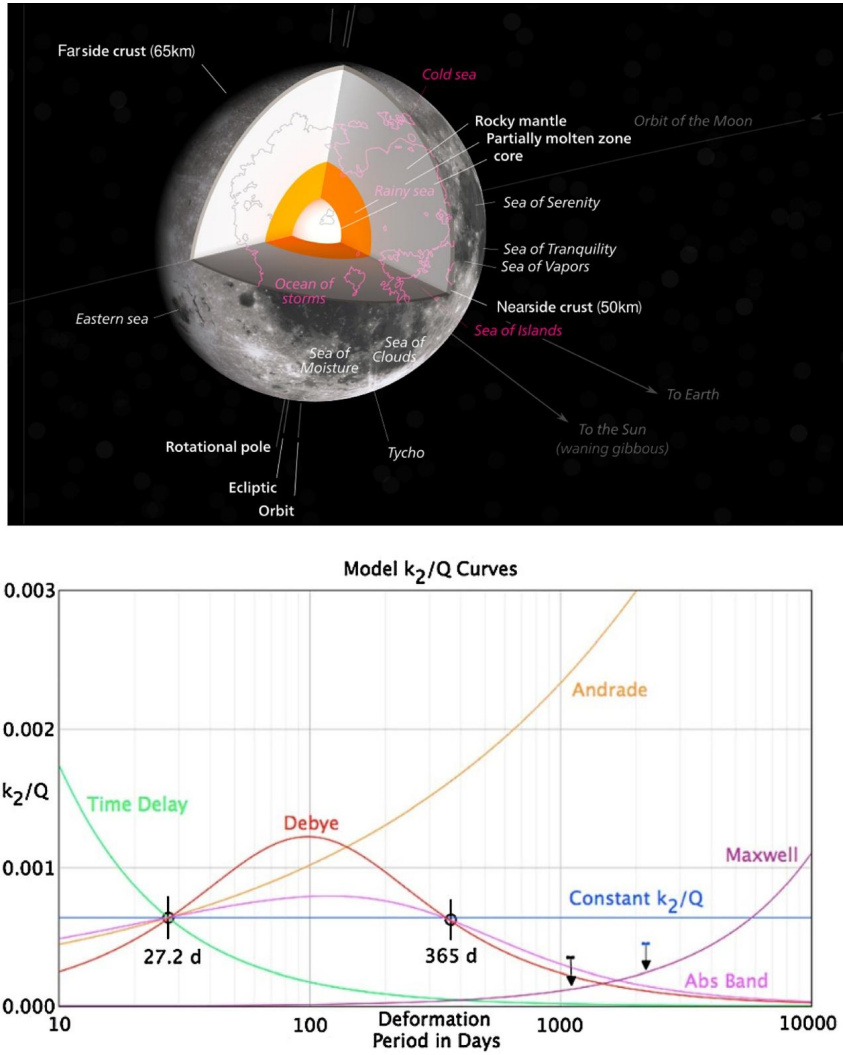

Figure 10 Top: Artistic view of the interior structure and surface features of the Moon; Bottom: Frequency dependence of k_2/Q for various lunar rheological models (in colors) and LLR measurements points and limits (in black). The absorption band and Debye model presents a kink reproducing the measurements (figure from Williams and Boggs (2015)).

al., 2020). Lunar seismic measurements will also help to better constrain the Moon's interior and to better understand tidal effects (Garcia et al., 2019). Finally, laboratory measurements of the dissipation processes of lunar and

supposedly lunar materials will help constrain the measurements and models currently used.

5.4 Mars

Owing to numerous successful missions, particularly in the past two decades, Mars has become the most geophysically-explored planet after the Earth. Similarly to the Moon, the lack of oceans eases the study of the solid body tides on Mars. As the only terrestrial planet except the Earth which has natural satellites, body tides in Mars are generated mainly by the Sun and Phobos, whereas the tides caused by Deimos are much weaker because of its small size and larger separation. A vast volume of information about Mars has been obtained from orbiting and landed spacecraft (Mars Pathfinder, Mars Global Surveyor, Mars Odyssey, Mars Reconnaissance Orbiter and Mars Express), and from the geodetic Doppler ranging data (Yoder et al., 2003; Bills et al., 2005; Lainey et al., 2007; Konopliv et al., 2006, 2011; Jacobson and Lainey, 2014; Konopliv et al., 2016, 2020b; Genova et al., 2016; Lainey et al., 2021). The Mars InSight lander touched down on the planet on November 2018, carrying on board a suite of geophysical instruments, including a seismometer, a magnetometer, a radio science experiment, and a heat flow probe to explore the planet's interior (Smrekar et al., 2019; Banerdt et al., 2020; Giardini et al., 2020; Lognonné et al., 2020). Before the recent improvements in our knowledge of the interior structure of Mars owing to the seismic measurements provided by InSight (Banerdt et al., 2020; Lognonné et al., 2020; Stähler et al., 2021; Khan et al., 2021; Durán et al., 2022; Knapmeyer-Endrun et al., 2021), geodetic measurements used to be the sole constraint on the Martian interior.

Constraining the tidal Love number of Mars can considerably help to understand the size and state of the Martian core (see Fig. 11). Along with that, the Martian tidal quality factor and its frequency-dependence can impose effective constraints on the mantle's temperature and rheological properties. Several studies based on different data sets have aimed at constraining Mars's tidal Love number, a summary of which can be found in Fig. 6 of Chapter 3 of this volume. Basing their analysis on the tracking data collected by the Mars Orbiter Laser Altimeter on the Mars Global Surveyor (MGS), Smith et al. (2001), obtained a Love number as low as 0.055 ± 0.008, as the first measurement of the Martian Love number. This value is very close to the k_2 of a Mars-size hypothetically homogeneous solid planet, which implies that the Martian core has solidified. Yet, a later analysis of the MGS Doppler and range data by Yoder et al. (2003), combined with the

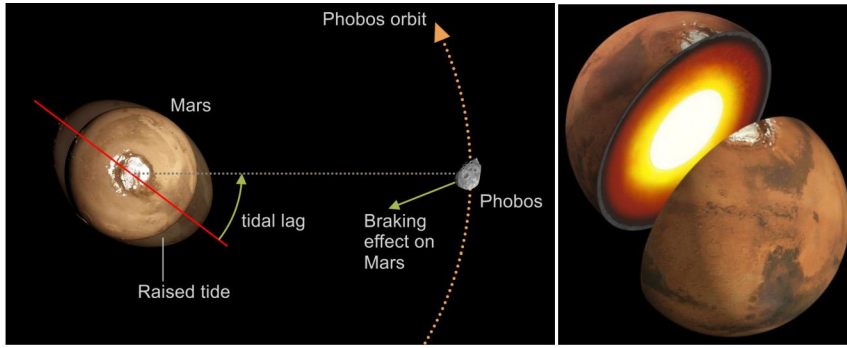

Figure 11 Artistic view of tides raised by Phobos on Mars (left) and interior of structure Mars with crust, mantle and core (right). Image credit: Left: David Ducros/IPGP, Right: NASA/JPL-CalTech.

information from Mars Pathfinder and Viking Lander, suggested a much larger tidal Love number of 0.153 ± 0.017 at the period of the Solar tides (11 hr 19 min). Such a large value is incompatible with the existence of a solid core, and instead indicates the presence of a large liquid core.

Yoder et al. (2003) obtained a liquid iron core of 1520–1840 km in radius based on their measured k_2. Using the measurement of the secular acceleration of Phobos, they proposed for the tidal quality factor a value of $Q = 92 \pm 11$. A caveat in computing the tidal quality factor is that the secular acceleration deals with the Phobos-raised tides at the synodic period (T = 5.55 hr), whereas the tidal Love number is measured at the semidiurnal tides period (T = 24.62 day), and it is not clear whether this difference is taken into account. By removing the anelastic effect, by analogy to the Earth's tidal response to the Moon, Yoder et al. (2003) also suggested that the elastic tidal Love number of Mars is in the range of 0.145 ± 0.017.

Several later studies dealt with constraining the tidal Love number and quality factor of Mars by analyzing the accumulated data from different Mars orbiters. The deduced values for the tidal Love number and quality factor were not dramatically different from those obtained by Yoder et al. (2003). Having collected six years of MGS tracking data and three years of Mars Odyssey tracking data, Konopliv et al. (2006) derived a global solution for Mars's gravity field, including the Solar-tide Love number of $k_2 = 0.152 \pm 0.009$ and the elastic tidal Love number of $k_2 = 0.148 \pm 0.009$. From the computed values of the Love numbers, these authors inferred the presence of a fluid core of a 1600–1800 km radius. Lemoine et al. (2006) employed six years of MGS data, starting from 1999, to obtain

$k_2 = 0.176 \pm 0.041$. Including tracking data from the MRO spacecraft, Konopliv et al. (2011) improved their previous finding and achieved a noticeable progress in determination of the high frequency portion of the spherical harmonic Mars gravity field. This resulted in a slightly larger value of the tidal Love number ($k_2 = 0.164 \pm 0.009$).

Using the Deep Space Network tracking data of the NASA Mars missions, Mars Global Surveyor, Mars Odyssey, and the Mars Reconnaissance Orbiter, Genova et al. (2016) presented a higher-order and high-degree spherical harmonic solution of the Martian gravity field, finding $k_2 = 0.1697 \pm 0.0027$. Note that Genova et al. (2016) directly take into account the atmospheric effects in their estimations, whereas all other studies need to correct for this effect after computing the Love number. Most recently, Konopliv et al. (2020b) analyzed several years of data to detect the Chandler wobble of the Martian pole, for the first time for any Solar system body other than the Earth. In line with several previous measurements, this study suggested $k_2 = 0.169 \pm 0.006$ at the Solar tides period without taking into account the atmospheric effects, and $k_2 = 0.174 \pm 0.008$ after correcting for this effect.

Pou et al. (2021) modeled the response of Mars to Phobos tides using tidal potential deduced from JPL Horizons ephemerides and predicted how the Very Broad Band seismometer (VBB) on the InSight lander can be used as a gravimeter to constrain the tidal response of Mars; however, after 3 years, extracting the tidal signal has proven to be more difficult and to require further data accumulation to reduce the signal-to-noise ratio to the necessary level.

The tidal quality factor of Mars has been constrained by measuring the secular acceleration of Phobos, as the most feasible method. Both Martian moons are very small, faint, and rapidly orbiting the planet, and are difficult to observe from the Earth-based instruments. Nevertheless, before the spacecraft era, several astrometric measurements had been carried out to constrain the orbital properties of the moons. The precision of most of those observations was, however, limited. A list of such observations can be found in Jacobson and Lainey (2014). Bills et al. (2005) used the observed transit of the shadow of Phobos from MOLA, to estimate the tidal quality factor of the planet, and found the secular acceleration of Phobos $\dot{s} = (1.367 \pm 0.006) \times 10^{-3}$ deg/yr^2. Therefore, these authors deduced the tidal quality factor to be $Q = 85 \pm 0.37$. Further analysis was performed by Rainey and Aharonson (2006); Lainey et al. (2007); Jacobson (2010); Lainey et al. (2021), with the aid of the Martian moons' ephemerides. In

summary, the quality factor derived by these studies resides in the range $78 \lesssim Q \lesssim 105$.

The observed tidal response, i.e., the values of the Martian tidal Love number and quality factor, can significantly improve our knowledge of its interior. Rivoldini et al. (2011) used the tidal Love number and the moment of inertia of Mars to constrain the core radius and sulfur content. They considered two main end-members of cold and hot interior models and found a core radius of 1794±65 km and a sulfur concentration of 16±2 wt%. These authors concluded that the geodetic data alone are not capable of constraining the mineralogy of the mantle and the crust. Note that Rivoldini et al. (2011) only considered an elastic Mars without taking into account the tidal dissipation in the planet.

Khan et al. (2018) utilized the knowledge on the Martian tidal response, along with mass and moment of inertia, to constrain, in the context of a probabilistic inversion method, the planet's major interior properties such as the size of the core, mantle, and crust, the composition of each part, the dissipative properties of the mantle, and the temperature profile. They employed a laboratory-based viscoelastic dissipation rheology (extended Burgers, as discussed in Section 2.4) to model the anelasticity of the Martian mantle, and used the known tidal response in inversion. They examined different crust and mantle compositions based on the analysis of Martian meteorites (i.e., Dreibus and Wanke, 1987; Morgan and Anders, 1979; Lodders and Fegley, 1997; Sanloup et al., 1999; Taylor, 2013). Fig. 12 from Khan et al. (2018) demonstrates the inversion results for the properties of the core. As shown in this figure, they obtained a core radius of 1730–1840 km and 15–18.5 wt% sulfur, similar to Rivoldini et al. (2011). The color code in the figure also shows the trade-off between the core radius and core density: the larger the radius, the lighter the core – and the more light elements in it, such as sulfur. Their results show that, except for the composition model of Morgan and Anders (1979), all models were able to fit the data, and hence are not distinguishable only based on the available geodetic measurements. Khan et al. (2018) also determined that the parameter α from the extended Burgers model (see Eq. (16) above) takes values in the range 0.24–0.38. They also found the temperature at the lithosphere to be in the range 1400–1460 °C.

In another recent study, (Plesa et al., 2018) used global thermal evolution models and calculated the tidal deformation of Mars using an Andrade pseudo-period model (Section 2.5 in this chapter, Jackson and Faul, 2010; Jackson, 2005). Model results indicate that a cold mantle that may result

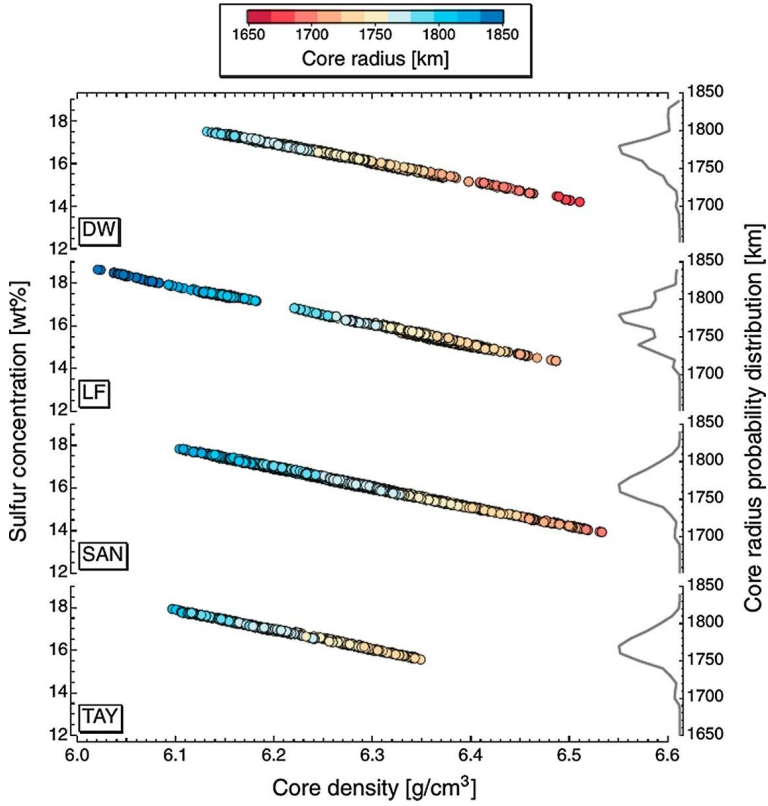

Figure 12 Sampled core properties in a probabilistic inversion method used by Khan et al. (2018): radius, sulfur content, and density for the four main compositions (defined as DW, LF, SAN, and TAY in Table 1 in Khan et al. (2018)). The histograms on the right axis show the probability distributions of core radius for each of the main compositions.

from concentrating nearly all radioactive heat producing elements in the crust would have a smaller quality factor Q (i.e., the mantle would not be dissipative enough) than the available estimates. Conversely, models with a hot interior, either due to the presence of a large amount of heat sources in the mantle or due to an inefficient heat transport caused by a high mantle viscosity, would be too dissipative to satisfy the constraint given by the tidal quality factor estimates. In order to match the values of the tidal Love number k_2 of Konopliv et al. (2016) and Genova et al. (2016), the combined thermal evolution and tidal deformation models of Plesa et al. (2018) indicated a core size larger than 1800 km with a preferred value of 1850 km,

a value range consistent to the core size estimates of Rivoldini et al. (2011) and Khan et al. (2018).

Bagheri et al. (2019) used an approach similar to Khan et al. (2018), but employed several viscoelastic models (as mentioned in Section 2) to constrain the interior properties of the planet, particularly the dissipation. They examined the extended Burgers, Andrade, power-law, Sundberg–Cooper, and Maxwell models to fit the observations. Their results show that all these models, except Maxwell, are capable of fitting the available tidal response measurement for Mars. The Maxwell model, however, can only fit the observed tidal response only at the expense of unrealistically low mantle viscosities. This is consistent with the conclusions from the work by Bills et al. (2005), in which a very low average viscosity of the mantle was found and was attributed to the possible presence of partial melt within the planet (Kiefer, 2003), or a more volatile-rich mantle, or a tidally forced flow of a fluid within a porous solid (Nield et al., 2004). However, the results of Khan et al. (2018) and Bagheri et al. (2019) demonstrate that the tidal dissipation rate in Mars can be explained by the anelastic strength of the mantle, without the need for the said phenomena. This observation reveals the necessity of utilizing more elaborate viscoelastic models for the planetary bodies, especially for tidal frequencies, because at these frequencies the anelastic relaxation is important. Bagheri et al. (2019) determined that the parameter α that appears in the Andrade and Sundberg–Cooper models, and in the power-law approximation should assume values in the interval of 0.22–0.42, which are higher than the Earth's value of 0.15 (McCarthy and Petit, 2004). This serves as another indication that the Martian interior is colder, because generally α tends to decrease with the increase of temperature, especially on approach to melting point (Fontaine et al., 2005; Bagdassarov and Dingwell, 1993), and it is possible that the value of α for the Earth is so low due to the presence of partial melt.

Bagheri et al. (2019) also found the tidal displacement Love numbers h_2 (0.22–0.24) and l_2 (0.037–0.040) for Mars. These authors provided estimations of dissipation (Q) at different periods, such as seismic waves, normal modes, and Solar tides, based on each viscoelastic model, and showed that while all models are capable of fitting the only available data point for dissipation (the Phobos tides), they do not predict similar dissipative behavior for other periods (Bagheri et al., 2019) (see Fig. 13). The recent findings of seismic attenuation and anelasticity at the Chandler-wobble period can further improve their finding.

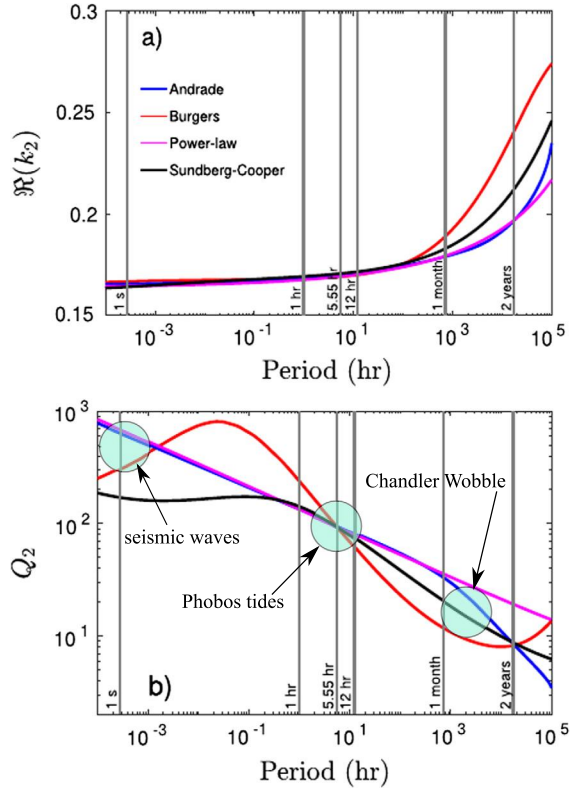

Figure 13 The potential Love number and quality factor of Mars as a function of period, for four rheological models: Andrade, Burgers, power-law, and Sundberg–Cooper. Green areas indicate the periods at which measurements currently exist. These are the period of tides raised by Phobos (∼5.55 hrs) and the periods of seismic waves (seconds) (Lainey et al., 2021; Lognonné et al., 2020).

Pou et al. (2022) considered modeling the tidal response of Mars with the aim of linking between the tidal and seismic attenuation using different viscoelastic models. Due to the proximity of Phobos to Mars, they take into account higher degrees of tidal response, up to and including degree 5 tides. They constrain the core radius as 1805±75 km and the average shear attenuation of the mantle in the range of 100 and 4000. The large uncertainty implies that the current available tidal observations are not precise enough to constrain the attenuation properties of the Martian mantle.

In the recent studies based on analyzing the seismic data from Marsquakes detected by InSight's Very Broad Band Seismic Experiment for Interior Structure (SEIS), the radius of the Martian core was pre-

cisely constrained (Stähler et al., 2021). The results show a liquid core of a 1830±40 km radius and the core density of 5700–6300 kg/m^3. These findings were refined with further analysis of the seismic data; Durán et al. (2022) used the analysis of the direct, reflected, and converted seismic waves to obtain the radius of the core as 1820–1870 km and its mean density (6000–6200 kg/m^3). Moreover, Khan et al. (2022) used a joint geophysical and cosmochemical approach to constrain the radius and density of the core as 1840±10 km and 6150±46 kg/m^3, respectively. These findings from precise seismic analysis compare very well with the conclusions based on the tides. This agreement illustrates the strength of the geodetic measurements in probing the large-scale planetary interior structure.

Studying tides in the Mars-Phobos-Deimos system does not only provide information about the interior of the planet, but also can be used to infer knowledge on the interior structure and origin of its two companion moons. Both moons are presently tidally locked in 1:1 spin-orbit resonance to Mars and given their small eccentricity and radius, the dissipation in the system is dominated by that within Mars. In a recent study, Bagheri et al. (2021) used the available information on the tidal response of Mars, in combination with a laboratory-based viscoelastic model and an advanced tidal theory, to integrate back in time the current orbital configuration of the Martian moons and obtain information on their origin. Both the tides produced in Mars by its moons and the tides produced in the moons by Mars contribute to these moons' orbital evolution due to higher eccentricity of the moons in the past. The results demonstrated that with a high probability, two moons are remnants of a disintegrated progenitor which was disrupted between 1–2.7 Gyrs ago. Moreover, based on the constraints obtained from the tidal evolution of the moons, they concluded that Phobos and Deimos are highly dissipative bodies and have a highly fractured and porous interior. In an earlier study of tidal evolution of Phobos and Deimos, Yoder (1982) used a simplified tidal model and, assuming that the tidal friction in Phobos is negligible, suggested that Phobos might have a substantial internal strength. Samuel et al. (2019) used the same assumption, i.e., a monolithic Phobos, to jointly study the orbital evolution of Phobos, along with thermal evolution of Mars. However, the assumption of a monolithic Phobos is not compatible with the constraints obtained by modeling the impact that have created the large Stickney crater on Phobos (Asphaug et al., 1998).

A question about Phobos and Deimos is their different tidal quality function (k_2/Q_2) obtained from studying their orbital evolution ($\sim 10^{-4}$ for

Deimos and $\sim 10^{-6}$ for Phobos). All such studies which consider an orbital evolution time of the moons longer than ~1 Gyrs remain to justify the large difference between the tidal quality function (k_2/Q_2) of the moons, as a measure of the interior structure. This difference results from the difference in the moons' present-day eccentricities, which is as large as two orders of magnitude, and considering the fact that tidal dissipation is responsible to have dampened the eccentricity jumps associate with their crossing several resonance periods in their history (Yoder, 1982; Bagheri et al., 2021). The puzzling origin of Phobos and Deimos is a long-standing problem and more details are out of the scope of this chapter. A complete review of the scenarios on the origin of the moons is provided by Rosenblatt (2011).

Although the two moons are tidally locked to Mars, their small orbital eccentricity can cause tides raised on them by Mars. Depending on the moons interior properties, such tides may be significant (e.g., Hurford et al., 2016; Le Maistre et al., 2013). Recently, Dmitrovskii et al. (2021) modeled the tidal deformations of Phobos to assess several possible interior structure models for the moon (see Fig. 14). They concluded that the currently available measurements are compatible with several models of the interior, including a rubble pile or monolithic body composed of rock or ice-rock mixtures (Campagnola et al., 2018; Usui et al., 2020). Similar conclusions were drawn by Rambaux et al. (2012); Le Maistre et al. (2013) and Le Maistre et al. (2019) based on libration measurements. These models will be examined with the upcoming Japanese Martian Moons eXploration (MMX) mission and along with the samples returned from the moons, will be able to further constrain the origin and interior properties of Phobos and Deimos.

5.5 Moons of giant planets

The tidal response of the moons of the giant planets became a topic of great interest after it was recognized that tidal dissipation in these moons' interiors can be a significant source of heat (Cassen et al., 1979) (Figs. 15 and 17). Like for other bodies addressed in Section 5, tidal forcing also plays a role in the evolution of the moon dynamical properties (spin, orbit), and tidal stress can drive tectonic activity on some of the moons. The most famous examples are Enceladus' Tiger stripes and associated jet activity whose temporal variability is correlated with tidal forcing (Hedman et al., 2013; Rovira-Navarro et al., 2022). Europa is another example, whose regional-scale ridges and cycloidal ridges have been produced from

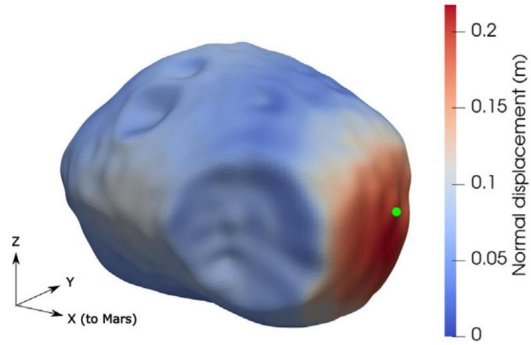

Figure 14 Normal component of tidal deformations on the surface of the Martian moon, Phobos for an example interior structure from Dmitrovskii et al. (2021). The colored dot indicates the location of the sub-Mars point. As shown in this figure, the tidal displacements on the surface of such a body can vary considerably due to the irregularities in the shape. This necessitates using an appropriate 3D approach for such bodies.

continuous forcing driving fatigue and eventual fracturing of surface material (Rhoden et al., 2021). In this section, we review the knowledge on the largest moons of giant planets with particular attention to the tidal dissipation as a heat source for different phenomenon within the interior of the moons. In Section 5.6, we will concentrate on the surface geological features as a result of tidal activity.

Io is the most volcanically active object in the Solar system (Fig. 16). Its tidal heating power is estimated between 65 and 125 TW (Lainey et al., 2009). Io's potential for significant tidal heating was suspected (Peale et al., 1979) even before Voyager 1 flew through the Jovian system. Despite several observations by missions and a sustained ground-based observation program, we still lack a full understanding of the mechanisms driving tidal heating in Io, and especially what this activity tells us about Io's deep interior. Galileo magnetic field observations hint that the moon could contain a deep magma layer, although its origin is debated (see Van Hoolst et al. (2020) for discussion). Using measurements of volcanic activity as a proxy for surface heat flow, based on spacecraft datasets covering several decades, Rathbun et al. (2018) found lower activity in the equatorial region at the anti-Jovian and sub-Jovian points. They also identified peak heat flow at midlatitudes and a fourfold symmetry of upwellings distribution in longitude. The distribution of high dissipation regions inside Io is very dependent on the localization of the dissipation: in the asthenosphere or the underlying mantle (see Fig. 16 for a definition of these terms). Kervazo

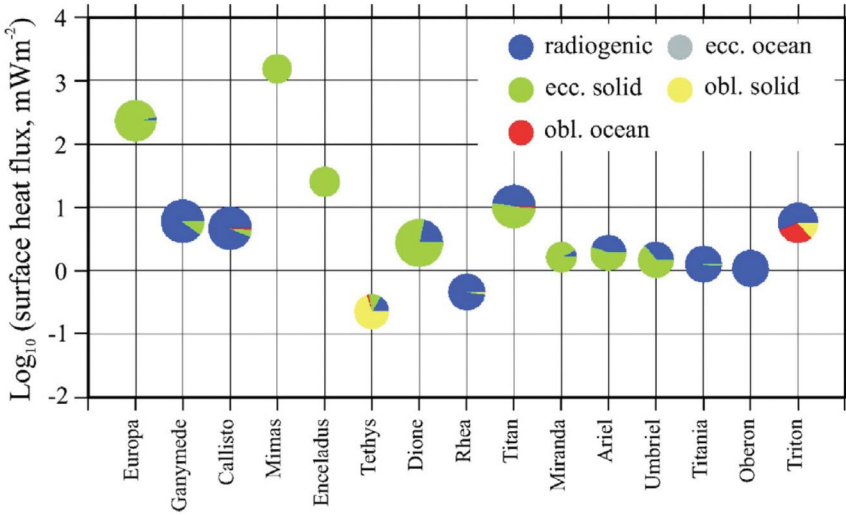

Figure 15 Thermal heat budget for outer Solar System satellites, broken down in terms of radiogenic heating, and eccentricity and obliquity tides applied to the ocean and solid layers of the moons. This example assumes $k_2 = 3/2$. From Chen et al. (2014), permission pending.

et al. (2022) demonstrated that the distribution of tidal heating between the mantle and the asthenosphere is very sensitive to the melt fraction in the asthenosphere. If this fraction is low (high), then dissipation may occur preferentially in the mantle (asthenosphere). This behavior is characterized by a drastic difference in the surface expression of tidal heating. Rathbun et al. (2018) suggested that their observations were consistent with the tidal heating model by Tackley et al. (2001) where large-scale convective pattern dominates the distribution of tidal heating, and smaller-scale asthenospheric instabilities spread out the surface heat flux. On the other hand, the presence of a deep magma ocean would shift the distribution of activity peaks by 30 deg. (Tyler et al., 2015) in comparison to the Rathbun et al. observations. Kervazo et al. (2022) predicted that the tidal Love numbers h_2 and especially l_2 are more sensitive than k_2 to the melt distribution and would allow distinguishing between a mantle-dominated and asthenosphere-dominated regimes. This difference is amplified by bulk heat production. Furthermore, Van Hoolst et al. (2020) found that the diurnal libration amplitude of Io is several times larger if Io has a magma ocean compared to a partially molten asthenosphere. These authors predicted that the libration amplitude could be greater than 1 km in the former case.

Upcoming missions, such as JUICE (JUpiter ICy moons Explorer, to be launched in 2023) and potential observations by Juno (two close Io flybys in 2023 and 2024) might be able to shed more light on Io's behavior.

The contribution of tidal heating to promoting global ice melting and then preserving a deep ocean over long-time scales is not well quantified in most bodies. Tidal forcing likely played a major role in the formation of a deep ocean in Enceladus, as the moon's small size and limited production from radioisotope decay would prevent global scale melting. It has been suggested that Saturn's inner moons (within Titan's orbit) formed in Saturn's rings and evolved outward as a result of tidal interactions with the rings and the planet (Charnoz et al., 2011). The moons could form from heterogeneous accretion of porous ice on silicate chards embedded in the rings. Then, they would exit the rings in sequence, with Rhea being the oldest moon and Mimas the youngest. This scenario could explain why the moons' densities do not follow a monotonic increase with distance to the planet, as would be expected if they formed in a circumplanetary disk. If the moons emerged from the ring, then they could have been subject to significant heating in their early history since they formed closer to the planet and their eccentricities were potentially excited by collisions with other emerging moons (Charnoz et al., 2011). However, an end-to-end evolution scenario of these bodies has not been investigated yet.

The feedback between tidal dissipation and orbital evolution can lead to a cycle of internal melting and freezing with geological expressions such as partial resurfacing (see for example Hussmann and Spohn (2004) for Europa and Section 5.6 for more details on surface features). Resonance crossing, when the orbital periods of two bodies become near-commensurate as a result of orbital migration, can trigger significant heating. For example, Uranus's moons Miranda and Ariel have recorded in their geology evidence of high heat flow, tens of mW/m^2 vs. < 0.01 mW/m^2 for their current eccentricities (e.g., Beddingfield et al. (2015), Beddingfield and Cartwright (2021)). This high heat flow has been attributed to the crossing of resonances: a possible 5:3 resonance between Ariel and Umbriel and a 3:1 resonance between Miranda and Ariel. In resonances, the eccentricities (and sometimes the inclinations) of moons are excited.

It was recently suggested that tidal forcing could also drive oceanic current (Rossby–Haurwitz waves) with potentially important implications (Tyler, 2014). Whether or not this mechanism could represent a long-term heat source in some of the moons is uncertain at this time. Chen et al. (2014) found that obliquity-driven tides in moon oceans could yield power

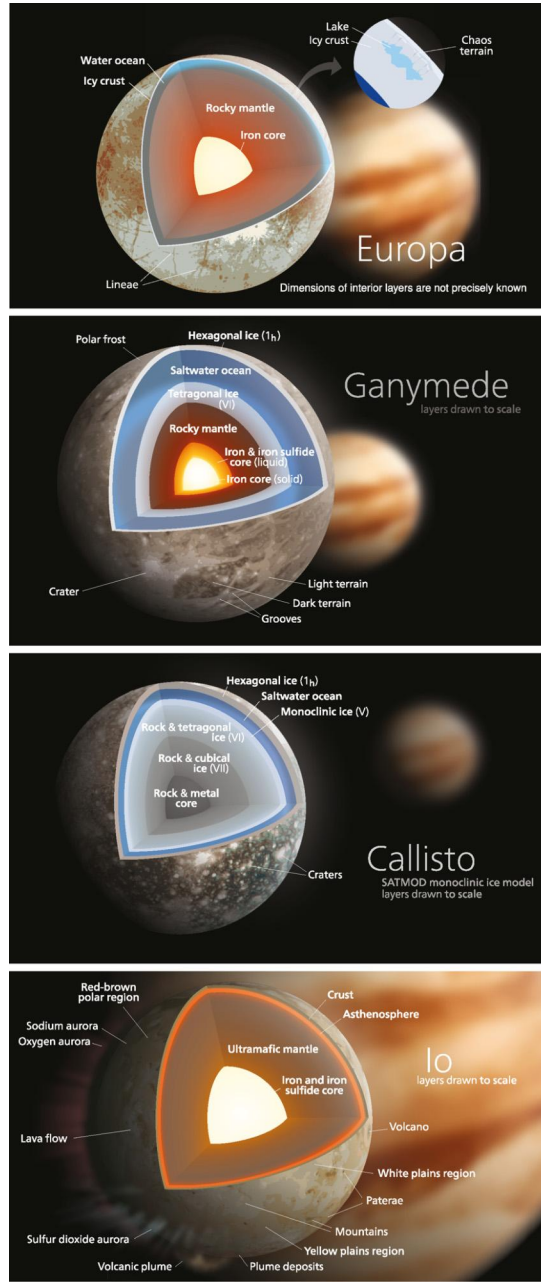

Figure 16 Cross-sections of the Galilean moons' interior structure based on the gravity data from Galileo mission. Various phases of ice and ice-silicate mixtures and metallic parts are present within the moons. This necessitates appropriate interior modeling of these objects.

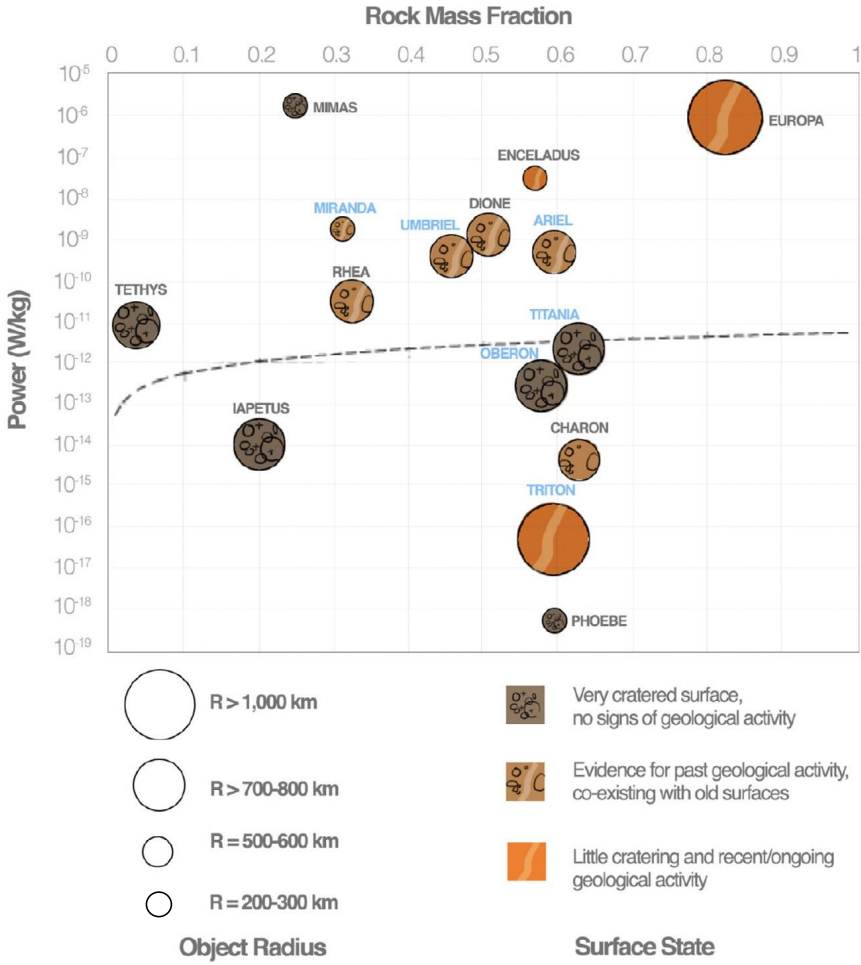

Figure 17 Icy satellite rock mass fractions and first-order tidal heating power (assuming $k_2/Q = 1$) with schematic representation of observed surface geology, which can reflect the potential for endogenic activity and the (past or current) presence of a subsurface ocean. The dashed line indicates current-day heating due to natural decay of radioisotopes in the rock. Based on Castillo-Rogez and Lunine (2012), with updated information on Charon from New Horizons data.

of the same order as radioactive decay heat (Fig. 15). In the case of Neptune's moon Triton, obliquity-driven tides might be the key to the moon's geologically young surface and ongoing activity (e.g., Nimmo and Spencer (2015); Hansen et al. (2021)). Indeed, obliquity-driven tides in the ocean could generate up to 300 GW (Nimmo and Spencer, 2015), which is about

five times greater than the power produced from radioisotope decay heat and six orders of magnitude greater than power generated from eccentricity tides. Recent work by Matsuyama et al. (2018) focusing on the coupling of the ocean to the ice shell showed that the outer ice shell tends to damp ocean tides and decrease their contribution to tidal heating. These authors highlighted that the obliquity phase lag is sensitive to ocean thickness and is large (18 deg. for a reference ocean thickness of 100 km below a 10-km thick shell) and may be measured by a future mission (e.g., Europa Clipper). Furthermore, Hay et al. (2022) computed that at high frequencies, tidal deformation driven by interactions among moons could be amplified by ocean dynamics. However, the amplitude of this high frequency tidal response is too small to be detectable via spacecraft.

In their work on the endogenic activity near the Enceladean south pole, Howett et al. (2011) proposed that the outgoing energy flow associated with the tiger stripes geysers is of the order of 16 GW. Many explanations have been suggested for this high power, most of which have been summarized by Nimmo et al. (2018). In a rough calculation, Efroimsky (2018b) modeled Enceladus with a homogeneous sphere composed of a Maxwell material, and calculated the amount of tidal power dissipated in it, with an input from forced libration in longitude taken into account. The so-obtained formula established a direct link between the power and the mean viscosity of Enceladus. The subsequent insertion of the measured value of heat outflow resulted in the value of the mean viscosity, which exactly coincided with the viscosity of ice near melting point. This simple estimate demonstrated that tides are sufficient to explain Enceladus's high heat power.

Among the recent developments in our understanding of the tidal dissipation in icy moons are more elaborate models, e.g., one permitting for water circulation in porous cores (fractured but solid, or rubble piles) (Choblet et al., 2017). Likely active in midsized moons (<1000 km radius, Neveu and Rhoden (2019)), this mechanism may be contributing to Enceladus's heat production, along with the significant dissipation in the ice shell and, potentially, in the ocean. Further insights in the surface geological activity of Enceladus will be provided in Section 5.6.

As mentioned earlier, the implications of tidal interactions between a moon and planet depend on the k_2/Q of the planet. For a long time, these parameters were almost unkown for any of the moons of giant planets as well as for the host planet itself. Indeed, tidal friction within Saturn causes its moons to migrate outwards, and tidal evolution determines their cur-

rent position. Based on astrometric observations obtained with the Cassini spacecraft, Lainey et al. (2017) showed that dissipation in Saturn is at least one order of magnitude larger ($k_2/Q = (1.59 \pm 0.74) \times 10^{-4}$) than assumed in past theoretical studies. These authors also identified that Saturn's tidal response might be frequency dependent by comparison between the tidal evolution of the midsized moons.

Disentangling the relationships between internal evolution and dynamical evolution offers prospects to explain the origin of the Saturnian moons (and maybe the Uranian moons when more observation becomes available). If the moons formed in Saturn's rings then, the evolution to their current locations can set constraints on Saturn's k_2/Q. On the other hand, if the moons formed near their current locations, then Saturn's Q needs to be high (about 80,000, Ćuk et al. (2016a)), which does not appear consistent with Enceladus's high dissipation. Additional observations with Cassini lead Lainey et al. (2020) to demonstrate that Titan is migrating away from Saturn faster than previously envisioned, leading to an estimate of Saturn's Q of about 100. These authors also inferred that Titan could have formed much closer to Saturn than its current location. Fuller et al. (2016) introduced the resonance locking theory between moons and internal oscillation modes of the planet as a way to address a number of observations in the Saturnian and Galilean systems. Resonance locking opposes the constant Q assumption used for decades. Fuller et al. (2016) inferred that this effect is the dominant driver of tidal dissipation in these systems and suggested that the resonance locking theory allows the large heating rate of Enceladus to be achieved in an equilibrium eccentricity configuration. Nimmo et al. (2018) pointed out that the astrometric observations at the basis of the resonance locking scenarios and follow on studies carry large uncertainties and only a narrow set of Saturn's k_2/Q allows the onset of resonances. These authors further noted that the impact of resonances on the internal evolution of satellites, especially under increase dissipation peak when they cross mean motion resonances is not accounted for. Tidal dissipation within the moons could counteract Saturn's influence by decreasing eccentricity and semimajor axis.

The thermal and orbital evolution of icy moons are coupled via the thermomechanical properties of their materials (see Section 3.2). There is evidence that Saturn's midsized moons have been very dissipative in their past, expressed in the geology (e.g., flexure relaxation, crater morphologies). This has been ascribed to resonance crossing (e.g., Chen and Nimmo (2008) for Tethys). Convective regions (e.g., convective plumes) can also be

areas of enhanced tidal heating. Sotin et al. (2002) suggested that tidal forcing can drive the formation of diapirs that may be involved in the formation of lenticulae and chaos regions at the surface of Europa. Tobie et al. (2003) further explored this idea and predict a heat flow of 35 to 40 mW/m^{-2} constant across Europa's surface. Further details on the surface geological activity on Europa will be provided in Section 5.6. In the case of Titan, Tobie et al. (2005a) found that a few percent of ammonia in the ocean is needed to limit the dissipation in the shell (by decreasing the basal temperature of the shell) and preserve a high eccentricity (0.009), although alternative models have been suggested to explain this high eccentricity (e.g., Ćuk et al. (2016a)) More work is needed to establish an end-to-end model of the evolution of the Saturnian moon system as a whole.

A recent analysis of the tidal evolution of the Uranian moons following their crossing mean motion resonances has led to constraints on their Q/k_2 (Ćuk et al., 2020). It ranges from 10^4 for Oberon (the farthest from Uranus) to 10^6 for Miranda (closest moon), suggesting a wide range of internal properties across the Uranian moons system. Considering the moon's k_2 may range from 10^{-3} to 10^{-2} (Hussmann et al., 2006), we infer dissipation factors in excess of 1000 in Miranda, and potentially also Oberon, suggesting that the moons are not dissipative at present and may be near frozen. Interestingly, the Uranian moon system is not in resonances at present.

Actual constraints on the tidal parameters of icy moons are few. Multiple flybys of Saturn's moon Titan by the Cassini orbiter led to the inference of $k_2 = 0.637 \pm 0.0220$ (Iess et al., 2014). This high value has been interpreted as evidence for a high density of the ocean, of the order of 1200 kg/m^3 (e.g., Mitri et al. (2014); Baland et al. (2014)). This high density points to a high content in salt (Baland et al., 2014) that cannot be uniquely explained by cosmochemical abundances but also involves a contribution of nonwater ice volatiles (e.g., CO_2, NH_3) to oceanic solutes (e.g., bi/carbonate and ammonium ions). This high density may also reflect a large abundance of clathrate hydrate, such as CO_2 hydrates, whose density is about 1100 kg/m^3 (Boström et al., 2021).

Despite the critical contribution of tidal stressing to the heat budgets of large icy moons, models miss input parameters that have been obtained in conditions relevant to these objects. By lack of knowledge on the internal properties of small moons (<1000 km radius), many studies assume a dissipation factor $Q = 100$ for these bodies, as well as a tidal Love number based on a homogeneous interior. However, as shown above, dissipation is a function of the material frequency-dependent mechanical response, which

itself depends on temperature and the history of the material. Dissipation in porous interiors (e.g., near Earth asteroids), mixtures of water ice, salts, and clathrates, that may be relevant to Europa or Titan, for example, are scarce. Tidal stresses at icy moons have a wide range of amplitudes that invoke different response mechanisms. Reproducing low stress and long forcing periods in laboratory is challenging and most cyclic forcing measurements have been obtained at frequencies greater than 10^{-4} Hz. Future experimental work should aim to retire some of these knowledge gaps that prevent more high-fidelity modeling of the moon internal evolution.

The Europa Clipper mission's gravity measurement is projected to yield Europa's tidal Love number k_2 with an accuracy of 0.015 (1-σ) (Mazarico et al., 2021). The combination of ground penetrating radar and imaging will yield h_2 (Steinbrügge et al., 2021) but the predicted accuracy is still a work in progress. The JUICE mission is also planning to obtain these parameters at Ganymede, in particular k_2 with an accuracy of 10^{-4} (e.g., Cappuccio et al., 2020).

5.6 Tidal signature on planetary surfaces

This chapter mainly addresses deciphering the interior structure based on measurements of tidal response presented in the form of Love numbers as well as the reciprocal effect of tidal heating and interior properties in the planetary bodies. However, it is important to mention how surface geological features as a result of tidal activities can also be used to constrain both the present-day interior and thermal-orbital evolution of the planetary bodies through their relationship to tidal stress and tidal evolution.

Hence, we dedicate this section to overview the effect of surface features as a result of tidal activities and their interpretations for the interior in different planetary bodies, particularly the icy moons. While, a more detailed review of the tidal signatures on the surface of the planets would need a dedicated study, here we only provide a summary of the most important findings on the interior as a result of studying the surface of the icy moons.

The extent to which the surface of a moon will be affected by tidal stress not only depends on the orbital elements such as eccentricity, obliquity, and the proximity to the parent planet, but also to the responsiveness of the interior of the body to tidal deformation, which in turn is strongly affected by the presence or absence of an ocean, the rheology of the interior, and the amount of internal heat being generated within the moon (e.g., Greenberg et al., 1998; Jara-Orué and Vermeersen, 2011; Rhoden and Walker, 2022). Thus, geologic features on the planetary objects can

provide insight as to their interior structures and thermal states. For example, the presence, absence, and style of tectonic activity can be diagnostic of a moon's thermal history (e.g., Rhoden et al., 2020). Similarly, the presence of eruptions, whether in the form of surface flows or geysers, can provide insight into the cooling history of a moon and the composition of its ocean (e.g., Rudolph et al., 2022). Lastly, indicators of past heat flows, through changes to crater morphology, can constrain the overall thermal history of a moon (e.g., Bland et al., 2012).

Although still an area of active study, some consistent links have been identified between certain geologic features and the inferred thermal-orbital history or interior structure of a moon. We begin with tectonics. The two icy satellites with extensive canyon systems, Tethys at Saturn and Charon at Pluto, both have negligible present-day orbital eccentricities, with reason to expect that they underwent rapid despinning and circularization (Peale, 1999; Neveu and Rhoden, 2019; Cheng et al., 2014). Neither moon is expected to have an ocean today due to a lack of potential heat sources, although observational constraints on Tethys's interior are quite limited (Castillo-Rogez et al., 2018). Tethys and Charon both have globally-distributed, but overall sparse, fracture systems that appear unrelated to either the canyons or tidal stress patterns (Castillo-Rogez et al., 2018; Rhoden et al., 2020). Their origin is currently unknown.

As described in Rhoden et al. (2020), the best explanation of the formation of the canyons on Tethys and Charon is that both moons began with high eccentricity orbits that generated oceans through tidal dissipation. As a result, the orbits circularized, and the lack of tidal heating led the oceans to freeze out. As oceans freeze, the thermal stresses and the increase in volume of the newly accreted ice at the base of the shell can create radial fractures within an ice shell (Rudolph and Manga, 2009; Rudolph et al., 2022). Hence, the cooling and freezing of the interior may have produced the initial fractures that developed into canyons through continued thickening of the ice shell. The lack of fractures associated with tidal stress patterns comes from the fact that circularization occurred before the ocean froze, so there were no tidal stresses available Rhoden et al. (2020). Thus, we can hypothesize that canyon systems are indicative of a past ocean that has completely frozen out.

One important difference between Charon and Tethys is that only Charon shows evidence of cryovolcanism. A potential explanation for this difference is that fractures formed through ocean freezing were able to crack through the entire ice shell at Charon but not at Tethys, perhaps because

the Tethys's interior did not warm up as much as Charon's, and the ice shell was correspondingly thicker. Given that Tethys is approximately 94% ice (Castillo-Rogez et al., 2018), it may have had too little rocky material to provide sufficient radiogenic heating to reach a similar level of melting as Charon, or it may have begun with a lower eccentricity that resulted in less tidal heating. The presence of ammonia within Charon's interior, as explored by Bagheri et al. (2022) could also facilitate eruptions and would likely be absent or less abundant within Tethys. In any case, comparing the geology of these two moons provides insight into differences in the thermal evolution of their interiors.

On the opposite end of the tectonic spectrum are the moons with oceans thicker than their overlying ice shells. Europa at Jupiter and Enceladus at Saturn (e.g., Nimmo and Pappalardo, 2016) are the two "confirmed" ocean worlds of this type. Both of these moons execute eccentric orbits while orbiting close to their parent planet; their subsurface oceans and warm ice shells allow for significant tidal deformation and stress in the overlying cold ice. Europa's surface is pervasively, and globally, fractured, and the fractures vary in their surface expression from linear to wavy to cycloidal (e.g., Kattenhorn and Hurford, 2009) (see Fig. 16). The shapes of cycloids, linked arcs that can span 100s of km, track the spatial and temporal changes in tidal stress throughout Europa's orbit (Greenberg et al., 1998; Hoppa et al., 2001; Rhoden et al., 2010, 2021). Fits to both individual cycloid shapes and the overall distribution of cycloids greatly improved when the effects of a small obliquity were added to the tidal stress model, illustrating the powerful link between the orbit, interior, and surface geology. Europa also displays strike-slip offsets along many fractures, long parallel bands formed from extension, and irregularly-shaped bands formed from compression/subsumption (see reviews by Kattenhorn and Hurford (2009); Prockter and Patterson (2009)). Many strike-slip offsets have been linked to tides (e.g., Rhoden et al., 2012), whereas band formation appears to result from large-scale plate motion (e.g., Kattenhorn and Prockter, 2014), which may be governed by different processes.

Enceladus displays tectonic features that are morphologically-similar to those at Europa, but Enceladus's tectonism is regional, with activity concentrated near the south pole (Spencer et al., 2006; Patthoff and Kattenhorn, 2011; Crow-Willard and Pappalardo, 2015). Also, Enceladus lacks cycloids, strike-slip offsets along fractures, and bands of any kind. The four, roughly parallel fractures within the south polar terrain (dubbed "Tiger Stripes") have orientations consistent with eccentricity-driven tidal stresses (Rho-

den et al., 2020), and the geyser-like eruptions emanating from the Tiger Stripes vary in output on a diurnal timescale, suggesting a link to tides (Nimmo et al., 2007; Hurford et al., 2007; Hedman et al., 2013). The ice shell thickness on Enceladus appears to vary considerably with location (e.g., Thomas et al., 2016; Beuthe et al., 2016; Čadek et al., 2019); the shell is thinnest at the south pole and thickest along the equator. In a heterogeneous ice shell, tidal stresses are enhanced at thin zones (Beuthe, 2019). Thus, the extent of tectonic activity may well be an indicator of ice shell thickness, with older tectonized regions representing past thin zones. This interpretation would suggest that, as at Europa, multiple generations of crisscrossing, ridge-flanked fractures are indicative of relatively thin ice shells and concentrated tidal stress.

Between these two extremes, there are a variety of heavily cratered moons with varying levels of tectonic activity, including Ganymede at Jupiter and Dione at Saturn. Both moons are thought to have thin oceans beneath much thicker ice shells, and they both orbit far enough from their parent planet to have reduced tidal heating and stress, which may be the reason for their limited geologic activity. Callisto at Jupiter and Rhea at Saturn orbit even farther away and both are heavily cratered with little other geologic activity. There is some evidence to suggest a deep, thin ocean within Callisto (Khurana et al., 1998), so it is possible that even heavily cratered worlds can have oceans; much less is known about the interior structure of Rhea (Tortora et al., 2016). Taken together, it seems that there is a correlation between ocean thickness, relative to total hydrosphere thickness, and the extent of tectonic activity.

One curious outlier is Saturn's smallest and innermost regular satellite, Mimas. With a higher eccentricity than its exterior neighbor, Enceladus, we might expect Mimas to be even more geologically active, akin to Io at Jupiter. However, Mimas is heavily cratered with few tectonic features and no evidence of volcanic activity. And yet, model fits to Cassini measurements of Mimas's physical librations indicate that Mimas is likely an ocean-bearing world and require that Mimas is differentiated into a rocky interior and outer hydrosphere (Tajeddine et al., 2014; Noyelles, 2017; Caudal, 2017). If Mimas does, indeed, have a subsurface ocean today, it may be a young ocean world, such that its surface has not had time to develop the characteristics features observed on moons such as Europa and Enceladus (see also Rhoden and Walker (2022)). In addition to tectonic and volcanic activity, craters can be quite diagnostic of the interior structure and heating history of a moon. Most obviously, the morphology of the initial

impact can be used to constrain the thickness of the outmost layer of the moon. For example, some craters have clearly cracked through Europa's entire ice shell to the ocean beneath (see Schenk and Turtle (2021), for an overview), whereas several of the midsized moons of Saturn have large (100s of km) impact basins that show no evidence of a subsurface ocean. However, tidal dissipation within an icy satellite can also have a more subtle, but still diagnostic, effect on craters.

As heat is transferred from the interior of a moon to the surface, it can modify the shapes of existing craters, creating flatter floors and overall subdued morphologies. The process, called crater relaxation, records the magnitude and longevity of heat flow through the ice shell. Crater relaxation on Enceladus, Tethys, Dione, and Rhea all indicate past episodes of higher heat flows (Bland et al., 2012; White et al., 2013, 2017). Even Enceladus, which has high present-day heat flows, would require a past epoch of considerably more dissipation to explain the observed crater shapes (Bland et al., 2012). For the other moons, to achieve the observed levels of relaxation would imply temperatures above the melting temperature of water ice, suggesting oceans within their surface ages. In contrast, Mimas's craters show no evidence of relaxation to within the observation limit imposed by image coverage. In that case, crater shapes provide an upper limit on the extent of tidal dissipation that could have taken place within Mimas. In all of these cases, it is the link between interiors, tidal dissipation, and surface geology that allows these features to provide additional insight as to the thermal-orbital evolution of the moons and their past and present interior structures.

6. Summary and conclusions

In this chapter, we have attempted to provide an overview of the past, present, and future use of tides as a means of procuring information on the interior structure of planets and moons from orbiting and landed spacecraft. Since tidal response measurements play an inordinate role in understanding the interiors of rocky and icy planetary bodies, we provided a detailed outline of the fundamental concepts connected to modeling the tidal response, including the viscoelastic behavior of planetary materials, and how the tides couple to the thermal structure within the planetary body to determine its subsequent orbital evolution. We also provided an overview of tidally generated surface geological features on icy moons, and

discussed interpretations of these features for these moons' interior structure and evolution.

Tides are also playing a key role in modeling and understanding of the evolution of extra-Solar planetary bodies and of these bodies' astrobiological potential. Related to this are the recent refunements of the tidal theory, like (Makarov and Efroimsky, 2013), as well as the extension of the tidal evolution formulae to allow for employment higher-order eccentricity functions needed to describe spin-orbit resonances, nonsynchronous rotation, and mean motion resonances (Renaud et al., 2021; Bagheri et al., 2021). For exoplanets trapped in a higher-order spin-orbit resonance for an extended amount of time, for example, important climate variations could ensue as a result of a new Solar configuration (Del Genio et al., 2019) and thus the potential for life to develop.

We provided an overview of the current state of investigation of the rocky bodies of our Solar system, including Mercury, Venus, the Moon, and Mars, and the icy moons of the giant planets from the point of view of tides that will invariably remain, relative to the more involved deployment of surface instrumentation, the most prominent means of inferring knowledge on the interior of the planets and satellites. The ongoing development of more refined tidal models, in combination with further experimental studies of the viscoelastic properties of planetary materials, and advances in geophysical models through continued analysis of geodetic and other large-scale measurements (e.g., InSight and LLR), promise new insights into the inner structure of terrestrial planets and moons of the Solar system.

Acknowledgments

We acknowledge informative discussions with Ian Jackson and Ulrich Faul on material viscoelasticity, and with Valeri Makarov on tides. A.B. was supported by a grant from the Swiss National Science Foundation (project 172508). J.C.'s contribution was developed at the Jet Propulsion Laboratory, California Institute of Technology, under contract with the National Aeronautics and Space Administration. M.W. and A.C.P. gratefully acknowledge the financial support and endorsement from the DLR Management Board Young Research Group Leader Program and the Executive Board Member for Space Research and Technology. The artistic views of the Moon and the Saturnian moons are taken or modified from https://commons.wikimedia.org/wiki/User:Kelvin13.

References

Al-Attar, D., Tromp, J., 2013. Sensitivity kernels for viscoelastic loading based on adjoint methods. Geophysical Journal International 196 (1), 34–77.

Alterman, Z., Jarosch, H., Pekeris, C.L., 1959. Oscillations of the Earth. Proceedings of the Royal Society of London Series A 252 (1268), 80–95. https://doi.org/10.1098/rspa.1959.0138.

Anderson, D.L., O'Connell, R., 1967. Viscosity of the Earth. Geophysical Journal International 14 (1–4), 287–295.

Anderson, F.S., Smrekar, S.E., 2006. Global mapping of crustal and lithospheric thickness on Venus. Journal of Geophysical Research: Planets 111 (E8).

Anderson, J.D., Colombo, G., Esposito, P.B., Lau, E.L., Trager, G.B., 1987. The mass, gravity field, and ephemeris of Mercury. Icarus 71, 337–349. https://doi.org/10.1016/0019-1035(87)90033-9.

Andrade, E.N.D.C., 1910. On the viscous flow in metals, and allied phenomena. Proceedings of the Royal Society of London. Series A, Containing Papers of a Mathematical and Physical Character 84 (567), 1–12.

Arakawa, S., Hyodo, R., Shoji, D., Genda, H., 2021. Tidal evolution of the eccentric moon around dwarf planet (225088) Gonggong. The Astronomical Journal 162 (6), 226.

Armann, M., Tackley, P.J., 2012. Simulating the thermochemical magmatic and tectonic evolution of Venus's mantle and lithosphere: Two-dimensional models. Journal of Geophysical Research: Planets 117 (E12), E12003. https://doi.org/10.1029/2012JE004231.

Asphaug, E., Ostro, S.J., Hudson, R., Scheeres, D.J., Benz, W., 1998. Disruption of kilometre-sized asteroids by energetic collisions. Nature 393 (6684), 437.

Auclair-Desrotour, P., Laskar, J., Mathis, S., 2017. Atmospheric tides in Earth-like planets. Astronomy and Astrophysics 603, A107. https://doi.org/10.1051/0004-6361/201628252.

Bagdassarov, N.S., Dingwell, D.B., 1993. Frequency dependent rheology of vesicular rhyolite. Journal of Geophysical Research: Solid Earth 98 (B4), 6477–6487. https://doi.org/10.1029/92JB02690.

Bagheri, A., Greenhalgh, S., Khojasteh, A., Rahimian, M., 2015. Dispersion of Rayleigh, Scholte, Stoneley and Love waves in a model consisting of a liquid layer overlying a two-layer transversely isotropic solid medium. Geophysical Journal International 203 (1), 195–212.

Bagheri, A., Khan, A., Al-Attar, D., Crawford, O., Giardini, D., 2019. Tidal response of Mars constrained from laboratory-based viscoelastic dissipation models and geophysical data. Journal of Geophysical Research: Planets 124, 2703–2727. https://doi.org/10.1029/2019JE006015.

Bagheri, A., Khan, A., Efroimsky, M., Kruglyakov, M., Giardini, D., 2021. Dynamical evidence for Phobos and Deimos as remnants of a disrupted common progenitor. Nature Astronomy 5 (6), 539–543. https://doi.org/10.1038/s41550-021-01306-2.

Bagheri, A., Khan, A., Deschamps, F., Samuel, H., Kruglyakov, M., Giardini, D., 2022. The tidal–thermal evolution of the Pluto–Charon system. Icarus 376, 114871.

Baland, R.-M., Tobie, G., Lefèvre, A., Van Hoolst, T., 2014. Titan's internal structure inferred from its gravity field, shape, and rotation state. Icarus 237, 29–41.

Banerdt, W.B., Smrekar, S.E., Banfield, D., Giardini, D., Golombek, M., Johnson, C.L., Lognonné, P., Spiga, A., Spohn, T., Perrin, C., et al., 2020. Initial results from the InSight mission on Mars. Nature Geoscience 13 (3), 183–189. https://doi.org/10.1038/s41561-020-0544-y.

Basaltic Volcanism Study Project, 1981. Basaltic Volcanism on the Terrestrial Planets. Pergamon Press, New York.

Beddingfield, C., Burr, D., Emery, J., 2015. Fault geometries on Uranus' satellite Miranda: Implications for internal structure and heat flow. Icarus 247, 35–52.

Beddingfield, C.B., Cartwright, R.J., 2021. A lobate feature adjacent to a double ridge on Ariel: Formed by cryovolcanism or mass wasting? Icarus 367, 114583.

Benjamin, D., Wahr, J., Ray, R.D., Egbert, G.D., Desai, S.D., 2006. Constraints on mantle anelasticity from geodetic observations, and implications for the J_2 anomaly. Geophysical Journal International 165, 3–16. https://doi.org/10.1111/j.1365-246X.2006.02915.x.

Benkhoff, J., van Casteren, J., Hayakawa, H., Fujimoto, M., Laakso, H., Novara, M., Ferri, P., Middleton, H.R., Ziethe, R., 2010. BepiColombo - Comprehensive exploration of Mercury: Mission overview and science goals. Planetary and Space Science 58, 2–20. https://doi.org/10.1016/j.pss.2009.09.020.

Bertone, S., Mazarico, E., Barker, M.K., Goossens, S., Sabaka, T.J., Neumann, G.A., Smith, D.E., 2021. Deriving Mercury geodetic parameters with altimetric crossovers from the Mercury Laser Altimeter (MLA). Journal of Geophysical Research: Planets 126 (4), e06683. https://doi.org/10.1029/2020JE006683.

Beuthe, M., 2013. Spatial patterns of tidal heating. Icarus 223 (1), 308–329. https://doi.org/10.1016/j.Icarus.2012.11.020.

Beuthe, M., 2019. Enceladus's crust as a non-uniform thin shell: II tidal dissipation. Icarus 332, 66–91.

Beuthe, M., Rivoldini, A., Trinh, A., 2016. Enceladus's and Dione's floating ice shells supported by minimum stress isostasy. Geophysical Research Letters 43 (19), 10–088.

Bierson, C.J., Nimmo, F., Stern, S.A., 2020. Evidence for a hot start and early ocean formation on Pluto. Nature Geoscience 13 (7), 468–472.

Bills, B.G., Neumann, G.A., Smith, D.E., Zuber, M.T., 2005. Improved estimate of tidal dissipation within Mars from MOLA observations of the shadow of Phobos. Journal of Geophysical Research: Planets 110, E07004. https://doi.org/10.1029/2004JE002376.

Biot, M.A., 1954. Theory of stress-strain relations in anisotropic viscoelasticity and relaxation phenomena. Journal of Applied Physics 25 (11), 1385–1391.

Bland, M.T., Singer, K.N., McKinnon, W.B., Schenk, P.M., 2012. Enceladus' extreme heat flux as revealed by its relaxed craters. Geophysical Research Letters 39 (17).

Bolmont, E., Breton, S.N., Tobie, G., Dumoulin, C., Mathis, S., Grasset, O., 2020. Solid tidal friction in multi-layer planets: Application to Earth, Venus, a Super Earth and the TRAPPIST-1 planets. Potential approximation of a multi-layer planet as a homogeneous body. Astronomy and Astrophysics 644, A165. https://doi.org/10.1051/0004-6361/202038204.

Borrelli, M.E., O'Rourke, J.G., Smrekar, S.E., Ostberg, C.M., 2021. A global survey of lithospheric flexure at steep-sided domical volcanoes on Venus reveals intermediate elastic thicknesses. Journal of Geophysical Research: Planets 126 (7), e2020JE006756.

Boström, M., Esteso, V., Fiedler, J., Brevik, I., Buhmann, S.Y., Persson, C., Carretero-Palacios, S., Parsons, D.F., Corkery, R.W., 2021. Self-preserving ice layers on CO_2 clathrate particles: Implications for Enceladus, Pluto, and similar ocean worlds. Astronomy & Astrophysics 650, A54.

Boué, G., Efroimsky, M., 2019. Tidal evolution of the Keplerian elements. Celestial Mechanics and Dynamical Astronomy 131 (7), 30.

Briaud, A., Fienga, A., Melini, D., Rambaux, N., Mémin, A., Spada, G., Saliby, C., Hussmann, H., Stark, A., 2022. Constraints on the Moon's deep interior from tidal deformation. In: 53rd Lunar and Planetary Science Conference. 7–11 March, 2022, The Woodlands, Texas. In: LPI Contributions, vol. 2678, p. 1349.

Burgers, J.M., 1935. Mechanical considerations-model systems-phenomenological theories of relaxation and of viscosity. First report on viscosity and plasticity 1.

Běhounková, M., Tobie, G., Čadek, O., Choblet, G., Porco, C., Nimmo, F., 2015. Timing of water plume eruptions on Enceladus explained by interior viscosity structure. Nature Geoscience 8 (8), 601–604. https://doi.org/10.1038/ngeo2475.

Čadek, O., Souček, O., Běhounková, M., Choblet, G., Tobie, G., Hron, J., 2019. Long-term stability of Enceladus' uneven ice shell. Icarus 319, 476–484.

Campagnola, S., Yam, C.H., Tsuda, Y., Ogawa, N., Kawakatsu, Y., 2018. Mission analysis for the Martian Moons Explorer (MMX) mission. Acta Astronautica 146, 409–417.

Canup, R.M., Asphaug, E., 2001. Origin of the Moon in a giant impact near the end of the Earth's formation. Nature 412 (6848), 708–712.

Cappuccio, P., Hickey, A., Durante, D., Di Benedetto, M., Iess, L., De Marchi, F., Plainaki, C., Milillo, A., Mura, A., 2020. Ganymede's gravity, tides and rotational state from JUICE's 3GM experiment simulation. Planetary and Space Science 187, 104902.

Cartier, C., Namur, O., Nittler, L.R., Weider, S.Z., Crapster-Pregont, E., Vorburger, A., Frank, E.A., Charlier, B., 2020. No FeS layer in Mercury? Evidence from Ti/Al measured by MESSENGER. Earth and Planetary Science Letters 534, 116108. https://doi.org/10.1016/j.epsl.2020.116108.

Cascioli, G., Hensley, S., De Marchi, F., Breuer, D., Durante, D., Racioppa, P., Iess, L., Mazarico, E., Smrekar, S.E., 2021. The determination of the rotational state and interior structure of Venus with VERITAS. Planetary Science Journal 2 (6), 220. https://doi.org/10.3847/PSJ/ac26c0.

Cassen, P., Reynolds, R.T., Peale, S., 1979. Is there liquid water on Europa? Geophysical Research Letters 6 (9), 731–734.

Castillo-Rogez, J., Lunine, J., 2012. Small habitable worlds. In: Frontiers of Astrobiology, pp. 201–228.

Castillo-Rogez, J., Hemingway, D., Rhoden, A., Tobie, G., McKinnon, W., 2018. Origin and evolution of Saturn's mid-sized moons. In: Enceladus and the Icy Moons of Saturn, pp. 285–306.

Castillo-Rogez, J.C., Banerdt, W.B., 2012. Impact of anelasticity on Mars' dissipative properties - application to the InSight mission. In: The Mantle of Mars: Insights from Theory, Geophysics, High-Pressure Studies, and Meteorites. In: LPI Contributions, vol. 1684, p. 4.

Castillo-Rogez, J.C., Efroimsky, M., Lainey, V., 2011. The tidal history of Iapetus: Spin dynamics in the light of a refined dissipation model. Journal of Geophysical Research: Planets 116 (E9), E09008. https://doi.org/10.1029/2010JE003664.

Caudal, G., 2017. The damping of forced librations of triaxial satellites with eccentric orbits: Consequences on the dynamics of Mimas. Icarus 286, 280–288.

Cavanaugh, J.F., Smith, J.C., Sun, X., Bartels, A.E., Ramos-Izquierdo, L., Krebs, D.J., McGarry, J.F., Trunzo, R., Novo-Gradac, A.M., Britt, J.L., Karsh, J., Katz, R.B., Lukemire, A.T., Szymkiewicz, R., Berry, D.L., Swinski, J.P., Neumann, G.A., Zuber, M.T., Smith, D.E., 2007. The Mercury laser altimeter instrument for the MESSENGER mission. Space Science Reviews 131 (1–4), 451–479. https://doi.org/10.1007/s11214-007-9273-4.

Cébron, D., Laguerre, R., Noir, J., Schaeffer, N., 2019. Precessing spherical shells: flows, dissipation, dynamo and the lunar core. Geophysical Journal International 219 (Supplement_1), S34–S57.

Chabé, J., Courde, C., Torre, J.-m., Bouquillon, S., Bourgoin, A., Aimar, M., Albanese, D., Chauvineau, B., Mariey, H., Martinot-Lagarde, G., et al., 2020. Recent progress in lunar laser ranging at Grasse laser ranging station. Earth and Space Science 7 (3), e2019EA000785.

Chabot, N.L., Wollack, E.A., Klima, R.L., Minitti, M.E., 2014. Experimental constraints on Mercury's core composition. Earth and Planetary Science Letters 390, 199–208. https://doi.org/10.1016/j.epsl.2014.01.004.

Chapront-Touzé, M., Chapront, J., 1988. ELP 2000-85-A semi-analytical lunar ephemeris adequate for historical times. Astronomy and Astrophysics 190, 342–352.

Chapront-Touzé, M., Chapront, J., 1991. Lunar tables and programs from 4000 B.C. to A.D. 8000.

Charnoz, S., Crida, A., Castillo-Rogez, J.C., Lainey, V., Dones, L., Karatekin, Ö., Tobie, G., Mathis, S., Le Poncin-Lafitte, C., Salmon, J., 2011. Accretion of Saturn's mid-sized moons during the viscous spreading of young massive rings: Solving the paradox of silicate-poor rings versus silicate-rich moons. Icarus 216 (2), 535–550.

Chawla, K.K., Meyers, M., 1999. Mechanical Behavior of Materials. Prentice Hall, Upper Saddle River.

Chen, E., Nimmo, F., 2008. Implications from Ithaca Chasma for the thermal and orbital history of Tethys. Geophysical Research Letters 35 (19).

Chen, E., Nimmo, F., Glatzmaier, G., 2014. Tidal heating in icy satellite oceans. Icarus 229, 11–30.

Cheng, W., Lee, M.H., Peale, S., 2014. Complete tidal evolution of Pluto–Charon. Icarus 233, 242–258.

Choblet, G., Tobie, G., Sotin, C., Běhounková, M., Čadek, O., Postberg, F., Souček, O., 2017. Powering prolonged hydrothermal activity inside Enceladus. Nature Astronomy 1 (12), 841.

Churkin, V., 1998. The Love numbers for the models of inelastic Earth. IPA Preprint 121.

Cooper, R.F., 2002. Seismic wave attenuation: Energy dissipation in viscoelastic crystalline solids. Reviews in Mineralogy and Geochemistry 51 (1), 253–290.

Cormier, V., 1989. Seismic attenuation: Observation and measurement. In: Jeames, D.E. (Ed.), Encyclopedia of Geophysics. Van Nostrand, pp. 1005–1018.

Correia, A.C.M., Laskar, J., de Surgy, O.N., 2003. Long-term evolution of the spin of Venus. I. Theory. Icarus 163 (1), 1–23. https://doi.org/10.1016/S0019-1035(03)00042-3.

Crawford, O., Al-Attar, D., Tromp, J., Mitrovica, J.X., Austermann, J., Lau, H.C., 2018. Quantifying the sensitivity of post-glacial sea level change to laterally varying viscosity. Geophysical Journal International 214 (2), 1324–1363.

Crow-Willard, E.N., Pappalardo, R.T., 2015. Structural mapping of Enceladus and implications for formation of tectonized regions. Journal of Geophysical Research: Planets 120 (5), 928–950.

Ćuk, M., Dones, L., Nesvorný, D., 2016a. Dynamical evidence for a late formation of Saturn's moons. The Astrophysical Journal 820 (2), 97. https://doi.org/10.3847/0004-637X/820/2/97.

Ćuk, M., Hamilton, D.P., Lock, S.J., Stewart, S.T., 2016b. Tidal evolution of the Moon from a high-obliquity, high-angular-momentum Earth. Nature 539 (7629), 402–406.

Ćuk, M., El Moutamid, M., Tiscareno, M.S., 2020. Dynamical history of the Uranian system. The Planetary Science Journal 1 (1), 22.

Darwin, G.H., 1879. On the analytical expressions which give the history of a fluid planet of small viscosity, attended by a single satellite. Proceedings of the Royal Society of London Series I 30, 255–278.

de Kleer, K., McEwen, A., Park, R., Bierson, C.J., Davies, A.G., DellaGustina, D.N., Ermakov, A.I., Fuller, J., Hamilton, C.W., Harris, C.D., et al., 2019a. Tidal Heating: Lessons from Io and the Jovian System-Final Report.

de Kleer, K., Nimmo, F., Kite, E., 2019b. Variability in Io's volcanism on timescales of periodic orbital changes. Geophysical Research Letters 46 (12), 6327–6332.

Dehant, V., 1987. Tidal parameters for an inelastic Earth. Physics of the Earth and Planetary Interiors 49 (1–2), 97–116.

Dehant, V., Oberst, J., Nadalini, R., Schreiber, U., Rambaux, N., 2012. Geodesy instrument package on the Moon for improving our knowledge of the Moon and the realization of reference frames. Planetary and Space Science 68 (1), 94–104.

Del Genio, A.D., Way, M.J., Amundsen, D.S., Aleinov, I., Kelley, M., Kiang, N.Y., Clune, T.L., 2019. Habitable climate scenarios for Proxima Centauri b with a dynamic ocean. Astrobiology 19 (1), 99–125.

Dell'Agnello, S., Delle Monache, G., Currie, D., Vittori, R., Cantone, C., Garattini, M., Boni, A., Martini, M., Lops, C., Intaglietta, N., et al., 2011. Creation of the new industry-standard space test of laser retroreflectors for the GNSS and LAGEOS. Advances in Space Research 47 (5), 822–842.
Dell'Agnello, S., et al., 2015. Advanced laser retroreflectors for astrophysics and space science. Journal of Applied Mathematics and Physics 3 (02), 218.
Dermott, S.F., 1979. Tidal dissipation in the solid cores of the major planets. Icarus 37 (1), 310–321. https://doi.org/10.1016/0019-1035(79)90137-4.
D'Incecco, P., Müller, N., Helbert, J., D'Amore, M., 2017. Idunn Mons on Venus: Location and extent of recently active lava flows. Planetary and Space Science 136, 25–33.
Dmitrovskii, A.A., Khan, A., Boehm, C., Bagheri, A., van Driel, M., 2021. Constraints on the interior structure of Phobos from tidal deformation modelling. Icarus, 114714.
Dobrovolskis, A.R., Ingersoll, A.P., 1980. Atmospheric tides and the rotation of Venus I. Tidal theory and the balance of torques. Icarus 41 (1), 1–17. https://doi.org/10.1016/0019-1035(80)90156-6.
Dreibus, G., Wanke, H., 1987. Volatiles on Earth and Mars - A comparison. Icarus 71, 225–240. https://doi.org/10.1016/0019-1035(87)90148-5.
Dumberry, M., 2011. The free librations of Mercury and the size of its inner core. Geophysical Research Letters 38 (16), L16202. https://doi.org/10.1029/2011GL048277.
Dumoulin, C., Tobie, G., Verhoeven, O., Rosenblatt, P., Rambaux, N., 2017. Tidal constraints on the interior of Venus. Journal of Geophysical Research: Planets 122 (6), 1338–1352.
Dunne, J.A., 1974. Mariner 10 Mercury encounter. Science 185 (4146), 141–142. https://doi.org/10.1126/science.185.4146.141.
Durán, C., Khan, A., Ceylan, S., Zenhäusern, G., Stähler, S., Clinton, J., Giardini, D., 2022. Seismology on Mars: An analysis of direct, reflected, and converted seismic body waves with implications for interior structure. Physics of the Earth and Planetary Interiors 325, 106851.
Efroimsky, M., 2012. Bodily tides near spin-orbit resonances. Celestial Mechanics and Dynamical Astronomy 112 (3), 283–330. https://doi.org/10.1007/s10569-011-9397-4.
Efroimsky, M., 2015. Tidal evolution of asteroidal binaries. Ruled by viscosity. Ignorant of rigidity. The Astronomical Journal 150 (4), 98.
Efroimsky, M., 2018a. Dissipation in a tidally perturbed body librating in longitude. Icarus 306, 328–354.
Efroimsky, M., 2018b. Tidal viscosity of Enceladus. Icarus 300, 223–226. https://doi.org/10.1016/j.icarus.2017.09.013.
Efroimsky, M., Makarov, V.V., 2013. Tidal friction and tidal lagging. Applicability limitations of a popular formula for the tidal torque. The Astrophysical Journal 764, 26. https://doi.org/10.1088/0004-637X/764/1/26.
Efroimsky, M., Makarov, V.V., 2014. Tidal dissipation in a homogeneous spherical body. I. Methods. Astronomical Journal 795 (1), 6.
Egbert, G.D., Ray, R.D., 2003. Semi-diurnal and diurnal tidal dissipation from TOPEX/Poseidon altimetry. Geophysical Research Letters 30 (17).
Esposito, L.W., 1984. Sulfur dioxide: Episodic injection shows evidence for active Venus volcanism. Science 223 (4640), 1072–1074.
Esposito, L.W., Copley, M., Eckert, R., Gates, L., Stewart, A., Worden, H., 1988. Sulfur dioxide at the Venus cloud tops, 1978–1986. Journal of Geophysical Research: Atmospheres 93 (D5), 5267–5276.
Farhat, M., Auclair-Desrotour, P., Boué, G., Laskar, J., 2022. The resonant tidal evolution of the Earth–Moon distance, arXiv preprint. https://doi.org/10.48550/arXiv.2207.00438.
Faul, U., Jackson, I., 2015. Transient creep and strain energy dissipation: An experimental perspective. Annual Review of Earth and Planetary Sciences 43, 541–569. https://doi.org/10.1146/annurev-earth-060313-054732.

Faul, U.H., Fitz Gerald, J.D., Jackson, I., 2004. Shear wave attenuation and dispersion in melt-bearing olivine polycrystals: 2. Microstructural interpretation and seismological implications. Journal of Geophysical Research Planets: Solid Earth (ISSN 2156-2202) 109 (B6), B06202. https://doi.org/10.1029/2003JB002407.

Findley, L., Onaran, K., 1965. Creep and Relaxation of Nonlinear Viscoelastic Materials. Dover Publications, New York.

Foley, B., Houser, C., Noack, L., Tosi, N., 2020. The heat budget of rocky planets. In: Planetary Diversity: Rocky Planet Processes and Their Observational Signatures, pages 4–1.

Fontaine, F.R., Ildefonse, B., Bagdassarov, N.S., 2005. Temperature dependence of shear wave attenuation in partially molten gabbronorite at seismic frequencies. Geophysical Journal International 163 (3), 1025–1038. https://doi.org/10.1111/j.1365-246X.2005.02767.x.

Frouard, J., Efroimsky, M., 2017. Tides in a body librating about a spin–orbit resonance: generalisation of the Darwin–Kaula theory. Celestial Mechanics and Dynamical Astronomy 129 (1–2), 177–214.

Fuller, J., Luan, J., Quataert, E., 2016. Resonance locking as the source of rapid tidal migration in the Jupiter and Saturn moon systems. Monthly Notices of the Royal Astronomical Society 458 (4), 3867–3879.

Garcia, R.F., Khan, A., Drilleau, M., Margerin, L., Kawamura, T., Sun, D., Wieczorek, M.A., Rivoldini, A., Nunn, C., Weber, R.C., et al., 2019. Lunar seismology: An update on interior structure models. Space Science Reviews 215 (8), 1–47.

Genova, A., Goossens, S., Lemoine, F.G., Mazarico, E., Neumann, G.A., Smith, D.E., Zuber, M.T., 2016. Seasonal and static gravity field of Mars from MGS, Mars Odyssey and MRO radio science. Icarus 272, 228–245. https://doi.org/10.1016/j.Icarus.2016.02.050.

Genova, A., Goossens, S., Mazarico, E., Lemoine, F.G., Neumann, G.A., Kuang, W., Sabaka, T.J., Hauck, S.A., Smith, D.E., Solomon, S.C., Zuber, M.T., 2019. Geodetic evidence that Mercury has a solid inner core. Geophysical Research Letters 46, 3625–3633. https://doi.org/10.1029/2018GL081135.

Genova, A., Hussmann, H., Van Hoolst, T., Heyner, D., Iess, L., Santoli, F., Thomas, N., Cappuccio, P., di Stefano, I., Kolhey, P., Langlais, B., Mieth, J.Z.D., Oliveira, J.S., Stark, A., Steinbrügge, G., Tosi, N., Wicht, J., Benkhoff, J., 2021. Geodesy, geophysics and fundamental physics investigations of the BepiColombo mission. Space Science Reviews 217 (2), 31. https://doi.org/10.1007/s11214-021-00808-9.

Gevorgyan, Y., 2021. Homogeneous model for the TRAPPIST-1e planet with an icy layer. Astronomy and Astrophysics 650, A141. https://doi.org/10.1051/0004-6361/202140736.

Ghail, R., 2021. How will EnVision improve our understanding of Venus? In: AAS/Division for Planetary Sciences Meeting Abstracts. In: AAS/Division for Planetary Sciences Meeting Abstracts, vol. 53, p. 315.02.

Ghail, R., Wilson, C.F., Widemann, T., 2016. EnVision M5 Venus orbiter proposal: Opportunities and challenges. In: AAS/Division for Planetary Sciences Meeting Abstracts# 48, volume 48, 216.08.

Giardini, D., Lognonné, P., Banerdt, W.B., Pike, W.T., Christensen, U., Ceylan, S., Clinton, J.F., van Driel, M., Stähler, S., Böse, M., et al., 2020. The seismicity of Mars. Nature Geoscience 13, 205–212.

Gold, T., Soter, S., 1969. Atmospheric tides and the resonant rotation of Venus. Icarus 11 (3), 356–366. https://doi.org/10.1016/0019-1035(69)90068-2.

Goldreich, P., 1966. Final spin states of planets and satellites. Astronomical Journal 71 (1).

Goossens, S., Renaud, J.P., Henning, W.G., Mazarico, E., Bertone, S., Genova, A., 2022. Evaluation of recent measurements of Mercury's moments of inertia and tides using a

comprehensive Markov Chain Monte Carlo method. The Planetary Science Journal 3 (2), 37. https://doi.org/10.3847/PSJ/ac4bb8.

Greaves, J.S., Richards, A.M.S., Bains, W., Rimmer, P.B., Sagawa, H., Clements, D.L., Seager, S., Petkowski, J.J., Sousa-Silva, C., Ranjan, S., Drabek-Maunder, E., Fraser, H.J., Cartwright, A., Mueller-Wodarg, I., Zhan, Z., Friberg, P., Coulson, I., Lee, E., Hoge, J., 2021. Phosphine gas in the cloud decks of Venus. Nature Astronomy 5, 655–664. https://doi.org/10.1038/s41550-020-1174-4.

Greenberg, R., Geissler, P., Hoppa, G., Tufts, B.R., Durda, D.D., Pappalardo, R., Head, J.W., Greeley, R., Sullivan, R., Carr, M.H., 1998. Tectonic processes on Europa: Tidal stresses, mechanical response, and visible features. Icarus 135 (1), 64–78.

Gribb, T.T., Cooper, R.F., 1998. Low-frequency shear attenuation in polycrystalline olivine: Grain boundary diffusion and the physical significance of the Andrade model for viscoelastic rheology. Journal of Geophysical Research Planets: Solid Earth 103 (B11), 27267–27279.

Gülcher, A.J.P., Gerya, T., Montési, L.G.J, Munch, J., 2020. Corona structures driven by plume–lithosphere interactions and evidence for ongoing plume activity on Venus. Nature Geoscience 13 (8), 547–554.

Haas, R., Schuh, H., 1996. Determination of frequency dependent Love and Shida numbers from VLBI data. Geophysical Research Letters 23 (12), 1509–1512.

Hamilton, D.P., Ward, W.R., 2004. Tilting Saturn. II. Numerical model. The Astronomical Journal 128 (5), 2510.

Hansen, C.J., Castillo-Rogez, J., Grundy, W., Hofgartner, J., Martin, E., Mitchell, K., Nimmo, F., Nordheim, T., Paty, C., Quick, L.C., et al., 2021. Triton: Fascinating moon, likely ocean world, compelling destination! The Planetary Science Journal 2 (4), 137.

Harada, Y., Goossens, S., Matsumoto, K., Yan, J., Ping, J., Noda, H., Haruyama, J., 2014. Strong tidal heating in an ultralow-viscosity zone at the core-mantle boundary of the Moon. Nature Geoscience 7, 569–572. https://doi.org/10.1038/ngeo2211.

Harada, Y., Goossens, S., Matsumoto, K., Yan, J., Ping, J., Noda, H., Haruyama, J., 2016. The deep lunar interior with a low-viscosity zone: Revised constraints from recent geodetic parameters on the tidal response of the Moon. Icarus 276, 96–101. https://doi.org/10.1016/j.icarus.2016.04.021.

Hauck, S.A., Margot, J.-L., Solomon, S.C., Phillips, R.J., Johnson, C.L., Lemoine, F.G., Mazarico, E., McCoy, T.J., Padovan, S., Peale, S.J., et al., 2013. The curious case of Mercury's internal structure. Journal of Geophysical Research: Planets 118 (6), 1204–1220.

Hay, H., Matsuyama, I., Pappalardo, R., 2022. The high-frequency tidal response of ocean worlds: Application to Europa and Ganymede. Journal of Geophysical Research: Planets, e2021JE007064.

Hay, H.C., Trinh, A., Matsuyama, I., 2020. Powering the Galilean satellites with moon-moon tides. Geophysical Research Letters 47 (15), e2020GL088317.

Hedman, M., Gosmeyer, C., Nicholson, P., Sotin, C., Brown, R.H., Clark, R., Baines, K., Buratti, B., Showalter, M., 2013. An observed correlation between plume activity and tidal stresses on Enceladus. Nature 500 (7461), 182–184.

Helbert, J., Müller, N., Kostama, P., Marinangeli, L., Piccioni, G., Drossart, P., 2008. Surface brightness variations seen by VIRTIS on Venus Express and implications for the evolution of the Lada Terra region, Venus. Geophysical Research Letters 35 (11).

Heller, R., Leconte, J., Barnes, R., 2011. Tidal obliquity evolution of potentially habitable planets. Astronomy & Astrophysics 528, A27.

Henning, W.G., Hurford, T., 2014. Tidal heating in multilayered terrestrial exoplanets. The Astrophysical Journal 789 (1), 30. https://doi.org/10.1088/0004-637X/789/1/30.

Hoppa, G.V., Tufts, B. Randall, Greenberg, R., Hurford, T.A., O'Brien, D.P., Geissler, P.E., 2001. Europa's rate of rotation derived from the tectonic sequence in the Astypalaea Region. Icarus 153 (1), 208–213. https://doi.org/10.1006/icar.2001.6663.

Howett, C., Spencer, J., Pearl, J., Segura, M., 2011. High heat flow from Enceladus' south polar region measured using 10–600 cm^{-1} Cassini/CIRS data. Journal of Geophysical Research: Planets 116 (E3).

Hurford, T., Helfenstein, P., Hoppa, G., Greenberg, R., Bills, B., 2007. Eruptions arising from tidally controlled periodic openings of rifts on Enceladus. Nature 447 (7142), 292–294.

Hurford, T., Asphaug, E., Spitale, J., Hemingway, D., Rhoden, A., Henning, W., Bills, B., Kattenhorn, S., Walker, M., 2016. Tidal disruption of Phobos as the cause of surface fractures. Journal of Geophysical Research: Planets 121 (6), 1054–1065.

Hussmann, H., Spohn, T., 2004. Thermal-orbital evolution of Io and Europa. Icarus 171 (2), 391–410.

Hussmann, H., Sohl, F., Spohn, T., 2006. Subsurface oceans and deep interiors of medium-sized outer planet satellites and large trans-neptunian objects. Icarus 185 (1), 258–273.

Hut, P., 1981. Tidal evolution in close binary systems. Astronomy and Astrophysics 99, 126–140.

Iess, L., Stevenson, D.J., Parisi, M., Hemingway, D., Jacobson, R.A., Lunine, J.I., Nimmo, F., Armstrong, J.W., Asmar, S.W., Ducci, M., Tortora, P., 2014. The gravity field and interior structure of Enceladus. Science 344, 78–80.

Ingersoll, A.P., Dobrovolskis, A.R., 1978. Venus' rotation and atmospheric tides. Nature 275 (5675), 37–38. https://doi.org/10.1038/275037a0.

Ivins, E.R., Caron, L., Adhikari, S., Larour, E., 2021. Notes on a compressible extended Burgers model of rheology. Geophysical Journal International 228 (3), 1975–1991.

Jackson, I., 2000. Laboratory measurement of seismic wave dispersion and attenuation: recent progress. In: Earth's Deep Interior: Mineral Physics and Tomography From the Atomic to the Global Scale, pp. 265–289.

Jackson, I., 2005. Laboratory measurement of seismic wave dispersion and attenuation at high pressure and temperature. In: Advances in High-Pressure Technology for Geophysical Applications. Elsevier, pp. 95–119.

Jackson, I., Faul, U.H., 2010. Grainsize-sensitive viscoelastic relaxation in olivine: Towards a robust laboratory-based model for seismological application. Physics of the Earth and Planetary Interiors 183, 151–163. https://doi.org/10.1016/j.pepi.2010.09.005.

Jackson, I., Gerald, J.D.F., Faul, U.H., Tan, B.H., 2002. Grain-size-sensitive seismic wave attenuation in polycrystalline olivine. Journal of Geophysical Research Planets: Solid Earth 107 (B12), ECV 5–1–ECV 5–16. https://doi.org/10.1029/2001JB001225. https://agupubs.onlinelibrary.wiley.com/doi/abs/10.1029/2001JB001225.

Jackson, I., et al., 2007. Properties of rock and minerals-physical origins of anelasticity and attenuation in rock. In: Treatise on Geophysics. Elsevier.

Jacobson, R., 2010. The orbits and masses of the Martian satellites and the libration of Phobos. Astronomical Journal 139 (2), 668.

Jacobson, R., Lainey, V., 2014. Martian satellite orbits and ephemerides. Planetary and Space Science 102, 35–44.

Jara-Orué, H.M., Vermeersen, B.L., 2011. Effects of low-viscous layers and a non-zero obliquity on surface stresses induced by diurnal tides and non-synchronous rotation: The case of Europa. Icarus 215 (1), 417–438.

Kamata, S., Nimmo, F., 2017. Interior thermal state of Enceladus inferred from the viscoelastic state of the ice shell. Icarus 284, 387–393. https://doi.org/10.1016/j.icarus.2016.11.034.

Karato, S., Spetzler, H.A., 1990. Defect microdynamics in minerals and solid-state mechanisms of seismic wave attenuation and velocity dispersion in the mantle. Reviews of Geophysics 28 (4), 399–421. https://doi.org/10.1029/RG028i004p00399. https://agupubs.onlinelibrary.wiley.com/doi/abs/10.1029/RG028i004p00399.

Karato, S.I., 2008. Deformation of Earth Materials. Cambridge University Press.

Karato, S.-i., 2013. Geophysical constraints on the water content of the lunar mantle and its implications for the origin of the Moon. Earth and Planetary Science Letters 384, 144–153. https://doi.org/10.1016/j.epsl.2013.10.001.

Karato, S.-i., Wu, P., 1993. Rheology of the upper mantle: A synthesis. Science 260 (5109), 771–778.

Kattenhorn, S.A., Hurford, T., 2009. Tectonics of Europa. Europa, 199–236.

Kattenhorn, S.A., Prockter, L.M., 2014. Evidence for subduction in the ice shell of Europa. Nature Geoscience 7 (10), 762–767.

Kaula, W.M., 1961. Analysis of gravitational and geometric aspects of geodetic utilization of satellites. Geophysical Journal 5 (2), 104–133. https://doi.org/10.1111/j.1365-246X.1961.tb00417.x.

Kaula, W.M., 1964. Tidal dissipation by solid friction and the resulting orbital evolution. Reviews of Geophysics 2 (4), 661–685.

Kervazo, M., Tobie, G., Choblet, G., Dumoulin, C., Běhounková, M., 2022. Inferring Io's interior from tidal monitoring. Icarus 373, 114737. https://doi.org/10.1016/j.icarus.2021.114737.

Khan, A., Connolly, J.A.D., Pommier, A., Noir, J., 2014. Geophysical evidence for melt in the deep lunar interior and implications for lunar evolution. Journal of Geophysical Research: Planets 119, 2197–2221. https://doi.org/10.1002/2014JE004661.

Khan, A., Liebske, C., Rozel, A., Rivoldini, A., Nimmo, F., Connolly, J.A.D., Plesa, A.-C., Giardini, D., 2018. A geophysical perspective on the bulk composition of Mars. Journal of Geophysical Research: Planets 123 (2), 575–611. https://doi.org/10.1002/2017JE005371.

Khan, A., Ceylan, S., van Driel, M., Giardini, D., Lognonné, P., Samuel, H., Schmerr, N.C., Stähler, S.C., Duran, A.C., Huang, Q., et al., 2021. Upper mantle structure of Mars from InSight seismic data. Science 373 (6553), 434–438.

Khan, A., Sossi, P., Liebske, C., Rivoldini, A., Giardini, D., 2022. Geophysical and cosmochemical evidence for a volatile-rich mars. Earth and Planetary Science Letters 578, 117330.

Khurana, K., Kivelson, M., Stevenson, D., Schubert, G., Russell, C., Walker, R., Polanskey, C., 1998. Induced magnetic fields as evidence for subsurface oceans in Europa and Callisto. Nature 395 (6704), 777–780.

Kiefer, W.S., 2003. Melting in the Martian mantle: Shergottite formation and implications for present-day mantle convection on Mars. Meteoritics & Planetary Science 38 (12), 1815–1832.

Kiefer, W.S., Hager, B.H., 1991. A mantle plume model for the equatorial highlands of Venus. Journal of Geophysical Research: Planets 96 (E4), 20947–20966.

Knapmeyer-Endrun, B., Panning, M.P., Bissig, F., Joshi, R., Khan, A., Kim, D., Lekić, V., Tauzin, B., Tharimena, S., Plasman, M., Compaire, N., Garcia, R.F., Margerin, L., Schimmel, M., Stutzmann, É., Schmerr, N., Bozdağ, E., Plesa, A.-C., Wieczorek, M.A., Broquet, A., Antonangeli, D., McLennan, S.M., Samuel, H., Michaut, C., Pan, L., Smrekar, S.E., Johnson, C.L., Brinkman, N., Mittelholz, A., Rivoldini, A., Davis, P.M., Lognonné, P., Pinot, B., Scholz, J.-R., Stähler, S., Knapmeyer, M., van Driel, M., Giardini, D., Banerdt, W.B., 2021. Thickness and structure of the martian crust from InSight seismic data. Science (ISSN 0036-8075) 373 (6553), 438–443. https://doi.org/10.1126/science.abf8966. https://science.sciencemag.org/content/373/6553/438.

Knibbe, J.S., van Westrenen, W., 2015. The interior configuration of planet Mercury constrained by moment of inertia and planetary contraction. Journal of Geophysical Research: Planets 120 (11), 1904–1923. https://doi.org/10.1002/2015JE004908.

Knibbe, J.S., van Westrenen, W., 2018. The thermal evolution of Mercury's Fe–Si core. Earth and Planetary Science Letters 482, 147–159. https://doi.org/10.1016/j.epsl.2017.11.006.

Konopliv, A., Yoder, C., 1996. Venusian k_2 tidal Love number from Magellan and PVO tracking data. Geophysical Research Letters 23 (14), 1857–1860.

Konopliv, A.S., Yoder, C.F., Standish, E.M., Yuan, D.-N., Sjogren, W.L., 2006. A global solution for the Mars static and seasonal gravity, Mars orientation, Phobos and Deimos masses, and Mars ephemeris. Icarus 182, 23–50. https://doi.org/10.1016/j.Icarus.2005.12.025.

Konopliv, A.S., Asmar, S.W., Folkner, W.M., Karatekin, Ö., Nunes, D.C., Smrekar, S.E., Yoder, C.F., Zuber, M.T., 2011. Mars high resolution gravity fields from MRO, Mars seasonal gravity, and other dynamical parameters. Icarus 211, 401–428. https://doi.org/10.1016/j.Icarus.2010.10.004.

Konopliv, A.S., Park, R.S., Yuan, D.-N., Asmar, S.W., Watkins, M.M., Williams, J.G., Fahnestock, E., Kruizinga, G., Paik, M., Strekalov, D., et al., 2013. The JPL lunar gravity field to spherical harmonic degree 660 from the GRAIL primary mission. Journal of Geophysical Research: Planets 118 (7), 1415–1434.

Konopliv, A.S., Park, R.S., Yuan, D.-N., Asmar, S.W., Watkins, M.M., Williams, J.G., Fahnestock, E., Kruizinga, G., Paik, M., Strekalov, D., et al., 2014. High-resolution lunar gravity fields from the GRAIL primary and extended missions. Geophysical Research Letters 41 (5), 1452–1458.

Konopliv, A.S., Park, R.S., Folkner, W.M., 2016. An improved JPL Mars gravity field and orientation from Mars orbiter and lander tracking data. Icarus 274, 253–260. https://doi.org/10.1016/j.Icarus.2016.02.052.

Konopliv, A.S., Park, R.S., Ermakov, A.I., 2020a. The Mercury gravity field, orientation, Love number, and ephemeris from the MESSENGER radiometric tracking data. Icarus 335, 113386. https://doi.org/10.1016/j.Icarus.2019.07.020.

Konopliv, A.S., Park, R.S., Rivoldini, A., Baland, R.-M., Le Maistre, S., Van Hoolst, T., Yseboodt, M., Dehant, V., 2020b. Detection of the Chandler wobble of Mars from orbiting spacecraft. Geophysical Research Letters 47 (21), e2020GL090568.

Krásná, H., Böhm, J., Schuh, H., 2013. Tidal Love and Shida numbers estimated by geodetic VLBI. Journal of Geodynamics 70, 21–27.

Lainey, V., Dehant, V., Pätzold, M., 2007. First numerical ephemerides of the Martian moons. Astronomy & Astrophysics 465, 1075–1084. https://doi.org/10.1051/0004-6361:20065466.

Lainey, V., Arlot, J.-E., Karatekin, Ö., Van Hoolst, T., 2009. Strong tidal dissipation in Io and Jupiter from astrometric observations. Nature 459 (7249), 957–959.

Lainey, V., Jacobson, R.A., Tajeddine, R., Cooper, N.J., Murray, C., Robert, V., Tobie, G., Guillot, T., Mathis, S., Remus, F., et al., 2017. New constraints on Saturn's interior from Cassini astrometric data. Icarus 281, 286–296.

Lainey, V., Casajus, L.G., Fuller, J., Zannoni, M., Tortora, P., Cooper, N., Murray, C., Modenini, D., Park, R.S., Robert, V., et al., 2020. Resonance locking in giant planets indicated by the rapid orbital expansion of Titan. Nature Astronomy 4 (11), 1053–1058.

Lainey, V., Pasewaldt, A., Robert, V., Rosenblatt, P., Jaumann, R., Oberst, J., Roatsch, T., Willner, K., Ziese, R., Thuillot, W., 2021. Mars moon ephemerides after 14 years of Mars Express data. Astronomy & Astrophysics 650 (11).

Lark, L.H., Parman, S., Huber, C., Parmentier, E.M., Head, J.W., 2022. Sulfides in Mercury's mantle: implications for Mercury's interior as interpreted from moment of inertia. Geophysical Research Letters 49 (6), e96713. https://doi.org/10.1029/2021GL096713.

Latychev, K., Mitrovica, J.X., Ishii, M., Chan, N.-H., Davis, J.L., 2009. Body tides on a 3-D elastic Earth: toward a tidal tomography. Earth and Planetary Science Letters 277 (1–2), 86–90.

Lau, H.C., Faul, U.H., 2019. Anelasticity from seismic to tidal timescales: Theory and observations. Earth and Planetary Science Letters 508, 18–29.

Lau, H.C., Mitrovica, J., Davis, J.L., Tromp, J., Yang, H.-Y., Al-Attar, D., 2017. Tidal tomography constrains Earth's deep-mantle buoyancy. Nature 551 (7680), 321.
Lau, H.C., Austermann, J., Holtzman, B.K., Havlin, C., Lloyd, A.J., Book, C., Hopper, E., 2021. Frequency dependent mantle viscoelasticity via the complex viscosity: cases from Antarctica. Journal of Geophysical Research: Solid Earth 126 (11), e2021JB022622.
Le Maistre, S., Rosenblatt, P., Rambaux, N., Castillo-Rogez, J.C., Dehant, V., Marty, J.-C., 2013. Phobos interior from librations determination using Doppler and star tracker measurements. Planetary and Space Science 85, 106–122.
Le Maistre, S., Rivoldini, A., Rosenblatt, P., 2019. Signature of Phobos' interior structure in its gravity field and libration. Icarus 321, 272–290.
Lekić, V., Matas, J., Panning, M., Romanowicz, B., 2009. Measurement and implications of frequency dependence of attenuation. Earth and Planetary Science Letters 282 (1–4), 285–293.
Lemoine, F., Bruinsma, S., Chinn, D., Forbes, J., 2006. Thermospheric studies with Mars global surveyor. In: AIAA/AAS Astrodynamics Specialist Conference and Exhibit, p. 6395.
Lemoine, F.G., Goossens, S., Sabaka, T.J., Nicholas, J.B., Mazarico, E., Rowlands, D.D., Loomis, B.D., Chinn, D.S., Caprette, D.S., Neumann, G.A., et al., 2013. High–degree gravity models from GRAIL primary mission data. Journal of Geophysical Research: Planets 118 (8), 1676–1698.
Lissa, S., Barbosa, N.D., Rubino, J., Quintal, B., 2019. Seismic attenuation and dispersion in poroelastic media with fractures of variable aperture distributions. Solid Earth 10 (4), 1321–1336.
Lodders, K., Fegley, B., 1997. An oxygen isotope model for the composition of Mars. Icarus 126, 373–394. https://doi.org/10.1006/icar.1996.5653.
Lognonné, P., Banerdt, W., Pike, W., Giardini, D., Christensen, U., Garcia, R., Kawamura, T., Kedar, S., Knapmeyer-Endrun, B., Margerin, L., et al., 2020. Constraints on the shallow elastic and anelastic structure of Mars from InSight seismic data. Nature Geoscience 13, 213–220.
Lourenço, D.L., Rozel, A.B., Ballmer, M.D., Tackley, P.J., 2020. Plutonic-squishy lid: a new global tectonic regime generated by intrusive magmatism on Earth-like planets. Geochemistry, Geophysics, Geosystems 21 (4), e2019GC008756.
Love, A.E.H., 1911. Some Problems of Geodynamics: Being an Essay to Which the Adams Prize in the University of Cambridge Was Adjudged in 1911, vol. 911. University Press.
MacDonald, G.J., 1964. Tidal friction. Reviews of Geophysics 2 (3), 467–541.
Maia, J.S., Wieczorek, M.A., 2022. Lithospheric structure of Venusian crustal plateaus. Journal of Geophysical Research: Planets 127 (2), e2021JE007004.
Makarov, V.V., Efroimsky, M., 2013. No pseudosynchronous rotation for terrestrial planets and moons. The Astrophysical Journal 764 (1), 27.
Marcq, E., Bertaux, J.-L., Montmessin, F., Belyaev, D., 2013. Variations of sulphur dioxide at the cloud top of Venus's dynamic atmosphere. Nature Geoscience 6 (1), 25–28.
Margerin, L., Campillo, M., Van Tiggelen, B., 2000. Monte Carlo simulation of multiple scattering of elastic waves. Journal of Geophysical Research: Solid Earth 105 (B4), 7873–7892.
Margot, J.-L., Peale, S., Jurgens, R., Slade, M., Holin, I., 2007. Large longitude libration of Mercury reveals a molten core. Science 316 (5825), 710–714.
Margot, J.-L., Peale, S., Solomon, S., Hauck, S., Ghigo, F., Jurgens, R., Yseboodt, M., Giorgini, J., Padovan, S., Campbell, D., 2012. Mercury's moment of inertia from spin and gravity data. Journal of Geophysical Research 117, E00L09. https://doi.org/10.1029/2012JE004161.
Margot, J.-L., Campbell, D.B., Giorgini, J.D., Jao, J.S., Snedeker, L.G., Ghigo, F.D., Bonsall, A., 2021. Spin state and moment of inertia of Venus. Nature Astronomy 5, 676–683. https://doi.org/10.1038/s41550-021-01339-7.

Martens, H.R., Rivera, L., Simons, M., Ito, T., 2016. The sensitivity of surface mass loading displacement response to perturbations in the elastic structure of the crust and mantle. Journal of Geophysical Research: Solid Earth 121 (5), 3911–3938.

Martens, H.R., Rivera, L., Simons, M., 2019. LoadDef: A Python-based toolkit to model elastic deformation caused by surface mass loading on spherically symmetric bodies. Earth and Space Science 6 (2), 311–323.

Matsumoto, K., Yamada, R., Kikuchi, F., Kamata, S., Ishihara, Y., Iwata, T., Hanada, H., Sasaki, S., 2015. Internal structure of the Moon inferred from Apollo seismic data and selenodetic data from GRAIL and LLR. Geophysical Research Letters 42 (18), 7351–7358. https://doi.org/10.1002/2015GL065335.

Matsuyama, I., Nimmo, F., 2009. Gravity and tectonic patterns of Mercury: Effect of tidal deformation, spin-orbit resonance, nonzero eccentricity, despinning, and reorientation. Journal of Geophysical Research: Planets 114 (E1).

Matsuyama, I., Nimmo, F., Keane, J.T., Chan, N.H., Taylor, G.J., Wieczorek, M.A., Kiefer, W.S., Williams, J.G., 2016. GRAIL, LLR, and LOLA constraints on the interior structure of the Moon. Geophysical Research Letters 43 (16), 8365–8375.

Matsuyama, I., Beuthe, M., Hay, H.C., Nimmo, F., Kamata, S., 2018. Ocean tidal heating in icy satellites with solid shells. Icarus 312, 208–230.

Mazarico, E., Barker, M.K., Neumann, G.A., Zuber, M.T., Smith, D.E., 2014a. Detection of the lunar body tide by the lunar orbiter laser altimeter. Geophysical Research Letters 41 (7), 2282–2288.

Mazarico, E., Genova, A., Goossens, S., Lemoine, F.G., Neumann, G.A., Zuber, M.T., Smith, D.E., Solomon, S.C., 2014b. The gravity field, orientation, and ephemeris of Mercury from MESSENGER observations after three years in orbit. Journal of Geophysical Research: Planets 119 (12), 2417–2436. https://doi.org/10.1002/2014JE004675.

Mazarico, E., Buccino, D.R., Castillo-Rogez, J., Dombard, A., Genova, A., Hussmann, H., Kiefer, W.S., Lunine, J.I., McKinnon, W.B., Nimmo, F., Park, R.S., Tortora, P., Withers, P., Roberts, J.H., Korth, H., Senske, D.A., Pappalardo, R.T., 2021. The Europa Clipper gravity/radio science investigation. In: 52nd Lunar and Planetary Science Conference, Lunar and Planetary Science Conference, p. 1784.

McCarthy, C., Castillo-Rogez, J.C., 2013. Planetary ices attenuation properties. In: The Science of Solar System Ices. Springer, pp. 183–225.

McCarthy, C., Cooper, R.F., 2016. Tidal dissipation in creeping ice and the thermal evolution of Europa. Earth and Planetary Science Letters 443, 185–194.

McCarthy, C., Takei, Y., Hiraga, T., 2011. Experimental study of attenuation and dispersion over a broad frequency range: 2. The universal scaling of polycrystalline materials. Journal of Geophysical Research Planets: Solid Earth (ISSN 2156-2202) 116 (B9), B09207. https://doi.org/10.1029/2011JB008384.

McCarthy, D.D., Petit, G., 2004. IERS conventions (2003). IERS Technical Note 32, 1.

Métivier, L., Conrad, C.P., 2008. Body tides of a convecting, laterally heterogeneous, and aspherical Earth. Journal of Geophysical Research: Solid Earth 113 (B11).

Mignard, F., 1979. The evolution of the lunar orbit revisited. I. The Moon and the Planets 20 (3), 301–315.

Mignard, F., 1980. The evolution of the lunar orbit revisited, II. The Moon and the Planets 23 (2), 185–201.

Mignard, F., 1981. Evolution of the Martian satellites. Monthly Notices of the Royal Astronomical Society 194 (2), 365–379.

Minster, J.B., Anderson, D.L., 1981. A model of dislocation-controlled rheology for the mantle. Philosophical Transactions of the Royal Society of London. Series A, Mathematical and Physical Sciences 299 (1449), 319–356. https://doi.org/10.1098/rsta.1981.0025.

Mitri, G., Meriggiola, R., Hayes, A., Lefevre, A., Tobie, G., Genova, A., Lunine, J.I., Zebker, H., 2014. Shape, topography, gravity anomalies and tidal deformation of Titan. Icarus 236, 169–177.

Mitrovica, J., Davis, J., Mathews, P., Shapiro, I., 1994. Determination of tidal h Love number parameters in the diurnal band using an extensive VLBI data set. Geophysical Research Letters 21 (8), 705–708.

Moczo, P., Kristek, J., 2005. On the rheological models used for time-domain methods of seismic wave propagation. Geophysical Research Letters 32 (1). https://doi.org/10.1029/2004GL021598. https://agupubs.onlinelibrary.wiley.com/doi/abs/10.1029/2004GL021598.

Moore, W.B., Schubert , G., 2000. NOTE: The tidal response of Europa. Icarus 147, 317–319. https://doi.org/10.1006/icar.2000.6460.

Morgan, J.W., Anders, E., 1979. Mars: a cosmochemical-geophysical estimate of bulk composition. In: Mars, p. 60.

Morris, S., Jackson, I., 2009. Implications of the similarity principle relating creep and attenuation in finely grained solids. Materials Science and Engineering: A 521, 124–127.

Mosegaard, K., Tarantola, A., 1995. Monte Carlo sampling of solutions to inverse problems. Journal of Geophysical Research Planets: Solid Earth (1978–2012) 100 (B7), 12431–12447.

Murphy, T., 2013. Lunar laser ranging: the millimeter challenge. Reports on Progress in Physics 76 (7), 076901.

Murray, C.D., Dermott, S.F., 1999. Solar System Dynamics. Cambridge University Press.

Ness, N.F., Behannon, K.W., Lepping, R.P., Whang, Y.C., Schatten, K.H., 1974. Magnetic field observations near Mercury: preliminary results from Mariner 10. Science 185 (4146), 151–160. https://doi.org/10.1126/science.185.4146.151.

Neveu, M., Rhoden, A.R., 2019. Evolution of Saturn's mid-sized moons. Nature Astronomy 3 (6), 543–552.

Nield, D.A., Kuznetsov, A.V., Xiong, M., 2004. Effects of viscous dissipation and flow work on forced convection in a channel filled by a saturated porous medium. Transport in Porous Media 56 (3), 351–367.

Nimmo, F., Faul, U., 2013. Dissipation at tidal and seismic frequencies in a melt-free, anhydrous Mars. Journal of Geophysical Research: Planets 118 (12), 2558–2569.

Nimmo, F., Pappalardo, R., 2016. Ocean worlds in the outer solar system. Journal of Geophysical Research: Planets 121 (8), 1378–1399.

Nimmo, F., Spencer, J., 2015. Powering Triton's recent geological activity by obliquity tides: Implications for Pluto geology. Icarus 246, 2–10.

Nimmo, F., Spencer, J., Pappalardo, R., Mullen, M., 2007. Shear heating as the origin of the plumes and heat flux on Enceladus. Nature 447 (7142), 289–291.

Nimmo, F., Faul, U.H., Garnero, E.J., 2012. Dissipation at tidal and seismic frequencies in a melt-free Moon. Journal of Geophysical Research: Planets 117, E09005. https://doi.org/10.1029/2012JE004160.

Nimmo, F., Barr, A.C., Behounková, M., McKinnon, W.B., 2018. The thermal and orbital evolution of Enceladus: observational constraints and models. In: Enceladus and the Icy Moons of Saturn, pp. 79–94.

Nowick, A.S., Berry, B., 1972. Anelastic Relaxation in Crystalline Solids. Academic Press.

Noyelles, B., 2017. Interpreting the librations of a synchronous satellite–How their phase assesses Mimas' global ocean. Icarus 282, 276–289.

Noyelles, B., Frouard, J., Makarov, V.V., Efroimsky, M., 2014. Spin-orbit evolution of Mercury revisited. Icarus 241, 26–44. https://doi.org/10.1016/j.Icarus.2014.05.045.

O'Rourke, J.G., Smrekar, S.E., 2018. Signatures of lithospheric flexure and elevated heat flow in stereo topography at coronae on Venus. Journal of Geophysical Research: Planets 123 (2), 369–389.

Padovan, S., Margot, J.-L., Hauck, S.A., Moore, W.B., Solomon, S.C., 2014. The tides of Mercury and possible implications for its interior structure. Journal of Geophysical Research: Planets 119 (4), 850–866. https://doi.org/10.1002/2013JE004459. https://agupubs.onlinelibrary.wiley.com/doi/abs/10.1002/2013JE004459.

Park, R.S., Folkner, W.M., Williams, J.G., Boggs, D.H., 2021. The JPL planetary and lunar ephemerides DE440 and DE441. The Astronomical Journal 161 (3), 105.

Patthoff, D.A., Kattenhorn, S.A., 2011. A fracture history on Enceladus provides evidence for a global ocean. Geophysical Research Letters 38 (18).

Pavlov, D.A., Williams, J.G., Suvorkin, V.V., 2016. Determining parameters of Moon's orbital and rotational motion from LLR observations using GRAIL and IERS-recommended models. Celestial Mechanics and Dynamical Astronomy 126 (1), 61–88.

Peale, S., 1999. Origin and evolution of the natural satellites. Annual Review of Astronomy and Astrophysics 37 (1), 533–602.

Peale, S., 2005. The free precession and libration of Mercury. Icarus 178 (1), 4–18.

Peale, S.J., 1976. Does Mercury have a molten core? Nature 262, 765–766. https://doi.org/10.1038/262765a0.

Peale, S.J., Cassen, P., Reynolds, R.T., 1979. Melting of Io by tidal dissipation. Science 203 (4383), 892–894.

Peale, S.J., Phillips, R.J., Smith, D.E., Zuber, M.T., 2002. A procedure for determining the nature of Mercury's core. Meteoretics and Planetary Science 37, 1269–1283. https://doi.org/10.1111/j.1945-5100.2002.tb00895.x.

Peltier, W., 1974. The impulse response of a Maxwell Earth. Reviews of Geophysics 12 (4), 649–669.

Petrov, L., 2000. Determination of Love numbers h and l for long-period tides using VLBI. In: Program and Abstracts of 14th Int. Symp. Earth Tides, vol. 16.

Petrova, N., Hanada, H., 2013. Computer simulation of observations of stars from the moon using the polar zenith telescope of the Japanese project ILOM. Solar System Research 47 (6), 463–476.

Plesa, A.-C., Padovan, S., Tosi, N., Breuer, D., Grott, M., Wieczorek, M., Spohn, T., Smrekar, S., Banerdt, W., 2018. The thermal state and interior structure of Mars. Geophysical Research Letters 45 (22), 12–198.

Pou, L., Nimmo, F., Lognonné, P., Mimoun, D., Garcia, R., Pinot, B., Rivoldini, A., Banfield, D., Banerdt, W., 2021. Forward modeling of the Phobos tides and applications to the first Martian year of the InSight mission. Earth and Space Science.

Pou, L., Nimmo, F., Rivoldini, A., Khan, A., Bagheri, A., Gray, T., Samuel, H., Lognonné, P., Plesa, A.C., Gudkova, T., Giardini, D., 2022. Tidal constraints on the Martian interior. In: LPI Contributions, vol. 2678, p. 1776.

Prockter, L.M., Patterson, G.W., 2009. Morphology and evolution of Europa's ridges and bands. In: Europa. University of Arizona Press, Tucson, pp. 237–258.

Qu, T., Jackson, I., Faul, U.H., 2021. Low-frequency seismic properties of olivine-orthopyroxene mixtures. Journal of Geophysical Research 126, e2021JB022504.

Rainey, E., Aharonson, O., 2006. Estimate of tidal Q of Mars using MOC observations of the shadow of Phobos. In: The 37th Annual Lunar and Planetary Science Conference. 13–17 March 2006.

Rambaux, N., Williams, J., 2011. The Moon's physical librations and determination of their free modes. Celestial Mechanics and Dynamical Astronomy 109 (1), 85–100.

Rambaux, N., Van Hoolst, T., Dehant, V., Bois, E., 2007. Inertial core-mantle coupling and libration of Mercury. Astronomy and Astrophysics 468 (2), 711–719. https://doi.org/10.1051/0004-6361:20053974.

Rambaux, N., Castillo-Rogez, J.C., Williams, J.G., Karatekin, Ö., 2010. Librational response of Enceladus. Geophysical Research Letters 37, L04202. https://doi.org/10.1029/2009GL041465.

Rambaux, N., Castillo-Rogez, J.C., Le Maistre, S., Rosenblatt, P., 2012. Rotational motion of Phobos. Astronomy and Astrophysics 548, A14. https://doi.org/10.1051/0004-6361/201219710.

Rambaux, N., Castillo-Rogez, J., Williams, J.G., Boggs, D., 2014. On the lunar dissipation law. In: European Planetary Science Congress, vol. 9.

Rathbun, J.A., Lopes, R.M.C., Spencer, J.R., 2018. The global distribution of active ionian volcanoes and implications for tidal heating models. The Astronomical Journal 156 (5), 207. https://doi.org/10.3847/1538-3881/aae370.

Ray, R.D., Eanes, R.J., Lemoine, F.G., 2001. Constraints on energy dissipation in the Earth's body tide from satellite tracking and altimetry. Geophysical Journal International 144, 471–480. https://doi.org/10.1046/j.1365-246X.2001.00356.x.

Remus, F., Mathis, S., Zahn, J.-P., Lainey, V., 2012. Anelastic tidal dissipation in multi-layer planets. Astronomy & Astrophysics 541, A165.

Renaud, J.P., Henning, W.G., 2018. Increased tidal dissipation using advanced rheological models: Implications for Io and tidally active exoplanets. Astronomical Journal 857 (2), 98.

Renaud, J.P., Henning, W.G., Saxena, P., Neveu, M., Bagheri, A., Mandell, A., Hurford, T., 2021. Tidal dissipation in dual-body, highly eccentric, and nonsynchronously rotating systems: Applications to Pluto–Charon and the exoplanet TRAPPIST-1e. The Planetary Science Journal 2 (1), 4.

Rhoden, A.R., Walker, M.E., 2022. The case for an ocean-bearing Mimas from tidal heating analysis. Icarus, 114872.

Rhoden, A.R., Militzer, B., Huff, E.M., Hurford, T.A., Manga, M., Richards, M.A., 2010. Constraints on Europa's rotational dynamics from modeling of tidally-driven fractures. Icarus 210 (2), 770–784.

Rhoden, A.R., Wurman, G., Huff, E.M., Manga, M., Hurford, T.A., 2012. Shell tectonics: A mechanical model for strike-slip displacement on Europa. Icarus 218 (1), 297–307.

Rhoden, A.R., Skjetne, H.L., Henning, W.G., Hurford, T.A., Walsh, K.J., Stern, S., Olkin, C., Spencer, J., Weaver, H., Young, L., et al., 2020. Charon: A brief history of tides. Journal of Geophysical Research: Planets 125 (7), e2020JE006449.

Rhoden, A.R., Mohr, K.J., Hurford, T.A., Henning, W., Sajous, S., Patthoff, D.A., Dubois, D., 2021. Obliquity, precession, and fracture mechanics: Implications of Europa's global cycloid population. Journal of Geophysical Research: Planets 126 (3), e2020JE006710.

Rivoldini, A., Van Hoolst, T., 2013. The interior structure of Mercury constrained by the low-degree gravity field and the rotation of Mercury. Earth and Planetary Science Letters 377, 62–72. https://doi.org/10.1016/j.epsl.2013.07.021.

Rivoldini, A., Van Hoolst, T., Verhoeven, O., 2009. The interior structure of Mercury and its core sulfur content. Icarus 201 (1), 12–30. https://doi.org/10.1016/j.Icarus.2008.12.020.

Rivoldini, A., Van Hoolst, T., Verhoeven, O., Mocquet, A., Dehant, V., 2011. Geodesy constraints on the interior structure and composition of Mars. Icarus 213, 451–472. https://doi.org/10.1016/j.Icarus.2011.03.024.

Roberts, J.H., Nimmo, F., 2008. Tidal heating and the long-term stability of a subsurface ocean on Enceladus. Icarus 194, 675–689. https://doi.org/10.1016/j.Icarus.2007.11.010.

Rolf, T., Steinberger, B., Sruthi, U., Werner, S.C., 2018. Inferences on the mantle viscosity structure and the post-overturn evolutionary state of Venus. Icarus 313, 107–123.

Rosenblatt, P., 2011. The origin of the Martian moons revisited. The Astronomy and Astrophysics Review 19 (1), 44.

Rosenblatt, P., Dumoulin, C., Marty, J.-C., Genova, A., 2021. Determination of Venus' interior structure with EnVision. Remote Sensing 13 (9), 1624.

Rovira-Navarro, A., Katz, G., Liao, Y., van der Wal, W., Nimmo, F., 2022. The tides of Enceladus' porous core. Journal of Geophysical Research: Planets. https://doi.org/10.1029/2021JE007117.

Rozel, A., Golabek, G., Jain, C., Tackley, P., Gerya, T., 2017. Continental crust formation on early Earth controlled by intrusive magmatism. Nature 545, 332–335. https://doi.org/10.1038/nature22042.

Rudolph, M.L., Manga, M., 2009. Fracture penetration in planetary ice shells. Icarus 199 (2), 536–541.

Rudolph, M.L., Manga, M., Walker, M., Rhoden, A.R., 2022. Cooling crusts create concomitant cryovolcanic cracks. Geophysical Research Letters 49 (5), e2021GL094421.

Rufu, R., Canup, R.M., 2020. Tidal evolution of the evection resonance/quasi-resonance and the angular momentum of the Earth–Moon system. Journal of Geophysical Research: Planets 125 (8), e2019JE006312.

Ryan, J., Clark, T., Coates, R., Ma, C., Wildes, W., Gwinn, C., Herring, T., Shapiro, I., Corey, B., Counselman, C., et al., 1986. Geodesy by radio interferometry: Determinations of baseline vector, Earth rotation, and solid Earth tide parameters with the Mark I very long baseline radio interferometry system. Journal of Geophysical Research: Solid Earth 91 (B2), 1935–1946.

Sabadini, R., Vermeersen, B., 2004. Global Dynamics of the Earth: Applications of Normal Mode Relaxation Theory to Solid-Earth Geophysics. Kluwer Academic Publishers, Dodrech, the Netherlands. ISBN 1-4020-2135-6.

Saillenfest, M., Lari, G., Boué, G., 2021. The large obliquity of Saturn explained by the fast migration of Titan. Nature Astronomy 5 (4), 345–349.

Samain, E., Mangin, J., Veillet, C., Torre, J., Fridelance, P., Chabaudie, J., Feraudy, D., Glentzlin, M., Van, J.P., Furia, M., et al., 1998. Millimetric lunar laser ranging at OCA (Observatoire de la Côte d'Azur). Astronomy & Astrophysics. Supplement Series 130 (2), 235–244.

Samuel, H., Lognonné, P., Panning, M., Lainey, V., 2019. The rheology and thermal history of Mars revealed by the orbital evolution of Phobos. Nature 569 (7757), 523.

Sanloup, C., Jambon, A., Gillet, P., 1999. A simple chondritic model of Mars. Physics of the Earth and Planetary Interiors 112, 43–54. https://doi.org/10.1016/S0031-9201(98)00175-7.

Saxena, P., Renaud, J.P., Henning, W.G., Jutzi, M., Hurford, T., 2018. Relevance of tidal heating on large TNOs. Icarus 302, 245–260.

Schenk, P.M., Turtle, E.P., 2021. Tectonics of Europa. University of Arizona Press, Tucsan, p. 181.

Segatz, M., Spohn, T., Ross, M.N., Schubert, G., 1988. Tidal dissipation, surface heat flow, and figure of viscoelastic models of Io. Icarus 75 (2), 187–206. https://doi.org/10.1016/0019-1035(88)90001-2.

Seitz, F., Kirschner, S., Neubersch, D., 2012. Determination of the Earth's pole tide Love number k2 from observations of polar motion using an adaptive Kalman filter approach. Journal of Geophysical Research: Solid Earth 117 (B9).

Shah, O., Helled, R., Alibert, Y., Mezger, K., 2022. Possible chemical composition and interior structure models of Venus inferred from numerical modelling. The Astrophysical Journal 926 (2), 217.

Shalygin, E.V., Markiewicz, W.J., Basilevsky, A.T., Titov, D.V., Ignatiev, N.I., Head, J.W., 2015. Active volcanism on Venus in the Ganiki Chasma rift zone. Geophysical Research Letters 42 (12), 4762–4769.

Shida, T., 1912. On the body tides of the Earth, a proposal for the International Geodetic Association. Proceedings of the Tokyo Mathematico-Physical Society. 2nd Series 6 (16), 242–258.

Shoji, D., Hussmann, H., Sohl, F., Kurita, K., 2014. Non-steady state tidal heating of Enceladus. Icarus 235, 75–85.

Singer, S., 1968. The origin of the Moon and geophysical consequences. Geophysical Journal International 15 (1–2), 205–226.
Smith, D.E., Kolenkiewicz, R., Dunn, P.J., 1973. Earth tidal amplitude and phase. Nature 244 (5417), 498–499.
Smith, D.E., Zuber, M.T., Neumann, G.A., 2001. Seasonal variations of snow depth on Mars. Science 294 (5549), 2141–2146.
Smith, D.E., Zuber, M.T., Phillips, R.J., Solomon, S.C., Hauck II, S.A., Lemoine, F.G., Mazarico, E., Neumann, G.A., Peale, S.J., Margot, J.-L., Johnson, C.L., Torrence, M.H., Perry, M.E., Rowlands, D.D., Goossens, S., Head, J.W., Taylor, A.H., 2012. Gravity field and internal structure from MESSENGER. Science 336 (6078), 214–217. https://doi.org/10.1126/science.1218809.
Smith, D.E., Zuber, M.T., Neumann, G.A., Mazarico, E., Lemoine, F.G., Head III, J.W., Lucey, P.G., Aharonson, O., Robinson, M.S., Sun, X., et al., 2017. Summary of the results from the lunar orbiter laser altimeter after seven years in lunar orbit. Icarus 283, 70–91.
Smrekar, S.E., Phillips, R.J., 1991. Venusian highlands: Geoid to topography ratios and their implications. Earth and Planetary Science Letters 107 (3–4), 582–597.
Smrekar, S.E., Stofan, E.R., Mueller, N., Treiman, A., Elkins-Tanton, L., Helbert, J., Piccioni, G., Drossart, P., 2010. Recent hotspot volcanism on Venus from VIRTIS emissivity data. Science 328 (5978), 605–608.
Smrekar, S.E., Davaille, A., Sotin, C., 2018. Venus interior structure and dynamics. Space Science Reviews 214 (5), 1–34.
Smrekar, S.E., Lognonné, P., Spohn, T., Banerdt, W.B., Breuer, D., Christensen, U., Dehant, V., Drilleau, M., Folkner, W., Fuji, N., et al., 2019. Pre-mission InSights on the interior of Mars. Space Science Reviews 215 (1), 3.
Smrekar, S.E., Hensley, S., Dyar, M., Helbert, J., Andrews-Hanna, J., Breuer, D., Buczkowski, D., Campbell, B., Davaille, A., DiAchille, G., et al., 2020. VERITAS (Venus Emissivity, Radio Science, InSAR, Topography, and Spectroscopy): A proposed Discovery mission. In: European Planetary Science Congress, p. 447. https://doi.org/10.5194/epsc2020-447.
Sohl, F., Solomonidou, A., Wagner, F., Coustenis, A., Hussmann, H., Schulze-Makuch, D., 2014. Structural and tidal models of Titan and inferences on cryovolcanism. Journal of Geophysical Research: Planets 119 (5), 1013–1036.
Solomon, S.C., McNutt, R.L., Gold, R.E., Domingue, D.L., 2007. MESSENGER mission overview. Space Science Reviews 131 (1), 3–39. https://doi.org/10.1007/s11214-007-9247-6.
Sotin, C., Head III, J.W., Tobie, G., 2002. Europa: Tidal heating of upwelling thermal plumes and the origin of lenticulae and chaos melting. Geophysical Research Letters 29 (8), 74.
Sotin, C., Tobie, G., Wahr, J., McKinnon, W.B., McKinnon, W., Khurana, K., 2009. Tides and tidal heating on Europa. Europa 11.
Spencer, J., 2013. Saturn's tides control Enceladus' plume. Nature 500 (7461), 155–156.
Spencer, J., Pearl, J., Segura, M., Flasar, F., Mamoutkine, A., Romani, P., Buratti, B., Hendrix, A., Spilker, L., Lopes, R., 2006. Cassini encounters Enceladus: Background and the discovery of a south polar hot spot. Science 311 (5766), 1401–1405.
Spencer, J.R., Barr, A.C., Esposito, L.W., Helfenstein, P., Ingersoll, A.P., Jaumann, R., McKay, C.P., Nimmo, F., Waite, J.H., 2009. Enceladus: An active cryovolcanic satellite. In: Saturn from Cassini-Huygens. Springer, pp. 683–724.
Stähler, S.C., Khan, A., Banerdt, W.B., Lognonné, P., Giardini, D., Ceylan, S., Drilleau, M., Duran, A.C., Garcia, R.F., Huang, Q., Kim, D., Lekic, V., Samuel, H., Schimmel, M., Schmerr, N., Sollberger, D., Stutzmann, É., Xu, Z., Antonangeli, D., Charalambous, C., Davis, P.M., Irving, J.C.E., Kawamura, T., Knapmeyer, M., Maguire, R.,

Marusiak, A.G., Panning, M.P., Perrin, C., Plesa, A.-C., Rivoldini, A., Schmelzbach, C., Zenhäusern, G., Beucler, É., Clinton, J., Dahmen, N., van Driel, M., Gudkova, T., Horleston, A., Pike, W.T., Plasman, M., Smrekar, S.E., 2021. Seismic detection of the martian core. Science (ISSN 0036-8075) 373 (6553), 443–448. https://doi.org/10.1126/science.abi7730. https://science.sciencemag.org/content/373/6553/443.

Steinberger, B., Werner, S.C., Torsvik, T.H., 2010. Deep versus shallow origin of gravity anomalies, topography and volcanism on Earth, Venus and Mars. Icarus 207 (2), 564–577. https://doi.org/10.1016/j.Icarus.2009.12.025.

Steinbrügge, G., Padovan, S., Hussmann, H., Steinke, T., Stark, A., Oberst, J., 2018a. Viscoelastic tides of Mercury and the determination of its inner core size. Journal of Geophysical Research: Planets 123 (10), 2760–2772.

Steinbrügge, G., Stark, A., Hussmann, H., Wickhusen, K., Oberst, J., 2018b. The performance of the BepiColombo Laser Altimeter (BELA) prior launch and prospects for Mercury orbit operations. Planetary and Space Science 159, 84–92. https://doi.org/10.1016/j.pss.2018.04.017.

Steinbrügge, G., Dumberry, M., Rivoldini, A., Schubert, G., Cao, H., Schroeder, D.M., Soderlund, K.M., 2021. Challenges on Mercury's interior structure posed by the new measurements of its obliquity and tides. Geophysical Research Letters 48 (3), e89895. https://doi.org/10.1029/2020GL089895.

Sundberg, M., Cooper, R., 2010. A composite viscoelastic model for incorporating grain boundary sliding and transient diffusion creep; correlating creep and attenuation responses for materials with a fine grain size. Philosophical Magazine 90 (20), 2817–2840. https://doi.org/10.1080/14786431003746656.

Tackley, P.J., Schubert, G., Glatzmaier, G.A., Schenk, P., Ratcliff, J.T., Matas, J.P., 2001. Three-dimensional simulations of mantle convection in Io. Icarus 149 (1), 79–93. https://doi.org/10.1006/icar.2000.6536.

Tajeddine, R., Rambaux, N., Lainey, V., Charnoz, S., Richard, A., Rivoldini, A., Noyelles, B., 2014. Constraints on Mimas' interior from Cassini ISS libration measurements. Science 346 (6207), 322–324.

Takei, Y., Karasawa, F., Yamauchi, H., 2014. Temperature, grain size, and chemical controls on polycrystal anelasticity over a broad frequency range extending into the seismic range. Journal of Geophysical Research Planets: Solid Earth (ISSN 2169-9356) 119 (7), 5414–5443. https://doi.org/10.1002/2014JB011146.

Takeuchi, H., Saito, M., Kobayashi, N., 1962. Statical deformations and free oscillations of a model Earth. Journal of Geophysical Research 67 (3), 1141–1154. https://doi.org/10.1029/JZ067i003p01141.

Tan, Y., Harada, Y., 2021. Tidal constraints on the low-viscosity zone of the Moon. Icarus 365, 114361. https://doi.org/10.1016/j.icarus.2021.114361.

Taylor, G.J., 2013. The bulk composition of Mars. Chemie der Erde 73, 401–420. https://doi.org/10.1016/j.chemer.2013.09.006.

Thomas, N., Hussmann, H., Spohn, T., Lara, L.M., Christensen, U., Affolter, M., Bandy, T., Beck, T., Chakraborty, S., Geissbuehler, U., Gerber, M., Ghose, K., Gouman, J., HosseiniArani, S., Kuske, K., Peteut, A., Piazza, D., Rieder, M., Servonet, A., Althaus, C., Behnke, T., Gwinner, K., Hüttig, C., Kallenbach, R., Lichopoj, A., Lingenauber, K., Lötzke, H.G., Lüdicke, F., Michaelis, H., Oberst, J., Schrödter, R., Stark, A., Steinbrügge, G., del Togno, S., Wickhusen, K., Castro, J.M., Herranz, M., Rodrigo, J., Perplies, H., Weigel, T., Schulze-Walewski, S., Blum, S., Casciello, A., Rugi-Grond, E., Coppoolse, W., Rech, M., Weidlich, K., Leikert, T., Henkelmann, R., Trefzger, B., Metz, B., 2021. The BepiColombo Laser Altimeter. Space Science Reviews 217 (1), 25. https://doi.org/10.1007/s11214-021-00794-y.

Thomas, P., Tajeddine, R., Tiscareno, M., Burns, J., Joseph, J., Loredo, T., Helfenstein, P., Porco, C., 2016. Enceladus's measured physical libration requires a global subsurface ocean. Icarus 264, 37–47.

Thor, R.N., Kallenbach, R., Christensen, U.R., Stark, A., Steinbrügge, G., Di Ruscio, A., Cappuccio, P., Iess, L., Hussmann, H., Oberst, J., 2020. Prospects for measuring Mercury's tidal Love number h2 with the BepiColombo Laser Altimeter. Astronomy & Astrophysics 633, A85.

Thor, R.N., Kallenbach, R., Christensen, U.R., Gläser, P., Stark, A., Steinbrügge, G., Oberst, J., 2021. Determination of the lunar body tide from global laser altimetry data. Journal of Geodesy 95 (1), 1–14.

Tobie, G., Choblet, G., Sotin, C., 2003. Tidally heated convection: Constraints on Europa's ice shell thickness. Journal of Geophysical Research: Planets 108 (E11).

Tobie, G., Grasset, O., Lunine, J.I., Mocquet, A., Sotin, C., 2005a. Titan's internal structure inferred from a coupled thermal-orbital model. Icarus 175 (2), 496–502.

Tobie, G., Mocquet, A., Sotin, C., 2005b. Tidal dissipation within large icy satellites: Applications to Europa and Titan. Icarus 177 (2), 534–549.

Tobie, G., Čadek, O., Sotin, C., 2008. Solid tidal friction above a liquid water reservoir as the origin of the south pole hotspot on Enceladus. Icarus 196 (2), 642–652. https://doi.org/10.1016/j.Icarus.2008.03.008.

Tortora, P., Zannoni, M., Hemingway, D., Nimmo, F., Jacobson, R.A., Iess, L., Parisi, M., 2016. Rhea gravity field and interior modeling from Cassini data analysis. Icarus 264, 264–273.

Touma, J., Wisdom, J., 1998. Resonances in the early evolution of the Earth–Moon system. The Astronomical Journal 115 (4), 1653.

Turyshev, S.G., Williams, J.G., Folkner, W.M., Gutt, G.M., Baran, R.T., Hein, R.C., Somawardhana, R.P., Lipa, J.A., Wang, S., 2013. Corner-cube retro-reflector instrument for advanced lunar laser ranging. Experimental Astronomy 36 (1), 105–135.

Tyler, R.H., 2008. Strong ocean tidal flow and heating on moons of the outer planets. Nature 456 (7223), 770–772.

Tyler, R.H., 2009. Ocean tides heat Enceladus. Geophysical Research Letters 36 (15).

Tyler, R.H., 2011. Magnetic remote sensing of Europa's ocean tides. Icarus 211 (1), 906–908.

Tyler, R., 2014. Comparative estimates of the heat generated by ocean tides on icy satellites in the outer Solar System. Icarus 243, 358–385.

Tyler, R.H., Henning, W.G., Hamilton, C.W., 2015. Tidal heating in a magma ocean within Jupiter's moon Io. The Astrophysical Journal. Supplement Series 218 (2), 22. https://doi.org/10.1088/0067-0049/218/2/22.

Usui, T., Bajo, K.-i., Fujiya, W., Furukawa, Y., Koike, M., Miura, Y.N., Sugahara, H., Tachibana, S., Takano, Y., Kuramoto, K., 2020. The importance of Phobos sample return for understanding the Mars-moon system. Space Science Reviews 216 (4), 1–18.

Van Hoolst, T., Jacobs, C., 2003. Mercury's tides and interior structure. Journal of Geophysical Research: Planets 108, 5121. https://doi.org/10.1029/2003JE002126.

Van Hoolst, T., Sohl, F., Holin, I., Verhoeven, O., Dehant, V., Spohn, T., 2007. Mercury's interior structure, rotation, and tides. Space Science Reviews 132 (2–4), 203–227. https://doi.org/10.1007/s11214-007-9202-6.

Van Hoolst, T., Baland, R.-M., Trinh, A., Yseboodt, M., Nimmo, F., 2020. The librations, tides, and interior structure of Io. Journal of Geophysical Research: Planets 125 (8), e2020JE006473.

Verma, A.K., Margot, J.-L., 2016. Mercury's gravity, tides, and spin from messenger radio science data. Journal of Geophysical Research: Planets 121 (9), 1627–1640.

Vermeersen, L.L.A., Sabadini, R., Spada, G., 1996. Compressible rotational deformation. Geophysical Journal International 126 (3), 735–761. https://doi.org/10.1111/j.1365-246X.1996.tb04700.x.

Vilella, K., Choblet, G., Tsao, W.-E., Deschamps, F., 2020. Tidally heated convection and the occurrence of melting in icy satellites: Application to Europa. Journal of Geophysical Research: Planets 125 (3), e2019JE006248.

Villanueva, G.L., Cordiner, M., Irwin, P.G.J., de Pater, I., Butler, B., Gurwell, M., Milam, S.N., Nixon, C.A., Luszcz-Cook, S.H., Wilson, C.F., Kofman, V., Liuzzi, G., Faggi, S., Fauchez, T.J., Lippi, M., Cosentino, R., Thelen, A.E., Moullet, A., Hartogh, P., Molter, E.M., Charnley, S., Arney, G.N., Mandell, A.M., Biver, N., Vandaele, A.C., de Kleer, K.R., Kopparapu, R., 2021. No evidence of phosphine in the atmosphere of Venus from independent analyses. Nature Astronomy 5, 631–635. https://doi.org/10.1038/s41550-021-01422-z.

Viswanathan, V., Fienga, A., Minazzoli, O., Bernus, L., Laskar, J., Gastineau, M., 2018. The new lunar ephemeris INPOP17a and its application to fundamental physics. Monthly Notices of the Royal Astronomical Society 476 (2), 1877–1888.

Webb, D., 1982. Tides and the evolution of the Earth–Moon system. Geophysical Journal International 70 (1), 261–271.

White, O.L., Schenk, P.M., Dombard, A.J., 2013. Impact basin relaxation on Rhea and Iapetus and relation to past heat flow. Icarus 223 (2), 699–709.

White, O.L., Schenk, P.M., Bellagamba, A.W., Grimm, A.M., Dombard, A.J., Bray, V.J., 2017. Impact crater relaxation on Dione and Tethys and relation to past heat flow. Icarus 288, 37–52.

Williams, J.G., Boggs, D.H., 2009. Lunar core and mantle. What does LLR see? In: Schilliak, S. (Ed.), Proceedings of the 16th International Workshop on Laser Ranging, Lunar and Planetary Science Conference. 13–17 October 2008, Poznań, Poland. Space Research Centre, Polish Academy of Sciences, Warsaw, pp. 101–120. http://cddis.gsfc.nasa.gov/lw16/docs/papers/proceedings_vol2.pdf. http://cddis.gsfc.nasa.gov/lw16/docs/papers/sci_1_Williams_p.pdf.

Williams, J.G., Boggs, D.H., 2015. Tides on the Moon: Theory and determination of dissipation. Journal of Geophysical Research: Planets 120 (4), 689–724.

Williams, J.G., Boggs, D.H., Yoder, C.F., Ratcliff, J.T., Dickey, J.O., 2001. Lunar rotational dissipation in solid body and molten core. Journal of Geophysical Research 106, 27933–27968. https://doi.org/10.1029/2000JE001396.

Williams, J.G., Turyshev, S.G., Boggs, D.H., 2014. The past and present Earth–Moon system: the speed of light stays steady as tides evolve. Planetary Science 3 (1), 1–9.

Winkler, K., Nur, A., Gladwin, M., 1979. Friction and seismic attenuation in rocks. Nature 277 (5697), 528–531.

Wisdom, J., Tian, Z., 2015. Early evolution of the Earth–Moon system with a fast-spinning Earth. Icarus 256, 138–146.

Wu, P., Peltier, W.R., 1982. Viscous gravitational relaxation. Geophysical Journal 70 (2), 435–485. https://doi.org/10.1111/j.1365-246X.1982.tb04976.x.

Yoder, C.F., 1981. The free librations of a dissipative Moon. Philosophical Transactions of the Royal Society of London. Series A, Mathematical and Physical Sciences 303 (1477), 327–338.

Yoder, C.F., 1982. Tidal rigidity of Phobos. Icarus 49, 327–346. https://doi.org/10.1016/0019-1035(82)90040-9.

Yoder, C.F., 1995. Venus' free obliquity. Icarus 117 (2), 250–286.

Yoder, C.F., Konopliv, A.S., Yuan, D.N., Standish, E.M., Folkner, W.M., 2003. Fluid core size of Mars from detection of the Solar tide. Science 300, 299–303. https://doi.org/10.1126/science.1079645.

Yuan, L., Chao, B.F., Ding, X., Zhong, P., 2013. The tidal displacement field at Earth's surface determined using global GPS observations. Journal of Geophysical Research: Solid Earth 118 (5), 2618–2632.

Zahnle, K.J., Lupu, R., Dobrovolskis, A., Sleep, N.H., 2015. The tethered moon. Earth and Planetary Science Letters 427, 74–82.

Zhang, S., Wimmer-Schweingruber, R.F., Yu, J., Wang, C., Fu, Q., Zou, Y., Sun, Y., Wang, C., Hou, D., Böttcher, S.I., et al., 2020. First measurements of the radiation dose on the lunar surface. Science Advances 6 (39), eaaz1334.

Zuber, M.T., Smith, D.E., Watkins, M.M., Asmar, S.W., Konopliv, A.S., Lemoine, F.G., Melosh, H.J., Neumann, G.A., Phillips, R.J., Solomon, S.C., et al., 2013. Gravity field of the Moon from the Gravity Recovery and Interior Laboratory (GRAIL) mission. Science 339 (6120), 668–671.

Serial Editor
Cedric Schmelzbach

Volume Editors
Cedric Schmelzbach and
Simon Christian Stähler

ACADEMIC PRESS
An imprint of Elsevier
elsevier.com/books-and-journals